

Lecture Notes in Mechanical Engineering

Lionel Ganippa  
R. Karthikeyan  
V. Muralidharan *Editors*

# Advances in Design and Thermal Systems

Select Proceedings of ETDMMT 2020

 Springer

# Lecture Notes in Mechanical Engineering

## Series Editors

Francisco Cavas-Martínez, Departamento de Estructuras, Universidad Politécnica de Cartagena, Cartagena, Murcia, Spain

Fakher Chaari, National School of Engineers, University of Sfax, Sfax, Tunisia

Francesco Gherardini, Dipartimento di Ingegneria, Università di Modena e Reggio Emilia, Modena, Italy

Mohamed Haddar, National School of Engineers of Sfax (ENIS), Sfax, Tunisia

Vitalii Ivanov, Department of Manufacturing Engineering Machine and Tools, Sumy State University, Sumy, Ukraine

Young W. Kwon, Department of Manufacturing Engineering and Aerospace Engineering, Graduate School of Engineering and Applied Science, Monterey, CA, USA

Justyna Trojanowska, Poznan University of Technology, Poznan, Poland

**Lecture Notes in Mechanical Engineering (LNME)** publishes the latest developments in Mechanical Engineering—quickly, informally and with high quality. Original research reported in proceedings and post-proceedings represents the core of LNME. Volumes published in LNME embrace all aspects, subfields and new challenges of mechanical engineering. Topics in the series include:

- Engineering Design
- Machinery and Machine Elements
- Mechanical Structures and Stress Analysis
- Automotive Engineering
- Engine Technology
- Aerospace Technology and Astronautics
- Nanotechnology and Microengineering
- Control, Robotics, Mechatronics
- MEMS
- Theoretical and Applied Mechanics
- Dynamical Systems, Control
- Fluid Mechanics
- Engineering Thermodynamics, Heat and Mass Transfer
- Manufacturing
- Precision Engineering, Instrumentation, Measurement
- Materials Engineering
- Tribology and Surface Technology

To submit a proposal or request further information, please contact the Springer Editor of your location:

**China:** Dr. Mengchu Huang at [mengchu.huang@springer.com](mailto:mengchu.huang@springer.com)

**India:** Priya Vyas at [priya.vyas@springer.com](mailto:priya.vyas@springer.com)

**Rest of Asia, Australia, New Zealand:** Swati Meherishi at [swati.meherishi@springer.com](mailto:swati.meherishi@springer.com)

**All other countries:** Dr. Leontina Di Cecco at [Leontina.dicecco@springer.com](mailto:Leontina.dicecco@springer.com)

To submit a proposal for a monograph, please check our Springer Tracts in Mechanical Engineering at <http://www.springer.com/series/11693> or contact [Leontina.dicecco@springer.com](mailto:Leontina.dicecco@springer.com)

**Indexed by SCOPUS. All books published in the series are submitted for consideration in Web of Science.**

More information about this series at <http://www.springer.com/series/11236>

Lionel Ganippa · R. Karthikeyan · V. Muralidharan  
Editors

# Advances in Design and Thermal Systems

Select Proceedings of ETDMMT 2020

 Springer



*Editors*

Lionel Ganippa  
Department of Mechanical and Aerospace  
Engineering  
Brunel University London  
Uxbridge, Middlesex, UK

R. Karthikeyan  
Department of Mechanical Engineering  
Birla Institute of Technology and Science  
Dubai, United Arab Emirates

V. Muralidharan  
Department of Mechanical Engineering  
B. S. Abdur Rahman Crescent Institute  
of Science and Technology  
Chennai, India

ISSN 2195-4356

ISSN 2195-4364 (electronic)

Lecture Notes in Mechanical Engineering

ISBN 978-981-33-6427-1

ISBN 978-981-33-6428-8 (eBook)

<https://doi.org/10.1007/978-981-33-6428-8>

© The Editor(s) (if applicable) and The Author(s), under exclusive license to Springer Nature Singapore Pte Ltd. 2021

This work is subject to copyright. All rights are solely and exclusively licensed by the Publisher, whether the whole or part of the material is concerned, specifically the rights of translation, reprinting, reuse of illustrations, recitation, broadcasting, reproduction on microfilms or in any other physical way, and transmission or information storage and retrieval, electronic adaptation, computer software, or by similar or dissimilar methodology now known or hereafter developed.

The use of general descriptive names, registered names, trademarks, service marks, etc. in this publication does not imply, even in the absence of a specific statement, that such names are exempt from the relevant protective laws and regulations and therefore free for general use.

The publisher, the authors and the editors are safe to assume that the advice and information in this book are believed to be true and accurate at the date of publication. Neither the publisher nor the authors or the editors give a warranty, expressed or implied, with respect to the material contained herein or for any errors or omissions that may have been made. The publisher remains neutral with regard to jurisdictional claims in published maps and institutional affiliations.

This Springer imprint is published by the registered company Springer Nature Singapore Pte Ltd. The registered company address is: 152 Beach Road, #21-01/04 Gateway East, Singapore 189721, Singapore

# Preface

We are delighted to present the special volume on the International Virtual Conference on **Emerging Trends in Design, Manufacturing, Materials and Thermal Sciences (ETDMMT 2020)**. The primary goal and feature of this conference is to bring academicians, technocrats and researchers together to exchange and share their experiences and findings about most aspects of research in science and technology. This forum has also provided opportunity to discuss the practical challenges encountered and to provide pragmatic solutions adopted. This book constitutes selected high-quality papers presented in the ETDMMT 2020, during 24 and 25 September 2020. This volume consists of 45 papers pertaining to materials and thermal sciences to address the issues related to mechanical, automobile and aerospace engineering. This book will be useful to the research scholars, academicians, fellow students and engineers working in the field as well as professionals involved in various sectors related to mechanical, automobile and aerospace engineering.

The conference had keynote sessions by eminent speakers addressing various aspects and different avenues for research in the field of mechanical, automobile and aerospace engineering. The support and participation tendered by the delegates is well acknowledged and makes the conference to sustain its success for a long time.

We would like to thank the organization members of the different committees and reviewers. They have toiled very hard in reviewing papers and rendered valuable suggestions for the authors to improve their work. We also would like to express our gratitude to the external reviewers, for providing extra help in the review process, and the authors for contributing their research result to the conference. The editors place a special thanks to Series Editors, Lecture Notes in Mechanical Engineering, Springer, for giving us the opportunity to publish this edited volume in the series.

Uxbridge, UK  
Dubai, United Arab Emirates  
Chennai, India

Lionel Ganippa  
R. Karthikeyan  
V. Muralidharan

# Contents

<b>Structural and Thermal Analysis of Composite Wind Turbine Blade for Wind Mill Applications</b> .....	1
K. Bak Mohamed, L. T. Augustin Lijo, R. Ramya, Priya Sri Lakshmi, R. Harini, and N. Ramasamy	
<b>The Effect of Novel Cryogenic Treatment in the Microstructure Analysis of Al 6101 Closed-Cell Foam</b> .....	19
Syed Zeenath Fathima, T. R. Tamilarasan, S. Rasool Mohideen, Milon Selvam Dennison, and Jayaraj Venkatesan	
<b>Development of Toxic Gas Monitoring and Alarm System</b> .....	39
Muniyandy Elangovan, D. Surya Prakash, and C. Hemadri	
<b>Predictive Modeling of Surface Roughness for Turning of Al-6061 Using Artificial Neural Network Model</b> .....	49
S. Rahul Rathnam, K. R. Anandh Natarajan, S. Gautam Kumar, N. Gobinath, and K. Rajan	
<b>Dynamic Supporting Wheels for Two-Wheeler Stability</b> .....	67
V. Deepan, P. D. Jeyakumar, and S. Sreenath	
<b>Microstructural Evolution, Phase Formation and Mechanical Behaviour of Al 7017 Alloy Produced by Powder Metallurgy (P/M) Technique</b> .....	81
M. Prashanth, R. Karunanithi, S. Rasool Mohideen, A. Karthik, and Prasanta Kumar Rout	
<b>Optimization of Solar Tunnel Dryer for Four Different Edible Products Using Response Surface Methodology</b> .....	95
V. Subbian, R. Christu Paul, R. Sathish Kumar, and V. Nadanakumar	
<b>Fault Detection in Single-Stage Helical Planetary Gearbox Using Support Vector Machine (SVM) and Artificial Neural Network (ANN) with Statistical Features</b> .....	119
Syed Shaul Hameed and V. Muralidharan	

<b>Characterization of Surface Roughness of Ground Specimens Using Image Processing</b> .....	133
S. Mohamed Fahad, J. Mahashar Ali, and H. Siddhi Jailani	
<b>Experimental Study on the Combustion, Performance and Emission Characteristics of a Diesel Engine Operated with the Blends of Waste Chicken Oil Biodiesel and Diesel</b> .....	143
V. Nadanakumar, R. Christupaul, Ravishankar Sathyamurthy, and R. Sathish Kumar	
<b>Experimental Investigation and Optimization of Process Parameters in EDM of Aluminum Metal Matrix Composites Using Selective Breeding Algorithm</b> .....	155
S. K. Rajesh Kanna, P. Sethuramalingam, N. Lingaraj, P. Sivasankar, and J. Sriharish	
<b>Analysis and Study of Tin Interlayer Aluminum Weld</b> .....	167
Sekar Anand, Sankaran Lokesh, Arunachalam Dharmalingam Srikeshav, and Jebaseelan Davidson	
<b>Effect of Heat Treatment on Wear and Corrosion Behavior of Electroless Ni–P–TiO<sub>2</sub>–Al<sub>2</sub>O<sub>3</sub> Nanocomposite Coatings on Magnesium AZ91D Alloy</b> .....	179
V. Krishnakumar and R. Elansezhian	
<b>Study of Varying Weight%, Particle Size and Artificial Aging of Al<sub>2</sub>O<sub>3</sub> on the Hardness and Wear Resistance of Al 6082 Alloy Composites by Stir Casting</b> .....	193
N. Sirajudeen, R. Karunanithi, and M. Abdur Rahman	
<b>A Comparative Study on the Characteristics of Crumb Rubber with Commercial Rubbers</b> .....	213
Sriram Srinivasan, Abbas Saifee Valsadwala, D. Karthik, D. Suganandam, and S. Shamshath Begum	
<b>The Addition of Polytetrafluoroethylene (PTFE) and Graphite on Acrylo Nitrile Butadiene Styrene (ABS) and Its Effects on Mechanical and Tribological Characteristics</b> .....	221
Basanta Kumar Behera and M. Thirumurugan	
<b>Design of Automotive Firewall Based on Thermal Analysis</b> .....	235
M. Karthikeyan and M. Venkatesan	
<b>Mechanical Characteristics of Paraffin Wax, Beeswax and HTPB as Rocket Propellant—A Comparative Study</b> .....	243
Vanchhit Kumar Dubey, Sri Nithya Mahottamananda, Afreen Abdul Khaleel, P. N. Kadiresh, and M. Thirumurugan	
<b>The Impact of Squeeze Casting in AMMC—Review</b> .....	253
A. Karthik, R. Karunanithi, A. S. Selvakumar, and S. A. Srinivasan	

**Analysis of Internal Hydrodynamic Behavior of Pressure Swirl Atomizer for Liquid Rocket Engines** ..... 261  
 Kabaleeswaran Manikandan, Boyapati Krishna Vamsi, Pola Anusha, and Chaturya Reddy

**Preparation of Low-Cost Oil Resistance Rubber Formulation for an Industrial Oil Seals from Leather Waste** ..... 271  
 N. Srirangarajalu, R. Dhanasekar, and S. Ponsubbiah

**Effect of Two-Step Sintering Cycle by Chen and Wang (TSS-CW) on Aluminium (Al) Metal Matrix Reinforced with Niobium Carbide (NbC)** ..... 283  
 R. Raj Mohan, R. Venkatraman, S. Raghuraman, P. Sunil Kumar, and S. Yokesh Kumar

**Drilling Performances of Kenaf Fibre/Steel Mesh Reinforced Hybrid Epoxy Composites** ..... 291  
 K. Jamesha Ibrahim, M. Thirumurugan, P. D. Jeyakumar, A. Arockia Julias, and S. Mohamed Fahad

**Hardness–Elastic Modulus Relationship for Nitrile Rubber and Nitrile Rubber–Polyvinyl Chloride Blends** ..... 301  
 D. Murali Manohar, Bikash C. Chakraborty, and S. Shamshath Begum

**Parametric and Nonparametric Modeling of Magnetorheological (MR) Damper** ..... 315  
 A. J. D. Nanthakumar, J. Jancirani, Aditya Mishra, and Parth Patel

**Product Development Process Concept—Industrial Perspective** ..... 331  
 Chitta Ranjan Tripathy and Arvind Katyayn

**Classification of Road Profile Using Golden Car Parameters for Quarter Car Model** ..... 341  
 A. J. D. Nanthakumar, Karan Jariwala, Kumawat Harshit, S. Yokeshwaran, and S. Madhankumar

**Development of Onboard Engine Management System—Prediction of Oil Degradation** ..... 349  
 K. Prabu, P. D. Jeyakumar, C. Dineshkumar, B. Vasanthan, A. Arockia Julius, and M. Thirumurugan

**Synthesis and Characterization of Water in Diesel Emulsions** ..... 361  
 Anumula Shiva Kumar, Mallampati Krishna Deepika, Chippa Sri Haasa, P. S. Raghavan, and Purushothaman Nandagopalan

**Design of Home Study Furniture for Students of 14–18 Years** ..... 373  
 Gurmeet Singh and T. Manu

<b>Mechanical Characteristics of Ethylene Vinyl Acetate Mixed Beeswax Fuel for Hybrid Rockets</b> .....	389
Jayapal Sri Nithya Mahottamananda, Dubey Vanchhit Kumar, Abdul Khaleel Afreen, S. Dinesh, Wahab Ashiq, P. N. Kadiresh, and M. Thirumurugan	
<b>Safety-Enhanced Driver Condition Monitoring System for Preventing Road Accidents in Automobile</b> .....	401
C. Dineshkumar, P. D. Jeyakumar, B. Mohamed Asarudeen, G. Mohamed Uvaize, and A. K. Ahamed Kabeer	
<b>Fabrication and Evaluation of Optimized Parametric Condition During EDM Machining of Al-CSA Composite Using Taguchi Orthogonal Array</b> .....	411
C. J. Rao, R. Siva Sankara Raju, D. Sreeramulu, and Y. Sagar	
<b>Prediction and Modeling of Tool Wear with Cutting Force and Fine Gaussian Support Vector Machine in Drilling</b> .....	421
G. Mahendran, M. A. Sai Balaji, J. Susai Mary, and D. Dinakaran	
<b>Toughness Property Evaluation of Additive Welded Low Carbon Steel Weldments</b> .....	431
Mohd Durvesh Mohiuddin and S. Rasool Mohideen	
<b>Performance Enhancement of Solar Water Heater Incorporated with Latent Heat Storage Material</b> .....	441
M. Ajees Aboobucker, N. Muthu Saravanan, R. Mayilraj Sathish, S. Aakhash, and M. Gunasekaran	
<b>Performance Analysis of Oil Expelling Using Vaagai Wood Crusher</b> ....	455
S. Stephen Bernard, M. Bakkiyaraj, Md. Javeed Ahmed, M. V. Niranjana, R. Nirmal, and K. Hemanand	
<b>The Effect of Quenching Mediums on Heat Treatment Properties of Multi-pass Welding of 0.3% C-Cr Mo V Steel</b> .....	463
K. Radhakrishnan and V. Muralidharan	
<b>A Study on the Welding and Heat Treatment of 0.3% C-Cr-Mo V Steel</b> .....	475
K. Radhakrishnan and V. Muralidharan	
<b>Investigation on Tribological Properties of Chromium-Filled Particle Damper During Hard Boring Process</b> .....	493
G. Lawrence, P. Sam Paul, R. Gokul, M. Subhash, M. Ezhil, and J. Ebi Ashish	
<b>Frictional Performance on Various Speed and Pressure for Cardanol as a Binder in High Friction Composite Material Using Pin on Disc</b> .....	501
G. K. Kannan, S. Stephen Bernard, Md. Javeed Ahmed, A. Ivon Paul, and G. Suresh	

**Studies on Mechanical and Physical Characteristics of Cardanol in a High-Friction Composite Material** ..... 509  
S. Stephen Bernard, G. Suresh, G. K. Kannan, S. R. Lohesh Srinath, M. Vishweshwaran, and Md. Javeed Ahmed

**Influence of 3-(8,11,14-Pentadecatrienyl) Phenol Cardanol as a Bio-Based Binder in a Brake Pad** ..... 519  
S. Stephen Bernard, S. Vivek, G. Suresh, and G. K. Kannan

**Effect of Barium Sulfate on Mechanical, DMA, Wear Analysis of Woven Hybrid with Wire Mesh Composite** ..... 529  
M. Arul Murugan and A. S. Selva Kumar

**Study on the Influence of Auxiliary Mass on Displacement Using Computational Static Analysis** ..... 541  
P. Sam Paul, D. S. Shylu, and G. Lawrance

# About the Editors

**Dr. Lionel Ganippa** is currently a Professor at the Mechanical and Aerospace Engineering Department, Brunel University, London. He received his PhD in Internal Combustion Engines, Chalmers University of Technology, Sweden. His area of research interest includes laser diagnostics In-cylinder combustion, soot processes diesel sprays, exhaust soot particle characterisation, diesel engine combustion and emissions control, alternative fuels, temperature measurements using laser-induced thermographic phosphorescence, phenomenological modelling and second law analysis of thermodynamic systems. He has published more than 100 research articles in various international peer-reviewed journals and conferences. Dr Ganippa has completed 8 funded projects sponsored by various international organisations. He is a Chartered Engineer (CEng), Fellow of Institution of Mechanical Engineers (FIMechE), Fellow of Higher Education Academy(FHEA) and member of Combustion institute.

**Dr. R. Karthikeyan** is currently a professor at the Department of Mechanical Engineering, BITS Pilani, Dubai campus, Dubai. He received his PhD in Production Engineering from Annamalai University, India. His research interests include robotics, modelling and simulation, composite materials and materials processing. He has guided 5 PhD scholars and published 92 research articles in various international journals and conferences. Dr Kartikeyan has completed 4 consultancy projects funded by AICTE and UAE agency. He is an active member of various professional societies and organised 4 international conferences.

**Dr. V. Muralidharan** is currently Associate Professor at the Department of Mechanical Engineering, B S Abdur Rahman Crescent Institute of Science and Technology, Chennai, India. He received his PhD from Karpagam University, India. His Areas of proficiency are in condition monitoring using techniques such as data mining, support vector machines and fuzzy logic. Dr Muralidharan is currently guiding 5 PhD Scholars and published 30 papers in various peer-reviewed international journals. He is reviewer for 5 international journals and organized 2 international conferences.



# Structural and Thermal Analysis of Composite Wind Turbine Blade for Wind Mill Applications



**K. Bak Mohamed, L. T. Augustin Lijo, R. Ramya, Priya Sri Lakshmi, R. Harini, and N. Ramasamy**

**Abstract** This study presents to investigate the mechanical properties and thermal properties of horizontal and vertical axis wind turbine (VAWT) blade using finite element analysis (FEA) Ansys software. The efficiency of the wind turbine is based on the design of wind turbine blade (WTB) and material used. The fiber-reinforced plastics (composite materials) such as glass fiber, carbon fiber and epoxy are used for model of wind turbine blade. After modeling of wind turbine blade using standard software CATIA, imported into software ANSYS for determining the structural and thermal strength of the wind turbine blades. The stress distributions observed on the horizontal axis wind turbine blade due to the applied structural load and thermal load. The maximum stress occurs on the surfaces (near the fixed end of hub) of the horizontal axis wind turbine blade (HAWT), and the minimum stress occurs near the tip end of the blade. Due to the applied thermal condition (temperature) on the blades, the heat flux generated almost equal to both the HAWT blade and VAWT blade. Based on the FEA Ansys results, horizontal wind turbine blade produces better structural strength and thermal strength than vertical wind turbine blade.

**Keywords** Wind turbine blade · Finite element analysis (ANSYS) · Composite materials · Strength properties · Thermal properties

---

K. Bak Mohamed (✉)

Department of Mechanical Engineering, BSAR Crescent Institute of Science and Technology, Chennai, Tamilnadu, India

e-mail: [mohamedbak@crescent.education](mailto:mohamedbak@crescent.education)

L. T. Augustin Lijo · R. Ramya · P. Sri Lakshmi · R. Harini

Department of Aeronautical Engineering, Hindusthan Institute of Technology, Coimbatore, Tamilnadu, India

N. Ramasamy

Department of Mechanical Engineering, Prathyusha Engineering College, Chennai, Tamilnadu, India

## 1 Introduction

In this work, finite element analysis (FEA) is conducted on horizontal axis wind turbine blade (HAWT) and vertical axis wind turbine blade (VAWT) with NACA 2412 and NACA 0018 aerofoil design. The blade optimization is carried out by considering the parameters like aerofoil profile, stresses and deformation on blade [1]. When designing a wind turbine, the aim is to attain the highest possible power output under particular atmospheric conditions, and this depends on the shape of the blade as well as on its material. The following basic aspects are considered for complex structure design of HAWT and VAWT blades such as selection of the aerodynamic shape, structural configuration and density of blade material [2, 3]. Yang et al. studied about the chord and twist linearization and geometry optimization required for blade geometry design [4]. Yang et al. [5] concluded that aerodynamics performance optimized using multi-point method at variable speeds to determine the maximum power point tracking dynamic process on wind turbine blades. Most linearization methods are focused on maximizing the aerodynamic efficiency based on the specific design wind speed and design tip speed ratio (TSR). However, blades designed based on particular design wind speeds and design TSRs exhibit maximum efficiency at specific wind speeds. Tahani et al. [6] used a linearization method to increase the precision of wind turbine blades with the highest efficiency that connect two adjacent points along with the theoretical blade span using blade momentum theory. The greater use of wind energy and the aerodynamic performance of wind turbine blade are important factor for the optimized design [7]. Model analysis of FEA used to determine the mechanical properties of structural design of wind turbine blades [8, 9].

The present work investigates the mechanical properties and thermal properties of horizontal and vertical axis composite wind turbine blade using FEA Ansys software. The efficiency of the wind turbine is based on the design of wind turbine blade and material used.

## 2 Modeling of Wind Turbine Blade (WTB)

### 2.1 Specifications of WTB

Horizontal and vertical axis wind turbine blades are modeled using Autodesk Fusion 360 platform. Table 1 contains the specifications for modeling of the horizontal axis wind turbine blade (HAWT).

**Table 1** Specifications of Wind Turbine Blade

Parameters	HAWT blade	VAWT blade
Aerofoil profile	NACA 2412	NACA 0018
Root chord length (mm)	1651	1651
Tip chord length (mm)	650	370
Length of blade (mm)	10,700	2800
Hub diameter (mm)	337.5	337.5
Hub length (mm)	1465	1465
Hub to blade length (mm)	1475	1475
Twist on blade tip (degree)	45	45

### 3 Analyzing of Wind Turbine Blade (WTB)

Analyzing of the wind turbine blade is carried using Ansys 16.2 software. The HAWT and VAWT blades are imported to the Ansys geometry modeler by using “Import External Geometry file” option.

#### 3.1 Meshing of WTB

Meshing is the preprocessing part in the analyzing process. After meshing, the whole component is divided into number of elements, and each element has its own stiffness while loading. For the linear arrangement of the elements, the face meshing is applied on the surfaces. For the surface, quadrilateral element is generated with fine mesh. For the spar body, hexahedral element is used to mesh. For the accurate result in the solving of HAWT blade, the geometry should have fine meshed structure [9–11]. The mesh connection is made on the surfaces with the edges of the spars to make the elements on spars and the elements in the surface to join. Figures 1 and 2 show the mesh method data given to the HAWT blade and VAWT blade. The quadrilateral dominant mesh method is given to the surfaces of the horizontal axis wind turbine blade. Surface thickness of 2 mm is defined to the horizontal axis wind turbine blade. The face size of 5 mm (element size) is given to the surfaces of the wind turbine blade. The mapped mesh method of hexahedral element is given for meshing the spars of the wind turbine blade. It clearly shows the number of nodes and the number of elements obtained on the vertical axis wind turbine blade while meshing the blade.

#### 3.2 Boundary Conditions of HAWT Blade and VAWT Blade

For the structural analysis of the HAWT blade, the pressure load is applied on the surfaces of the blade. Pressure is applied normally to the blade. Hub edge is fixed

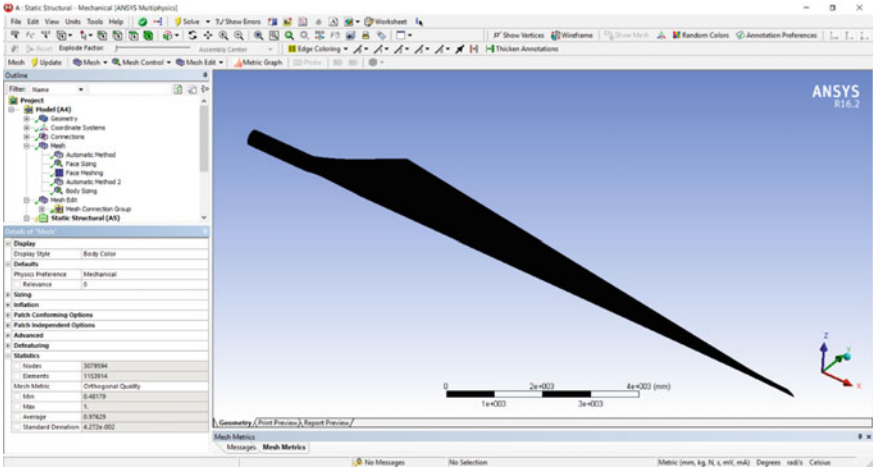


Fig. 1 Meshed HAWT blade

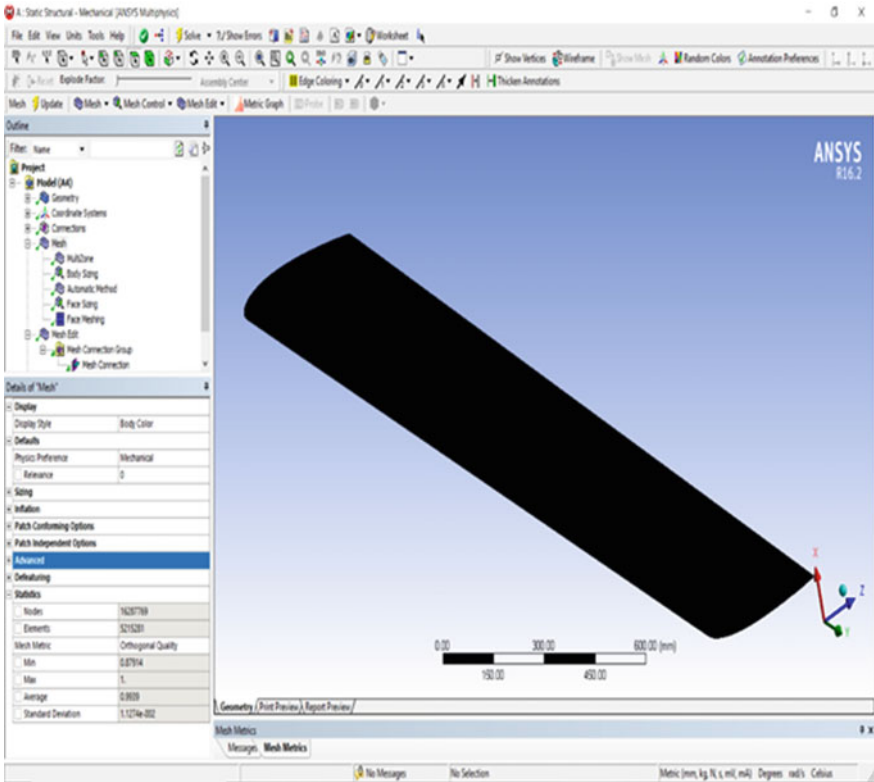
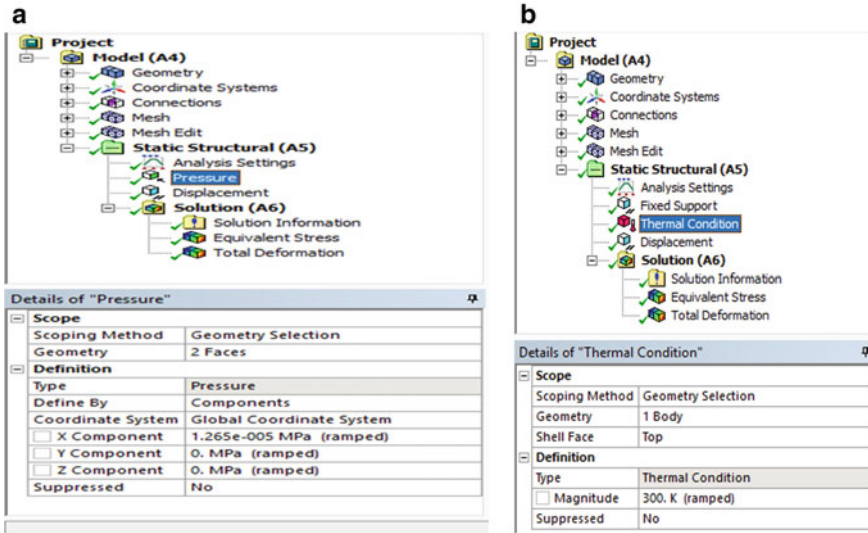


Fig. 2 Meshed VAWT blade



**Fig. 3** a Applied pressure values for wind turbine blade (boundary conditions). b Temperature values for wind turbine blade (boundary conditions)

using fixed support. Displacement on X- and Y-axis is constrained, and Z-axis is made free to move. For the structural and thermal analysis of the models, determine the stress, strain, deformation of the structures caused by the loads that do not induce damping effect. For the thermal analysis of the HAWT and VAWT blades, thermal condition (temperature) is applied on the static structural module and the steady-state thermal module in the workbench as shown in Figs. 3a, b.

The red color indicates that the pressure is applied on the outer surfaces of the horizontal axis wind turbine blade as shown in Fig. 4. The magnitude of 1.265e—005 MPa is applied normal to the blade for the analyzing of structural strength of the blade. Figure 5 shows the applied thermal condition (temperature) for the thermal analysis of HAWT blade. The magnitude of thermal condition applied is visualized by red-colored indication.

Figure 6 shows the applied load (pressure) condition over the VAWT blade where the normal axis is made free to move. The X component is made free, and the Y and Z components are constrained to move. The magnitude of 1.265e—005 MPa is applied over the surface of the wind turbine blade. Figure 7 shows the VAWT blade with the applied thermal condition (temperature) over the surface of the wind turbine blade. The portion where the thermal conditions are applied is identified by red color.

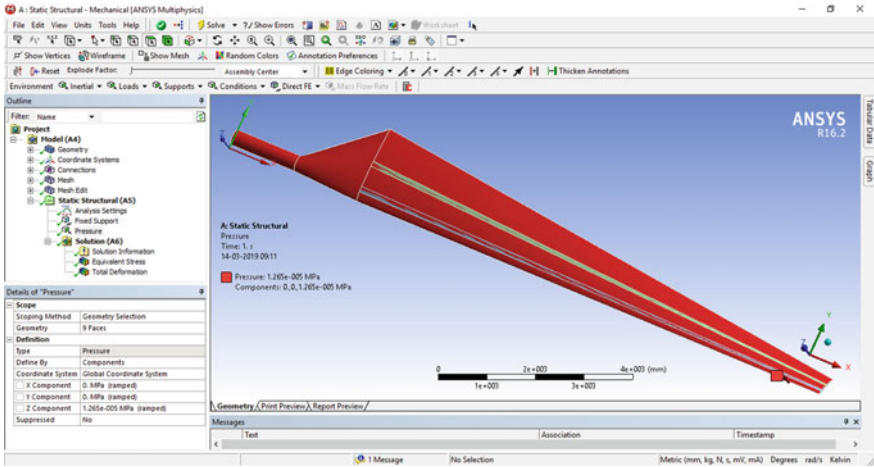


Fig. 4 Applied pressure on the surface of the HAWT blade

## 4 Result and Discussion

### 4.1 Structural Analysis for Horizontal Axis Wind Turbine Blade (HAWT)

The stress distributions observed on the HAWT blade due to the applied structural load and thermal load [9, 11]. The stress developed on the blade caused deformation over the blade surfaces. This makes the structure to get fail. Here, the hub edges are made fixed. Figure 8 shows the solved HAWT blade and stress over the structure is distributed. It clearly shows the maximum and minimum stress developed point and how much the stress value is obtained on the blade. The maximum stress occurs on the surfaces (near the fixed end of hub) of the HAWT blade, and the minimum stress occurs near the tip end of the blade. Figure 9 shows the maximum and the minimum stress values generated on the HAWT blade and also shows in which body the maximum and minimum stress occurs on the tip of wind turbine blade by applying pressure load.

### 4.2 Thermal Analysis of HAWT Blade

Figure 10 shows the von Mises stress distribution over the HAWT blade due to the applied thermal condition (temperature). It clearly shows the maximum and minimum stresses occurred on the root end of the HAWT blade. Figure 11 shows the von Mises stresses obtained by applying thermal load over the surfaces of the HAWT blade.

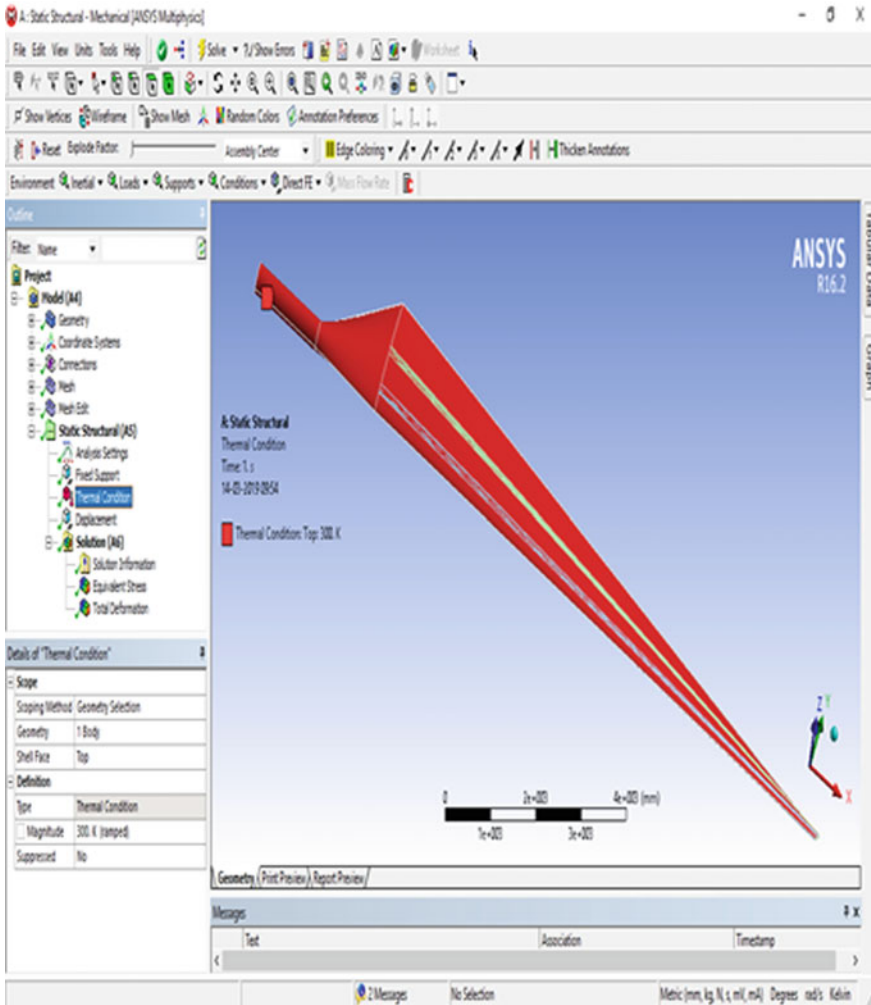


Fig. 5 Applied thermal condition on the surfaces of HAWT blade

Here, the maximum stress of 1.1764 MPa occurs on the surface of the wind turbine blade, and the minimum stress of  $1.4383e-003$  MPa occurs on the solid body.

Figure 10 shows the heat flux generated on the HAWT blade by applying thermal load (temperature) over the surface of the blade. The maximum heat flux developed on the spar section of the blade, and the minimum heat flux developed on the outer surface of the wind turbine blade. The maximum heat flux value of  $2.5141e-015$  W/mm<sup>2</sup> occurs on the solid body of the wind turbine blade, and the minimum heat flux value of  $3.6481e-023$  W/mm<sup>2</sup> occurs on the surfaces of the wind turbine blade.

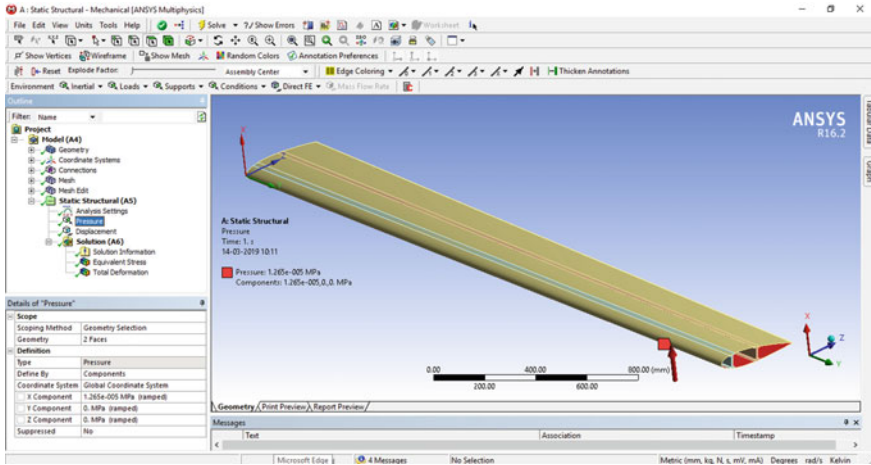


Fig. 6 Applied pressure on the surface of the VAWT blade

### 4.3 Structural Analysis for Vertical Axis Wind Turbine Blade (VAWT)

In the VAWT blade, the stress distribution obtained due to the applied structural and thermal load over the wind turbine blade. The deformation also occurs on the blade due to the applied load. Displacement over the blade is constrained in Y- and Z-axis. Figure 11 shows the von Mises stress occurs on the VAWT blade while applying structural load (pressure Load) over the surfaces of the wind turbine blade. It clearly shows the stress developed on the trailing edge of the vertical axis blade surfaces. The maximum and the minimum stresses areas are shown in different color notations. The maximum stress of 0.58482 MPa occurs on the solid body (spars) of the wind turbine blade, and the minimum stress of 1.8731e-005 MPa occurs on the surface of the VAWT blade.

### 4.4 Thermal Analysis for VAWT Blade

Figure 12 shows the von Mises stress distribution over the VAWT blade due to the applied thermal load. This load distribution is solved in the static structural solver using Ansys workbench. The values of maximum stresses and the minimum stresses are specified on the blade. It clearly shows the maximum stress developed on the surface (near the tip end of the blade) and the minimum stress developed on the spars of the blade. Figure 13 shows the heat flux distribution over the vertical axis wind turbine blade. Due to the applied thermal load (temperature), the low heat flux is



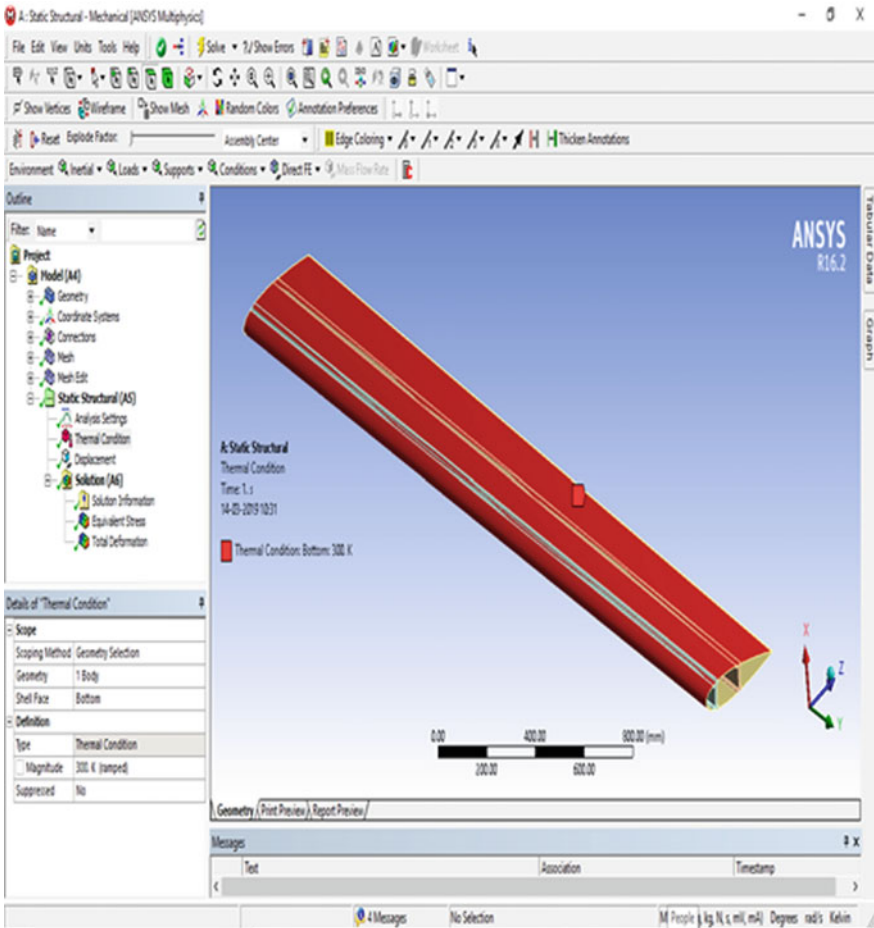


Fig. 7 Applied thermal condition on the surfaces of VAWT blade

generated on the blade on the surfaces and maximum values on the spars of the wind turbine blade.

Figure 14 shows the von Mises stress value occurs on the VAWT blade due to the applied thermal load (temperature). The maximum and the minimum values occur on the wind turbine blade are 0.78156 MPa and 7.0908e−004 MPa, respectively. The maximum value occurs on the surface of the blade, and the minimum value occurs on the solid body (spars) of the blade. Figure 15 shows the heat flux value occurs on the VAWT blade due to the applied thermal load over the surface of the wind turbine blade. The maximum value of heat flux occurs is 2.5754e−015 W/mm<sup>2</sup> over the solid body of blade, and the minimum value of heat flux occurs is 5.2255e−022 W/mm<sup>2</sup> over the surface of the wind turbine blade.

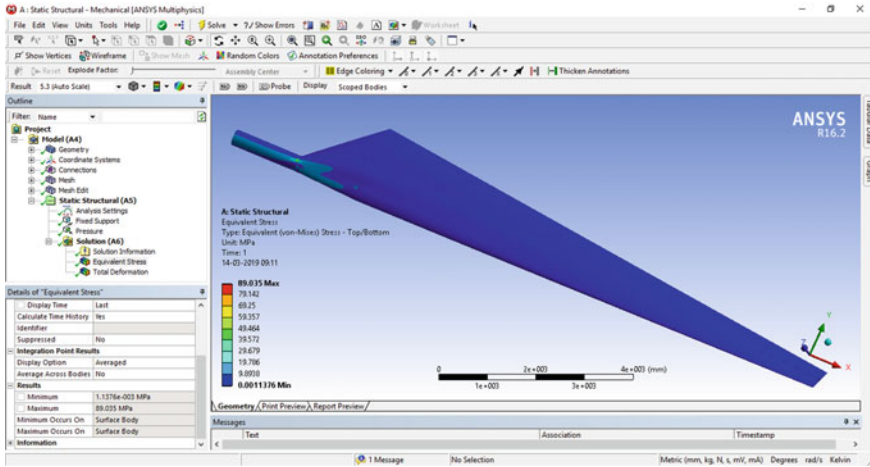


Fig. 8 von Mises stress distribution over HAWT blade due to pressure load-GFRP

## 5 Comparing the Results of HAWT and VAWT Blade

### 5.1 Comparison of von Mises Stresses Due to Structural Load

Table 2 shows the values of von Mises stresses developed on the blades (HAWT and VAWT). Comparison of equivalent stress in two blades shows that the HAWT blade developed more stress than VAWT blade. By fixing the hub edge of the horizontal axis wind turbine blade, it acts as the blade fixed on the wind turbine. Due to these conditions, the stress concentration over the blade is created on the root end of the blade. This makes the maximum stress occur on the root section of the HAWT blade. In the VAWT blade, it shows the stress occurs on the tip of the blade. This is due to constrained boundary conditions (Y and Z components are constrained, and X component is free) on the blade it gives the nature of VAWT blade is working in vertical wind mill. From the discussion, it shows that by means of weight force acting on the blade the more stress is created on the HAWT blade than VAWT blade.

### 5.2 Comparison of von Mises Stresses Due to Thermal Load

Table 3 shows the comparison von Mises stresses values in MPa, it clearly gives that the HAWT blade developed more equivalent stress than VAWT blade by applying thermal condition over the blade surfaces. The thermal stresses developed on the HAWT blade and VAWT blade are created by applying the thermal condition over the blade. Due to the thermal properties (thermal expansion) of epoxy and glass

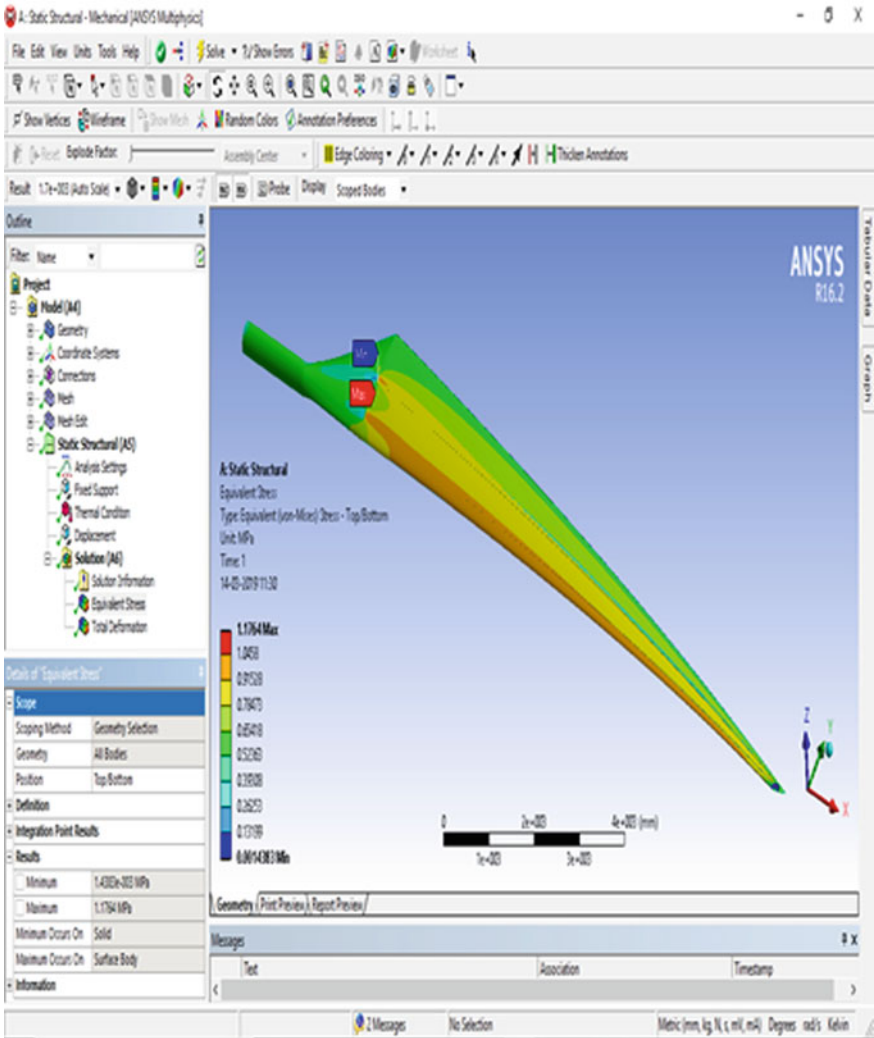


Fig. 9 von Mises stress distribution over HAWT blade due to pressure load-CFRP

fiber composite material are low, the stresses are generated on the HAWT blade and VAWT blade.

### 5.3 Comparison of Total Heat Flux Due to Thermal Load

Table 4 shows the comparison value of total heat flux generated on the wind turbine blades. This shows the minimum and maximum heat flux values on the wind turbine

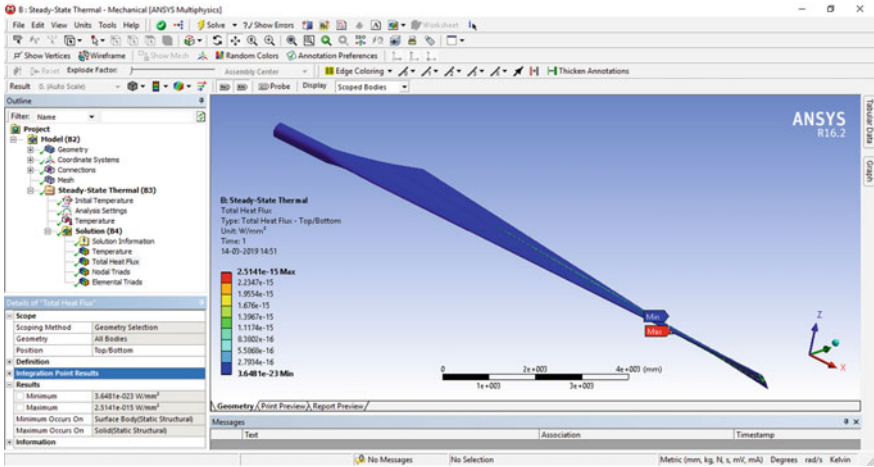


Fig. 10 Total heat flux distribution over the HAWT blade due to thermal load

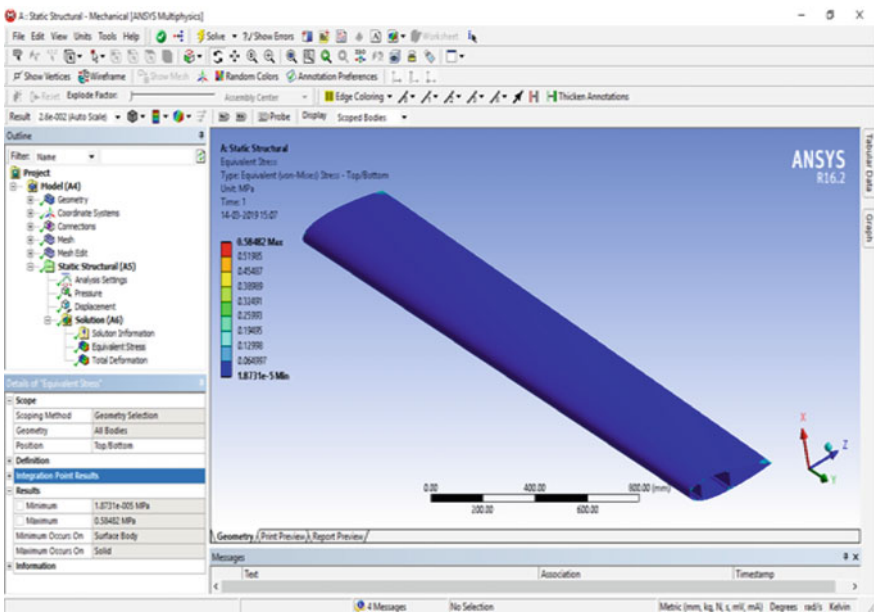


Fig. 11 von Mises stress distribution over VAWT blade due to pressure load

blades. Due to the applied thermal condition (temperature) on the blades, the heat flux generated is almost equal to both the HAWT blade and VAWT blade.

The heat flux generated on the HAWT and VAWT blade, this is due to the thermal conductivity of the material used in the wind turbine blades. The spars have the more

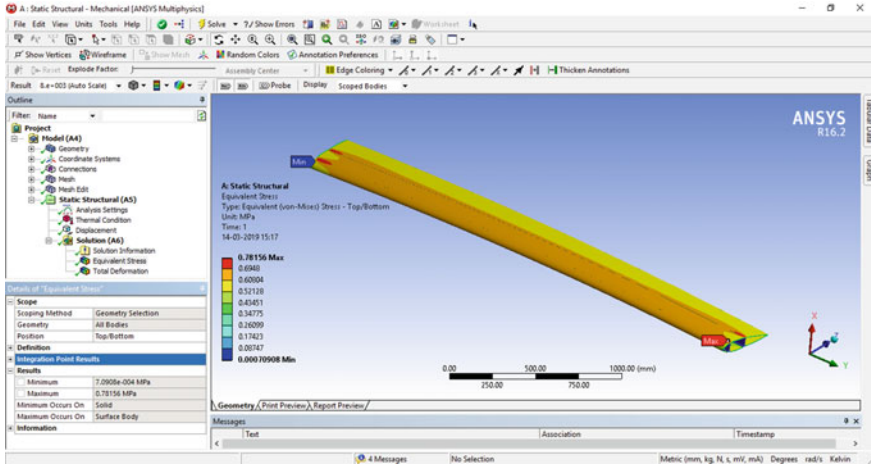


Fig. 12 von Mises stress distribution over VAWT blade due to thermal load (static structural solver)

heat flux values, this is due to the spars having the more bonded atoms, and it is not supposed to free atmospheric air, but surfaces of the blades were directly in contact with the surrounding atmosphere. This results in low heat flux value occurs on the surfaces of the blade.

## 6 Conclusion

In this work, the HAWT blade and VAWT blade are modeled with the help of aerofoil geometries using CATIA standard software and transferred to finite element analysis (Ansys) for solving the structural and thermal analysis. From Ansys simulations, it has been observed that,

The structural strength of both HAWT blade and VAWT blade obtained from Ansys simulation is 89.035 and 0.58482 MPa under the pressure of  $1.265 \times 10^{-5}$  Mpa, which is compared with the previously research paper [8] of values 183.93 and 0.10845 Mpa for HAWT and VAWT. The error obtained for both HAWT and VAWT is 94.895 and 0.47637 MPa.

The thermal strength of both HAWT and VAWT obtained from Ansys simulation is 1.1764 and 0.78156 Mpa under the temperature of 300 K, which shows that the thermal stress obtained is equivalent for HAWT blade and VAWT blade.

The heat flux obtained in both the HAWT and VAWT blade obtained from ANSYS simulation is  $2.514 \times 10^{-15}$  and  $2.5754 \times 10^{-15}$  W/mm<sup>2</sup> under the temperature of 300 K, which shows that the heat flux created is equivalent for HAWT blade and VAWT blade.

Based on this work, wind turbine blade geometry design was modeled using blade element momentum (BEM) theory, and structural performance analyses have been

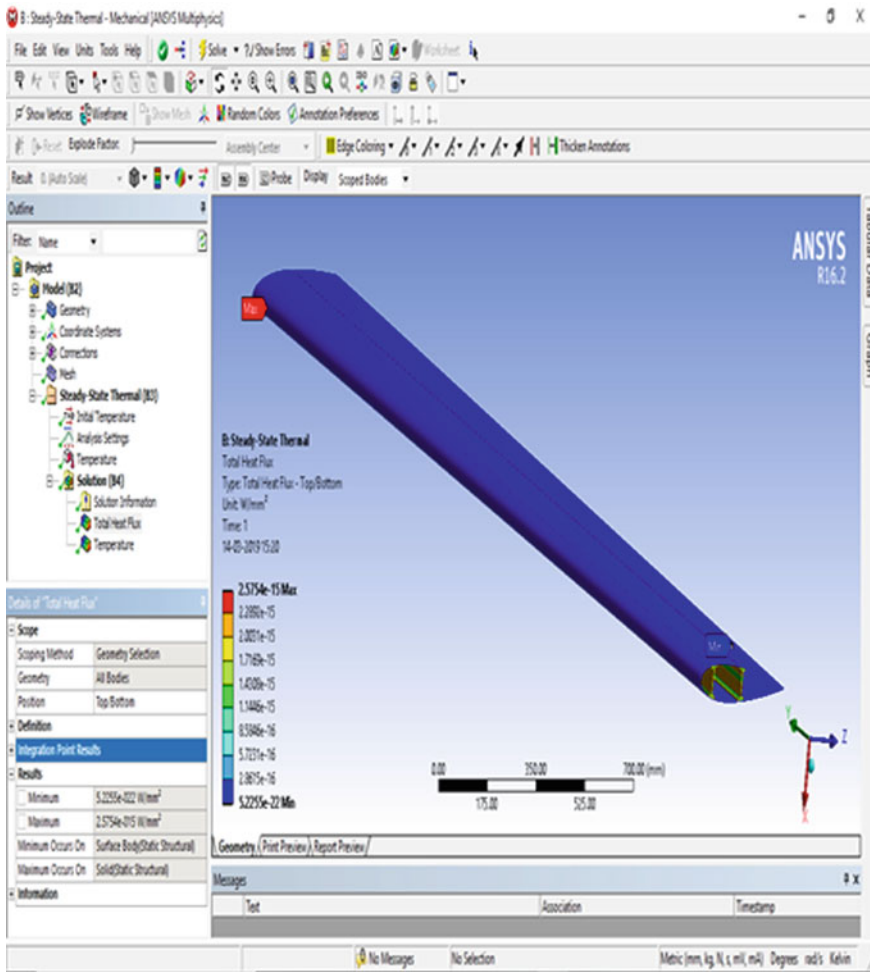


Fig. 13 Total heat flux distribution over the VAWT blade due to thermal load (steady-state thermal)

conducted using FEA. The vertical wind turbine blade twist profile mainly affects low wind speeds depending on the size of the incremental angle, and its effect on the structural-aerodynamic performance at high wind speeds is compared with horizontal wind turbine blade [6, 8].

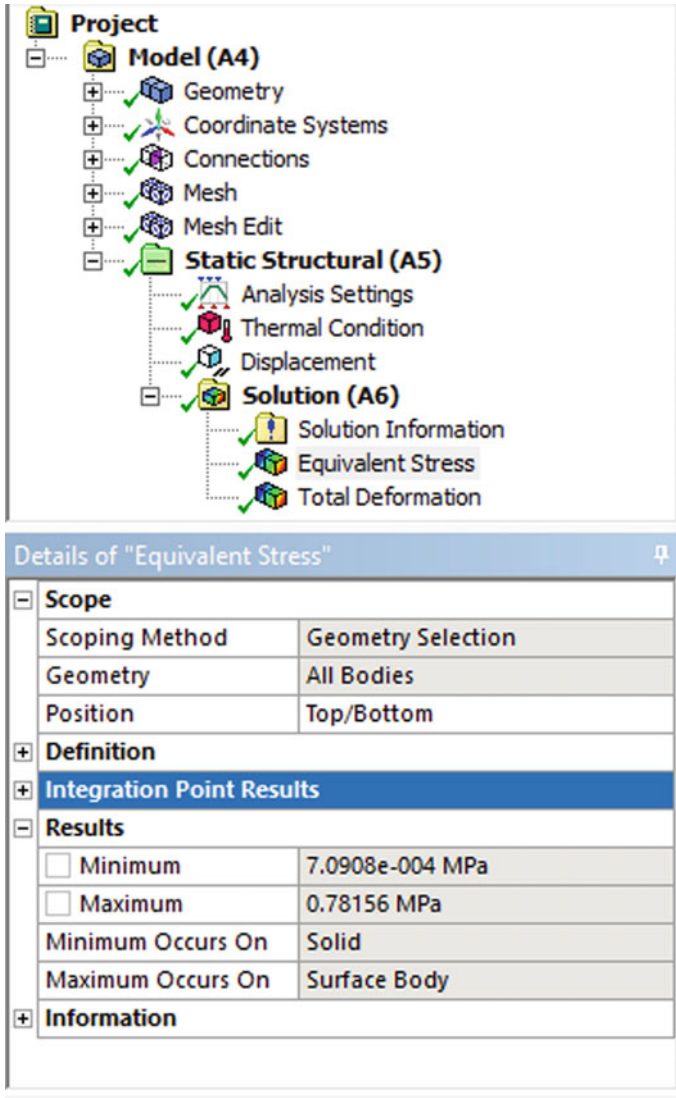


Fig. 14 von Mises stress values obtained on VAWT blade due to thermal load



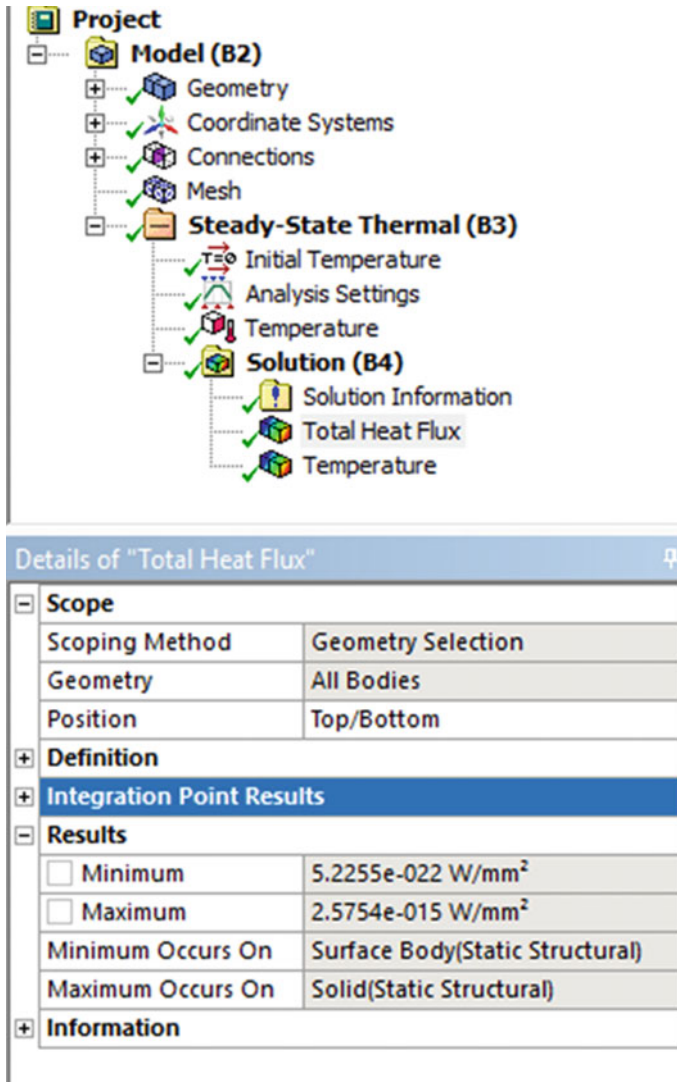


Fig. 15 Heat flux values obtained on VAWT blade due to thermal load

Table 2 Comparison of von Mises stress due to applied structural load by static structural solver

Sl. No.	Blade	Maximum stress (MPa)	Minimum stress (MPa)
1	HAWT Blade	89.035	0.0011376
2	VAWT Blade	0.58482	1.87e-5



**Table 3** Comparison of von Mises stress due to applied thermal load in static structural solver

Sl. No.	Blade	Maximum stress (MPa)	Minimum stress (MPa)
1	HAWT Blade	1.1764	0.001438
2	VAWT Blade	0.78156	0.00071

**Table 4** Comparison of total heat flux due to applied thermal load in steady-state thermal solver

Sl. No.	Blade	Maximum heat flux (W/mm <sup>2</sup> )	Minimum heat flux (W/mm <sup>2</sup> )
1	HAWT Blade	2.514e-15	3.648e-23
2	VAWT Blade	2.5754e-15	5.225e-22

## References

1. Manwell JF, McGowan JG, Rogers AL (2010) Wind energy explained: theory, design and application. Wiley, Chichester, UK
2. Johansen J, Madsen HA, Gaunaa M, Bak C, Srensen NN (2009) Design of a wind turbine rotor for maximum aerodynamic efficiency. *Wind Energy* 12:261–273
3. Liu X, Wang L, Tang X (2013) Optimized linearization of chord and twist angle profiles for fixed-pitch fixed-speed wind turbine blades. *Renew Energy* 57:111–119
4. Yang K (2020) Geometry design optimization of a wind turbine blade considering effects on aerodynamic performance by linearization. *J Energy* 13:2320. <https://doi.org/10.3390/en13092320>
5. Yang Z, Yin M, Xu Y, Zhang Z, Zou Y, Dong ZY (2016) A multi-point method considering the maximum power point tracking dynamic process for aerodynamic optimization of variable-speed wind turbine blades. *Energies* 9:425
6. Tahani M, Kavari G, Masdari M, Mirhosseini M (2017) Aerodynamic design of horizontal axis wind turbine with innovative local linearization of chord and twist distributions. *Energy* 131:78–91
7. Pour rajabian A, Afshar PAN, Ahmadizadeh M et al (2016) Aero-structural design and optimization of a small wind turbine blade. *Renew Energy* 87:837–848
8. Tenguria N, Mittal ND, Ahmed S (2011) Modal analysis for blade of horizontal axis wind turbine. *Asian J Sci Res* 4(4):326–334
9. Bechly ME, Clausen PD (1997) Structural design of a composite wind turbine blade using finite element analysis. *Comput Struct* 63(3):639–646
10. Mohamed Bak K, KalaiChelvan K, VijayaRaghavan GK, Arumugam V (2013) Study on effect of adhesive thickness of single lap joints in composite laminate using AE and FEA. *BINDT-Int J Insight—Non-Destructive Testing and Condition Monitoring* 55(1):35–41(7) (Impact Factor:0.56). ISSN:0007-1137
11. Mohamed Bak K, KalaiChelvan K (2012) Parametric study of bonded, riveted and hybrid joints using FEA. *J Appl Sci* 12(10):1058–1062

# The Effect of Novel Cryogenic Treatment in the Microstructure Analysis of Al 6101 Closed-Cell Foam



Syed Zeenath Fathima, T. R. Tamilarasan, S. Rasool Mohideen, Milon Selvam Dennison, and Jayaraj Venkatesan

**Abstract** This research work is to explicit the surface morphology, material composition and crystal structure of a closed-cell aluminium foam subjected to various treatments such as heat treatment (HT), cryogenic treatment (CT) and cryogenic heat treatment (CHT). The closed-cell aluminium foam utilized for this research is made of Al 6101 aluminium alloy with high purity. The microstructure, material composition and crystal structure of the treated samples are evaluated by a high-resolution scanning electron microscope, energy dispersive X-ray technique and X-ray diffraction technique, respectively. From the results, significant observations were made in the surface morphology of the Al 6101 foam samples subjected to various treatments.

**Keywords** Al 6101 · Closed-cell foam · Heat treatment · Cryogenic treatment · Microstructure · Material composition · Crystal structure

## Nomenclature

GFC Ltd.,	Good Fellow Cambridge Limited
CT	Cryogenic treatment
SCT	Shallow cryogenic temperature
$^{\circ}\text{C}/\text{min}$	Degree Celsius per minute
CHT	Cryogenic heat treatment
UT	Untreated

---

S. Zeenath Fathima (✉) · T. R. Tamilarasan · S. Rasool Mohideen  
Department of Mechanical Engineering, B.S. Abdur Rahman Crescent Institute of Science and Technology, Chennai, Tamil Nadu 600048, India  
e-mail: [zeenukhan2002@gmail.com](mailto:zeenukhan2002@gmail.com)

M. S. Dennison  
Department of Mechanical Engineering, School of Engineering & Applied Sciences, Kampala International University (Western Campus), Kampala, Uganda

J. Venkatesan  
Department of Mechanical Engineering, Higher College of Technology, Muscat, Oman

HT	Heat treatment
ASTM	American society of testing and materials
$\mu\text{m}$	Micrometre
nm	Nanometre
$\mu\text{A}$	Micro-ampere
O	Oxygen
C	Carbon
Fe	Iron
Na	Sodium
Si	Silicon
Mg	Magnesium
Wt	Weight
At	Atomic
SEM	Scanning electron microscope
EDAX	Energy dispersive X-ray
XRD	X-ray diffraction
GP	Guinier–Preston
Al	Aluminium
GR	Grains refinement

## 1 Introduction

The present world seeks for the novel idea of artificial materials with advanced mechanical and chemical properties to satisfy the necessary applications [1]. Aluminium is the common recyclable engineering material that is used in all lightweight-related engineering [2]. Ultra-light metal foams are considered as an attractive material in both scientific research areas and industrial applications [3, 4]. In particular, closed-cell aluminium alloy foams are lightweight, recyclable, high stiffness with very low density and it has good sound and energy absorption properties. These foams have the capability of vibration damping and absorbing impact energy [5, 6]. In recent years, closed-cell aluminium foam is one of the important cellular foams which has been manufactured by the number of cost-effective processes [7]. The applications of closed-cell aluminium foams are extensively used in automotive, aerospace and other lightweight-dependent industries. The established applications of closed-cell aluminium foams include heat exchangers, pump housings and baffles to absorb traffic noise and as cladding on buildings, hydraulic components and lightweight structures for aerospace applications and includes automobile firewalls, components for rail-transport systems [8].

In material science, the cryogenic treatment is witnessed to be a supplementary process that enhances the chemical and mechanical properties of metals and thus the product life of the material would enhance [9, 10]. Due to the apparatus setup and consumables required for treating the materials, cryogenic treatment is accounted

to be an expensive surface treatment process. From various literature readings, it is evident that cryogenically treated components exhibit improved microstructure and stabilize the product dimension prevents material deformation [11]. The deep cryogenic treatment of aluminium alloys would enhance the wear resistance due to the formation of the Guinier–Preston (GP) zone, and the result revealed from a microstructural analysis [12].

The cryogenically treated specimens reported low wear rates when examined for microstructural analysis. The generations of the supplementary Guinier–Preston zones as the cause of the enhanced wear resistance [13]. The case of AA 5182 alloys yield strength, tensile strength and uniform elongation rise when the temperature is decreased from room temperature to  $-196\text{ }^{\circ}\text{C}$  [14, 15]. The case of 2024-T351 aluminium alloy subjected to cryogenic handling contributed to the enhancement of tensile properties by removing the second and the third categories of tensile residual stresses with the improvement of plasticity. Besides, they hypothesized the phenomenon of grains refinement (GR) was found throughout the microstructure uniformly due to the shrinking effect of dimples in the fracture zone after cryogenic treatment [16]. The cryogenic processing is the optimistic approach to enhance the mechanical properties and it is reported as one of the favourable processes in the published literature to improve the wear resistance mainly on cutting tools, moulds and the final products and to reduce the surface roughness and improve the grain refinement for various materials [17]. The deep cryogenic treatment is one of the prosperous treatments to refine the precipitates (uniform allocation of  $\eta'$ - $\text{MgZn}_2$ - and  $\eta$ -phase precipitates) and increase the consistency of the precipitate allocation, thereby improving the plasticity and strength of the 7A99 aluminium alloy [18].

Most of all cryogenic studies were dealt with ferrous materials. Limited research papers are published with non-ferrous materials for engineering applications and the enhancement of microstructural analysis. However, very little research has focused on the effect of deep cryogenic treatment on the microstructures of aluminium alloy closed-cell foam. The focus of this research is to study the microstructural analysis of heat and deep cryogenic-treated Al 6101 closed-cell foam.

## 2 Investigational Facts

### 2.1 Selection of Material

The closed-cell aluminium foam selected for this investigation is made of Al6101 aluminium alloy with 98.5% of purity. The foam material is directly procured from GFC Ltd., England and the material is confirmed by chemical composition test in its raw form and the text report is given in Table 1. The closed-cell aluminium foam made of Al6101 alloy exhibit unique mechanical properties such as high strength to weight ratio, high surface area to volume and isotropic stress response. Also, this type of foam exhibits other properties such as corrosion resistance, electrical and

**Table 1** Chemical composition of the aluminium foam (AL003860) made of Al6101 alloy

Element	Percentage composition	
	Standard	Tested
Magnesium	0.35–0.80	0.510
Silicon	0.30–0.70	0.430
Zinc	0.10 max	0.060
Chromium	0.030 max	0.030
Manganese	0.030 max	0.030
Boron	0.060 max	0.040
Copper	0.10 max	0.070
Aluminium	Rest	98.830

**Table 2** Specifications of the aluminium foam (AL003860) made of Al6101 alloy

Specification	Value
Porosity	93.0%
Thickness	30 mm
Mass density	0.20 g/cm <sup>3</sup>
Purity	98.5%
Pores/cm	16

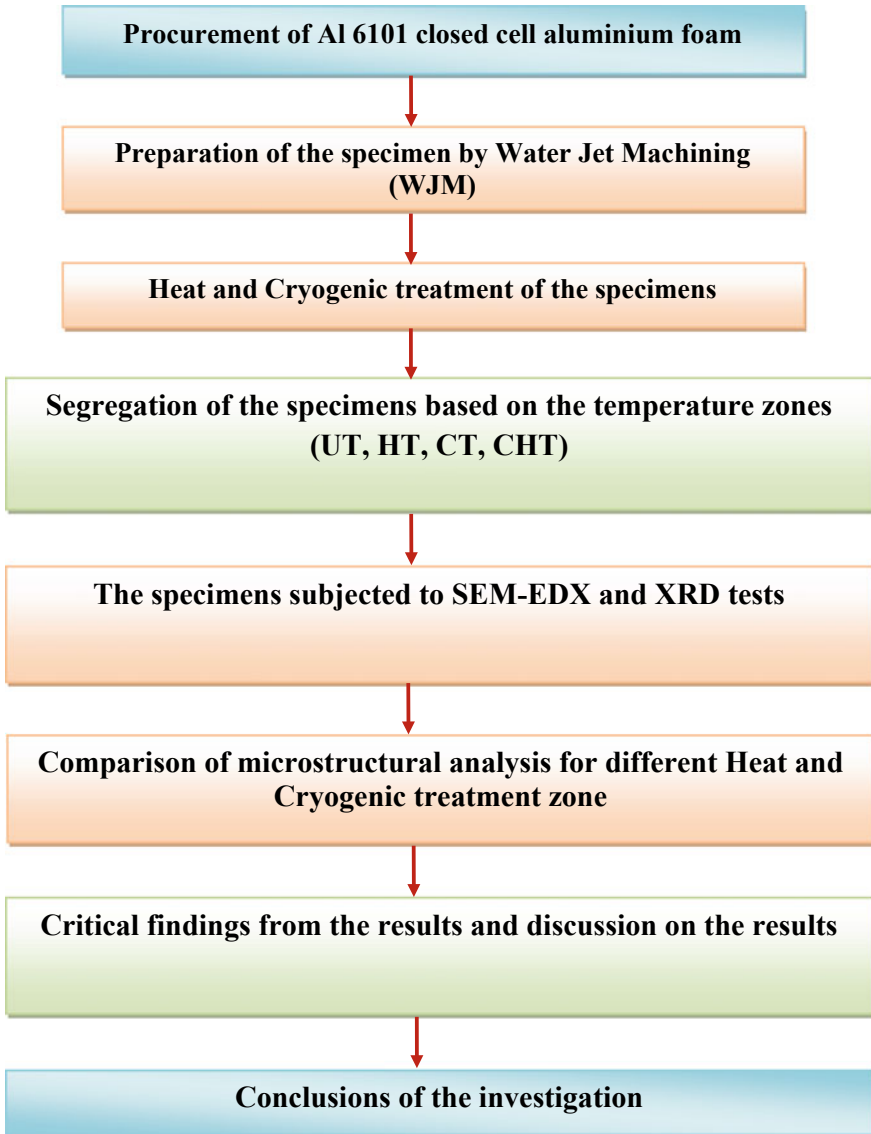
thermal conductivity. This was the reason for selecting Al6101 alloy foam for this investigation. The specifications of the closed-cell aluminium foam of product code ‘AL003860’ used for this investigation are given in Table 2. The steps involved in this investigation are portrayed in Fig. 1.

## 2.2 Specimen Preparation

Sample preparation is a challenge for SEM-EDX analysis because Al 6101 closed-cell foam is very much delicate to handle for 1 mm thickness. Water jet machine (Dardi DWJ3020-BB) is used to cut the SEM samples of (55 × 10 × 1 mm<sup>3</sup>) size as shown in Fig. 2 and it is made with the size of (4 × 4 × 1 mm<sup>3</sup>) for SEM observation with different angular locations as per the standard practice.

## 2.3 Heat Treatment (HT)

In the present investigation, the Al 6101 closed-cell foam specimen was kept in the furnace at a temperature of 350 °C for 3 h and progressively the specimen was cooled back to room temperature. The annealing temperature of aluminium alloys



**Fig. 1** Steps involved in this investigation

6XXX grade lies in between the temperature of 300–400 °C starting from 30 min to 3 h. The time and temperature for annealing depend on the size of the part and the composition of the alloy. The purpose of annealing is to reset the crystalline grain structure, relieve the internal stresses, restoring slip planes and making it possible to continue shaping the part without requiring excessive force. Hence, the average



Fig. 2 Specimen picture for SEM analysis

temperature of 350 °C has been maintained and the maximum time of 3 h for heat treatment (HT) trailed by cooling at room temperature.

### 2.4 Cryogenic Treatment (CT)

The scientific process of cryogenic treatment (CT) typically starts from a slow rate of cooling at 1 °C/min until it reaches the shallow cryogenic temperature (SCT) at -84 °C and it should continue until it reaches the temperature of -196 °C and followed by maintaining in the same temperature for 24 h and slowly back to room temperature. The temperature profile for cryogenic treatment is shown in Fig. 3.

For the commencement of the cryogenic treatment (CT), the batch of specimens was cleaned to remove the impurities and the dust particles on the surface. In the current examination, the Al6101 closed-cell foam was gradually cooled from room

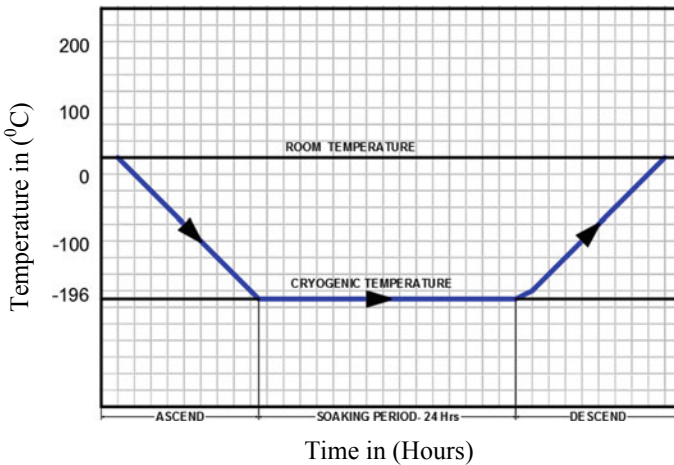
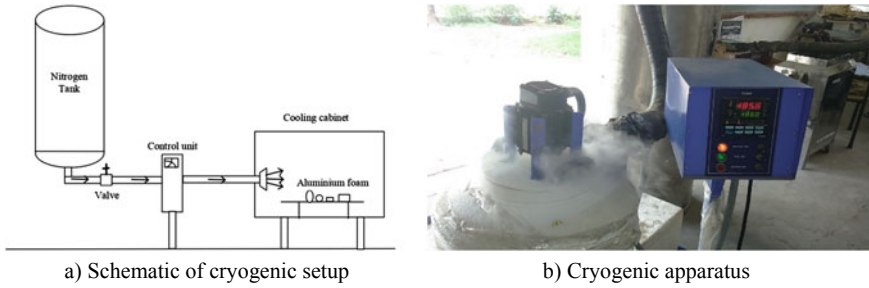


Fig. 3 Cryogenic treatment cycle for Al 6101 foam



**Fig. 4** Cryogenic treatment setup. **a** Schematic of cryogenic setup. **b** Cryogenic apparatus

temperature at the pace of  $-0.5\text{ }^{\circ}\text{C}/\text{min}$  until it comes to  $-196\text{ }^{\circ}\text{C}$  followed by keeping up at the same temperature for 24 h and gradually back to room temperature. Modernized control cryogenic treatment processor is utilized for accomplishing the cycle of cryogenic treatment. The cryogenic treatment schema and the processor are shown in Fig. 4.

The working fluid of the cryogenic processor is liquid nitrogen when it evaporates, it releases a large volume of gas, which is highly dangerous to the human body and so it is kept in the well-insulated chamber. A vacuum insulated hose connects the cryogenic treatment chamber with the liquid nitrogen tank. The cryogenic treatment chamber has gotten the temperature sensors that sense the temperature inside the chamber. The PID temperature controller operates in response to the temperature sensor and it controls the solenoid valve to regulate the liquid nitrogen flow. The liquid nitrogen passes through the spiral heat exchanger and it is converted to nitrogen gas and it enters the duct which is located at the bottom of the chamber. The blower which is at the top of the chamber plays an important role to reduce the chamber temperature by circulating the gas inside the chamber. The important process parameters are soaking time, temperature and cooling rate of the deep cryogenic treatment is controlled by the programmable temperature controller which is placed in the cryogenic process chamber. The deep CT processes are well documented with the help of a data acquisition system.

### 2.5 Cryogenic Heat Treatment (CHT)

The deep CHT is carried out after completing the CT in the previous step and the specimen is removed from the cryogenic chamber and it has been transformed into a stress relief annealing process in such a way that heating the specimen at  $350\text{ }^{\circ}\text{C}$  for 3 h and followed by cooling in room temperature. The process of deep cryogenic treatment and heat treatment is given in Table 3.



**Table 3** Various heat regime and conditions

Nomenclature	Heat regime	Condition
UT	Untreated	The Al 6101 closed-cell foams were not subjected to any type of treatment
HT	Heat treatment	The Al 6101 closed-cell foam samples were subjected to HT at 350 °C for 3 h and subsequently by cooling at ambient temperature
CT	Cryogenic treatment	The Al 6101 closed-cell foam samples were subjected to CT at –196 °C for 24 h
CHT	Cryogenic heat treatment	Subsequent to the CT the Al 6101 closed-cell foam samples were subjected to an annealing process executed at 350 °C for 3 h followed by cooling at ambient temperature

## 2.6 Surface Characterization

The surfaces of the Al 6101 closed-cell foam samples were etched with 2% of nital solution and cleaned using methanol for 30 s. Before recording the images in SEM, the residual damage generated during the sample preparation was removed. The residual damage in the foam samples was carefully removed prior to the microstructure evaluation using a high-resolution scanning electron microscope (SEM). At last, the perfect spot of the microstructure with suitable splendour and amplification has been chosen in the samples. The choice of this spot of interest is essential, which chooses whether the picture information is significant or not. It is attractive to catch the total research objects included in the selected volume, which can be remade to quantitative investigation.

Then, the surface morphology of Al 6101 foam specimens with the different regimes was examined employing a high-resolution SEM in a different angular location with the secondary electron image resolution of 1 nm at 15 kV and backscattered electron image resolution of 3 nm at 15 kV YAG detector to recognize the microstructure and the internal grain structure before and after cryogenic treatment were obtained with JEM-2000FX. The elemental identification and quantitative compositional information of Al 6101 foam were determined by Bruker energy dispersive X-ray analyser (EDAX). The crystal structure of the Al 6101 foam specimens was evaluated with an X-ray diffraction (XRD) technique. The XRD patterns of the foams were documented at ambient temperature using an X-ray powder diffractometer (Bruker binary) with CuK $\alpha$  radiation ( $\lambda = 1.5405 \text{ \AA}$ ) in a wide sort of Bragg angles  $2\theta$  ( $10^\circ \leq 2\theta \leq 90^\circ$ ) at a scanning pace of  $2^\circ/\text{min}$ .

### 3 Results and Discussion

#### 3.1 *Microstructure and Material Composition Analysis*

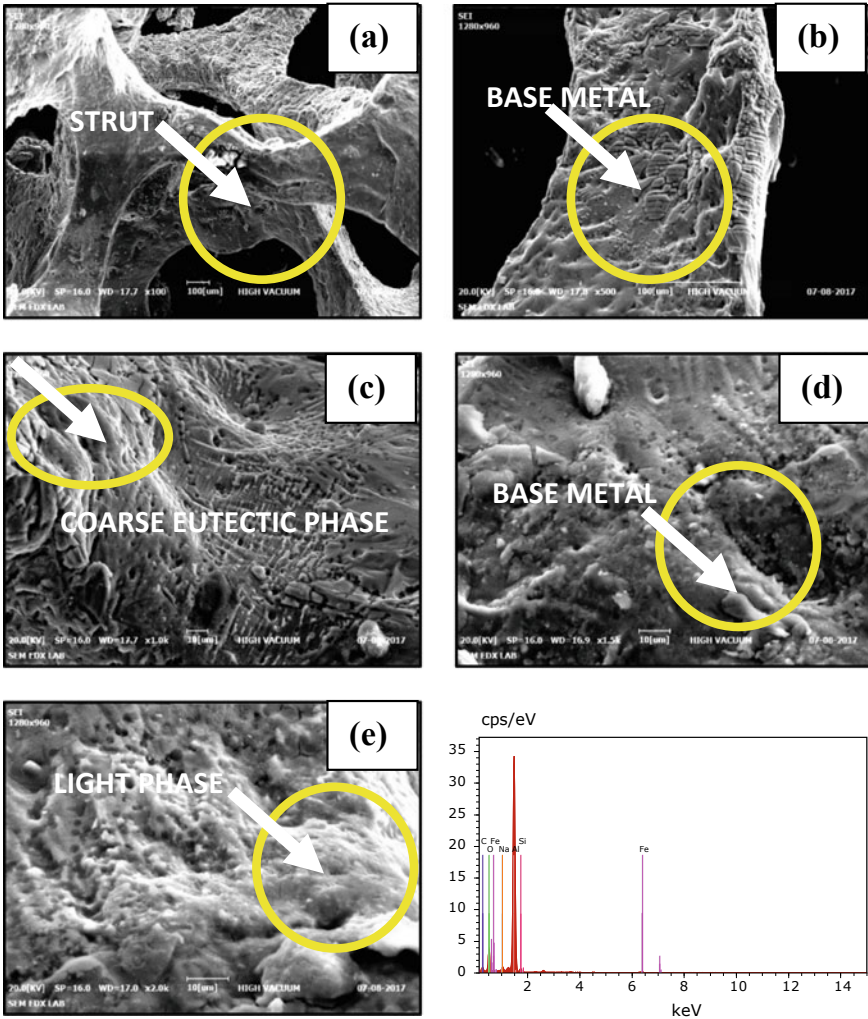
The microstructure investigation was carried out to find the possible differences among the UT, HT, CT, CHT samples. The surface morphology of Al 6101 closed-cell foam was subjected to SEM-EDAX analysis and to investigate the changes in the microstructure and the impact of the cryogenic treatment in the composition of the foam due to the presence of liquid nitrogen in the cryogenic treatment.

As the microstructure of the aluminium was influenced by the cryogenic process, the bright surface indicates the aluminium structure and the dark marks are precipitates. Each set of SEM image shows the observations in different positions to show the foam structure distinctly. The following methodologies are followed in the research steps, i.e., microstructure examination by SEM images of UT, HT, CT, CHT samples.

Untreated (UT) specimens of SEM-EDAX images are shown in Fig. 5a–e, normally the cells are reticulated open type and the appearance is clumsy and there is no clearance in the boundaries. Figure 6a–e shows the surface morphology of the heat-treated (HT) SEM-EDAX specimen the SEM investigations revealed the inter-metallic phases distributed solely in the network and the cells are expanded due to the heat treatment and hence there are some macro and micro-sized pores appear on the surface.

The cryogenic-treated (CT) SEM-EDAX images are shown in Fig. 7a–e, due to the cryogenic treatment the surface morphology is clear and there is a formation of GP zones and closely packed cell structure can be seen as well. Due to the dense packing of atoms, there may not be any more dislocations. Hence, it leads to the improvement of mechanical properties like brittle strength, wear, fatigue, etc. Figure 8a–e shows cryogenic heat-treated (CHT) SEM-EDAX images where the surface has undergone by heat and cold treatment, and the grains are closely packed and here also there is a formation of GP zones due to the deep cryogenic treatment the surface morphology looks enhanced when compared with the cryogenic treatment zone specimen.

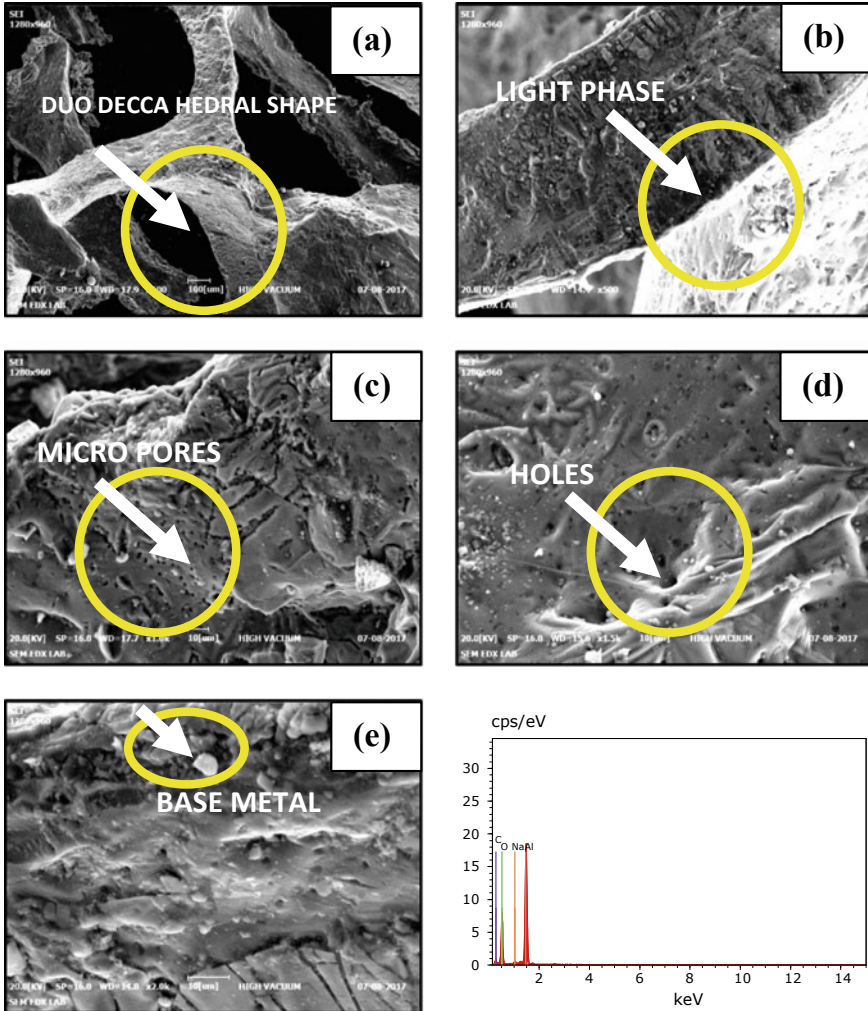
The EDAX beam always incorporates the substrate around the precipitates. There are two kinds of precipitates that were found with this metallographic analysis. The percentage of concentrations found for all elements are listed in Table 4. As the precipitations are very small, therefore, aluminium is always present in all the measurements. The grey rod-shaped marks are characteristic for  $Mg_2Si$  and  $Al_xFe_xSi_x$  precipitates and the smaller round shaped black precipitates would be  $SiO_2$ . The occurrence of Mg and Fe is found in the characteristic of  $Al_xFe_xSi_x$  and the  $Mg_2Si$  precipitates which is there in CT and CHT regime. The presence of Fe is found in UT and CT zone, but it is disappearing in HT and CHT zones. It shows evidence that the elements Al,  $O_2$  and C present in all the zones. Therefore, it can be mentioned that the cryogenic heat treatment did not have any visually evident outcome with optical investigation methods rather than forming the above-mentioned precipitates.



**Fig. 5** SEM-EDAX images of untreated specimen (UT). **a** Visibility of strut structures 20.0[k v] SP = 16.0 WD = 17.7 × 100, 100 [μm], **b** observation of base metal 20.0[k v] SP = 16.0 WD = 17.8 × 500, 100 [μm], **c** observation of coarse eutectic phase 20.0 [kv] SP = 16.0 WD = 17.6 × 1000, 10 [μm], **d** visibility of light phase and base metal 20.0 [kv] SP = 16.0 WD = 1 6.9 × 1500, 10 [μm], **e** visibility of light phase 20.0 [kv] SP = 16.0 WD = 17.0 × 2000, 10 [μm]

### 3.2 XRD Analysis

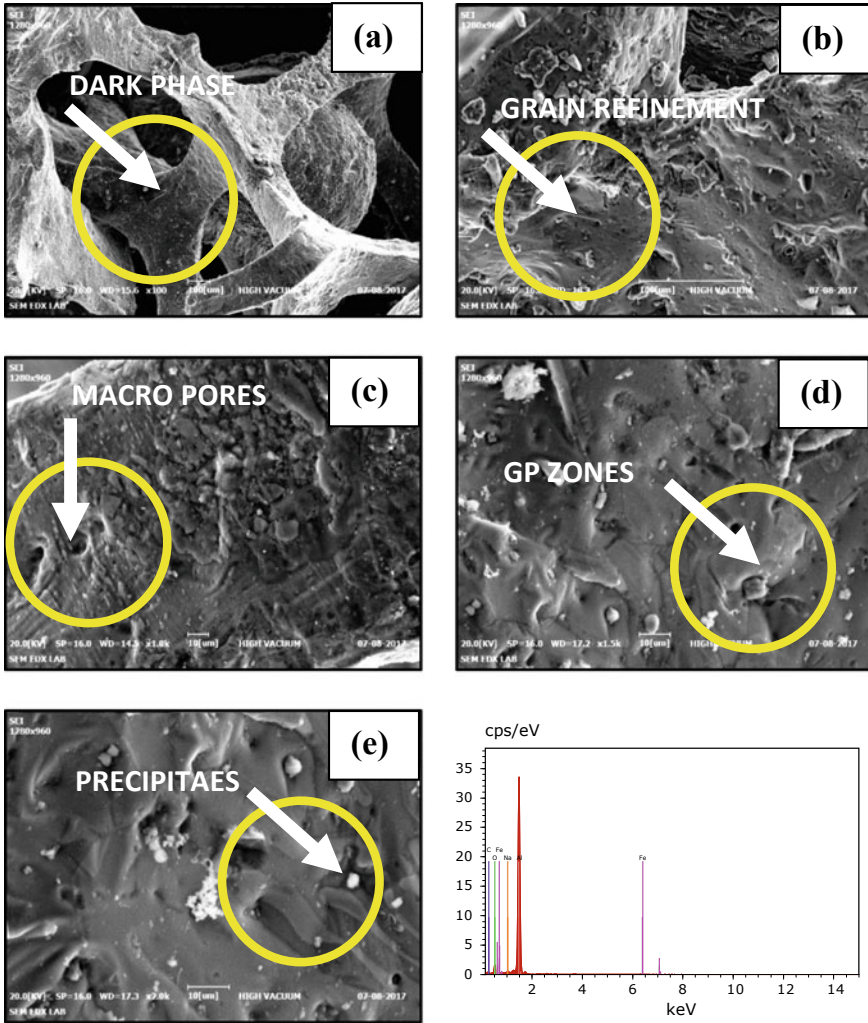
X-ray powder diffraction (XRD) is a scientific research technique that is used to identify the crystal structure of a material and dimensions of a unit cell. Figure 9 shows the enlarged XRD patterns of the Al 6101 foam in the ranges of 2θ from 10° to



**Fig. 6** SEM-EDAX images of heat-treated specimen (HT). **a** Visibility of duo-decahedral shape 20.0 [k v] SP = 16.0 WD = 17.9 × 100, 100 [μm], **b** observation of light phase 20.0[k v] SP = 16.0 WD = 14.4 × 500, 100 [μm], **c** identification of micropores 20.0 [k v] SP = 16.0 WD = 17.7 × 1000, 10 [μm], **d** formation of holes 20.0 [k v] SP = 16.0 WD = 15.6 × 1500, 10 [μm], **e** base metal identification 20.0 [k v] SP = 16.0 WD = 14.8 × 2000, 10 [μm]

90° to analyse the changes in the crystal structure in the HT and CT Al 6101 closed-cell foam samples. By knowing the crystal structure of any material, it is important to understand the behaviour of materials under stress, temperature, alloy formation and phase transformations.

The angular positions of the diffraction peaks can be defined by the size and shape of the unit cell and the relative intensities of the peaks determine the arrangement of

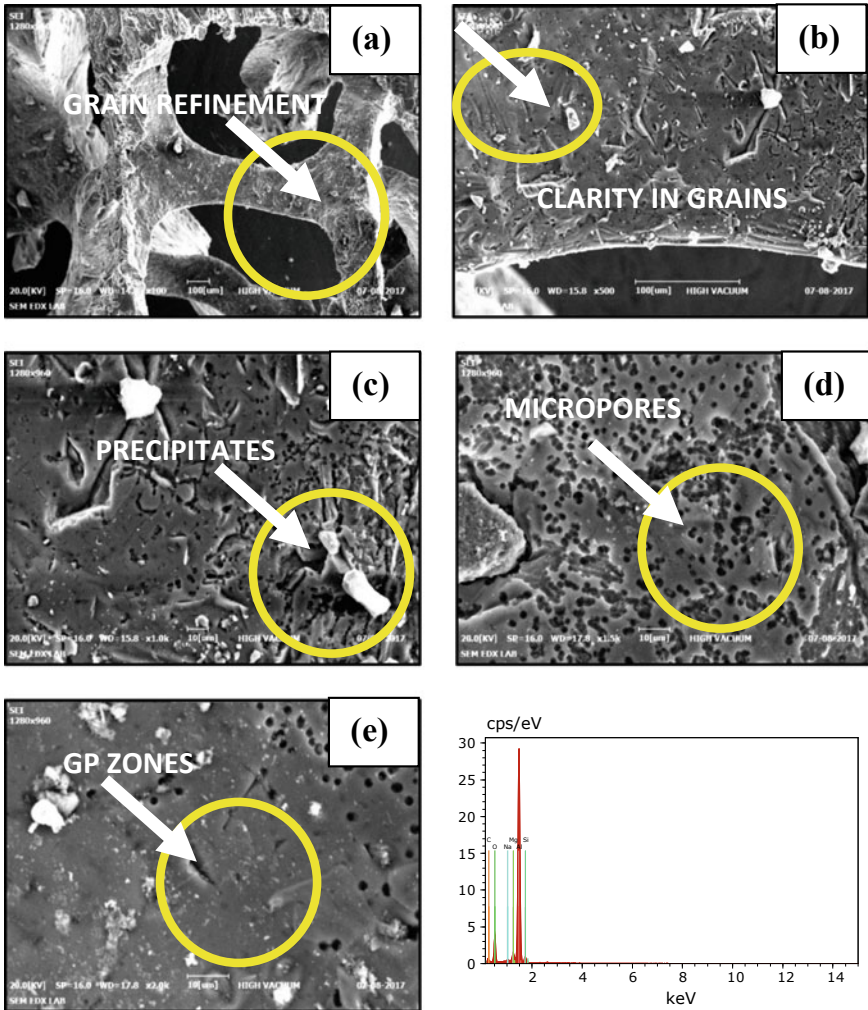


**Fig. 7** SEM-EDAX images of cryogenic-treated specimen (CT). **a** Observation of dark phase 20.0[k v] SP = 16.0 WD = 15.6 × 100,100[μm], **b** observation of grain refinement 20.0[k v] SP = 16.0 WD = 18.3 × 500,100[μm], **c** observation of macropores 20.0 [kv] SP = 16.0 WD = 14.5 × 1000, 10 [μm], **d** formation of Guinier–Preston (GP) zones 20.0 [kv] SP = 16.0 WD = 17.2 × 1500, 10 [μm], **e** formation of Guinier–Preston (GP) zones and observation of precipitates 20.0 [kv] SP = 16.0 WD = 17.3 × 2000, 10 [μm]

the atoms within the unit cell. The lattice factors for each peak are shown in Fig. 9 and the calculation of the common coefficient for all the regimes are given in Table 5.

By comparing the results with the sequences of  $h^2 + k^2 + l^2$  values to identify the Bravais lattice and the corresponding lattice factor shows that all  $hkl$  values resemble





**Fig. 8** SEM-EDAX images of cryogenic heat-treated specimen (CHT). **a** Observation of grain refinement 20.0 [k v] SP = 16.0 WD = 14.8 × 500, 100 [μm], **b** observation of clarity in grains 20.0 [k v] SP = 16.0 WD = 15.8 × 500, 100 [μm], **c** formation of precipitates 20.0 [k v] SP = 16.0 WD = 15.8 × 1000, 10 [μm]-CHT, **d** formation of microholes 20.0 [k v] SP = 16.0 WD = 17.8 × 1500, 10 [μm], **e** formation of Guinier–Preston (GP) zones 20.0 [k v] SP = 16.0 WD = 17.8 × 2000, 10 [μm]

the FCC structure in the HT and CHT zones and the calculation of common coefficient for the regimes shows that there is a common coefficient 0.14 in  $\text{Sin}^2\theta$ ,  $\text{Sin}^2\theta/2$ ,  $\text{Sin}^2\theta/3$  columns which resembles the standard FCC structure. The higher range of XRD diffraction peak intensity of Al 6101 foam in the CT zone suggested that CT can

**Table 4** Precipitations of the aluminium alloy foam

UT-spectrum: acquisition 7952							
Elements	Al	O	Cu	Fe	Na	Si	Mg
C norm.[wt%]	54.89	22.38	17.77	2.44	1.32	1.19	NIL
C atom. [at.%]	40.23	27.67	29.26	0.87	1.14	0.84	NIL
HT-spectrum: acquisition 7953							
C norm.[wt%]	38.55	45.92	14.27	NIL	1.25	NIL	NIL
C atom. [at.%]	25.78	51.79	21.44	NIL	0.98	NIL	NIL
CT-spectrum: acquisition 7951							
C norm.[wt%]	69.09	14.73	13.93	1.32	0.93	NIL	NIL
C atom. [at.%]	54.23	25.97	18.44	0.5	0.85	NIL	NIL
CHT-spectrum: acquisition 7954							
C norm.[wt%]	54.37	25.06	14.72	NIL	2.31	0.97	2.57
C atom. [at.%]	40	31.09	24.34	NIL	1.63	0.84	2.1

induce the (311) peak preferred orientation. In the process of cooling, a lot of dislocations and subgrains were generated within the material due to the volume shrinkage effect. In the following process of cryogenic heat treatment recovery, recrystallization occurred with grains of aluminium alloy rotating on the preferred orientation, which led to the formation of recrystallization texture. The grain orientation would be used to inhibit dislocation motion, thereby increasing the strength of the Al 6101 closed-cell foam.

In the investigation of microstructure analysis of Al 6101 foam with the deep cryogenic and heat treatment, the observed results are summarized in Table 6.

## 4 Conclusions

This investigation has arrived with the following conclusions;

- $Al_xMg_xSi_x$  precipitates are the major reason to discover Guinier–Preston zone aids understanding of precipitation. The arrangement of the GP zone in the CT regime quickens the precipitation course, refines the precipitates and expands the consistency of the hasten dispersion, consequently, bringing about improved quality of the Al 6101 closed-cell foam.
- The SEM-EDAX analysis implies that the deep cryogenic treatment under the CHT regime changes the morphology of Al 6101 foam due to the formation of GP zones which showed the improvement in the microstructure of cryogenically treated specimen in the CT, CHT regime compared with the untreated samples in the UT, HT regime.

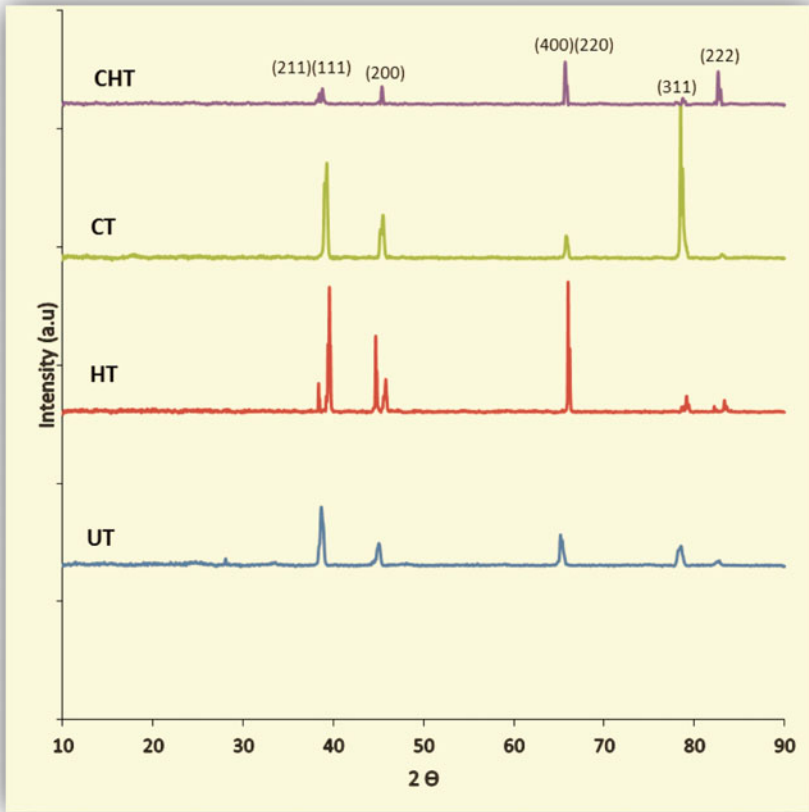


Fig. 9 XRD patterns of the Al 6061 foam

- The higher range of XRD diffraction peak intensity of Al 6101 foam in the cryogenic zone suggested that cryogenic treatment can induce the (311) peak preferred orientation. The formation of recrystallization texture due to cryogenic heat treatment and grain orientation would be used to inhibit dislocation motion, thereby increasing the strength of the Al 6101 closed-cell foam.
- Consequently, the investigation also concludes that the increase in dimensional stability can be achieved due to the formation of the precipitates  $Al_xFe_xSi_x$  and the  $Mg_2Si$ .
- In summary, CT improves the strength and ductility of the Al 6101 foam mainly by accelerating precipitation, refining the size of the precipitates and increasing the dispersion of the precipitates, thereby increasing the strength of the foam.
- In an outline, CT improves the quality and malleability of the Al 6101 foam for the most part by accelerating precipitation, refining the size of the cell structure



**Table 5** Diffraction peak intensity of the Al 6061 foam

UT					
Peak No	Pos. [°2Th.]	Height [cts]	Sin <sup>2</sup> θ	Sin <sup>2</sup> θ/2	Sin <sup>2</sup> θ/3
1	28.046	55.22	0.0587	0.0293	0.0195
2	33.4232	14.97	0.0826	0.0413	0.0275
3	38.6369	487.66	0.1093	0.0546	0.0364
4	45.1552	149.91	0.1473	0.0736	0.0491
5	65.1588	254.22	0.2897	0.1448	0.0965
6	78.5591	159.65	0.4006	0.2003	0.1335
7	82.7682	35.7	0.4369	0.2184	0.1456
HT					
1	38.3904	159.27	0.1081	0.054	0.036
2	39.5557	1053.6	0.1144	0.0572	0.0381
3	44.6788	636.7	0.1444	0.0722	0.0504
4	45.7942	265.19	0.1513	0.0756	0.0504
5	66.0141	1095.4	0.2966	0.1483	0.0988
6	66.201	535.76	0.2982	0.1491	0.0994
7	79.1856	89.86	0.4061	0.203	0.1353
8	83.3207	78.53	0.4418	0.2209	0.1472
CT					
1	39.2775	788.02	0.1128	0.0564	0.0376
2	45.5014	363.84	0.1495	0.0747	0.0498
3	65.7757	180.79	0.2947	0.1473	0.0982
4	78.491	1318.1	0.4001	0.2	0.1333
CHT					
1	38.6782	61.45	0.1095	0.0547	0.0365
2	45.3627	145.8	0.1486	0.0743	0.0495
3	65.6609	337.42	0.2939	0.1469	0.0979
4	78.7878	40.12	0.4027	0.2013	0.1342
5	82.6581	275.56	0.4359	0.2179	0.1453

and expanding the scattering of the precipitates and refining the quality of the foam.

**Table 6** Summary of results

Heat Regimes	SEM-EDAX	XRD
UT—Without any treatment	The cells are reticulated open type and the appearance is clumsy and there is no clearance in the boundary	The result shows that there is a common coefficient 0.14 in $\text{Sin}^2\theta$ , $\text{Sin}^2\theta/2$ , $\text{Sin}^2\theta/3$ columns which resembles the standard FCC structure
HT—Heat treatment	SEM investigations revealed the intermetallic phases distributed solely in the network and the cells are expanded due to the heat treatment and hence there are some macro and micro-sized pores appear on the surface	The result shows that there is a common coefficient 0.14 in $\text{Sin}^2\theta$ , $\text{Sin}^2\theta/2$ , $\text{Sin}^2\theta/3$ columns which resembles the standard FCC structure
CT—Cryogenic treatment	SEM-EDAX analysis shows that the presence of Mg and Fe in the $\text{Al}_x\text{Fe}_x\text{Si}_x$ and the $\text{Mg}_2\text{Si}$ precipitates, in the CT zone apart from the major components of aluminium $\text{Al}_x\text{Mg}_x\text{Si}_x$ precipitates are the major reason to discover Guinier–Preston zone aids understanding of precipitation The arrangement of the GP zone in the CT regime quickens the precipitation course, refines the precipitates and expands the consistency of the hasten dispersion, consequently, bringing about improved quality of the Al 6101 closed-cell foam	The higher range of XRD diffraction peak intensity of Al 6101 foam in the cryogenic zone suggested that cryogenic treatment can induce the (311) peak preferred orientation. The formation of recrystallization texture due to cryogenic heat treatment and grain orientation would be used to inhibit dislocation motion thereby increasing the strength of the Al 6101 closed-cell foam
CHT—Cryogenic heat treatment	SEM-EDAX analysis shows that the presence of Mg and Fe in the $\text{Al}_x\text{Fe}_x\text{Si}_x$ and the $\text{Mg}_2\text{Si}$ precipitates in the CHT zone apart from the major components of aluminium The SEM-EDAX analysis implies that the deep CT under the CHT regime changes the surface morphology of Al 6101 foam due to the formation of GP zones compared with the UT and HT regime samples	The result shows that there is a common coefficient 0.14 in $\text{Sin}^2\theta$ , $\text{Sin}^2\theta/2$ , $\text{Sin}^2\theta/3$ columns which resembles the standard FCC structure. When compared to CT regime there is no peak intensity in the CHT zone

## References

1. Ullah F, Othman MBH, Javed F, Ahmad Z, Akil HM (2015) Classification, processing and application of hydrogels: a review. *Mater Sci Eng C* 57:414–433. <https://doi.org/10.1016/j.msec.2015.07.053>
2. Koricho EG, Belingardi G (2015) An experimental and finite element study of the transverse bending behaviour of CFRP composite T-joints in vehicle structures. *Compos B Eng* 79:430–443. <https://doi.org/10.1016/j.compositesb.2015.05.002>
3. Syed ZF, Tamilarasan TR, Mohideen SR, Dennison MS (2020) Mechanical properties and surface characterisation of aluminium foam made of Al 6101 subjected to cryogenic treatment—a comparative study. *Int J Mater Eng Innov* 11(3):244–263. <https://doi.org/10.1504/IJMATEI.2020.108884>
4. Xiong J, Mines R, Ghosh R, Vaziri A, Ma L, Ohrndorf A, Christ HJ, Wu L (2015) Advanced micro-lattice materials. *Adv Eng Mater* 17(9):1253–1264. <https://doi.org/10.1002/adem.201400471>
5. Zhang Q, Yang X, Li P, Huang G, Feng S, Shen C, Han B, Zhang X, Jin F, Xu F, Lu TJ (2015) Bioinspired engineering of honeycomb structure—using nature to inspire human innovation. *Prog Mater Sci* 74:332–400. <https://doi.org/10.1016/j.pmatsci.2015.05.001>
6. Karuppasamy R, Barik D, Sivaram NM, Dennison MS (2020) Investigation on the effect of aluminium foam made of A413 aluminium alloy through stir casting and infiltration techniques. *Int J Materials Eng Innov* 11(1):34–50. <https://doi.org/10.1504/IJMATEI.2020.104790>
7. Rashed MG, Ashraf M, Mines RAW, Hazell PJ (2016) Metallic microlattice materials: a current state of the art on manufacturing, mechanical properties and applications. *Mater Des* 95:518–533. <https://doi.org/10.1016/j.matdes.2016.01.146>
8. Duarte I, Vesenjak M, Krstulović-Opara L, Anžel I, Ferreira JM (2015) Manufacturing and bending behaviour of in situ foam-filled aluminium alloy tubes. *Mater Des* 66:532–544. <https://doi.org/10.1016/j.matdes.2014.04.082>
9. Chopra SA, Sargade VG (2015) Metallurgy behind the cryogenic treatment of cutting tools: an overview. *Mater Today: Proc* 2(4–5):1814–1824. <https://doi.org/10.1016/j.matpr.2015.07.119>
10. Jawahir IS, Attia H, Biermann D, Dufflou J, Klocke F, Meyer D, Newman ST, Pusavec F, Putz M, Rech J, Schulze V (2016) Cryogenic manufacturing processes. *CIRP Annals* 65(2):713–736. <https://doi.org/10.1016/j.cirp.2016.06.007>
11. Arslan Y, Uygur I, Jazdzewska A (2015) The effect of cryogenic treatment on microstructure and mechanical response of AISI D3 tool steel punches. *J Manuf Sci Eng* 137(3):034501. <https://doi.org/10.1115/1.4029567>
12. Kong LB, Huang Y, Que W, Zhang T, Li S, Zhang J, Dong Z, Tang D (2015) Ceramic powder synthesis. In: *Transparent ceramics*. Springer, Cham, pp 93–189. [https://doi.org/10.1007/978-3-319-18956-7\\_2](https://doi.org/10.1007/978-3-319-18956-7_2)
13. Franco Steier V, Ashiuchi ES, Reißig L, Araújo JA (2016) Effect of a deep cryogenic treatment on wear and microstructure of a 6101 aluminium alloy. *Adv Mater Sci Eng*. <https://doi.org/10.1155/2016/1582490>
14. Li CM, Cheng NP, Chen ZQ, Guo N, Zeng SM (2015) Deep-cryogenic-treatment-induced phase transformation in the Al-Zn-Mg-Cu alloy. *Int J Miner Metall Mater* 22(1):68–77. <https://doi.org/10.1007/s12613-015-1045-7>
15. Li X, Li T, Lo KH, Kwok CT, Chen F (2017) Influences of thermomechanical treatments on the cryogenic treatability of a slightly unstable austenitic stainless steel. *Mater Manuf Process* 32(11):1239–1247. <https://doi.org/10.1080/10426914.2016.1257806>
16. Zhou J, Xu S, Huang S, Meng X, Sheng J, Zhang H, Li J, Sun Y, Boateng EA (2016) Tensile properties and microstructures of a 2024-T351 aluminium alloy subjected to cryogenic treatment. *Metals* 6(11):279. <https://doi.org/10.3390/met6110279>

17. Panicker SS, Singh HG, Panda SK, Dashwood R (2015) Characterization of tensile properties, limiting strains, and deep drawing behaviour of AA5754-H22 sheet at elevated temperature. *J Mater Eng Perform* 24(11):4267–4282. <https://doi.org/10.1007/s11665-015-1740-6>
18. Wang Y, Song Y, Xia Y (2016) Electrochemical capacitors: mechanism, materials, systems, characterization and applications. *Chem Soc Rev* 45(21):5925–5950. <https://doi.org/10.1039/C5CS00580A>

# Development of Toxic Gas Monitoring and Alarm System



Muniyandy Elangovan, D. Surya Prakash, and C. Hemadri

**Abstract** Nowadays, safety awareness brings more attention to the people, and safety is first in all industries. Safety plays major role in the current technology's world, and it is unavoidable to adopt a good safety system in working place and apartment. Because of the technology development in sensors and IoT, lots of researches are going to improve safety in every industry. Though most of the company has the safety system but not connected to each other in the safety process. A sprinkler is one of the systems that work automatically that too in the well-established company. Most of the company is still managing with the manually operated fire-fighting system. Knowing the needs of the industry, the authors have decided to develop a safety system to monitor and react when there is a need for action after the incident. The main objective of the work is to design a toxic gas detecting using sensors and activates the alerting device/system to react to an incident. The toxic gases like NO<sub>2</sub>, CO, CO<sub>2</sub>, methane, butane, hydrogen sulfide (H<sub>2</sub>S), and propane were monitored, and if these gases exceed the threshold limit, then a system can activate alarm followed by visual identification. Sensors are the vital component used in this system, which is meant for detecting different combustible/toxic gas and suitable for different applications. As this application is targeted for small-scale industries, the best price sensors were selected without compromising on requirements to keep the budget low. Once the sensor detects the toxic gas, the alarm sound is activated, which gives a sound indication of any toxic gas presence in the working environment and then automatically exhaust fan gets switched on. Sometime, fresh air fan gets activated to increase the quantity of fresh air and diluting the toxicity level till it comes to normal condition. To verify the design, a model was developed by placing a sensor, and the fan was activated after the gas was detected. Therefore, this automated system is verified in the model, and the complete system is working fine. The main advantages of this automated detection, monitoring, and alarming systems over the manual method are that it offers a quick response in time and accurate detection of an emergency and in turn leading a faster diffusion of the normal condition. The authors believe that this safety system can be used in any industry as well as a commercial building.

---

M. Elangovan (✉) · D. Surya Prakash · C. Hemadri  
Mechanical Department, Vel Tech Rangarajan Dr. Sagunthala R&D Institute of Science and  
Technology, Chennai, India  
e-mail: [drmelangovan@veltech.edu.in](mailto:drmelangovan@veltech.edu.in)

This newly designed and verified safety system can improve safety and is easy to adopt.

**Keywords** Gas · Alarm · Safety · Health and automation

## 1 Introduction

Hazardous gases and or vapor-producing liquids are being used which are transported or stored, and there exists the opportunity to leak into the surrounding area accidentally. Therefore, monitoring of such hazards is an essential part of any safety system on continuous basis. In the area of monitoring applications, the gas detection system is specifically designed to safe guard human life [1–5]. The gas detection system can be used with several different types of sensors in area monitoring with the latest communications and reporting functionalities.

Gas exposure can be fatal in the industry. In everyday life, people are exposed to a different type of gasses, which are at low concentration levels. If the gases are within the acceptable limit or controlled, it does not harm or danger. In the case of a buildup of the combustible gas system, it can leak and cause an explosion. In the buildup of toxic gas situations, even carbon monoxide can be fatal.

In the nineteenth and early twentieth centuries, coal mining is the mass production industry and many incidents happens that working life ended because of expected gas. Initially, coal miners were carrying out the gas detection by wearing a wet blanket and attach a wick with the end lit on fire. The lit wick is moved along the walls of the mine, it gets fire/ignite when there exist a pockets of methane gas [6, 7]. Therefore, blankets are used a safety tester for human safety. However, in some cases, a large amount of methane pockets caused the entire work area to be engulfed in flames. From the statistical data of accidental cases, it was realized to have an alternate method to identify the dangerous gas presents in the area. This test needs to be done before entering into the working area which can improve the safety in mines.

Canaries were decided to use for gas detection. The nervous system of canaries resembles the human breathing. The canaries are known for having a loud and melodious chirp. Miners would bring canaries in birdcages into the mine tunnels; it is monitored on the songbirds regularly. When it is observed that a canary gets started shaking cages and stopped singing. With this signal, miners understand that methane gas presents and people need to be evacuated from the area immediately.

The detection methods for gas leak are so important after seeing the effects of harmful gases on human life. Before the modern electronic sensors technology development, earlier detection methods have a low probability on safety of human life.

With the latest technology, gas detection instruments are produced as a product of safety that is preferably used to protect workers and ensure safety at the plant. These technologies are dedicated to detect dangerous gas concentrations and then trigger

alarms [1]. Same time, it activates countermeasures before being hazardous for the employees, assets, and the environment.

There are two types of gas detection systems—portable gas measuring instruments and fixed installed gas detection systems.

- Portable gas detection system
  - (a) Multi-gas detectors
  - (b) Single-gas detectors
- Fixed gas detection system

In typical gas detection systems, it is used to monitor the density of gas condition and send an alarm. Depending on the working area and expected gas, safety system decide the single-gas or multiage detection system. Due to economic issue, single-gas detector is preferred in some of the places. In most of the mines, system was implemented with multiage detection system, so that higher level of security is assured for the working people.

It is recommended to analyze the gases present in the area on continues basis. So that required sensor can be added to identify the danger and same time increase the safety system for better work environment. Portable detectors are used when there is no continuous work or only for testing purpose. In hazardous industry or working places where the production or manufacturing is going on continues basis, there is a need of fixed gas detection system.

## 2 Objectives

The automatic toxic gas monitoring and alarm system will be used in most industries for detecting the presence of toxic gas in the nearby environment and to alert the personnel is working with toxic gas. By using this gas monitoring and alarm system, it is quite possible to identify any type of leak of dangerous gases from the system, and then, necessary action can be initiated by the working personnel toward safeguarding the facilities and human beings as well.

Depending upon the type of gas that is expected to release from the system, the method of detection and type of sensing elements will be deployed for timely detection and alerting. Based on the application, the sensing element is to be selected and installed in the system, and the leaked out gas is to be sent out from the working environment for safeguarding the personnel within the working vicinity.

By providing the automatic toxic gas detection and alarming system at any industry, the following benefits will be ensured.

- Timely detection of toxic gas enables us to isolate the sources or escape from the hazards.

- The toxic gas can be driven out by using the exhaust fan, and inside toxic gas can be diluted by taking the fresh air from the outside atmosphere using a high speed intake fan other country.

### 3 Problem Definition and Methodology

When a toxic gas is leaked in any plant from the processing circuit or from the storage vessel, it will try to occupy the entire volume of the containment/confined space. Since there is always a possibility of the presence of human beings in the plant where the manual activities are involved, there must be an alerting system to indicate the potential hazards

Even low concentration (low ppm) vapors will try to displace the normal atmospheric air outside the room/plant and create asphyxiation. If the leaked gas is poisonous like H<sub>2</sub>S, arsine, and bromine, then the gas may cause damage to the internal organs and even can cause death. Gas detection system approach is show in Fig. 1.

### 4 Design of Gas Monitoring Alarm System

Toxic fluids storage building dimension

Length: 10 m

Breadth: 10 m

Height: 7 m

Total volume of the building:  $10 \times 10 \times 7 = 700 \text{ m}^3$

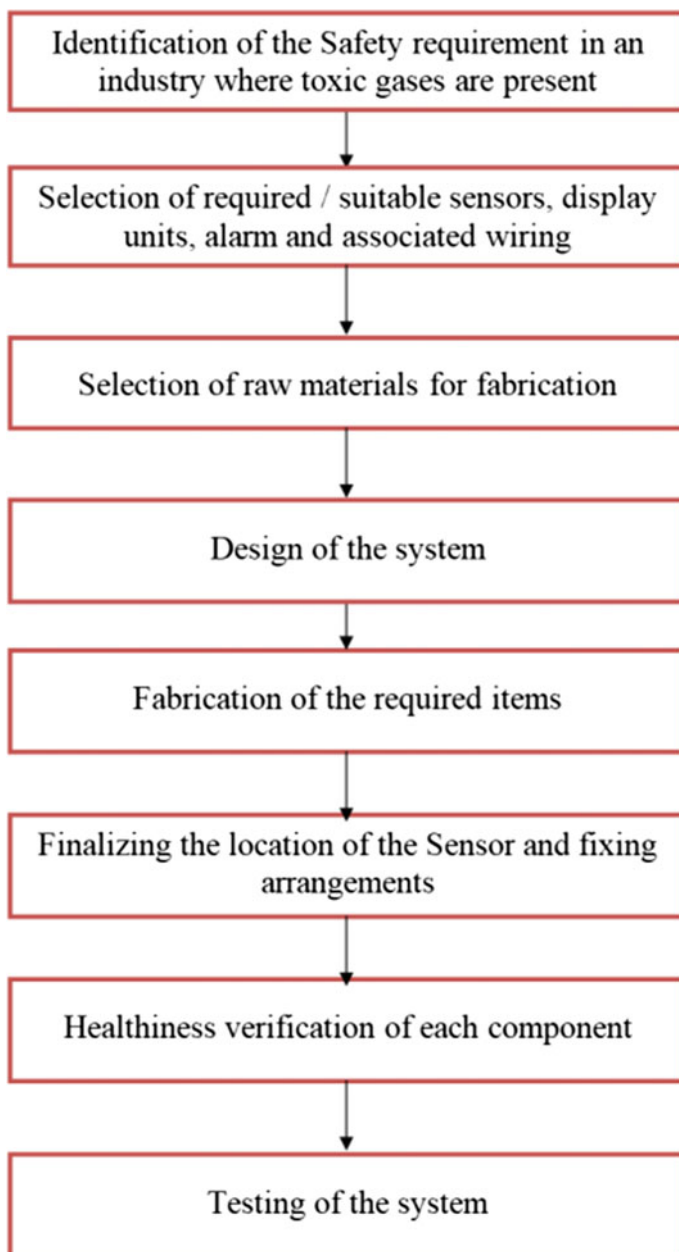
Air delivery capacity of exhaust fan:  $900 \text{ m}^3/\text{h}$

Time required for replacing the gas one time:  $700/900 = 0.77 \text{ h}$

#### 4.1 Hardware Requirements

- Step-down transformer
- Relay and power supply board
- Toxic gas sensor
- Exhaust fan
- Fresh air intake fan
- 2 no's of LEDs
- Alarm sounder





**Fig. 1** Methodology flowchart

## 4.2 Power Supply

To have continuous monitoring safety system, there is a need of power supply and need regular supply without any interruptions. The limit of current and voltages are to be controlled, and needs are to be supplied without much fluctuation.

Some basic components used in power supply:

### Transformers

Transformers are used to increase or decrease the voltage by a proper winding system. The performance of the transformer is decided by the quality wire used for winding and the number of windings.

In a transformer, both terminations have two wires at each side of the coil. On the transformer, one side will have three terminals and the other will have two terminals. The one with the three terminals is the wandered down yield of the transformer, and the one with the two terminals is the place that the data voltages are to be acclimated.

### Rectifier:

A rectifier is a small unit which is diodes. When two diodes are combined for allowance of light of the path, then there can be a voltage drop of 1.4v. Since every diode has voltages drop of 0.7 V. However, on account of full-wave connect rectifier, there will be a voltage drop of 0.7 V as it was. The voltage controller needs 2 V more than its yield voltage. For the event, we are interfacing 12 V connector for our motivation, and henceforth, we require 14 V according to the yield voltage. Simple circuit of rectifier is shown in Fig. 2.

The yield of the diodes (which goes into the voltage controller) will be more than or vague to 14 V. According to the diode data voltage, the diode voltage in the voltage controller will be 14 V. The voltage drop will be 1.4 V totally, so the proportionate aggregate voltage will be 15.4 V of which 14 V in addition to 1.4 V. So it is ideal to utilize 18-V venture down transformer from 220 V input voltage. In this manner transformer, yield voltage will be of 3.4 V of rough esteem.

### Capacitors:

The capacitors stores electrical energy, and it is released when there is reduction in electrical energy. There are many types of capacitors and need to select the right

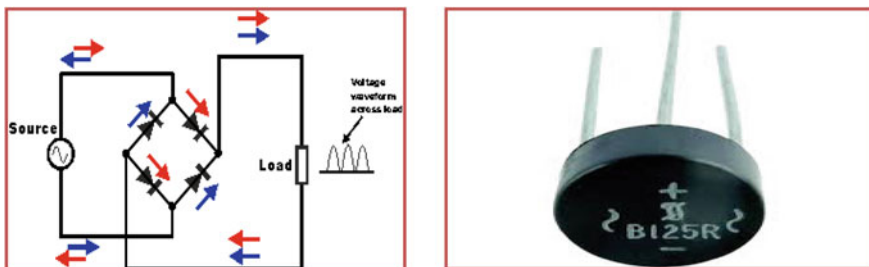


Fig. 2 Rectifier circuit

model based on the requirement. The rectifier is utilized to get throbbing DC voltage which is utilized as a part of the light of the present destiny and from the connector.

### **Voltage Regulators:**

This voltage regulator is used to send the voltage without any fluctuation. The XX speaks to the voltage of which the voltage controller delivers as the yield to the specific gadget. 7805 will deliver and control the yield voltage of 5 voltage and the 7812 will create the yield voltage of 12 voltage.

### **Gas Sensor**

Sensor systems are low cost and suitable for different applications. The sensor is sensitive to flammable gas and smoke to detect without any failure. The smoke sensor is given 5 V to power it. The smoke sensor indicates smoke by the voltage, and it is displayed as output or set alarm. The output is proportional to smoke and vice versa. A potentiometer is provided to adjust the sensitivity of smoke. The SnO<sub>2</sub> sensor is used for the low conductivity, when the air is clean. When smoke exists, an analog output is produced based on the concentration of smoke. The power is given to the heater by VCC and GND from the power supply. The circuit has a variable resistor, and the resistance across the pin depends on the smoke in the air. The resistance is lowered if the current is more and the voltage is increased between the sensor and the load resistor.

Specifications:

- It is wide range of sensitivity to combustible gas
- It has better sensitivity to propane, LPG, and hydrogen gas
- Low cost and better life duration
- Drive circuit is simple.
- Sensor type is semiconductor
- Concentration is between 300 and 10000 ppm (combustible gas)
- Supplied voltage is 5 V

Applications:

- Home safety
- Control the air quality
- Measurement of gas level and set alarm

### **Relay**

This controls the low power supply signal, a relay comes in places and is used to control a circuit. It is also used in places where only one signal is sufficient to control a lot of circuits. The application of relays switch is heated up during the invention of telephones to manage many contacts at a time. They played an important role in switching calls in the telephone exchange center. It is also used in a long-distance telegraphy operation. After the invention of computers, they were also used to perform Boolean and other logical operations in the computational system. The

high-end applications of relays require high power-driven by electric motors and so on.

### **Exhaust and Fresh Air Intake Fan**

In any system, proper ventilation is required to reduce the temperature during the operation. An exhaust ventilation system removes the air and also removed airborne contaminates from the working area. The supply system adds air to workroom to dilute contaminants in the workplace and to lower the contaminant concentrations.

The blades of the exhaust fan are aerodynamically designed, and it can remove the stale air more effectively. The fan sports have a sturdy construction, and it requires minimal maintenance. The body and the blade of the exhaust fan are powder coated, and it ensures that the fan remains rust-free. By installing the right exhaust fan, the working room maintains fresh air and a healthy environment

## **5 Online Publication in SpringerLink**

In this project, gas sensor continuously monitors the concentration of toxic gases/harmful gases present in the controlled surroundings environment. If the concentration of harmful gas goes beyond the threshold value, then automatically relay turns on both fans which will be switched on along with LEDs glow. Designed gas detection leakage system is shown in Fig. 3 which is prepared in 3D software. Gas detection must be placed in proper location. Then, it can easily detect without any failure of system. Experienced person can identify the location to fix the gas detection sensor. Same was modeled and tested in our laboratory which is show in Fig. 4.

Fresh air intake fan is designed with 1000 CFM (cubic feet per minute) capacity, which is meant for flooding the intake of fresh air into the room from the outside atmosphere.

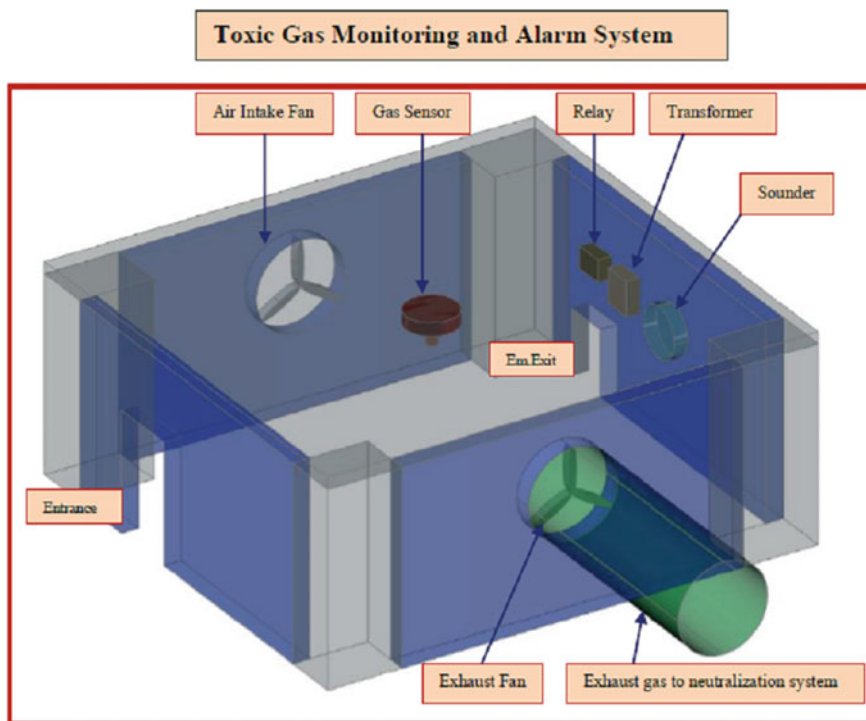
The exhaust fan is designed with 900 CFM, less capacity compare to the air intake fan, which is used for throwing out the toxic gases to the outside from the inside room for preventing the exposure of the working team from the toxic gases.

The toxic gases released from the room through low capacity exhaust fan will be routed through the scrubbing system, in which the toxic gases will be neutralized while passing in the neutralization solution, and then, the fresh air only will be delivered into the outside atmosphere.

Advantages:

- Quick detection and alarming
- Reduces air pollution
- Easy to maintain the system
- Low cost and more efficient

Applications:



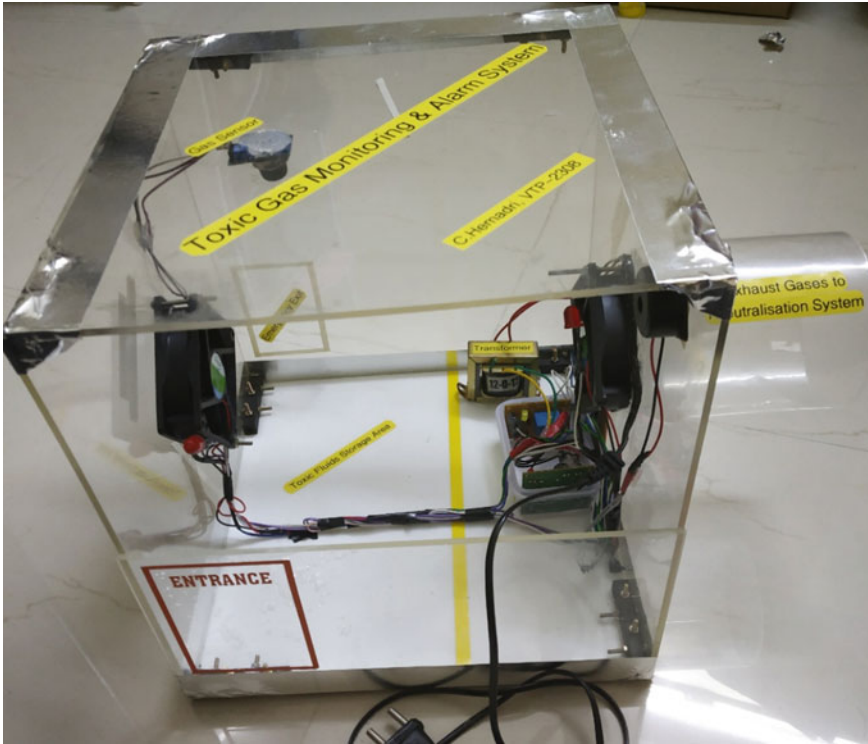
**Fig. 3** Toxic gas monitoring and Alarm system

- Used in industries and in home applications.
- Used in automobile application.
- Used in agriculture pesticides manufacturing plant and other chemical industries.

## 6 Open Conclusions and Future Scope of Work

This report addresses the safeguarding of personnel working in a toxic gas environment, by designing and installing the automatic toxic gas monitoring and alarming system using a highly reliable gas detection sensor. Hence, usage of toxic gas monitoring and alarming system is very important, efficient, and cost-effective. It is also important to establish and enforce the same system where the team is working with toxic/hazardous gases for preventing any type of eventuality at the work site.

- The system should be equipped with a different types of additional sensors for detecting most of the toxic gases.
- Monitoring system shall be provided with oxygen monitoring sensors also to check the O<sub>2</sub> level in the working area.



**Fig. 4** Practical setup of the safety system

- The system generated alarm/toxic levels shall be obtained remotely using GSM module (IOT based).

## References

1. OSHA Field Safety and Health Manual (2018)
2. NFPA 72: National Fire Alarm Code (2019)
3. IEC 60079-29 Series standards and IEC 62990 Series standards under development, a life safety gas system does more than detect the presence of combustible and toxic gases
4. ANSI/ISA 12.13.01: Gas detectors—Installation & Performance requirements of detectors for gases (2013)
5. BS EN 60079-29-2: Explosive Atmospheres. Gas Detectors, Selection, Installation, Use and Maintenance of Detectors for Flammable Gases and Oxygen
6. BS EN 60079-10-1 Explosive Atmospheres. Classification of Areas. Explosive Gas Atmospheres (2015)
7. BS EN 50402:2005 + A1:2008: Electrical Apparatus for the Detection and Measurement of Combustible or Toxic Gases or Vapours or of Oxygen (2008)

# Predictive Modeling of Surface Roughness for Turning of Al-6061 Using Artificial Neural Network Model



S. Rahul Rathnam, K. R. Anandh Natarajan, S. Gautam Kumar, N. Gobinath, and K. Rajan

**Abstract** Achieving outstanding quality with minimum wastage has been an ever-standing thumb rule in manufacturing industry, for which many statistical approaches are continuously examined. This work intends to study the influence of input variables over the output parameters such as surface roughness, cutting force, and temperature on turned sample of aluminum. Four different values for each input variables such as 510–900 rpm (Spindle speed), 0.135–0.28 mm/rev (Feed rate), 0.2–1.7 mm (Depth of cut) are chosen for the present experimental investigation. Artificial intelligence is implemented in the present work and a predictive neural network model is developed using the experimental results obtained from the full factorial study. A model of 3-5-3-1 configuration is created and trained with the experimental data, which is found to have a mean absolute percentage error (MAPE) of 5.24% and mean squared error (MSE) as 0.035, for the test data. Also, the developed model is compared to a multiple regression model and found to be more accurate in predicting the surface roughness of the turned sample. Moreover, the surface roughness is found to be predominantly influenced by feed rate followed by depth of cut and cutting speed.

**Keywords** Turning · ANN · Machine learning · Surface roughness · Cutting force

---

S. Rahul Rathnam · K. R. Anandh Natarajan · S. Gautam Kumar · N. Gobinath (✉)  
School of Mechanical and Building Sciences, VIT Chennai, Chennai 600063, India  
e-mail: [Gobinath.n@vit.ac.in](mailto:Gobinath.n@vit.ac.in)

S. Rahul Rathnam  
e-mail: [rahul.rathnam@gmail.com](mailto:rahul.rathnam@gmail.com)

K. R. Anandh Natarajan  
e-mail: [anandhnatarajankr@gmail.com](mailto:anandhnatarajankr@gmail.com)

S. Gautam Kumar  
e-mail: [gautamkumar30897@gmail.com](mailto:gautamkumar30897@gmail.com)

K. Rajan  
Department of Computer Engineering, Muthiah Polytechnic College, Chidambaram 608002, India  
e-mail: [mptcse@gmail.com](mailto:mptcse@gmail.com)

## Nomenclature

V	Spindle speed
D, DoC	Depth of Cut
DoF	Degree of Freedom
F	Feed rate
AISI	American Iron and Steel Institute
ANN	Artificial neural network
ANOVA	Analysis of variance
APE	Absolute percentage error
MRR	Material removal rate
MAPE	Mean absolute percentage error
MSE	Mean squared error
MS	Mean square
$P$	Results probability under null hypothesis
$R_a$	Surface roughness
SS	Sum of squares

## 1 Introduction

Ever since machining is an irreplaceable process in manufacturing industry and hence faced huge developments among various machining operations, in the past decades. Lathe operation is the most widely used primitive machining process which is in practice in several industries to achieve the finished components through the removal of unwanted material from the raw material. Computer numerical controls (CNC's) opened up the pathway for precise and good quality machining components with more accurate dimensions, in automated lathe. Surface roughness, the key factor that challenges the quality of assembly of the parts machined from a lathe, plays a vital role in determining the types of fit and hence decides the operational reliability of the functional parts. It is highly influenced by the cutting force that generates during machining of parts from a single point cutting tool and it is also happened to be deciding factor of the product quality in terms of fatigue life improvement, corrosion resistance, and even for the aesthetics [1]. In further, the cutting force controls tool wear and specific power consumption of the machining operation. Additionally, the parameters associated to machining such as the speed, depth of cut, cutting feed rate, nose radius (tool), lubrication rate, machine vibrations, tool wear also contribute for the accuracy of finished parts [2]. Many studies are reported in understanding the extent of influence of such input parameters on the output characteristics of machining parts [3–5] and various models are developed to choose the input parameters for better operating conditions [6–8]. Makadia and Nanavati [3], in their three-level full factorial experiments on AISI 410 steel, selected the cutting speed, feed, depth of cut, and nose radius as the input parameters. The authors observed the level of influence



of each input parameter on the roughness of the workpiece and is arranged in their decreasing priority as follows, feed rate > nose radius (tool) > speed > depth of cut. Similar results are reported by Qehaja et al. [4], who studied the effects of feed rate, nose radius, and cutting time on surface roughness in dry turning with coated tungsten carbide inserts. Also, the authors presented a regression model to find the optimal selection of the input parameters. Deepak and Rajendra [5] performed turning operations on Al-6061 across three-levels of cutting speed, feed rate, and depth of cut and revealed that an increase in the input parameters' magnitude resulted drastic increase of the surface roughness of the aluminum alloy. Furthermore, the effect of depth of cut was seemed to be highly significant compared to the feed rate. Machining temperature, apart from the aforementioned parameters, is also considered to be a potential parameter in respect of a viable machining process.

Arefi et al. [6] developed a procedure using Taguchi method to obtain a combination of optimum process parameters for achieving minimum surface roughness and machining temperature. Roy et al. [7], based on the turning experiments using tungsten carbide inserts on aluminum alloys, have confirmed that the depth of cut is highly significant on the aluminum surface roughness while the feed rate was found to be the least significant, in their work. Balasubramaniam et al. [8] studied the effects of input parameters such as electric current, pulse in time, flushing pressure on the material removal rate (MRR), electrode wear rate (EWR) and circularity (CIR) of copper, brass, and tungsten electrodes in an EDM process. The authors developed a model in artificial neural network (ANN) using front feed-forward back-propagation method to formulate the relationship among the input parameters and output characteristics. In another study, Mikolajczyk et al. [9] utilized ANN approach to predict the tool life in a CNC end-milling process and found that their model is closely matched with the experimental results. Mahdavinejad et al. [10] conducted studies toward improving the capability of ANN models and found that the network structure, number of training and testing data, network algorithm and eventually, transfer, training, learning, and performance functions are of greater importance in minimizing the deviations of ANN models from experimental data. Muthukrishnan and Davim [11] developed a model for optimizing the machining parameters using ANN and analysis of variance (ANOVA). ANOVA was used to ascertain the percentage of influence of each input parameter over the output results and the back-propagation (BP) neural network configuration 3-10-1 with 18 patterns was used to train the model. Yet, in a different study, Palanisamy et al. [12] used genetic algorithm (GA) to develop the prediction model for end-milling operations.

From the comprehensive survey of the literature, it is observed that there are limited works on the prediction models using ANN approach. There are many scopes to build an appropriate model through full factorial experiments and to train and test the complete set of experimental data with the model, as well. The present work aims at creating prediction models using ANN and multiple regression (MR) through the experimentally measured roughness values of Al-6061 in a turning operation, and to identify the effective model that gives more reliable results when compared to the experimental data. Three machining parameters (Speed, Feed rate, Depth of cut) with four different values for each parameter are set as the input. The MR model has

been tested using ANOVA. A feed-forward back-propagation ANN model is built and tested with complete set of data. The models are cross-verified for their accuracy and the results are reported.

## 2 Experimental Work

The turning experiments are conducted on a lathe “ESTEAMETM—356” located at our laboratory premises and the associated data are collected for aluminum material (Al-6061) of billet size 16 mm ( $\Phi$ )  $\times$  100 mm (L) in dry machining condition. Throughout the experiments, carbide insert (TNMG160404) is used as the cutting tool. A total of 64 experiments is performed following a full-factorial design of experiment. The selected spindle speeds between 510 and 900 rpm (step ratio = 1.2), feed rates, and depth of cuts for the present experimental work are shown in Table 1. Cutting force, temperature, and surface roughness are the output parameters of interest that are measured from the present work.

The cutting forces are measured during the experiments along the coordinate axes (x, y & z) using a cutting force dynamometer by connecting it to the tool holder, as shown in Fig. 1. At any specific input condition, the total cutting force is the resultant of the three components measured along the coordinate axes. High temperatures developed during machining are detrimental to the tool and also to the job which in further leads to rapid tool wear, built-up edge formation in the tool. In further,

**Table 1** Input values—speed, feed, and depth of cut

Spindle speed (rpm)	Feed rate (mm/rev)	Depth of cut (mm)
510	0.135	0.2
585	0.177	0.7
770	0.233	1.2
900	0.280	1.7



**Fig. 1** Cutting force dynamometer readings

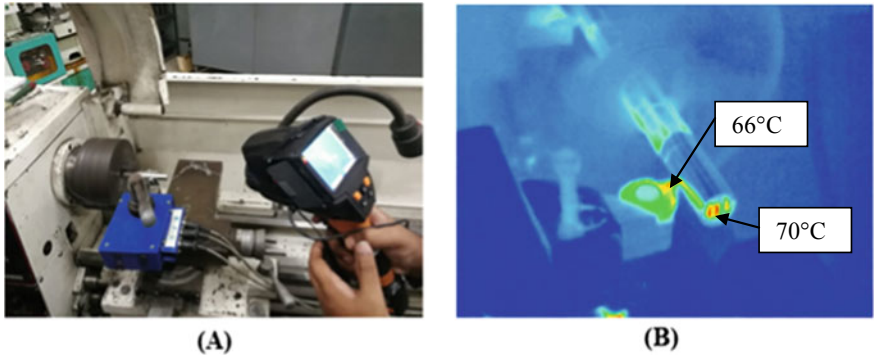


Fig. 2 a IR-Thermal imager. b Thermogram from the imager

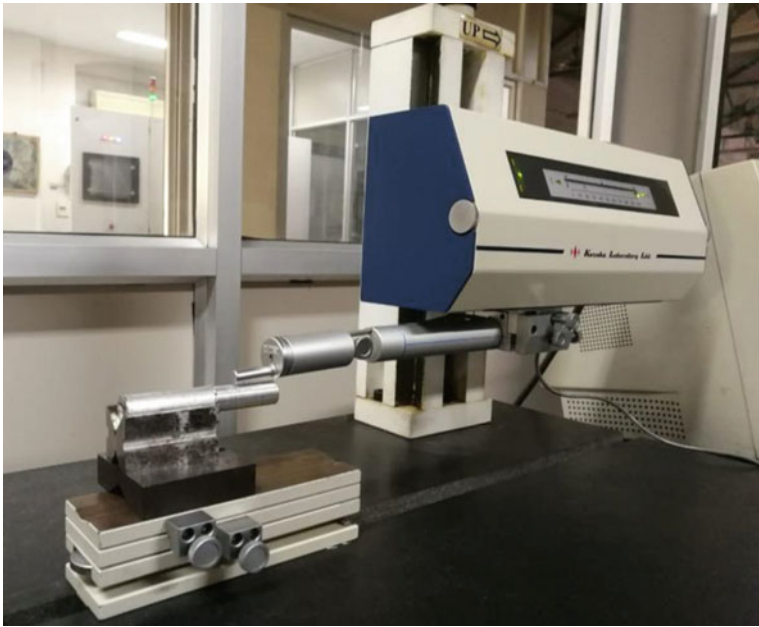
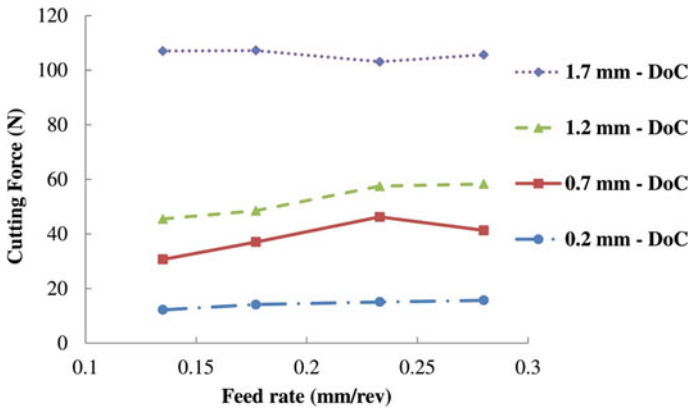


Fig. 3 Surface roughness tester (Contact type)

it leads to dimensional inaccuracy and surface damages. Henceforth, studying the trend of temperature variation at the cutting point is included in the present work. An infra-red (IR) thermal imager with an accuracy of  $\pm 0.1$  °C, as shown in Fig. 2, is used to capture the temperature at the contact point between the tool and the job during machining. The average surface roughness ( $R_a$ ) value of the machined surface along the cutting tool direction is measured using a contact-type surface roughness



**Fig. 4** Variation of cutting force at 510 rpm

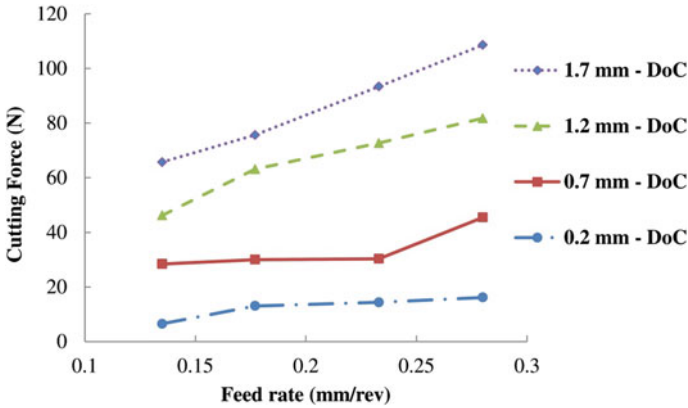
tester SE3500 as shown in Fig. 3, with 0.8 mm cut-off length and 5.6 mm sample length.

### 3 Results and Discussions—Experiments

#### 3.1 Cutting Force

In any machining process, the cutting force has the direct role in controlling the specific power consumption and also plays a vital role in maintaining the system's stability. As a primitive measure of having control over the whole experiments, the cutting forces that generate at the machining juncture are monitored continuously and the peak values observed from the dynamometer plots are taken for comparison. Figure 4 shows the variation of cutting force (Resultant) magnitude with variations in feed rate and depth of cut, measured at the spindle speed of 510 rpm.

It is witnessed from Fig. 4 that increasing the feed rate at any constant depth of cut would result in a marginal increase in the cutting force magnitude. An increase in feed rate from 0.135 to 0.280 mm/rev caused a maximum of 28% increase in cutting force at 1.2 mm depth of cut. So far, the cutting force does not show more than 10% increase in its value at the remaining depth of cuts in the present work. However, it is significantly increased with increase in depth of cut value. At any constant feed rate, raising the depth of cut value from 0.2 to 1.2 mm results in 2.7 times increment in the cutting force. Furthermore, raising the depth of cut from 1.2 to 1.7 mm, a tremendous increase of 135 and 81% in cutting force is observed at the feed rates 0.135 and 0.280 mm/rev, respectively. The drastic increase in cutting force due to the small increase in depth of cut from 1.2 to 1.7 mm at all feed rates would result in huge increase in power consumption, which is not justifiable for the case.



**Fig. 5** Variation of cutting force at 900 rpm

Similar trend is observed for cutting force values at the spindle speed of 900 rpm, as shown in Fig. 5. Yet, at low feed rate the rise in cutting force is gradual while at higher feed rates, the cutting force steeply increases with increase in depth of cut values. Also, it is evidenced together from Figs. 4 and 5 that increasing the spindle speed reduces the cutting force values at all feed rates with any depth of cut values. These trends are cross-verified with the established results and found matching.

### 3.2 Temperature

The temperature that is generated once the metal-metal contact is established during the experiment, if left untreated, will lead to a poor surface finish and ultimately affects the quality of the machined part. In the process of optimizing the machining parameters to achieve the best possible output characteristics for the machining parts, machining temperature is also considered in the current work and the results are presented in this section. Figure 6 shows the influence of feed rates on the machining temperature of Al-6061 with carbide tool, at different depth of cuts. The machining temperature is much affected by the change in depth of cuts rather than that of the feed rates. At any constant depth of cut, the machining temperature increase with increase in the feed rate is only marginal. The spindle speed can also contribute to increase the machining temperature. As given in Fig. 7, increase in spindle speed considerably increases the machining temperature but only at higher depth of cuts. At low depth of cut (0.2 mm in the present study), the temperature remains unchanged even at higher speeds which shows the supremacy of depth of cut on the machining temperature generation. Since the current experiments are happened to be under dry conditions, no coolants are involved in order to examine the temperature values. The detrimental effects of temperature could be minimized using high pressure coolants which could improve the surface finish [13].

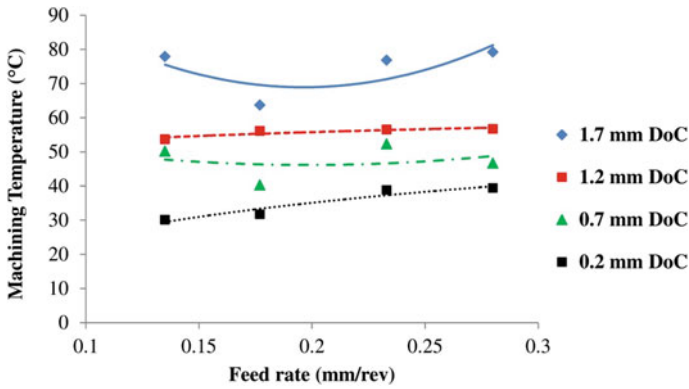


Fig. 6 Effect of feed rate on machining temperature at various DoC's

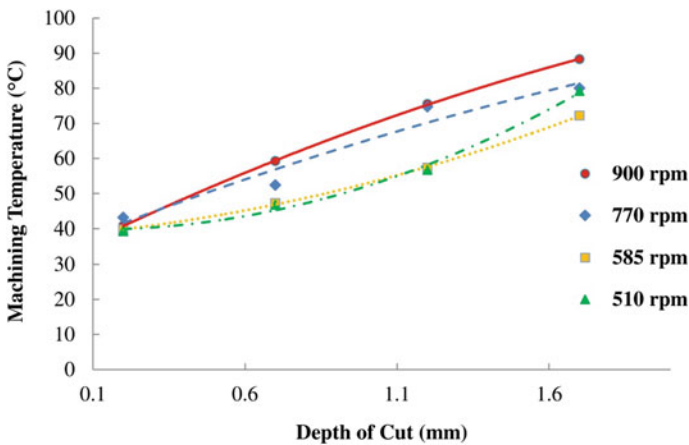
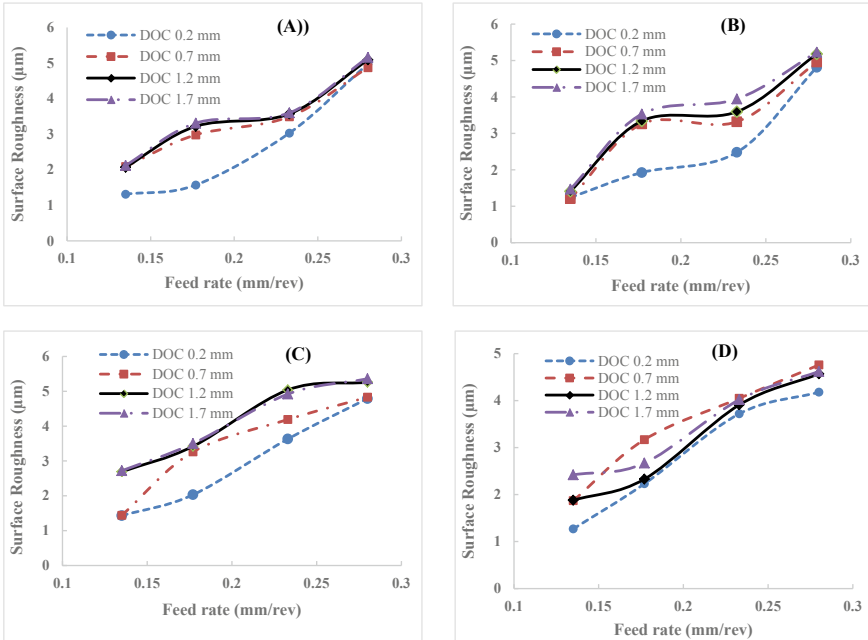


Fig. 7 Effect of depth of cut on machining temperature at various rpm

### 3.3 Surface Roughness

In any conventional machining processes, the accurate surface will be achieved at a higher machining cost because of its poor material removal rate at lower feed rates. In order to feed the details of the influence of feed rates on the surface roughness at various spindle speeds in ANN, experiments are conducted and the trend in the roughness variations are cross verified. Figure 8 shows the surface roughness variations with feed rates at various spindle speeds.

As witnessed from the graphs shown in Fig. 8, increase in surface roughness due to increase in depth of cut values is less predominant than the increase due the increase in feed rate values. Little anomalies in the trend as observed in Fig. 8 can be attributed to certain experimental conditions such as chip formation.



**Fig. 8** Trend of variations in surface roughness with feed rates at **a** 510 rpm, **b** 585 rpm, **c** 770 rpm, **d** 900 rpm

## 4 Prediction Models

### 4.1 Multiple Regression

In general, multiple regression is used to understand the relationship among the continuous dependent variable and two or more independent/predictor variables [14]. In order to account for a more realistic model, to determine the surface roughness, a regression equation of second order is selected for the present work as given by Eq. (1).

$$R_a = b_0 + b_1V + b_2F + b_3D + b_4V * V + b_5V * F + b_6F * F + b_7F * D + b_8D * V + b_9D * D + b_{10}V * F * D \quad (1)$$

where,  $R_a$ ,  $V$ ,  $F$ ,  $D$ , and  $b$  stand for the surface roughness, speed, feed, depth of cut, and the corresponding coefficients, respectively. The extent of influence of each predictor variable on the dependent variable is determined using analysis of variance (ANOVA).

## 4.2 ANN

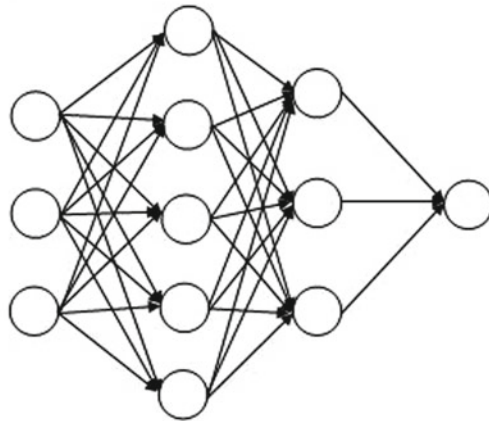
A feed-forward artificial neural network with back-propagation is used for creating the prediction model using the experimental data in MATLAB. All the data are normalized to ensure no influence of the input parameters' scale over the training of the model. A feed-forward-back-propagation algorithm consists of two passes. All the weights are fixed in the forward pass and the weights are updated during the backward pass based on the difference arising between the actual output and the desired output of the network. These weights, when updated continuously, result in a model where the network output and desired output are close enough to be accepted.

Levenberg-Marquardt algorithm was selected for training in order to minimize the computational effort required. In order to improve the model's performance, two hidden layers are selected. Through trial and error, the best results are found to be obtained with 3-5-3-1 network configuration, wherein each number represents the neuron numbers in the following layers in order; input layer, first hidden layer, second hidden layer, and output layer (Fig. 9). Since manual selection of training, validation and testing datasets might lead to a bias in the model's performance, ten-fold cross-validation technique is used to facilitate the training, validation, and testing of all possible combinations of data.

Mean absolute percentage error (MAPE) and mean squared error (MSE) are used to evaluate the performance of the created model.

Fig. 9 ANN configuration

*Input Layer      Hidden Layers 1 & 2      Output Layer*





## 5 Model Validation

The prediction models created using multiple regression technique and ANN method are verified for its accuracy with the experimental data and the results are reported in this section.

### 5.1 Multiple Regression Model

The second-order equation to predict the surface roughness value from the input machining parameters has been developed through multiple regression technique using the experimental data, which is given by Eq. (2).

$$\begin{aligned}
 R_a = & -7.08497 + 0.0127595V + 26.5402F + 1.84262D - 8.12288e - 006V * V \\
 & -0.00330362V * F - 2.67842F * F - 1.0031F * D \\
 & + 6.9255e - 005D * V - 0.44375D * D - 0.00197434V * F * D \quad (2)
 \end{aligned}$$

The feed rate is the most dominant factor, followed by depth of cut and then spindle speed. In addition, the interaction between feed rate and depth of cut is found to be more influential as compared to interactions between any two other predictor variables. The adjusted  $R^2$  value is 89.15%. The predicted  $R^2$  value (87.15%) is close to the general  $R^2$  value (90.87%). This proves that the model is not over-fitted. The results of ANOVA obtained from Minitab software are tabulated as shown in Table 3.

The overall  $P$ -value obtained from the  $F$ -test is found to be very less ( $<0.000001$ ), which implies that the predictor variables have an influence on the dependent variable much larger than what could be expected by chance. Therefore, the model is significant. In general, any null hypothesis from the  $F$ -test can be neglected since the  $P$ -value is less than 0.05, for the present study.

### 5.2 ANN Model

An ANN model is created in MATLAB with the input parameters mentioned in Table 2, and the coefficient of correlation ( $R$ ) obtained for training, validation, and testing from the created ANN model is shown in Fig. 10. The finalized model has the MAPE value of 5.24% and MSE of 0.035, which is found to be acceptable (Table 3).

**Table 2** Training parameters of the ANN model

Parameter	Value
Number of layers	4
Number of neurons in input layer	3
Number of neurons in the two hidden layers	5 & 3
Number of neurons in output layer	1
Activation function	Hyperbolic tangent sigmoid
Normalization range	-1 to +1
Learning rate	0.05
Momentum constant	0.95
Maximum number of iterations	10,000
Training ratio	0.8
Validation ratio	0.1
Testing ratio	0.1

### 5.3 Model Comparison

The prediction models developed using multiple regression technique and ANN methods are compared using their performance metrics in order to identify the accuracy of the methods. Out of the two models, ANN is found to be the best method which resulted high coefficient of determination while estimating the surface roughness, for the given input machining parameters as shown in Table 4. Comparison of experimental data and predictive model outputs is provided in the appendix.

## 6 Conclusions

The results obtained from the full factorial design of experiments in a turning operation using aluminum alloy (Al-6061) are as given below,

- The experimental results showed major trends between the input parameters and output characteristics like surface roughness, cutting force, and temperature.
  - a. Feed rate influences the surface roughness predominantly, followed by depth of cut and cutting speed.
  - b. Cutting force is found to be profoundly influenced by feed rate and depth of cut, while the effect of spindle speed is less.
  - c. The influence on temperature is found to be similar to that of cutting force with feed rate and depth of cut being significant influences.

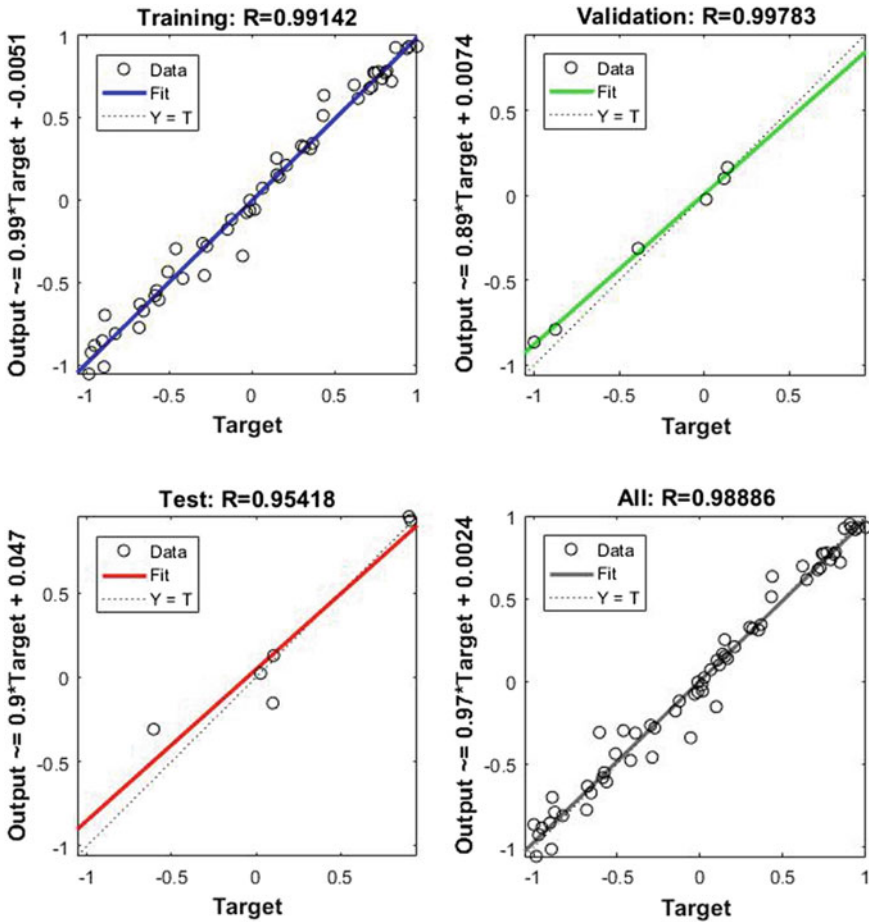


Fig. 10 Coefficient of correlation from ANN method

- The predictive model created using ANN is found to be more accurate than the one created using multiple regression.
- The model was able to predict the surface roughness values for any combination of input machining parameters between the extremums of the training range with a MAPE of 5.24%.
- The model could further be used in order to determine the optimal input settings to achieve the desired surface roughness.

**Table 3** Results of *F*-test

Source	DoF	Sequential SS	Adjusted SS	Adjusted MS	<i>P</i> -value
Regression	10	93.067	93.0669	9.30669	0.000000
V	1	0.151	0.9017	0.90174	0.027870
F	1	84.432	0.7272	0.72721	0.047315
D	1	6.250	0.1997	0.19974	0.292038
V*V	1	0.925	0.9247	0.92472	0.026035
F*F	1	0.002	0.0023	0.00229	0.909630
D*D	1	0.788	0.7877	0.78766	0.039290
V*F	1	0.122	0.0127	0.01275	0.789091
F*D	1	0.339	0.0028	0.00285	0.899354
D*V	1	0.054	0.0001	0.00015	0.976891
V*F*D	1	0.006	0.0055	0.00553	0.860103
Error	53	9.346	9.3464	0.17635	
Total	63	102.413			

**Table 4** Comparison of model metrics

Model	Mean squared error	Mean absolute percentage error	Coefficient of determination ( )
Multiple regression	0.146037	11.76768	0.8915
ANN	0.035515	5.238133	0.97784

## Appendix

Experimental data Vs predictive model outputs (Multiple regression and ANN)

S.No.	Inputs			Output	Multiple regression			ANN	
	<i>V</i>	<i>F</i>	<i>D</i>		Measured <i>R<sub>a</sub></i>	Predicted <i>R<sub>a</sub></i>	APE (%)	Predicted <i>R<sub>a</sub></i>	APE (%)
1	510	0.135	0.2	1.31	0.92	29.78	1.45	10.82	
2	510	0.135	0.7	2.09	1.52	27.11	2.14	2.52	
3	510	0.135	1.2	2.07	1.91	7.96	2.08	0.44	
4	510	0.135	1.7	2.12	2.07	2.59	2.03	4.38	
5	510	0.177	0.2	1.57	1.91	21.77	1.60	2.05	
6	510	0.177	0.7	2.98	2.47	17.01	2.92	2.16	
7	510	0.177	1.2	3.22	2.81	12.65	3.13	2.94	
8	510	0.177	1.7	3.31	2.93	11.47	3.24	2.14	
9	510	0.233	0.2	3.03	3.22	6.26	3.04	0.32	

(continued)

(continued)

S.No.	Inputs			Output	Multiple regression		ANN	
	V	F	D	Measured $R_a$	Predicted $R_a$	APE (%)	Predicted $R_a$	APE (%)
10	510	0.233	0.7	3.49	3.72	6.73	2.97	14.96
11	510	0.233	1.2	3.57	4.01	12.27	3.63	1.66
12	510	0.233	1.7	3.60	4.07	13.04	3.60	0.02
13	510	0.28	0.2	4.98	4.30	13.57	4.90	1.52
14	510	0.28	0.7	4.87	4.76	2.21	4.90	0.57
15	510	0.28	1.2	5.09	5.00	1.80	5.20	2.20
16	510	0.28	1.7	5.16	5.01	2.86	5.26	1.91
17	585	0.135	0.2	1.24	1.17	5.38	1.09	11.77
18	585	0.135	0.7	1.21	1.77	46.24	1.49	23.27
19	585	0.135	1.2	1.41	2.14	52.05	1.51	7.18
20	585	0.135	1.7	1.47	2.30	56.21	1.65	12.04
21	585	0.177	0.2	1.93	2.15	11.88	1.89	1.94
22	585	0.177	0.7	3.26	2.70	17.04	3.15	3.32
23	585	0.177	1.2	3.34	3.03	9.18	3.33	0.23
24	585	0.177	1.7	3.53	3.14	11.03	3.49	1.06
25	585	0.233	0.2	2.48	3.45	38.95	2.64	6.38
26	585	0.233	0.7	3.32	3.94	18.57	3.16	4.72
27	585	0.233	1.2	3.60	4.21	16.97	3.81	5.95
28	585	0.233	1.7	3.95	4.25	7.77	3.95	0.07
29	585	0.28	0.2	4.82	4.52	6.18	4.89	1.53
30	585	0.28	0.7	4.96	4.96	0.05	4.88	1.64
31	585	0.28	1.2	5.18	5.18	0.09	5.21	0.63
32	585	0.28	1.7	5.23	5.17	1.12	5.19	0.83
33	770	0.135	0.2	1.43	1.41	1.55	1.18	17.29
34	770	0.135	0.7	1.44	1.99	37.90	1.83	27.36
35	770	0.135	1.2	2.69	2.34	12.94	2.33	13.25
36	770	0.135	1.7	2.72	2.48	8.97	2.70	0.63
37	770	0.177	0.2	2.03	2.36	16.22	2.65	30.36
38	770	0.177	0.7	3.26	2.88	11.52	3.28	0.55
39	770	0.177	1.2	3.42	3.19	6.80	3.43	0.38
40	770	0.177	1.7	3.50	3.27	6.61	3.55	1.46
41	770	0.233	0.2	3.63	3.61	0.46	3.57	1.53
42	770	0.233	0.7	4.19	4.07	2.92	4.60	9.81
43	770	0.233	1.2	5.04	4.30	14.68	4.78	5.21
44	770	0.233	1.7	4.92	4.31	12.38	4.81	2.21
45	770	0.28	0.2	4.79	4.65	2.86	4.71	1.71

(continued)

(continued)

46	770	0.28	0.7	4.83	5.05	4.51	4.89	1.19
47	770	0.28	1.2	5.26	5.22	0.74	5.21	0.86
48	770	0.28	1.7	5.36	5.17	3.50	5.22	2.70
49	900	0.135	0.2	1.27	1.24	2.37	1.36	7.44
50	900	0.135	0.7	1.87	1.81	3.47	1.68	10.32
51	900	0.135	1.2	1.88	2.15	14.27	1.97	4.89
52	900	0.135	1.7	2.42	2.27	6.21	2.30	5.15
53	900	0.177	0.2	2.23	2.17	2.63	2.38	6.71
54	900	0.177	0.7	3.17	2.68	15.52	2.58	18.63
55	900	0.177	1.2	2.33	2.96	27.17	2.67	14.59
56	900	0.177	1.7	2.67	3.03	13.33	2.74	2.50
57	900	0.233	0.2	3.72	3.40	8.64	3.72	0.03
58	900	0.233	0.7	4.05	3.83	5.50	4.00	1.32
59	900	0.233	1.2	3.91	4.03	3.18	3.96	1.39
60	900	0.233	1.7	4.02	4.02	0.01	3.93	2.25
61	900	0.28	0.2	4.18	4.42	5.63	4.35	3.97
62	900	0.28	0.7	4.76	4.78	0.40	4.68	1.58
63	900	0.28	1.2	4.57	4.92	7.67	4.73	3.51
64	900	0.28	1.7	4.62	4.84	4.77	4.56	1.27

## References

1. Rao CJ, Nageswara Rao D, Srihari P (2013) Influence of cutting parameters on cutting force and surface finish in turning operation. *Procedia Eng* 64:1405–1415
2. Ratnam MM (2017) Factors affecting surface roughness in finish turning. *Compr Mater Finish* 1:1–25 (Elsevier Publications)
3. Makadia AJ, Nanavati JI (2013) Optimisation of machining parameters for turning operations based on response surface methodology. *Measurement* 46(4):1521–1529
4. Qehaja N, Jakupi K, Bunjaku A, Bruçi M, Osmani H (2014) Effect of machining parameters and machining time on surface roughness in dry turning process. In: 25th DAAAM international symposium on intelligent manufacturing and automation, Vienna, Austria. doi:10.1016/j.proeng.2015.01.351
5. Deepak D, Rajendra B (2016) Optimization of machining parameters for turning of Al6061 using robust design principle to minimize the surface roughness. *Procedia Technol* 24:372–378
6. Arefia GA, Dasa R, Sahooa AK, Routaraa BC, Nanda BK (2017) A study on the effect of machining parameters in turning of lead alloy. *Mater Today: Proc* 4(8):7562–7572
7. P. Roy, S.K. Sarangi, A. Ghosh, A.K. Chattopadhyay, Machinability study of pure aluminum and Al-12% Si alloys against uncoated and coated carbide inserts, *International Journal of Refractory Metals and Hard Materials*, 27, 535–544

8. Balasubramaniam V, Baskar N, Narayanan CS (2014) Optimization of electrical discharge machining parameters using artificial neural network with different electrodes. In: 5th international & 26th all India manufacturing technology, design and research conference, 2014, Assam, India
9. Mikolajczyk T, Nowicki K, Bustillo A, Pimenov DY (2018) Predicting tool life in turning operations using neural networks and image processing. *Mech Syst Signal Process* 104:503–513
10. Mahdavinejad RA, Khani N, Fakhrabadi MMS (2012) Optimization of milling parameters using artificial neural network and artificial immune system. *J Mech Sci Technol* 26(12):4097–4104
11. Muthukrishnan N, Davim JP (2009) Optimization of machining parameters of Al/SiC-MMC with ANOVA and ANN analysis. *J Mater Process Technol* 209(1):225–232
12. Palanisamy P, Rajendran I, Shanmugasundaram S (2006) Optimization of machining parameters using genetic algorithm and experimental validation for end-milling operations. *Int J Adv Manuf Technol* 32(7–8):644–655
13. Kaminski J, Alvelid B (2010) Temperature reduction in the cutting zone in water-jet assisted turning. *Int J Mach Tools Manuf* 52:925–932
14. Asiltürk İlhan, Çunkas Mehmet (2011) Modeling and prediction of surface roughness in turning operations using artificial neural network and multiple regression method. *Expert Syst Appl* 38:5826–5832

# Dynamic Supporting Wheels for Two-Wheeler Stability



V. Deepan, P. D. Jeyakumar, and S. Sreenath

**Abstract** Two wheelers are cheap and most efficient way of transportation; however, it still requires a rider (human) to balance a vehicle at low speeds and traffic conditions to complete the process of moving from point to point. Although a bike is a relative advantage, it still possesses a greater threat in form of accidents. Newspapers in daily basis report such motorcycle accident like skidding to be a major spoiler of a much-enjoyed mode of travel. It requires great deal of physical strength. Consider an aged person who is suffering from diabetes requires heavy relaxation for a duration after prolonged riding, thereby causing a great deal of fatigue. Therefore, it is necessary to bring about modifications to the existing vehicle because they make the riding a lot safer under low speed travel on dry sand surfaces which are common on Indian roads. The motorcycle by itself is self-balancing using their side legs at low speeds and traffics thereby facing many problems like joint pain, fracture, in the worst cases even ligament fracture, etc. The end result is about bringing up the supporting wheel concept on two wheelers is that the two-wheeler would balance itself and can be stabilized against any impact as well as zero velocity equally. Increased maintenance as well as the reduction in fuel economy in four wheels are on the ground all the time and also increases confidence in riding the vehicle entirely for a long period of time. Also, it would not demand much of leg reflexes to act upon the road or the brake foot pedal.

**Keywords** Self-balancing · Supporting wheels · Stability · Dynamic balancing

---

V. Deepan (✉) · S. Sreenath

Department of Automobile Engineering, B.S. Abdur Rahman Crescent Institute of Science and Technology, Chennai, India

e-mail: [vijayandeepan@gmail.com](mailto:vijayandeepan@gmail.com)

P. D. Jeyakumar

Department of Mechanical Engineering, B.S. Abdur Rahman Crescent Institute of Science and Technology, Chennai, India



# 1 Introduction

Two-wheeler vehicles are an essential part of transportation which is widely preferred in all countries for dynamic abilities as well as performance wise aspect. However, on one hand the fact which makes it a convenient ride, the other hand it possesses a lot of danger, and it has all possible chances to skid from its course of slowing down at traffic, while cornering at turns, while riding in unmetaled road makes the rider prone to injuries and sometimes even fatality [1]. The total factor of stability is totally dependent upon the rider, and any sort of irregularity in the riding position or the angle of lean can lead to chances of topple.

It constantly needs a rider to balance it at low speed and traffic. It is very difficult one for aged person to balancing at low speed, speed breakers, uneven road surface sometimes they a facing body, and joint pain due to balance through legs. It also affects disabled people to be active or mobile outside their wheelchair [2]. Cases of two-wheeler turning-over and skidding are an everyday case due to mismanagement of handling and efforts to secure it [3]. So as an aim to reduce efforts and increase comfort of riding in overall basis, supporting wheels for a two-wheeler provide stability at low speeds [4].

Reference [3] Balance through permanent supports would spoil the geometry of the design the motorcycle was created for primarily and would also add weight to the frame whereby spoiling the dynamics of the vehicle. Supporting wheels for a two-wheeler to provide stability at low speeds under the influence of signals from Arduino which is connected to the sensor connected to the wheels would monitor the rpm of the support that should retract under thereby making it temporary support for the whole system and hence canceling the chances of skid [5]. It also affects disabled people to be active or mobile outside their wheelchair [2]. Cases of two-wheeler turning-over and skidding are an everyday case due to mismanagement of handling and efforts to secure it [3]. So as an aim to reduce efforts and increase comfort of riding in overall basis, supporting wheels for a two-wheeler provide stability at low speeds [4].

The supporting wheel concept on two wheelers is that the two-wheeler would balance itself and can be stabilized against any impact and in zero velocity as well [6]. Increased maintenance as well as the reduction in fuel economy in four wheels are on the ground all the time. This idea proposal puts the safety and fuel economy issue to rest and at the same time not spoil the dynamics of the look of the motorcycle to any large extent. Using DC motor, Arduino board and proximity sensor controls the to and fro motion of the supporting wheel which is programmed through the PC integral development environment (IDE). Initially the Arduino board is programmed for the required system, i.e., the supporting wheels should be lowered to ground if and only if the vehicle velocity goes below 20 km/h and the same way the supporting wheels should be brought back to its original position when the vehicle velocity goes above 20 km/h or else the dynamics is spoiled [1].

Reference [7] The supporting wheels provide stability and also quite good ergonomic for the beginners who ride with fear of meeting with accident also well as

for handicapped [8], while the gyroscopic effect that has been mounted in most bike designs is to allow front wheel steering in the direction of leaning. This phenomenon is named, and the rate an object precesses at is inversely proportional to its spin rate. Therefore, for slower front wheel turns, as the bike leans, the faster it precesses, vice versa.

Reference [2] As the front wheel does by pressure of the tires on the ground, the rear wheel is stopped from precessing, and therefore tends to lean as if it was not turning. Therefore, gyroscopic forces do not give tipping resistance [9]. The precession of the front wheel is too high at low forward speeds, leading to the propensity of an unstable bike to over steer, start leaning the other direction and finally oscillating and dropping over [1]. The precession is typically too weak at high speeds, owing to the propensity of an unstable bike to go under the steering wheel and eventually tip over without ever hitting the upright location. This volatility is very sluggish, at the order of seconds, and is easy to overcome for most riders. So a fast bike could feel secure even though it is not actually self-stable and might fall over if it were unregulated.

## 2 Methodology

Dynamic supporting wheels for two-wheeler stability method on two wheelers is that the two-wheeler would balance itself and can be stabilized against any impact and in zero velocity as well [6]. This idea proposal puts the safety issue to rest and at the same time not spoil the dynamics of the look of the motorcycle to any large extent. Using DC motor, Arduino board and proximity sensor controls the to and fro motion of the supporting wheel is programmed through the PC integral development environment (IDE).

Initially the Arduino board is programmed for the required system, i.e., the supporting wheels should be lowered to ground if and only if the vehicle velocity goes below 20 km/h and the same way the supporting wheels should be brought back to its original position when the vehicle velocity goes above 20 km/h or else the dynamics is spoiled [1]. The complete assembly of supporting wheels is shown in Figs. 1 and 2.

When the vehicle reaches speed greater than 20 km/h, the proximity sensor signals the Arduino board, then motor starts lifting the supporting wheels via lead screw and movable nut as the motor lowers the supporting wheel at less than 20 km/h. The motor rotates the lead screw as it moves to and fro motion of wheels. It consists of monitor display that indicates the speed. Battery is the power source for Arduino circuit and DC motor [10, 11]. With the assistance of connecting wires, the proximity sensor, motor driver, and battery are attached to the Arduino board; the field mechanism in the motor creates a circular field through which the armature rotates. It is consisted of several salient poles [11]. The magneto motive force that the coils generate creates a magnetic flux that moves through the components of the shaft, the air space, the armature, and the frame. Armature and field carriers being made of

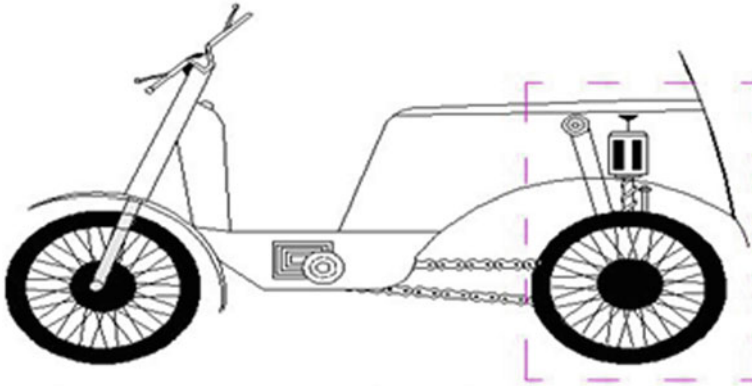
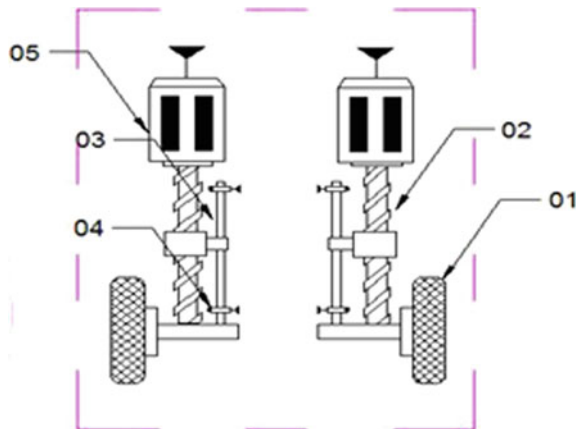


Fig. 1 2D diagram of the support system installed motorcycle

Fig. 2 2D diagram of the support system accessory in position. (1) Wheel, (2) leads screw, (3) guide rod, (4) proximity sensor, (5) motor



permeable material as most of the magneto motive force of field coils is needed to induce flux in the air gap. Armature winding where “working” emf is induced. Stator and rotor are the stationary and since axis movement component. The stator could be a magnet of the field, interacting with the armature to create motion, depending on the characteristics of a spinning electromotive device; or It may act as an armature, gaining its effect from shifting field coils on the rotor wires, and the motor’s magnetic field is arranged in such a way that a torque forms around the rotor axis. In certain prototypes, the rotor serves as the motor’s armature, across which the I/P volt range is given.

Reference [12] When geometry and mechanics in general are concerned, suspension systems serve a dual purpose—which is making the travel smooth, as well as protecting the frame from surface irregularities. It is necessary for the suspension to hold the road wheel in contact with the road surface as far as possible, so all the road or ground forces operating on the vehicle achieve so through the tire impact

patches, according to which the motor operates on the lead screw, as this suspension requires some nominal stiffness. The joint which connects the frame and the supporting retractable side arm which carries the wheels for treading on the surface when the speed is below the optimum for stability before contact failure a hinge joint between the joint aids the unidirectional motion about both coordinates [5]. For all that motion to occur, the proximity sensor primarily detects obstacles under a certain limit as a result of which proximity sensor often emits electromagnetic field to the target. The capacitance takes a relatively long time to sense in capacitive proximity sensors, the maximum switching range of a proximity sensor at about 50 Hz. While the signal is being sent to the motor via the Arduino Uno via the regulated output pins through wires, a lead screw translating radial motion into linear motion allows the support wheels to drop down gradually [13]. A lead screw nut and screw pair with rubbing surfaces, resulting in comparatively high friction and static friction, is compared to rotating components matting rolling surfaces and rolling bearings. Backlash is reduced by the use of a second nut to create preload. The commercially available computer integrates a number of machine components into a single chip. It has processors, peripheral, and memory built into make it a miniature computer.

That was based primarily on an 8-bit microprocessor device in the past. AT89C51 is the Atmel group manufactured 40 pins, 8-bit microcontroller [11]. This is reprogrammable flash form memory. The drawback of this flash drive is that after a few minutes we will delete the program. It has 4 kb on-chip ROM and 128 bytes of internal RAM and 32 I/O pin arranged as port 0 to port 3 each has 8-bit bay. Port 0 contains 8 data line (D0-D7) and low order address line (AO-A7). This is a unit of the Uno board within which the AR89C51 is a part of relying on the input power given by the battery unit and coding done thorough the IDE. The 8051 features two 16-bit registers consisting of program counter (PC) and reference pointer (DPTR). Just one is used to maintain a word's address in memory. Software instruction bytes are extracted from memory locations that the machine is addressing. Program ROM can be on the chip at the addresses 000 h to FFFh, external to the address chip which exceeds FFFh, or fully external to all addresses from 0000 h to FFFFh [10].

The stack is a region of internal RAM which is used to easily store and retrieve data in combination with such opcodes. 8051 uses the 8-bit stack pointer (SP) register to store an internal RAM address that is considered the top of the stack. The address maintained in the SP register is the internal RAM location where the last data byte is stored by a stack operation. The SP increases as data is to be put on the stack before data is deposited on the stack, meaning that the stack expands as data is processed. When data is extracted from the stack, the byte is read from the stack, and then the SP decreases to lead to the next stored data byte open. Stack feature as seen above, and SP. The SP is set to 07 h when the 8051 is reset, and the programmer may change it to any internal RAM address, i.e., the default stack pointer address position is 07 h. Using a command to transfer data, we may change the position of the stack pointer.

The stack is limited in height to the inner RAM. The stack has the ability to write useful data in the bit-addressable RAM, register banks, and general purpose (scratchpad) RAM areas over (if the programmer is not careful to restrain its growth).

## 2.1 Actuation Control Module

The software is designed to ensure that the stack does not expand beyond predefined boundaries. The stack is usually put high in internal RAM by selecting the number found in the SP register, in order to avoid interference with the internal RAM areas of log, bit and scratchpad. A running machine must have program memory to handle the code, mainly in ROM and RAM memory for variable data which can be altered while the program runs. For certain functions, the 8051 has internal RAM and ROM memory. The 8051 is structured in such a manner that data memory and computer code memory can be found in two totally separate physical memory entities. They also have the same set of addresses. User variables that need to be updated regularly or at high speed will use the remaining 80 bytes of internal RAM, from addresses 30 h through 7Fh. Even the microcontroller uses this area as a storage area for the running stack. This fact significantly restricts the stack of the 8051, as the field reserved for the stack is only 80 bytes, as shown in the memory diagram, and is typically smaller because these 80 bytes have to be exchanged between stack and user variables. The 8051 uses 8 “R” registers, which in many of its instructions are used. These registers “R” are numbered between 0 and 7 (R0, R1, R2, R3, R4, R5, R6, and R7). Generally, these registers are used to help modify values and transfer data from one memory location to another. Microcontroller implementations include the tracking of external events such as the frequency of a pulse train, or the generation or measurement of internal time differences between device actions. All of these tasks may be performed using computational methods, but counting or pacing program loops holds the processor active enough that other, maybe more important, operations are not executed (Fig. 3).

To alleviate the processor from this pressure, two 16-bit up counters, called T0 and T1, are made available for the programmer’s general use. Counter can be programmed to count internal clock pulses, serve as a timer, or programmed as a counter for counting external pulses. The counters are split into two- to eight-bit registers called bytes low timer (TL0, TL1) and high (TH0, TH1). In the timer mode control register (TMOD), the timer/counter control register (TCON), some program commands, and all counter operations are controlled by bit statuses.

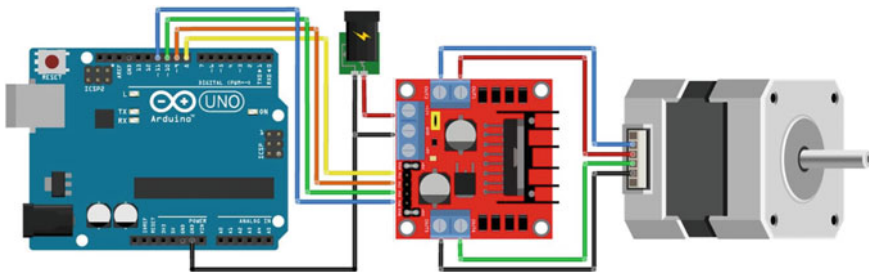


Fig. 3 Schematic diagram for a unit stepper motor

Computers in new, multiprocessor distributed networks must be able to connect with other computers. One of the most efficient means of communication is the serial transmission and receiving of data bits. The 8051 has a serial data exchange circuit that uses SBUF for data keeping log. Register SCON controls data exchange, register PCON controls traffic speeds, and serial data network links the RXD (P3.0) and TXD (P3.1) pins. Register SCON controls data exchange, register PCON controls traffic speeds, and serial data network links the RXD (P3.0) and TXD (P3.1) pins.

Physically, SBUF is a two-register. One is just writing and is used to carry data that is to be transmitted via TXD from 8051. The other is read only and contains data obtained via RXD from external sources. Both registers are mutually exclusive and use address 99 h. There are four programmable serial data transmission modes which are picked by setting the SMX bits in SCON. Baud rates are determined according to the chosen mode. The heart of the 8051 is that it produces the pulse of the clock which synchronizes all internal operations [14].

## 2.2 Material Analysis

Owing to its already comparatively poor tensile strength, mild steel is used as the tool for the retractable arms; the surface stiffness can be improved by carburizing. Low-carbon steels experience yield-point run out if there are two yield points for the material. The first point of yield or upper point of yield is above the second point, and the yield decreases substantial after the upper point.

## 3 Program Coding

The base coding on an Arduino Uno R3 is a simple C program involving selection strings to target the output pins to the actuators when necessary at 1.5 V delivery line to the stepper motor shield where the signal is bypassed and reaches the stepper motor that actuates the stepper motor.

**PROGRAM CODE IDE**—Attached to the supporting document *Annexure*

## 4 Formula Derivation and Construction of Supporting Wheels

Pitch of the lead screw = 2.5 mm.

Speed of the motor,  $N = 500$  rpm (is the speed at which the thread path is followed).

Lead screw linear velocity =  $500 \times 2.5 = 1250$  mm/minute (Angular ( $\theta$ ) to Linear).

Lead screw angular velocity =  $2 \times \pi \times N/60 = 52.33 \text{ rad/s}$ .

Lead screw motor power,  $P = 12 \text{ W}$ .

Motor torque =  $P \times (60/2 \times \pi \times N) = 0.229 \text{ Nm}$ .

Absolute capacity resistance =  $[\text{Torque } (\tau)/\text{lead screw radius}(r)] = 0.229/0.005 \text{ N}$

#### 4.1 Calculation for DC Motor

*Descriptive Details of the particular:*

Angular speed (N) = **30 rpm**.

Electric potential (V) = **12 Volts**.

Current flow (I) = **0.3 Amps (at loading condition)**.

Current flow (I) = **0.06 Amps (at no loading Condition)**.

Power

$$P = V * I \text{ (in Watts)}$$

Wherein

P—Power (W)

I—Current (A)

V—Applied potential (V)

$$= 12 \times 0.3 = 3.6 \text{ Watts}$$

Power consumed by the system as a whole under loading and no load conditions.

$$P = 48 \times 10^{-4} \text{ HPs}$$

**Efficiency of the Motor = 36%**

Electric power of motor:

$$P_I = I \times V$$

Where

$P_I$ —Input power (W)

The mechanical output of the motor:

$$P_O = \tau \times \omega$$

Wherein

$P_O$ —Output power (W)

- $\tau$ —Torque (Nm)
- $\omega$ —Angular speed (rad/s)

Calculating angular velocity engine rotational velocity (rpm) is known:

$$\omega = N \times 2 \times \pi / 60$$

Wherein

- $\omega$ —Angular speed (rad/s)
- $\pi = 3.14$ .
- 60—Seconds per minute.

Motor efficiency is measured as:

$$E = P_O / P_I \text{ (Hence)}$$

$$P_O = P_I \times E$$

$$\tau \times \omega = I \times V \times E \{ \omega = 2\pi N / 60 \}$$

$$\tau \times N \times 2\pi / 60 = I \times V \times E$$

**Motor Torque:-**

Calculation of torque:

$$\tau = (I \times V \times E \times 60) / (N \times 2 \times \pi)$$

$$= (0.3 \times 12 \times 0.36 \times 60) / (30 \times 2 \times \pi)$$

$$\tau = 4.2 \text{ kg cm} = 4.12 \times 10^{-1} \text{ Nm}$$

**4.2 Dimensions of the Component**

- Wheel diameter—72 mm;
- Wheel thickness—32 mm;
- Clamp length—56 mm;
- Clamp breadth—36 mm;
- Clamp thickness—2.3 mm;
- Distance between center of the hole in clamp to the bottom of the spring—46 mm.
- Hole size—10 mm;
- Compressed spring length—72 mm;
- Crest—4.5 mm;
- Number of coils—10;



Spacer length—107.5 mm;  
 Spacer diameter—25.4 mm;  
 Washer thickness—2.5 mm;  
 Washer diameter—41.5 mm;  
 M16 thread bolt—(metric  $\text{Ø}16$ );  
 Total length of the hollow rod—200 mm;  
 Top and bottom threaded space—15 mm each.

## 5 Result and Discussion

Dynamic supporting wheels for two-wheeler stability based on the principle of when the vehicle reaches speed greater than 20 km/h the proximity sensor signals the Arduino board, then motor starts lifting the supporting wheels via lead screw and movable nut as the motor lowers the supporting wheel at less than 20 km/h. The motor rotates the lead screw as it moves to and fro motion of wheels. It consists of monitor display that indicates the speed.

### 5.1 *Without Load (at a Steady State of Rest in Side Stands)*

Vehicle mass—120 kg (total mass included wheels)  
 Load at front wheel—55 kg (suspension, handlebar, and electronics)  
 Load at rear wheel—65 kg (drive train and frame along with suspension)  
 Load at supporting wheel—22 kg, (at initial)  
 Thus, the mass 22 kg acted on without load self-balancing in standard model motorcycle was found theoretically.

### 5.2 *Adding a Rider (First Step to Exerting Force on the Vehicle)*

Weight of the rider—58 kg (at normal)  
 Load at front wheel—74 kg (change in load exerted on the front wheel upon addition)  
 Load at rear wheel—106 kg (change in weight occurred due to addition of rider)  
 Load at supporting wheel—35.33 kg (includes all the down force exerted)  
 Thus, the mass 35.33 kg (includes all the down force exerted) acted on adding a rider self-balancing in standard model motorcycle was found theoretically.

### ***5.3 Adding a Pillion (Pillion Weight Amounts to the Additional Unsprung Mass) and Hence Reduces the Effective Distance Between the Support Mounting and the Ground***

Pillion rider weight—67 kg (at normal steady position of contact with the surface)

Load at front wheel—81 kg (which includes the rider effort and leaning weight of the pillion excluding conditions of braking)

Load at rear wheel—159 kg (the weight including the pillion amounted to weight which is sustained during the run)

Load at supporting wheels—53 kg (includes the payload alone which confides to motion in a straight line)

Thus, the mass 53 kg (includes the payload alone which confides to motion in a straight line) acted on adding a pillion (pillion weight amounts to the additional unsprung mass) self-balancing in standard model motorcycle was found theoretically.

TVS flame DS125 type of motorcycle was used for dynamic supporting system on two wheelers. Supporting wheels system is fitted to the steel frame; this system included DC motor, Arduino board, and proximity sensor controls. To and fro motion of the supporting wheel is programmed through the PC integral development environment (IDE). The supporting wheels should be lowered to ground if and only if the vehicle velocity goes below 20 km/h and the same way the supporting wheels should be brought back to its original position when the vehicle velocity goes above 20 km/h or else the dynamics is spoiled. The complete assembly of supporting wheels is shown in Fig. 4.

## **6 Conclusion**

From this study, we concluded that the developed solution can be seen to improve the level of stability by a large margin, and it is also found that under curve negotiation so done to create force balance is used to make transportation easier for people and thereby increasing fuel economy. And it carried out by making an impressive task in stability at low speed and even during speed breakers irrespective of the surface stability of the terrain. It is very useful for any two-wheeler rider who is highly particular about safety. Moreover, it is applicable to implement in any two wheelers.

**Fig. 4** Supporting wheel installed to the motorcycle



## References

1. Mandlik SM, Pastapure SS (2017) Safety analysis of two-wheeler side wheel attachment for differently-abled people. *IJERT* 6(08) (August)
2. Whetson Meynard C (1958) Retractable support wheels are assembled to the two-wheeler to convert it into a tricycle with retractable motorcycle stop support wheels. US Patent 2995378 (May)
3. Murata Y, Ueda Y, Hashimoto Y (2008) Motorcycle with auxiliary support. US Patent 7396033 B2, Honda Motor Co., Ltd., Tokyo (July)
4. Sakita M (1989) Two-wheel vehicle with auxiliary support system. US Patent No 4826194 (May)
5. del Rosso V, Andreucci A, Boria S, Corradini ML, Giambo R, Ranalli A (2018) Self-balancing electric motorcycle, modelling at low speed: preliminary results. In: 6th European conference

- on computational mechanics (ECCM 6), 7th European conference on computational fluid dynamics (ECFD 7), June 2018, Glasgow, UK
6. Willman DM (1991) Retractable motorcycle stop support wheels. US Patent 5029894 (July)
  7. Engelbach TS (1987) System for automatically preventing turnover of two-wheeled vehicles. US Patent No 4691798 (September)
  8. Sears A, Segala A, White J (2012) Low-speed motorcycle stabilization device
  9. Corno M, Panzani G, Savaresi SM (2015) Single track vehicle dynamics control: state of the art and perspective. *IEEE/ASME Trans Mechatron* 20(4) (Aug)
  10. Bhunte GV, Deshmukh TR (2015) A review on design and analysis of two wheeler chassis. *Int J Res Emerging Sci Technol* 2(1) (January)
  11. Sherth Babu S, Shivayogiharmath Raj S, Malsoor B (2016) Stability enhancement of a powered two wheeler vehicle under curve negotiation. *Int Refer J Eng Sci (IRJES)* 5(5) (May)
  12. Hari Sudhan H, Ganesh Kumar K, Udhaya-Prakash A, Anu Roopa Devi S, Sathiya P (2015) Arduino ATMEGA-328 Microcontroller. *Int J Innov Res Electr Electron Instrum Control Eng* 3(4) (April)
  13. Singhania S, Kageyama I, Karanam VM (2019) Study on low-speed stability of a motorcycle. Steering, Torque & Yaw Motion disturbances of a single track automotive (June)
  14. Brennan L (1905) Means for passing-on stability to naturally constructed unstable bodies. US Patent 796893 (August)

# Microstructural Evolution, Phase Formation and Mechanical Behaviour of Al 7017 Alloy Produced by Powder Metallurgy (P/M) Technique



M. Prashanth, R. Karunanithi, S. Rasool Mohideen, A. Karthik, and Prasanta Kumar Rout

**Abstract** This research was to assess the microstructure, formation of secondary phases and mechanical behaviour of Al 7017 alloy by mechanical alloying for different milling time at room temperature followed by unidirectional cold compaction and sintering technique. Sintered samples analysed for homogeneous distribution of alloy elements were perceived through field emission scanning electron microscope. X-ray diffraction of sintered samples confirmed peak broadening and disclosed the reduction in crystal size and lattice parameter with the increase in lattice strain. Archimedes principle was implemented to analyse the density of the sintered sample and observed that there is decrease in the relative density with increase in milling time. Vickers's microhardness increased with respect to milled time duration due to refinement of the grain size.

**Keywords** Al 7017 alloy · Mechanical alloying (MA) · Uniaxial cold compaction · FE-SEM · XRD · VHN

## 1 Introduction

The microstructure, mechanical and stress corrosion cracking of 7xxx series which are mainly used in automobile and aerospace industries were reported by Wu et al.

---

M. Prashanth · R. Karunanithi (✉) · S. Rasool Mohideen · A. Karthik  
Department of Mechanical Engineering, B.S. Abdur Rahman Crescent Institute of Science and Technology, Chennai 600048, India  
e-mail: [karunaponni@gmail.com](mailto:karunaponni@gmail.com)

M. Prashanth  
e-mail: [prashanthmuralishankar@gmail.com](mailto:prashanthmuralishankar@gmail.com)

M. Prashanth · R. Karunanithi  
Department of Aerospace Engineering, B.S. Abdur Rahman Crescent Institute of Science and Technology, Chennai 600048, India

P. K. Rout  
Department of Material Science and Engineering, Tripura University (Central University), Tripura 799022, India

[1]. Liao et al. proposed the structural and morphological behaviour of aluminium and 7.6% of magnesium were ball-milled under cryogenic condition and investigated using transmission electron microscope (TEM) [2]. Prabhu et al. studied on high-energy ball milling (HEBM) that was used to fabricate aluminium reinforced with alumina for different volume percentage. From the results, homogeneous distribution of alumina is observed in pure aluminium and there is no formation of intermetallic compounds after milling for more than 20 h of the chemical powder [3]. Al 7075 alloy was examined for mechanical and microstructure behaviour of cold pressed and hot extrusion technique. From the results, uniform dispersal of  $MgZn_2$  second phase particle and grains has been recrystallized and was stated by Jabbari Taleghani et al. [4]. Azimi et al. projected on mechanical alloying of 7068 aluminium alloy and fabricated through hot-pressed technique. Crystal size was found to be 27 nm for 40-h-milled samples, and the intermetallic compound was formed during compacting [5]. Van Der Zwan et al. investigated on 7075 aluminium alloy that is fabricated through mechanical alloying followed by unidirectional compaction and sintering to analyse the microstructure, physical and mechanical behaviour of sintered samples [6]. Many researchers have analysed on compaction pressure which has a dominant role during compaction of Al 7075 alloy. The various parameters which were considered during compaction are size, shape and dispersal of alloy powder during unidirectional compaction [7, 8].

Crystal size on the material is calculated from XRD peak broadening analysis using Scherrer's equation where there is no strain on the material that was reported by many researchers [9, 10]. Gubicza et al. studied on Al–Mg alloy produced through ball mill to examine the crystal size and lattice parameter as related to milling time. From the experiment outcomes, decrease in crystal size with increase in lattice parameter as a function of milling time [11]. Williamson–Hall method is the precise method to calculate the lattice strain and crystal size on the cubic structure for lower diffraction angle that was investigated by Williamson et al. [12]. I. Estrada Guel et al. studied on microstructure and mechanical behaviour of Al 7075 alloy, and the formation of flake like structure on the samples is seen, whereas hardness and tensile strength were increased from 101.2 BHN and 283.71 MPa to 108.8 BHN and 400.86 MPa [13]. K. John Joshua et al. researched on metallurgical, and microhardness of Al7068 alloy was fabricated through cold compaction and sintering technique. Optical micrograph shows the formation of uniform distribution of spherical pores on the base alloy and the hardness was found to be 33 VHN [14]. Crystal size and lattice parameter as a function of milling time for aluminium 7075 alloy were ball-milled followed by hot-pressing technique. Das et al. [15] reported that XRD revealed the reduction in crystal size, and increase in dislocation density for different milling time and Hall–Petch relation was used to evaluate the hardness value.

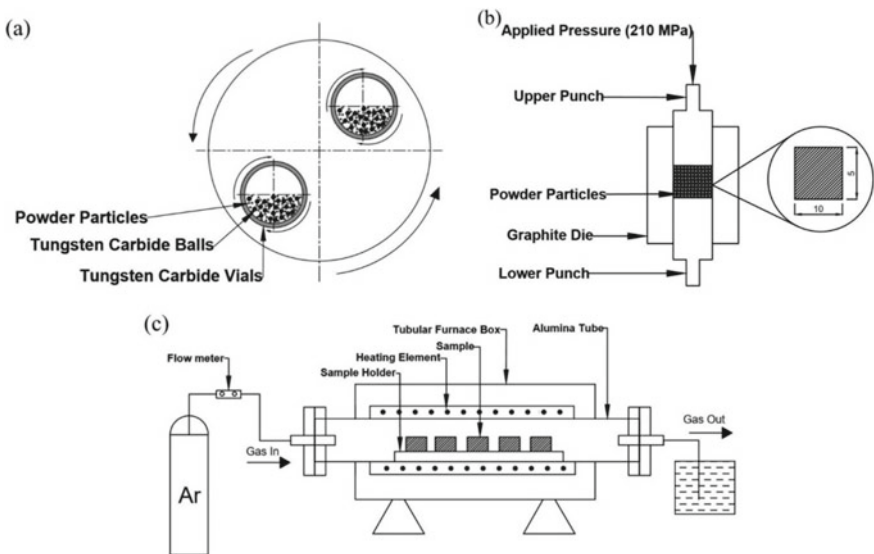
Many researchers have investigated on 7xxx series with Al–Zn–Mg as a major element. The grain size was observed to be less than 10  $\mu\text{m}$  [16, 17]. However, the purpose of this work was to fabricate Al7017 alloy for different milling time duration (0, 5, 10 and 20 h) through P/M technique and to discuss their microstructure behaviour, structural analysis, relative density and Vickers microhardness of sintered alloy samples for different milling time duration.

## 2 Materials and Methods

### 2.1 Preparation of the Sample

Al 7017 alloy used in this work was procured from Alfa Aesar, USA. Pure aluminium powder with purity 98% and particle size of 45  $\mu\text{m}$  was used as the major element. Other minor elements and their weight percentage composition such as zinc (5.2%), magnesium (2.3%), copper (0.12), silicon (0.082), chromium (0.35), manganese (0.30) and titanium (0.15) with particle size of 45  $\mu\text{m}$  were used. Chemical powders were milled using Fritsch planetary ball mill as shown in Fig. 1a under wet milling condition using toluene as a process control agent and various milling parameter such as 10-mm diameter tungsten carbide balls, 300 rpm speed and ball-to-powder ratio 10:1 under atmospheric temperature for different milling time duration (0, 5, 10 and 20 h). The chemical powders were milled for 1 h and allowed to cool for 45 min to reduce the significant temperature rise.

Milled alloy powders were cold compacted into a pellet of 10-mm diameter and 5-mm height using unidirectional hydraulic press of 100-ton capacity. Zinc stearate is used as a lubricant which is applied on the surface of the die and punch to reduce heat and friction. The samples were pressed at 210 MPa for 3 min holding time and the sintering is carried out in argon atmosphere at 580  $^{\circ}\text{C}$  and 2 h of holding time and then they are allowed to cool at ambient temperature. The schematic diagram of the compaction and sintering is shown in Fig. 1b, c.



**Fig. 1** Schematic diagram. **a** High-energy ball mill; **b** hydraulic press and **c** tubular furnace

## 2.2 Characterization of the Sintered Samples

Microstructural analysis was performed on pellet samples using field emission scanning electron microscope (FE-SEM) along with EDAX for different milling time duration. Before the examination, the samples were mechanically polished with series of SiC grit papers such as 600, 800, 1000, 1200 and 1500, respectively. Finally, mirror polishing was done on the samples to get the fine microstructure of the samples.

XRD pattern of Al 7017 alloy sintered samples for different milling time are analysed using Bruker D8 advance X-ray diffractometer using  $\text{CuK}\alpha$  ( $\lambda = 0.154078$  nm) radiations. The  $2\theta$  range was from  $30^\circ$  to  $90^\circ$  with a scan speed of  $1^\circ/\text{min}$ . X-ray peak broadening analyses were examined with the help of full-width half maximum (FWHM) for various structural parameters such as crystal size and lattice parameter with respect to milling time.

Density test was evaluated using Archimedes principle on Al 7017 alloy sintered samples. Vickers microhardness test (MMT-X7B, Matsuzawa, Japan) [15, 18] was performed on the cold uniaxial-pressed samples based on ASTM E92-82. The samples were measured at three different positions, and the average value was obtained for the applied load of 100 gf and dwell time of 10 s.

## 3 Results and Discussion

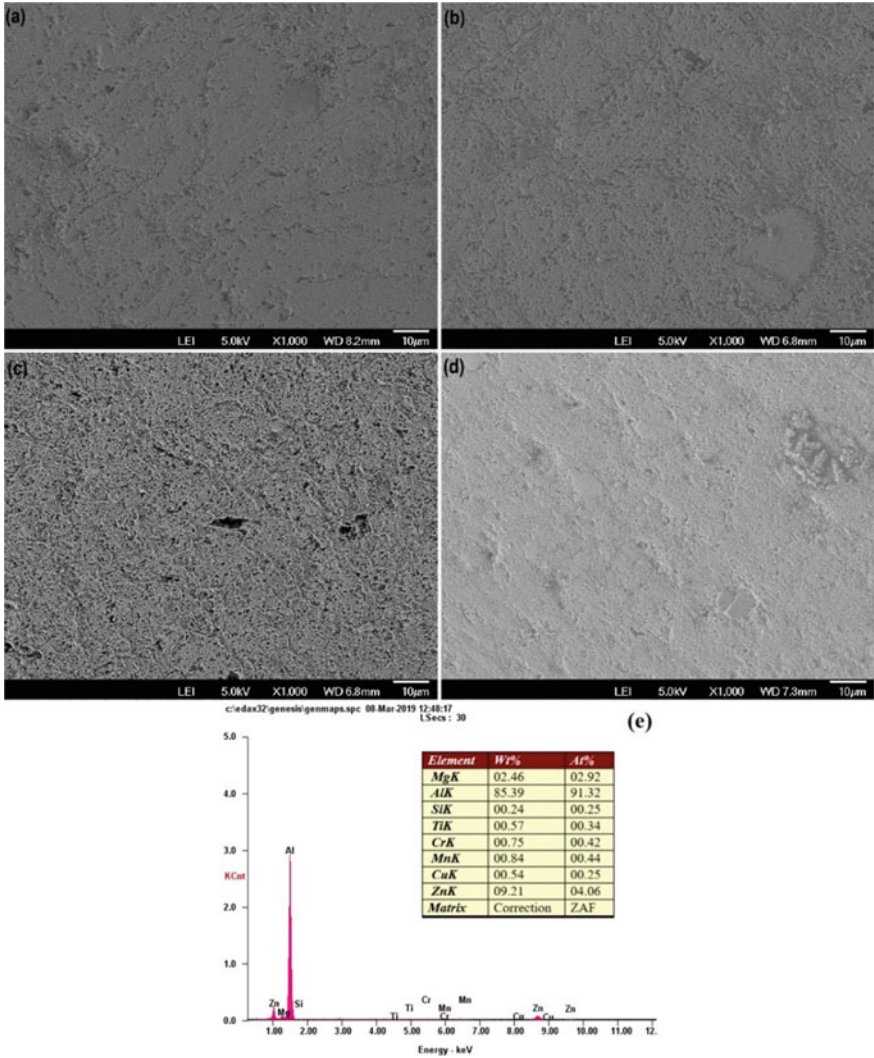
### 3.1 Effect of Milling Hour on Sintered Samples for FE-SEM Analysis

Figure 2a–d is furnished with the microstructure of base alloy. The selected alloy samples were scrutinized using Supra 40, Zesis FE-SEM and EDAX. From the microstructure, it is evident that during milling time the powder particles have undergone welding and fragmentation along the grain boundaries. In addition, as the milling time increases there is reduction in crystal size with increase in lattice strain of the material which is proved in XRD and SEM analysis. The formation of  $\text{MgZn}_2$  intermetallic compounds is during cold compaction technique for 20-h-milled sintered samples. Figure 2e EDAX shows the various elements present in the sintered sample.

### 3.2 Effect of Milling Hour on Structural Evaluation of Al 7017 Alloy

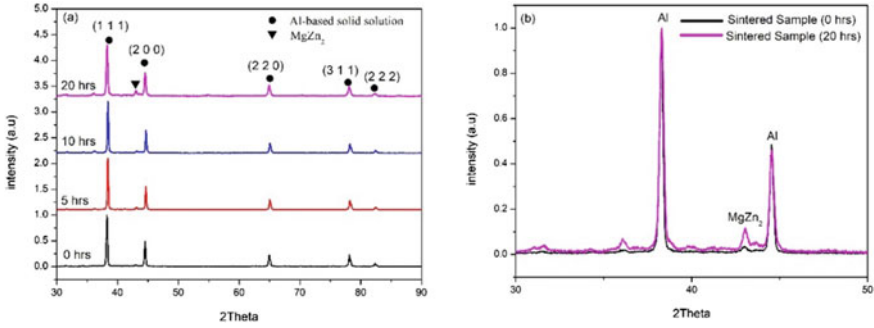
Figure 3a shows the XRD pattern of Al 7017 alloy sintered sample for different milling time (0, 5, 10 and 20 h). XRD results for sintered samples revealed the major





**Fig. 2** Microstructure of Al 7017 alloy sintered sample of different milling time. **a** 0 h; **b** 5 h; **c** 10 h; **d** 20 h; and **e** EDAX of Al 7017 alloy elements

peaks of aluminium were recognized as FCC crystal structure and they are indexed using X-pert High Score software. The major peaks of aluminium were observed at  $2\theta$  values of 38.6833, 44.9178, 65.3067, 78.4407 and 82.6415 and their corresponding (h, k, l) values were given by (111), (200), (220), (311) and (222), respectively. XRD pattern shows there is a formation of  $MgZn_2$  [15] intermetallic compounds during the milling of Al 7017 alloy. The peak broadening of Al 7017 alloy was observed in Fig. 3b which indicates the reduction in powder particles from micro- to nanosize



**Fig. 3** Diffraction pattern of Al 7017 alloy sintered sample for different milling time. **a** XRD graph and **b** peak broadening

as the milling time increases. Moreover, minor components present in Al 7017 alloy were not noticeable because of the lower weight per cent of the component.

X-ray peak broadening is mainly due to the crystal size of the material as well as the instrumental broadening. So, before evaluating the crystal size, instrumental broadening effect must be corrected. Instrumental broadening of full width at half maximum was estimated from the X-ray diffraction peaks by the following equation [19, 20].

$$\beta_{hkl} = [(\beta_{hkl})_{\text{Measured}}^2 - (\beta_{hkl})_{\text{Instrumental}}^2]^{1/2} \tag{1}$$

The average crystal size of the base alloy is obtained from the peak broadening. Crystal size of the Al 7017 alloy sintered samples is analysed using Scherrer's equation [21, 22], and it was given by

$$D = \frac{k\lambda}{\beta \cos \theta} \tag{2}$$

where  $k$  is the shape factor (0.9),  $\lambda$  the incident wavelength,  $\theta$  the diffraction angle and  $\beta$  the full width at half maximum (FWHM) and  $D$  the crystal size. The graph has been plotted between milling time and crystal size Fig. 4.

Scherrer's equation was used to evaluate only crystal size of the material, whereas the strain in the material was analysed using X-ray peak broadening with the help of Williamson–Hall method for uniform deformation model (W–H UDM) to inspect the crystal size and lattice strain. In this method, the strain in the material is assumed to be uniform, hence the material is isotropic in nature. Crystal size and lattice strain were given by the following equation [19, 22]

$$\beta \cos \theta = \frac{k\lambda}{D} + 4\epsilon \sin \theta \tag{3}$$

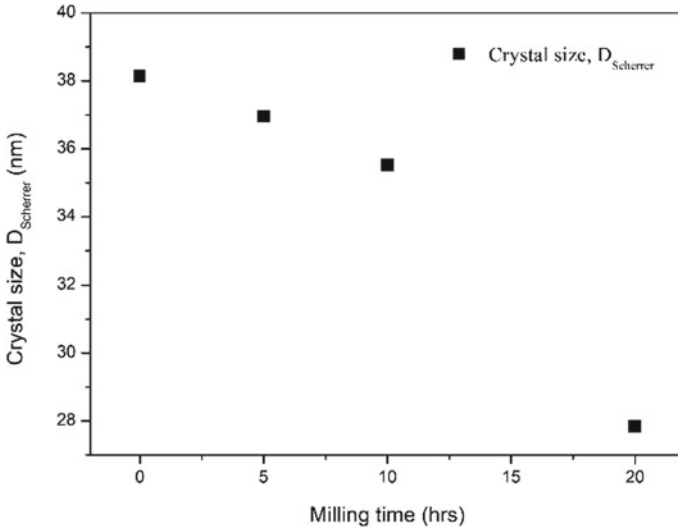


Fig. 4 Milling time on crystal size using Scherrer’s equation

From Eq. (3), graph was plotted between  $\beta \cos \theta$  in Y-axis and  $4 \sin \theta$  in X-axis to obtain the crystal size and lattice strain from intercept and slope using linear regression fit plot.

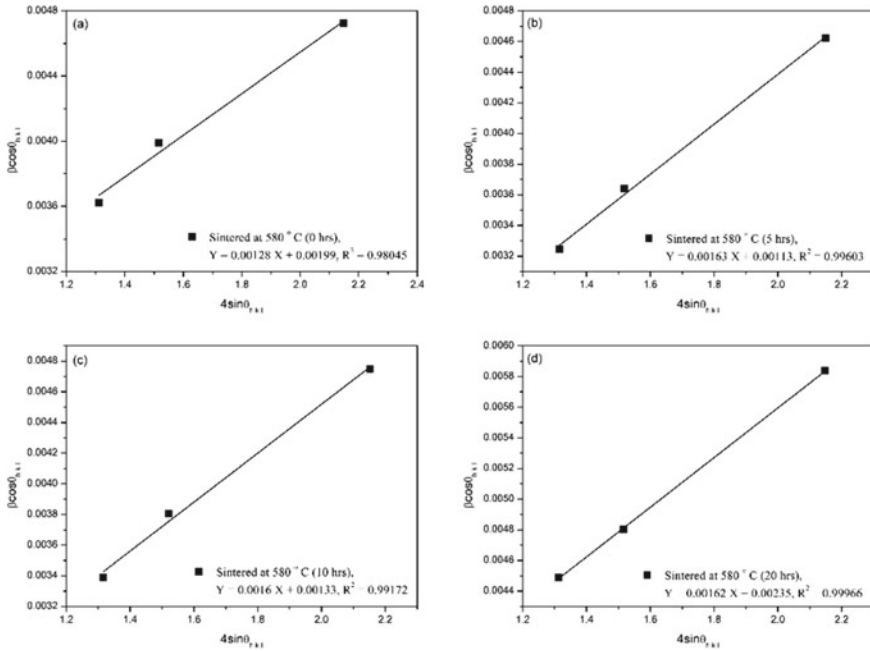
As stated by W–H UDM, the changes in crystal size [20, 21] and lattice strain for different milling time of sintered samples are signified in Fig. 5a–d. The reduction in crystal size with an increase in lattice strain is due to the grain refinement and development of structural defects on the material for various milling time. The decrease in crystal size and increase in lattice strain were found to be 58.89 nm and 0.0021% for 20-h-milled sintered sample, whereas 0 h sample was found to be 69.65 nm and 0.0013%, respectively.

Uniform stress deformation model (USDM) [23] strain is evaluated from Hook’s law where stress is proportional to the strain within the elastic limit of  $\sigma = E\varepsilon$  where  $\varepsilon$  represents the strain,  $\sigma$  represents the stress and  $E$  represents the Young’s modulus. Equation (3) can be rewritten for modified Williamson–Hall method for USDM and the equation was given by

$$\beta \cos \theta = \frac{k\lambda}{D} + 4 \frac{\sigma \sin \theta}{E_{h,k,l}} \tag{4}$$

The Young’s modulus of the material can be evaluated with below mentioned equation for cubic crystal structure.

$$\frac{1}{E_{h,k,l}} = \frac{S_{11} - 2(S_{11} - S_{12} - S_{44})(k^2l^2 + l^2h^2 + h^2k^2)}{(h^2 + k^2 + l^2)^2} \tag{5}$$



**Fig. 5** W-HUDM method for Al 7017 alloy sintered sample of different milling time. **a** 0 h; **b** 5 h; **c** 10 h; and **d** 20 h

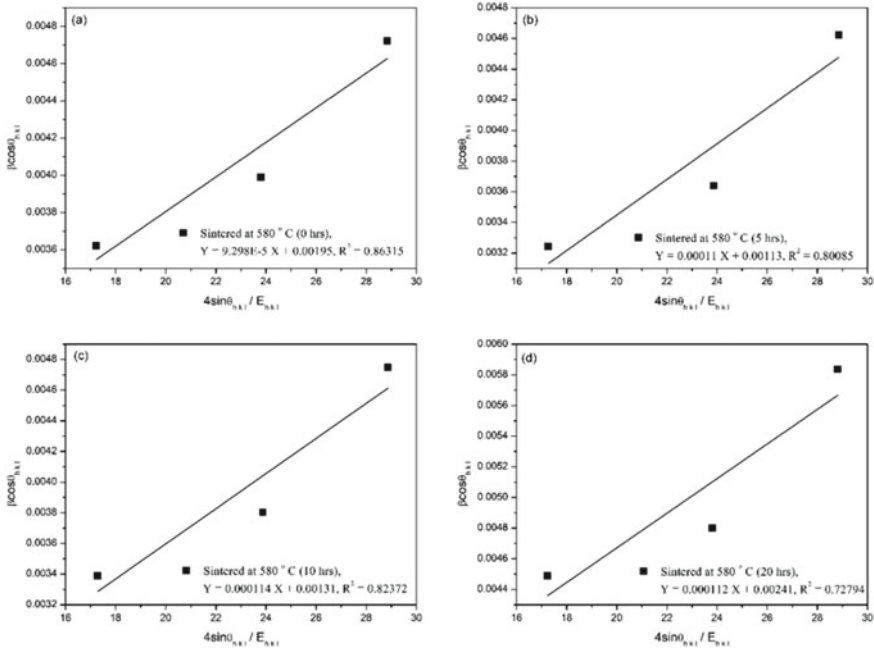
From the above equation, the elastic compliances of pure aluminium are given by  $S_{11}$  ( $15.7 \text{ TPa}^{-1}$ ),  $S_{12}$  ( $-5.70 \text{ TPa}^{-1}$ ) and  $S_{44}$  ( $3.51 \text{ TPa}^{-1}$ ), respectively. The slope and intercept can be obtained through linear fit analysis by plotting the graph between  $(4 \sin \theta / E_{h,k,l})$  in X-axis and  $(\beta \cos \theta)$  in Y-axis for stress and crystal size. However, strain on the material can be calculated using Hooke's law.

According to W-H USDm, the variation in crystal size and lattice strain for varying milling time of sintered samples is signified in Fig. 6a–d. The decrease in crystal size with increase in lattice strain is due to the severe plastic deformation and development of various defects such as dislocation, stacking fault and twinning on the material for various milling time. 20-h-milled sintered sample shows the reduction in crystal size and rise in lattice strain was found to be 57.46 nm and 0.002%.

Uniform deformation energy density model (UDEDm) is examined for crystal size [23, 24] and energy density using following equations

$$\beta \cos \theta = \frac{K\lambda}{D} + \left[ 4(2/E_{h,k,l})^{\frac{1}{2}} \sin \theta \right] u^{\frac{1}{2}} \tag{6}$$

From the above equation, the crystal size and energy density were calculated from intercept and slope through linear fit analysis by plotting the graph between



**Fig. 6** W–H USDM method for Al 7017 alloy sintered sample of different milling time. **a** 0 h; **b** 5 h; **c** 10 h; and **d** 20 h

$4 \sin \theta (2 / E_{hkl})^{1/2}$  in X-axis and  $\beta \cos \theta$  in Y-axis. In UDEDM method, the strain is assumed to be anisotropic in nature and it was determined by  $2u / E_{hkl}$ .

According to W–H UDEDM, the difference in crystal size and lattice strain for varying milling time of sintered samples is shown in Fig. 7a–d. The decline in crystal size with the improvement in lattice strain is due to cold welding and fragmentation and change in lattice deformation and crystal imperfection leads to high dislocation density for various milling time. The drop in crystal size and rise in lattice strain were found to be 60.49 nm and 0.0044% for 20-h-milled sintered sample.

Lattice parameter was calculated from Bragg’s angle of diffraction, and the graph was plotted between lattice parameter and  $\cos^2 \theta_{hkl} / \sin \theta_{hkl}$  to obtain the precise lattice parameter from the intercept using linear fit analysis. For sintered sample, the aluminium matrix was found to increase with an increase in milling time duration. This is mainly due to the isolation of negligible quantity of other elements present in the Al 7017 alloy. The lattice parameter [23] of sintered samples declines during sintering process is clearly depicted in Fig. 8.

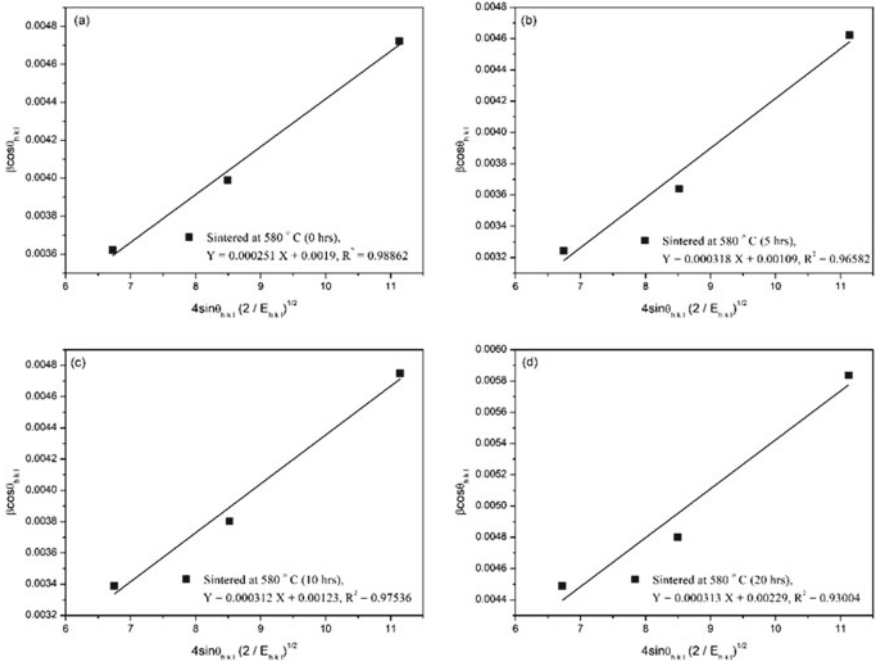
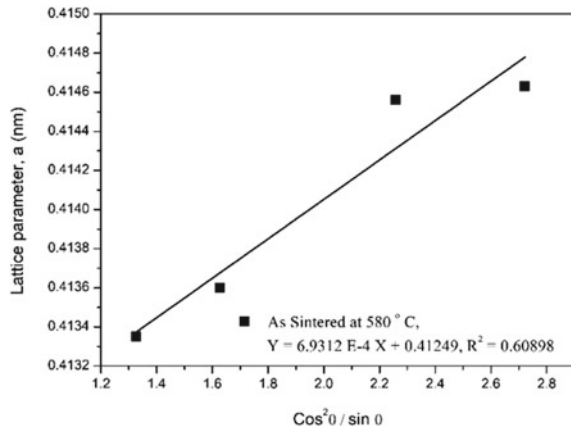
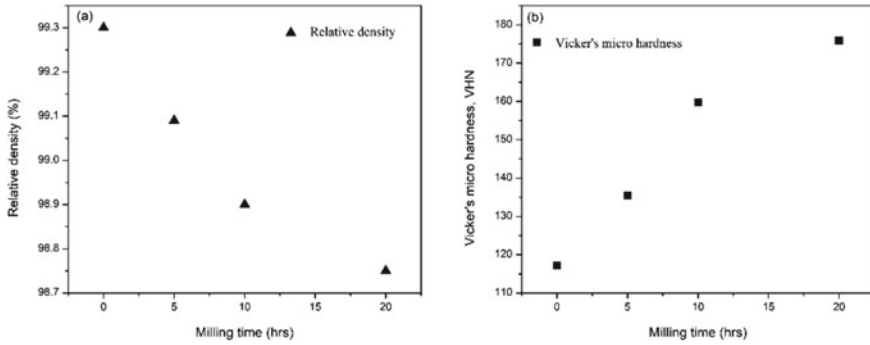


Fig. 7 W–H UEDM method for Al 7017 alloy sintered sample of different milling time. a 0 h; b 5 h; c 10 h; and d 20 h

Fig. 8 Lattice parameter for Al 7017 alloy sintered sample





**Fig. 9** Effect of milling time as a function of **a** relative density and **b** Vickers's microhardness

### 3.3 Effect of Milling Hour on Physical and Mechanical Behaviour of Al 7017 Alloy

Figure 9a shows the changes in relative density [25–27] and Vickers's microhardness [15, 18] of Al 7017 alloy pellet samples for different milling time. The relative density Al 7017 alloy compacted sample is noticeable and found to decrease from 99.3 to 98.75% with the increase in milling time. Moreover, it can be seen that the compacted density of the materials depends on the microstructure of the powder, along with compaction and sintering parameter. In addition to it, decrease in particle size for longer milling time duration increases the rate of diffusion. Figure 9b shows the variation of Vickers's microhardness for sintered Al 7017 alloy samples for different milling time, and it was observed to increase from 123 to 175 VHN, respectively. The percentage improvement of hardness for 20-h-milled sintered sample was found to be 29.71% compared to 0 h samples. The changes in the hardness were mainly due to the fine grain refinement and high dislocation density on the boundaries of the sintered samples.

## 4 Conclusion

The following conclusions were presented based on the microstructural, phase transformation and mechanical behaviour on uniaxial cold compacted Al 7017 alloy samples.

- (1) Microstructure of nanocrystallite Al 7017 alloy was showed the homogeneous distribution of the elements with the presence of secondary elements, and minor pores were reduced on the sintered samples during the sintering process.
- (2) The peak broadening analysis due to crystal size, lattice strain and lattice parameter was examined through Scherrer and W–H method on the sintered samples for Al 7017 alloy.

- (3) The relative density of the sintered alloy is decreased with increase in milling time. The lowest relative density 98.75% was observed for higher milling time compared with that of 0-h sintered sample.
- (4) Superior Vickers's microhardness was observed for 20-h-milled sintered sample of 175 VHN, about 29.71% increase in comparison with the 0-h sample.

**Acknowledgements** We thank Dr. R. Nagarajan, Head of Chemical Engineering Department, IIT Madras, India, for his valuable support in providing the laboratory facilities which helped us to carry out this research work.

## References

1. Wu L-M, Wang W-H, Hsu Y-F, Trong S (2007) Effects of microstructure on the mechanical properties and stress corrosion cracking of an Al–Zn–Mg–Sc–Zr alloy by various temper treatments. *Mater Trans* 48:600–609. <https://doi.org/10.2320/matertrans.48.600>
2. Liao XZ, Huang JY, Zhu YT, Zhou F, Lavernia EJ (2003) Nanostructures and deformation mechanisms in a cryogenically ball-milled Al–Mg alloy. *Phil Mag* 83:3065–3075. <https://doi.org/10.1080/1478643031000152799>
3. Prabhu B, Suryanarayana C, An L, Vaidyanathan R (2006) Synthesis and characterization of high-volume fraction Al–Al<sub>2</sub>O<sub>3</sub> nanocomposite powders by high-energy milling. *Mater Sci Eng A* 425:192–200. <https://doi.org/10.1016/j.msea.2006.03.066>
4. Jabbari Taleghani MA, Ruiz Navas EM, Torralba JM (2014) Microstructural and mechanical characterisation of 7075 aluminium alloy consolidated from a premixed powder by cold compaction and hot extrusion. *Mater Des* 55:674–682. <https://doi.org/10.1016/j.matdes.2013.10.028>
5. Azimi A, Shokuhfar A, Zolriasatein A (2014) Nanostructured Al–Zn–Mg–Cu–Zr alloy prepared by mechanical alloying followed by hot pressing. *Mater Sci Eng A* 595:124–130. <https://doi.org/10.1016/j.msea.2013.11.094>
6. Van Der Zwan J, Siskens CAM (1982) The compaction and mechanical properties of agglomerated material. *Powder Technol* 33:43–54. [https://doi.org/10.1016/0032-5910\(82\)85037-7](https://doi.org/10.1016/0032-5910(82)85037-7)
7. Razavi Hesabi Z, Hafizpour HR, Simchi A (2007) An investigation on the compressibility of aluminium/nano-alumina composite powder prepared by blending and mechanical milling. *Mater Sci Eng A* 454:89–98. <https://doi.org/10.1016/j.msea.2006.11.129>
8. Chen W, Malghan SG (1994) Investigation of compaction equations for powders. *Powder Technol* 81:75–81. [https://doi.org/10.1016/0032-5910\(94\)02861-3](https://doi.org/10.1016/0032-5910(94)02861-3)
9. Cullity BD (1978) *Elements of X-ray diffraction*, 2nd edn. Addison Wesley, London. ISBN 0201011743 9780201011746
10. Hall BD, Zanchet D, Ugarte D (2003) Estimating nanoparticle size from diffraction measurements. *J Appl Cryst* 33:1335–1341. <https://doi.org/10.1107/S0021889800010888>
11. Gubicza J, Kassem M, Ribárik G, Ungár T (2004) The microstructure of mechanically alloyed Al–Mg determined by X-ray diffraction peak profile analysis. *Mater Sci Eng A* 372:115–122. <https://doi.org/10.1016/j.msea.2003.12.016>
12. Williamson GK, Hall WH (1953) X-ray line broadening from filed aluminium and wolfram. *Acta Metal* 1:22–31. [https://doi.org/10.1016/0001-6160\(53\)90006-6](https://doi.org/10.1016/0001-6160(53)90006-6)
13. Estrada-Guel I, Carreño-Gallardo C, Mendoza-Ruiz DC, Miki-Yoshida M, Rocha-Rangel E, Martínez-Sánchez R (2009) Graphite nanoparticle dispersion in 7075 aluminium alloy by means of mechanical alloying. *J Alloys Compd* 483:173–177. <https://doi.org/10.1016/j.jallcom.2008.07.190>



14. John Joshua K, Vijay SJ, Philip Selvaraj D (2018) Effect of nano TiO<sub>2</sub> particles on microhardness and microstructural behaviour of AA7068 metal matrix composites. *Ceram Int* 44:20774–20781. <https://doi.org/10.1016/j.ceramint.2018.08.077>
15. Tuhin Das R, Karunanithi AS, Ghosh KS, Bera S (2016) Deformation decomposition and hardening behaviour of nano Al7075 alloy prepared by mechanical milling and hot pressing. *ADV Powder Technol* 27:1874–1877. <https://doi.org/10.1016/j.apt.2016.05.010>
16. Molnárová O, Málek P, Lukáč F, Chráska T (2016) Spark plasma sintering of a gas atomized Al7075 alloy: microstructure and properties. *Materials* 9:1004. <https://doi.org/10.3390/ma9121004>
17. Becker H, Dopita M, Stráská J, Málek P, Vilémová M, Rafaja D (2015) Microstructure and properties of spark plasma sintered Al–Zn–Mg–Cu alloy. *Acta Phys Pol A* 128:602–605. <https://doi.org/10.12693/APhysPolA.128.602>
18. Feijoo I, Cabeza M, Merino P, Pena G, Perez MC, Cruz S, Rey P (2019) Estimation of crystal size and lattice strain in nano sized TiC particle reinforced 6005A aluminium alloy from X-ray diffraction line broadening. *Powder Technol* 343:19–28. <https://doi.org/10.1016/j.powtec.2018.11.010>
19. Maity S, Sinha A, Bera S (2018) A novel study on mechanically alloyed Al–Mg system by X-ray diffraction technique. *Nano-Struct Nano-Obj* 16:63–68. <https://doi.org/10.1016/j.nanoso.2018.04.005>
20. Rane GK, Welzel U, Meka SR, Mittemeijer EJ (2013) Non-monotonic lattice parameter variation with crystallite size in nanocrystalline solids. *Acta Mater* 61:4524–4533. <https://doi.org/10.1016/j.actamat.2103.04.021>
21. Jeyasimman D, Sivasankaran S, Sivaprasad K, Narayanasamy R, Kambali RS (2014) An investigation of the synthesis, consolidation and mechanical behaviour of Al6061 nanocomposites reinforced by TiC via mechanical alloying. *Mater Des* 57:394–404. <https://doi.org/10.1016/j.matdes.2013.12.067>
22. Rajesh Kumar B, Hymavathi B (2017) X-ray peak profile analysis of solid state sintered alumina doped zinc oxide ceramics by Williamson–Hall and size strain plot methods. *J Asian Ceram Soc* 5:94–103. <https://doi.org/10.1016/j.jascer.2017.02.001>
23. Sivasankaran S, Sivaprasad K, Narayanasamy R, Satyanarayana PV (2011) X-ray peak broadening analysis of AA 6061100–x–x wt.% Al<sub>2</sub>O<sub>3</sub> nanocomposite prepared by mechanical alloying. *Mater Charact* 62:661–672. <https://doi.org/10.1016/j.matchar.2011.04.017>
24. Prabhu YT, Rao KV, Kumar VSS, Kumari BS (2014) X-ray analysis by Williamson–Hall and size-strain plot methods of ZnO nanoparticles with fuel variation. *J NanoSci Eng* 4:21–28. <https://doi.org/10.4236/wjnse.2014.41004>
25. Toozandehjani M, Matori KA, Ostovan F, Abdul Aziz S, Mamat MS (2017) Effect of milling time on the microstructure, physical and mechanical properties of Al–Al<sub>2</sub>O<sub>3</sub> nanocomposite synthesized by ball milling and powder metallurgy. *Materials* 10:2–17. <https://doi.org/10.3390/ma10111232>
26. dos Santos Torres C, Schaeffer L (2010) Effect of high energy milling on the microstructure and properties of WC–Ni composite. *Mater Res* 13:293–298. <https://doi.org/10.1590/S1516-14392010000300004>
27. Sharma P, Sharma S, Khanduja D (2015) On the use of ball milling for the production of ceramic powders. *Mater Manuf Process* 30:1370–1376. <https://doi.org/10.1080/10426914.2015.1037904>

# Optimization of Solar Tunnel Dryer for Four Different Edible Products Using Response Surface Methodology



V. Subbian, R. Christu Paul, R. Sathish Kumar, and V. Nadanakumar

**Abstract** The work analyzes the performance of a solar tunnel dryer for drying four different products (mango slice, citrus, beef, fish) under forced convection by using a DC blower run by a photovoltaic panel (200 w). An experimental setup of solar tunnel dryer has been designed and fabricated. Experiments have been performed during summer season. The system is operated between 30 and 69 °C. The dryer is simple in construction, at a low cost, with locally available materials. The performance of the designed drier is evaluated by carrying drying experiments at Nagercoil, Tamil Nadu, India (8.1700 °N, 77.4300 °E). RSM software was used to investigate estimation of capacity optimization and acceptability using desirability for four different products. The independent variables or responses were time, air temperature, and solar radiation. These researches are applicable to various process industries to analyze the probable utilization in various forms.

**Keywords** Solar energy · Solar dryer · Experimental performance · Drying capacity · Response surface methodology

## 1 Introduction

Mangoes cultivated in South Asia for thousands of years reached East Asia between the fifth and fourth centuries BC. Commercial and subsistence fishers hunt fish in wild fisheries or ponds or cages in the ocean. Beef is the third most widely consumed meat in the world, accounting for about 25% of meat production worldwide, after pork and poultry at 38% and 30%, respectively. A drying process is needed to preserve and inverse the shelf life of such edible end products, and an open drying process under direct sunlight is an efficient system of utilizing solar energy [1, 2]. The effectiveness

---

V. Subbian

Department of Mechanical Engineering, ACE College of Engineering, Thiruvananthapuram, Kerala, India

R. Christu Paul · R. Sathish Kumar (✉) · V. Nadanakumar

Department of Automobile Engineering, Hindustan Institute of Technology and Science, Chennai, Tamil Nadu 603103, India

e-mail: [sathish.rajamanickam@gmail.com](mailto:sathish.rajamanickam@gmail.com)

of continuous solar dryer, integrated with desiccant thermal storage for drying cocoa beans, has to improve specific energy consumption and drying time has been reported [3].

Solar dryer performance with forced convection and experimentally proved to be efficient compared to other plants [4]. This work was carried out using the simulation method which is suitable for design of passive solar dryers to find the optimum mass airflow [5]. A report on the mixed-mode solar dryer with packed bed PCM, capable of storage of thermal energy in the form of latent heat and sensible heat during daytime, had been presented by Jain and Tewari [3].

A review of various types of solar dryers for drying various commodities was made, and a computer-based technology was designed leading to many simulation tools to investigate the process characteristic of any system before its fabrication [6]. In this drying process, a diagonal batch dryer was developed for batch uniformity using energy utilization, energy utilization ratio, and exergy losses increased with the increase in drying air temperature and decreased with the increase in potato slice thickness [7]. Mish et al. [3] had studied the performance of a solar-assisted solid desiccant dryer for kenaf core fiber drying under low radiation (average  $394 \text{ W/m}^2$ ).

The experimental investigation and economic evaluation of a new mixed-mode solar greenhouse dryer for drying red pepper and grape in the open sun and under the greenhouse effect in the falling rate period were carried out and reported by Aymen [8]. Chan et al. [9] have conducted the study and reported that the drying efficiency of the dryer which was 35.7% while the total specific energy (including solar radiation) was  $9.475 \text{ MJ/kg}^1$  of water evaporated. Borah et al. [3] had presented their works on drying kinetics of whole and sliced turmeric rhizome in a solar conduction dryer where the overall thermal efficiency was 55%. Mustayen et al. [10] had studied the performance of different solar dryers. The use of solar energy allows reducing the electric energy inputs, with thermal efficiencies varying between 0.22 and 0.67 [11]. CFD fluent software 6.3 was used in the simulation and validation of the vanilla drying process in an indirect solar dryer [11].

The results of an experimental drying study as pineapple in a new solar hybrid dryer were studied and reported [12, 13] had presented his work on optimization of the pistachio nut roasting process using response surface methodology for color parameters in the modeling and optimization. The artificial neural network models and response surface methodology were used to enable optimization and acceptability using desirability was performed [14]. Drying experiments were carried out using a dryer consisting of a centrifugal fan that forces heated air from the heating elements to the sampling drum [15]. In this paper, the air drier consists of three basic units, a fan providing the desired velocity, a heat exchanger using saturated steam controlling the temperature of the drying air, and an air chamber [16–20].

## 2 Materials and Methods

### 2.1 Experimental Setup

The dryer essentially consists of a flat plate air heating collector and a tunnel drying unit as shown in Fig. 1. Both the collector and the drying unit are covered with UV stabilized plastic sheets. The product to be dried is placed in a single layer on a wire mesh inside the tunnel drier. Thermocol, pebbles, and sawdust are used as insulation materials in different layers to reduce the heat loss from the bottom of the drier. Thermocouples are provided to measure the temperatures during drying period. A chimney is provided to maintain the airflow at the end of the dryer toward atmosphere. The whole system is placed horizontally on a raised platform. Atmospheric air enters the system through the inlet by forced convection. Solar radiation passes through the transparent cover of the collector and heats the absorber. Ambient air enters through the collector by the DC blower run by power from photovoltaic cells. Heat is transferred from absorber plate to air above the collector; heated air from collector while passing over the products absorbs moisture from the products. Figure 2 shows a schematic view of the solar tunnel dryer with DC blower. Heat by solar radiation also helps drying the products. This enhances the drying rate and the temperature in the drier rises to the range of 30–69 °C.



**Fig. 1** Photographic view of solar tunnel dryer

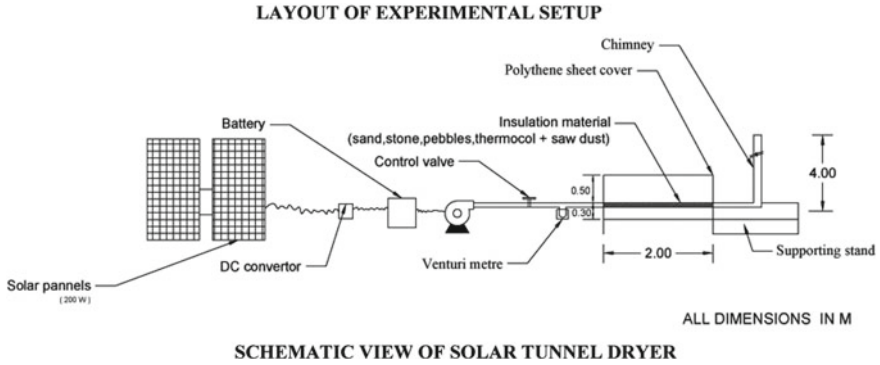


Fig. 2 Schematic view of the solar tunnel dryer with DC blower

## 2.2 Experimental Procedure for Drying Products

All the parameters affecting the performance of the drier were measured. A thermocouple was used to measure the drying air temperature along the flow direction of the air inside the dryer, and a solar meter was used to measure the incident radiation. The ambient temperature of the air is measured with a thermometer. The velocity of drying air was measured by an anemometer. Weight loss of the product during drying period was also measured with an electronic balance. The direct sun-dried samples (of 1 kg) were also weighed. All these data were recorded at 1 h intervals. The samples of drying products were placed on the wire mesh of the drier in a single layer. Experiment was started at about 6.00 am and was stopped at about 6.00 pm. To compare the performance of the tunnel drier with that of the direct sun drying, samples of mango slice, citrus, beef, and fish were placed on trays in single layer inside the drier.

## 3 Results and Discussion

### 3.1 Drying of Mango Slice

The variation of solar radiation and thermal efficiency during experimentation is shown in Fig. 3. A maximum solar intensity of  $850 \text{ W m}^{-2}$  was observed. The moisture content and the moisture removal process are fully depending upon the temperature and mass flow rate. According to the solar radiation, the moisture is reduced to 29.00% shown in Fig. 4. The thermal efficiency increases from 0% to such a peak value of 10.86% and then decreases to 4% as shown in Fig. 3.

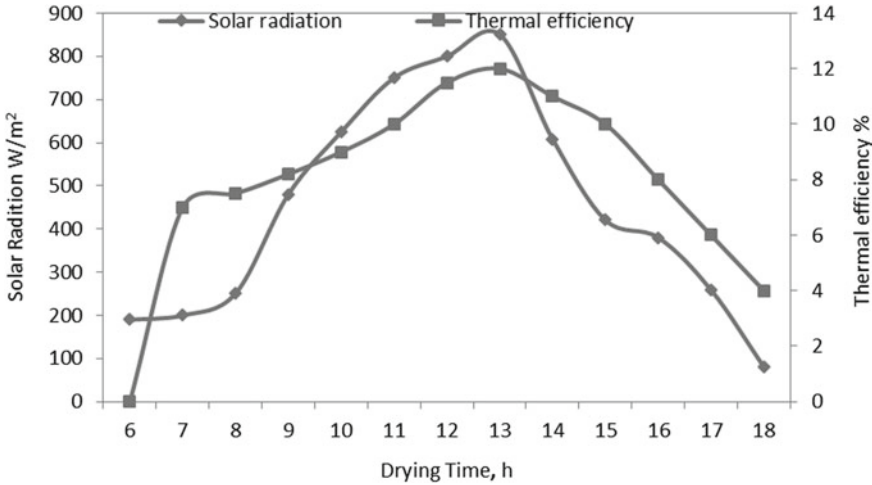


Fig. 3 Variation of solar radiation and thermal efficiency with drying time for mango slice

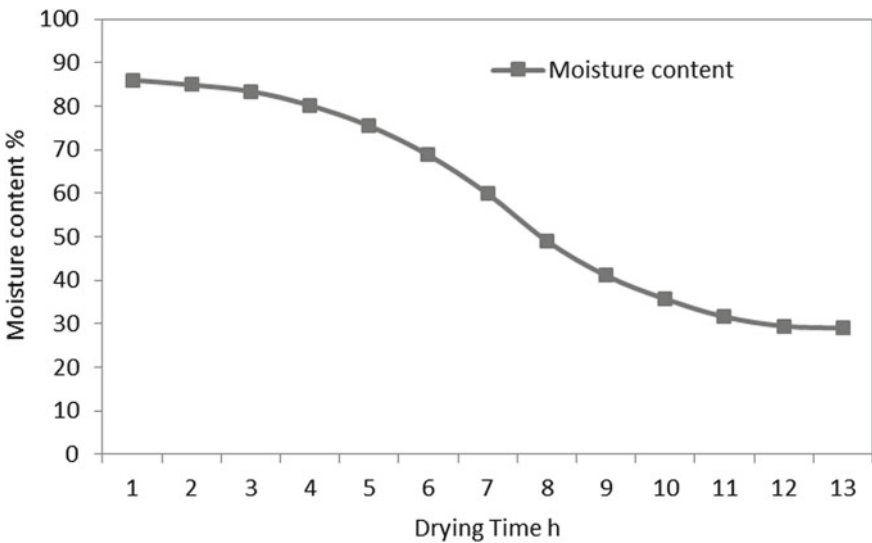
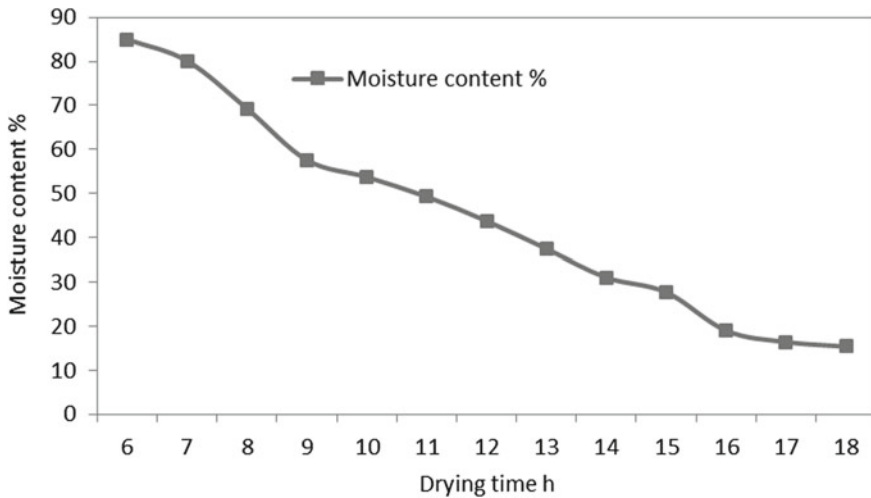
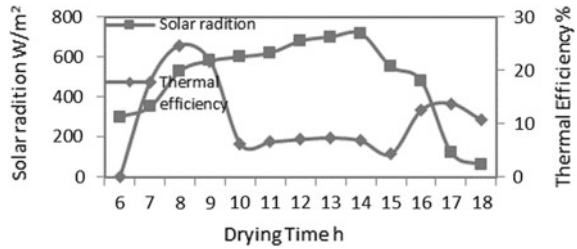


Fig. 4 Variation of moisture content with drying time for mango slice

### 3.2 Drying of Citrus

The variation of solar radiation and thermal efficiency during experimentation is shown in Fig. 5. A maximum solar intensity of  $715 W m^{-2}$  was observed. The moisture content and the moisture removal process are fully depending upon the temperature and mass flow rate. The moisture is reduced to 15.39% shown in Fig. 6.

**Fig. 5** Variation of solar radiation and thermal efficiency with drying time for citrus



**Fig. 6** Variation of moisture content with drying time for citrus

The thermal efficiency is also varying from 0 to 10.61%. The maximum thermal efficiency is 24% shown in Fig. 5.

### 3.3 Drying of Beef

The variation of solar radiation and thermal efficiency during experimentation is shown in Fig. 7. A maximum solar intensity of 880 W m<sup>-2</sup> had been observed. The moisture content and the moisture removal process are fully depending upon the temperature and mass flow rate. The moisture is reduced to 2.43% shown in Fig. 8. The thermal efficiency is also varying from 0 to 47.26%. The maximum thermal efficiency is 63% shown in Fig. 7.

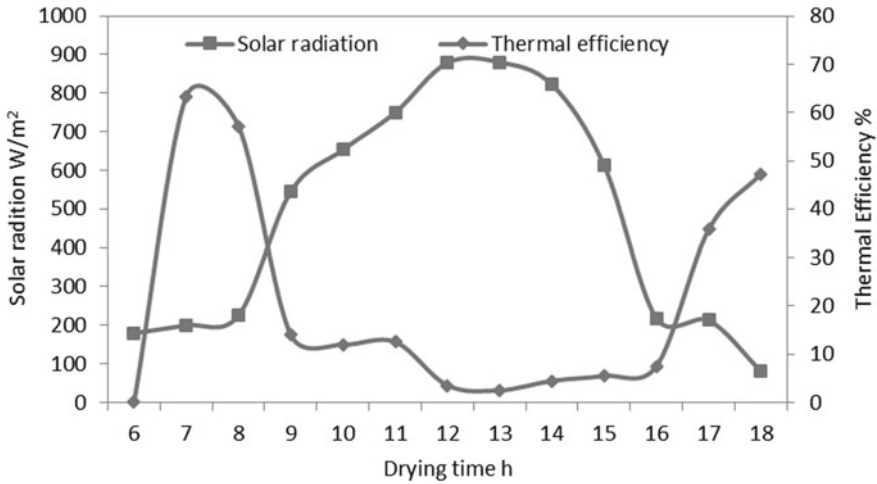


Fig. 7 Variation of solar radiation and thermal efficiency with drying time for beef

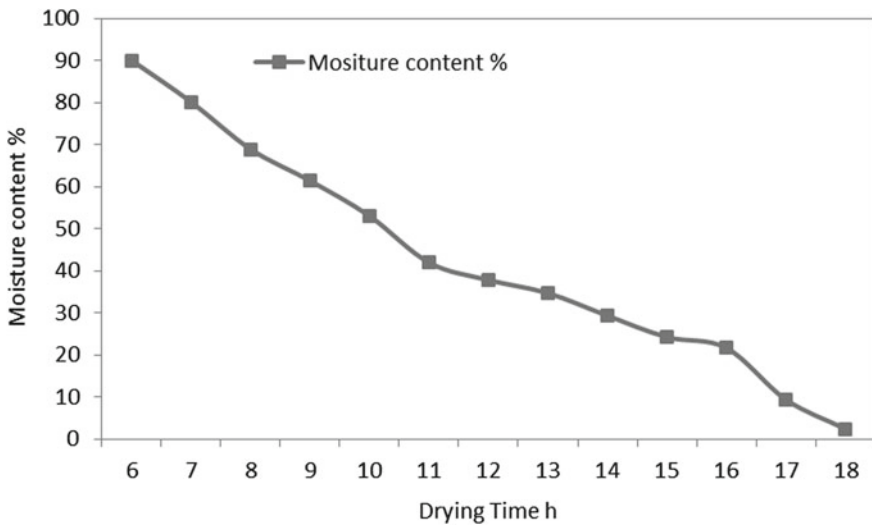


Fig. 8 Variation of moisture content and drying time for beef

### 3.4 Drying of Fish

The variation of solar radiation and thermal efficiency during experimentation is shown in Fig. 9. A maximum solar intensity of  $715 \text{ W m}^{-2}$  had been observed. The moisture content and the moisture removal process are fully depending upon the temperature and mass flow rate. The moisture is reduced to 13.17% shown in



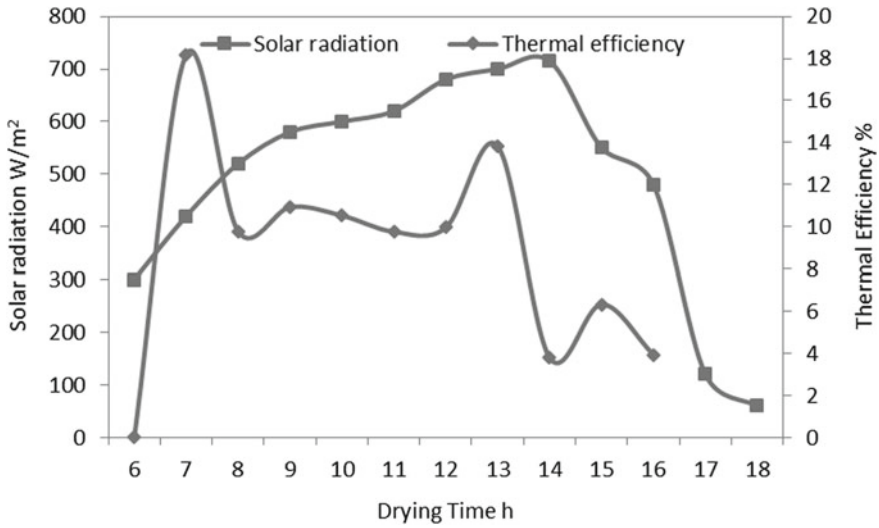


Fig. 9 Variation of solar radiation and thermal efficiency with drying time for fish

Fig. 10. The thermal efficiency is also varying from 0 to 3.9%. The maximum thermal efficiency is 18.18% shown in Fig. 9.

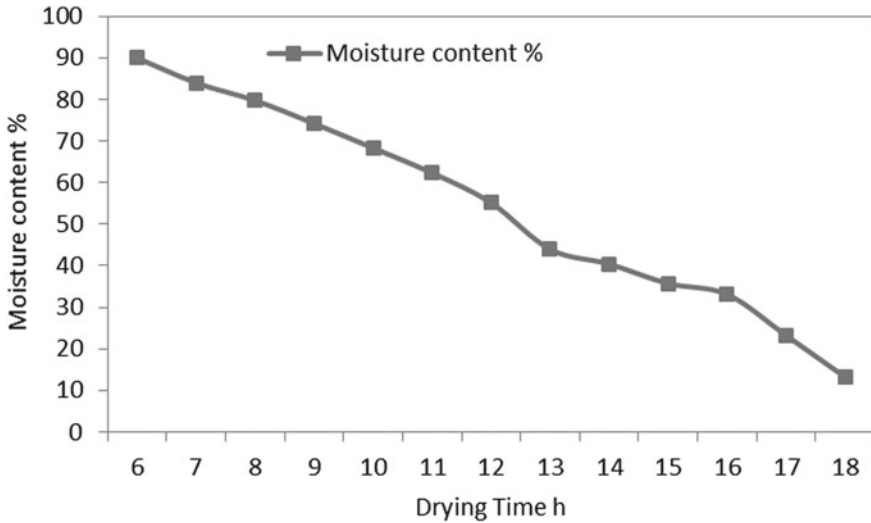


Fig. 10 Variation of moisture content and drying time for fish

### 4 Statistical Analysis

The experimental results were analyzed using the central composite design method to obtain the best fit empirical mathematical model. The type of polynomial model obtained for the responses is linear, two-factor interaction (2F1), quadratic, and cubic. ANOVA was conducted to determine significant effects of process variable on each response and to fit second-order polynomial models to experimental data. Regression equation coefficients of the proposed models and statistical significance of all main effect calculated for each response were obtained. ANOVA also showed that the lack of fit was not significant for all response surface models at 95% confidence level. To visualize the combined effects of three factors on any response, the response surface and contour plots were generated for each of fitted models of three independent variables.

#### 4.1 Statistical Analysis for Mango Slice

The type of polynomial model obtained for the responses is quadratic. Two different response surface plots (Figs. 11, 12, 13 and 14) were illustrated by maintaining

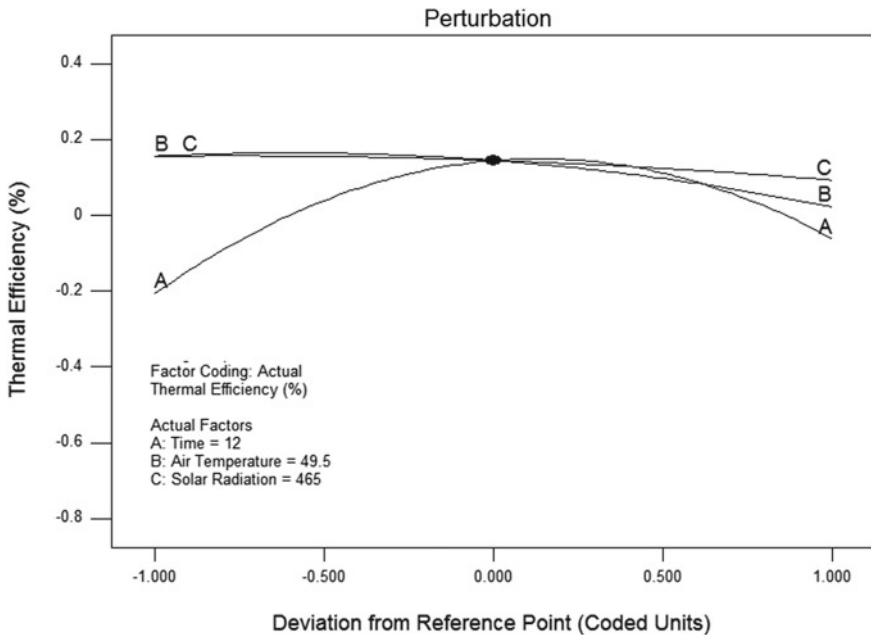


Fig. 11 Perturbation graph showing the effect of independent variable on thermal efficiency (mango slice)

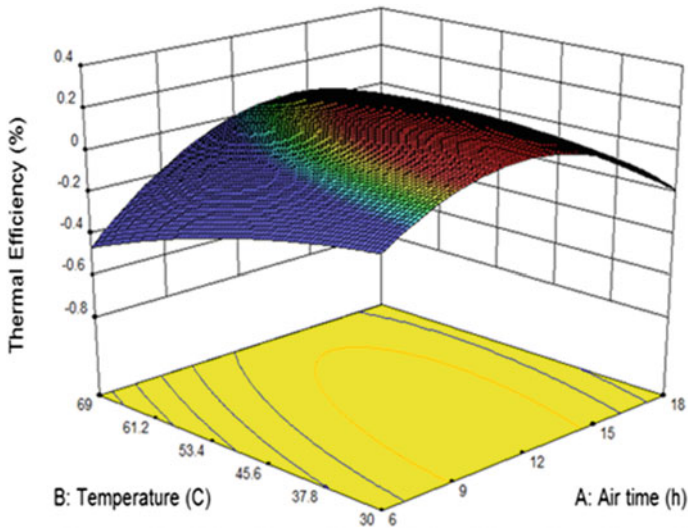


Fig. 12 Response surface and contour plots for thermal efficiency (mango slice)

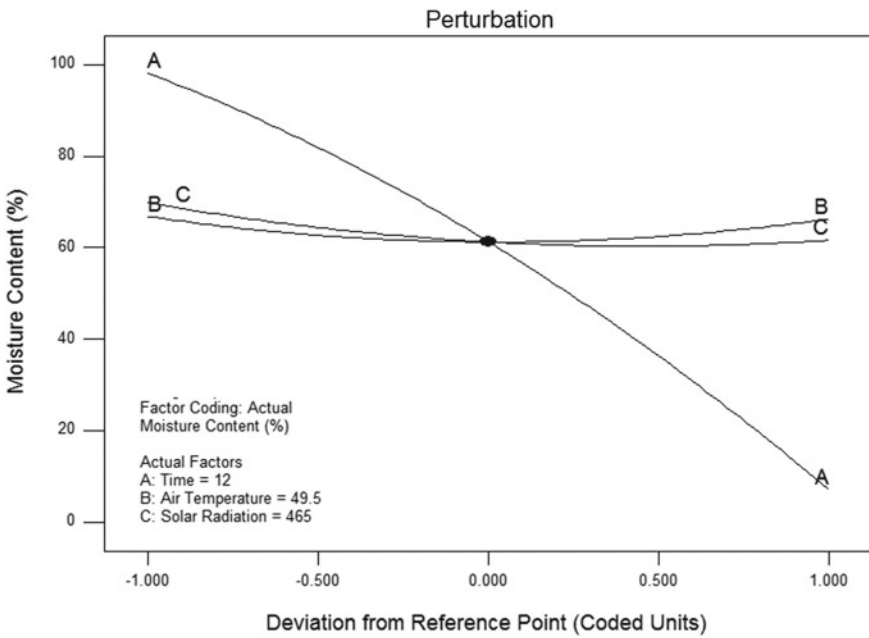


Fig. 13 Perturbation graph showing the effect of independent variable on moisture content (mango slice)

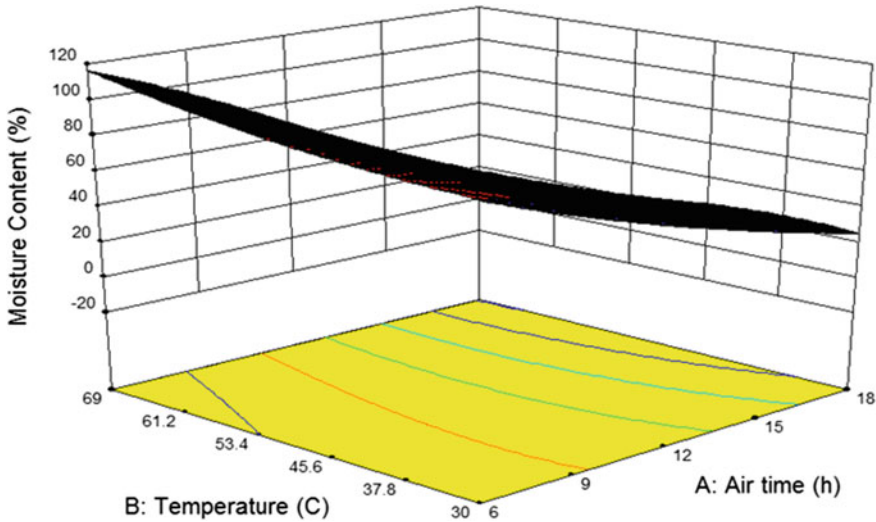


Fig. 14 Response surface and contour plots for moisture content (mango slice)

one factor constant for each figure. The effect of variables on response was seen by the evaluation of these plots. The effects that are not significant ( $p > 0.05$ ) and predicted  $R^2$ . A predicted- $R^2$  comparable to fitted  $R^2$  implies that the fit is adequate for predicting. The effects of independent variables on the responses as represented in perturbation graphs (Fig. 11) revolves that air temperature and solar radiation showed a lowering effect regarding thermal efficiency. The linear effect of air temperature and solar radiation in Table 1 shows a negative effect on thermal efficiency. The interactive effect of BC has a positive effect on thermal efficiency. These results indicate an increase in thermal efficiency with an increase in time and air temperature. Figure 12 also indicates the more pronounced effect of thermal efficiency compared to the time and air temperature. The quadratic terms of air temperature and solar radiation harm thermal efficiency. The effects of independent variables on the responses as represented in perturbation graphs (Fig. 13) revolve that time, air temperature and solar radiation showed a lowering effect regarding moisture content. The linear effect of all variables in Table 1 shows a negative effect on moisture content. Figure 14 indicates a decrease in moisture content with an increase of time and temperature at process duration. The quadratic terms of temperature have a positive effect on moisture content. The models as fitted provide an adequate approximation to the true system.

$$\begin{aligned}
 \text{Thermal efficiency} = & +0.15 + 0.073 * A - 0.067 * B - 0.032 * C \\
 & + 0.13 * AB - 0.065 * AC + 0.14 * BC - 0.28 * A^2 \\
 & - 0.056 * B^2 - 0.021C^2
 \end{aligned}
 \tag{1}$$

**Table 1** Analysis of variance and coefficients for predicted models

Source	DF	Thermal efficiency (TE)			DF	Moisture content (MC)		
		Coefficient	Sum of squares	P value		Coefficient	Sum of squares	P value
Model	9	0.15	0.021	<0.0001	9	61.29	8471.46	<0.0001
A	1	0.073	$4.750 \times 10^{-4}$	0.0004	1	-45.58	187.62	<0.0001
B	1	-0.067	$4.154 \times 10^{-4}$	0.0007	1	-0.26	$6.392 \times 10^{-3}$	0.6520
C	1	-0.032	$2.848 \times 10^{-4}$	0.0026	1	-4.08	4.71	<0.0001
AB	1	0.13	$1.133 \times 10^{-4}$	0.0310	1	-13.22	1.17	<0.0001
AC	1	-0.065	$5.748 \times 10^{-5}$	0.1042	1	-7.38	0.75	0.0005
BC	1	0.14	$5.263 \times 10^{-5}$	0.1180	1	-6.23	0.10	0.0921
A <sup>2</sup>	1	-0.28	$2.489 \times 10^{-3}$	<0.0001	1	-8.65	2.38	<0.0001
B <sup>2</sup>	1	-0.056	$1.977 \times 10^{-5}$	0.3193	1	5.31	0.18	0.0340
C <sup>2</sup>	1	-0.021	$5.138 \times 10^{-6}$	0.6048	1	4.47	0.24	0.0167
Residual	10		$1.799 \times 10^{-4}$		10		0.30	
Lack of fit	3		$1.799 \times 10^{-4}$		3		0.30	
Pure error	7		0.000		7		0.000	
Total	19				19			
R <sup>2</sup>		0.9916				1.0000		
Adj-R <sup>2</sup>		0.9840				0.9999		
Pre-R <sup>2</sup>		0.9286				0.9994		
Adeq precision		41.741				468.236		

$p < 0.05$  is significant at  $\alpha = 0.05$ ; lack of fit is not significant at  $p > 0$

$$\begin{aligned}
 \text{Moisture content} = & +61.29 - 45.58 * A - 0.26 * B - 4.08 * C - 13.22 * AB \\
 & - 7.38 * AC - 6.23 * BC - 8.65 * A^2 + 5.31 * B^2 + 4.47 * C^2
 \end{aligned}
 \tag{2}$$

### 4.2 Statistical Analysis for Citrus

The type of polynomial model obtained for the responses are quadratic model in thermal efficiency. Two different response surface plots (Figs. 15, 16, 17 and 18) were illustrated by maintaining one factor constant for each figure. The effect of independent variables on the responses is represented in perturbation graphs (Fig. 15). The increase of time and solar radiation had an increase in thermal efficiency response. The linear effect of air temperature in Table 2 shows negative effect on thermal efficiency. Figure 16 also indicates the more pronounced effect of thermal efficiency compared to time and air temperature. The quadratic terms of air temperature have negative effect on thermal efficiency. The interactive effect of BC has positive effect on thermal efficiency. The effect of independent variables on the responses as represented in perturbation graphs (Fig. 17) revolves that time and solar radiation showed lowering effect with reference to moisture content. The type of polynomial model obtained for the responses are linear model in moisture content. The linear effect of the variable in Table 2 shows time and solar radiation have negative effect on moisture content. Figure 18 indicates decrease in moisture content with increase of time and temperature at process duration. The model as fitted provides an adequate approximation to the true system.

$$\text{Thermal efficiency} = -8.04 + 74.49 * A - 81.48 * B + 68.98 * C$$

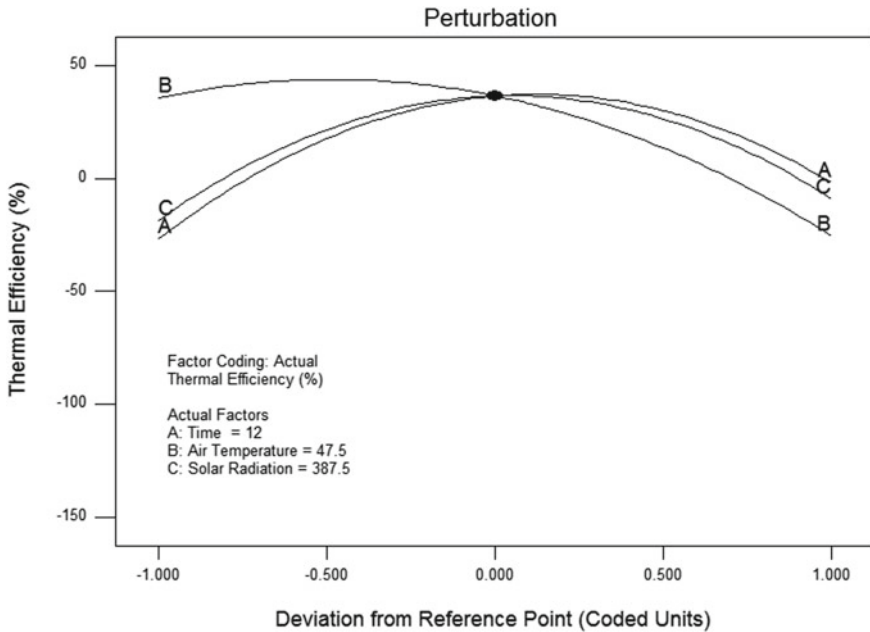


Fig. 15 Perturbation graph showing the effect of independent variable on thermal efficiency (citrus)

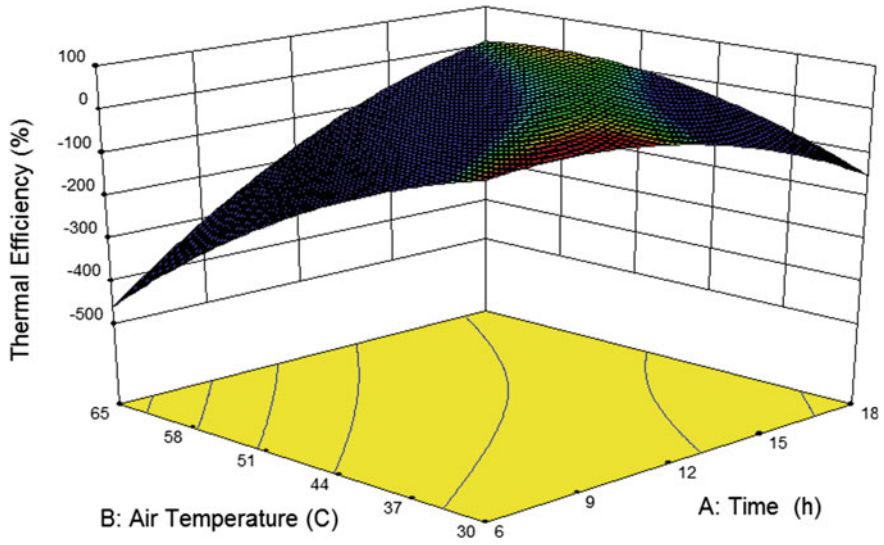


Fig. 16 Response surface and contour plots for thermal efficiency (citrus)

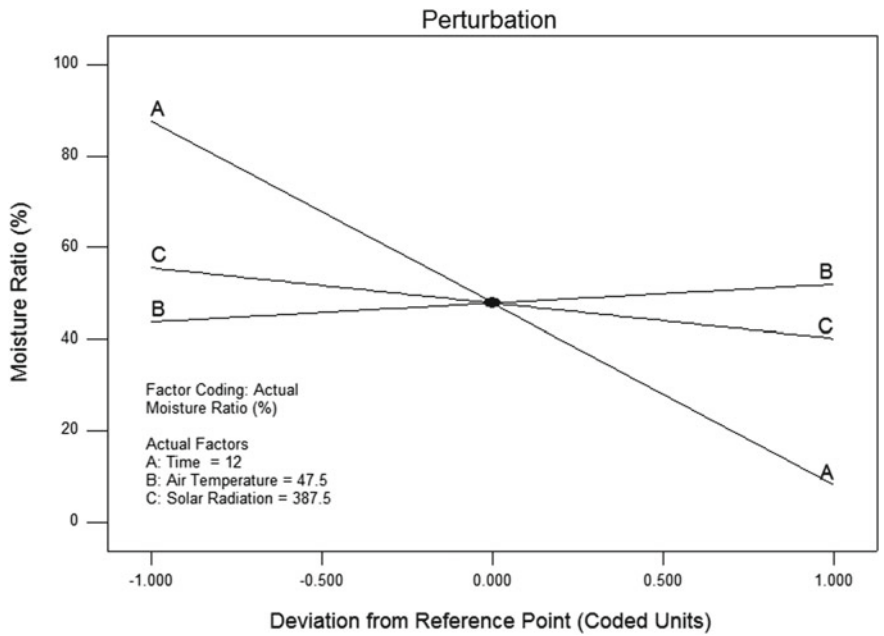


Fig. 17 Perturbation graph showing the effect of independent variable on moisture content (citrus)

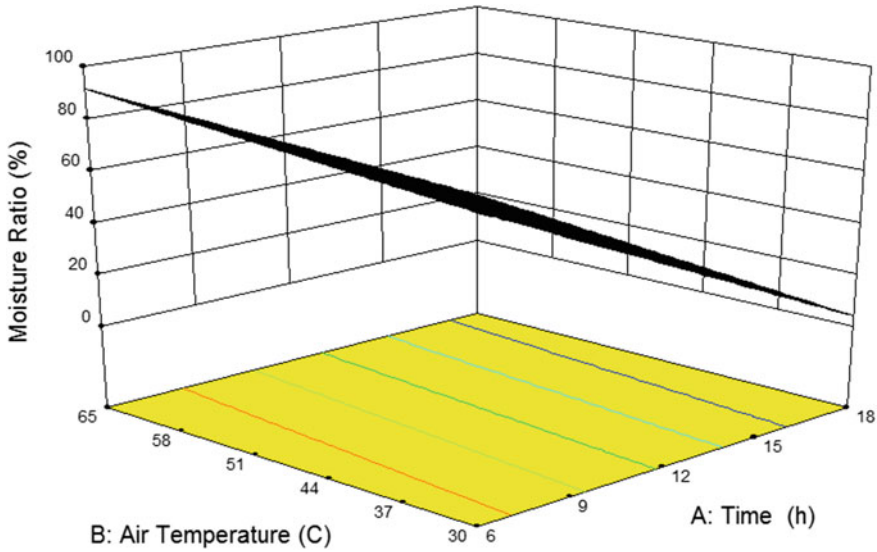


Fig. 18 Response surface and contour plots for moisture content (citrus)

$$\begin{aligned}
 &+ 161.82 * AB - 144.47 * AC + 141.38 * BC - 71.10 * A^2 \\
 &- 62.92 * B^2 - 70.57 * C^2
 \end{aligned}
 \tag{3}$$

$$\text{Moisture content} = +47.86 - 39.77 * A + 4.12 * B - 7.68 * C
 \tag{4}$$

### 4.3 Statistical Analysis for Beef

The type of polynomial model obtained for the responses is linear and quadratic. Two different response surface plots (Figs. 19, 20, 21 and 22) were illustrated by maintaining one factor constant for each figure. The effect of independent variables on the responses is represented in perturbation graphs (Fig. 19). The increase in time and solar radiation had an increased thermal efficiency response. The linear effect of air temperature in Table 3 shows a negative effect on thermal efficiency. Figure 20 also indicates the more pronounced effect of thermal efficiency compared to the time and air temperature. The quadratic terms of air temperature harm thermal efficiency. The interactive effect of BC has a positive effect on thermal efficiency. The effect of independent variables on the responses as represented in perturbation graphs (Fig. 21) revolves that time and solar radiation showed a lowering effect concerning moisture content. The type of polynomial model obtained for the responses is the linear and quadratic model in moisture content. The linear effect of the variable in Table 2 shows



**Table 2** Analysis of variance and coefficients for predicted models

Source	DF	Thermal efficiency (TE)			DF	Moisture content (MC)		
		Coefficient	Sum of squares	P value		Coefficient	Sum of squares	P value
Model	9	-8.04	943.51	0.0084	3	47.86	9431.02	<0.0001
A-time	1	74.49	173.92	0.0149	1	-39.77	3046.70	<0.0001
B-air temperature	1	-81.48	183.29	0.0131	1	4.12	21.50	0.0367
C-solar radiation	1	68.98	272.22	0.0043	1	-7.68	102.01	0.0001
AB	1	161.82	284.34	0.0038				
AC	1	-144.47	483.59	0.0006				
BC	1	141.38	281.84	0.0039				
A <sup>2</sup>	1	-71.10	145.88	0.0228				
B <sup>2</sup>	1	-62.92	227.90	0.0073				
C <sup>2</sup>	1	-70.57	217.11	0.0083				
Residual	10		202.00		16		66.23	
Lack of fit	3		202.00		9		66.23	
Pure error	7		0.000		7		0.000	
Total	19		1145.52		19		9497.25	
R <sup>2</sup>		0.8237				0.9930		
Adj R-squared		0.6649				0.9917		
Pred R <sup>2</sup>		-30.3740				0.9859		
Adeq precision		6.673				80.203		

$p < 0.05$  is significant at  $\alpha = 0.05$ ; lack of fit is not significant at  $p > 0$

time and solar radiation harmed moisture content. Figure 22 indicates a decrease in moisture content with an increase of time and temperature at process duration. The model as fitted provides an adequate approximation to the true system.

$$\begin{aligned}
 \text{Thermal efficiency} = & +26.38 + 73.03 * A - 128.56 * B + 6.69 * C + 62.52 * AB \\
 & - 4.48 * AC + 149.93 * BC - 189.59 * A^2 \\
 & - 37.99 * B^2 + 28.17 * C^2
 \end{aligned} \tag{5}$$

$$\begin{aligned}
 \text{Moisture content} = & +29.68 - 13.69 * A - 16.34 * B + 3.94 * C \\
 & + 36.53 * AB - 4.07 * AC - 2.87 * BC - 6.18 * A^2 \\
 & - 0.070 * B^2 + 13.86 * C^2
 \end{aligned} \tag{6}$$

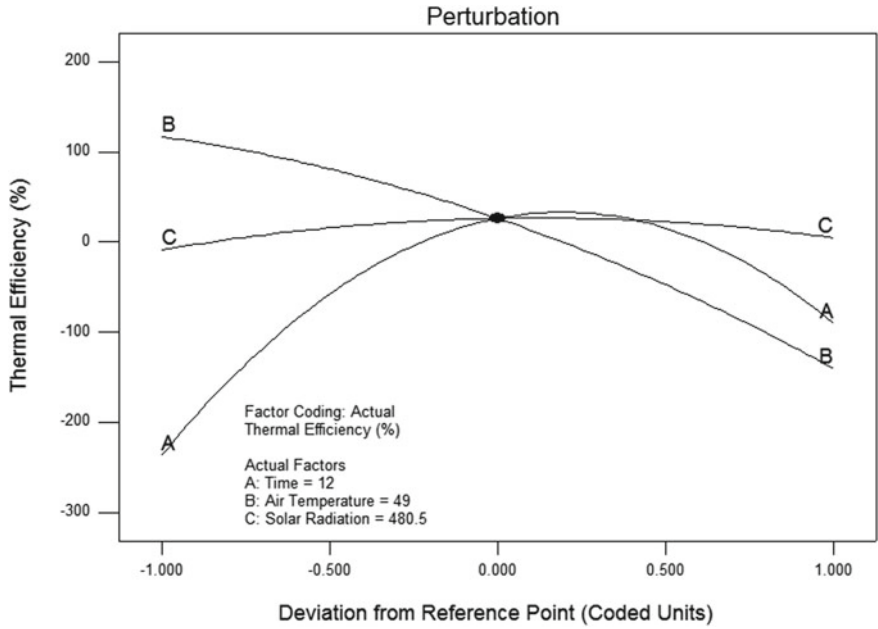


Fig. 19 Perturbation graph showing the effect of independent variable on thermal efficiency (beef)

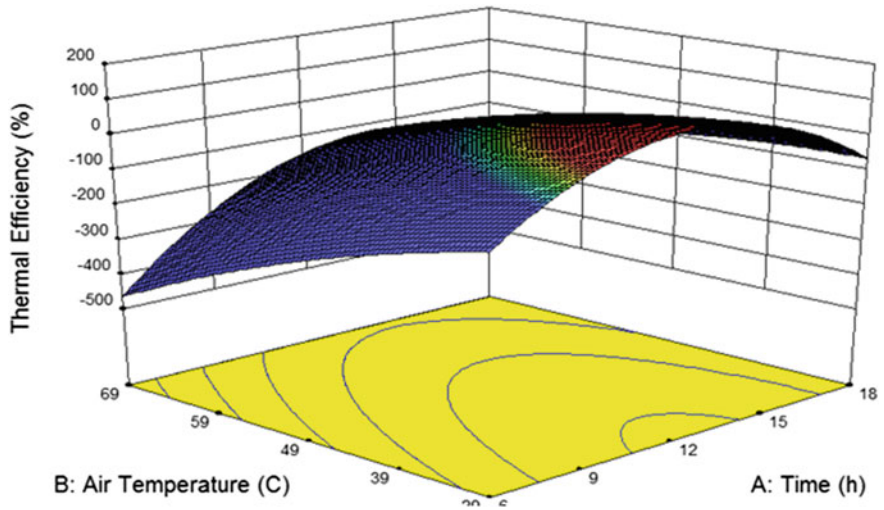


Fig. 20 Response surface and contour plots for thermal efficiency (beef)

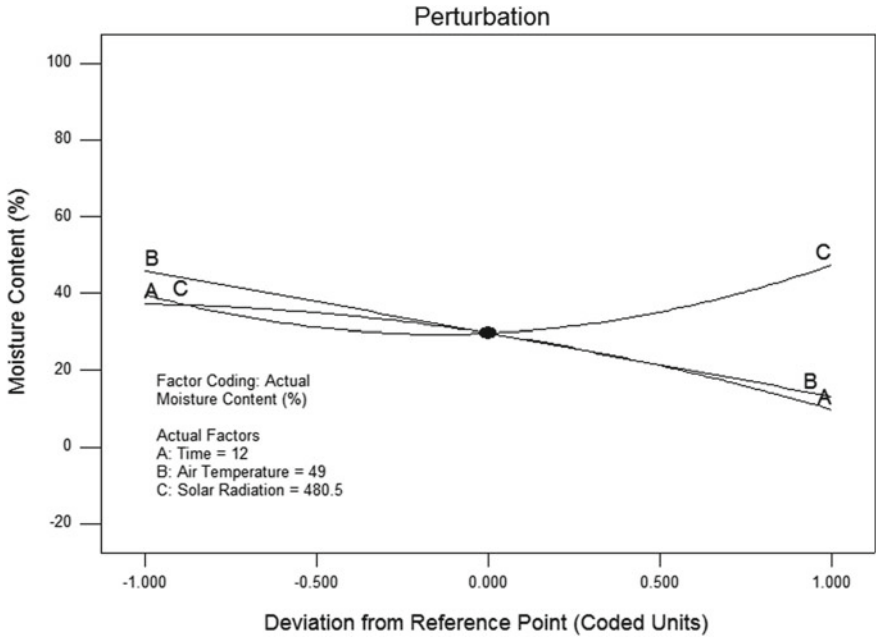


Fig. 21 Perturbation graph showing the effect of independent variable on moisture content (beef)

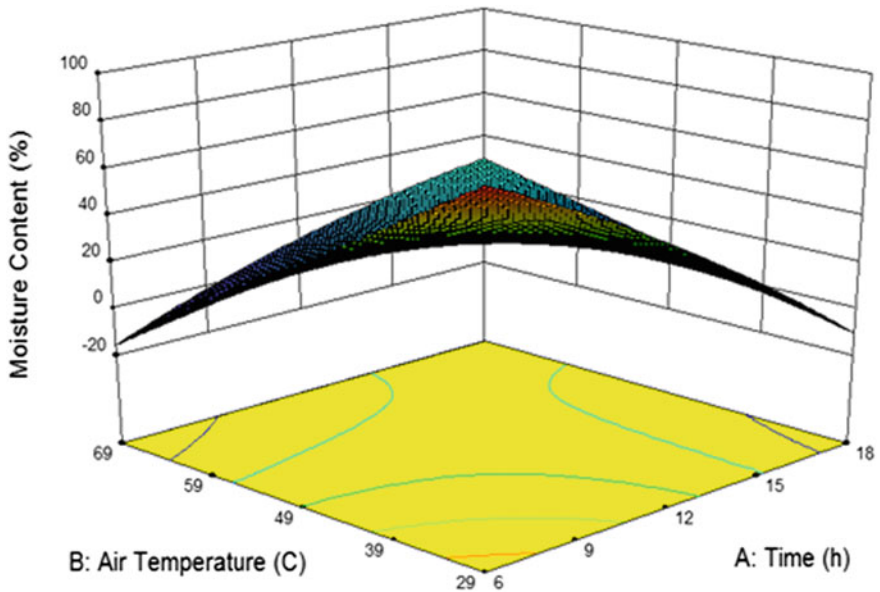


Fig. 22 Response surface and contour plots for moisture content (beef)

**Table 3** Analysis of variance and coefficients for predicted models

Source	DF	Thermal efficiency (TE)			DF	Moisture content (MC)		
		Coefficient	Sum of squares	P value		Coefficient	Sum of squares	P value
Model	9	-8.04	943.51	0.0084	9	47.86	9431.02	<0.0001
A	1	74.49	173.92	0.0149	1	-39.77	3046.70	<0.0001
B	1	-81.48	183.29	0.0131	1	4.12	21.50	0.0367
C	1	68.98	272.22	0.0043	1	-7.68	102.01	0.0001
AB	1	161.82	284.34	0.0038	1			
AC	1	-144.47	483.59	0.0006	1			
BC	1	141.38	281.84	0.0039	1			
A <sup>2</sup>	1	-71.10	145.88	0.0228	1			
B <sup>2</sup>	1	-62.92	227.90	0.0073	1			
C <sup>2</sup>	1	-70.57	217.11	0.0083	1			
Residual	10		202.00		10		66.23	
Lack of fit	3		202.00		3		66.23	
Pure error	7		0.000		7		0.000	
Total	19		1145.52		19		9497.25	
R <sup>2</sup>		0.8237				0.9930		
Adj-R <sup>2</sup>		0.6649				0.9917		
Pre-R <sup>2</sup>		-30.3740				0.9859		
Adeq precision		6.673				80.203		

$p < 0.05$  is significant at  $\alpha = 0.05$ ; lack of fit is not significant at  $p > 0$

### 4.4 Statistical Analysis for Fish

The type of polynomial model obtained for the responses is quadratic in thermal efficiency. Two different response surface plots (Figs. 23, 24, 25 and 26) were illustrated by maintaining one factor constant for each figure. The effect of independent variables on the responses is represented in perturbation graphs (Fig. 23). The increase in air temperature and solar radiation had an increased thermal efficiency response. The linear effect of time in Table 4 shows a negative effect on thermal efficiency. Figure 24 also indicates the more pronounced effect of thermal efficiency compared to the time and air temperature. The quadratic terms of time and air temperature harm thermal efficiency. The interactive effect of BC has a positive effect on thermal efficiency. The effect of independent variables on the responses as represented in perturbation graphs (Fig. 25) revolves that time and air temperature showed a lowering effect concerning moisture content. The type of polynomial model obtained for the responses is two-factor interaction and quadratic model in moisture content. The linear effect of the

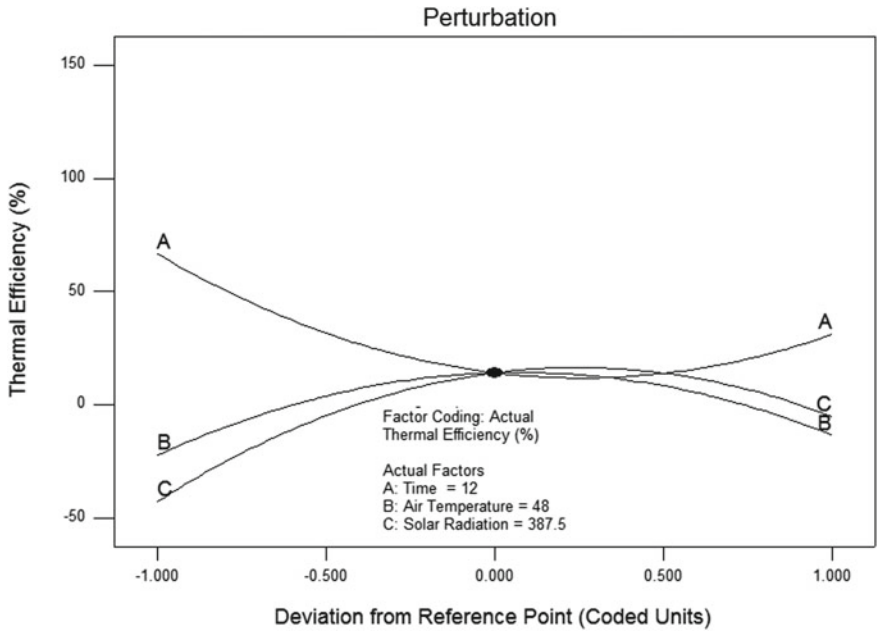


Fig. 23 Perturbation graph showing the effect of independent variable on thermal efficiency (fish)

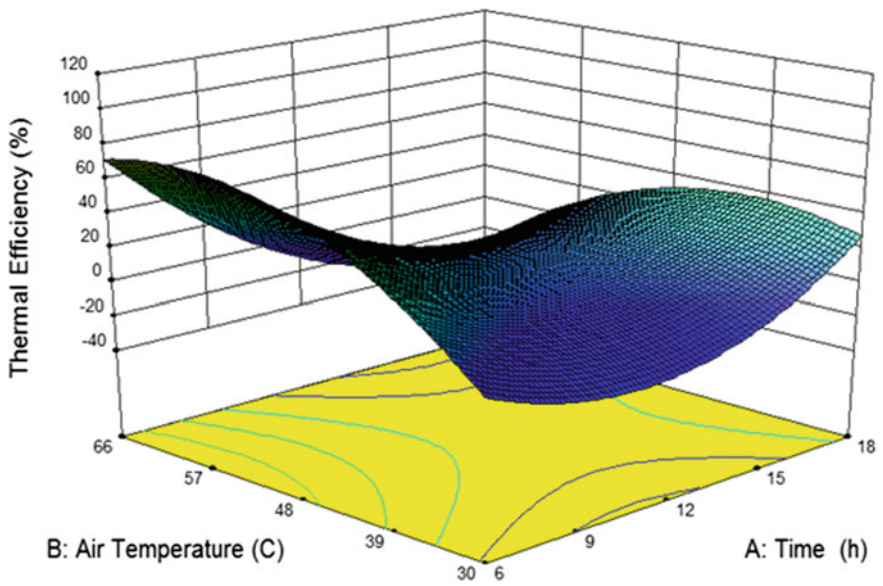


Fig. 24 Response surface and contour plots for thermal efficiency (fish)

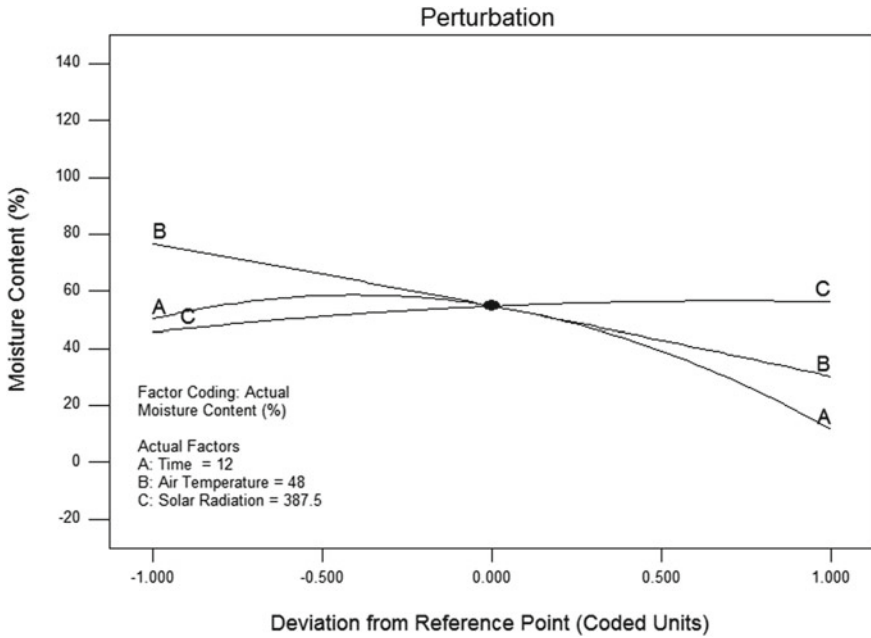


Fig. 25 Perturbation graph showing the effect of independent variable on moisture content (fish)

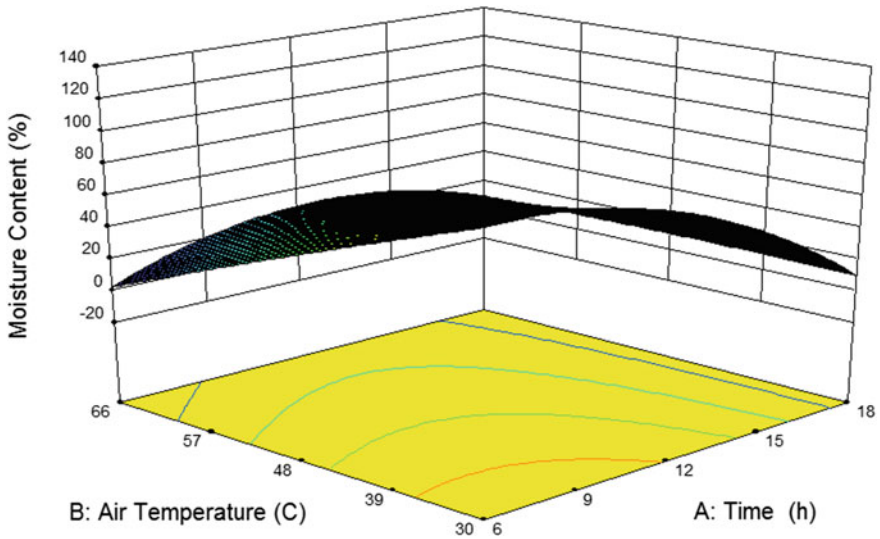


Fig. 26 Response surface and contour plots for moisture content (fish)

**Table 4** Analysis of variance and coefficients for predicted models

Source	Thermal efficiency (TE)		Moisture content (MC)					
	Coefficient	Sum of squares	Coefficient	Sum of squares				
Model	9	14.13	11,085.65	<0.0001	9	54.79	9814.72	<0.0001
A	1	-17.80	0.79	0.8235	1	-19.34	0.94	0.1967
B	1	4.44	0.020	0.9719	1	-23.09	0.54	0.3199
C	1	18.84	1.14	0.7893	1	5.29	0.090	0.6773
AB	1	-32.92	0.92	0.8102	1	22.82	0.44	0.3643
AC	1	-62.23	12.74	0.3803	1	-2.04	0.014	0.8707
BC	1	71.95	3.23	0.6539	1	9.99	0.062	0.7288
A <sup>2</sup>	1	34.72	2.40	0.6989	1	-23.90	1.14	0.1587
B <sup>2</sup>	1	-32.01	3.55	0.6386	1	-1.41	6.914 × 10 <sup>-3</sup>	0.9077
C <sup>2</sup>	1	-38.17	5.64	0.5551	1	-3.80	0.056	0.7422
Residual	10		151.23		10		4.89	
Lack of fit	3		151.23		3		4.89	
Pure error	7		0.000		7		0.000	
Total	19		11,236.88		19		9819.62	
R <sup>2</sup>			0.9865				0.9995	
Adj-R <sup>2</sup>			0.9744				0.9991	
Pre-R <sup>2</sup>			0.7806				0.9950	
Adeq precision			37.758				155.103	

$p < 0.05$  is significant at  $\alpha = 0.05$ ; lack of fit is not significant at  $p > 0$

variable in Table 4 shows time and air temperature harm moisture content. Figure 26 indicates a decrease in moisture content with an increase of time and temperature at process duration. The model as fitted provides an adequate approximation to the true system.

$$\begin{aligned} \text{Thermal efficiency} = & +4.13 - 17.80 * A + 4.44 * B + 18.84 * C \\ & - 32.92 * AB - 62.23 * AC + 71.95 * BC + 34.72 * A^2 \\ & - 32.01 * B^2 - 38.17 * C^2 \end{aligned} \quad (7)$$

$$\begin{aligned} \text{Moisture content} = & +54.79 - 19.34 * A - 23.09 * B + 5.29 * C \\ & + 22.82 * AB - 2.04 * AC + 9.99 * BC - 23.90 * A^2 \\ & - 1.41 * B^2 - 3.80 * C^2 \end{aligned} \quad (8)$$

## 5 Conclusion

In this work, the aim is to perform an experimental analysis using solar dryer for drying food products such as mango slice, citrus, beef, and fish. After performing the experimental analysis, results such as thermal efficiency and moisture content with respect to time and solar radiation had been plotted. Response surface methodology is a powerful tool for modeling of extrusion processing of drying products. Thermal efficiency and moisture content for the drying of mango slice, citrus, beef, and fish can be predicted by the model as fitted. The predicted values obtained from the perturbation and contour plots were closer to the experimental values in the graphical optimization technique. This approach can be extended to solve similar problems to have a detailed comparative study and applications of processing industries.

## References

1. Bala BK, Woods JL (1994) Simulation of the indirect convection solar drying of rough rice. *Sol Energy* 53:259–266
2. Rathore NS, Panwar NL (2011) Design and development of energy efficient walk-in type solar tunnel dryer for industrial. *Appl Environ Progress* 13:125–132
3. Borah A, Hazarika K, Khayer SM (2015) Drying kinetics of whole and sliced turmeric rhizome (*curcuma longa* L.) in a solar conduction dryer. *Inf Process Agric* 2(2):85–92
4. Benhamou A, Fazouane F, Benyoucel B (2014) Simulation of solar dryer performances with forced convection experimentally proved. *Phys Proc* 55:96–105
5. Duran G, Condor M, Altobelli F (2015) Simulation of a passive solar dryer to charqui production using temperature and pressure networks. *Sol Energy* 119:310–318
6. Kumar M, Sansaniwal SK, Khatak P (2016) Progress in dryers for drying various commodities. *Renew Sustain Energy Rev* 55:346–360



7. Amjad W, Hensel O, Munir A, Esper A, Sturm B (2016) Thermodynamics analysis of drying process in a diagonal-batch dryer developed for batch uniformity using potato slices. *J Food Eng* 169:238–249
8. Elkhadraouri A, Kooli S, Hamdi I, Farhat A (2015) Experimental investigation and economic evaluation of a new mixed mode solar greenhouse dryer for drying of red pepper and grape. *Renew Energy* 77:1–8
9. Chan Y, Nining Dyah TM, Kamaruddin A (2015) Solar dryer with pneumatic conveyor. *Energy Proc* 65:378–385
10. Mustayen AGMB, Mekhilef S, Saidur R (2014) Performance study of different solar dryer: a review. *Renew Sustain Energy Rev* 34:463–470
11. Reyes A, Mahn A, Vasquea F (2014) Mushroom dehydration in a hybrid-solar dryer, using a phase change material. *Energy Convers Manage* 83:241–248
12. Gudino-Ayala D, Calderon-Topete A (2014) Pineapple drying using a new solar hybrid dryer. *Energy Proc* 57:1642–1650
13. Kahyaoglu T (2008) Optimization of the pistachio nut roasting process using response surface methodology and gene expression programming. *LWT* 41:26–33
14. Karimi F, Rafiee S, Taheri-Garavand A, Karimi M (2012) Optimization of an air drying process for *Artemisia absinthium* leaves using response surface and artificial neural network models. *J Taiwan Inst Chem Eng* 43:29–39
15. Abbasi Surki A, Sharifzade F, Tavakkol Afshari R, Manjnoun Hosseini N, Gazor HR (2010) Optimization of processing parameters of soybean seeds dried in a constant-bed dryer using response surface methodology. *J Agric Sci Technol* 12:409–423
16. Corozo O, Bracho N, Vasquez A, Pereira A (2008) Optimization of a thin layer drying process for coroba slice. *J Food Eng* 85:372–380
17. Jain D, Tewari P (2015) Performance of indirect through pass natural convective solar crop dryer with phase change thermal energy storage. *Renew Energy* 80:244–250
18. Mish S, Mat S, Ruslan MH, Salleh E, Sopian K (2015) Performance of a solar assisted solid desiccant dryer for kenaf core fiber drying under low radiation. *Sol Energy* 112:194–204
19. Romero VM, Cerezo E, Garcia MI, Sanchez MH (2014) Simulation and validation of vanilla drying process in an indirect solar dryer prototype using CFD fluent program. *Energy Proc* 57:1651–1658
20. Dina SF, Farel HA, Napitupulu H, Kawai H (2015) Study on effectiveness of continuous solar dryer integrated with desiccant thermal storage for drying cocoa beans. *Case Stud Therm Eng* 5:32–40

# Fault Detection in Single-Stage Helical Planetary Gearbox Using Support Vector Machine (SVM) and Artificial Neural Network (ANN) with Statistical Features



Syed Shaul Hameed and V. Muralidharan

**Abstract** Drive train failures are most common in wind turbines. Lots of effort have been made to improve the reliability of the gearbox but the truth is that these efforts do not provide a lifetime solution. Majority of failures are caused by bearing and gearbox. Also, wind turbine gearbox failure causes the highest downtime as repair must be done at original equipment manufacturer (OEM). This work aims to predict the failures in planetary gearbox (PGB) using fault diagnosis technique and machine learning algorithms. In the proposed method, the failing parts of planetary gearbox are monitored with the help of accelerometer sensor mounted on the planetary gearbox casing which will record the vibrations. A prototype has been fabricated as a miniature of single-stage planetary gearbox. The vibrations of healthy gearbox under sun defect, planet defect, and ring defect during loaded conditions are obtained. The signals show the characteristics of gearbox condition. Statistical feature analysis was performed on the obtained signals and predominant statistical features which represent the fault condition were selected using decision tree (J48) algorithm. Using these features, the support vector machine (SVM) and artificial neural network (ANN) algorithm was trained to classify the faults. The prediction accuracy of the machine learning algorithm greatly helps in deciding the optimum time to carry out the required maintenance operation.

**Keywords** Fault diagnosis · Planetary gearbox · Statistical features · Support vector machine · Artificial neural network · Vibration measurement

---

S. S. Hameed (✉) · V. Muralidharan  
Department of Mechanical Engineering, B S Abdur Rahman Crescent Institute of Science and Technology, Vandalur, Chennai 600048, India  
e-mail: [syedshaulhameed@gmail.com](mailto:syedshaulhameed@gmail.com)

V. Muralidharan  
e-mail: [v.muralidharan2@gmail.com](mailto:v.muralidharan2@gmail.com)

## 1 Introduction

The planetary gearbox (PGB) are widely used in industrial sectors due to its advantages over fixed axis gearbox, such as high torque capability, compact size, and high reduction ratios. Failure in PGB will cause significant downtime and high maintenance cost due to its high-end applications such as wind turbine, helicopters, and earth mining machines. Catching signs of failing parts at an early stage by continuously monitoring its condition will help in understanding the machine condition and schedule maintenance which can shorten the downtime and improved machine reliability. Fault diagnosis is a process of monitoring the machine behavior by inducing a premeasured fault condition and by acquiring data from the sensors. Further data analytics is performed on the acquired data. Each fault condition will have a signature pattern, and these patterns are identified and classified using machine learning algorithms. The common failure mode in the helical gear planetary gearbox is localized defects such as tooth breakage, pitting, cracks, and planet bearing damage [1, 2]. These defects are mainly caused due to fatigue, misalignment, imbalance, improper meshing of gears, and some small foreign particle in the lubricants. A defect in one gear will cause damage with meshing gear thus reducing the overall performance of the gearbox. A planetary gear set consists of a ring gear which is held stationary, a sun gear which rotates about its axis, and planet gears, they not only rotate about its axis but also revolve around the sun gear. Therefore, determining the severity of the fault in PGB is very complex.

Recent works have explored the following defects in fault diagnosis of the planetary gearbox (chipped and missing tooth of sun gear [3], the cracked tooth on ring gear [4], pitting damage of planet gear [5], inner and outer race defects in planet bearings [6], and combined gear defects [7]). These defects cause transient behavior to the normal signal. Vibration [8, 9], sound [10, 11], and acoustic emission [12]-based approaches have been used noticeably for fault diagnosis of rotating systems. Out of above three methods, vibration-based approach has been preferred widely because of its simplicity and ease of handling data. For this study, time domain and vibration-based approach are followed. Usually in condition-based maintenance, signals are obtained from the transducer and features such as statistical, histogram, and wavelets are extracted from the signal and then classified to assess the condition of the machine. In order to reduce the classification process time, algorithms like a decision tree, best tree, and random tree are used to select the prominent features from the pool of features [13, 14]. These algorithms are tree-based knowledge representation, which automatically generates rules for feature sets. In machine learning, fault diagnosis is only possible by comparing signals of a different condition. Support vector machine (SVM) has been used in pattern recognition problems extensively because of its classification accuracy. In recent past, many researchers have been reported using SVM in the field of fault diagnosis namely spur and helical gearbox [15, 16], roller bearings [13], pumps [9], and shafts. From the literature, SVM has worked well with vibration signals and statistical features. Similarly, artificial neural networks (ANNs) have been used extensively [17, 18]. It is evident from the literature

that SVM and ANN have large scope in the field of fault diagnosis and condition monitoring.

The present work focuses on four different machine conditions (good condition, planet gear tooth defect, sun gear tooth defect, and ring gear tooth defect) of the planetary gearbox. Vibration signals are acquired using Kistler accelerometer. Statistical parameters of the vibration signals were extracted. J48 algorithm is used to select the prominent features from the pool of statistical features. The selected prominent features for different gear conditions are then classified using SVM and ANN. The results are then compared. The detailed methodology is shown in Fig. 1. The ability of the algorithms to predict the defect will help in taking maintenance decisions.

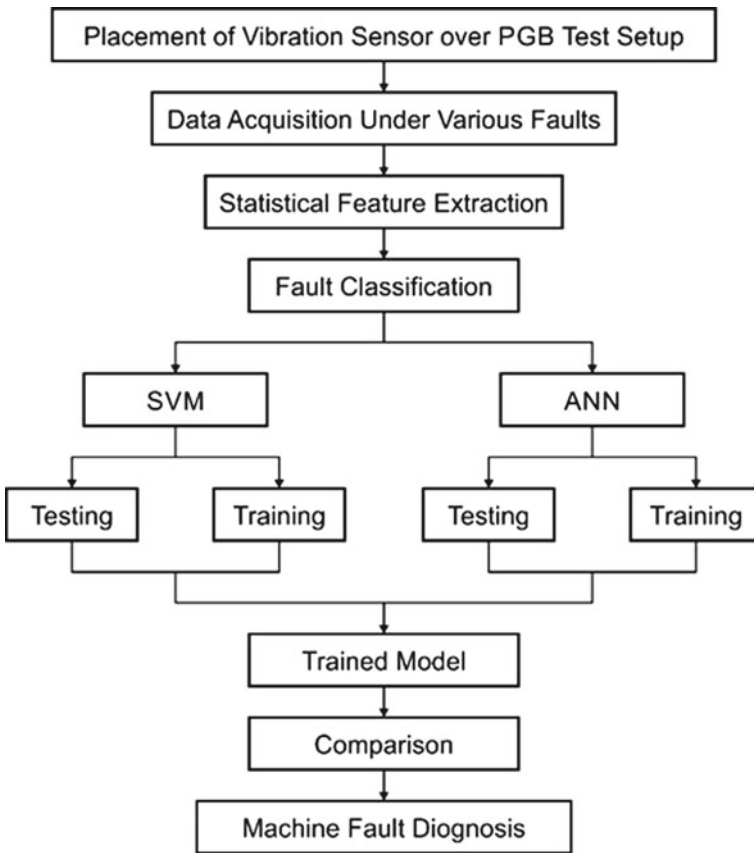
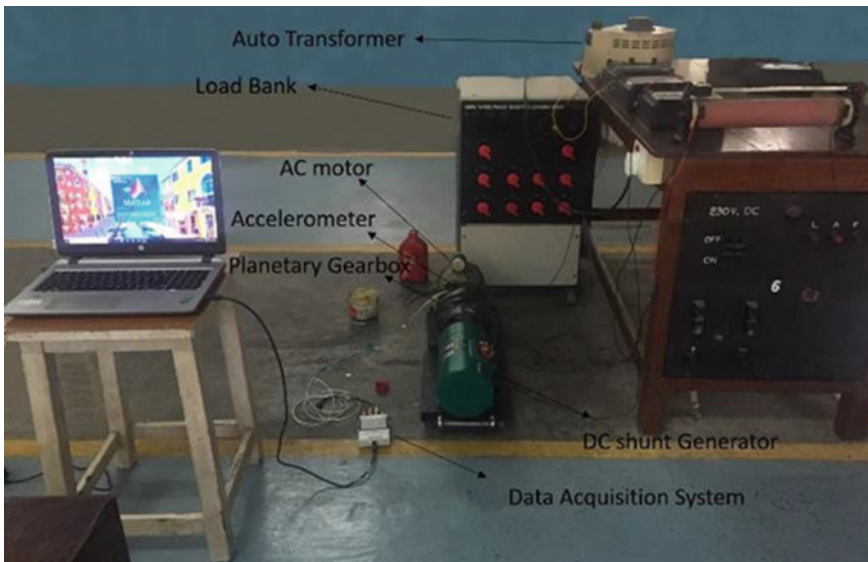


Fig. 1 Detailed methodology adopted in this study

## 2 Experimental Setup and Procedure

### 2.1 Experimental Setup

The test setup consists of a single-phase induction motor, a planetary gearbox, and a DC load motor. The input shaft of the gearbox is coupled with the single-phase induction motor. The planetary gearbox output shaft is then coupled with DC load motor. The DC motor is then connected to DC load bank to provide electrical load on to the gearbox. The input shaft of the gearbox is sun gear, and the output shaft of the gearbox is the planetary carrier. The ring gear is held stationary. The entire assembly is mounted on a thick 20 mm base plate. This is provided with legs, and these legs are well damped such that reduce ground vibrations. The test setup is represented in Fig. 2. The detailed specification of gearbox is shown in Table 1.



**Fig. 2** Planetary gearbox test setup

**Table 1** Specification of planetary gearbox

Gear parameters	Sun	Planet	Ring
No. of teeth	48	23	96
Diameter (mm)	66.48	33	135.6
Addendum (mm)	1.359	1.35	1.394
Module	1.329	1.32	1.383
Tooth thickness (mm)	2.08	2.07	2.17

## 2.2 Experimental Procedure

The test was conducted on four different conditions.

- Good condition
- Sun gear tooth defect
- Planet gear tooth defect
- Ring gear tooth defect.

Vibration signals from the piezoelectric accelerometer mounted on the planetary gearbox housing was acquired. The sensitivity of accelerometer is 100 mV/g. Initially the setup was made to run for some time before acquiring the signals, and this allows the components in the gearbox to sync properly with the driving speed. The motor driving speed is set at its rated speed of 1400 rpm. A load of 1.5 kW was applied from the load bank to the DC load motor which was separately excited. The accelerometer was connected to National Instruments sound and vibration measurement data acquisition hardware NI 9234. The output of the data acquisition hardware was then interfaced with PC. The hardware is configured with the help of Matlab2018a, and the acquired data were stored. The sampling frequency was set to 2048 Hz, and the sample time was set to 10 s. Therefore, for each trial 20,480, data were stored. For each test condition, 100 sample readings were collected. The fault in the sun, planet, and ring gear was introduced using electric discharge machining. Figure 3 illustrates defective gear used for experimentation.

## 3 Feature Extraction

100 sample readings were acquired for each gear condition. A representative time domain plot of each condition is shown in Fig. 4. It requires specific domain expertise to clearly identify and interpret the raw signal for defects. Therefore, from the raw

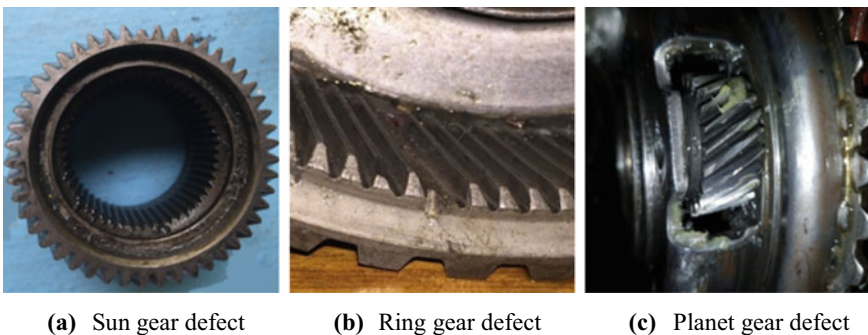


Fig. 3 Gear defects

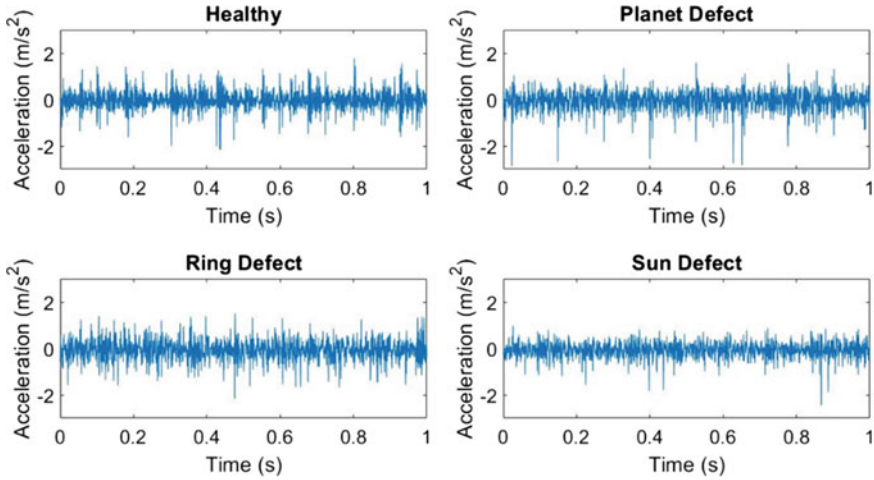


Fig. 4 Raw time domain vibration signals

signals, key statistical parameters have been computed. The parameters computed are represented in Table 2.

where

$x_i$ — $i$ th sample value,  $n$ —Total number of samples,  $\bar{x}$ —sample mean and  $\sigma$ —standard deviation.

Table 2 Extracted statistical features

Feature description	Formula
<b>Mean</b> ( $\bar{x}$ ) is the arithmetic average of the sample signal	$\bar{x} = \sum_i^n \frac{x_i}{n}$
<b>Standard deviation</b> ( $\sigma$ ) is the dispersion of the data point from the average	$\sigma = \sqrt{\sum_i^n (x_i - \bar{x})^2}$
<b>Kurtosis</b> is a measure of peakness in the distribution	$\sum_i^n \frac{(x_i - \bar{x})^4}{n \cdot \sigma^4}$
<b>Skewness</b> is a measure of symmetricity of the distribution	$\sum_i^n \frac{(x_i - \bar{x})^3}{n \cdot \sigma^3}$
<b>Variance</b> depicts the variation of the data point with respect to mean of the distribution	$\sum_i^n \frac{(x_i - \bar{x})^2}{n}$
<b>Standard error</b> represents the deviation of sample mean with respect to the true mean of the distribution	$\frac{\sigma}{\sqrt{n}}$
<b>Median</b> is a numerical value which separates the higher half and lower half with its middle value when arranged in order	$\frac{(\frac{n}{2})\text{th term} + (\frac{n}{2} + 1)\text{th term}}{2}$
<b>Mode</b> is a numerical value appearing more frequently in the data set	NA
<b>Maximum</b> is the highest value in the distribution	$\max(x_{i=1...n})$
<b>Minimum</b> is the lowest value in the distribution	$\min(x_{i=1...n})$
<b>Range</b> is the difference between maximum and minimum value	$x_{(i)\max} - x_{(i)\min}$

A total of 11 statistical features was extracted for each signal and for all conditions. These features are then arranged, and the corresponding class was labeled. Prominent features are those which clearly distinguish the class variable. These prominent features are identified using a decision tree J48 algorithm. This algorithm automatically creates simple ‘If then’ rules and depicts the feature usefulness in the form of a tree. The tree top most node is called root node and moving down the tree are the branch nodes. The end of each branch is the leaf node which represents class variable. The branching continues to take place until a homogeneous set is achieved.

$$\text{Entropy}(S) = \sum_{i=1}^n -p_i * \log_2 * p_i \tag{1}$$

where  $c$  is the number of class in our case is  $c$  is 4. And  $p_i$  is the proportion of  $S$  belonging to class  $i$ .

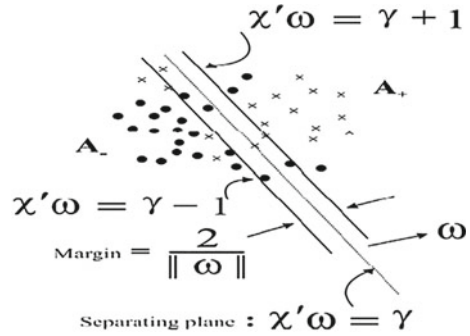
## 4 Classifier

### 4.1 Support Vector Machine

Support vector machine is a supervised machine learning algorithm. It is a data classification technique which involves separating the classes (conditions of the gearbox) by means of a hyperplane. The hyperplane is constructed in such a way that the margins between the classes are large. The points on either side of the margins are known as support vectors. There can be any number of classes for a particular SVM model. The features selected using the decision trees are used as dimensions for classifying the various classes. Based on the number of features selected by the decision tree, the number of dimensions in the SVM will vary. When a new input data is given to the system, based on the features (dimensions), the SVM classifies the data into anyone of the classes. The SVMs can be further optimized using the ‘C-parameter.’ When the value for the C-parameter is small then the hyperplane does not classify all the data correctly but will have a larger margin on the other hand if the ‘C-parameter’ value is high then the hyperplane will classify all the data correctly but the margin size will be minimized. The gamma ( $\gamma$ ) parameter is used to determine which data will have more influence over the hyperplane. If the ‘ $\gamma$ ’ value is large then the vectors near the hyperplane will have more weight and if the value is small, then the vectors which are further away from the hyperplane will have more weight. When the classes are difficult to classify kernels can be used. Kernel adds one more dimension to the existing model and separates the classes using a hyperplane. Figure 5 shows the SVM model.

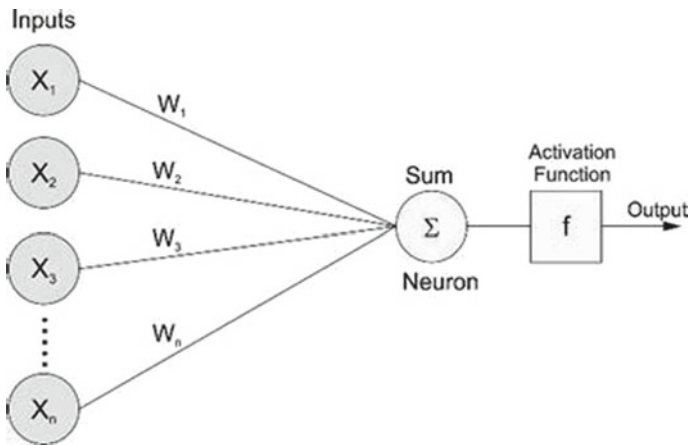


**Fig. 5** Support vector machine model



### 4.2 Artificial Neural Network

Artificial neural networks are computer models whose architecture mimics that of the biological neurons present in the human brain. ANN are neural computing technique designed specifically to perform a particular task unlike human brain. In humans, the neurons are linked with one other through synaptic in a highly nonlinear fashion, and the strengths of these connection depend on the learning. The artificial neurons in ANN are also connected in similar manner, and their strengths are assigned with some weights. The neurons receive information from the outside world and inputs given to it. ANN generally constitutes of three layers, (1) input layer, (2) hidden layer, and (3) output layer as shown in Fig. 6. The input layer is where the network receives information given as features. The hidden layer is where these features are processed, and in the output layer, the processed output is compared with that of the desired class.



**Fig. 6** Schematic artificial neural network model

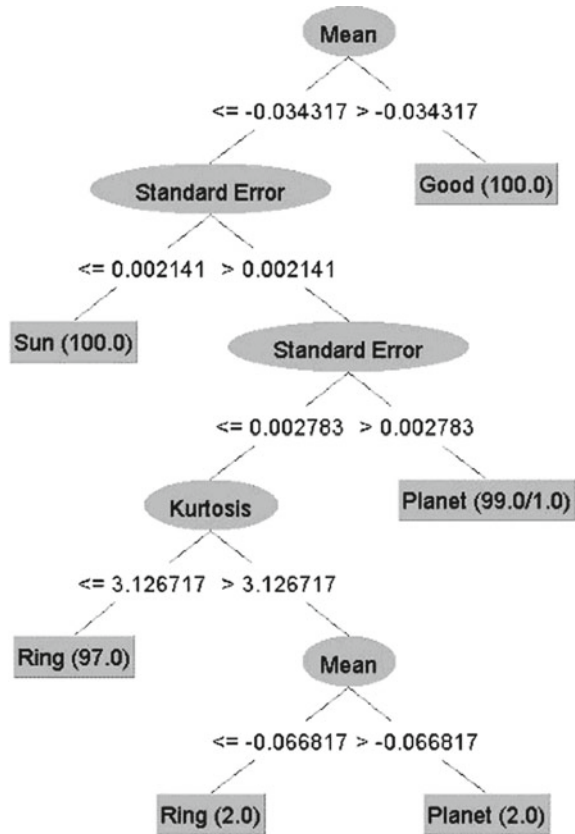
In our case, the inputs to the model are the statistical features. The neuron collectively receives the net sum of the features and its corresponding weights ( $x_1 * w_1 + x_2 * w_2 + x_3 * w_3 + \dots + x_n * w_n$ ) and sends this information to the transfer function for processing. The output from the activation function is the net actual output. Since ANN is a supervised learning classifier, the desired output is labeled to class variables. Then the sum of squared error (SSE) is computed. Accordingly, the weights are adjusted such that the SSE is minimized. The rate at which the weights are adjusted 'learning rate' is very critical as faster convergence will lead to instability of the algorithm. The learning is stopped until the stopping criteria are met. ANN is generally preferred in pattern recognition and classification problem as it can mask the hidden information.

## 5 Results and Discussion

In the present work, a set of eleven statistical features was extracted from the vibration signals that are given as input to the J48 algorithm, and the output is the decision tree.

1. The decision tree is a tree-based knowledge representation displaying qualified features. The features which are of most important are obtained shown in Fig. 7.
2. Out of eleven features, three features mean, standard error, and kurtosis proved their dominance
3. Fig. 8 represents the scatter plot of three dominant features among four class. Good features are those whose variation inside the class is minimum and maximum separation among other classes
4. The simple five if the rule formed by the decision tree shown in Fig. 7 is as follows.
  - (a) If mean greater than  $-0.034317$  all 100 data points of good class can be distinguished.
  - (b) Mean less than or equal to  $-0.034317$  and standard error less than equal to 0.002141 all 100 data points of sun defects can be classified.
  - (c) Mean less than or equal to  $-0.034317$  and standard error greater than equal to 0.002141 and standard error greater than 0.002783, 99 data points of planet defect class are correctly classified.
  - (d) Mean less than or equal to  $-0.034317$  and standard error greater than equal to 0.002141 and standard error less than 0.002783 and kurtosis less than 3.126717, 97 data points of ring defect can be separated from other classes.
  - (e) Mean less than or equal to  $-0.034317$  and standard error greater than equal to 0.002141 and standard error less than 0.002783 and kurtosis greater than 3.126717 and mean less than or equal to  $-0.066817$  the two data points of ring gear was separated and mean greater than to  $-0.066817$ , the missed out two data points of planet gear where distinguished by this rule.

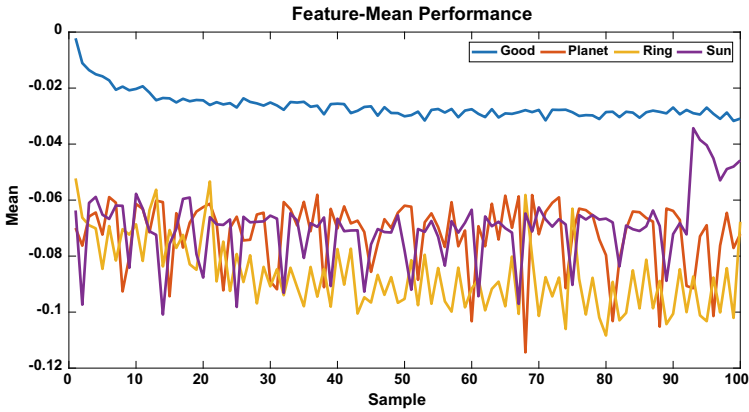
Fig. 7 Prominent features



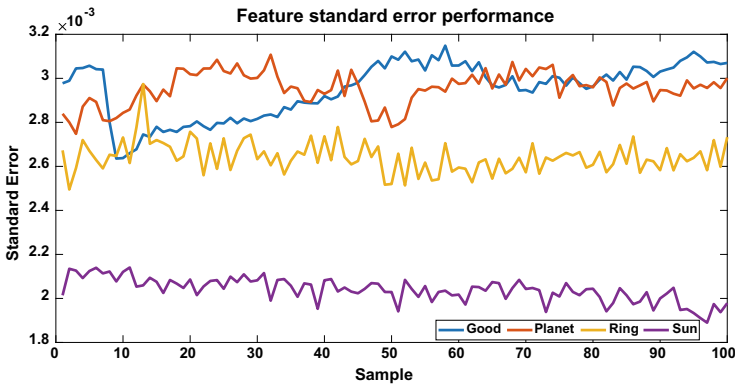
The features were given as input to both SVM and ANN algorithms for classification. The classification process is of two steps. The first step constitutes of training or learning, and the latter is for testing. The test method adopted for both classifiers was tenfold cross-validation. Cross-validation is a statistical method used to estimate the ability machine learning algorithm. In this method, the original sample is randomly partitioned into  $k$ -equal size subsamples. Of the  $k$  subsamples, a single subsample is retained as the validation data for testing the model, and the remaining  $k - 1$  subsamples are used as training data. Further observations were made on classifier performance with full features and selected features. The results are presented in the form of histogram Fig. 9.

Therefore, from Fig. 9 it is clear by feature reduction the classification time of both algorithms has been shortened and enhancement of classifier performance. On comparison of both algorithms, ANN has surpassed SVM in terms of prediction accuracy and SVM has surpassed ANN in terms of classification time.

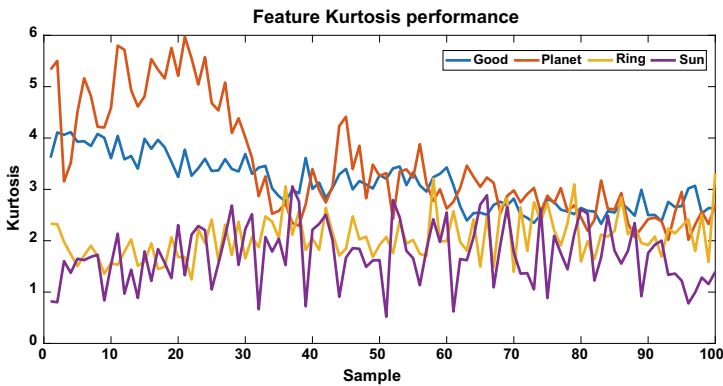
The detailed output of the algorithms is shown in the form of confusion matrix for selected three features Tables 3 and 4.



(a) Scatter plot for mean feature.



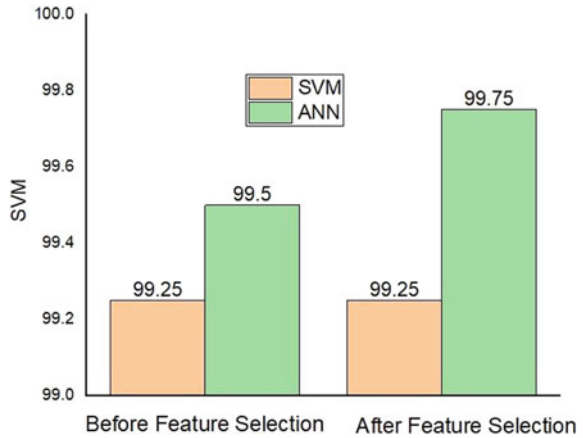
(b) Scatter plot for standard error feature.



(c) Scatter plot for kurtosis feature.

Fig. 8 Scatter plot of prominent features

**Fig. 9** Classifier performance



**Table 3** Confusion matrix of SVM

Predicted					
Good	Planet	Ring	Sun	Condition	
100	0	0	0	Good	Actual
1	99		0	Planet	
0	0	100	0	Ring	
0	4	1	99	Sun	

**Table 4** Confusion matrix of ANN

Predicted					
Good	Planet	Ring	Sun	Condition	
100	0	0	0	Good	Actual
1	99	0	0	Planet	
0	0	100	0	Ring	
0	0	0	100	Sun	

From Tables 3 and 4, the actual vs prediction accuracy of classifier in each class is represented. The diagonal elements represent the correctly classified instances in each class and the off-diagonal elements represent the misclassified instances. The overall accuracy can be calculated by summing up the correctly classified diagonal instances and dividing it by total number of instances. The accuracy of the algorithm greatly helps in deciding and scheduling maintenance of the gearbox.

## 6 Conclusion

This work outlines how statistical features can be applied on vibration signals produced by planetary gearbox for accessing the fault condition. The faults used in this study were the sun, planet, and ring gear tooth defects. Feature selection was done using J48 algorithms, and the importance of feature selection in enhancing classifier performance has been discussed. The prediction accuracy of ANN and SVM has been compared, and the results were encouraging. It was found that ANN had better classification accuracy with that of SVM. This work thus concludes that artificial neural networks have higher potential in fault diagnosis of planetary gearbox.

## References

1. Lei Y, Lin J, Zuo MJ, He Z (2014) Condition monitoring and fault diagnosis of planetary gearboxes: a review. *Meas J Int Meas Confed* 48:292–305. <https://doi.org/10.1016/j.measurement.2013.11.012>
2. Amarnath M, Jain D, Sugumaran V, Kumar H (2013) Fault diagnosis of helical gear box using decision tree through vibration signals. *Int J Perform Eng* 9:221–233
3. Lei Y, Han D, Lin J, He Z (2013) Planetary gearbox fault diagnosis using an adaptive stochastic resonance method. *Mech Syst Signal Process* 38:113–124. <https://doi.org/10.1016/j.ymssp.2012.06.021>
4. Barszcz T, Randall RB (2009) Application of spectral kurtosis for detection of a tooth crack in the planetary gear of a wind turbine. *Mech Syst Signal Process* 23:1352–1365. <https://doi.org/10.1016/j.ymssp.2008.07.019>
5. Feng Z, Zuo MJ (2012) Vibration signal models for fault diagnosis of planetary gearboxes. *J Sound Vib* 331:4919–4939. <https://doi.org/10.1016/j.jsv.2012.05.039>
6. Feng Z, Ma H, Zuo MJ (2016) Vibration signal models for fault diagnosis of planet bearings. *J Sound Vib* 370:372–393. <https://doi.org/10.1016/j.jsv.2016.01.041>
7. Shaul Hameed S, Vaithyanathan M, Kesavan M (2019) Fault detection in single stage helical planetary gearbox using artificial neural networks (ANN) and decision tree with histogram features. <https://doi.org/10.4271/2019-28-0151>
8. Muralidharan V, Ravikumar S, Kangasabapathy H (2014) Condition monitoring of self aligning carrying idler (SAI) in belt-conveyor system using statistical features and decision tree algorithm. *Measurement* 58:274–279. <https://doi.org/10.1016/j.measurement.2014.08.047>
9. Muralidharan V, Sugumaran V, Sakthivel NR (2011) Wavelet decomposition and support vector machine for fault diagnosis of monoblock centrifugal pump. *Int J Data Anal Tech Strateg* 3:159. <https://doi.org/10.1504/ijdots.2011.039849>
10. Amarnath M, Sugumaran V, Kumar H (2013) Exploiting sound signals for fault diagnosis of bearings using decision tree. *Meas J Int Meas Confed* 46:1250–1256. <https://doi.org/10.1016/j.measurement.2012.11.011>
11. Saimurugan M, Ramprasad R (2018) A dual sensor signal fusion approach for detection of faults in rotating machines. *J Vib Control* 24:2621–2630. <https://doi.org/10.1177/1077546316689644>
12. Eftekharijad B, Mba D (2009) Seeded fault detection on helical gears with acoustic emission. *Appl Acoust* 70:547–555. <https://doi.org/10.1016/j.apacoust.2008.07.006>
13. Sugumaran V, Muralidharan V, Ramachandran KI (2007) Feature selection using Decision Tree and classification through Proximal Support Vector Machine for fault diagnostics of roller bearing. *Mech Syst Signal Process* 21:930–942. <https://doi.org/10.1016/j.ymssp.2006.05.004>

14. Srivastava A, Singh A, Sugumaran V, Amarnath M (2016) Fault diagnosis of helical gear box using vibration signals through random tree and wavelet features. *Ind J Sci Technol* **9** (2016). <https://doi.org/10.17485/ijst/2016/v9i33/101330>.
15. Praveenkumar T, Sabhrish B, Saimurugan M, Ramachandran KI (2018) Pattern recognition based on-line vibration monitoring system for fault diagnosis of automobile gearbox. *Measurement* **114**:233–242. <https://doi.org/10.1016/j.measurement.2017.09.041>
16. Amarnath M, Jain D, Sugumaran V, Kumar H (2015) Fault diagnosis of helical gear box using naïve Bayes and Bayes net. *Int J Decis Support Syst* **1**:4. <https://doi.org/10.1504/ijdss.2015.067252>
17. Sugumaran V, Muralidharan V, Hegde BK (2010) Intelligent process selection for NTM—A neural network approach 87–96 (2010)
18. Praveenkumar T, Saimurugan M, Ramachandran KI (2017) Comparison of vibration, sound and motor current signature analysis for detection of gear box faults. *Int J Progn Heal Manag* **8** (2017)

# Characterization of Surface Roughness of Ground Specimens Using Image Processing



S. Mohamed Fahad, J. Mahashar Ali, and H. Siddhi Jailani

**Abstract** Conventional measurement of surface roughness is primarily stylus-based. One of the disadvantage is the physical contact of the stylus with the measuring surface altering the nano-peaks and the other major disadvantage is the filtering effect by the stylus end-radius. A vision-based surface roughness technique which is proposed in this study has various advantages, such as good accuracy, and 100% inspection of components can be achieved in a non-contact mode. First, the stylus parameters  $R_a$ ,  $R_{da}$  and  $R_{dq}$  are computed for all the ground specimens. On the other hand, a complementary metal oxide semiconductor camera and red LED light sources were used for white light image capturing of the same ground specimens. The surface image contains the pixel intensity matrix. A signal vector was created from the ground surface images. Using MATLAB software, the image pixel intensity distribution parameter means were calculated for each of the signal vectors of the ground specimen images. It was found that the stylus parameters having linear correlation with image parameters. Especially, the  $R_a$  has a correlation coefficient of 0.88 with image parameter, showing a strong potential in online characterization of ground specimens for a roughness range between 0.07 and 0.22  $\mu\text{m}$ .

**Keywords** Grinding · Surface roughness · Hybrid roughness parameters · White light image · Image processing · Vision system

## 1 Introduction

The surface roughness measurement is next important to dimension control in realizing a machined component. Traditional or normal method of surface roughness measurement is of stylus-based. The limitation of the stylus-based method is the stylus cannot have an ability to reach all the valleys of the surface due to the radius of the stylus tip which is seen as an offline process consuming more time. So, the requirement of highly dependable online surface roughness measuring systems is

---

S. Mohamed Fahad · J. Mahashar Ali (✉) · H. Siddhi Jailani  
Department of Mechanical Engineering, B S Abdur Rahman Crescent Institute of Science and Technology, Chennai 600048, India  
e-mail: [mahashar@crscent.education](mailto:mahashar@crscent.education)



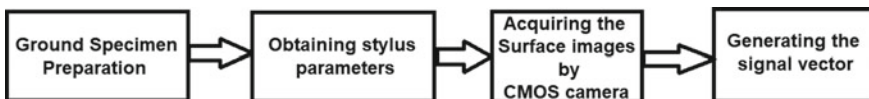
in great need. Over the years, lot of improvements occurred in image processing of satellite imaging and biometrics applications [1–3]. A vision-based characterization for surfaces machined with EDM from the white light images adopting integrated risk information system (iris) identification methodology is done by Ali et al. [4]. The speckle image lay hold of using laser was contemplated for surface roughness measurements in many literatures [5–8].

The normalization procedure of images to reduce the lighting variations was described by Ma et al. [9]. Shahabi and Ratnam [10] captured the cutting tool nose area using a CCD camera and assessed the surface roughness from that profile. They have used this method to find the dimensional deviations of the work piece also. Zhao et al. [11] suggest an in situ and in-process scrutiny and assessment the methodology of machined surfaces based on image processing method. A new characterization system for roughness of the milled specimens was presented by Cuka et al. [12]. Mahashar and Murugan [13] narrowed down the distribution parameters of the white light images of turned surfaces to forecast the surface roughness. The unprocessed photograph was processed and changed in to form of signal matrices. To compute the image intensity values of these signal vector matrices, statistical image parameters were used. It was established that the image parameters were match well with the stylus parameters. Rodriguez et al. [14] suggest contrast intensity technique, binary image technique, and speckle spot technique. They found that these techniques having good correlation with typical methods for different speckle characterization. Wavelet transform analysis is another patch used for surface roughness assessment of machined surfaces. Ali et al. [15, 16] characterized milled and surfaces machined with EDM using biorthogonal wavelets. They embraced the iris recognition methodology for characterizing the machined surfaces.

In this investigation, iris recognition methodology is adopted to assess the roughness of the flat ground specimens by correlating the  $R_a$ ,  $R_{da}$ , and  $R_{dq}$  parameters with the image parameters acquired from the surface white light images.

## 2 Methodology

The methodology consists of the following steps which is shown in Fig. 1.



**Fig. 1** Methodology

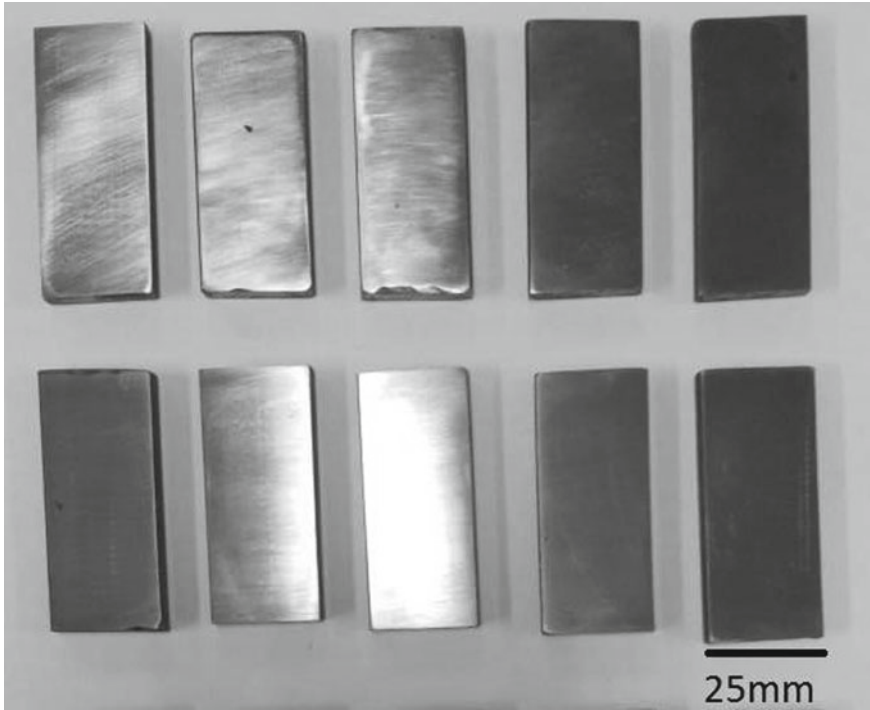


Fig. 2 Ground specimen

### 2.1 Ground Specimen Preparation

Specimen preparation—There are ten different specimens were ground with different values of cross feed and depth of cut which are shown in Fig. 2.

### 2.2 Obtaining Stylus Parameters

Conventional surface roughness measurement is done using the talysurf for all ground surfaces. The talysurf stylus tip radius is  $2\ \mu\text{m}$ . The instrument is shown in Fig. 3 and the actual profile of a ground specimen shown in Fig. 4 and the stylus parameters  $R_a$  and  $R_{da}$  and  $R_{dq}$  are tabulated in Table 1.



Fig. 3 Taylor and Hobson surface roughness tester (Talysurf)

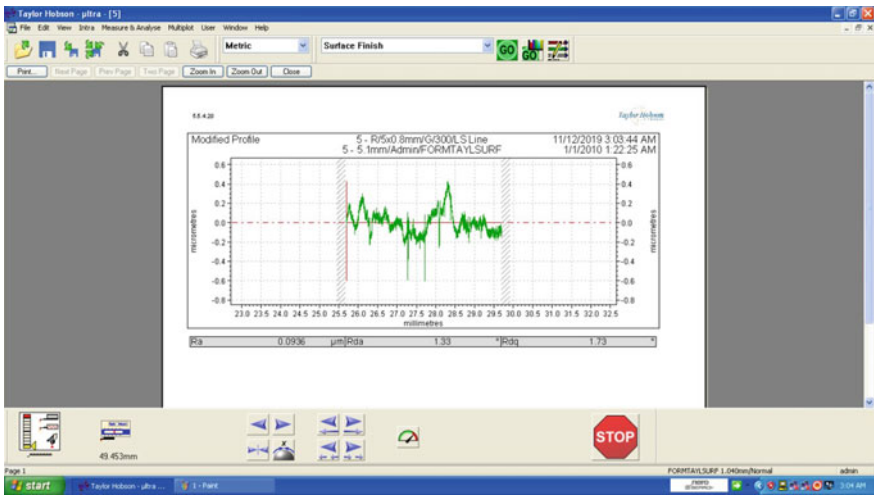
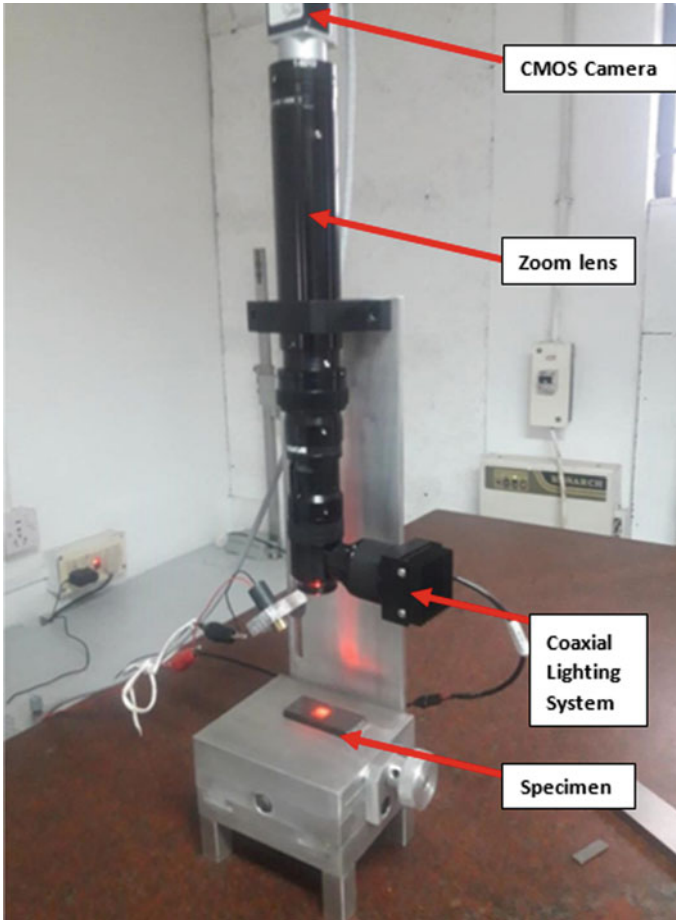


Fig. 4 Surface profile of ground specimen

Table 1 Stylus parameters of ground specimens measured using Talysurf

S. No.	Depth of cut (mm)	Cross feed (mm)	$R_a$ ( $\mu\text{m}$ )	$R_{da}$	$R_{dq}$
1	0.04	0.8	0.0798	1.07	1.42
2	0.04	1.5	0.1938	1.36	2.20
3	0.05	1.5	0.0910	1.18	1.59
4	0.05	1.0	0.0936	1.33	1.73
5	0.06	1.5	0.2177	1.41	1.90
6	0.06	1.0	0.1273	1.27	1.65
7	0.09	0.8	0.0717	1.01	1.71
8	0.08	1.5	0.1059	1.17	1.76
9	0.08	1.0	0.0917	1.07	1.45
10	0.08	0.8	0.0843	1.10	1.44



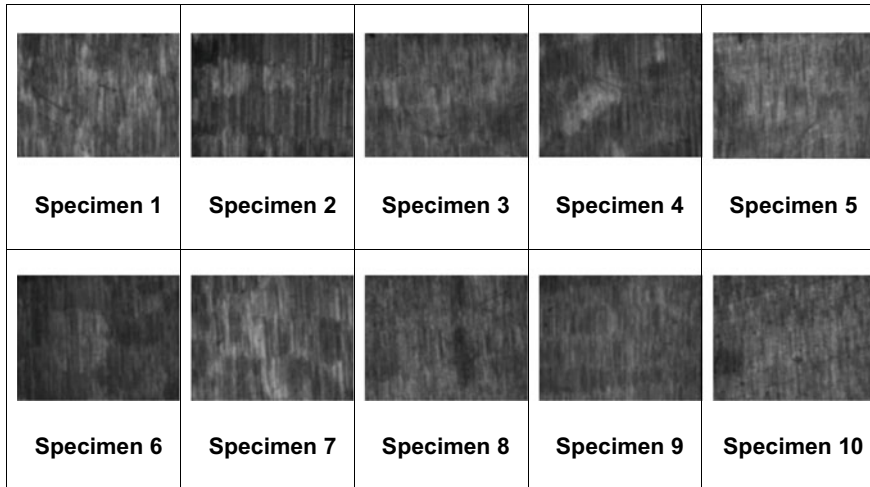
**Fig. 5** Experimental set-up

### ***2.3 Acquiring the Surface Images by CMOS Camera***

A CMOS camera with a  $45\times$  zoom lens is used for acquiring the surface images. The camera is held by a stand at an angle  $90^\circ$  to the specimen surface. Figure 5 shows the experimental setup and the captured white light images are shown in Fig. 6.

### ***2.4 Generating the Signal Vectors***

Approximately, the center portion of the image was used to arrive the signal vector. There are three adjacent pixel rows of image intensity matrix used. These three rows



**Fig. 6** White light images of specimen

**Table 2** Image parameter of the ground specimens

S. No.	Depth of cut (mm)	Cross feed (mm)	Stylus parameters			Image parameter
			$R_a$ ( $\mu\text{m}$ )	$R_{da}$	$R_{dq}$	Mean
1	0.04	0.8	0.08	1.07	1.42	90.04
2	0.04	1.5	0.19	1.36	2.20	69.39
3	0.05	1.5	0.09	1.18	1.59	88.41
4	0.05	1.0	0.09	1.33	1.73	82.88
5	0.06	1.5	0.21	1.41	1.90	57.85
6	0.06	1.0	0.13	1.27	1.65	86.97
7	0.09	0.8	0.07	1.01	1.71	90.75
8	0.08	1.5	0.11	1.17	1.76	86.43
9	0.08	1.0	0.09	1.07	1.45	94.84
10	0.08	0.8	0.08	1.10	1.44	95.07

are equivalent to the size of the stylus tip diameter. The signal vector of one row of length 2400 pixels was arrived by taking the mean of the pixel intensity of three rows. A database of image signal vector was obtained and stored using MATLAB.

### 3 Results and Discussions

The image parameter and the stylus parameter correlations were obtained. Table 2 shows the stylus parameter and the image parameter. The comparison of the stylus

parameters  $R_a$ ,  $R_{da}$ , and  $R_{dq}$  with image parameters revealed that we can get the result of the test surface roughness from the image parameters. Table 2 shows image parameters and the graph of mean intensity versus  $R_a$ ,  $R_{da}$ , and  $R_{dq}$  are shown in Figs. 7, 8, and 9.

From the Figs. 7, 8, and 9, it is noticed that the image parameter (mean) is inversely proportional to  $R_a$  and  $R_{da}$  and  $R_{dq}$ . The central tendency of the image intensity is linked with the roughness of the surface. The low image intensity value exhibits well in the signal vector and hence the signal vector displays a lower value of mean.

The  $R^2$  value between the image parameter and the  $R_a$  is 0.882,  $R_{da}$  is 0.722, and with  $R_{dq}$  is 0.632. Decreasing value of central tendency of the pixel intensity with increasing  $R_a$ ,  $R_{da}$ , and  $R_{dq}$  indicates rougher surface, which when illuminated with a white light source causes more scattering of light and results in an image that has more brightness and having less variation in the image intensity values

It is evident that the mean of the uni-dimensional intensity matrix of white light images has a strong content for the in situ characterization of flat ground surfaces with  $R_a$ , for a range of specimen roughness value 0.07–0.22  $\mu\text{m}$ .

### 4 Conclusion

- An image-based surface roughness characterization for the noncontact and in situ measurement of surface roughness of ground specimens for a roughness ( $R_a$ ) range of 0.07–0.22  $\mu\text{m}$  is proposed.

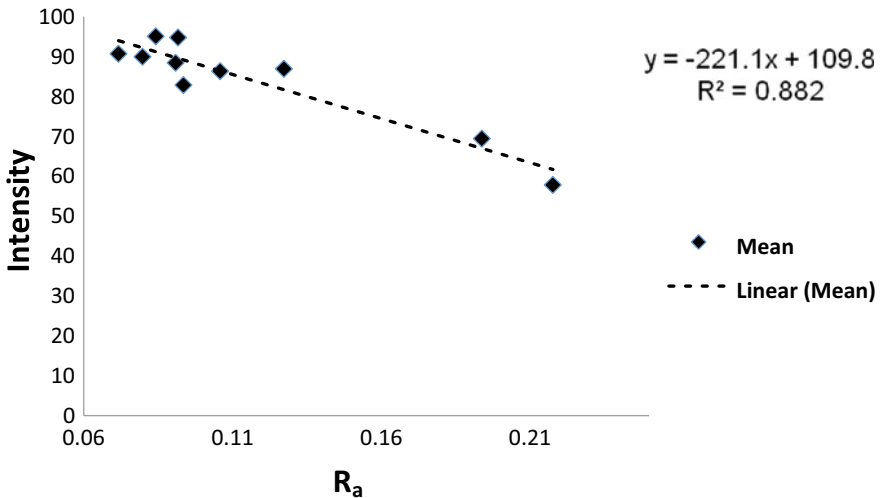


Fig. 7 Mean of image intensity versus  $R_a$

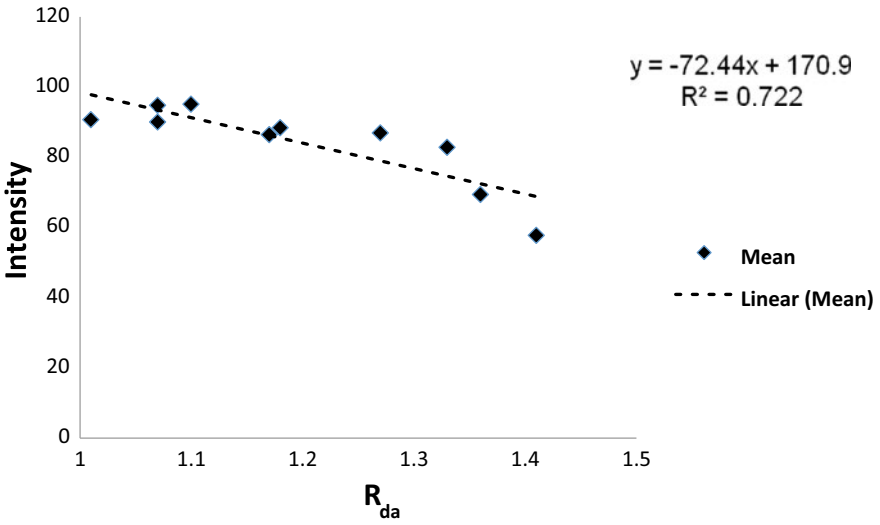


Fig. 8 Mean of image intensity versus R<sub>da</sub>

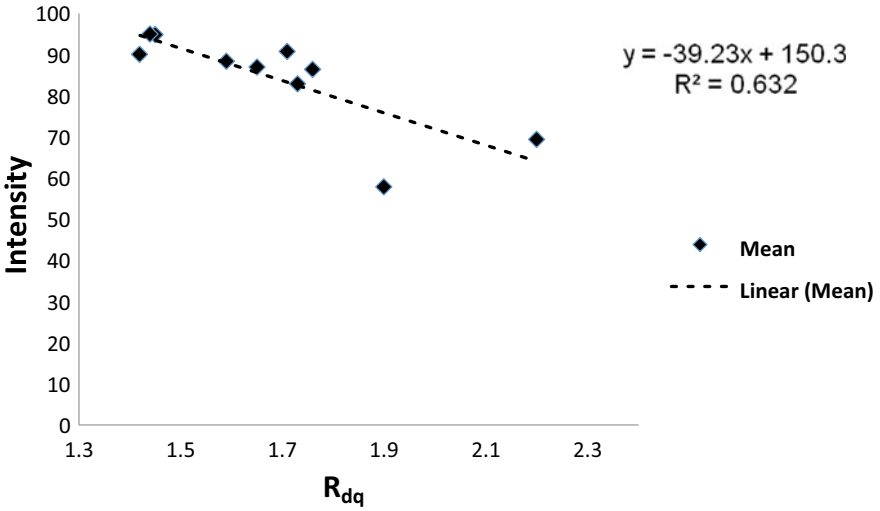


Fig. 9 Mean of image intensity versus R<sub>dq</sub>

- The specimen was illuminated using a LED source and the white light image was obtained
- For validating the concept, ground specimens were prepared and their surface roughness measured using the stylus instrument. The new metrics, mean from the image signal vectors of white light image illuminated work-piece was computed.

- It found from the trends that the mean value of the uni-dimensional image vector correlates well with roughness parameter  $R_a$ ,  $R_{da}$ , and  $R_{dq}$  with a linearity of 0.882, 0.722, and 0.632, respectively.
- The further reliability of the metrics and its applicability can be established through further experiments with larger sample size with varying range of roughness.

## References

1. Daugman J (2009) How iris recognition works. In: The essential guide to image processing. Elsevier, Amsterdam, pp 715–739
2. Alkoot FM (2012) A review on advances in iris recognition methods. *Int J Comput Eng Res* 3(1):1–9
3. Abhyankar A, Schuckers S (2010) A novel biorthogonal wavelet network system for off-angle iris recognition. *Pattern Recogn* 43(3):987–1007
4. Ali M, Jailani S, Mariappan M, Anandan M, Pavithran V (2019) Vision based surface roughness characterization of flat surfaces machined with EDM. SAE Technical Paper
5. Fujii H, Asakura T (1977) Roughness measurements of metal surfaces using laser speckle. *JOSA* 67(9):1171–1176
6. Fujii H, Asakura T, Shindo Y (1976) Measurement of surface roughness properties by using image speckle contrast. *JOSA* 66(11):1217–1222
7. Fujii H, Asakura T (1974) Effect of surface roughness on the statistical distribution of image speckle intensity. *Opt Commun* 11(1):35–38
8. Fujii H, Asakura T (1975) Statistical properties of image speckle patterns in partially coherent light. *Nouvelle Revue d'Optique* 6(1):5
9. Ma L, Tan T, Zhang D (2004) Efficient iris recognition by characterizing key local variations. *IEEE Trans Image Process* 13:739–750
10. Shahabi H, Ratnam M (2010) Noncontact roughness measurement of turned parts using machine vision. *Int J Adv Manuf Technol* 46(1–4):275–284
11. Zhao YJ, Li HN, Song KC, Yan YH (2017) In-situ and in-process monitoring of optical glass grinding process based on image processing technique. *Int J Adv Manuf Technol* 93(9–12):3017–3031
12. Cuka B, Cho M, Kim D-W (2018) Vision-based surface roughness evaluation system for end milling. *Int J Comput Integr Manuf* 31(8):727–738
13. Ali JM, Murugan M (2017) Surface roughness characterisation of turned surfaces using image processing. *Int J Mach Mach Mater* 19(4):394–406. <https://doi.org/10.1504/ijmmm.2017.086166>
14. Rodríguez F, Cotto I, Dasilva S, Rey P, Van der Straeten K (2017) Speckle characterization of surface roughness obtained by laser texturing. *Proced Manuf* 13:519–525
15. Ali JM, Jailani HS, Murugan M (2020) Surface roughness evaluation of electrical discharge machined surfaces using wavelet transform of speckle line images. *Measurement* 149:107029
16. Ali J, Jailani H, Murugan M (2019) Surface roughness evaluation of milled steel surfaces using wavelet transform of laser speckle line images. *Lasers in Engineering (Old City Publishing)* 44



# Experimental Study on the Combustion, Performance and Emission Characteristics of a Diesel Engine Operated with the Blends of Waste Chicken Oil Biodiesel and Diesel



V. Nadanakumar, R. Christupaul, Ravishankar Sathyamurthy, and R. Sathish Kumar

**Abstract** The decline in the availability of fossil fuel, increase in cost and the stringent emission norms are the main concerns identified in the automotive sector during the recent years. Biodiesel is one of the hopeful alternate resources for the mineral diesel to address the above-listed problems. In the present investigation, waste chicken fat biodiesel has been prepared and used to investigate the performance features of single cylinder naturally aspirated direct injection diesel engine. The waste chicken fat biodiesel is prepared using transesterification process, and the yield is found to be 94.8%. The physicochemical characteristics of the waste chicken fat methyl ester have been tested and found in line with ASTM standards. The blends of waste chicken fat biodiesel with mineral diesel have been prepared and experimented in a single cylinder standard compression ignition diesel engine without any modifications. The combustion, performance and emission characteristics have been studied, and it is found that the blend B20 resulted in higher performance and lesser emissions among the other test fuels.

**Keywords** Waste chicken fat · Biodiesel · Diesel engines · Performance · Emission

## 1 Introduction

In this modern age, growing reliance on fossil-diesel fuel in cars and other industries has ultimately led to the quest for renewable energy sources to replace diesel

---

V. Nadanakumar · R. Christupaul · R. Sathish Kumar (✉)  
Department of Automobile Engineering, Hindustan Institute of Technology and Science, Chennai  
603103, Tamil Nadu, India  
e-mail: [sathish.rajamanickam@gmail.com](mailto:sathish.rajamanickam@gmail.com)

R. Sathyamurthy  
Department of Mechanical Engineering, KPR Institute of Engineering and Technology,  
Coimbatore 641407, Tamil Nadu, India

minerals. Owing to growing reliance on petroleum goods, the oil shortage and environmental degradation, green energy technologies are widely used when investigated. Biofuels are often seen as one of the significant forms of naturally replenishing energy [1–6]. Even though, it is recommended that energy is obtained from renewable sources through the energy of solar, geothermal, wind, biomass and other sustainable resources that do not cause environmentally sensitive pollutions [7], Biofuel is found to be a best alternate among those renewable energy sources. Many researchers were investigating the methodology of producing biodiesel from waste animal's fats in laboratory scales. In various countries depending upon the biofuels availability, states adopt possibility of future fuels to resolve their energy demands under the global norms of green energy and environment.

Biodiesel is non-poisonous, recyclable, carbon-neutral oil, emits lower sulfur, unburnt hydrocarbon, carbon monoxide emissions and an environmentally sustainable source of energy [8]. Some of the biodiesel resources are edible oils extracted from coconut, peanut, sunflower, olive, rapeseed and soybean, while majority resources are non-edible such as jatropha, pongamia pinnata, neem, linseed, cotton seed and castor oil [9]. Biodiesel has the greatest potential since recent experiments have shown that the burning of biodiesel substantially decreases pollution, so biodiesel is also the most widely used form of renewable energy. While operating the engine, the safe CO<sub>2</sub> is released during fuel combustion. National Renewable Energy Laboratory (NREL) had revealed that utilizing biodiesel releases safe CO<sub>2</sub> emission. Thus, biodiesel's life cycle study showed that total CO<sub>2</sub> emissions were decreased by 78% relative to other fuels [10].

Transesterification is the conversion mechanism between organic group of an alcohol and an ester. Transesterification is the reaction between oil/fat and an alcohol producing biodiesel in the presence of an effective catalytic agent. Oils with a high amount of free fatty acid contents can be converted to biodiesel by transesterification. Although vegetable or plant-based oils are mainly used to synthesize biodiesel, the use of vegetable oils is restricted by certain major challenges such as feedstocks supplies, feeding stuff costs, transport and fuel storage over long periods [11]. Recently, the attention of energy producers was drawn to animal fat containing triglycerides. The beef tallow in Brazil accounts for 17% of the feedstock for the production of biodiesel [12]. Apart from beef tallow, chicken fat was also recognized as one of the resources for biodiesel synthesis.

Statistics of the Indian government suggest a consumed annual consumption of about 800,000 tons of chicken meat [13] and discard of around 79,000 tons of chicken fat because it is harmful to the public. The waste chicken consists of lipids which could be used for biodiesel production [14–16].

## 2 Materials and Methods

### 2.1 Preparation of Waste Chicken Fat Oil

The chicken waste collected from the hatchery shops in and around Kelambakkam, Chennai, India and was dried in a temperature controllable hot air thermal oven at a hotness of 70 °C. The dried chicken waste was collected, grinded and filtered using 600- $\mu$ m sieve to obtain a particle size of 0.5 mm. 50 gm of the sieved waste chicken powder has been taken in a Soxhlet apparatus along with hexane for solvent extraction process. The reaction was maintained for a period of 7–8 h. On completion of the process, hexane was recovered by batch distillation. Traces of solvent are removed by rotary evaporator.

The oil obtained was collected, and the properties of the oil were founded. From the properties, it is evident that the viscous of the oil was found to be higher. Due to the higher viscosity, the oil cannot be used directly for operating the engine as it may affect injection parameters as well as it may clog the filters. Hence, it was decided to perform transesterification in order to convert the oil into fatty acid methyl esters.

### 2.2 Transesterification

The process of transesterification is widely used to convert oils into methyl esters, and it is a process in which organic alkyl group of oil, lipids is mixed with the methyl group and catalytic agent in order to convert the oils and lipids into esters [17].

The required quantity of waste chicken oil is taken in a flask, and appropriate molar ratio of methanol and the catalyst KOH were added. The flask is kept in a magnetic stirrer cum heater, and the reaction is made to happen at the required temperature with adequate time and proper stirring for the completion of reaction. Upon completion, the mixture is transferred into a glass conical separating flask and placed idle for 24 h for the separation of methyl esters and glycerine. The collected methyl esters were heated in an open pan for removing the traces of methanol, and then, it washed with water. Several trials of this process are made, and the following parameters were set for obtaining the maximum conversion. The catalyst used is KOH with 2 (%wt) catalyst concentration, 65 °C reaction temperature, 11:1 molar ratio of methanol to chicken fat oil and 60 min reaction time. The maximum yield of waste chicken oil biodiesel obtained is 94.5%.

The biodiesel obtained in blended with mineral diesel in the following proportions on volume basis.

B10 WCOBD – 10% WCFME + 90% Diesel

B20 WCOBD – 20% WCFME + 80% Diesel

B30 WCOBD – 30% WCFME + 70% Diesel

**Table 1** Comparative statement of the properties

Property	Waste chicken oil	Waste chicken oil biodiesel	Unit
Density	0.897	0.837	g/cc
Calorific value	36,500	38,400	kJ/kg
Pour point	12	-16	°C
Viscosity	12.57	4.37	mm <sup>2</sup> /s
Cloud point	10	-12	°C
Flash point	172	79	°C

These mixtures of biodiesel waste chicken oil with diesel were used to operate a DI engine to investigate the parameters of combustion, efficiency and emission (Table 1).

### 2.3 Experimental Setup

All the experiments were conducted in a naturally aspired, four stroke, water cooled, single cylinder, direct injection constant speed engine. The make and type of the engine is Kirloskar TV1, and the same is in connection to a SAJ AG10 type eddy current dynamometer for loading. A surge tank fitted with a manometer was coupled to the inlet manifold in order to reduce the pulsations occurred by the engine. Appropriate instruments like fuel flow transmitter, piezo sensor, and crank angle sensor were employed for monitoring and measuring the fuel consumption, cylinder pressure and the crank angle, respectively. An acquisition device has been used for acquiring the data, and the same was stored in computer for further calculations. Apart from the data acquisition device, manual readings for fuel consumed were recorded using a standard burette and digital stopwatch.

Measurement of the exhaust was made using AVL Digas 444 five gas analyzer, in which the gases carbon monoxide, nitrous oxides NO<sub>x</sub> and hydrocarbon were measured (Fig. 1; Table 2).

### 2.4 Test Procedure

The diesel blends of the waste chicken biodiesel are prepared and used to run the engine. The engine runs at a steady speed of 1500 rpm, and the fuel supply hoses, water cooling lines have been tested for any leakage before the engine is operated. Initially, the engine was run with diesel fuel to take the basic readings. The engine was permitted to run for certain period to reach stability before taking the readings. The engine is encumbered by the eddy current dynamometer which is paired to the crank shaft. Initial reading was taken with no load, and further, the engine was loaded



**Fig. 1** Pictorial view of engine setup

**Table 2** Specifications of the engine

Engine type	4 stroke, diesel engine
Number of cylinders	1
Rated RPM	1500
Max power @ rated RPM (kW)	3.5
Stroke (mm)	110
Bore (mm)	87.5
Displacement (cc)	661
Injection timing	23° BTDC
Injection pressure	200 bar
Compression ratio	17.5

with 25, 50, 75 and 100% load, respectively, for recording the characteristics. Period required for a 10 cc fuel intake is recorded using a stopwatch, exhaust temperature, and the emission measurements CO, NO<sub>x</sub>, UBHC were noted accordingly, other readings such as the pressure, angle of the crank and the heat release rate are recorded using data acquisition system. For each reading, three set of trials were run, and the

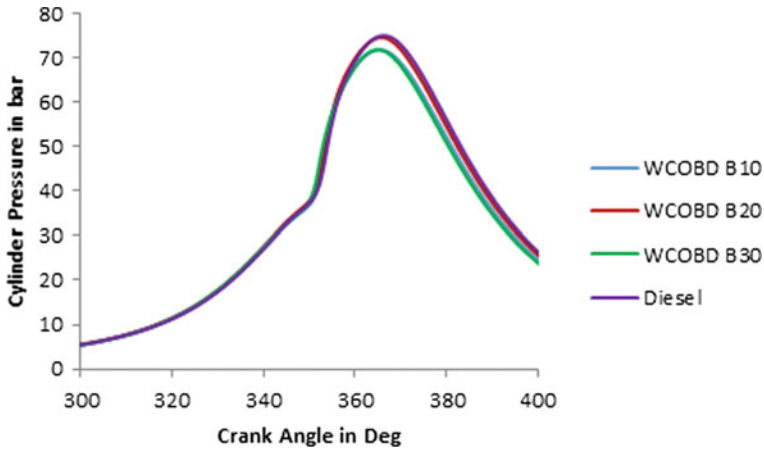


Fig. 2 Cylinder pressure versus crank angle

average is used for calculations. The entire fuel line is purged by diesel after using a particular fuel blend.

### 3 Result and Discussion

#### 3.1 Cylinder Pressure

Figure 2 compares the influence of the in-cylinder pressure versus crank angle for the blends of waste chicken biodiesel with that of diesel fuel.

All the WCOBD blends show a similar trend in-cylinder pressure curve, B20 of WCOBD shows a slightly higher pressure than the other blends. The higher peak pressure is obtained by diesel which is slightly higher than that of B20 blend. WCOBD B20 blend recorded a higher pressure of 75.04 bar, while other blends are slightly lower. This may be contributed to the inherent oxygen content, viscosity and calorific value of the fuel. Even though the calorific value of WCOBD B20 is slightly lower than WCOBD B10, better combustion might have been resulted due to good atomization as the viscous is lower when compared to WCOBD B10.

#### 3.2 Heat Release Rate

Figure 3 shows the variation of rate of net heat release with crank angle for the blends of waste chicken biodiesel with that of diesel fuel. The negative heat release observed is due to the heat utilized by the fuel droplets for vaporization. The heat release rate

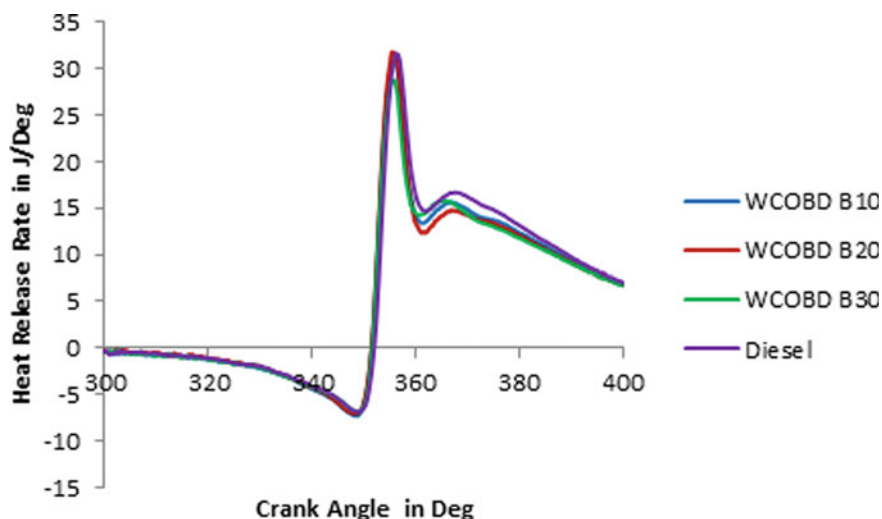


Fig. 3 Heat release rate versus crank angle

of the blend B20 recorded a better trend in comparison with the other fuel blends. Any how the diesel showed superior heat release rate than that of all other blends due to the calorific value. The maximum heat released by diesel is 31.7 kJ, while B20 which is higher among fuel blends recorded 30.71 kJ.

### 3.3 Brake Thermal Efficiency

The relationship between brake mean effective pressure (BMEP) and brake thermal efficiency (BTE) is given in Fig. 4. The BTE of all the test fuels increases with the increase in BMEP, which may be due to the more increase in engine power with increase in the load and loss of heat may be lesser in higher load [6]. It is found that the BTE of WCOBD B20 is 28.6% at maximum load which is higher BTE when related to other blends of waste chicken oil biodiesel. This may be contributed to the mutual influence of the viscosity and the calorific value with respect to the other blends. Although the diesel fuel's calorific value is greater than the biodiesel blends, the diesel's brake thermal performance is achieved at 29.43% and is better than any other fuels.

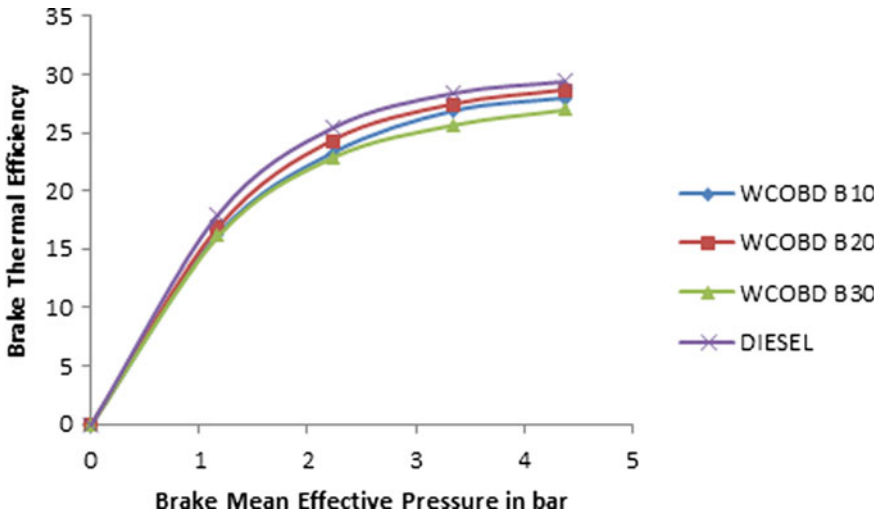


Fig. 4 Brake thermal efficiency versus brake mean effective pressure

### 3.4 Brake-Specific Fuel Consumption

Figure 5 shows the relation between brake-specific fuel consumption (BSFC) versus BMEP for the blends of WCOBD and diesel. The BSFC shall be described as the amount of fuel spent per unit of engine brake power. Moreover, BSFC is the measure of conversion of fuel energy into work output, and hence, lower BSFC is highly expected. From the graph, the BSFC is lowered as the load of the engine is increased. From the graph, the BSFC of the WCOBD B20 recorded lower than all other blends,

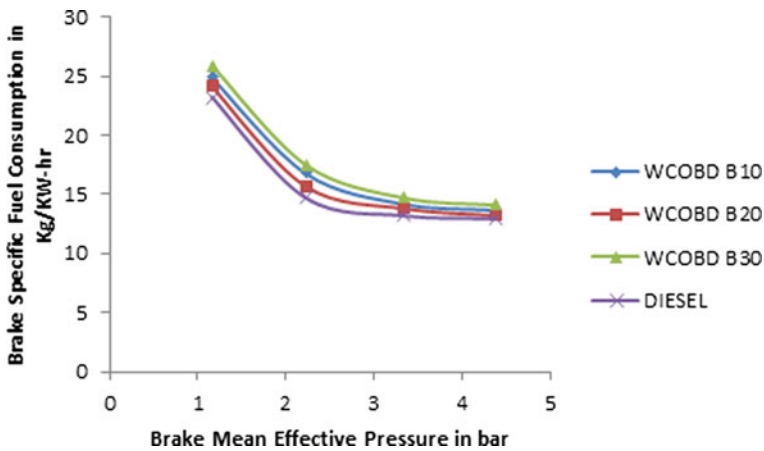


Fig. 5 Brake-specific fuel consumption versus brake mean effective pressure



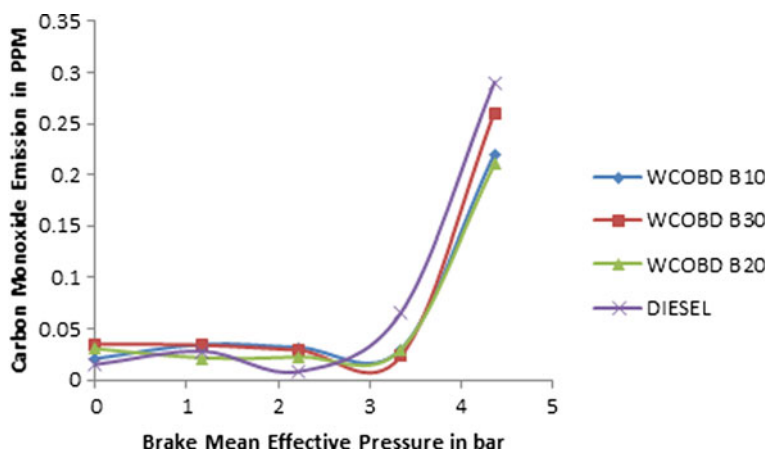


Fig. 6 Carbon monoxide versus brake mean effective pressure

and diesel has lowest BSFC. As the calorific value of the fuel is lesser than that of diesel and in order to maintain the rated speed of the engine for the given load, additional fuel is consumed which resulted in the increase in the BSFC of the blends.

### 3.5 Carbon Monoxide Emission

Figure 6 depicts the emission of carbon monoxide with relation to BMEP. CO emissions are generally formed due to rich mixtures [18]. The lack of oxygen at fuel rich zones is the major cause for CO emission. At peak load, the CO emission of all the WCOBD mixtures was found to be lower than that of diesel, which may be due to the existence of innate oxygen available in the fuel. Among the biodiesel blends, WCOBD B20 recorded lowest CO emission. In order to maintain a constant speed at higher loads, more volume of fuel is injected which in turn increases fuel-rich zones leading to more CO emission.

### 3.6 Unburned Hydrocarbon Emission

Figure 7 shows the relationship between the unburned hydrocarbons versus BMEP for diesel, blends of WCOBD. The emission of hydrocarbon is due to improper combustion of the fuel. The fuel which gets deposited in the crevices of the piston and valves is the main sources of hydrocarbon. UBHC emissions are observed to be higher than diesel, as the biofuel chain contains more hydrocarbons. The emission of the blends WCOBD B20 is found to be lower as the combustion is better than the other blends of WCOBD.

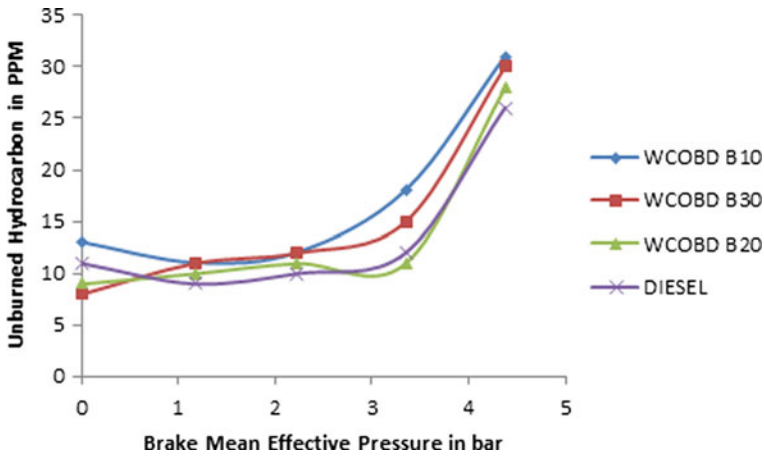


Fig. 7 Unburned hydrocarbon versus brake mean effective pressure

### 3.7 NOx Emission

Figure 8 shows the NOx emission versus BMEP for diesel, blends of waste chicken oil methyl ester. It is detected that the NOx emission is increased for all fuels as the load increases. Higher NOx emission is observed for all the biodiesel blends than diesel, which is because of better combustion as the fuel contains inherent oxygen molecules that would have been resulted in a higher flame temperature resulting in higher NOx emission [19]. From the figure, it is clear that B20 exhibits higher NOx emission. This rise in NOx emissions is attributed to the increased oxygen content on lead in the cylinder temperature relative to other combustion mixtures.

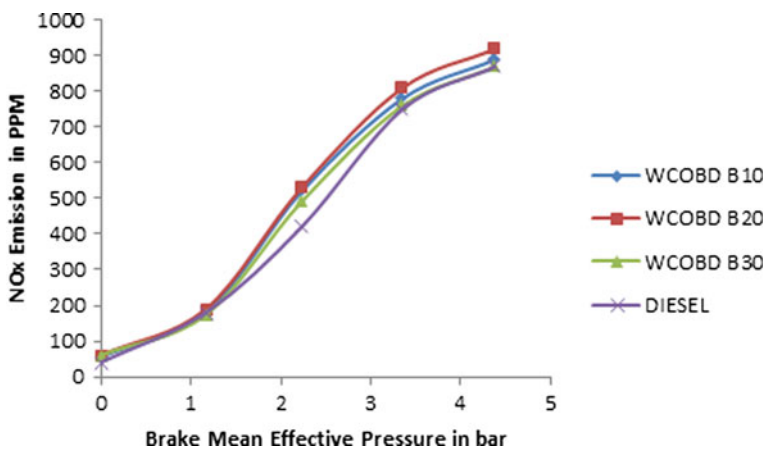


Fig. 8 NOx emission versus brake mean effective pressure

## 4 Conclusion

The experimental study has been done to analyze the combustion, performance and the emission characteristics of different blends B10, B20, B30 of waste chicken oil biodiesel, and the same was compared with diesel. Based on the experimental observations, the following conclusions have been summed up:

The maximum biodiesel yield was obtained as 94.5% with 2% wt of catalyst concentration, 65 °C reaction temperature, 11:1 methanol to oil molar ratio and 60 min of reaction time.

The BTE of B20 is 28.6 which higher than all other blends due to the mutual influence of the viscosity and calorific value.

The emission of the blend B20 of waste chicken oil is found to be lower in case of unburned hydrocarbon and carbon monoxide while higher in case of NO<sub>x</sub> when compared to diesel.

Hence, it has been identified that waste chicken oil biodiesel can be utilized to run a diesel engine without any modifications.

## References

1. Subramaniam M, Solomon JM, Nadanakumar V, Anaimuthu S, Sathyamurthy R (2020) Experimental investigation on performance, combustion and emission characteristics of DI diesel engine using algae as a biodiesel. *Energy Rep* 6:1382–1392
2. Sundar PS, Vijayabalan P, Balachandar M, Sathyamurthy R, Chamkha AJ (2020) Influence of oxygen enrichment on performance, combustion, and emission characteristics of a stationary diesel engine fuelled with *Calophyllum Inophyllum* biodiesel blend. *Asia-Pac J Chem Eng*
3. Karuppan D, Manokar AM, Vijayabalan P, Sathyamurthy R, Madhu B, Mageshbabu D, Bharathwaaj R, Muthiya SJ (2020) Experimental investigation on pressure and heat release HCCI engine operated with chicken fat oil/diesel-gasoline blends. In: *Materials today: proceedings*
4. Balaji D, Pillai TM, Gnanasekaran K, Balachandar M, Ravikumar TS, Sathish S, Sathyamurthy R (2019) Dataset for compression ignition engine fuelled with corn oil methyl ester biodiesel. *Data Brief* 27:104683
5. Sekhar SC, Karuppasamy K, Sathyamurthy R, Elkelawy M, Bastawissi HAED, Paramasivan P, Sathiyamoorthy K, Edison P (2019) Emission analysis on compression ignition engine fueled with lower concentrations of *Pithecellobium dulce* biodiesel-diesel blends. *Heat Transf—Asian Res* 48(1):254–269
6. Kirubakaran M, Selvan VAM (2018) A comprehensive review of low cost biodiesel production from waste chicken fat. *Renew Sustain Energy Rev* 82:390–401
7. Freedman BEHP, Pryde EH, Mounts TL (1984) Variables affecting the yields of fatty esters from transesterified vegetable oils. *J Am Oil Chem Soc* 61(10):1638–1643
8. Gnanaprakasam A, Sivakumar VM, Surendhar A, Thirumarimurugan M, Kannadasan T (2013) Recent strategy of biodiesel production from waste cooking oil and process influencing. *Rev J Energy, Parameter*
9. Çaynak S, Gürü M, Biçer A, Keskin A, İçingür Y (2009) Biodiesel production from pomace oil and improvement of its properties with synthetic manganese additive. *Fuel* 88(3):534–538
10. Nouredini H, Gao X, Philkana RS (2005) Immobilized *Pseudomonas cepacia* lipase for biodiesel fuel production from soybean oil. *Biores Technol* 96(7):769–777

11. Keskin A, Gürü M, Altıparmak D, Aydın K (2008) Using of cotton oil soapstock biodiesel–diesel fuel blends as an alternative diesel fuel. *Renew Energy* 33(4):553–557
12. Soegiantoro GH, Chang J, Rahmawati P, Christiani MF, Mufrodi Z (2019) Home-made eco green biodiesel from chicken fat (CIAT) and waste cooking oil (PAIL). *Energy Procedia* 158:1105–1109
13. Chakraborty R, Gupta AK, Chowdhury R (2014) Conversion of slaughterhouse and poultry farm animal fats and wastes to biodiesel: parametric sensitivity and fuel quality assessment. *Renew Sustain Energy Rev* 29:120–134
14. Singh SP, Singh D (2010) Biodiesel production through the use of different sources and characterization of oils and their esters as the substitute of diesel: a review. *Renew Sustain Energy Rev* 14(1):200–216
15. Atabani AE, Mahlia TMI, Badruddin IA, Masjuki HH, Chong WT, Lee KT (2013) Investigation of physical and chemical properties of potential edible and non-edible feedstocks for biodiesel production, a comparative analysis. *Renew Sustain Energy Rev* 21:749–755
16. Qi DH, Yang K, Zhang D, Chen B (2017) Combustion and emission characteristics of diesel tung oil-ethanol blended fuels used in a CRDI diesel engine with different injection strategies. *Appl Therm Eng* 111:927–35. <https://doi.org/10.1016/j.applthermaleng.2016.09.157>
17. Zhang J, Liu J, Ma H (2012) Esterification of free fatty acids in *Zanthoxylum bungeanum* seed oil for biodiesel production by stannic chloride. *J Am Oil Chem Soc* 89(9):1647–1653
18. Imtenan S, Masjuki HH, Varman M, Kalam MA, Arbab MI, Sajjad H et al (2014) Impact of oxygenated additives to palm and jatropha biodiesel blends in the context of performance and emissions characteristics of a light-duty diesel engine. *Energy Convers Manag* 83:149–58
19. Nabi MN, Rasul MG (2018) Influence of second generation biodiesel on engine performance, emissions, energy and exergy parameters. *Energy Convers Manag* 169:326–33

# Experimental Investigation and Optimization of Process Parameters in EDM of Aluminum Metal Matrix Composites Using Selective Breeding Algorithm



S. K. Rajesh Kanna, P. Sethuramalingam, N. Lingaraj, P. Sivasankar, and J. Sriharish

**Abstract** In the digital manufacturing era, to forbid the challenges and complexity in manufacturing of the geometrically complicated shapes or machining the harder materials or precise cutting of materials, electrical discharge machining has been used by the manufacturing sectors. The output performance of the electric discharge machining depends on its input process parameter values. So in this current research, these input parameters such as supply current, pulse on time and pulse off time have been considered and optimized its value for achieving higher material removal rate, enhanced surface roughness and lesser tool wear rate for Al6061 SiC stir casted metal matrix composites using selective breeding algorithm. Selective breeding algorithm is applied to optimize the said multiple performance characteristics. This experimental research revealed that current value is having major influence over the output performance parameter.

**Keywords** Al6061 · Metal matrix composite · Electrical discharge machining · Selective breeding algorithm

## 1 Introduction

The digital revolution in the industries creates a void for lightweight, high-strength materials for the machine tools. So the manufacturers are focusing on the aluminum and its alloys, which is light in weight and having satisfactory strength. On the other hand, the aluminum alloys are having the limited capability and not able to satisfy the desired need of the manufacturers. So the researchers are adding specific metals to the aluminum matrix in order to yield the desired properties, and the process is called as reinforcement. The resulted material is called aluminum metal matrix composite (MMC) [1]. The commonly used reinforcement materials for the aluminum matrix are nanotubes [2], TiC and SiC [3], because of its properties like

---

S. K. Rajesh Kanna (✉) · P. Sethuramalingam · N. Lingaraj · P. Sivasankar · J. Sriharish  
Rajalakshmi Institute of Technology, Chennai, India  
e-mail: [skrkanna@gmail.com](mailto:skrkanna@gmail.com)

higher temperature resistant and enhanced mechanical properties which are highly needed for the industries such as automotive and aerospace. MMC increases the wear rate and thereby increases the performance and the life of the material [4]. MMCs can also yield the considerable weight saving without compromising the strength-to-weight ratio, so it can be used for the various engineering and domestic applications [5]. Even though the researchers can extract the desired properties from the aluminum MMCs, prospective being predominantly restricted during manufacturing, because of the cost, machining difficulty, complex profile formations, etc. It is common phenomenon that the enhanced properties of the MMC will lead to the machining difficulty, higher tool wear and breakage during the machining [5]. The improved strength due to the availability of the reinforced particles in MMCs causes difficulty in machining [6]. Later by the researchers, it has been explored that the machining of the MMC using the conventional methods might be quite complicated [7], and machining by the abrasive particle's like electrical discharge machining, stir casting method, spark plasma sintering [8], liquid infiltration, squeeze casting method, powder metallurgy, etc. is producing better results [9]. However, electrical discharge methods are widely used for machining the MMC, due to its economic aspects and material independent machining of arbitrary profiles [9].

Electrical discharge machining (EDM) is categorized under the unconventional machining process, which has been specifically developed to fabricate intricate complex profiles on the conductive work piece, irrespective to the material properties like hardness, toughness, etc. [10]. In this EDM process, continuous discharges of electrons have been passed with high pressure and force, which removes the materials from the workpiece by creating the arc between the electrode tool and the workpiece [11]. The removed materials have been removed by the dielectric fluid medium. Thus, EDM machining opens an era for the researchers and as the outcome of the machinability analysis by the various researchers, it have been found that the significance of EDM process parameters such as supply current, duration of pulse on time, off time, flushing pressure of the dielectric, etc. plays a major role in the performance measures. Also the particles used as the reinforcement and its size plays major role in the EDM performance. Researchers also determined the best possible combination process parameters for multi-objective conflicting optimization problems by implementing various optimization techniques such as Taguchi, grayscale analysis [12], genetic algorithm [13], ant colony algorithm [14], hybrid algorithms [15], firefly algorithm [16], stochastic methods, etc., because the experimental and the trial-and-error methods consume more cost and time.

For these type of NP-hard problems, many solution methodologies have been proposed by the researchers like genetic algorithm, fuzzy logic, neural network, selective breeding, PSO, etc. Among these algorithms, selective breeding algorithm plays a vital role, as this algorithm generates the breed from the generated breed. Thus, the best solution obtained from the better solutions. Christopher and Ian [17] implemented the selective breeding to enable long-term genetic improvement of broodstock. Zhi and Yuan [18] used the selective breeding concept in enhancing the crossover operation in the genetic algorithm and stated that the results had excellent improvements. Boris et al. [19] used selective breeding concept for segregating

the genes with acute functional tolerance to the effect of ethanol. Srirama & B. Parvathavarthini [20] applied the selective breeding algorithm for optimizing the one dimensional bin packing problems.

In this current research, the experimental trails had been devised for L27 orthogonal array to optimize the supply current (A), pulse on time (PoT) and the particle size (Ps) to achieve the maximum material removal rate (MRR), minimal tool wear rate (TWR) and better surface roughness (Ra). The multiple objective optimization has been achieved in this research by implementing the selective breeding algorithm (SBA).

## 2 Experimental Implementation

Aluminum 6061 Alloy has been used as the matrix material for the experimentation, because the AL6061 is having better castability for thinner/intricate sections along with the higher corrosion resistance, which can be the desired properties for the many industrial applications. Further to enhance the mechanical properties of the matrix, SiC has also been added into the matrix, because SiC enhanced the matrix to a very hard material with lesser wear rate [21]. In this present experimentation, Al6061-SiC MMC comprising alumina (Al6061) with the SiC reinforcement of the particle size 15, 20 and 30  $\mu\text{m}$ , fabricated by stir casting method has been used to identify the optimal value for the EDM machining process parameters such as supply current, pulse on time and the particle size to obtain higher MRR, lesser TWR and better Ra. Al6061 alloy was melted in the furnace at the constant temperature of 850  $^{\circ}\text{C}$ , and then the SiC particles of the sizes 15, 20 and 25  $\mu\text{m}$  are added into the molten matrix [22]. Before adding to the SiC particles, these particles were pre-heated to 450  $^{\circ}\text{C}$  to achieve the homogeneous MMC mixture in the muffle furnace. Then, the mixture is stirred with 450 rpm for 15 min continuously to obtain the homogeneous mixture and dissemination of the SiC particles all over the matrix material. Then, the blend was maintained at the 800  $^{\circ}\text{C}$  to retain the fluidity of the mixture, then the molten blend was poured into the standard rectangular prismatic dies to fabricate the work specimens, and three different workpiece were fabricated for the experimentation by varying the SiC particle sizes.

In this research, for experimentation, Electronica EDM machine with the copper electrode of 12-mm-diameter tool was used to drill the blind hole of 3-mm-depth on the 5-mm-thick work piece with the kerosene as the dielectric fluid to flush away the removed materials. Machining parameters set for the experimentation have been shown in Table 1.

The MRR and TWR were measured by calculating the weight before and after machining with the precision weighing machine. Similarly, the surface roughnesses were measured using Mitutoyo surface roughness tester. In order to avoid the manual error in measuring, every data have been recorded thrice and the averages of the recorded value have been taken for the research. The obtained value from the experimentation is shown in Table 2 for L27 array.

**Table 1** Input machining parameters for experimentation

EDM parameters	Notation	Unit	1	2	3
Current	I	Amps	4	8	12
Pulse on time	POT	$\mu$ s	200	300	400
Voltage	V	Volts	30	30	30
Flushing pressure	Pr	MPa	0.0200	0.0200	0.0200
Particle size	Ps	$\mu$ m	15	20	25

**Table 2** Experimental input and output

Trials	Current (A)	POT ( $\mu$ s)	Volt (V)	Pressure (MPa)	Ps ( $\mu$ m)	MRR (g/Min)	TWR (g/min)	Ra ( $\mu$ m)
1	4	200	30	0.02	15	0.0315	0.0021	1.52
2	4	200	30	0.02	20	0.0321	0.0023	1.74
3	4	200	30	0.02	25	0.0329	0.0035	1.69
4	4	300	30	0.02	15	0.0318	0.0023	1.56
5	4	300	30	0.02	20	0.0336	0.0029	1.76
6	4	300	30	0.02	25	0.0344	0.0036	1.71
7	4	400	30	0.02	15	0.0329	0.0024	1.57
8	4	400	30	0.02	20	0.0356	0.0032	1.65
9	4	400	30	0.02	25	0.0365	0.0034	1.78
10	8	200	30	0.02	15	0.0342	0.0031	1.85
11	8	200	30	0.02	20	0.0378	0.0039	1.93
12	8	200	30	0.02	25	0.0396	0.0046	2.02
13	8	300	30	0.02	15	0.0384	0.0038	1.88
14	8	300	30	0.02	20	0.0413	0.0041	1.99
15	8	300	30	0.02	25	0.0408	0.0049	2.06
16	8	400	30	0.02	15	0.0396	0.0039	1.92
17	8	400	30	0.02	20	0.0426	0.0045	1.97
18	8	400	30	0.02	25	0.0426	0.0052	2.11
19	12	200	30	0.02	15	0.0411	0.0051	2.15
20	12	200	30	0.02	20	0.0457	0.0053	2.18
21	12	200	30	0.02	25	0.0481	0.0062	2.41
22	12	300	30	0.02	15	0.0457	0.0052	2.16
23	12	300	30	0.02	20	0.0478	0.0057	2.26
24	12	300	30	0.02	25	0.0496	0.0064	2.45
25	12	400	30	0.02	15	0.0489	0.0062	2.41
26	12	400	30	0.02	20	0.0492	0.0059	2.46
27	12	400	30	0.02	25	0.0498	0.0064	2.49



These experimental observations will bridge the gap to take decision on the parameters such as discharge current, pulse on time and particle size which are influencing the MRR, TWR and surface roughness. These observed values have been given as the input the developed selective breeding algorithm for optimization of the input machining parameters.

### 3 Selective Breeding Algorithm Optimization

In this research, for optimizing the EDM machining parameters, selective breeding algorithm has been used. Selective breeding algorithm (SBA) is derived from the behavior of the animals, i.e., inherits the behavior breeding the chicken or animal breeding by identifying and enhancing the property of the best chromosome to the desired level from the available chromosomes and generating 'n' number of hybrid breeds. Thus, the generated breeds are inherited only the best properties from the parents and thereby they are having the desired properties. Again the same procedure of breeding the child from the parents has to be repeated till the desired property achieved. Thus, the final breeds are having the user-defined characteristics or the breed without undesirable properties. In this study, the values of the input machining parameters are assumed to be the genes formulated a chromosome. In general, in SBA, the length for a chromosome or number of genes in a chromosome is mapped to the number of instances responsible for optimization or the factors influencing the performance. In this research, the number of instances influencing the machining parameters is the A, PoT and Ps, so the size of the chromosome is set to three. As the size of the chromosome is very less, the outcome of the optimization might not yield the best results. So to compensate the lesser length chromosomes, the number of breeding iterations has to be increased, so in this optimization module, the number of breeding iterations increased to 250 with the minimal step ratio of 1 Amps, 10  $\mu$ s and 1  $\mu$ m for the supply current, pulse on time and particle size, respectively. Thus, the search space has been increased to 24,000 combinations of genes. Initially, the chromosomes are allowed to generate at random and allowed to breed its children's to reduce the MRR, increase the TWR and enhance the Ra. SBA module is carried out in five stages to get the optimal values.

Random generation of the initial population is the initial stage of the SBA. In this stage, for the defined chromosome size, genes are generated at random using roulette wheel generation. Similarly, the chromosomes are generated for the user-defined numbers. There is no specific methodology derived for the number of chromosomes and has to be set by conducting the sensitivity analysis. In this research work, sensitivity analysis has been performed and found that the further increase in the chromosomes above 250 numbers has yield only the similar results, because the size of the chromosome is limited to three. Each gene or string in the chromosome represents the input machining parameters in binary-coded chromosomes [23].

The binary digits are in the order of supply current, pulse on time and particle size, respectively. For explanation, the randomly generated sample 10 numbers of

Parent 1: 011100 1011000111 0110010001 001000 00000000 00000000 00000000  
 Parent 2: 000111 1111000101 0100110010 011001 00000000 00000000 00000000  
 Parent 3: 001001 1010001010 0101110001 000011 00000000 00000000 00000000  
 Parent 4: 010011 0001111010 0001110010 010110 00000000 00000000 00000000  
 Parent 5: 001101 0101010000 0110000100 000100 00000000 00000000 00000000

**Fig. 1** Sample parent chromosomes

chromosome are shown in Fig. 1. The binary digital numbers represent the EDM machining parameters, i.e., the first six digits denote the value of the supply current followed by the decimal value of the current for next ten digits, the next ten digits denote the pulse on time duration, the next six digits denote the particle size, and the last 24 digits denote the flag value for the SBA. While decoding, the binary values are converted to the decimal values and then mapped to the specific units mentioned in Table 1. Similarly in this stage, 250 parents have been generated at random using the roulette wheel selection method.

In the second stage, breeding factor (Bf) values, i.e., the objective function value for the above randomly generated parents has to be calculated. The breeding factor function is given in Eq. 1.

$$Bf(x) = 1/(\max(MRR) + \min(TWR) + C * Ra) \tag{1}$$

In general, the machining performance of a methodology has been assessed by the MRR, TWR and Ra of the machined workpiece. The traditional way of calculating the MRR is given in Eq. 2.

$$MRR = (\text{Material removed})/(\text{Time Taken})(\text{grams/min}) \tag{2}$$

The amount of material removed during machining is the difference in the weight of the workpiece before and after the machining process, and the obtained value is given in Table 2. As there is more than one parameter with the conflicting nature involved, a need arises for the multi-objective function. The multi-objective function for this research has been obtained from the Minitab software, and the obtained formulation for MRR, TWR and Ra is given in the Eqs. 3, 4 and 5, respectively.

$$\begin{aligned} MRR = & 0.0951 e^{-004} + (4.0652 e^{-050} \times I) + (2.2582 e^{-008} \times Ps) \\ & + (3.2113 e^{-009} \times PoT) - (2.9081 e^{-008} \times I \times Ps) \\ & - (0.1257 e^{-008} \times PoT \times Ps) \end{aligned} \tag{3}$$

From Eq. 3, it is clear that the current supplied is directly proportional to the MRR, i.e., MRR value increases proportionally with increase in the current value. For the TWR model given in Eq. 4, it is clear that the supply current is inversely proportional to the EDM parameters. Thus, the optimization problem became the multi-objective conflicting non-deterministic problem, which cannot be solved by

the traditional optimization methods.

$$\begin{aligned} \text{TWR} = & 6.2247 e^{-005} + (4.0452 e^{-003} \times I) + (5.6854 e^{-008} * \text{Ps}) \\ & + (8.2354 e^{-009} \times \text{PoT}) - (9.910 e^{-008} \times I \times \text{Ps}) \\ & - (6.3123 e^{-004} \times \text{PoT} \times \text{Ps}) \end{aligned} \quad (4)$$

For the Ra model given in Eq. 5, it is clear that the particle size is directly proportional to the surface roughness. Higher the size of the particle, removes the extra material from the surface and vice versa. So it became necessary to decide the particle size before blending with the matrix.

$$\begin{aligned} \text{Ra} = & 2.2102 + (2.4542 \times I) + (8.3254 \times \text{Ps}) - (4.2135 e^{-004} \times \text{PoT}) \\ & - (4.0150 e^{-003} \times I \times \text{Ps}) - (2.2082 \times \text{PoT} \times \text{Ps}) \end{aligned} \quad (5)$$

The randomly generated chromosome values have been decoded to the actual values and substituted in the Eqs. 1–5 to obtain the breeding factor value. The obtained breeding factor values have been normalized to make the homogenous unit for the factor. Based on the obtained values, the parents are sorted in the ascending order to elect the higher rank parents.

Once the breeding factor values have been calculated, then the parents have to be allowed to operate by the segregation operator, which is the third stage of the SBA. In this module, the SAB segregates the available parents into dominant and recessive parent sets based on the breeding fitness value. The parents with the higher fitness set are called the dominant parent set, i.e., best chromosome parents going to dominant in the population generation and remaining parent sets are called as recessive parent set, i.e., worst property parents. Once the parents have been segregated, then the next stage is the breeding stage. In the breeding stage, one dominant parent and one recessive parent have been selected in sequence from each set, and they have to be permitted to breed their children's. Similarly, the same process of breeding has to be done with the other available parents in the sets. For example, in the above sample given in Fig. 1, five dominant parents (D1, D2, D3, D4, D5) and five recessive parents (r1, r2, r3, r4, r5) were obtained, and they have to be paired for breeding operation stages, i.e., stage 1—D1r1, stage 2—D2r2, stage 3—D3r3, stage 4—D4r4 and stage 5—D5r5. The stage and the pairs depend on the number of parent in the population selected for breeding in the initial stage.

The fourth stage is the breeding stage, in which all the probabilities of the combinations of the genes in the chromosomes have to breed their child and the probable combinations for the above stated example are as follows for the parents given in Fig. 1 are as follows,

$$\begin{aligned} & D1r1 \times D2r2; D2r2 \times D3r3; D3r3 \times D4r4; D4r4 \times D5r5; \\ & D1r1 \times D3r3; D2r2 \times D4r4; D3r3 \times D5r5; \\ & D1r1 \times D4r4; D2r2 \times D5r5; \end{aligned}$$

$$D1r1 \times D5r5.$$

At the end of this breeding stage, 80 breded children were generated for the above-mentioned combination of parent sets of sample size 10. The fusion point plays a major role in the breeding; in this research, it has been set to 50%, i.e., two fusion points at random for each and every breed. The fusion points are used to swap the genes between the dominant parent and the recessive parent. The common phenomenon in all the animal behavior and evolutionary algorithms is that by swapping only the genes among the parent will lead to stagnation of the solution at the local optimal peaks and in SBA it is called as in-breeding depression. So to avoid the phenomenon, mutation like operations has been performed, which muted certain genes in the chromosomes, but this paved the way for unfeasible solutions [24]. So in SBA, there is no mutation and there is no replacement of the parents to retain all the best in the population, 10% of random parents have been generated and included in the population. Thus, the population size increased to another 10% of the total population. Thus, for the sample population considered above, the total parents for the next generation became 99 numbers (10 initial parent, 80 breded child + 9 in-breed child).

The final fifth stage of SBA is the termination stage, in this stage, best chromosomes have to be identified from the available updated breed population. Again it has been done by sorting the chromosomes based on the breeding factor values. The identified top 10 chromosomes will be selected for the next breeding iteration and the similar sequence of the procedure have to be followed till the desired or pre-defined termination conditions reached. In this research, the desired condition is to make the breed factor to 1, and the termination condition is that the number of iterations reached 100. The numbers of iterations have to be set based on the global optimal point reachability, i.e., the same parameter values have to be repeated for more number of parents in the population indicates the solution reached the global optimal and the iteration have to be set for the SBA termination condition. Once the termination conditions have been satisfied, the top ranked chromosome values will be considered to be the best optimal values for the machining parameters.

## 4 Results and Discussion

The main objective of this research is to increase the MRR for the reduced roughness and tool wear rate as the index of higher performance measure through the selective breeding algorithm. In this present investigation, the obtained best optimal result for a sample study by the developed SBA module is '01000 110101011 101000010 10101 1011100 1011001 1010001,' which decodes to 8.427 amps value for the supply current, 322  $\mu$ s for the pulse on time, 21  $\mu$ m for the SiC particle size and the flag values for the MRR, TWR and Ra are 0.92, 0.89, 0.81, respectively.

The objective function for the MRR is the maximization function, i.e., higher the MRR better category. The relations of the MRR with respect to the supply current,

pulse on time and particle size are shown in Fig. 2. From the Fig. 2, it is clearly perceived that the MRR is proportionally getting increased with the supply current, pulse on time and particle size. Because increase in the supply current will increase the discharge energy pulses from low to high level and thereby increases the heat flux over the aluminum metal matrix composites. Thus, more materials removed from the surface. Similarly by increasing the pulse on time for a long period increases the flux contact time and thereby increases the heat flux. From this research investigation, it is proved that the supply current has predominant effect over the MRR in the EDM process of aluminum metal matrix composites.

Tool wear rate plays a major role in the performance of the machining, as it decides the shape, finish, cost, machining time, and accuracy of the workpiece. The effect plot for the TWR with the EDM machining parameters are shown in Fig. 3. As the TWR is correlated with the melting point of the electrode materials, current increase then the TWR increases. But the pulse on time and the particle size have not much influencing effect over the TWR.

In general, the machining performance decided by the surface roughness and should be minimum as possible. The plot on the effect input parameters over the roughness is shown in Fig. 4. Form the research, it is clear that the surface roughness is higher for the higher current and for the better surface finish, the material has to be removed at the slower rate and the with lesser tool wear. Similarly for the smaller particle size, better the surface finish. Apart from these parameters, the flushing pressure lays a vital role in the roughness attainment. Because of the continuous discharge of the metal, it results in the formation of the metal pool over the surface and has to be removed properly and at the meantime, more the flushing pressure,

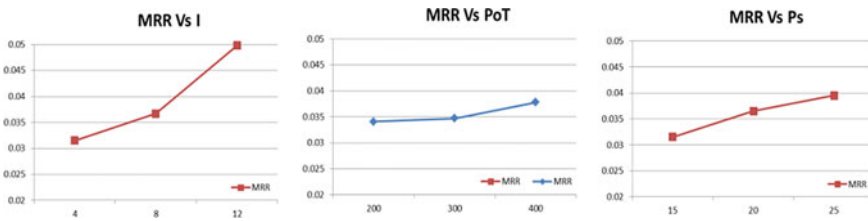


Fig. 2 Effect plot for the MRR (X-axis) versus I, PoT and Ps (Y-axis)

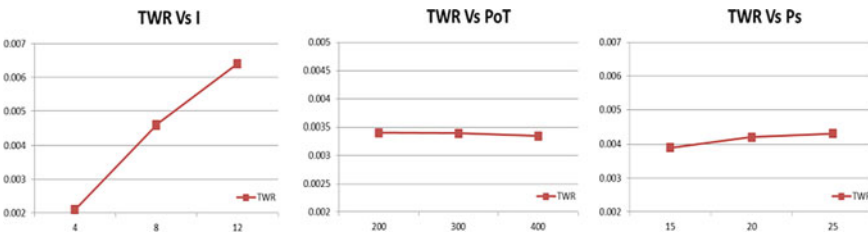
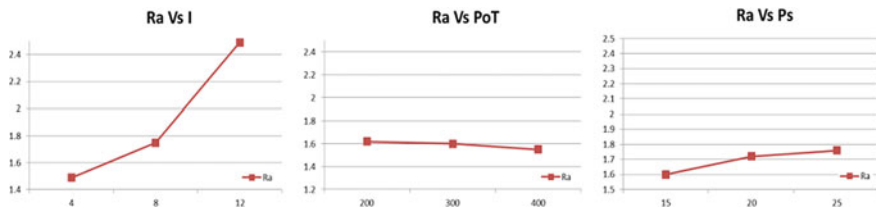


Fig. 3 Effect plot for the TWR (X-axis) versus I, PoT and Ps (Y-axis)



**Fig. 4** Effect plot for the Ra (X-axis) versus I, PoT and Ps (Y-axis)

**Table 3** Comparison of EDM parameters

Trial	Current	POT	TWR	TWR [12]	Ra	Ra [12]
1	4	200	0.0021	0.00865	1.52	3.0
2	4	400	0.0024	0.00471	1.57	5.9
3	8	200	0.0031	0.01497	1.85	8.81
4	8	400	0.0039	0.00618	1.92	5.76
5	12	200	0.0051	0.01962	2.15	5.76
6	12	400	0.0062	0.01598	2.41	7.24

lesser the roughness. So only by optimizing the I, PoT and Ps will not able to attain the higher surface finish. The effect plot for the Ra during EDM process is shown in Fig. 4.

Further to validate the experimentation, the obtained values have been compared with the dataset of Singh et al. [12] and have been provided in Table 3. Form the comparison, it is clear that the developed algorithm performs better.

## 5 Conclusions

The alumina (Al6061) strengthened with SiC particulate specimens have been prepared from the process of stir casting. The prepared test specimens were machined in the EDM by varying the machining parameters and obtained the data for L27 arrays. The machining process variables such as supply current, pulse on time and particle size for electrical discharge machining of Al6061-SiC MMCs have optimized for material removal rate, tool wear rate and surface roughness with selective breeding algorithm. The experimental results proved that the SBA is found to be more suitable optimization tool for multi-objective conflicting optimization machining problems. The identified optimal values are 8.5 amps value for the supply current, 320  $\mu$ s for the pulse on time, 20  $\mu$ m for the SiC particle size and the output normalized values for the MRR, TWR and Ra are 0.92, 0.89 and 0.81, respectively, based on the SBA methodology. The results are again machined and tested for the performance, in which the SBA data and the experimental data are in line. Selective breeding

algorithm results reveals that the supply current is playing a predominant role in controlling the EDM machining process, and it is the significant process parameter in affecting the characteristics of the workpiece and the tool, so more weightage have to be given to the supply current while optimizing with the multi-objective functions. Then, it is followed by the pulse on time in the similar pattern of the supply current in the controllable fashion. But the reinforcement particle size plays a significant role in the machining performance, as those materials only enhances the properties of the materials. Apart from these parameters, flushing pressure of the dielectric fluid plays a role in obtaining the better surface finish.

## References

1. Muller F, Monaghan J (2001) Non-conventional machining of particle reinforced metal matrix composites. *J Mater Process Technol* 118:278–285
2. Saba F, Abdolkarim S, Simin S, Mohsen H, Jaafar H-S, Babayi SH (2019) A novel approach to the uniformly distributed carbon nanotubes with intact structure in aluminum matrix composite. *Adv Compos Hybrid Mater* 2(3):540–548
3. Muller F, Monaghan J (2000) Non-conventional machining of particle reinforced metal matrix composite. *Int J Machine Tools Manuf* 40:1351–1366
4. Brazil D, Monaghan J, Aspin Wall K (1997) Wear characterization of various diamond tooling when single point turning a particle reinforced metal matrix composite. In: *Proceeding of the IMC-14 conference*, pp 143–152
5. Vijayarangan S, Rajamanickam N, Sivananth V (2003) Evaluation of metal matrix composite to replace spheroidal graphite iron for a critical component, steering knuckle. *Mater Des* 43:532–541
6. Chadwick GA, Heat P (1989) The machining of metal matrix composites with polycrystalline diamond tools. In: *Proceedings of the seventh conference on materials resolutions through the 90s*, pp 1–33
7. Lau WS, Yue TM, Lee TC, Lee WB (1995) Un-conventional machining of composite machining. *J Mater Process Technol* 48:199–205
8. Sadeghi B, Cavaliere P, Azimi G, Martin R, Morteza N, Trembosova Stefan SV, Nagy Niloofar E (2019) Hot rolling of MWCNTs reinforced Al matrix composites produced via spark plasma sintering. *Adv Compos Hybrid Mater* 2(3):549–570
9. Yigezu BS, Jha PK, Mahapatra MM (2013) The key attributes of synthesizing ceramic particulate reinforced Al-based matrix composites through stir casting process: a review. *J Mater Manuf Process* 969–979
10. Crookall JR, Heuvelman CJ (1971) Electro-discharge machining the state of the art. *Ann CIRP* 20 2:113–120
11. Taha MA (2003) Practicalization of cast metal matrix composites (MMCCs). *Mater Des* 22:431–441
12. Singh PN, Raghukandan K, Pai BC (2004) Optimization by Grey relational analysis of EDM parameters on machining Al–10% SiCP composites. *J Mater Process Technol* 155:1658–1661
13. Rajesh Kanna SK, Udaiyakumar KC, Dinesh Kumar S, Lingaraj N (2018) 3D heterogeneous bin packing framework for multi constrained problems using hybrid genetic approach. *IOP Conf Ser Mater Sci Eng* 402:1–9
14. Rajesh Kanna SK, Jaisree B, Bharanikumar (2015) Optimization of 3D constrained rectangular bin packing problem using recursive ant colony algorithm. *IOSR J Mechan Civil Eng* 12(4):65–70

15. Rajesh Kanna SK, Malliga P, Sarukesi K (2012) A 3D-multi constrained arbitrary sized heterogeneous box packing optimization using hybrid genetic approach. *J Adv Mater Res* 479–481:1825–1830
16. Rajesh Kanna SK, Udaiyakumar KC (2017) A complete framework for multi-constrained 3d bin packing optimization using firefly algorithm. *Int J Pure Appl Math* 114(6):267–282
17. Hollenbeck CM, Johnston IA (2018) Genomic tools and selective breeding in molluscs. *Front Genet* 9(253):1–15
18. Chen Z-Q, Yin Y-F (2012) An new crossover operator for real-coded genetic algorithm with selective breeding based on difference between individuals. *IEEE Explor.* <https://doi.org/10.1109/ICNC.2012.6234556>
19. Tabakoff B, Bhave SV, Hoffman PL (2003) Selective breeding, quantitative trait locus analysis, and gene arrays identify candidate genes for complex drug-related behaviors. *J Neurosci* 23(11):4491–4498
20. Sriramya P, Parvathavarthini B (2012) Performance analysis of selective breeding algorithm on one dimensional bin packing problems. *J Instit Eng India Ser B* 93:255–258
21. Fan X, Yin X (2018) Progress in research and development on matrix modification of continuous fiber-reinforced silicon carbide matrix composites. *Adv Compos Hybrid Mater* 1(4):685–695
22. Suresh S, Harinath G, Deva Kumar MLS (2018) Wear behaviour of Al 7075/SiC/Mg metal matrix nano composite by liquid state process. *Adv Composit Hybrid Mater* 1(4):819–825
23. Rajesh Kanna SK, Malliga P (2012) Multi-constrained optimization of rectangular bin packing problem using binary coded evolutionary algorithm. *Int J Mater Manuf Optim* 3(1):27–35
24. Rajesh Kanna SK, Dinesh Kumar (2011) Overloading orientation constraint over genetic mutation for solving 3D heterogeneous bin packing problem. *Eur J Sci Res* 66(3):366–376



# Analysis and Study of Tin Interlayer Aluminum Weld



Sekar Anand, Sankaran Lokesh, Arunachalam Dharmalingam Srikeslav,  
and Jebaseelan Davidson

**Abstract** Friction stir welding is a solid-state welding process and is used to join dissimilar metals effectively. Moreover, they are used to weld Aluminum alloys which are widely used in aerospace, vehicle body parts, and plenty more applications. In our study, two Aluminum plates were joined by inserting a small strip or wire of another material using friction stir welding. This dissimilar non-ferrous welding changes the properties of the material at the specified location, i.e., near the weld joint region. This change of material properties only in a particular region is useful for many applications. The objectives of our study were to improve the properties of the Aluminum alloy (Al6061), especially near the weld region. Two sets of Aluminum plates were taken, and friction stir welding was carried out. The Tin strip was introduced between one set of Aluminum plates while welding and other set is welded normally using friction stir. The destructive tests and Rockwell hardness test were carried out to check the efficiency of the weld joint. It was observed that the tensile strength and compressive strength of the weld joint was higher when the Tin strip is introduced between the Aluminum samples while welding. Further, the elongation of Tin introduced Aluminum sample is less compared to the Aluminum without Tin insertion. From the hardness test, hardness near the weld zone was higher in the Tin-inserted Aluminum sample. Thus, it could conclude that the insertion of the Tin strip between Aluminum can be further studied for various lightweight applications that require specific properties at defined locations.

**Keywords** Aluminum · Tin · Solid-state welding · Tensile property

---

S. Anand (✉) · S. Lokesh · A. D. Srikeslav · J. Davidson  
School of Mechanical Engineering, Vellore Institute of Technology, Chennai Campus, Vandalur -  
Kelambakkam Road, Chennai 600127, Tamil Nadu, India  
e-mail: [s.anand2016@vitstudent.ac.in](mailto:s.anand2016@vitstudent.ac.in)

S. Lokesh  
e-mail: [s.lokeslav2016@vitstudent.ac.in](mailto:s.lokeslav2016@vitstudent.ac.in)

A. D. Srikeslav  
e-mail: [ad.srikeslav2016@vitstudent.ac.in](mailto:ad.srikeslav2016@vitstudent.ac.in)

J. Davidson  
e-mail: [Davidson.jd@vit.ac.in](mailto:Davidson.jd@vit.ac.in)

## 1 Introduction

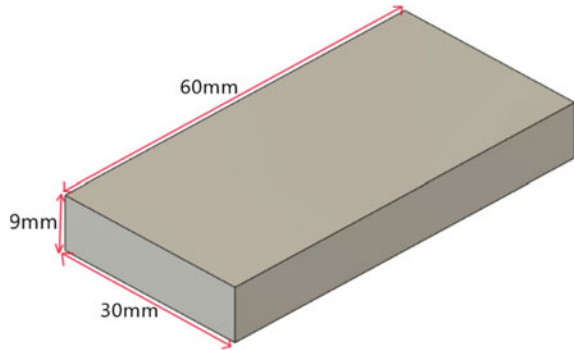
Aluminum has a wide range of applications from the aircraft industry to construction. Its mechanical property, ease of manufacturing, and availability are major reasons for it [1]. Aluminum can be welded by friction stir welding, a solid-state welding technique, with dissimilar metal as well as with its dissimilar Aluminum alloy. There was numerous research carried out on friction stir welding of Aluminum. The lap shear strength and the fatigue properties of friction stir welded dissimilar AZ31B-H24 Mg alloy and Al alloy (AA) 5754-O was evaluated and was found to increase [2]. The research was carried out in which copper and Aluminum were tried to join using friction stir welding and was successfully welded [3]. Moreover, the mechanical and microstructural properties of 2024 and 7075 Aluminum sheets joined by friction stir welding were investigated [4]. In another research paper, a nanoparticle deposition system is combined with friction stir spot welding of dissimilar Al alloys to fabricate a carbon/Aluminum metal matrix compo-site joint [5]. In addition to that Tin interlayer, 6061-T6 Aluminum extrusions were friction stir welded in a 90° butt-weld configuration. [6]. Furthermore the fatigue behavior of notched specimens of friction stir-welded Aluminum alloy 6063-T6 was studied [7]. Interlayers are added while welding to improve the quality of the weld. Aluminum (Al 6060) was welded with Copper in a lap joint with a Zinc interlayer to reduce the formation of intermetallic compounds [8]. Stainless Steel was connected with Titanium using Aluminum interlayer in a friction welding to reduce the formation of Steel–Titanium intermetallic compounds [9]. An investigation was performed on the friction stir welding of Aluminum to Titanium with a Niobium interlayer [10]. Similarly, Zinc interlayers are used while welding dissimilar metals to reduce the formation of the intermetallic compound [11–13]. Also, Tin and Zinc interlayers were used to reduce the intermetallic formed during welding of Magnesium with Aluminum [14]. In most of the studies, interlayers have been used to reduce the intermetallic formation. However, the idea of this study was that interlayers can also be used to vary the properties of the material near the weld region. The advantage of using an interlayer is that the composition of a base metal can be changed near the weld zone while in other regions, the compositions remain unaffected. Thus, in this study, Aluminum 6061 was welded with a Tin interlayer to improve its mechanical properties and was compared with a control set where the Aluminum billets were welded without interlayer.

## 2 Methodology

### 2.1 Sample Procurement

Pure Aluminum is a soft material, but when combined with alloying materials it can produce a wide range of mechanical properties. Aluminum sample (Al6061) of

**Fig. 1** Dimensions of the aluminum plate



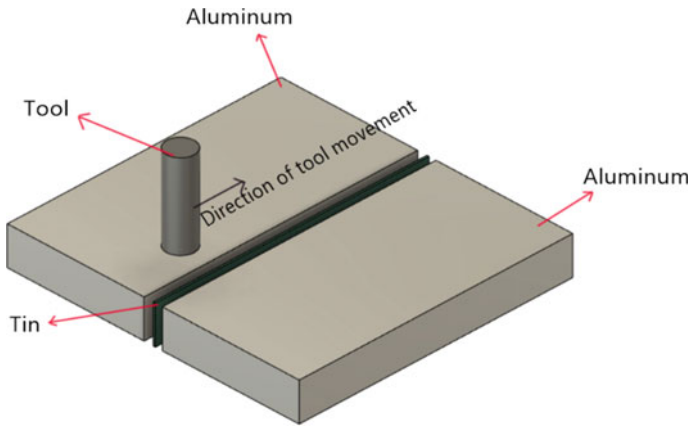
dimension 60 mm × 30 mm × 9 mm was procured along with a Tin sheet of 0.5 mm thickness. The pictorial representation of the Aluminum sample is shown in Fig. 1. The thickness of 0.5 mm was taken to test the validity for thin sheet welding process.

## 2.2 Experiment Procedure

The friction stir welding (FSW) was performed on two sets. At first, two Aluminum billets were welded by FSW with the plunge depth of 0.9 cm with an incremental feed of 10 mm/min. This served as the control set. Another pair of Aluminum billets were welded by FSW by placing an interlayer made of Tin. The interlayer was cut from the Tin sheet to the dimensions of 60 mm × 9 mm × 0.5 mm. The friction stir welding parameters were initialized based on the literature studies and the trials conducted, and it remains the same for both the sets which are given in Table 1. The visualization of the friction stir welding of the sample is shown in Fig. 2. The mechanical testing like the Rockwell hardness test, the tensile test, and the compressive test were performed on both the sets of samples.

**Table 1** Welding parameters

Parameter	Values
Speed	1000 rpm
Total head tilt angle	5° on either side
Incremental feed	10 mm/min
Plunge depth	0.9 cm



**Fig. 2** Friction stir welding of the sample

### 3 Results and Discussion

#### 3.1 Hardness Test

Rockwell hardness was performed on the samples in three regions (on weld zone, on heat-affected zone (HAZ) and on-base metal). 1/16 diamond ball indenter was used with 100 Kgf load. The Rockwell hardness of samples was found and is given below in Table 2. It can be inferred from the table that there was a significant reduction in the hardness value in heat-affected zone (HAZ) of the Tin interlayer Aluminum weld sample than that of the control set. However, the hardness of the Tin interlayer Aluminum weld was higher than the control set. The increased hardness indicates the increase in the brittleness of the sample as hardness is defined as the material's resistance to the plastic deformation. [15]

**Table 2** Hardness test results

Sample/location	Aluminum–Aluminum	Tin interlayer aluminum
Base metal	B10	B11
HAZ	B15	B7.5
Weld metal	B7.5	B11.7

### 3.2 Tensile Test

The tensile property of both the samples was studied using a universal testing machine (UTM). The welded samples were held on the edges parallel to the weld zone, and force is applied with a constant speed of 2 mm/min which can be seen in Fig. 3.

Aluminum–Aluminum weld– The results from the UTM for this sample is given in Table 3 along with the stress–strain and force–displacement response curves as shown in Figs. 4 and 5, respectively.

Tin interlayer Aluminum weld– The results from the UTM for this sample is given in Table 4 along with the stress–strain and force–displacement response curves as shown in Figs. 6 and 7, respectively.

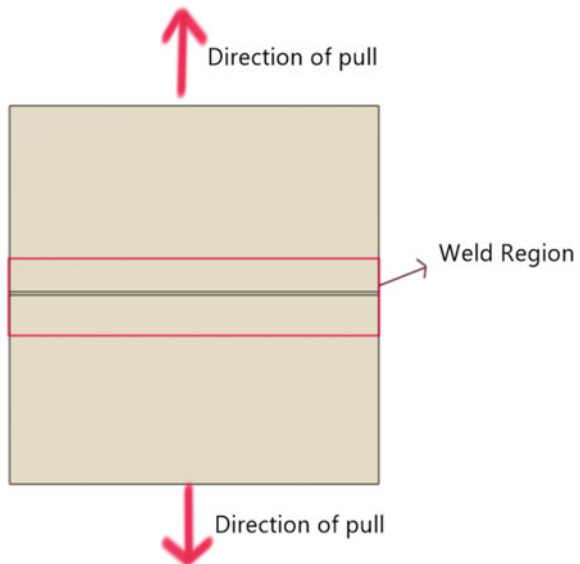
By comparing Figs. 4 and 6, it can be observed that the yield point stress of both the sets is almost the same (13.0239 MPa for the control set and 12.8589 MPa for Tin interlayer Aluminum–Aluminum weld). However, the max stress of the Tin interlayer Aluminum–Aluminum weld occurred at 35.2400 MPa while the control set’s max stress is around 30.0114 MPa. Thus, a slight increase in the maximum stress was observed. The increase in the percentage of the tensile strength of Tin interlayer Aluminum–Aluminum weld sample can be given below,

$$\text{Increase in tensile strength} = 5.2286 \text{ MPa}$$

$$\text{Increase percentage} = 17.42\%$$

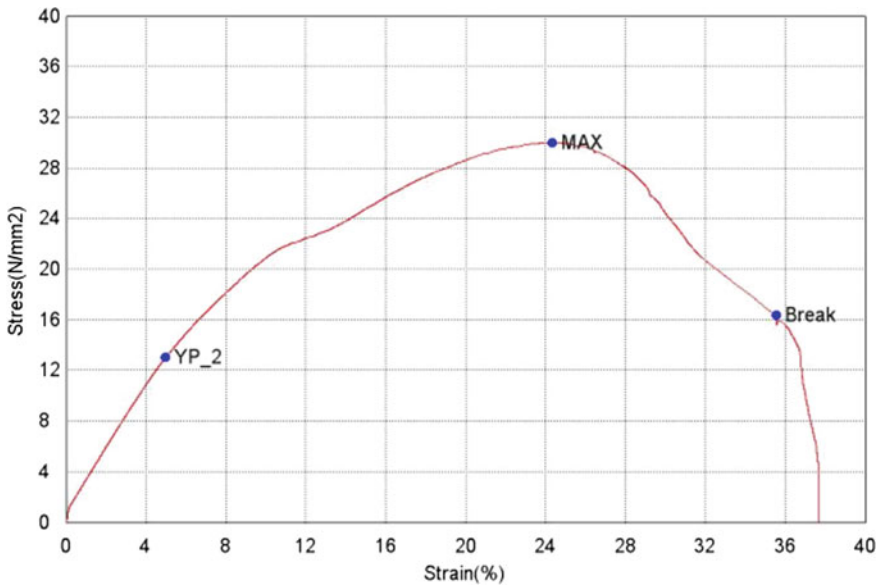
From Figs. 5 and 7, the maximum force the weld withstood before the failure can be inferred. The force values of the Tin interlayer Aluminum-Aluminum weld sample (21144 N) is quite high than the Aluminum-Aluminum weld (18006.8 N).

**Fig. 3** Tensile test orientation



**Table 3**  
Aluminum–Aluminum  
welded property

Parameter	Value	Unit
Max_Force	18006.8	N
Max_Stress	30.014	N/mm <sup>2</sup>
Max_Stroke	4.86323	mm
Max_Strain	24.3162	%
Max_Time	145.930	sec
Break_Force	9796.24	N
Break_Stress	16.3271	N/mm <sup>2</sup>
Break_Stroke	7.1123	mm
Break_Strain	35.5612	%
Yield point force	7814.34	N
Yield point stress	13.0239	N/mm <sup>2</sup>
Yield point stroke	0.99992	mm
Yield point strain	4.99958	%



**Fig. 4** Stress–strain relationship of Aluminum–Aluminum weld sample

Further, there is less displacement or the deformation of the Tin interlayer Aluminum–Aluminum weld sample (around 3 mm) compared to the control set (around 5 mm) before the failure. The tensile strength of the weld samples correlates with the hardness because higher hardness indicates improved tensile strength [15].

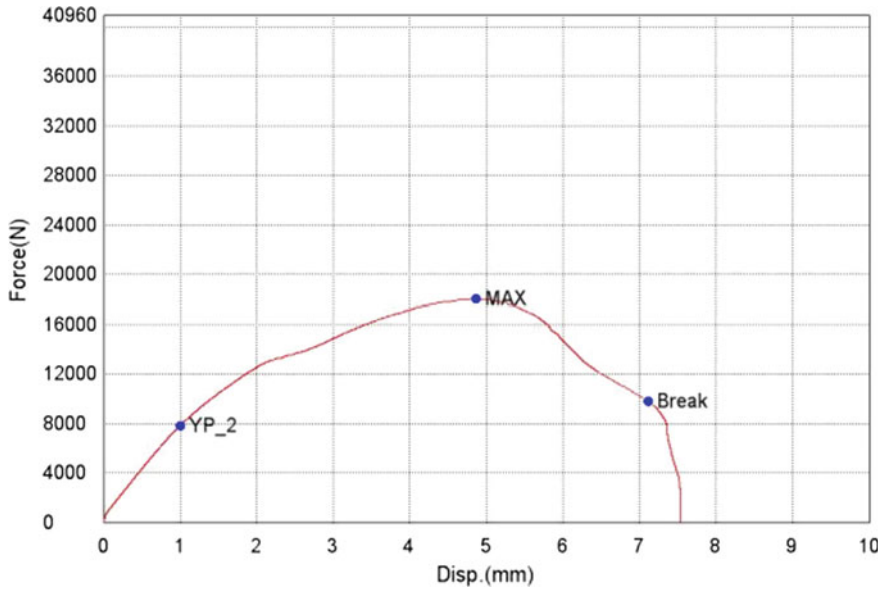


Fig. 5 Force–displacement relationship of Aluminum–Aluminum weld sample

**Table 4**  
Aluminum–Tin–Aluminum  
welded property

Parameter	Value	Unit
Max_Force	21144	N
Max_Stress	35.2400	N/mm <sup>2</sup>
Max_Stroke	3.18423	mm
Max_Strain	15.9212	%
Max_Time	95.5600	sec
Break_Force	–	N
Break_Stress	–	N/mm <sup>2</sup>
Break_Stroke	–	mm
Break_Strain	–	%
Yield point force	7715.34	N
Yield point stress	12.8589	N/mm <sup>2</sup>
Yield point stroke	0.99992	mm
Yield point strain	4.99958	%

### 3.3 Compression Test

**Aluminum–Aluminum Weld** The compression test is carried out for Aluminum–Aluminum weld specimen. The input parameters and the results are given in Tables 5 and 6. The load versus crosshead travel is depicted in Fig. 8.

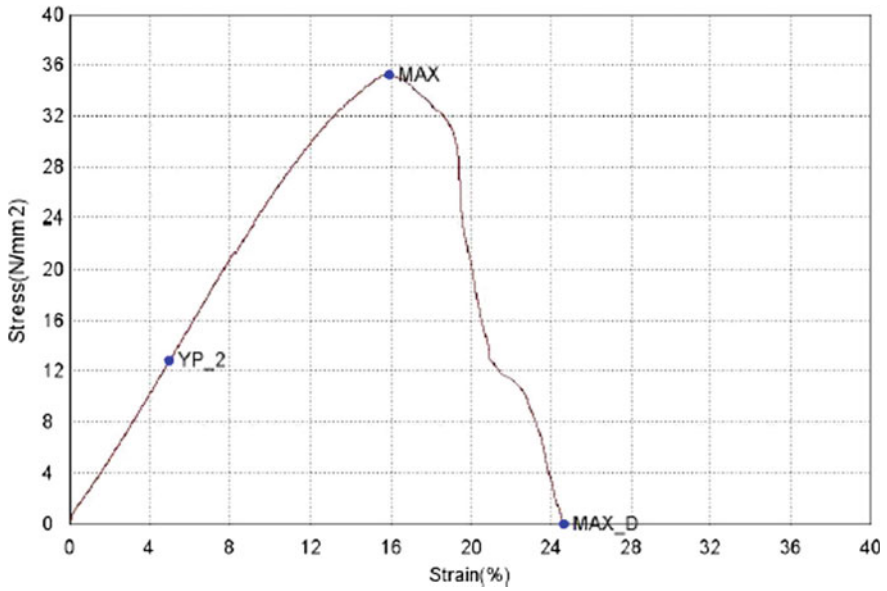


Fig. 6 Stress–strain relationship of Tin-interlayered Aluminum weld sample

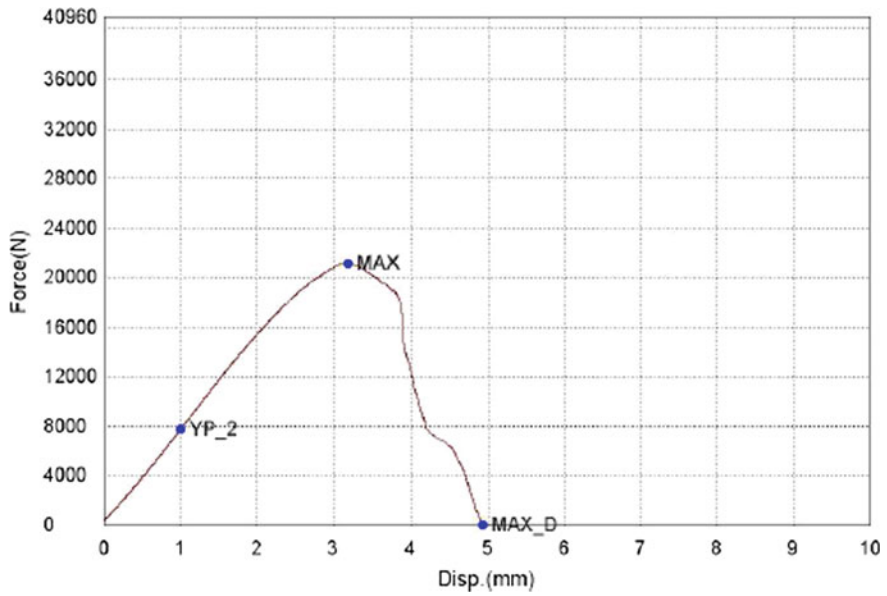


Fig. 7 Force–displacement relationship between Tin interlayer Aluminum weld sample

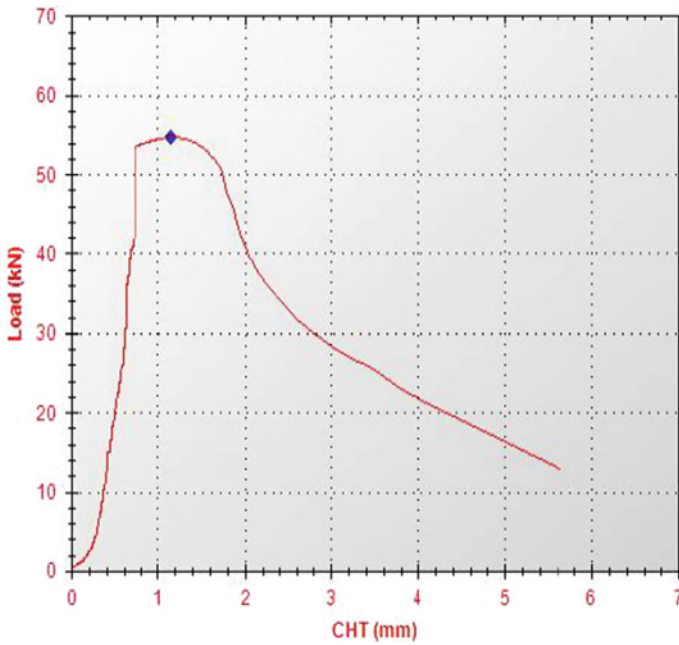


**Table 5** Input parameters for compression strength testing of Aluminum–Aluminum weld specimen

Input parameters	Values
Max load	400 kN
Max elongation	200 mm
Specimen cross-sectional area	540 mm <sup>2</sup>
Specimen width	60 mm
Specimen thickness	9 mm

**Table 6** Compressive strength of Aluminum–Aluminum weld specimen

Output parameters	Values
Load at peak	54.640 kN
Elongation at peak	1.2 mm
Compression strength	88.129 N/mm <sup>2</sup>



**Fig. 8** Load versus crosshead travel relationship of Aluminum–Aluminum weld specimen

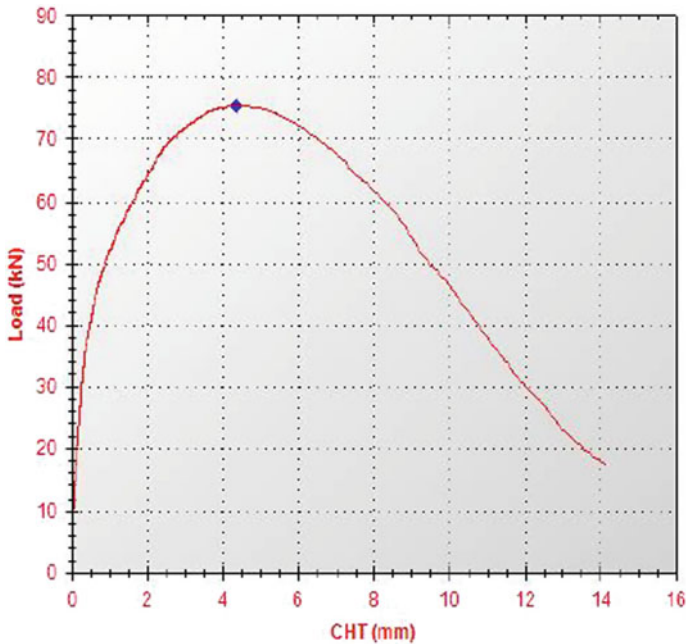
**Tin interlayer Aluminum weld** The compression test is carried out for the Tin interlayer Aluminum weld specimen. The input parameters and the results are given in Tables 7 and 8. The load versus crosshead travel is depicted in Fig. 9.

**Table 7** Input parameters for compression strength testing of Tin interlayer Aluminum weld specimen

Input parameters	Values
Max load	400 kN
Max elongation	200 mm
Specimen cross-sectional area	540 mm <sup>2</sup>
Specimen width	60 mm
Specimen thickness	9 mm

**Table 8** Compressive strength of Tin interlayer Aluminum weld specimen

Output parameters	Values
Load at peak	75.280 kN
Elongation at peak	4.520 mm
Compression strength	121.419 N/mm <sup>2</sup>



**Fig. 9** Load versus crosshead travel relationship of Tin interlayer Aluminum–Aluminum weld specimens

From the above results, the maximum compressive strength of the Aluminum–Aluminum welded sample is 88.129 N/mm<sup>2</sup> and that of Tin interlayer Aluminum–Aluminum welded sample is 121.419 N/mm<sup>2</sup>. The percentage increase in the compressive strength of the Tin interlayer Aluminum–Aluminum weld sample can be inferred below,

Increase in compression strength =  $33.29 \text{ MPa}$   
Percentage increase in compressive strength =  $37.77\%$

Further, the peak load and the deformation of the Tin interlayer Aluminum–Aluminum weld (75.280 kN, 4.520 mm) is higher than the Aluminum–Aluminum weld sample (54.640 kN, 1.2 mm). This corroborates to the increased brittleness of Tin interlayer Aluminum–Aluminum weld sample.

## 4 Conclusion

Friction stir welding was carried out on two sets with the above-given parameters. First, two Aluminum billets were welded together which acts as a control set, and other pair of Aluminum billets were welded along with the Tin interlayer. Rockwell hardness test, tensile test, and compressive test were executed on the samples. The hardness of the Tin interlayer Aluminum–Aluminum weld sample near the weld zone is higher than that of the Aluminum–Aluminum weld sample. Further, from the tensile test, it was observed that the deformation of the Tin interlayer Aluminum–Aluminum weld before the failure is less than the control set. The increased hardness and the reduced deformation of the Tin interlayer Aluminum–Aluminum weld sample could attribute to the increase in the brittleness of the material. The increase in the strength of the Tin interlayer Aluminum–Aluminum weld sample was around 17.42%. Further, the Tin interlayer Aluminum–Aluminum weld sample was able to withstand a more compressive load than the control set which signifies the improved brittleness of the Tin interlayer Aluminum–Aluminum weld sample. The improvement in the compressive strength was around 37.77%. Thus, it can be concluded that using an interlayer of the Tin sheet between Aluminum billets could improve the tensile properties of the weld and also increase hardness of the material near the weld. However, this process can increase brittleness of the material and would increase susceptibility for cracking. Future studies should be carried out on visualizing the microstructure weld zone through scanning electron microscope (SEM) and X-ray diffraction (XRD) which could provide more information about the reason for the increase in the brittleness of the Tin interlayer Aluminum–Aluminum weld compared to the conventional Aluminum–Aluminum weld.

## References

1. Royal Society of Chemistry. <https://www.rsc.org/periodic-table/element/13/Aluminum>
2. Chowdhury SH, Chen DL, Bhole SD, Cao X, Wanjara P (2013) Lap shear strength and fatigue behavior of friction stir spot welded dissimilar magnesium-to-Aluminum joints with adhesive. Mater Sci Eng, A 562:53–60. <https://doi.org/10.1016/j.msea.2012.11.039>

3. Panaskar N, Terkar R (2016) A review on recent advances in friction stir lap welding of aluminum and copper. In: International conference on advancements in aeromechanical materials for manufacturing (ICAAMM-2016), Hyderabad, pp 8387–8393. <https://doi.org/10.1016/j.matpr.2017.07.182>
4. Cavaliere P, Nobile R, Panella FW, Squillace A (2006) Mechanical and microstructural behavior of 2024–7075 Aluminum alloy sheets joined by friction stir welding. *Int J Mach Tools Manuf* 46(6):588–599. <https://doi.org/10.1016/j.ijmactools.2005.07.010>
5. Hong S-T, Das H, Oh H-S, Alam Al Nasim MNE, Chun D-M (2017) Combination of nano-particle deposition system and friction stir spot welding for fabrication of carbon/Aluminum metal matrix composite joints of dissimilar Aluminum alloys. *CIRP Ann* 66(1):261–264. <https://doi.org/10.1016/j.cirp.2017.04.115>
6. Azo materials. <https://www.azom.com/article.aspx?ArticleID=9120>
7. Moreira PMGP, Oliveira FMF, Castro PMST (2008) Fatigue behaviour of notched specimens of friction stir welded Aluminum alloy 6063-T6. *J Mater Process Technol* 207(1–3):283–292. <https://doi.org/10.1016/j.jmatprotec.2007.12.113>
8. Akbari M, Bahemmat P, Haghpanahi M, Besharati Givi M-K (2013) Enhancing metallurgical and mechanical properties of friction stir lap welding of Al–Cu using intermediate layer. *Sci Technol Weld Joining* 18(6):518–524. <https://doi.org/10.1179/1362171813Y.0000000130>
9. Cheepu MM, Muthupandi V, Katakam S (2014) The influence of aluminium intermediate layer in dissimilar friction welds. *Int J Mater Res* 105(4):350–357. <https://doi.org/10.3139/146.111031>
10. Kar A, Choudhury SK, Suwas S, Kailas SV (2018) Effect of niobium interlayer in dissimilar friction stir welding of aluminum to titanium. *Mater Charact* 14:402–412. <https://doi.org/10.1016/j.matchar.2018.09.007>
11. Saputra LA, Nurul Muhayat T (2018) Effect of Zn interlayer particles on mechanical properties and microstructure of friction stir spot welding aluminum alloy. In: The 1st international conference on industrial, electrical and electronics (ICIEE 2018), Anyer, Indonesia. <https://doi.org/10.1051/mateconf/201821804005>
12. Kar A, Kailas SV, Suwas S (2018) Effect of zinc interlayer in microstructure evolution and mechanical properties in dissimilar friction stir welding of aluminum to titanium. *J Mater Eng Perform* 27:6016–6026. <https://doi.org/10.1007/s11665-018-3697-8>
13. Niu S, Ji S, Yan D, Meng X, Xiong X (2019) AZ31B/7075-T6 alloys friction stir lap welding with a zinc interlayer. *J Mater Process Technol* 263:82–90. <https://doi.org/10.1016/j.jmatprotec.2018.08.009>
14. Liu L, Ren D, Liu F (2014) A review of dissimilar welding techniques for magnesium alloys to aluminum alloys. *Materials* 7(5):3735–3757. <https://doi.org/10.3390/ma7053735>
15. Callister WD Jr, Rethwisch DG (2010) *Materials science and engineering: an introduction*, 8th edn. Wiley, USA

# Effect of Heat Treatment on Wear and Corrosion Behavior of Electroless Ni–P–TiO<sub>2</sub>–Al<sub>2</sub>O<sub>3</sub> Nanocomposite Coatings on Magnesium AZ91D Alloy



V. Krishnakumar and R. Elansezhian

**Abstract** The effect of electroless Ni–P–TiO<sub>2</sub>–Al<sub>2</sub>O<sub>3</sub> nanocomposite coatings on AZ91D magnesium alloys was investigated in this study. Nickel phosphorus (Ni–P) was deposited on nano-TiO<sub>2</sub> and Al<sub>2</sub>O<sub>3</sub> alloys at various concentrations (0.5–0.5), (1–1), (1.5–1.5), (2–2) g/L using electroless coating. The coated samples were heat-treated at 450 °C for 1 h. The heat-treated nanocomposite deposit on the surface properties of the alloy was characterized by an optical microscope (OM), a scanning electron microscopy (SEM), an energy-dispersive X-ray dispersion (EDS). The rate of wear and corrosion was calculated by pin-on-disc and salt spraying equipment. The findings indicate that improved microhardness (623 VHN<sub>100</sub>), low friction coefficient (0.22), and high wear resistance at a low specific wear rate of  $1.4693 \times 10^{-5}$  mm<sup>3</sup>/Nm at an optimal concentration (1.5–1.5) g/L of nanoparticles. Similarly, the corrosion rate at (1.5–1.5) g/L was the lowest 0.000286 MPY compared to other heat-treated nano co-deposits. This improvement in microhardness, wear resistance, and corrosion resistance is substantially dependent on the addition of nanoparticles and heat treatment. However, also after heat treatment, the findings demonstrated a converse pattern when nanoparticle concentrations exceeded the optimal concentration (1.5–1.5) g/L due to agglomeration.

**Keywords** Electroless · Nanocomposite coatings · Heat treatment · Wear rate · Corrosion rate · SEM · EDAX

## 1 Introduction

Magnesium's unique properties make it the ideal option for many applications with ultra-light low-density and cost-effective competition with other lightweight magnesium materials, especially in transport and manual handling, and a simple choice for use in the aerospace industry, high-performance cars have long-used magnesium to boost their performance. Standard automotive steel makes up about 65% of its parts.

---

V. Krishnakumar (✉) · R. Elansezhian  
Department of Mechanical Engineering, Pondicherry Engineering College, Puducherry, India  
e-mail: [krishbio.kumar@gmail.com](mailto:krishbio.kumar@gmail.com)

It is vital for safety, but reducing the overall vehicle weight can improve its fuel efficiency if magnesium alloys are both robust and lightweight. Magnesium alloys are also used in aerospace aircraft helicopter missiles all have magnesium alloy components, so the most significant benefit to magnesium alloys is that they are lightweight. The application of magnesium in the automotive industry is based on weight limitation, and the reduction of magnesium alloys is very light and robust. It has high thermal radiation properties, as well. The magnesium alloy is, therefore, suitable for use in automotive and aircraft components with high-temperature magnesium alloys, pressure tightness, and the ability to produce complex shapes. Magnesium with versatile creeps resistant properties and physical properties that enable us to do extraordinary things [1–8]. However, magnesium was prohibitive because many people were worried about the corrosion and flammability associated with it [9–12].

Nickel coating (EN) is a process of chemical reduction based on the process of chemical reduction of nickel ions and the subsequent insertion of nickel metal without electrical energy. This process is widely used in materials such as valves and pipe components because of its outstanding corrosion resistance and high hardness. A right adhesive and excellent service performance can be achieved at EN with a wide range of submarine and external steels with a correct pre-adjustment sequence and precise process control [13, 14]. Nanocomposite coatings are formed by confining two types of particles, one of which is hard and the other is soft particles to the electroless Ni–P matrix [15]. Wear resistance and longevity of the Ni–P–Al<sub>2</sub>O<sub>3</sub> deposits with the co-deposition of Al<sub>2</sub>O<sub>3</sub> and heat treatment of 400 °C are due to the formation of the Ni<sub>3</sub>P process [16]. The hardness of the nanocomposites embedded with the concentration of aluminum particles is a result critical the temperature rise [17]. The temperature helps to improve the structure and adherence of the first nodular smooth surface morphology. The improvement of wear resistance of the Ni–P composite coatings is preferably more than 350 °C, due to its composition, resilience, crystalline nickel hardening, and phosphides, and solid particle size enhancement [18]. Aluminum particle trapping in the Ni–P matrix of Ni–P–Al<sub>2</sub>O<sub>3</sub> enhances the composite coating endurance, resulting in abrasive wear. Due to the amount of non-coherent precipitates, the temperature is transformed into a semi-coherent Ni<sub>3</sub>P, which increases wear resistance and hardness. Heating up to 500 °C will increase the lifespan of Ni–P by 1 h, but additional heating is limited by grain softening and thickening [19].

Although few researchers have reported nanocomposite coatings on magnesium alloys, they were limited to ternary composite coatings only. Quaternary nanocomposite coatings on magnesium alloy have not been reported. Furthermore, the effect of heat treatment on the quaternary composite coatings has not been studied. The purpose of our research was, therefore, to extend the nanocomposite coatings from ternary coating to quaternary coatings and study the effect of heat treatment on coatings. For this reason, using electroless coating, Ni–P–TiO<sub>2</sub>–Al<sub>2</sub>O<sub>3</sub> nanocomposite coatings were deposited at different concentrations on magnesium alloy and heat-treated to examine surface morphology, microhardness wear, and corrosion behavior of the coatings.

**Table 1** Composition of bath

Material considerations	Chemical composition (g/L)
NiSO <sub>4</sub> (nickel Sulfate)	35
NaPO <sub>2</sub> H <sub>2</sub> (sodium hypophosphate)	30
Na <sub>3</sub> C <sub>6</sub> H <sub>5</sub> O <sub>7</sub> (tri-sodium citrate)	45
NH <sub>4</sub> Cl (ammonia chloride)	50

## 2 Experiment

### 2.1 Coating Procedure

Magnesium AZ91D alloy (30 × 20 × 20 mm) was used as a base material, while TiO<sub>2</sub> and Al<sub>2</sub>O<sub>3</sub> reinforcements were used. Different quantities of TiO<sub>2</sub> and Al<sub>2</sub>O<sub>3</sub> of 100 nm particle size at various concentrations (0.5–0.5), (1–1), (1.5–1.5), (2–2) g/L were co-deposited using the electroless process with the base matrix material. Before coating, magnesium AZ91D alloy substrates were pre-treated for 60 min at 25 °C to ensure that they were free of contamination, allowing the base surface to act as a better deposition catalyst. For this purpose, magnesium alloys AZ91D were treated with acetone and then with methanol to remove impurities in the alloy. Magnesium substrate was activated with hydrogen fluoride to improve the adhesion of the substrate, the Ni–P matrix, and the reinforcement particles. For the coating process, the electrolyte bath was heated by a water bath. The composition of the bath is selected following the procedure followed by our earlier works [20–22], as shown in Table 1. Bath pH was adjusted to 8.0 by adding an adequate amount of ammonia solution, and the required chemical was continuously stirred at 400 rpm using a magnetic stirrer for 5 min. Magnesium AZ91D alloys and reinforcements were immersed in a 90° furnace bath for deposition. For all the different concentrations of nanomaterials, the composition and the same process were repeated. The coated samples were then heated to 450 °C for 1 h using a muffle furnace. In the end, after heating, the substrate was removed from the furnace and tested.

### 2.2 Characterization Details

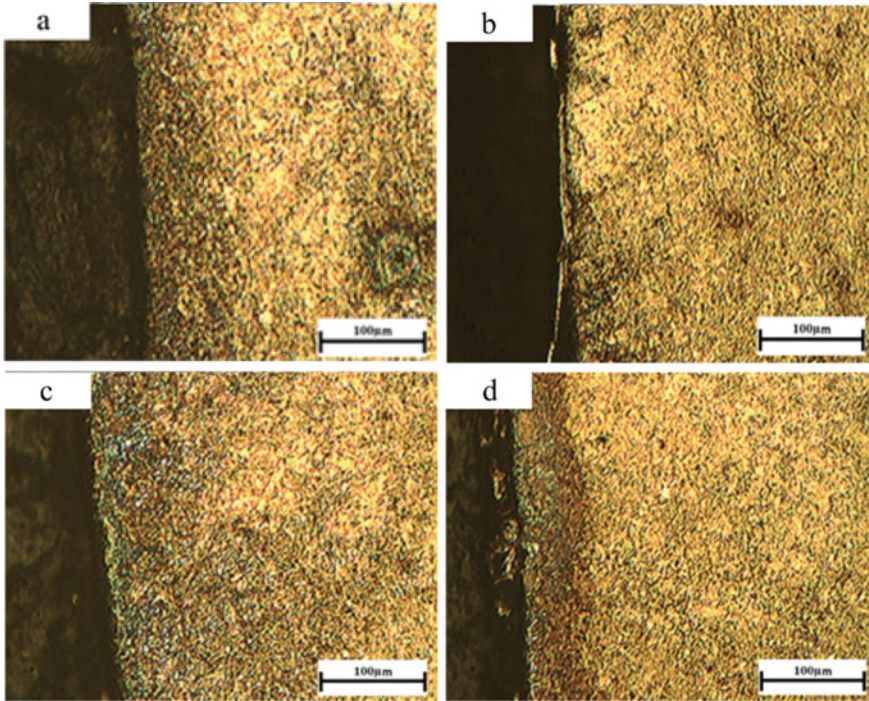
The rate of wear was calculated using a pin-on-disc device. The sample is cleaned, machined to the standard according to the procedure followed by each sample size (length: 30 mm; diameter: 1 mm, Fig. 5). The initial sample weight is calculated using an electronic weighing machine. The sliding wear test was performed with a 10 N load with a sliding speed of 5 m/s and a sliding distance of 2000 m for a continuous period of 10 min. Upon completion of the wear tests, worn surfaces of the

substrates were analyzed for wear characteristics. The worn surface was then debris micrographed using a scanning electron microscope (SEM) to examine the wear characteristics. Scanning electron microscope images of worn areas were obtained at 100X magnification with a working distance of 100  $\mu\text{m}$  and a voltage of 15 kV. The samples were tested for corrosion in the salt spray chamber. The device consists of a salt solution tank, a fog chamber, an air supply correctly compressed, and one or more nozzles. The solution of salt was achieved by weight dissolving five sodium chloride sections of the water solution in ninety-five portions. The exposure area of the salt spray chamber is maintained at 25  $^{\circ}\text{C}$ . To ensure proper humidification, the water solution level must be maintained automatically. Each sample was taken (30  $\times$  20  $\times$  20 mm) and placed in the salt spray chamber for 100 h. During the test, the sample weight is determined both first and last. The cross section of the substrate deposits was observed using an optical microscope. Surface morphology and elemental analysis were performed using a field emission scanning electron microscope (FESEM) aided by energy-dispersive X-ray analysis (EDAX). The composite coating process was established using X-ray diffraction (XRD).

### 3 Result and Discussion

The optical microscope (OM) indicates that nanocomposite coatings were deposited, and almost all compositions apart from (2–2) g/L were confirmed with uniform deposition (Fig. 1). The optical microscope image shows coated deposits with a thickness of approximately 10  $\mu\text{m}$ . Energy-dispersive analysis of X-rays detects the presence of various concentrations of nano  $\text{TiO}_2$  and  $\text{Al}_2\text{O}_3$  in the composite coatings (Fig. 3). Table 2 lists the different materials and their oxides present in the coating. For (0.5–1.5), (1–1), (2–2), (0.5–0.5) g/L respectively, nickel was observed to have a maximum weight of 91.26, 93.45, 93.84, and 93.92 wt% for percentage minutes of the coating. Combined  $\text{TiO}_2$ – $\text{Al}_2\text{O}_3$  percentage presence was observed with maximum weight percentages of 7.56, 6.12, and 5.92 and 5.28. A scanning electron microscope was used to examine deposits of surface layers at various concentrations. The  $\text{TiO}_2$ – $\text{Al}_2\text{O}_3$  concentrations of (1.5–1.5) g/L are high, compact, and uniformly distributed compared to other compositions. Also, the coating adherence to the surface layer is excellent (Fig. 2a), and Fig. 2d indicates a rough and irregular surface due to severe agglomeration at (2–2) g/L. Figure 4 shows the XRD patterns of Ni–P coating with  $\text{TiO}_2$ – $\text{Al}_2\text{O}_3$  concentrations heat-treated at 450  $^{\circ}\text{C}$  for 1 h. Amorphous Ni–P broad peaks were achieved without heat treatment. The  $\text{Ni}_3\text{P}$  phase was acquired at a temperature of 450  $^{\circ}\text{C}$  with the highest peak intensity. A mix of polycrystalline phases was produced by this heat treatment.





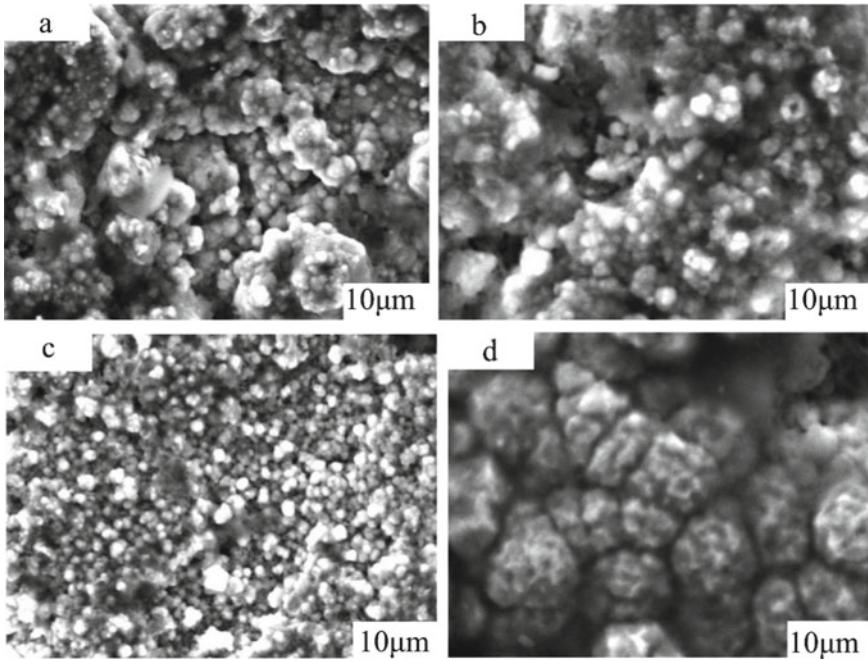
**Fig. 1** Cross-sectional OM image of different  $TiO_2-Al_2O_3$  concentrations heat-treated at  $450\text{ }^\circ C$ ; **a** (0.5–0.5), **b** (1–1), **c** (1.5–1.5), **d** (2–2) g/L

**Table 2** EDAX for coating composition of deposits

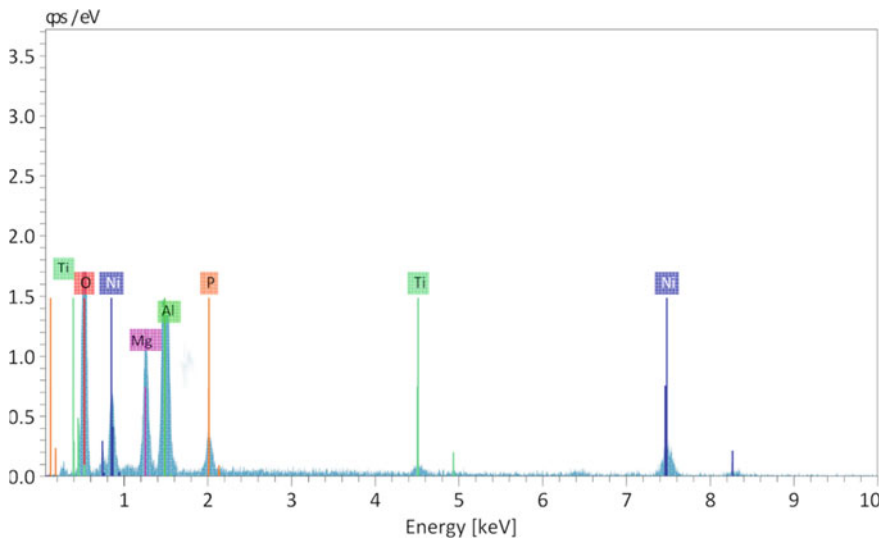
At different $TiO_2-Al_2O_3$ concentrations (g/L)	Combined $TiO_2-Al_2O_3$ percentage		Nickel	
	Wt. in percentage	Atom in percentage	Wt. in percentage	Atom in percentage
(1.5–1.5)	7.56	14.21	91.26	87.62
(1–1)	6.12	13.62	93.45	88.53
(2–2)	5.92	12.36	93.84	88.78
(0.5–0.5)	5.28	11.45	93.92	89.23

### 3.1 COF, Wear Rate, and Microhardness

Wear analysis was performed with the same load for different with  $TiO_2-Al_2O_3$  concentrations heat-treated at  $450\text{ }^\circ C$  for 1 h. Figures 7 and 8 show the impact on wear and COF values of the same load conditions of Ni–P nanocomposites combined with various concentrations of  $TiO_2-Al_2O_3$ . The wear rate of the composites can be seen to decrease with increased  $TiO_2-Al_2O_3$  content in the Ni–P matrix. At (1.5–1.5) g/L, low friction coefficient (0.22) and a low specific wear rate of  $1.4693 \times 10^5$



**Fig. 2** SEM of different  $\text{TiO}_2\text{-Al}_2\text{O}_3$  concentrations heat-treated at  $450^\circ\text{C}$ ; **a** (0.5–0.5), **b** (1–1), **c** (1.5–1.5), **d** (2–2) g/L



**Fig. 3** EDAX image of  $\text{TiO}_2\text{-Al}_2\text{O}_3$  at (1.5–1.5) concentrations heat-treated at  $450^\circ\text{C}$

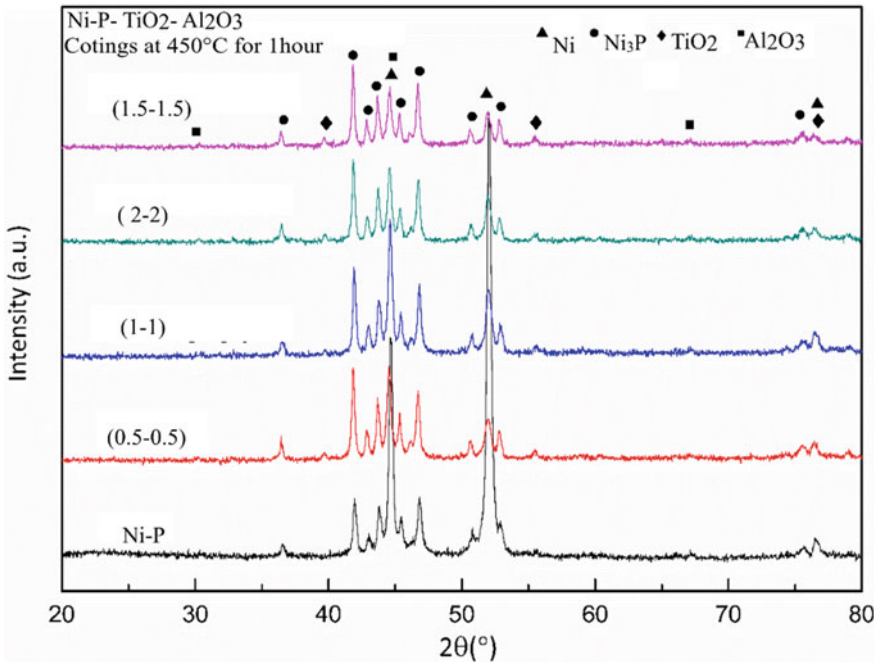
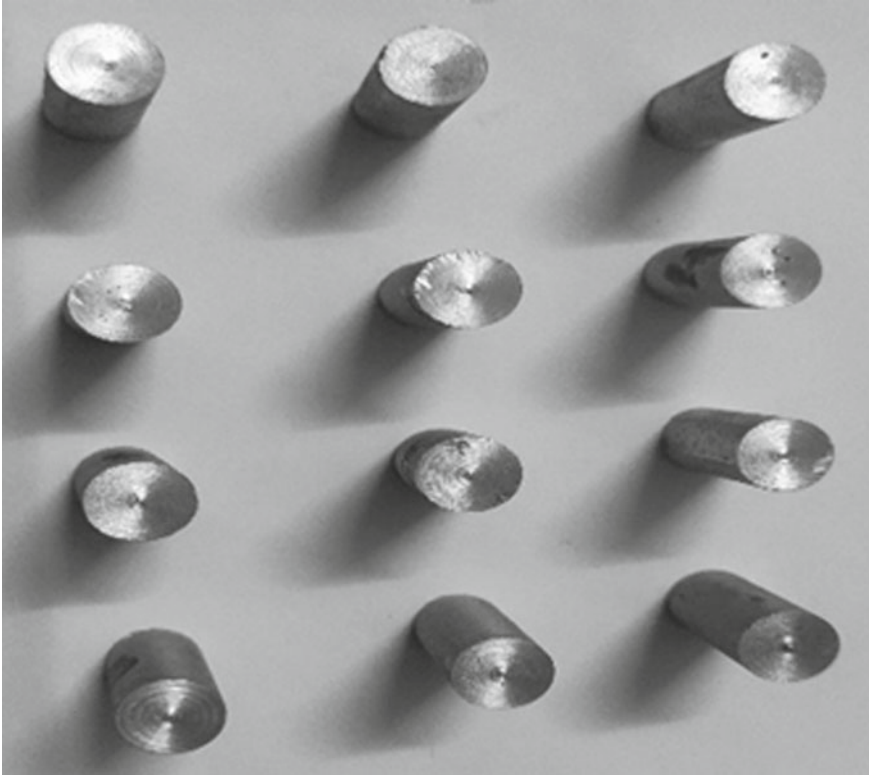


Fig. 4 XRD of different  $\text{TiO}_2\text{-Al}_2\text{O}_3$  concentrations heat-treated at 450 °C for 1 h

$\text{mm}^3/\text{Nm}$  were observed. The heat treatment transformed the amorphous Ni-P matrix into a stable nanocrystalline  $\text{Ni}_3\text{P}$  phase with  $\text{TiO}_2\text{-Al}_2\text{O}_3$  particles. The transition in the crystallinity phase from the amorphous phase was supposed to lead to a reduced rate of wear. Additionally, this improved reduced wear and COF could be due to a low phosphorous fraction in the Ni-P. At (1.5–1.5) g/L, the composite microhardness (623  $\text{VHN}_{100}$ ) was the maximum because of the formation of a strong inter-diffusion layer on the substrate/coating and hard nanocrystalline  $\text{Ni}_3\text{P}$  precipitate after heating (Fig. 6). Heat treatment and uniform distribution of nano- $\text{TiO}_2\text{-Al}_2\text{O}_3$  prevent plastic deformation that helps reduce the wear of composites. Magnesium substrate coated at a concentration of (0.5–0.5), (1–1) g/L possessed a lower rate of wear and hardness compared to the other two coatings due to fragile interfacial bonding between the substrate and agglomeration of nano- $\text{TiO}_2\text{-Al}_2\text{O}_3$ .

### 3.2 Wear Track Morphology of the Composite

The wear tracks were analyzed using an electron scanning microscope after the specimen was tested for wear. Figure 9 shows the pattern of wear on the nanocomposite coatings containing grooves. Figure 9d shows at (1.5–1.5) g/L, the wear debris



**Fig. 5** Machined samples after solidification for wear analysis

grooves were much lower than different compositions, and this is due to the uniform and seamless distribution of  $\text{TiO}_2$  and  $\text{Al}_2\text{O}_3$  in the nickel-phosphorus matrix. There is a substantial increase in wear resistance to the application of nanoparticles, enabled by the delay in cracking the wear surfaces. Also, heat treatment resulted in a strong interfacial bond between the matrix and reinforcement that reduced the wear debris. It was also found that post-heat treatment transforms the coating to a crystalline form that increases corrosion resistance. Therefore, the composite deposit wear tracks decrease with the increasing percentage of  $\text{TiO}_2$  and  $\text{Al}_2\text{O}_3$  reinforcements and heat treatment. However, at (2–2) g/L, even after heat treatment, severe damage to coatings due to reduced hardness adhesion was observed; this shows rigorous adhesive wear owing to nano-agglomeration.

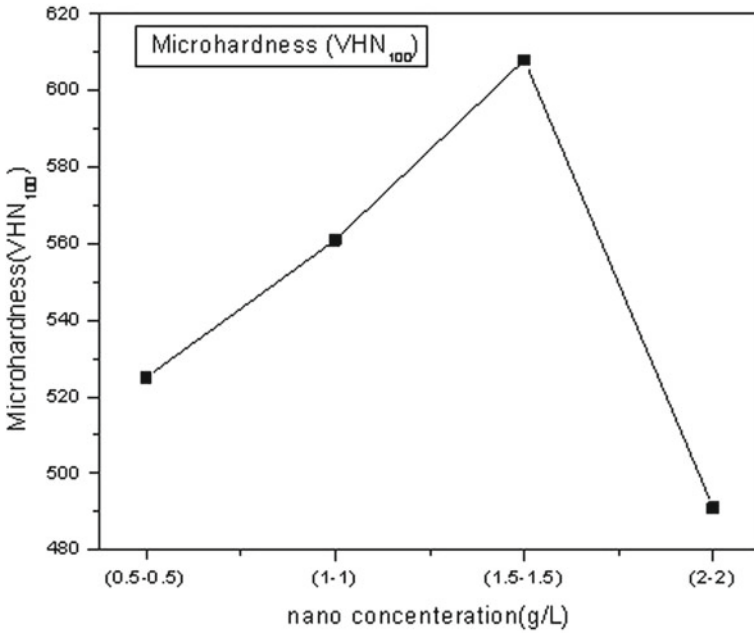


Fig. 6 Microhardness of different TiO<sub>2</sub>-Al<sub>2</sub>O<sub>3</sub> concentrations heat-treated at 450 °C

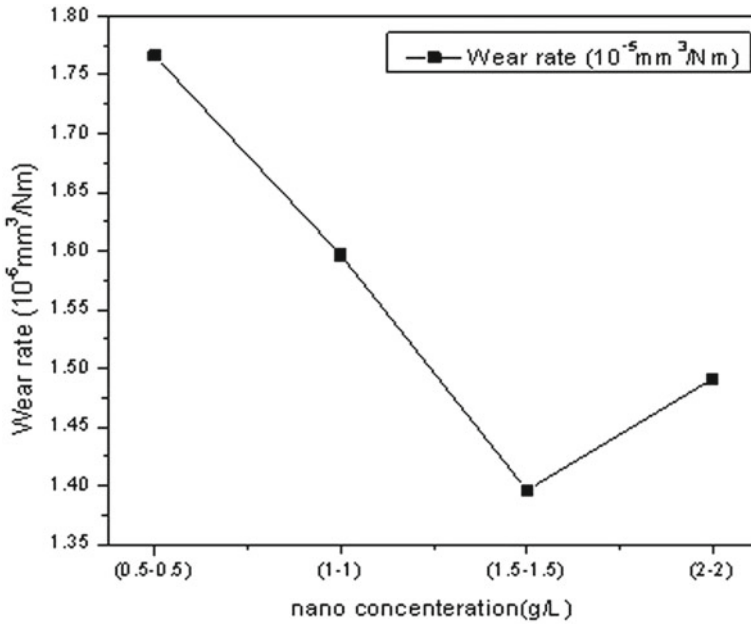
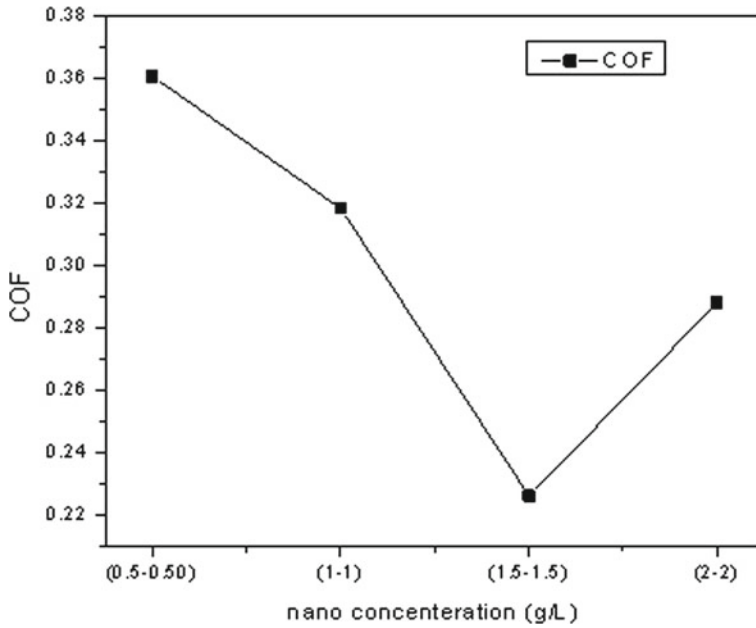
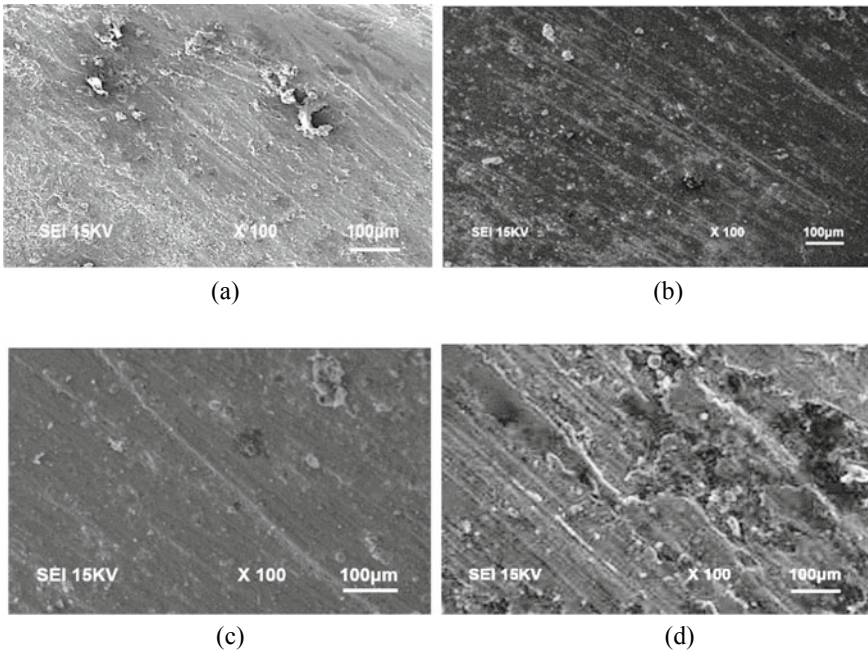


Fig. 7 Wear rate of different TiO<sub>2</sub>-Al<sub>2</sub>O<sub>3</sub> concentrations heat-treated at 450 °C

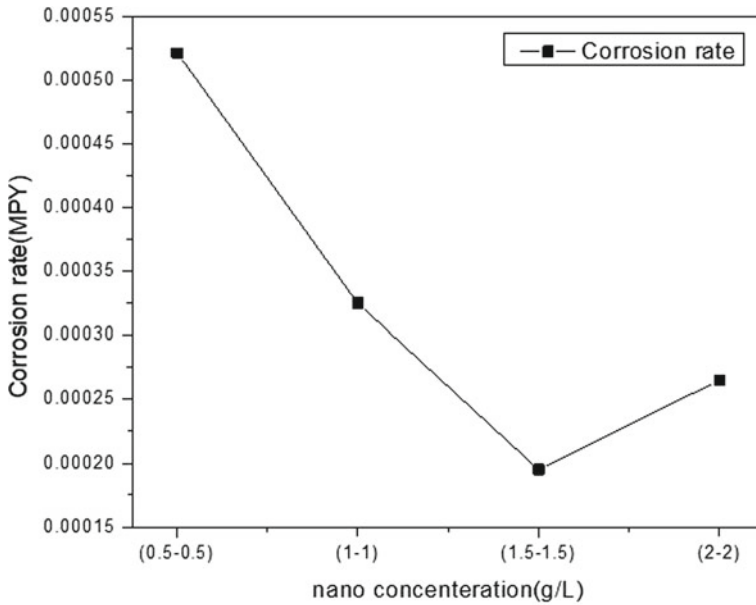




**Fig. 8** COF of different  $\text{TiO}_2\text{-Al}_2\text{O}_3$  concentrations heat-treated at  $450^\circ\text{C}$



**Fig. 9** Wear track SEM of different  $\text{TiO}_2\text{-Al}_2\text{O}_3$  concentrations heat-treated at  $450^\circ\text{C}$ ; **a** (0.5–0.5), **b** (1–1), **c** (1.5–1.5), **d** (2–2) g/L



**Fig. 10** Corrosion rate of different  $\text{TiO}_2\text{-Al}_2\text{O}_3$  concentrations heat-treated at  $450^\circ\text{C}$

### 3.3 Corrosion Test

Figure 10 shows the corrosion rate of different nanocomposites coatings at different  $\text{TiO}_2\text{-Al}_2\text{O}_3$  concentrations heat-treated at  $450^\circ\text{C}$ . At  $(1.5\text{-}1.5)$  g/L, the corrosion rate was at least  $(0.000286)$  MPY comparisons to other heat-treated nanocoatings. This lowest corrosion rate is attributed to proper post-heat bonding of the Ni-P matrix with reinforcement considerably improved coverage density, leading to increased corrosion resistance. It was also found to increase the P content of post-heat-treatment, transforming the coatings into a crystalline structure that increases corrosion resistance. Furthermore, the uniform distribution of nano- $\text{TiO}_2\text{-Al}_2\text{O}_3$  over the metal magnesium substrate reduced the contact area of the alloy exposure to the environment. At the same time, at  $(2\text{-}2)$  g/L, the loss of corrosion due to nano-coatings is observed cracking and delamination, which in turn increases metal exposure to the atmosphere and thus leads to corrosion. In addition, the agglomeration of nanomaterials at  $(2\text{-}2)$  g/L results in a decrease in corrosion resistance due to irregular deposits on the surface of the substrate

## 4 Conclusion

Using electroless coating, Ni–P–TiO<sub>2</sub>–Al<sub>2</sub>O<sub>3</sub> nanocomposite coatings were deposited on magnesium alloy particles at various concentrations (0.5–0.5), (1–1), (1.5–1.5), (2–2) g/L and were heat-treated at 450 °C for 1 h. The experiment showed the following results:

- (1) Increased microhardness (623 VHN100), low friction coefficient (0.22), and high wear resistance at a low specific wear rate of  $1.4693 \times 10^{-5} \text{ mm}^3/\text{Nm}$  at an optimum concentration (1.5–1.5) g/L of nanoparticles due to heat treatment that transformed the amorphous Ni–P matrix into a stable nanocrystalline Ni<sub>3</sub>P phase with TiO<sub>2</sub>–Al<sub>2</sub>O<sub>3</sub> particles.
- (2) The corrosion rate at a concentration of (1.5–1.5) g/L showed the lowest rate of 0.000286 MPY comparisons with other heat-treated nanocoatings as a result of heat treatment, transforming the coatings into a crystalline structure that increased corrosion resistance.

**Acknowledgements** The authors acknowledge the infrastructure and support provided by the Mechanical Department, Pondicherry Engineering College (PEC), Puducherry, and B. S. Abdur Rahman Crescent Institute of Science and Technology, Chennai.

## References

1. Ramalingam VV, Ramasamy P, Kovukkal MD, Myilsamy G (2019) Research and development in magnesium alloys for industrial and biomedical applications: a review. *Metals Mater Int* 1–22
2. Mordike BL, Ebert T (2001) Magnesium: properties—applications—potential. *Mater Sci Eng A* 302(1):37–45
3. Easton M, Beer A, Barnett M, Davies C, Dunlop G, Durandet Y et al (2008) Magnesium alloy applications in automotive structures. *Jom* 60(11):57
4. Mehta DS, Masood SH, Song WQ (2004) Investigation of wear properties of magnesium and aluminum alloys for automotive applications. *J Mater Process Technol* 155:1526–1531
5. Kulekci MK (2008) Magnesium and its alloys applications in automotive industry. *Int J Adv Manuf Technol* 39(9–10):851–865
6. Pegguleryuz MO, Kaya AA (2003) Creep resistant magnesium alloys for powertrain applications. *Adv Eng Mater* 5(12):866–878
7. Rambabu PPNKV, Prasad NE, Kutumbarao VV, Wanhill RJH (2017) Aluminium alloys for aerospace applications. In: *Aerospace materials and material technologies*. Springer, Singapore, pp. 29–52
8. Furuya H, Kogiso N, Matunaga S, Senda K (2000) Applications of magnesium alloys for aerospace structure systems. In: *Materials science forum*, vol 350. Trans Tech Publications Ltd., pp 341–348
9. Esmaily M, Svensson JE, Fajardo S, Birbilis N, Frankel GS, Virtanen S et al (2017) Fundamentals and advances in magnesium alloy corrosion. *Prog Mater Sci* 89:92–193
10. Ambat R, Aung NN, Zhou W (2000) Evaluation of microstructural effects on corrosion behaviour of AZ91D magnesium alloy. *Corros Sci* 42(8):1433–1455



11. Alvarez-Lopez M, Pereda MD, Del Valle JA, Fernandez-Lorenzo M, Garcia-Alonso MC, Ruano OA, Escudero ML (2010) Corrosion behaviour of AZ31 magnesium alloy with different grain sizes in simulated biological fluids. *Acta Biomater* 6(5):1763–1771
12. Song G, Bowles AL, StJohn DH (2004) Corrosion resistance of aged die cast magnesium alloy AZ91D. *Mater Sci Eng, A* 366(1):74–86
13. Mallory GO, Hajdu JB (eds) (1990) *Electroless plating: fundamentals and applications*. Cambridge University Press
14. Loto C (2016) A electroless nickel plating—a review. *Silicon* 8(2):177–186
15. Sudagar J, Lian J, Sha W (2013) Electroless nickel, alloy, composite and nano coatings—a critical review. *J Alloy Compd* 571:183–204
16. Novak M, Vojtěch D, Vítů T (2010) Influence of heat treatment on tribological properties of electroless Ni–P and Ni–P–Al<sub>2</sub>O<sub>3</sub> coatings on Al–Si casting alloy. *Appl Surf Sci* 256(9):2956–2960
17. Shrestha NK, Hamal DB, Saji T (2004) Composite plating of Ni–P–Al<sub>2</sub>O<sub>3</sub> in two steps and its anti-wear performance. *Surf Coat Technol* 183(2–3):247–253
18. Oguocha INA, Taheri R, Yannacopoulos S, Uju WA, Sammynaiken R, Wettig S, Hu YF (2010) Temperature effects on the chemical composition of nickel–phosphorus alloy thin films. *Thin Solid Films* 518(8):2045–2049
19. Alirezai S, Monirvaghefi SM, Salehi M, Saatchi A (2007) Wear behavior of Ni–P and Ni–P–Al<sub>2</sub>O<sub>3</sub> electroless coatings. *Wear* 262(7–8):978–985
20. Krishnakumar V, Elansezhian R (2020) Wear and corrosion resistance of electroless Ni-P-ZnO-SiO<sub>2</sub> nanocomposite coatings on magnesium AZ91D alloy. In: AIP conference proceedings, vol 2235, no 1. AIP Publishing LLC, p 020001
21. Elansezhian R, Ramamoorthy B, Nair PK (2009) The influence of SDS and CTAB surfactants on the surface morphology and surface topography of electroless Ni–P deposits. *J Mater Process Technol* 209(1):233–240
22. Elansezhian R, Ramamoorthy B, Nair PK (2008) Effect of surfactants on the mechanical properties of electroless (Ni–P) coating. *Surf Coat Technol* 203(5–7):709–712

# Study of Varying Weight%, Particle Size and Artificial Aging of Al<sub>2</sub>O<sub>3</sub> on the Hardness and Wear Resistance of Al 6082 Alloy Composites by Stir Casting



N. Sirajudeen, R. Karunanithi, and M. Abdur Rahman

**Abstract** In this study, the effect of artificial aging, particle size, different weight fractions (1, 1.5, 2, and 2.5%) of Al<sub>2</sub>O<sub>3</sub> on the hardness and wear resistance of Al 6082 alloy composite produced by stir casting method is studied. Al 6082 alloy composite specimens strengthened individually with Al<sub>2</sub>O<sub>3</sub> particles of 45 μm and 40–50 nm were produced by stir casting method. The composite specimens were first solutionized followed by artificial aging at 180 °C for various time periods (1, 2, 4, 6, 8, 10, 12, 14, 16, 18 and 20 h). The hardness and wear tests were performed on the heat-treated and non-heat-treated specimens. Vickers microhardness tests demonstrated a tremendous improvement in the composites' VHN values due to artificial aging and the addition of varying wt% of micron/nano-sized Al<sub>2</sub>O<sub>3</sub> reinforcement. The T6-treated Al 6082 alloy composite specimens reinforced with nano-Al<sub>2</sub>O<sub>3</sub> particles showed an enhancement in VHN microhardness and wear resistance when compared to the pure Al 6082 alloy and composite specimens reinforced with micron-sized Al<sub>2</sub>O<sub>3</sub> reinforcement. Pin-on-disc wear testing demonstrated that T6 specimens reinforced with nano-Al<sub>2</sub>O<sub>3</sub> exhibited enhanced wear resistance than the composite specimens reinforced with micron-sized ceramic reinforcement. Worn surface morphology was carried out using FESEM to study the mode of wear.

**Keywords** Stir casting · Nano alumina · Al metal matrix composite · Aging · Wear

## 1 Introduction

Aluminium matrix composites (AMCs) are widely used for the manufacture of automobile, aerospace, marine and military components due to their excellent mechanical, tribological and corrosion properties. Investigations are going on in a large scale all over the world to enhance its properties by using innovative production methods and also by the inclusion of reinforcements [1–3]. The addition of certain particulates to the base metal matrix enhances its properties in terms of increase in strength,

---

N. Sirajudeen · R. Karunanithi (✉) · M. Abdur Rahman  
Department of Mechanical Engineering, B.S.A.R Crescent Institute of Science and Technology,  
Chennai 600048, India  
e-mail: [karunanithi@crescent.education](mailto:karunanithi@crescent.education)

hardness, wear, thermal and corrosion resistance. Thus, the particulate-reinforced aluminium matrix composites (PRMMC) are rapidly replacing the conventional aluminium matrix composites owing to their superior performance. A lot of research work is going on to produce them with enhanced properties, especially for aerospace, structural and military applications [4–7]. The addition of strengthening media to the base aluminium matrix causes many beneficial changes like grain refinement, enhanced dislocation density and the ability of the base matrix to transfer the applied load to the ceramic reinforcement thereby increasing its strength [8, 9]. Among aluminium alloys, the age hardenable, Al–Mg–Si alloy commonly referred as 6XXX series alloys are widely used for structural applications possess a lower density, good strength, exceptional formability, and good corrosion resistance [10–12]. PRMMCs are fabricated by many techniques like liquid metal infiltration, mechanical alloying, squeeze casting, friction stir processing, etc. and among them, the stir casting technique has proven to be a highly economical route. Recent studies have revealed the possibility of attaining a good homogenous dispersion of the reinforcement particles in the base alloy matrix by optimizing the stir casting process parameters like stirring speed, pouring time, controlled atmosphere, the temperature of the liquid metal, preheating of the mould, etc. [13, 14].

The fabrication of composite involves melting of the metal, addition of ceramic particulates and mechanically mixing them uniformly in the molten matrix using a stirrer setup [15]. The commonly used ceramic reinforcements for enhancing the mechanical, tribological and corrosion behaviour of the metal matrix composites are SiC, boron carbide,  $\text{Al}_2\text{O}_3$  and zirconia [16–21].

Among them the  $\text{Al}_2\text{O}_3$  particles are widely used as reinforcement material owing to its exceptional mechanical, wear and corrosion properties [22]. Among the 6XXX series age hardenable alloys, the Al 6082 alloy with outstanding mechanical properties occupies a significant place for lightweight applications [23]. GP zones develop due to nucleation of precipitates during solution treatment of age hardenable alloys [24].

Previous research studies on age-hardenable alloys have indicated the development of (intermetallic) phases [25]. Although the effect of varying particulate size and weight fraction of ceramic reinforcement has been studied previously, very less research has been done on the effect of heat treatment and varying particle of  $\text{Al}_2\text{O}_3$  on the hardness and wear behaviour of the Al 6082 alloy composite. Thus, the novelty of the present investigation is to study the combined influence of artificial aging (1, 2, 4, 6, 8, 10, 12, 14, 16, 18 and 20 h) and varying particle/weight% of  $\text{Al}_2\text{O}_3$  particles on the hardness and wear resistance of Al 6082 alloy composite by stir casting route. The other novelty of this research is apart from comparing the effect of T6 aging; it studies the effect of T7 or overaging (heat treatment) on the hardness of Al 6082 alloy composite specimens reinforced separately with coarse and nano- $\text{Al}_2\text{O}_3$  reinforcement particles. The wear resistance of the test specimens is studied using a pin-on-disc wear tester under varying load conditions.

## **2 Materials and Methods**

### **2.1 Sample Preparation**

The commercially available Al 6082-T6 alloy and Al<sub>2</sub>O<sub>3</sub> powder of 45 μm size was chosen as the matrix and reinforcement material, respectively. Toluene was added to avoid a rise in temperature and clustering. The particle size analysis (Zeta Nano ZS, Malvern, UK) showed that the final particle size after ball milling of micro-sized Al<sub>2</sub>O<sub>3</sub> was 40–50 nm. Preheated (250 °C), Al<sub>2</sub>O<sub>3</sub> reinforcement particles with varying weight % (1, 1.5, 2, and 2.5%) and size (45 μm/ 40–50 nm) were added individually to the base matrix to get two sets of cast specimens, i.e., one set of samples was reinforced with coarse alumina and the next set of samples with nano-alumina. Stirring time and speed were fixed as 10mins and 300 RPM, respectively, to obtain a vortex. Stirring temperature was maintained between 830 and 850 °C. Hexachloroethane (C<sub>2</sub>Cl<sub>6</sub>) tablets were used to get rid of the trapped gases.

Later the two different sets of Al 6082 alloy composite reinforced separately with varying weight fraction of coarse and nano-Al<sub>2</sub>O<sub>3</sub> particles were poured into a preheated die, of 20 mm diameter and 200 mm height. After the solidification process, the cast samples were ejected from the die and machined to ASTM standard dimensions for hardness and wear tests.

### **2.2 Aging**

The specimens were initially solutionized at 480 °C for a period of 1 h in an induction furnace. The solutionized specimens were quenched followed by artificial aging for various time periods of 1, 2, 4, 6, 8, 10, 12, 14, 16, 18 and 20 h at 180 °C.

### **2.3 Hardness Measurement**

VHN measurement was performed on a Vickers microhardness testing machine with a load capacity of 50 kgf and a ball indenter diameter of 5 mm. The test was repeated at five different locations for reproducibility, and the average values were tabulated.

### **2.4 Wear Test**

Wear test of the composite was analysed under varying load (15 N, 20 N, 25 N and 30 N) conditions. Machining was performed on the stir cast specimens such that it had a diameter and a height of 6 mm and 15 mm, respectively. Volumetric wear rate of

the specimens was performed on a pin-on-disc wear testing machine (Model: TR20-LE) with a sliding speed of  $2 \text{ ms}^{-1}$  against EN32 steel disc (500HV) of 100 mm track diameter. Acetone was used as a cleaning substance for the specimens.

## 2.5 XRD and FESEM

The cast composite specimens were mechanically polished using 800, 1000, 1200, 1500 gr SiC emery sheets. The polished samples were cleaned with distilled water and acetone, further cloth polishing of the specimens was performed by applying a diamond paste ( $0.5 \mu\text{m}$ ). The specimens were later etched using Keller's reagent, before conducting the FESEM (Model: SUPRA 55-CARL ZEISS, GERMANY) and XRD analysis (PANalytical X-ray diffractometer).

## 3 Results and Discussion

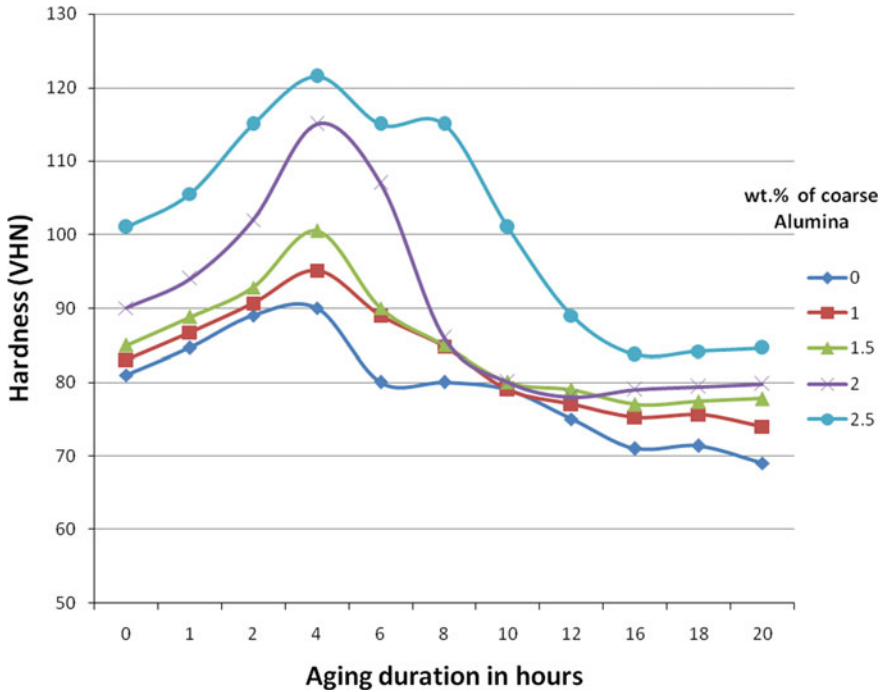
### 3.1 Vickers Microhardness

Vickers microhardness testing machine was used for hardness test for both the non-aged and aged specimens of Al 6082 alloy composites. The VHN plot shown in Figs. 1 and 2 shows that the microhardness of Al 6082 alloy composite increases due to the addition of both coarse or nano- $\text{Al}_2\text{O}_3$  reinforcement. Nevertheless, the nano- $\text{Al}_2\text{O}_3$ -reinforced specimens outperformed its coarse  $\text{Al}_2\text{O}_3$ -reinforced counterpart. The specimens reinforced with 2.5 wt.% of nano  $\text{Al}_2\text{O}_3$  reinforcement attained a maximum VHN of 238, i.e., peak aged hardness was attained after 6 h of aging. This can be ascribed to precipitation hardening as well as the hard nature of the nano sized  $\text{Al}_2\text{O}_3$  particulates, which acted as barriers to dislocation motion resisting the loads related to indentation during VHN tests [26, 27].

Based on the VHN microhardness results, the aged samples can be categorized into underaged, peak aged and overaged samples. The increase or decrease in the hardness of the specimens can be related to the kinetics of aging which affects the shape, size and dispersion of precipitates in the base alloy matrix [28].

The graphs in Figs. 1 and 2 indicate an enhancement of VHN microhardness values due to the addition of both coarse and nano-sized reinforcement; however, it is worth noting that the aged specimens outperformed the non-aged samples. The other reason for the improvement of VHN can be attributed to the addition of nano-sized reinforcement particles [29].

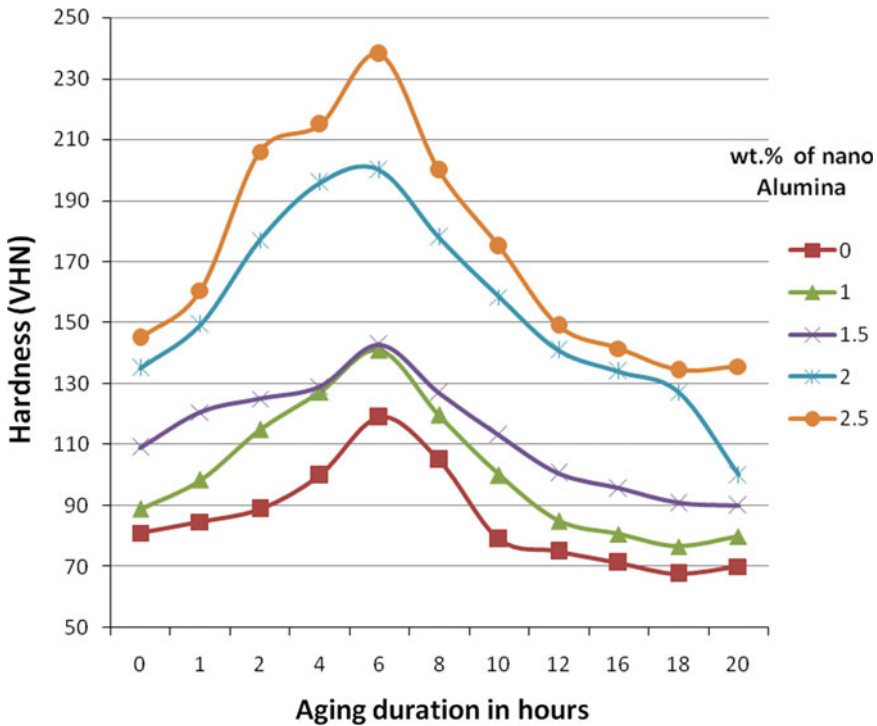
With an increase in the weight fraction of alumina particles of nano-size, a higher dislocation density existed due to the thermal mismatch between the nano  $\text{Al}_2\text{O}_3$  and the base Al 6082 alloy matrix. This increased dislocation density in the base matrix increased the hardness of the composite [30].



**Fig. 1** VHN versus aging duration plot of the Al 6082 alloy composite reinforced with coarse Al<sub>2</sub>O<sub>3</sub> particles

It is clear from Figs. 1 and 2 that artificial aging of both the unreinforced Al 6082 alloy and its reinforced composite specimens led to an increase in the VHN microhardness. The graphs indicate a sharp increase in the VHN microhardness immediately after the solution treatment followed by artificial aging. The coarse Al<sub>2</sub>O<sub>3</sub>-reinforced composite specimens (refer Fig. 1) show a tremendous increase in VHN microhardness up to 122 VHN (peak aged hardness) after 4 h of aging beyond which the specimens showed a gradual decrease in its VHN value. The peak aged (T6) hardness values of composite specimens reinforced with 1, 1.5, 2, 2.5% of coarse Al<sub>2</sub>O<sub>3</sub> particles are 90, 95, 101, 115 and 122 VHN, respectively. Overaging (T7) occurred in the range of 18–20 h when the samples reinforced with different wt.% of coarse Al<sub>2</sub>O<sub>3</sub> particles attained their lowest hardness.

Figure 2 shows the VHN values of aged specimens reinforced with 1, 1.5, 2 and 2.5% of nano Al<sub>2</sub>O<sub>3</sub> particles as 119, 141, 143, 200 and 238 VHN, respectively, after 6 h of aging. Similarly overaging (T7) occurred in the range of 18–20 h during which the samples reinforced with nano-Al<sub>2</sub>O<sub>3</sub> particles reached their lowest microhardness values. Nevertheless, the nano-Al<sub>2</sub>O<sub>3</sub>-reinforced samples outperformed the coarse Al<sub>2</sub>O<sub>3</sub>-reinforced samples even at overaging (T7) conditions in terms of microhardness values. Thus, the VHN microhardness results reveal that the nano-Al<sub>2</sub>O<sub>3</sub>-reinforced Al 6082 alloy composite samples bettered the coarse Al<sub>2</sub>O<sub>3</sub> reinforced



**Fig. 2** VHN versus aging duration plot of the Al 6082 alloy composite reinforced with nano- $\text{Al}_2\text{O}_3$  particles

Al 6082 alloy composite specimens. Usually, grain boundary acts as the preferential place for the nucleation of precipitate phases. During heat treatment, the diffusion of Mg and Si is quite significant for the formation of  $\text{Mg}_2\text{Si}$  precipitates. After the attainment of a supersaturated solid solution, artificial aging is performed by heating the specimens at a suitable temperature of 180 °C, which will speed up the process of Mg and Si diffusion, leading to the formation of (stable)  $\text{Mg}_2\text{Si}$  precipitate [31]. It has been reported that the decomposition of supersaturated solid solution occurs as a result of aging. Hence, with aging rate is proportional to the degree of supersaturation [32]. During age hardening, the rearrangement of atoms within the crystal lattice occurs. Next forms the clusters and GP zones. In this stage, mechanical properties are improved due to the occurrence of microstrains in the crystal lattice. When compared to the pure alloy, the composite specimens undergo accelerated aging due to the occurrence of a large dislocation density near the Al 6082 matrix— $\text{Al}_2\text{O}_3$  interface [33]. Previous studies on the Al 6XXX alloys show the following sequence of aging: [31, 34].

Initially, the supersaturated solid solution transforms into cluster of solute atoms followed by primitive Guinier–Preston zones which transform into needle-shaped GP zones which are rod-shaped, metastable, hexagonal and semi-coherent- $\beta$  phase.

The formation of GP zones is a complex process which involves the formation of clusters of vacancies and silicon atoms followed by the precipitation of Mg atoms on nuclei [35]. Then forms the stable, incoherent, cubic,  $Mg_2Si$  precipitate ( $\beta$  phase). It has also been reported that the solutionizing temperature plays a crucial role in increasing the strength of the Al 6061 Al/SiC composite. The report also suggests a correlation between the hardness and the aging temperature/duration owing to the phase transformations occurring during heat treatment [34].

XRD graphs of both the T6-aged Al 6082 alloy (refer Fig. 3) and the T6-aged Al 6082 alloy composite reinforced with 2.5 wt% of nano  $Al_2O_3$  (refer Fig. 4) reveal the formation of the stable  $Mg_2Si$  precipitates on account of the precipitation hardening phenomenon.

The enhanced VHN microhardness of the Al 6082 alloy composite compared to the unreinforced alloy could be attributed to its better aging kinetics behaviour. The acceleration of aging occurs due to a high concentration of dislocations near the vicinity of the alloy matrix–ceramic reinforcement interface [36]. The presence of high density of dislocations paved the way for the occurrence of heterogeneous nucleation sites which are precursors for the formation of precipitates and enhances higher diffusivity of alloying elements [34–36].

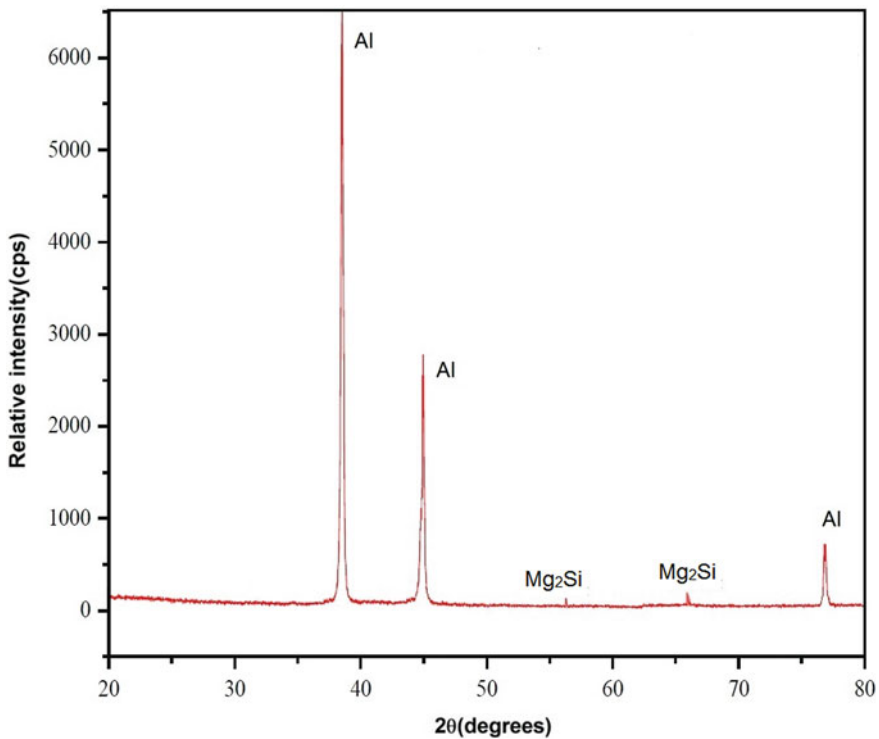


Fig. 3 XRD plot of Al 6082 alloy subjected to T6 aging



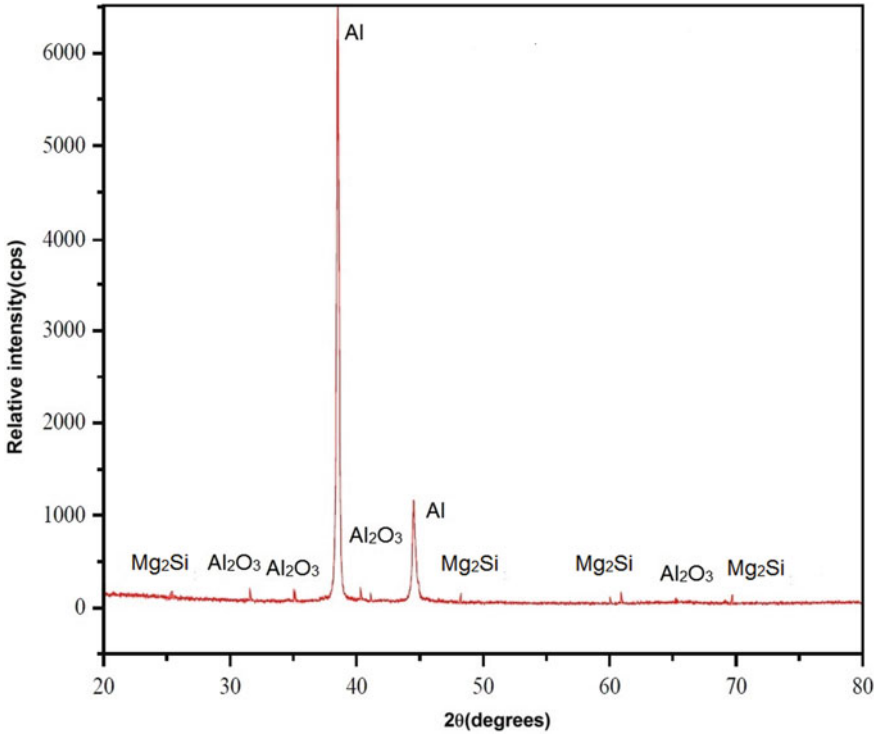


Fig. 4 XRD plot of Al 6082 alloy reinforced with 2.5 wt% of nano Al<sub>2</sub>O<sub>3</sub> subjected to T6 aging

### 3.2 Wear Test

Wear tests were performed on both the non-aged and T6-aged samples with and without reinforcement (micro/nano). Figures 5, 6, 7, 8, 9, 10, 11 and 12 demonstrate an enhancement of wear resistance of the test specimens due to the addition of varying weight fraction and particle size of the reinforcement. With the increase in the applied

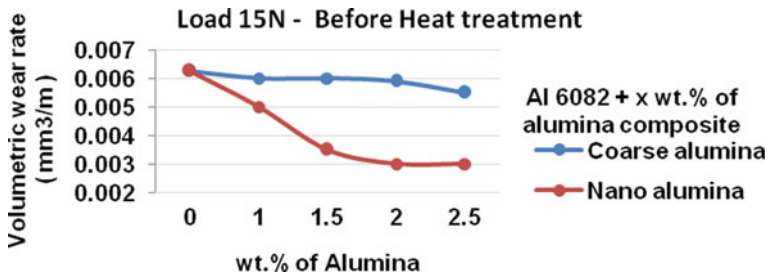


Fig. 5 Wear rate of Al 6082 alloy composite at load of 15 N, before heat treatment

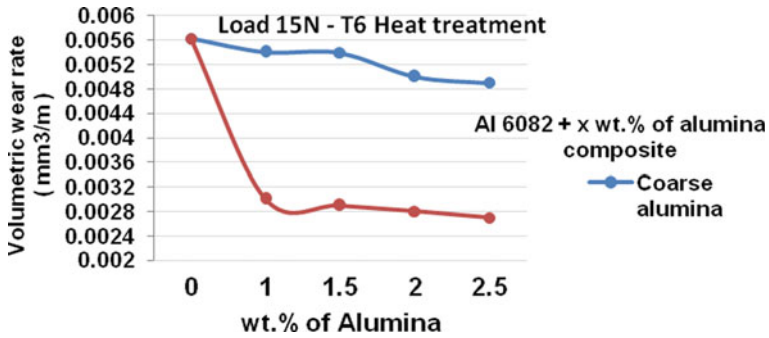


Fig. 6 Wear rate of Al 6082 alloy composite at load of 15 N, after T6 aging treatment

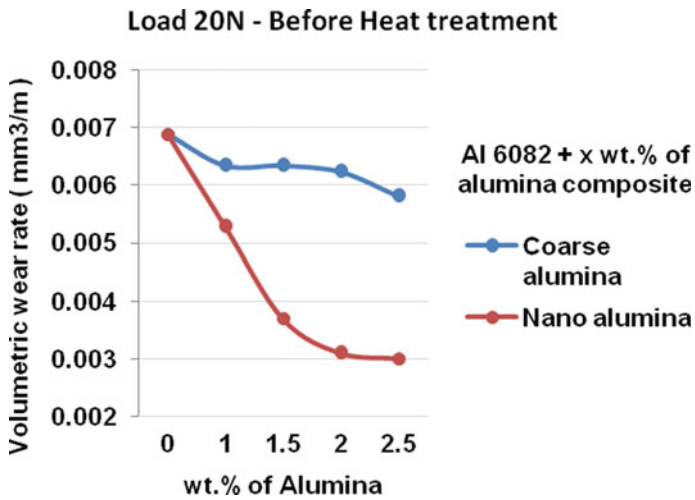


Fig. 7 Wear rate of Al 6082 alloy composite at load of 20 N, before heat treatment

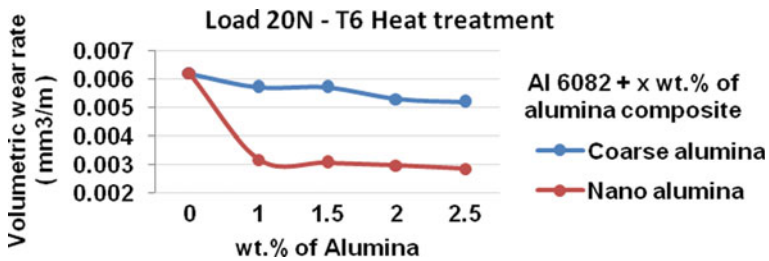


Fig. 8 Wear rate of Al 6082 alloy composite at load of 20 N, after T6 aging treatment

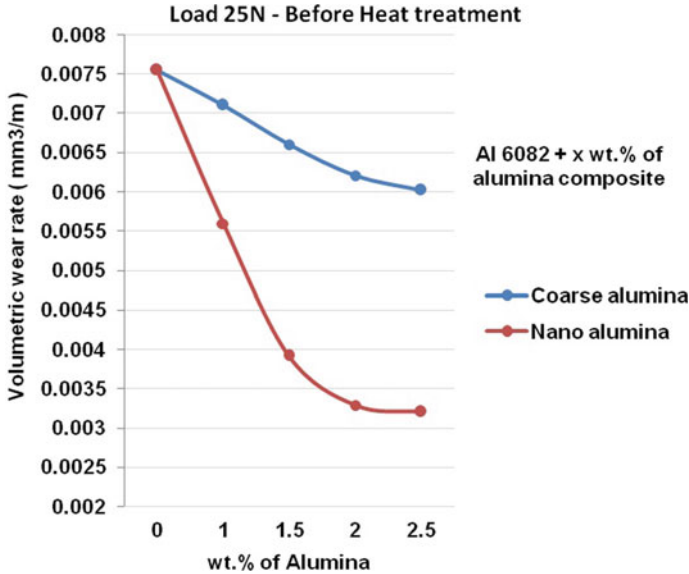


Fig. 9 Wear rate of Al 6082 alloy composite at load of 25 N, before heat treatment

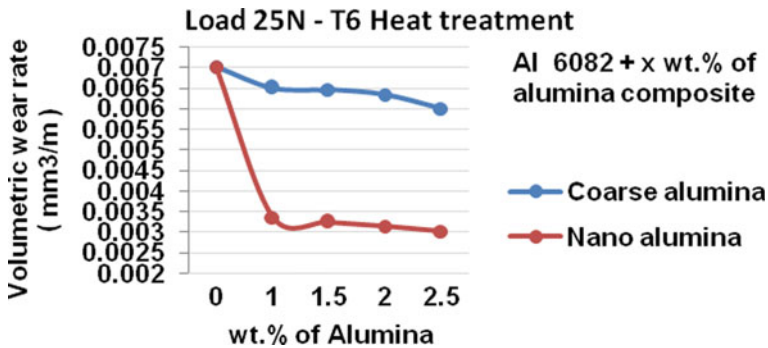
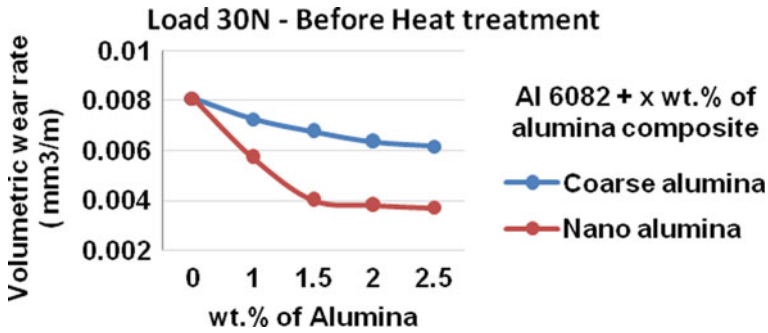
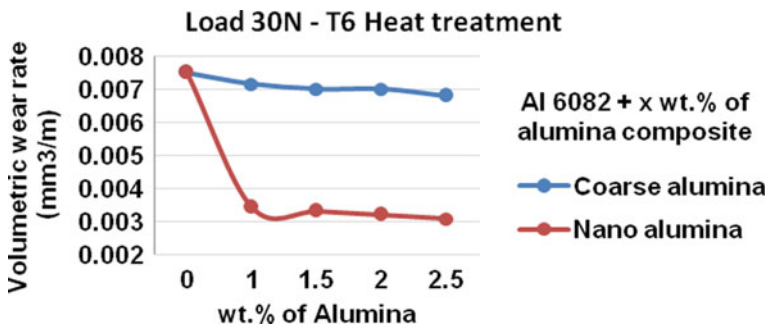


Fig. 10 Wear rate of Al 6082 alloy composite at load of 25 N after T6 aging treatment

load, the rate of volumetric wear also increases. Nevertheless, the volumetric wear rate of the pure alloy and the coarse  $Al_2O_3$ -reinforced samples were higher than that of the nano- $Al_2O_3$ -reinforced Al 6082 alloy composite specimens indicating enhanced resistance to wear due to the addition of nano- $Al_2O_3$  particles. The wear graphs also show that the T6-aged specimens reinforced with nano- $Al_2O_3$  particles outperformed the other sets of specimens, i.e., unreinforced Al 6082 alloy and the coarse  $Al_2O_3$ -reinforced Al 6082 alloy composite (under both aged and non-aged conditions) showing an enhanced wear behaviour. Thus, the pin-on-disc wear testing results (refer Figs. 6, 8, 10 and 12) showed that the T6-aged, nano- $Al_2O_3$ -reinforced



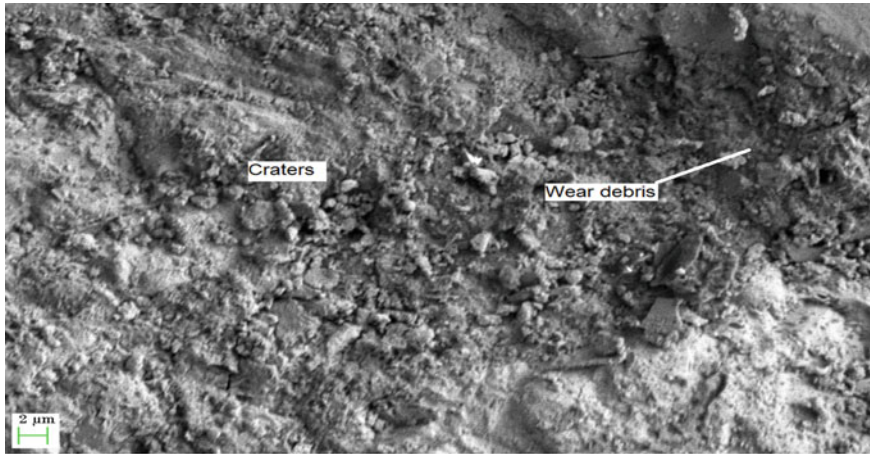
**Fig. 11** Wear rate of Al 6082 alloy composite at load of 30 N before heat treatment



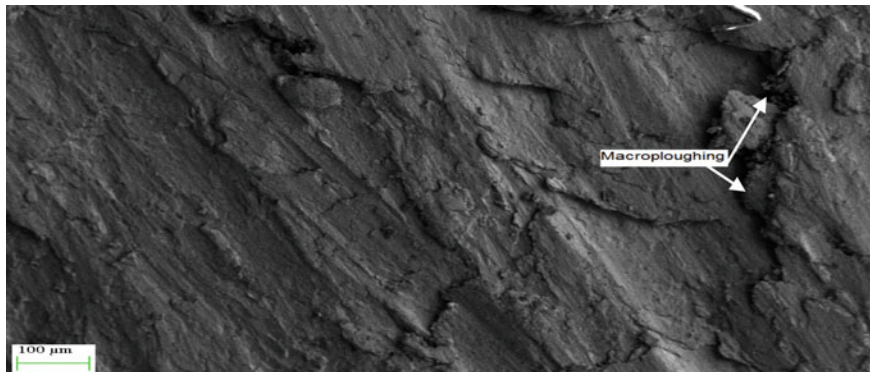
**Fig. 12** Wear rate of Al 6082 alloy composite at load of 30 N after T6 aging treatment

Al 6082 alloy composite specimens demonstrated an enhanced wear resistance under varying applied loads of 15, 20, 25 and 30 N.

SEM micrographs of the worn samples of T6-aged and non-aged composite specimens as well as the unreinforced specimens are shown in Figs. 13, 14, 15, 16, 17, 18 and 19. SEM images clearly indicate that the non-aged Al 6082 alloy and its composites have suffered more damage compared to the aged specimens. Development of microcracks as indicated in Figs. 15, 17 and 19 could be ascribed to the occurrence of fatigue wear due to repeated loading during wear test runs. Figure 16 shows the formation of deep grooves of various sizes which lead to subsurface crack propagation along the direction of sliding. With the increase in the applied load, delamination mode of wear occurs (refer Fig. 18). The pure Al 6082 alloy’s worn surface (refer Fig. 13) is characterized by large craters, indicating that the specimen has undergone severe plastic deformation due to its inability to resist the repeated loads during sliding test runs. The size of cracks and grooves of the pure Al 6082 alloy indicates the occurrence of abrasive mode of wear due to severe plastic deformation. The peeling away of the outer layer which is occupied by the hard nano- $Al_2O_3$  particles also indicates that the mechanism of wear is abrasive in nature (refer Figs. 13 and 14). The severe damage could also be attributed to the direct contact between the metal to



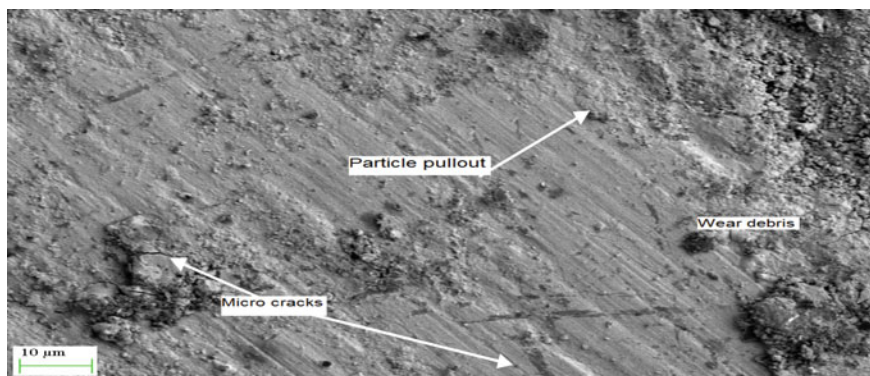
**Fig. 13** SEM micrograph of (non-aged) unreinforced Al 6082 alloy revealing craters and the accumulation of wear debris



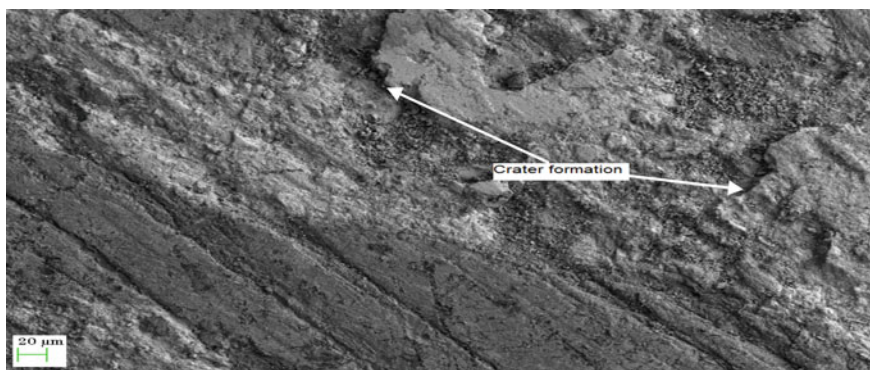
**Fig. 14** SEM micrograph of (non-aged) unreinforced Al 6082 alloy revealing severe damage due to macroplooughing

metal interface between the matrix and the counter steel disc. The increase in the applied load softens the base matrix leading to more material loss. The worn surface of the reinforced specimens is characterized by particle pull out associated with fine to distinctive groove formations (refer Fig. 15). With the increase in the applied load, the protrusion of ceramic particles from the worn surface leads to abrasive type of wear. This could be ascribed to the high plastic strain which destabilizes the ceramic particle from the worn surface. During sliding wear, the loosening of the ceramic particles takes place which later get confined between the faying surfaces. A mechanism known as three-body abrasion occurs. The tribo-film comprises of confined  $\text{Al}_2\text{O}_3$  particles and wear debris emerging between the faying surfaces of Al 6082 alloy matrix and the counter steel disc surface. This wear-resistant film decreases the

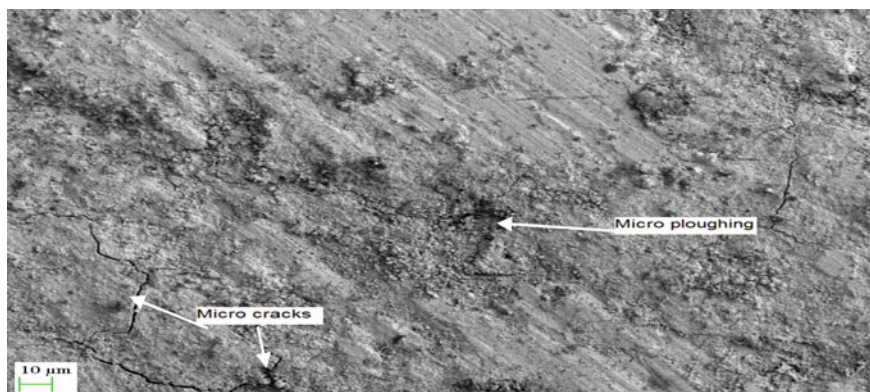




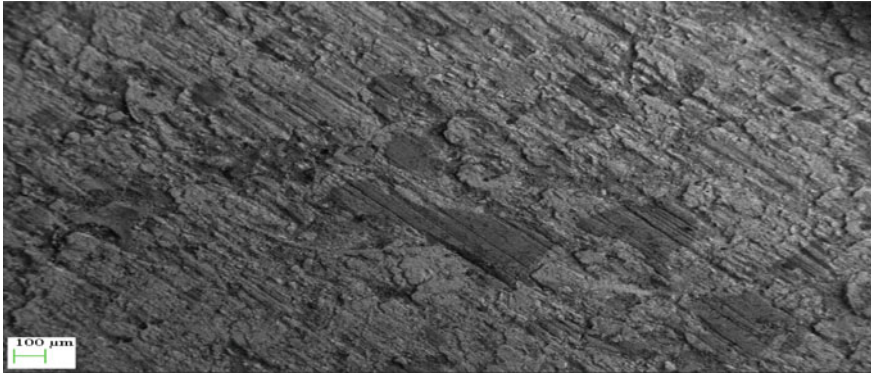
**Fig. 15** SEM micrograph of T6-aged Al 6082 alloy with 1 wt % of coarse Al<sub>2</sub>O<sub>3</sub> revealing particle pullout, wear debris and micro cracks



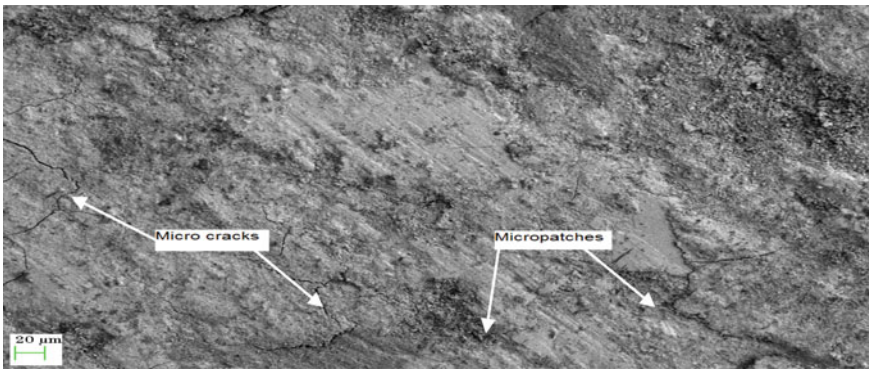
**Fig. 16** SEM micrograph of non-aged Al 6082 with 1.5 wt% of coarse Al<sub>2</sub>O<sub>3</sub> revealing crater formation due to macroploughing



**Fig. 17** SEM micrograph of T6-aged Al 6082 alloy with 1.5 wt% of nano Al<sub>2</sub>O<sub>3</sub> showing microcracks and microploughing



**Fig. 18** SEM micrograph of T6-aged Al 6082 with 2 wt% of coarse Al<sub>2</sub>O<sub>3</sub> at an applied load of 30 N



**Fig. 19** SEM micrograph of T6-aged Al 6082 alloy with 2 wt% of nano Al<sub>2</sub>O<sub>3</sub> revealing micropatches and microcracks due to microplothing

shear loads during sliding operation due to which the damage on account of plastic deformation reduces, thus contributing to reduced wear rate of the reinforced and aged specimens. Another contributing factor is the formation of oxide layer on the pin's surface. As the sliding continues, the distortion and fragmentation of the pin mating surface occurs. The displacement of oxides occur with an increase in the applied load; however, a small portion of the oxides between the faying surfaces continues to exist. Dislodging of oxides takes place during the course of sliding; however, a meagre amount of oxides present between the mating surfaces diminishes the metallic contact on account of which the specimens suffer a very reduced wear damage, in other words an increase in wear resistance [37, 38].

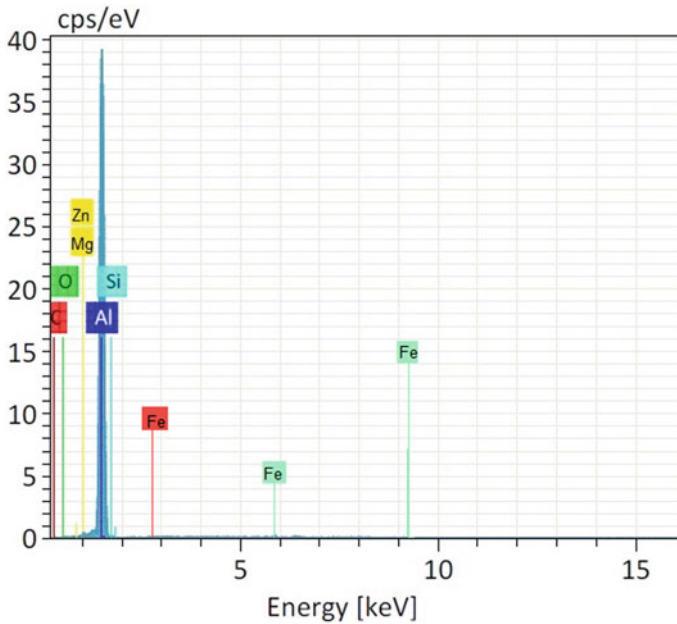
The enhancement of wear behaviour of the T6-aged and reinforced specimens can be ascribed to the stable lubricating film, which forms on the surface of the Al 6082

alloy composite. The wear test results showed that not only the addition of nanoparticles but also the heat treatment given to the test specimens play a very significant role in enhancing the wear resistance of the samples. The composite specimens reinforced with nano- $\text{Al}_2\text{O}_3$  particles showed an enhanced wear behaviour in terms of reduced volumetric wear loss (refer Figs. 6, 8, 10 and 12). The pin-on-disc tests conducted also indicated that the T6-aged specimens reinforced with nano- $\text{Al}_2\text{O}_3$  outperformed the non-aged and coarse  $\text{Al}_2\text{O}_3$ -reinforced samples in terms of increase in wear resistance under varying load conditions. The fragmentation and fracture of the reinforcement media lead to a direct contact between the composite's surface and the counter steel disc. The higher wear resistance of the ceramic-reinforced composite specimens is because of the better load bearing ability of the nano-sized  $\text{Al}_2\text{O}_3$  reinforcement [37]. The worn surface of the composite specimens shows a mechanically mixed layer deposits as a result of transfer of material from the counter steel disc surface. During pin-on-disc wear testing, the presence of hard ceramic particles acts as stress absorbers during the application of varying applied loads which leads to scratching on the counter steel disc surface.

During sliding operations at varying loads, exposure of the embedded ceramic particles causes localized milling on the counter steel disc surface leading to transfer of steel fragments on the pin's surface. When the composite pin slides against the counter steel disc surface, the disc undergoes severe plastic deformation and leads to the ploughing out of the Iron (Fe) from the rotating counter steel disc surface, which acts as a precursor for the formation of what is known as the mechanically mixed layer (MML). Thus, the test specimen's surface comprises of layers of Fe and FeO which can be confirmed by the EDS analysis as shown in Fig. 20. The decrease in the volumetric wear rate of the reinforced specimens could be attributed to the increase in the weight% of  $\text{Al}_2\text{O}_3$  particles which reduces the direct contact between the pin's surface and the counter steel disc. When the applied load is less, the effect due to strain hardening is very minimal hence its effect on the wear rate is also very less. Nevertheless, with an increase in the applied load, debonding and fragmentation of ceramic particles from the base matrix occurs. This condition also leads to three-body abrasion. Thus, the increase in wear rate of the samples with an increase in the applied load could be due to the freely moving ceramic particles which act as three-body abrasive elements during pin-on-disc wear testing operations.

At the inception of the pin-on-disc wear testing, the sliding of the pin's surface against the rotating steel disc gradually increases the temperature between the faying surfaces. The effect due to friction between the faying surfaces increases the extent of plastic deformation and hence increases further loss of material. The applied load also has a significant impact on the volumetric wear rate of the composite samples. The rate of wear increases with the increase in the applied load for both unreinforced and reinforced samples. The unreinforced specimens suffer severe damage (plastic deformation) due to direct contact between the pin and counter steel disc surface resulting in a large amount of material removal and subsurface cracking. However, the ceramic particulate-reinforced Al 6082 alloy composite comparatively suffered less damage due to the ability of the  $\text{Al}_2\text{O}_3$  reinforcement to absorb and withstand the applied load thereby protecting the softer matrix of the base alloy.





**Fig. 20** EDS analysis of T6-aged Al 6082 alloy composite

Thus, the main purpose of the ceramic reinforcement is to reduce surface damage due to plastic deformation and abrasion between the composite pin and steel disc surface thereby reducing the material loss [39, 40].

The addition of reinforcement led to an increase in the dislocation density on account of thermal mismatch between the alloy and the ceramic reinforcement. Due to the presence of large amount of dislocation densities along with the ceramic reinforcement, strain hardening occurs leading to hindrance of dislocation motion contributing to reduced wear rate. With increase in the applied load, a large amount of stress on the contact asperities leads to its fragmentation and particle pull out [40]. The presence of hard asperities in the pin erodes the rotating steel disc surface. Initially, the sharp asperities causes abrasive action on the steel disc causing some portion of the material from the steel disc surface to get transferred to the pin's surface. A previous study [41] demonstrates that the wear resistance of overaged Al-based composites reduces on account of the coarsening of precipitates. On the other hand, the T6 (peak aged) specimens demonstrate an enhanced wear resistance due to the load bearing capacity of the ceramic particulates and the stable  $Mg_2Si$  precipitates. The stable  $Mg_2Si$  precipitates not only enhanced the bonding between the  $Al_2O_3$  reinforcement and the base matrix but also provided high temperature (thermal) resistance during dry sliding wear tests [40, 43, 43].

Thus, a combination of artificial aging and the addition of increasing weight fraction and decreasing particle size of  $Al_2O_3$  enhanced the hardness and wear resistance of the ceramic-reinforced Al 6082 alloy composite [39–41, 43–47].

## 4 Conclusions

Al 6082 alloy and Al 6082 alloy composite samples reinforced with varying weight fraction and particle size of alumina particles were synthesized by stir casting process. The solutionized composite specimens were subjected to various durations of heat treatment (i.e., artificial aging) to study its effect on hardness and wear behaviour. XRD analysis confirms the formation of the stable  $Mg_2Si$  precipitates. The VHN microhardness results showed that peak aged hardness was attained after 6 h of heat treatment at 180 °C. A maximum peak aged (T6-aged) hardness of 238 VHN was obtained for composite samples reinforced with 2.5% of nano- $Al_2O_3$ . The VHN results demonstrated that the composite samples reinforced with nano- $Al_2O_3$  particles outperformed the coarse  $Al_2O_3$  reinforced samples with a maximum hardness of 122 VHN after 4 h of aging. Overaging for both sets of samples (coarse and nano- $Al_2O_3$  reinforced) occurred in the range of 18–20 h. Thus, hardness test showed a better behaviour for alumina added composite due to precipitation hardening. The pin-on-disc wear tests conducted under varying loads, also indicate that the T6-aged samples reinforced with  $Al_2O_3$  particles outperformed the aged as well as non-aged unreinforced Al 6082 alloy samples in terms of reduced volumetric wear rate. Worn surface morphology (FESEM) of the unreinforced sample shows severe damage due to macropolishing revealing poor resistance to wear. The T6-aged samples demonstrated lesser amount of damage compared to the non-aged samples demonstrating enhancement of its hardness and wear resistance. The formation of precipitates which acted as obstacles to dislocation motion during artificial aging acted as stress absorbing elements, resisting the applied loads during dry sliding wear tests. Thus, the present investigation reveals the beneficial influence of both T6 aging as well as the addition of increasing weight fraction and decreasing particle size of  $Al_2O_3$  particles in enhancing the hardness and wear behaviour of Al 6082 alloy.

**Acknowledgements** The authors would like to acknowledge Dr. N. Srirangarajulu, MIT, Chennai, India, for providing the facilities to do the research work.

## References

1. Rahimian M, et al (2009) The effect of particle size, sintering temperature and sintering time on the properties of Al– $Al_2O_3$  composites, made by powder metallurgy. *J Mater Process Technol* 209.14(2009):5387–5393
2. Sharifi EM, Karimzadeh F, Enayati MH (2011) Fabrication and evaluation of mechanical and tribological properties of boron carbide reinforced aluminum matrix nanocomposites. *Mater Design* 32(6):3263–3271
3. Hemanth J (2009) Quartz ( $SiO_2$ ) reinforced chilled metal matrix composite (CMMC) for automotive applications. *Materials & Design*, 30(2), 323–329.
4. Moses JJ, Dinaharan I, Sekhar SJ (2016) Predicting the influence of process parameters on tensile strength of AA6061/TiC aluminum matrix composites produced using stir casting.

5. Zhu QJ, Wang BB, Zhao X, Zhang BB (2018). Robust micro arc oxidation coatings on 6061 aluminum alloys via surface thickening and microvoid reducing approach. In *Solid State Phenomena*, , Trans Tech Publications Ltd, vol 279, pp. 148–152
6. Dong GJ, Bi J, Du B, Chen XH, Zhao CC (2017) Research on AA6061 tubular components prepared by combined technology of heat treatment and internal high pressure forming. *J Mater Process Technol* 242:126–138
7. Yu LI, Li QL, Dong LI, Wei LIU, Shu GG (2016) Fabrication and characterization of stir casting AA6061—31% B4C composite. *Trans Nonferrous Metal Soc China* 26(9):2304–2312
8. Kang YC, Chan SLI (2004) Tensile properties of nanometric Al<sub>2</sub>O<sub>3</sub> particulate-reinforced aluminum matrix composites. *Mater Chem Phys* 85(2–3):438–443
9. Namini AS, Azadbeh M, Asl MS (2017) Effect of TiB<sub>2</sub> content on the characteristics of spark plasma sintered Ti–TiB<sub>w</sub> composites. *Adv Powder Technol* 28(6):1564–1572
10. Sharma, P., Khanduja, D., & Sharma, S. (2014). Metallurgical and Mechanical characterization of Al 6082-B4C/Si<sub>3</sub>N<sub>4</sub> hybrid composite manufactured by combined ball milling and stir casting. In *Applied Mechanics and Materials* (Vol. 592, pp. 484–488). Trans Tech Publications Ltd.
11. El-Danaf EA, El-Rayes MM (2013) Microstructure and mechanical properties of friction stir welded 6082 AA in as welded and post weld heat treated conditions. *Mater Design* 46:561–572
12. Thangarasu A, Murugan N, Mohankumar R, Thangapandi P (2014) Processing and characterization of AA6082/TiC composites by stir casting. *Emer Mater Res* 3(3):123–129
13. Ravi KR, Sreekumar VM, Pillai RM, Mahato C, Amaranathan KR, Pai BC (2007) Optimization of mixing parameters through a water model for metal matrix composites synthesis. *Mater Design* 28(3):871–881
14. Kok M (2005) Production and mechanical properties of Al<sub>2</sub>O<sub>3</sub> particle-reinforced 2024 aluminium alloy composites. *J Mater Process Technol* 161(3):381–387.
15. Mazahery, A., & Shabani, M. O. (2012). Tribological behaviour of semisolid–semisolid compocast Al–Si matrix composites reinforced with TiB<sub>2</sub> coated B4C particulates. *Ceram Int* 38(3):1887–1895
16. Suresh S, Moorthi NSV, Vettivel SC, Selvakumar N (2014) Mechanical behavior and wear prediction of stir cast Al–TiB<sub>2</sub> composites using response surface methodology. *Mater Design* 59:383–396
17. Razavizadeh K, Eyre TS (1982) Oxidative wear of aluminium alloys. *Wear* 79(3):325–333
18. Lai J, Zhang Z, Chen XG (2013) Precipitation strengthening of Al–B<sup>4</sup>C metal matrix composites alloyed with Sc and Zr. *J Alloy Comp* 552:227–235
19. Bueno S, Ferrari B, Melandri C, De Portu G, Baudín C (2010) Processing of alumina-coated tetragonal zirconia materials and their response to sliding wear. *Ceram Int* 36(5):1545–1552
20. Su H, Gao W, Feng Z, Lu Z (2012) Processing microstructure and tensile properties of nano-sized Al<sub>2</sub>O<sub>3</sub> particle reinforced aluminum matrix composites. *Mater Design* (1980–2015), 36:590–596
21. Zhang Q, Ma X, Wu G (2013) Interfacial microstructure of SiCp/Al composite produced by the pressureless infiltration technique. *Ceram Int* 39(5):4893–4897
22. El-Sabbagh AM, Soliman M, Taha MA, Palkowski H (2013) Effect of rolling and heat treatment on tensile behaviour of wrought Al-SiCp composites prepared by stir-casting. *J Mater Process Technol* 213(10):1669–1681
23. Mohamed MS, Foster AD, Lin J, Balint DS, Dean TA (2012) Investigation of deformation and failure features in hot stamping of AA6082: experimentation and modelling. *Int J Mach Tool Manuf* 53(1):27–38
24. Shaeri MH, Salehi MT, Seyyedein SH, Abutalebi MR, Park JK (2014) Microstructure and mechanical properties of Al-7075 alloy processed by equal channel angular pressing combined with aging treatment. *Mater Design* 57:250–257
25. Cong FG, Gang ZHAO, Jiang F, Ni TIAN, Li RF (2015) Effect of homogenization treatment on microstructure and mechanical properties of DC cast 7X50 aluminum alloy. *Trans Nonferrous Metals Soc China* 25(4):1027–1034

26. Kk M, zdin K (2007) Wear resistance of aluminium alloy and its composites reinforced by  $Al_2O_3$  particles. *J Mater Process Technol* 183(2–3):301–309
27. Surappa MK, Prasad, SV, Rohatgi PK (1982) Wear and abrasion of cast Al-alumina particle composites. *Wear*, 77(3):295–302
28. Appendino P, Badini C, Marino F, Tomasi, A (1991) 6061 aluminium alloy-SiC particulate composite: a comparison between aging behavior in T4 and T6 treatments. *Mater Sci Eng A* 135:275–279
29. Kumar, G. V., Pramod, R., Gouda, P. S., & Rao, C. S. P. (2018). Effect of tungsten carbide reinforcement on the aluminum 6061 alloy. *J Test Evaluat* 47(4):2613–2629
30. Ramesh CS, Safiulla M (2007) Wear behavior of hot extruded Al6061 based composites. *Wear* 263(1–6):629–635.
31. Chawla KK, Esmaeili AH, Datye AK, Vasudevan AK (1991) Effect of homogeneous/heterogeneous precipitation on aging behavior of SiCPAl 2014 composite. *Scripta Metallurgica et Materialia*, 25(6):1315–1319
32. Yilmaz O, Buytoz S (2001) Abrasive wear of  $Al_2O_3$ -reinforced aluminium-based MMCs. *Compos Sci Technol* 61(16):2381–2392
33. Kaushik NC, Rao RN (2016) Effect of grit size on two body abrasive wear of Al 6082 hybrid composites produced by stir casting method. *Tribol Int* 102:52–60
34. Kaushik NC, Rao RN (2016) Effect of applied load and grit size on wear coefficients of Al 6082-SiC-Gr hybrid composites under two body abrasion. *Tribol Int* 103:298–308
35. Salvo L, L'esperance G, Suery M, Legoux JG (1994) Interfacial reactions and age hardening in Al Mg Si metal matrix composites reinforced with SiC particles. *Mater Sci Eng: A* 177(1–2):173–183
36. Udayashankar, N. K., Rajasekaran, S., & Nayak, J. (2012). The effect of protective coatings on the oxidation behavior of 6061Al/SiC composite at high temperatures. In *Advanced Materials Research*, Trans Tech Publications Ltd. vol 383, pp 3949–3953
37. Savařkan T, Hekimođlu AP, Prek G (2004) Effect of copper content on the mechanical and sliding wear properties of monotectoid-based zinc-aluminium-copper alloys. *Tribol Int* 37(1):45–50
38. Prasad Reddy A, Vamsi Krishna P, Rao RN (2019) Two-body abrasive wear behaviour of AA6061-2SiC-2Gr hybrid nanocomposite fabricated through ultrasonically assisted stir casting. *J Compos Mater* 53(15):2165–2180
39. Mazahery A, & Shabani MO (2013) Microstructural and abrasive wear properties of SiC reinforced aluminum-based composite produced by compocasting. *Trans Nonferrous Metal Soc China* 23(7):1905–1914
40. Gurcan AB, Baker TN (1995) Wear behaviour of AA6061 aluminium alloy and its composites. *Wear* 188(1–2): 185–191
41. Gavgali M, Totik Y, Sadeler R (2003) The effects of artificial aging on wear properties of AA 6063 alloy. *Mater Let* 57(24–25): 3713–3721
43. Song WQ, Krauklis P, Mouritz AP, Bandyopadhyay S (1995) The effect of thermal ageing on the abrasive wear behaviour of age-hardening 2014 Al/SiC and 6061 Al/SiC composites. *Wear* 185(1–2):125–130
44. Das S, Mondal DP, Sawla S, Ramakrishnan N (2008) Synergic effect of reinforcement and heat treatment on the two body abrasive wear of an Al-Si alloy under varying loads and abrasive sizes. *Wear* 264(1–2):47–59
45. Dasgupta R (2010) Sliding wear resistance of Al-alloy particulate composites: An assessment on its efficacy. *Tribol Int* 43(5–6):951–958
46. Alaneme KK, Adegun MH, Archibong AG, Okotete EA (2019) Mechanical and wear behaviour of aluminium hybrid composites reinforced with varied aggregates of alumina and quarry dust. *J Chem Technol Metallurgy* 54(6)
47. Bonny K, De Baets P, Vleugels J, Van der Biest O, Salehi A, Liu W, Lauwers B (2009) Reciprocating sliding friction and wear behavior of electrical discharge machined zirconia-based composites against WC-Co cemented carbide. *Int J Refract Metals Hard Mater* 27(2):449–457

# A Comparative Study on the Characteristics of Crumb Rubber with Commercial Rubbers



Sriram Srinivasan, Abbas Saifee Valsadwala, D. Karthik, D. Suganandam,  
and S. Shamshath Begum

**Abstract** There is abundant amount of polymeric materials produced and used every day. After their usage period, only little amount is being recycled or reused. The recycled polymeric material has several properties similar to or better than that of the virgin, and their usage as a final product is cost-effective. Among these materials, rubber is the most used especially in manufacturing of various tyres (light, medium and heavy tyres). Rubber can be recycled in several ways using mechanical and thermal means producing shredded rubber and fuels, respectively. In this investigation, crumb rubber which was obtained from tyre has been used. It was molded by compression under uniform temperature and pressure in form of a sheet and was then cut for different characterisation tests as per the standards. Mechanical properties such as tensile strength, hardness and flex fatigue test, resilience property using rebound resilience were tested and compared with the corresponding commercial rubbers like styrene butadiene rubber (SBR), butyl rubber (BR), and nitrile butadiene rubber (NBR). Surprisingly, crump rubber was found to have high hardness value with respect to the commercial rubbers.

**Keywords** Recycling · Rubber · Rubber crumb · Tyres · Mechanical

---

S. Srinivasan · A. S. Valsadwala · D. Karthik · D. Suganandam · S. Shamshath Begum (✉)  
Department of Polymer Engineering, B.S. Abdur Rahman Crescent Institute of Science and  
Technology, Vandalur, Chennai 600048, India  
e-mail: [msshamu@gmail.com](mailto:msshamu@gmail.com)

S. Srinivasan  
e-mail: [sriramsrinivasn28@yahoo.com](mailto:sriramsrinivasn28@yahoo.com)

A. S. Valsadwala  
e-mail: [abbasvalsadwala@gmail.com](mailto:abbasvalsadwala@gmail.com)

D. Karthik  
e-mail: [karthikjustdoit2000@gmail.com](mailto:karthikjustdoit2000@gmail.com)

D. Suganandam  
e-mail: [trendsuda@gmail.com](mailto:trendsuda@gmail.com)

## 1 Introduction

Materials in general have played pivotal roles in the development of various countries, one among which is 'rubber.' Rubber, is a polymeric material which is available in nature and manufactured by industries as well. Rubber materials have found predominant application in various fields and domains because of their unique properties such as flexibility, and elasticity, etc. In general, all rubbers have negative glass transition temperature ( $T_g$ ) which accounts for its flexible and viscoelastic nature. They also have decent properties of damping noise and vibration [1].

Rubber (Cis-1,4 polyisoprene) is obtained from the tree called *Hevea brasiliensis* which originated from Para port, Amazon valley. Rubber is extracted from the tree through a series of steps like tapping (the process of obtaining raw latex from the tree using a small knife) which is then followed by processing of latex. The different products of natural rubber are either sulfur or urethane vulcanized. This vulcanization gives good strength, dynamic properties and resistance to wear and abrasion in rubbers. This makes it suitable for its applications in the production of tyre tread. Also because of its low heat generation and high resistance to cutting, it is made suitable for usage in earthmover (vehicles that moves off the road on a wet soil) tyres [2–4].

Many rubbers are also synthesized for commercial applications which include styrene butadiene rubber (SBR), butyl rubber (BR), nitrile butadiene rubber (NBR), ethylene propylene diene monomer (EPDM), fluoroelastomer, and chloroprene rubber, etc. Among these, SBR is produced the most and accounts for more than half of the total rubber synthesized. This is because of two main factors, i.e., the precursor (styrene and butadiene) being available readily from fossils and their compatibility between the two which results in easier processing. The initial production of SBR started during the First World War where Germany used butadiene sourced from methyl rubber. Generally speaking, SBR is usually synthesized through an emulsion process follows free radical mechanism due to its good binding strength with various processing ingredients. The  $T_g$  of SBR also varies depending on the process, thereby making it available for a wide range of applications. It is important to know that 75% of this rubber is employed in the tyre industry. Other applications include foot wears, waterproof materials, and other miscellaneous applications [5, 6].

Another important synthetic rubber is BR, which is produced by rapid cationic catalyst copolymerization of isoprene with isobutylene including aluminium trichloride ( $AlCl_3$ ) dissolved in methyl chloride ( $CH_3Cl$ ) as catalyst. Different grades of BR are available based on their molecular weight distribution (MWD) and percentage unsaturation of the moles of isoprene. It is a low-functionality elastomer with good resistance to ozone and desirable oxidation characteristics. In addition to it, six main properties make BR very unique and versatile which includes resistance to weathering, chemical and moisture resistance, higher frictional coefficient, vibration damping, thermal stability and its low gas permeation. They are usually vulcanized by dioxine curing, accelerated sulfur vulcanization and resin curing. They find their application mostly in the tyre field which comprises their usage in the inner liner

of tubeless tyres, tyre side wall components and heat-resistant truck inner tubes. In addition to it, this rubber also finds its application in gaskets, bridge bearing pads, tank lining and pharmaceutical stoppers, etc. [7–11].

Another significant commercial rubber extensively used is NBR. It was first produced and utilized by Germany in 1935 by an industry called Perbunan. It consists of two main components, one being acrylonitrile and the other butadiene. Similar to SBR, it is also produced by free radical emulsion copolymerization technique. The amount of acrylonitrile ranging from 15 to 50% of the total rubber decides the grade and properties of it. The most crucial characteristic exhibited by this rubber is its excellent oil resistance. It also contains some percentage of gel which enables green strength. NBR is usually modified by the addition of carboxyl groups to increase the abrasion resistance and flame retardant properties. It is largely used for hoses in transporting liquid oil and some gases like nitrogen ( $N_2$ ), oxygen ( $O_2$ ), etc. [12–14].

Tyre being the main application of rubber results in a large amount of waste generated every year. Statistics show around 14 million tons (MT) of rubber products were produced in 2018 and are expected to increase around 5% every year, but only 13% of the total production has been recycled. They can be reused in various applications after being converted to its crumb form. It can either be directly used or can be modified for enhancement in its properties. In this investigation, the mechanical properties of crumb rubber were compared with vulcanized commercial rubbers.

## 2 Materials and Methods

### 2.1 Raw Materials Used

The commercial rubbers (SBR, NBR, and BR) were purchased from Reliance Industries Limited. Crumb tyre rubber was purchased from Manmeet Engineering Works, Chennai. Zinc oxide as activator, stearic acid which plays the role of filler reinforcing material and also as softener, carbon black of N660 grade as a filler and sulphur as a vulcanizing agent were the different ingredients chosen for the present study. Additionally, accelerators like 2,2 dibenzo thiazyl disulphide (MBTS) and tetra methyl thiuram disulphate (TMTD) were also used in this investigation.

### 2.2 Compounding

A formulation was developed as given in Table 1. The ingredients were compounded with the rubber as per the formulation using a two-roll mill manufactured by Ravi Engineering Works, New Delhi. The two rollers were set to rotate at a speed ratio of 1:1.5. The raw rubber was added first into the two-roll mill followed by zinc oxide,

**Table 1** Formulation table

Materials	Parts per hundred rubber (PHR)
Rubber	100
Zinc oxide	5
Stearic acid	15
Carbon black	20
Sulfur	1.5
MBTS	1.3
TMTD	0.2

stearic acid and carbon black. Once the black mixing was completed, the remaining ingredients MBTS, TMTD and sulfur were introduced in the respective order.

### 2.3 Moulding

Once the compounding was finished, the compounded rubber was then placed in a mould of dimensions  $0.15 \text{ m} \times 0.15 \text{ m} \times 0.003 \text{ m}$ . Subsequently, the sheet was formed using a hydraulic press manufactured by Ravi Engineering work, New Delhi, at a temperature of  $160 \text{ }^\circ\text{C}$  and maintaining a constant pressure of  $23.16 \text{ N/mm}^2$ . Similarly, the crumb rubber was moulded into a sheet of same dimensions.

### 2.4 Testing

The mechanical properties of the commercial rubbers were compared to that of crumb rubber. For tensile strength, the sample was cut as per ASTM D412 standards. The value of tensile strength and percentage elongation was determined by using ZwickRoell Universal Testing Machine (UTM) which has a load cell of 2 ton capacity. The hardness of the rubber was studied by using Shore A hardness meter as per the ASTM D2240 standard. Flex test was conducted as per the ASTM D813 standard in a Dematia flex tester manufactured by prolific engineers. The rebound resilience (ASTM D7121) of the rubber sheets was measured by using rebound resilience tester.



### 3 Results and Discussion

#### 3.1 Hardness

The range of hardness values confirms and gives an idea about the specific applications of elastomers. This test is used to estimate the hardness of any sample either rubber or plastic. When subjected to Shore A durometer, the hardness was found to be higher for the crumb rubber sheet than the other three samples. The average hardness after trials was estimated to be 24.19% less in case of BR, 22.03% and 12.9% lower for NBR and SBR sheets, respectively when compared to the average hardness values of crumb rubber. The hardness values depend on the creep strength of the rubber which in turn is directly proportional to Young’s modulus [15]. The Shore A hardness values obtained for different rubbers are shown in Fig. 1.

#### 3.2 Rebound Resilience

Rebound resilience is a test where elasticity and comfort of the material can be revealed [16]. The resilience value depends on the modulus of the material but in an negative way, i.e., resilience is inversely proportional to modulus [17]. This test is used to determine the resilience, a physical characteristic of the rubber sheet prepared in laboratory. On the whole, BR sample was found to have the least value of resilience in the present study. It was found that NBR had twice the resilience value of BR, whereas crumb rubber and SBR had rebound resilience of 2.4 and 3.8 times, respectively, to that of BR. Rebound resilience test results of the rubber samples are shown in Fig. 2.

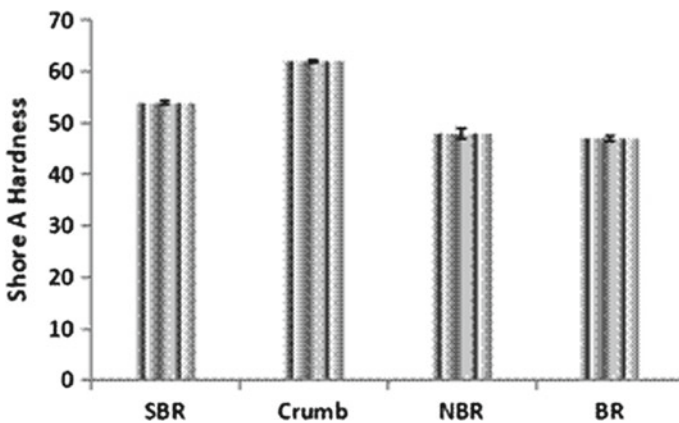
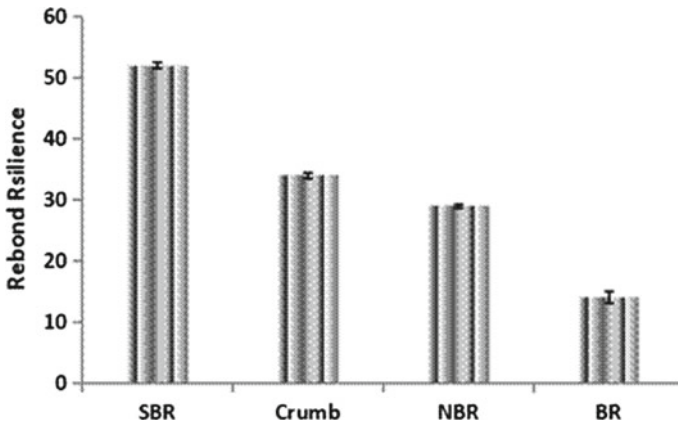


Fig. 1 Shore A hardness values of SBR, BR, NBR and crump rubber samples



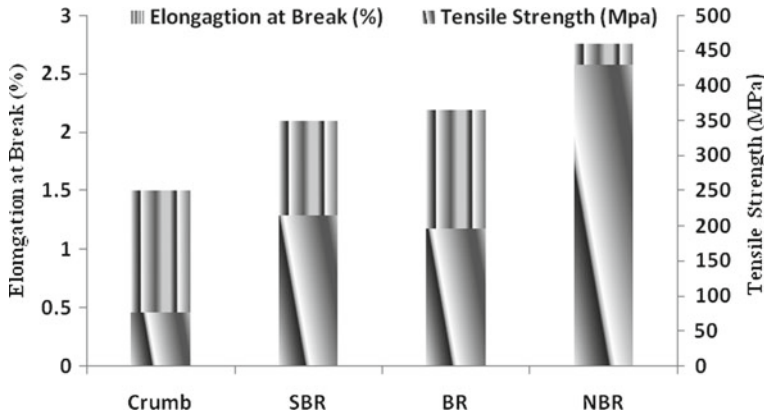
**Fig. 2** Rebound resilience of SBR, BR, NBR, and crump rubber samples

### 3.3 Flex Test

This test reports the number of dynamic loading cycles required for the propagation of the initiated crack. As the specimen is loaded under dynamic condition, there is heat build up on the specimen. This built-up heat causes the propagation of the crack as the number of cycles increases [18]. It was found that the crack was propagated throughout the crumb rubber specimen in a very less time, whereas reached around  $1.1 \times 10^6$  cycles with very less propagation in SBR. The no. of cycles were found to be 50 and 75% for NBR and BR, respectively, lesser in comparison with SBR.

### 3.4 Tensile Strength

Not only for rubbers, in case of any materials, the force pulling the specimen causes stress in the molecules. At the middle of the specimen, stress concentration takes place thereby causing the specimen to break [19]. Tensile strength is the capability of the material to withstand this stress. Any material could bear stress till a particular limit and faces deformation after that. This condition gives a physical property of that particular material which is known as tensile strength [20]. In this test, the amount of load the material can withstand before failure and the % elongation at the break of the specimen were found. From the test, it can be inferred that the tensile strength and the percentage elongation was poor for crumb rubber, while the best results were obtained for NBR with 2.75 MPa. Tensile strength and elongation at break (%) are shown in Fig. 3.



**Fig. 3** Tensile strength and elongation at break (%) of SBR, BR, NBR, and crump rubber samples

## 4 Conclusion

In this study, the crumb rubber was compared with commercial rubbers such as SBR, BR, and NBR after being moulded in terms of their mechanical properties. Tensile strength, hardness, and resilience properties were found to be more in case of crumb rubber than the commercial ones, but show an anomaly by giving least flex strength. The present investigation confirms that crumb rubber can be used for various applications similar to commercial rubbers but not suitable under dynamic loading conditions.

## References

1. Santana MH (2018) Design of a new generation of sustainable SBR compounds with good trade-off between mechanical properties and self-healing ability. *Eur Polym J* 106:273–283
2. Hasma H (1984) Lipids in the latex and rubber of *Hevea brasiliensis* Muell. Arg. and their effects on some properties of natural rubber. Thesis, Rijksuniversiteit Ghent, vol 128
3. Sattayanurak S, Sahakaro K, Kaewsakul W, Dierkes WK, Louis Reuvekamp AEM, Blume A, Noordermeer JWM (2020) Synergistic effect by high specific surface area carbon black as secondary filler in silica reinforced natural rubber tire tread compounds. *Polym Testing* 81
4. Ginting EM, Bukit N, Frida E, Bukit BF (2020) Microstructure and thermal properties of natural rubber compound with palm oil boilers ash for nanoparticle filler. *Case Stud Thermal Eng* 17
5. Synthetic rubber manual, international institute of synthetic rubber producers, 9th edn., Houston, Texas (1983)
6. Wang R, Gao P, Tian M, Dai Y (2019) Experimental study on mechanical and waterproof performance of lightweight foamed concrete mixed with crumb rubber. *Constr Build Mater* 209:655–664
7. Thomas RM, Sparks WJ (1963) Synthetic rubber. In: Whitby GS (ed) Wiley, New York, p 24

8. Hermenegildo G, Bischoff E, Mauler RS, Giovanela M, Carli LN, Crespo JS (2017) Development of chlorobutyl rubber/natural rubber nanocomposites with montmorillonite for use in the inner liner of tubeless ride tires. *J Elastomers Plast* 49(1):47–61
9. Du P, Tuo J, Wang X, Xie S (2019) Research on the properties of compressed rubber sheet gasket reinforced by non-asbestos fiber. In: *IOP conference series: earth and environmental science*, vol 242, no 3, pp 1–5
10. Harmsworth N (1995) Butyl rubber in pharmaceutical applications experience. *Knowl Trends* 48:38–43
11. Terashita F, Takagi S, Kohjiya S, Naito Y (2005) Airtight butyl rubber under high pressures in the storage tank of CAES-G/T system power plant. *J Appl Polym Sci* 95:173–177
12. Morrill JP (1973) Nitrile and polyacrylate rubbers in rubber technology. In: Morton M (ed) 2nd edn. Van Nostrand Reinhold, New York
13. Omran AM, Youssef AM, Ahmed MM, Abdel-Bary EM, Hellipolis Cairo RTL (2010) Mechanical and oil resistance characteristics of rubber blends based on nitrile butadiene rubber. *Elastomers Plastics* 197–202
14. Ansalonia L, Alcock B, Thijs A, Petersa (2020) Effects of CO<sub>2</sub> on polymeric materials in the CO<sub>2</sub> transport chain: a review. *Int J Greenhouse Gas Control* 94
15. Lan H, Venkatesh TA (2014) On the relationships between hardness and the elastic and plastic properties of isotropic power-law hardening materials. *Philos Mag* 94(1):35–55
16. Thilagarajan P, Syed Naveed A, Shamshath Begum S, Abdul Majeed SSM, Vijayarani S, Sindhu KP, Krishnamoorthy V, Gayathiri S (2016) Improvement in the property of flexible polyurethane foam by addition of nano-silica. *IARJSET* 3(5):138–142
17. Bassi AC (1978) Dynamic modulus of rubber by impact and rebound measurements. *Polym Eng Sci J* 18(10):750–754
18. Le Saux VY, Calloch MS, Charrier P, Taveau D (2013) Heat build-up of rubber under cyclic loadings: validation of an efficient demarch to predict the temperature fields. *Rubber Chem Technol* 86(1):38–56
19. Yamamoto G, Onodera M, Koizumi K, Watanabe J, Okuda H, Tanaka F, Okabe T (2019) Considering the stress concentration of fiber surfaces in the prediction of the tensile strength of unidirectional carbon fiber-reinforced plastic composites. *Compos Part A: Appl Sci Manuf* 121:499–509
20. Kaleeswar J, Savio J, Begum S, Abdul Majeed SSM, Vijayarani S, Gayathri R (2015) Studies on flexible polyurethane foam with improved flame retardancy. *Int J Adv Eng Res Dev* 2(5):1–7

# The Addition of Polytetrafluoroethylene (PTFE) and Graphite on Acrylo Nitrile Butadiene Styrene (ABS) and Its Effects on Mechanical and Tribological Characteristics



Basanta Kumar Behera and M. Thirumurugan

**Abstract** The polymeric materials are getting more attention in engineering applications due to its weight reduction, reduced costs and easy handling, and thus the metallic materials are replaced with polymeric materials. Acrylonitrile butadiene styrene (ABS) thermoplastic matrix is blended with the solid lubricant fillers of PTFE and graphite to improve the friction and wear characteristics of neat ABS. The composites were prepared in different weight ratios of graphite powder 3, 6 and 9%, with a fixed 5% PTFE for the all three compositions. The three different weight ratios of graphite were blended with ABS and PTFE by using Berstorff twin screw extruder (German). The microscopic analysis showed well-distributed graphite and PTFE particles in the ABS matrix. The specimens for the mechanical and pin-on-disk tests were prepared using L&T Demag 60 ton injection molding machine. The tensile test showed that addition of graphite fillers in ABS/PTFE composite decreases the mechanical strength. The friction and wear characteristics of ABS/PTFE/graphite composites were found out against steel using a pin-on-disk instrument as per ASTM standard, for the normal load of 10 N and the speed at 1 m/s. The coefficient of friction, specific wear rate and the weight loss of the prepared composite materials are analyzed. Addition of PTFE and graphite in ABS matrix decreases the coefficient of friction, specific wear rate and weight loss up to 3 wt% of graphite.

**Keywords** ABS · PTFE · Graphite · Mechanical properties · Coefficient of friction · Wear rate

---

B. K. Behera (✉)

Department of Polymer Engineering, B.S. Abdur Rahman Crescent Institute of Science and Technology, Chennai 600048, India

e-mail: [bkbehera@crescent.education](mailto:bkbehera@crescent.education)

M. Thirumurugan

Department of Mechanical Engineering, B.S. Abdur Rahman Crescent Institute of Science and Technology, Chennai 600048, India

## 1 Introduction

Polymers and polymer composites are widely used as replacing materials in various fields of aerospace, automobile and construction applications. The polymer composites are subjected to scratch and wear in many applications. Many of the automobile and medical equipment are made from acrylo butadiene styrene (ABS). This material has very good toughness, moderate rigidity and high resistance to heat, chemical and environmental stresses. The selections of materials are important to manufacture bearings, clutches, cams and gears. For these applications, high strength, high modulus, high operating temperature environment, low coefficient and good wear resistant polymers are required. Pure ABS material alone cannot meet all these requirements, and the additions of fillers can improve the friction and wear behavior of polymer materials without much compromise on mechanical properties. When fillers are added in polymer, the resultant material is known as polymer composite.

The polytetrafluoroethylene (PTFE) contains carbon fluorine compounds, which has the characteristics of high melting point, high strength, self-lubrication and protection from all chemicals and water. PTFE finds in many applications including sliding activity of parts like bearings, gears and medical equipment. The PTFE materials do not have a layered structure, and the coefficient of friction of PTFE is very low compared to many other solid lubricants. The graphite has layered structure which is also a solid lubricant can able to reduce the friction between two sliding surfaces. The graphite materials can operate up to a higher temperature.

Better tribological properties can be obtained for polymers filled with nanoscale fillers compared to that filled with microscale particles. As a result, the friction and wear resistance of these composites are found to increase with increasing filler concentration [1].

During last few years, many researches were made with the different polymer composites with ABS, PC and PEEK as matrix and added the different types of fillers such as PC, Mica, PTFE, ZnO, short carbon fiber (SCF), graphite flakes, OMMT, TiO<sub>2</sub> and Zn to improve the tribological properties. The increase in wt. percentage of graphite in ABS composite decreases the mechanical properties. The addition of graphite particles in ABS matrix exhibits lower coefficient of friction and weight losses [2].

It was found that the surface treated mica fillers in PC/ABS composites reduce the tensile strength, elongation at break and impact properties [3]. The PTFE blended ABS polymer composites, the addition of PTFE particles increased the interfacial bonding between polymer matrix and fillers and enhanced the self-lubrication properties like mass loss, specific wear rate and coefficient of friction [4]. The mechanical and tribological properties of ABS/ZnO polymer composites are improved due to the addition of filler material [5].

The combination of ABS, PTFE and graphite composites can be useful for the tribological applications with the enhanced mechanical properties. In this work, the aim is to fabricate the ABS/5%PTFE composites with varying concentrations of graphite (3, 6 and 9 wt%) and to analyze the mechanical and tribological properties of the composites.

## 2 Experimental Methods

### 2.1 Raw Materials and Sample Preparation

Matrix material ABS (granular form) was purchased from Formulated Polymers Limited, Chennai, Tamil Nadu, India. PTFE (powder 30  $\mu\text{m}$ ) and graphite (powder 70  $\mu\text{m}$ ) were procured in powder form a chemical supplier Chem O Chem, Chennai, Tamil Nadu, India.

### 2.2 Formulation

Table 1 shows the composition of ABS/PTFE/Graphite composites.

**Table 1** Different compositions of ABS/PTFE/graphite composites

S. No.	Sample code	Composition
1	A0	Neat ABS
2	APG3	ABS + 5%PTFE + 3%Graphite
3	APG6	ABS + 5%PTFE + 6%Graphite
4	APG9	ABS + 5%PTFE + 9%Graphite

**Table 2** Specifications of the twin screw extruder

Length in mm	4000
Weight approx. (kg)	3500
Output in kg/hr	40
Flight depth in mm	7.1
<i>L/D</i> ratio	38
Max. screw speed in rpm	450
Drive power in KW	146
Torque in Nm	$2 \times 580$

### 2.3 Compounding of ABS/PTFE/Graphite

The raw materials of ABS and PTFE materials were dried in an oven (Vijaya Scientific company, Chennai, India, of size  $300 \times 300 \times 300$  mm, 800 W and temperature ranges from 50 to 250 °C) at 80 °C for 4 h to remove the moisture content. Then the fillers were added manually to the ABS matrix as 5% of PTFE and 3, 6 and 9% of graphite powder in wt%. The mixed ABS/PTFE/graphite mixture was then fed into Berstorff Twin Screw Extruder (Make: German), and the specifications of extruder are given in Table 2. The temperature ranges in the extruder were maintained between 220 and 260 °C, and the speed of the rotating screw was maintained at 250 rpm. Then the different concentrations of ABS/PTFE/graphite mixtures were extruded through the die, and then the extruded mixture was cooled in the water bath. The cooled extruded mixture was then passed through pelletizer to make constant size granules.

### 2.4 Injection Molding Procedure to Prepare Sample

The ABS/PTFE/graphite composite granules were fed into injection molding machine (Make: L&T DEMAG 60 tonnage capacity, Department of Polymer Engineering, B.S. Abdur Rahman Crescent Institute of Science & Technology, Chennai) through hopper. Before the compounded material was fed into the hopper of injection molding machine, the composite granules were pre-dried at 80 °C for 3 h. The injection pressure was set at 85 bar, and the holding pressure was maintained at 50 bar for 30 s to fill the cavities. The temperatures of the three zones in the injection molding machine were maintained at 210, 230 and 240 °C. The required test (tensile strength, hardness, elastic modulus, flexural strength, impact strength) samples were prepared using a family type two plate injection mold. The samples of required dimensions (as per ASTM standards) were obtained by injecting the composite into the mold (Fig. 1).





**Fig. 1** Injection molding machine to prepare the samples as per ASTM standards



**Fig. 2** Universal testing machine to conduct tensile tests of samples

## ***2.5 Tensile Test Procedure***

To analyze the mechanical characteristics of the ABS/PTFE/graphite composites, it is necessary to measure the tensile strength, hardness, flexural strength and impact strength for the end use applications. The tensile test of the prepared composites was found out using a universal testing machine (Kamal Metal Industries, India, model UTM 201 of 5 ton capacity in the department of Polymer Engineering) as per the ASTM D638 standard and the speed of the cross-head was 50 mm/min. The nominal dimensions of the specimen were 170 mm  $\times$  10 mm  $\times$  4 mm. The load and displacement values were measured from the universal testing machine, and the tensile strength was calculated (Figs. 2 and 3).

## ***2.6 Flexural Test Procedure***

The flexural strength of the prepared samples was measured as per ASTM D790 standard. The same cross-head speed was maintained, and the nominal dimensions

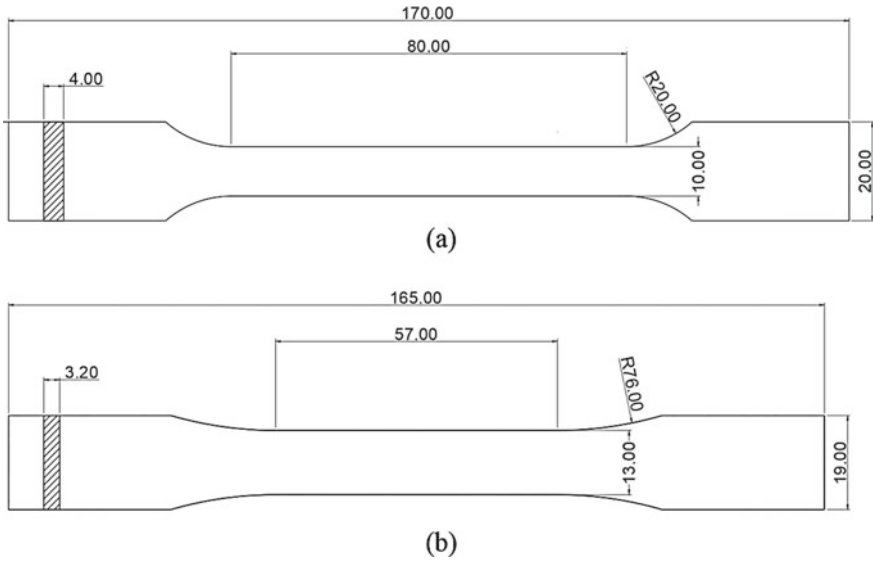


Fig. 3 a and b Standard tensile test specimen of the prepared composite

of the specimen were 165 mm length  $\times$  10 mm width  $\times$  3.2 mm thickness for which gauge length was kept as 57 mm (Fig. 4).

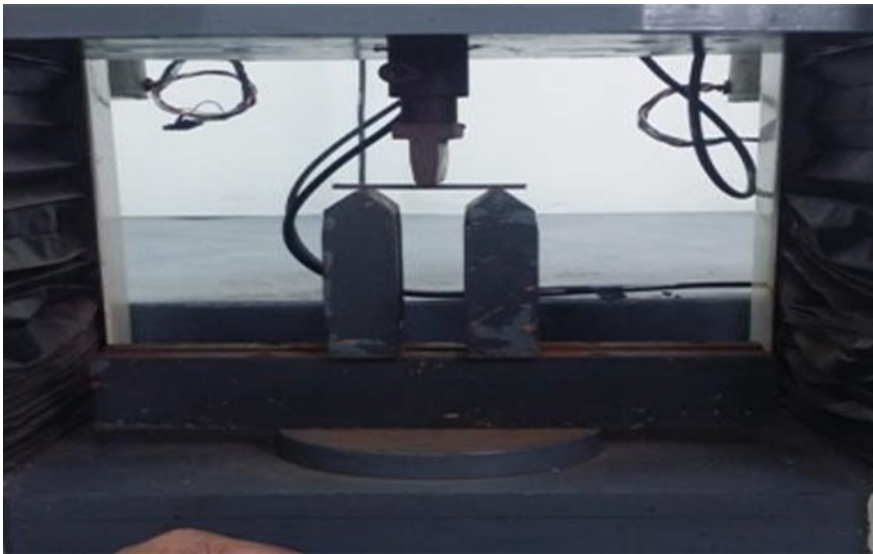
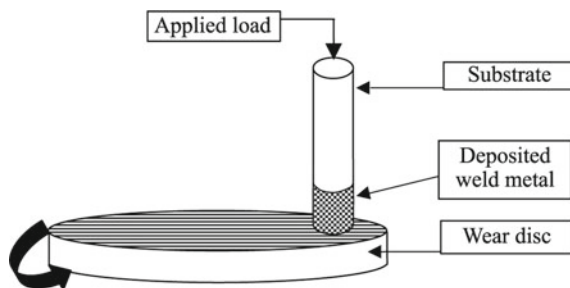


Fig. 4 Universal testing machine to conduct flexural test of composite

**Fig. 5** Pin-on-disk (2D sketch)



## 2.7 Impact and Hardness Test Procedure

The impact strength of the prepared samples was found out using Charpy Izod impact test machine available in the Plastic Testing Laboratory in the department of Polymer Engineering, B. S. Abdur Rahman Crescent Institute of Science & Technology, Chennai, India, according to standard ASTM D256. The nominal dimension of the specimen was 80 mm × 10 mm × 3 mm.

## 2.8 Wear Analysis

Wear analysis was performed on pin-on-disk equipment type friction and wear monitoring test rig as per ASTM G 99. The counter body was a disk made of hardened ground steel. The specimen is held stationary, and disk was rotated while a normal force is applied through a lever mechanism. Circular specimen of diameter 10 mm and height 30 mm was prepared, and the surface roughness of the specimen was 0.8 μm (Figs. 5 and 6).

## 3 Result and Discussion

### 3.1 Tensile Strength of ABS Polymer Composites

The tensile strength of neat ABS composite and the composites with addition of 5% (wt%) PTFE and 3, 6, 9% (wt%) graphite fillers were evaluated with an universal testing machine. The effects of various wt% of graphite are shown in Fig. 7, and the results show that the tensile strength of ABS/PTFE/graphite composites decreases with increase amount of graphite fillers. The tensile strength of neat ABS is 32 MPa, and it decreases to 30 MPa, 29 MPa and 28 MPa, respectively, for APG3, APG6 and APG9 samples, when the percentage of PTFE filler was maintained constant at 5 wt%. The tensile strengths of specimen show that due to the addition of graphite



Fig. 6 Pin-on-disk tester

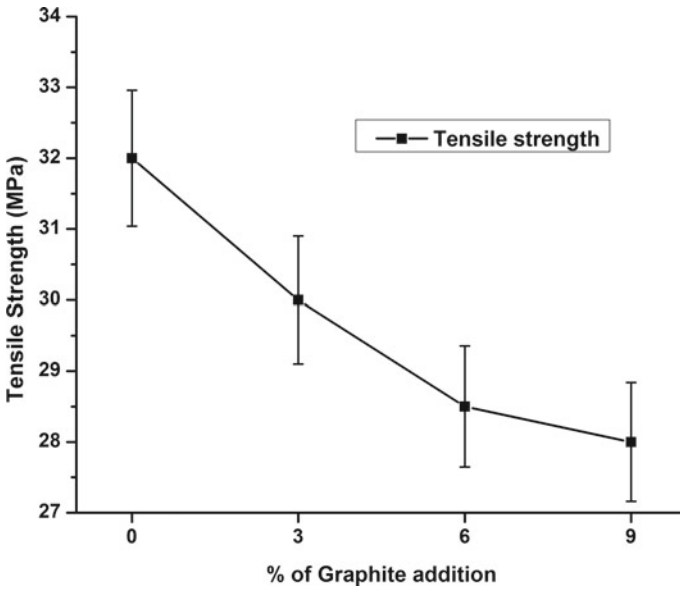


Fig. 7 Tensile strength versus wt%age of graphite graph

filler, the tensile strength of ABS/PTFE composite is reduced by a small margin. It is due to poor chemical bonding between the matrix and fillers of PTFE and graphite. The addition of the fillers may also increase the agglomeration, and it reduces the tensile strength of the composites.

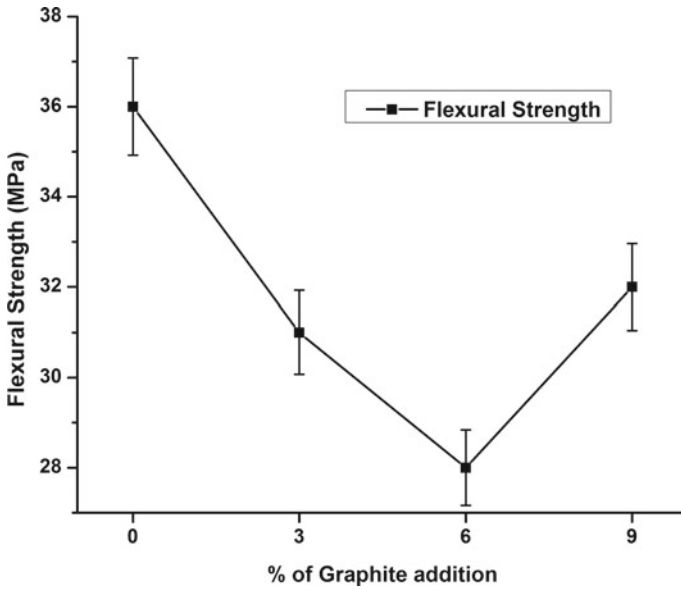


Fig. 8 Graph of flexural strength versus w %age of graphite

### 3.2 Flexural Strength of ABS Polymer Composites

The flexural test specimens were prepared in injection molding using reciprocating screw injection machine. The flexural strength of the composites found out from flexural test is shown in Fig. 8, and the plotted graph shows that the flexural strength of neat ABS is 36 MPa. The flexural strength decreases from 31 to 29 MPa for APG3 and APG6 composites. But the magnitude of flexural strength increases to 33 MPa.

### 3.3 Impact Strength of ABS Polymer Composite

The impact strength of the prepared composite was determined using ASTM D256 standard method. In this method, the impact strength of prepared sample calculated through the amount of energy absorbed by the material. The impact strength of neat and composites filled with PTFE and graphite fillers was measured using Charpy Izod test, and the results obtained are shown in Fig. 9. From the result, it is observed that the PTFE and graphite fillers in ABS matrix have significant effect in the impact strength of ABS/PTFE/graphite composite. The impact strength of neat ABS is 0.8 J/cm, and the value decreased as the %age of fillers increased. The impact strength is 0.25 J/cm for APG3 (5% of PTFE), and there is a small increment in the impact strength for APG9 composites.

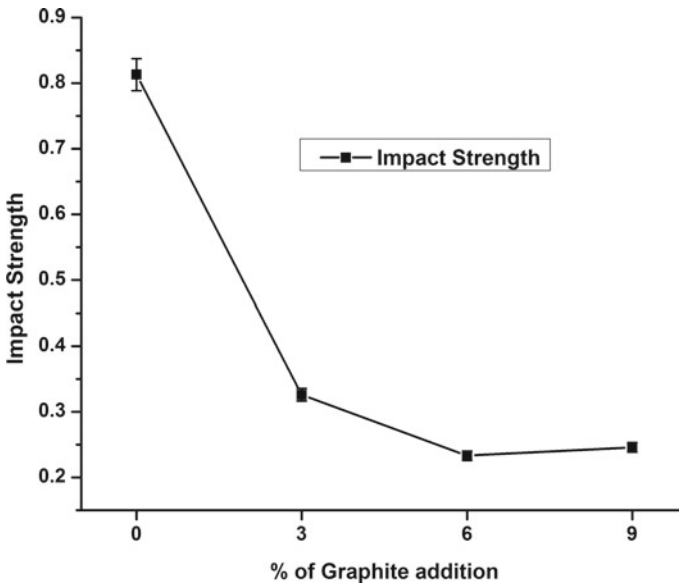


Fig. 9 Graph of impact strength versus wt%age of graphite

### 3.4 Hardness of ABS Polymer Composite (Shore D)

It is an ASTM D2240 standard method of determining hardness of plastic materials. The hardness of neat and filled composites is presented in Fig. 10. The graph indicates that the hardness of PTFE/graphite composites decreases gradually with increase in the wt. %age of filler content. The hardness values of neat A0, APG3, APG6 and APG9 are 83, 82, 81 and 79, respectively. The hardness values are presented in Fig. 10 as shown.

### 3.5 Result of Tribological Properties for ABS Composites

The friction and wear characteristics of the composite samples were found out using a pin-on-disk apparatus. Figures 11, 12 and 13 show the mass loss, coefficient of friction and specific wear rate of neat and filled (5% PTFE + 3%, 6% and 9% graphite) composites. The mass loss of neat ABS is 0.021 g. But the mass loss is reduced with increase amount of filler percentage in the composite. The mass loss is the lowest of 0.013 g for APG3, and there is an increase in mass losses for APG6 and APG9. The specific wear rate has a similar trend like the mass losses. The specific wear rate decreased up for APG3, and then there is increase in specific wear rate for APG6 and APG9. The coefficient of friction of the composites is presented in Fig. 12, it reveals that there is high coefficient of friction of unfilled composite (neat

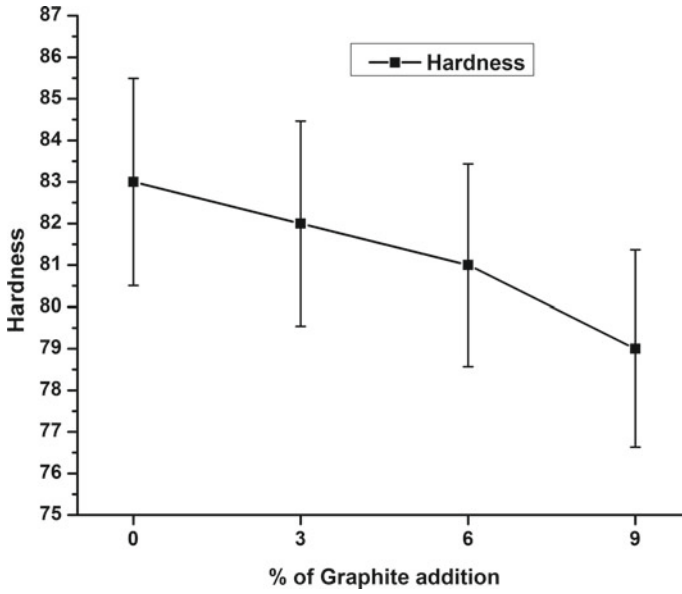


Fig. 10 Graph of hardness versus wt%age of graphite

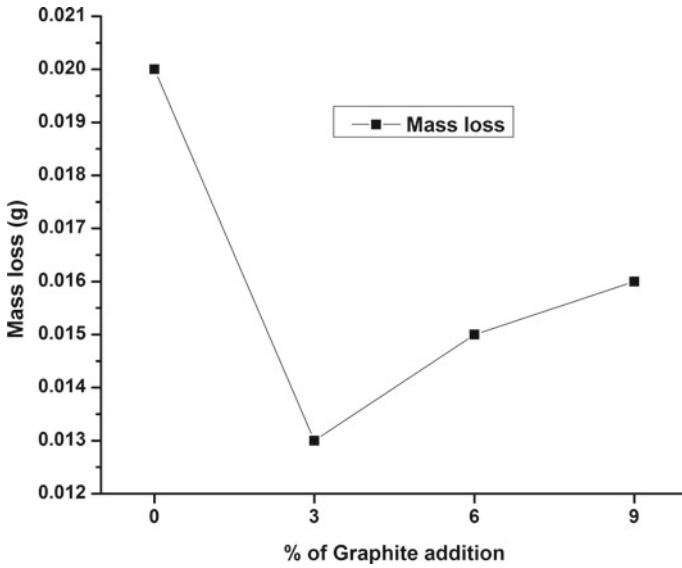


Fig. 11 Graph of mass loss versus wt%age of graphite

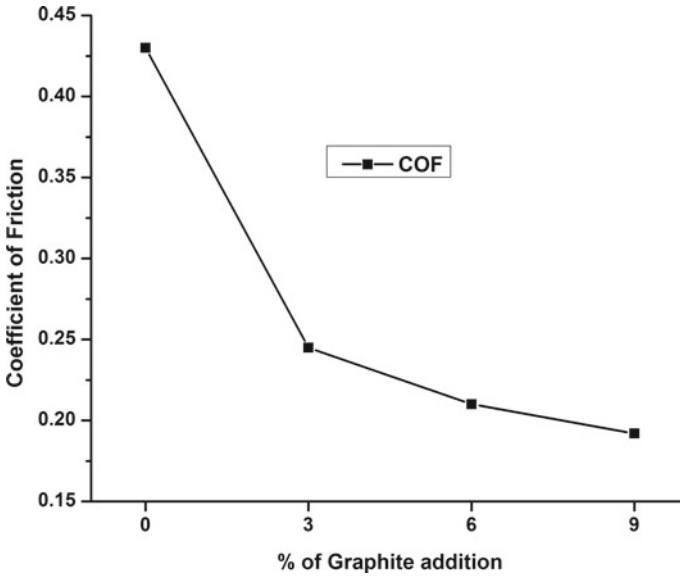


Fig. 12 Graph of coefficient of friction versus wt%age of graphite

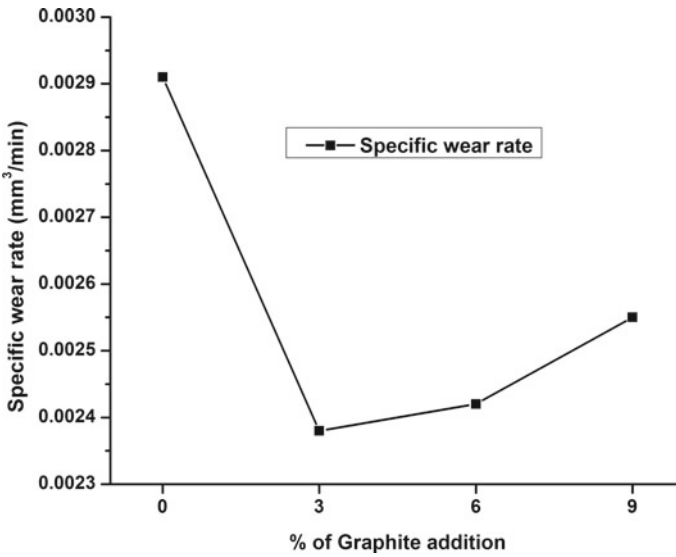


Fig. 13 Graph of specific wear rate versus %age of graphite



ABS) of more than 0.4, and as the percentage of graphite filler content increases (5% PTFE), the value of coefficient of friction decreases. The coefficient of friction is the lowest for APG9.

## 4 Conclusion

Various weight percentages (3–9%) of graphite filler were added in acrylonitrile butadiene styrene ABS/PTFE (5% wt). ABS/PTFE/graphite composites were compounded in twin screw extruder for proper mixing, and samples for mechanical and tribological characterization were prepared using fully automatic injection molding machine. The mechanical and tribological characteristics of the prepared composite were investigated systematically. The mechanical properties of the composite were tested in universal testing machine, and Charpy and Izod instruments were used to measure the impact strength. The test results revealed that with increase in graphite powder in ABS/PTFE, it reduced the tensile, flexural, hardness and impact strength. The friction and wear characteristics of the composites were measured using pin-on-disk instrument as per ASTM standard. The results for wear test indicate that the increased percentage of graphite powder reduces the coefficient of friction approximately by 50%. But the mass loss and the specific wear rate of the prepared composites were reduced up to 3 wt% of graphite and again increased slightly at 6 and 9 wt% of graphite. From the results, it can be concluded that the addition of solid lubricants like PTFE and graphite changes the tribological properties, and the composite can be recommended for tribological applications in automotive and other industries.

## References

1. Alay AA (2012) Friction and wear of polymer composites filled by nano-particles: a review, *World. J Nano Sci Eng* 2:32–39
2. Ben Difallah B, Kharrat M, Dammak M, Monteil G (2012) Mechanical and tribological response of ABS polymer matrix filled with graphite powder. *Mater Des* 34:782–787
3. Asyadi F, Jawaid M, Hassan A, Wahit MU (2013) Mechanical properties of mica filled polycarbonate/poly(acrylonitrile butadiene styrene) composites., *Polym Plastics Technol Eng* 52:727–736
4. Maheshkumar R, Rajini N, SenthilMuthukumara T, Mayandi K, Siengchin S, Ismail SO (2019) Thermal and structural characterization of ABS copolymer blends with PTFE particulate composite. *Mater Exp* 6:085330
5. Sudeepan J, Kumar K, Barman TK, Sahoo P (2015) Study of mechanical and tribological properties of ABS/ZnO polymer composite 181–183(2):624–631

# Design of Automotive Firewall Based on Thermal Analysis



M. Karthikeyan  and M. Venkatesan 

**Abstract** The function of the automotive firewall is to insulate the heat and damp the vibrations occurring from the engine, and it also protects the passenger compartment by resisting the intrusion of the engine noise. The proposed work is to create a double-walled firewall made of glass fiber-reinforced polypropylene (GFRP) with sandwiched honeycomb structure than the pressed steel plate which conventionally used. GFRP found to have better thermal properties than the pressed steel plate, it has a high strength-to-weight ratio, corrosion and thermal resistance have less dense. The cavity between the two plates is filled with ‘honeycomb’ structure, and it has excellent sound and vibration damping characteristics because of the high-volume fraction of void space within each cell. The study shows that using GFRP was thermally more stable than the single-walled firewall, which made up of pressed steel. The density of the GFRP is lesser than that of pressed steel, and using GFRP reduces the weight of the firewall structure, which in turn improves the efficiency of the vehicle.

**Keywords** Firewall · GFRP composites · Honeycomb structure

## 1 Introduction

The current automotive vehicle designers focus on passenger comfort, safety, and reducing fuel consumption by various methods. One of the methods improving these functions is reducing the temperature inside the passenger cabin [1]; this study carried out to reduce the thermal conductivity of under hood which affect the comfort level of passenger shows improvement needed in the passenger cabin in thermal aspects. The current study focuses on reducing the thermal conductivity of the firewall.

The firewall of a car connects to the under hood and chassis which separates the engine and the passenger cabin. It serves many purposes, as a heat insulator for the

---

M. Karthikeyan (✉) · M. Venkatesan  
School of Mechanical Engineering, SASTRA Deemed to be University, Thanjavur, India  
e-mail: [karthikeyan@mech.sastra.edu](mailto:karthikeyan@mech.sastra.edu)

M. Venkatesan  
e-mail: [venkatesan@sastra.ac.in](mailto:venkatesan@sastra.ac.in)

passenger cabin from the intense heat of the engine, and as protection during the incidence of fire [1]. It prevents the intrusion of the engine parts into the passenger cabin at the time of the collision and transfers the load to underbody and chassis structure to reduce cabin displacement; thus, the firewalls form a crucial part of a car's unibody crash-protection 'cocoon.' [2], and also it helps to reduce the vibration and noise transfer from the engine [3]. Most of the studies focus on acoustic control of firewall [4, 5], the panel and firewall have the most contribution to the noise transfer [4], which shows improvement needed in firewall in terms of noise control. The comparison of double steel plate with viscoelastic material and single plate one side with viscoelastic material the quasi steel plate shows more damping at resonant condition [6] and developed an active control of firewall to reduce the noise transferred to the passenger compartment with input as velocity feedback with inertial actuator and positive position feedback with piezoelectric actuator; both methods are able to damp the noise [7]. An experiment on the thermal parameter for layered material and compound material using fiber glass and aluminized silica as insulating material with the steel plate which resembles a firewall, the paper suggests that instead of analyzing it as a layered material compound material gives a comparable result with the experiment [8].

The idea is to develop a double-walled composite firewall sandwiched honeycomb structure, the purpose of using composite material is weight reduction and higher damping factor. Several studies show that fiber reinforcement polymers (FRP) has high strength, damping characteristics, resistance to heat transfer, impact and wear [9], matrix composites rely on the bond strength between the matrix and fiber. The bond strength may manipulate to enhance the toughness by absorbing energy in interface debonding [10]. The firewall with composite material provides increased protection against engine intrusion at the time of the collision. It has various application; In civil, GFRP concrete is used for fire resistance [11], and in automobile, parts made up of composite material show not only the weight reduction and also enhance the stability and strength [9, 12], the honeycomb structure provides better heat insulation made of plastic filled with microspheres [13], double-walled firewall sandwiched with honeycomb structure is comparatively more heat can be insulated, and noise from engine can be damped. So that the passenger will experience an even more comfortable ride. From the above works of literature, thermal analysis of firewall is having minimum work. This study conducted on a novel design of thermal analysis of double-walled composite sandwiched firewall.

## 2 Modeling of Firewall

The dimensions of the firewall taken from the reference of Honda City from the Honda forum website. The dimension is  $1700 \times 2 \times 401.25$  mm. The part drawing of this design done in Creo Parametric Software concerning the corresponding dimensions Fig. 1a. With the same dimensions, another wall projected in front of the previous firewall at a distance of 10 cm Fig. 1b.

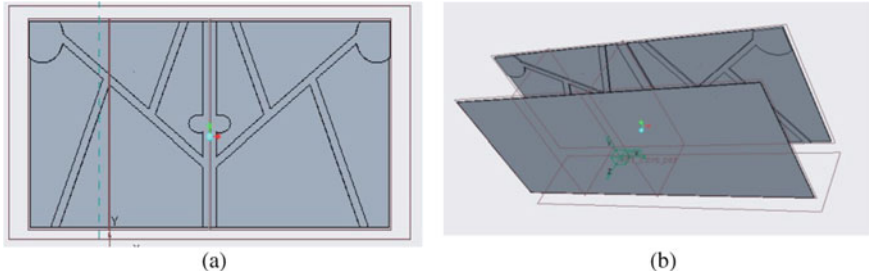


Fig. 1 Double-walled composite firewall

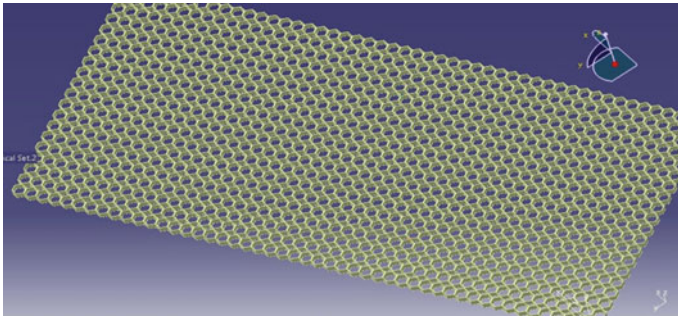


Fig. 2 Hexagonal honeycomb structure

### 3 Development of Honeycomb Structure

The gap between the firewalls filled by constructing a hexagonal honeycomb structure between plates Fig. 2. Mechanical properties of honeycombs are anisotropic: Tensile and compressive strengths are greatest in a direction parallel to the cell axis. Honeycomb structures also have excellent sound and vibration damping characteristics because of the high-volume fraction of void space within each cell. The void space has filled with ‘filler material’—composite foam. Composite foam is an excellent acoustic insulator, temperature-resistant, permanently elastic, excellent absorber of impact energy.

### 4 Simulation of Firewall

After the completion of the part drawing, the model imported to ANSYS for thermal analysis. Thermal analysis in ANSYS is done through the steady-state thermal condition. Conduction equation is used to solve the analysis with four assumptions: (1) Heat is transferred in steady-state, heat transfer occurring with respect to space, (2)

thermal conductivity is constant, (3) heat flow in a single direction, and (4) there is no heat generation and storage. The analysis was done by solving the conservation of energy Eq. (1).

$$\rho c \frac{\partial T}{\partial t} = \frac{\partial}{\partial x} \left[ k \frac{\partial T}{\partial x} \right] \quad (1)$$

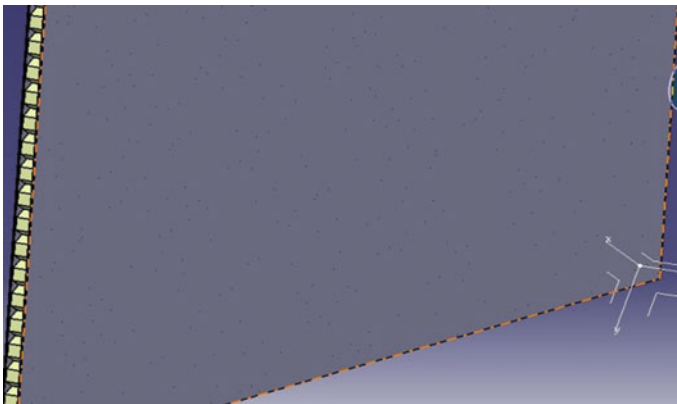
And then if we consider the assumption, the equation will be

$$\frac{\partial^2 T}{\partial x^2} = 0 \quad (2)$$

Then by applying the boundary condition  $x = x_0$  and  $T(x) = T_0$   
By solving the Eq. (2), we will get the heat transfer,

$$\dot{Q} = -kA \left[ \frac{\partial T}{\partial x} \right]_{x_0} \quad (3)$$

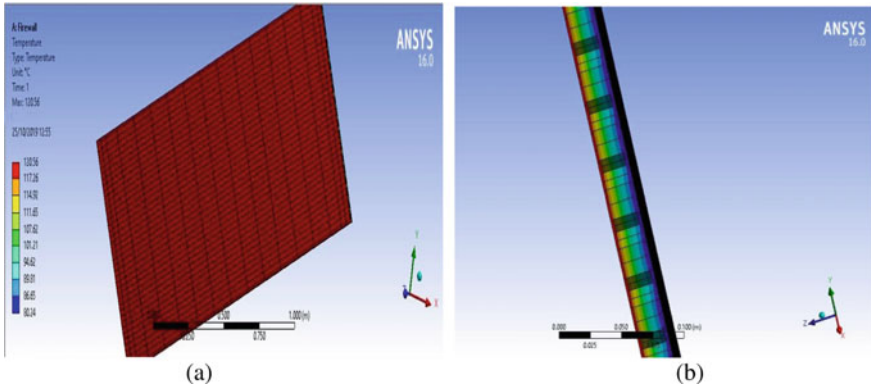
The above equations are solved using the finite element method. Required constraints are given, namely temperature and heat flow, perfectly insulated in other dimensions shown in Fig. 3. Temperature is given to the surface where heat is going to be faced (engine side firewall), and the magnitude of the temperature is given say 120 °C. Convection is given to all the surfaces except the temperature facing the region. Film coefficient is given by selecting ‘Stagnant air simplified case.’ After all the constraints were given, the solution is obtained by selecting thermal, total heat flux, and directional heat flux. The same procedure is to be followed for the thermal analysis of conventional (single-walled) firewall. Material is chosen as pressed steel, and the properties are given for analysis Table 1. All the constraints are given as same as for the double-walled firewall of 20% glass fiber-reinforced polypropylene.



**Fig. 3** Assemble view of double-walled firewall

**Table 1** Properties of materials

Properties	Pressed steel	GFRP
Density (g/cm <sup>3</sup> )	7.85	2.58
Tensile Strength (Mpa)	1020	420
Poisson’s ratio	0.29	0.21
Thermal conductivity (W/mK)	46	0.2



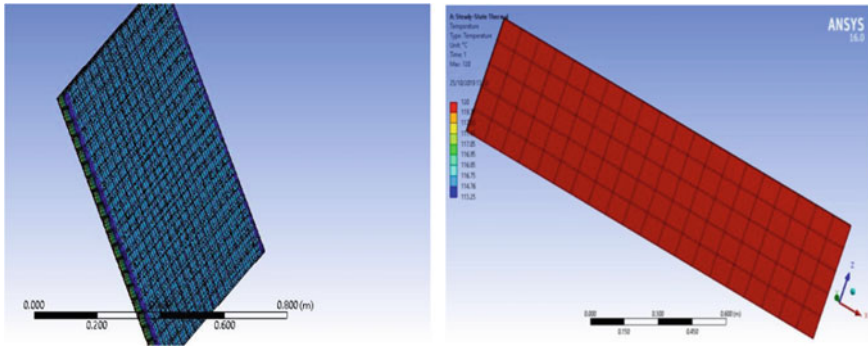
**Fig. 4** Frontal view and heat reduction of double-walled firewall

**Table 2** Passenger-side temperature in firewall

Single-walled firewall (°C)	Double-walled firewall (°C)
120	120
119.75	117.26
117.25	114.92
117.15	111.65
117.05	107.62
116.95	101.21
116.85	94.62
116.75	89.81
114.76	86.65
113.25	80.24

## 5 Result and Discussion

It has been found from thermal analysis when using GFRP as a material for firewall, the temperature has been reduced. The convective heat transfer makes the double-walled firewall to release more amount of heat. Initially, temperature from the engine hitting the firewall is given as 120.56 °C. After passing through the subsequent



**Fig. 5** Frontal view and heat reduction in single-walled firewall

honeycomb structure and passenger side firewall, the temperature observed was 80.24 °C.

Figure 4 shows the frontal side of the double-walled firewall. Heat transfer has been observed in Fig. 4b, and the reduction in the temperature is observed through yellow, green, cyan, and blue fringes. Figure 5 shows the analysis done for the single-walled (conventional) firewall, and the temperature difference obtained is only around 7 °C. Initially, as like the same given for the double-walled firewall, the temperature on the engine side firewall is given as 120 °C. The temperature received on the passenger side firewall is 113.25 °C.

The above results from the analysis clearly show that firewall incorporated with GFRP as the core material has better thermal reduction characteristics when compared to the firewall using pressed steel as its core material. The temperature difference was about 40 °C for double-walled firewall whereas; it was only 7 °C as the difference for the conventional firewall. Even in the cars which are using a conventional firewall, the passenger doesn't feel any heat inside the cabin and even at the back of the gas pedal. By using double-walled firewall, we will have even more insulated cabin and the workload given for air-conditioning system is considerably reduced which in turn increases the efficiency of the vehicle. The effect of double-walled composite firewall is shown in Table 2

## 6 Conclusion

Thus, the double-walled firewall modeled by inserting honeycomb between the structure and the thermal analysis has been done. The obtained result from the analysis proved that the double-walled firewall constructed using GFRP was thermally more stable than the single-walled firewall which is made up of pressed steel. The density of the GFRP is lesser than pressed steel thus reduces the weight of the firewall structure which in turn improves the efficiency of the vehicle. In addition to the heat of

insulation, dampening of the vibrations occurring from the engine would happen. It also protects the passenger compartment by resisting the intrusion of the engine noise.

## References

1. Misciagna DT, Landi DJ (2005) Integrated ceramic composite firewall. SAE Tech Pap. <https://doi.org/10.4271/2005-01-3430>
2. Dwivedi P, Kulkarni A, Chalipat S, Pardeshi M (2011) Protection devices to improve frontal pendulum impact performance of heavy commercial vehicles. SAE Tech Pap 1–9. <https://doi.org/10.4271/2011-26-0099>.
3. Shivle S, Murthy AV (2010) Improvement in noise transmission across firewall of a passenger car. SAE Tech Pap. <https://doi.org/10.4271/2010-01-0751>
4. Mahale PS, Kalsule DJ, Muthukumar A, Raju S (2005) Vehicle interior noise source identification and analysis for benchmarking. SAE Tech Pap <https://doi.org/10.4271/2005-26-048>
5. Florentin, J., Durieux, F.: A Steel Solution for a Firewall Using a Hybrid Test / CAE Approach Yukihiisa Kuriyama and Toyoki Yamamoto. (2018).
6. González M, Jordan R, Gerges SNY (2008) Modeling of firewall panel with laminated metal using experiment and numerical methods. SAE Tech Pap. <https://doi.org/10.4271/2008-36-0514>
7. Haase F, Kauba D, Mayer D, van der Auweraer H, Gajdatsy P, de Oliveira L, Sas P, Deraemaeker A (2008) Active vibration control of an automotive firewall for interior noise reduction. Proc Adapt Congr
8. McMasters RL IV, Wichman IS (2002) Compound material thermal parameters for a layered material resembling an automobile firewall. Heat Transf Eng 23:44–56. <https://doi.org/10.1080/01457630290090491>
9. Senthilvelan S, Gnanamoorthy R (2006) Fiber reinforcement in injection molded nylon 6/6 spur gears. Appl. Compos. Mater. 13:237–248. <https://doi.org/10.1007/s10443-006-9016-9>
10. Andrew JJ, Srinivasan SM, Arockiarajan A, Dhakal HN (2019) Parameters influencing the impact response of fiber-reinforced polymer matrix composite materials: a critical review. Compos Struct 224. <https://doi.org/10.1016/j.compstruct.2019.111007>.
11. Correia JR, Bai Y, Keller T (2015) A review of the fire behaviour of pultruded GFRP structural profiles for civil engineering applications. Compos Struct 127:267–287. <https://doi.org/10.1016/j.compstruct.2015.03.006>
12. Osborn CJ, Kennedy JM (2004) Integrating advanced composite materials into the chassis of a sports car. Am Soc Mech Eng Des Eng Div 117:915–932. <https://doi.org/10.1115/IMECE2004-61865>
13. Ryzhenkov AV, Lapin EE, Loginova NA, Sitdikov DR, Grigor'ev SV (2016) Evaluation of the thermal efficiency of a high-temperature heat-insulation structure based on honeycomb plastic. Therm Eng 63:445–448. <https://doi.org/10.1134/S0040601516060057>



# Mechanical Characteristics of Paraffin Wax, Beeswax and HTPB as Rocket Propellant—A Comparative Study



Vanchhit Kumar Dubey, Sri Nithya Mahottamananda,  
Afreen Abdul Khaleel, P. N. Kadiresh, and M. Thirumurugan

**Abstract** Waxes and hydroxyl-terminated polybutadiene (HTPB) are identified as a feasible and efficient replacement for conventional rocket fuels and are capable of providing good mechanical and thermal performances with good structural stability. In this work, paraffin wax, beeswax and HTPB are taken for the analysis of the mechanical characteristics. These materials were tested to understand their grain structure, quality and mechanical strength. The scanning electron microscope (SEM) examination was carried out to analyze the surface and morphological characteristics. The purity of the samples was confirmed through FTIR spectrum analysis. The HTPB revealed the clear and distinct grain structure and morphology, whereas the beeswax and paraffin wax showed the traces of pellets with small microcracks. The beeswax exhibited the highest density compared to paraffin wax and HTPB. Tensile strength of pure paraffin recorded the maximum value of  $102.311 \times 10^4 \text{ N/m}^2$  and Young's modulus of  $116.3 \times 10^6 \text{ N/m}^2$ . Tensile strength and Young's modulus values of beeswax were recorded as  $93.96 \times 10^4 \text{ N/m}^2$  and  $36.63 \times 10^6 \text{ N/m}^2$ , respectively. The HTPB has shown the lowest tensile strength properties compared with the other two materials with the highest elongation rates.

**Keywords** Beeswax · Paraffin wax · HTPB · Tensile test · Young's modulus · Stress · Strain · FTIR · SEM

## Nomenclature

HTPB Hydroxyl-terminated polybutadiene  
FTIR Fourier transform infrared spectroscopy

---

V. K. Dubey (✉) · S. N. Mahottamananda · A. A. Khaleel · P. N. Kadiresh  
Department of Aerospace Engineering, B.S.Abdur Rahman Crescent Institute of Science and  
Technology, Chennai 600048, India  
e-mail: [vanchhitdubey@gmail.com](mailto:vanchhitdubey@gmail.com)

M. Thirumurugan  
Department of Mechanical Engineering, B.S.Abdur Rahman Crescent Institute of Science and  
Technology, Chennai 600048, India

SEM Scanning electron microscope  
UTM Universal testing machine  
ASTM The American Society for Testing and Materials

## 1 Introduction

In the primitive days, usage of gasoline and other jet fuels for rocket engine combustion was predominant. But conventional liquid fuels pose a large number of complications and complexities such as storage problems and handling issues. As an alternative, gaseous fuels were used for a certain period of time, but they too have several disadvantages. Gases require more storage space due to higher volume, leading to an unnecessary increase in total weight of the rocket body. To overcome these issues, enormous researches are being done on fuels, and one such discovery was hybrid fuels which came into the picture outweighing the usage of solid and liquid fuels. Hybrid rocket exhibits several advantages compared to solid and liquid rockets [1]. Hybrid rocket fuels have a booming future in space applications.

Solid hybrid fuels exhibit several advantages when used as rocket fuels. They are convenient to store, carry and portable in nature. On the other hand, they also serve as reinforcing structural member to rocket body, providing rocket body with better structural integrity [2]. Like two sides of a book, the solid propellants pose certain limitations. They have low combustion efficiency, low volumetric efficiency and low specific impulse with zero throttling [3–8]. But all these limitations are negligible, comparing the structural integrity and better handling properties that are achieved by the usage of the hybrid propellants. Few researchers tried to improve the mechanical properties of paraffin wax and HTPB [9, 10], but fuels required mechanical properties were needed more exploration. Present work involves the comparison of mechanical properties of HTPB, paraffin waxes and beeswax such as analysis of tensile strength, percentage of elongation and Young's modulus of prepared fuels samples. The surface morphology and chemical composition of fuel samples were analyzed using scanning electron microscope and FTIR spectra.

## 2 Experimentation

### 2.1 Preparation of Fuel Samples

Test specimens were prepared with paraffin wax and beeswax. The preparation was carried out by hammering the wax crystals into small pieces followed by melting to a melting temperature is in the range of 60–70 °C. The reason of choosing this temperature range is that above this temperature there is a good probability of vaporization. The melted waxes were casted into dog bone shape samples in a mold with

gradual cooling in room temperature. The HTPB fuel sample was prepared with necessary ingredients and cured with 55 °C because it has lower melting temperature than paraffin wax and beeswax. The chemical compositions of prepared fuel were analyzed using FTIR.

## 2.2 Density Test and Surface Morphology Experimentation

The prepared samples were tested for quality and ability to provide better thrust properties. The density test of these samples was performed using Archimedes principle, and the reference fluid used was ethanol (density 789 kg/m<sup>3</sup>). The surface morphology of prepared fuel samples was analyzed using scanning electron microscope (Fig. 1).

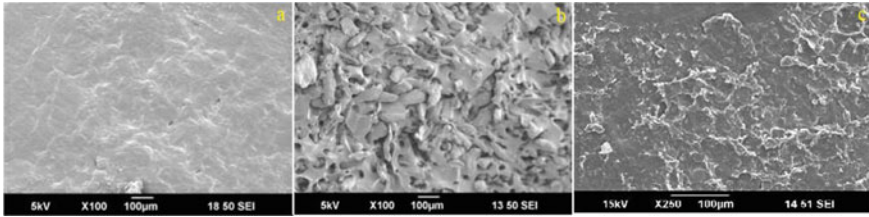
## 2.3 Tensile Testing for Fuel Samples

In order to determine the tensile strength and other important behavioral parameters of the specimen, tension test was performed using Instron UTM machine of 9000 Series, shown in Fig. 2. The maximum stress, strain and Young's modulus of the sample were determined. For this purpose, three samples were prepared and tested for each composition. ASTM standard D412 was followed in sample preparation in order to maintain standard sizing. Figure 3 depicts the die prepared as per the ASTM standard D412.

# 3 Results and Discussion

## 3.1 Surface Morphological Comparison for Pure Paraffin Wax, HTPB and Beeswax

Figure 1 depicts the SEM images taken for paraffin wax (Fig. 1a), HTPB (Fig. 1b) and beeswax (Fig. 1c) compositions. To acquire better knowledge of the innate behavior of individual components before mixing to make solid fuel compositions, SEM analysis and the comparison of paraffin wax, HTPB and beeswax in natural form were carried out. These characteristics were considered as exemplary for all other compositions. In comparison with beeswax, paraffin wax exhibits better homogeneous surface characteristics. The presence of slight flakes on the beeswax sample (Fig. 1c) indicates that it is brittle when in pure form when compared to paraffin wax. These material characteristics can be improved by the addition of *bonding agents*. On the other hand, pure HTPB (Fig. 1b) shows a greater amount of porosity in the structure



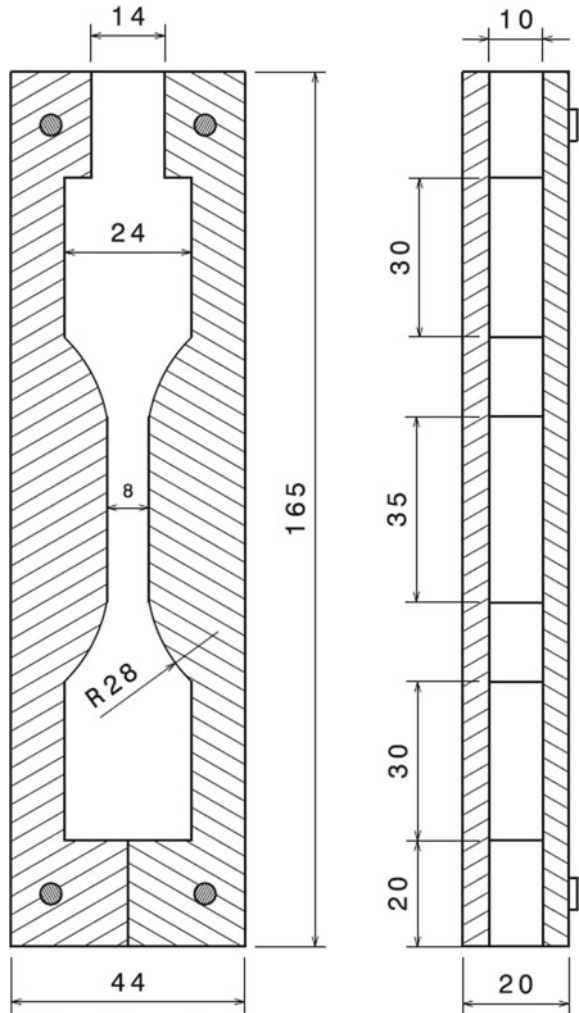
**Fig. 1** SEM images of **a** 100%Paraffin Wax; **b** 100% HTPB; **c**100% Beeswax

compared to other samples under study. Among all the samples observed, the lowest porosity is exhibited by paraffin wax (Fig. 1a). Thus, the individual characteristics can be improved when HTPB is combined either with beeswax or paraffin wax for better morphological characteristics than all the three in their natural form [11, 12].

**Fig. 2** UTM 9000 series



**Fig. 3** ASTM standard D412—die



### 3.2 Density Analysis of the Samples

The rocket propellants are rated in terms of impulse and (or) thrust produced by them. Since mass flow rate is the principal parameter for thrust, the mass flow rate completely depends on density and regression rates, which makes density a major design parameter for any propellant [4]. We have calculated and observed the density for all three samples and presented in Table 1. Although there is no much difference in values, but still considerable density variation was observed. Beeswax has shown the highest density among these three followed by HTPB and paraffin wax. It can be stated that beeswax might produce a higher mass flow rate with comparatively lesser required volume of storage.

### 3.3 *Strength and Elongation Analysis for the Samples*

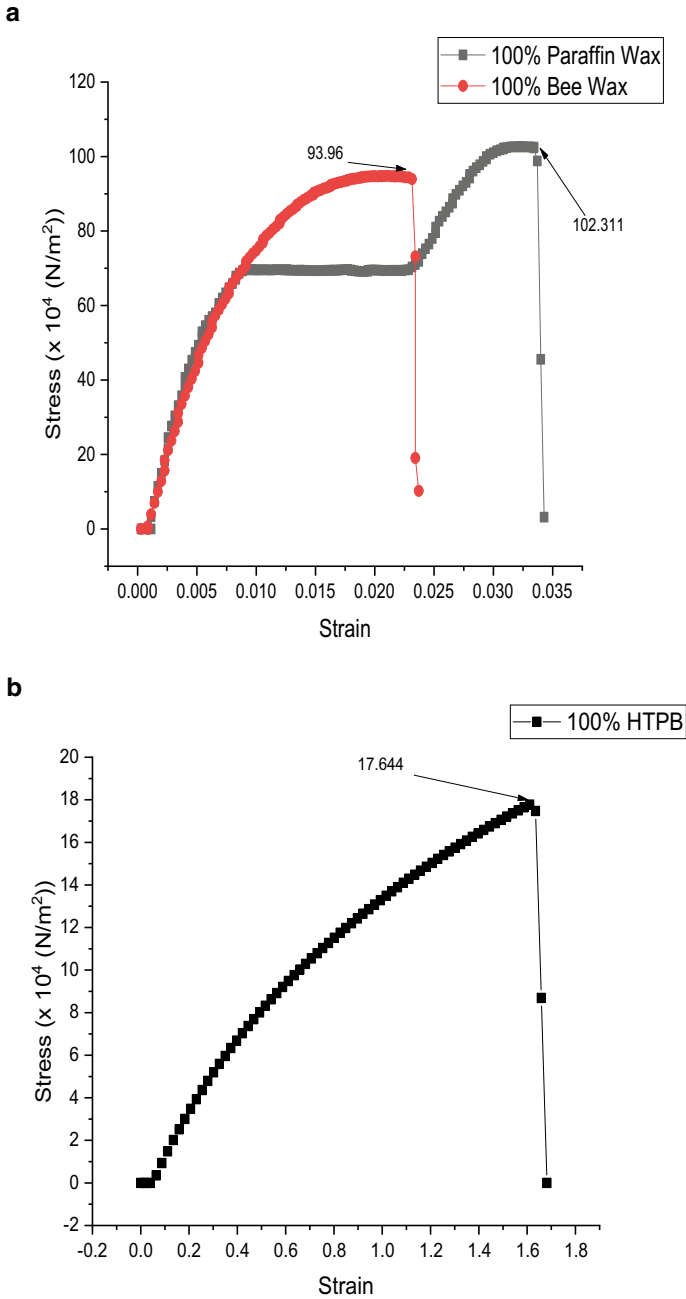
The samples of paraffin wax, HTPB and beeswax were prepared as per ASTM standards, and the tensile test was carried out with the moving head velocity of 5 mm/min. For the repeatability, three tensile samples were tested for each composition, and the stress vs strain values are recorded. Figure 4 shows the stress versus strain plot for paraffin wax, beeswax and HTPB samples at room temperature.

Observation from the strain–strain plot of these waxes shows the variation of properties of these three compositions. The Table 2 shows the stress, strain and Young's modulus values for paraffin wax, HTPB and beeswax which states that, the paraffin wax shows the highest value of maximum stress ( $102.311 \times 10^4 \text{ N/m}^2$ ), while the maximum stress was observed minimum for HTPB which is much lesser than paraffin wax [13] and beeswax. But the trend for beeswax was very near to paraffin wax. Beeswax recorded the maximum stress of  $93.96 \times 10^4 \text{ N/m}^2$  which is closer to paraffin wax. On the other hand, observation of maximum strain values of these samples was quite interesting with a lot of variations. The maximum strain (1.6585) was observed for HTPB which is much higher than both paraffin wax and beeswax. Paraffin wax and beeswax recorded the maximum strain values of 0.03427 and 0.02313, respectively.

We can deduce to the conclusion that although paraffin wax and beeswax provided far better strength but lacked elongation properties [14], meanwhile, HTPB provides much better elongation properties but completely lacked strength characteristics and cannot be used as a propellant (100% HTPB). Since for an ideal rocket propellant, both strength and elongation properties are desired, so use of a blend of these waxes and HTPB could be a better option to try as a rocket propellant.

### 3.4 *Chemical Composition of Paraffin Wax, Beeswax and HTPB*

The FTIR spectra of paraffin wax, HTPB and beeswax are presented in Fig. 5. The peaks of the samples at 2918 and 2849  $\text{cm}^{-1}$  represent aliphatic C–H stretching vibration of the  $-\text{CH}_3$  and  $-\text{CH}_2$  groups, respectively [15]. For HTPB, the peak at 1734  $\text{cm}^{-1}$  corresponds to the urethane groups, and the absorption wavelength at 962  $\text{cm}^{-1}$  represents the bending vibrations of the C=C band. For beeswax, the absorption wavelength at 2914 and 2848  $\text{cm}^{-1}$  corresponds to the methylene ( $-\text{CH}_2$ ) C-H asymmetrical/symmetrical stretch. The wavelength 1464 and 1375  $\text{cm}^{-1}$  corresponds to the methylene and methyl C-H asymmetrical/symmetrical bend, respectively. The wavenumber 722  $\text{cm}^{-1}$  corresponds to the methylene  $\{-(\text{CH}_2)_n-$ ; where  $n \geq 3$ ) aliphatic chain rocking. The wavenumbers 2914, 2848, 1463 and 722 collectively confirm the presence of an aliphatic chain compound. Thus, the result helps in confirming that there are no impurities in the samples used [16, 17].



**Fig. 4** Stress versus strain curve for **a** paraffin wax, beeswax **b** HTPB sample

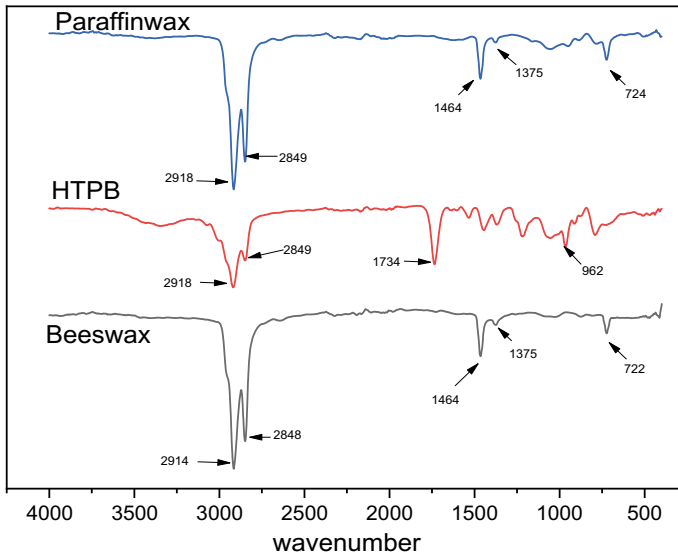


Fig. 5 FTIR spectra of paraffin wax, beeswax and HTPB samples

## 4 Conclusion

In order to observe and compare the mechanical properties of different waxes to be used as hybrid rocket propellant, a series of studies were carried out. Three distinct compositions like paraffin wax, beeswax and HTPB had been analyzed through SEM, density analysis, tensile testing and FTIR test. The results of this study can be summarized as follows:

- (1) Density analysis of the wax samples describes the volumetric loading of fuel. In this study, it was observed that beeswax exhibits a higher density than paraffin wax and HTPB.
- (2) Tensile test analysis shows that paraffin wax exhibits maximum stress and Young's modulus of elasticity higher than that of beeswax and even much higher than that of HTPB, while maximum strain was observed to be maximum for HTPB which is much greater than both paraffin wax and HTPB.
- (3) Scanning electron microscopy (SEM) examination reveals the morphological characteristics of pure beeswax, pure paraffin wax and HTPB. It is observed that all fuel samples are homogeneous in nature.
- (4) The purity of the paraffin wax, beeswax and HTPB was observed and verified on the basis of the presence of functional group among them by using FTIR, and it was found to be in order (Table 2).



**Table 1** Experimental density and theoretical density of paraffin, beeswax and HTPB

Sample name	Experimentaldensity (kg/m <sup>3</sup> )	Theoretical density (kg/m <sup>3</sup> )	Porosity (%)
Paraffin wax	894	900	0.666
Beeswax	952.4	961	0.895
HTPB	920.3	932.9	1.350

**Table 2** Maximum stress, maximum strain and Young's modulus of paraffin wax, HTPB and beeswax

Sample	Max. Stress $\times 10^4$ N/m <sup>2</sup>	Maximum strain	Young's Modulus (MPa)
Paraffin wax	102.311	0.03427	116.1
HTPB	17.644	1.6585	0.145
Beeswax	93.96	0.02313	36.63

## References

1. Mahottamananda SN, Joshi PC (2016) Combustion study of HTPB–sugar hybrid fuel with gaseous oxygen. *J Therm Anal Calorim* 123:1927–1934. <https://doi.org/10.1007/s10973-015-4608-y>
2. Kuo KK, Chiaverini MJ (2007) Fundamentals of hybrid rocket combustion and propulsion. American Institute of Aeronautics and Astronautics, Inc. <https://doi.org/10.2514/4.866876>
3. Sutton GP, Biblarz O (2010) Rocket propulsion elements, 8th edn Wiley, Hoboken
4. Zishan Akhter M, Hassan MA (2018) Characterisation of paraffin-based hybrid rocket fuels loaded with nano-additives. *J Exp Nanosci*. <https://doi.org/10.1080/17458080.2018.1431848>
5. Lee TS, Tsai HL (2008) Combustion characteristics of a paraffin- based fuel hybrid rocket. In: 9th Asian Pacific international symposium on combustion and energy utilization, Beijing, China, November
6. Chen S, Tang Y, Zhang W, Shen R, Yu H, Ye Y, DeLuca LT (2019) Innovative methods to enhance the combustion properties of solid fuels for hybrid rocket propulsion. In: MDPI Aerospace
7. Young G, Risha GA, Connell TL, Jr., and Richard A. Yetter, (2019) Combustion of HTPB based solid fuels containing metals and metal hydrides with nitrous oxide. *Propellants, Explos, Pyrotech*. <https://doi.org/10.1002/prop.201800380>
8. Rajiv Kumar R, Ramakrishna PA (2016) Studies on EVA-based wax fuel for launch vehicle applications. *Propellants, Explos., Pyrotech*. <https://doi.org/10.1002/prop.201500172>
9. Maruyama S, Ishiguro T, Shinohara K, Nakagawa I (2011) Study on the mechanical characteristics of paraffin-based fuel. In: Eighth international conference on flow dynamics. Sendai, Japan
10. Mahottamananda SN, Kadiresh PN (2020) Mechanical Characteristics of Paraffin Wax-HTPB Based Hybrid Rocket Fuel Lecture Notes in Mechanical Engineering. Springer, Singapore. [https://doi.org/10.1007/978-981-15-4756-0\\_9](https://doi.org/10.1007/978-981-15-4756-0_9)
11. Sumit Verma PA, Ramakrishna, (2014) Dependence of density and burning rate of composite solid propellant on mixer size. *Acta Astronaut* 93(2014):130–137
12. Reimer L (1985) Scanning electron microscopy: physics of image formation and microanalysis. <https://doi.org/10.1088/0957-0233/11/12/703>
13. Mahottamananda SN, Kadiresh NP, Pal Y Regression rate characterization of HTPB-Paraffin based solid fuels for hybrid rocket. *propellants, explosives, pyrotechnics*. <https://doi.org/10.1002/prop.202000051>.

14. Sakote R, Yadav N, Karmakar S, Joshi PC, Chatterjee AK (2014) Regression rate studies of paraffin wax-HTPB hybrid fuels using swirl injectors. *Propellants, Explos, Pyrotech*. <https://doi.org/10.1002/prop.201300207>
15. DeSain J, Brady B, Metzler K, Curtiss T, Albright T (2009) Tensile tests of paraffin wax for hybrid rocket fuel grains. In: 45thAIAA/ASME/SAE/ASEE joint propulsion conference & exhibit. <https://doi.org/10.2514/6.2009-5115>
16. Coates J (2006) Interpretation of infrared spectra, a practical approach. *Encyclopedia of Analytical Chemistry*. <https://doi.org/10.1002/9780470027318.a5606>
17. Berthomieu C, Hienerwadel R (2009) Fourier transform infrared (FTIR) spectroscopy. *Photosynth Res*. <https://doi.org/10.1007/s11120-009-9439>

# The Impact of Squeeze Casting in AMMC—Review



A. Karthik, R. Karunanithi, A. S. Selvakumar, and S. A. Srinivasan

**Abstract** This current review deals with the influence of squeeze casting on the mechanical property and microstructure of aluminium matrix composites. The squeeze casting is also known as the liquid forging technique in which the liquid aluminium matrix is forged by applying squeeze pressure during solidification. Squeeze casting has an ability to offer excellent cast microstructure, which in turn enhances the mechanical property and also avoids conventional process-oriented defects. Squeeze casting improves the heat transfer rate during solidification due to its process capability. The solid solubility of AMMC is excellent than to other casting processes. The optimum governance of the process parameter of squeeze casting influences the performance of AMMC under tribological environment. The several benefits and applications offered by squeeze casting lead to exploring the process. A certain area in the casting process needs to be cautious and reviewed before commercial use of the squeeze casting process.

**Keywords** Squeeze casting · Cast microstructure · Mechanical property · Solid solubility · Process parameter · Benefits

## 1 Introduction

The development of AMMC gained widespread acceptance in automobiles and aerospace structure applications due to the charisma of aluminium matrix such as low weight density, high load-bearing capacity, tailor-made manufacturing process, and

---

A. Karthik · A. S. Selvakumar

Department of Mechanical Engineering, B.S. Abdur Rahman Crescent Institute of Science and Technology, Chennai 600048, India

R. Karunanithi (✉)

Department of Aerospace Engineering, B.S. Abdur Rahman Crescent Institute of Science and Technology, Chennai 600048, India

e-mail: [karunaponni@gmail.com](mailto:karunaponni@gmail.com)

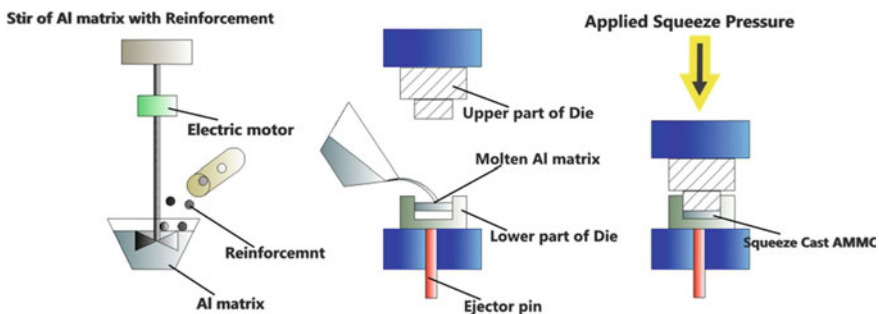
S. A. Srinivasan

Department of MME, National Institute of Technology, Trichy 620015, India

high stiffness, which leads to enhanced performance in-service condition [1]. The high strength to density ratios of AMMC improved domestic consumer vehicles' fuel economy in the recent decade, strong reasons for replacing conventional steel material by AMMC [2]. Several scientists reported that carbide ceramics and oxides' reinforcements have significantly enhanced the mechanical properties of AMMC, i.e., hardness, tensile strength, toughness, density, and wear resistance to meet the engineering requirement in the current decade when compared with base AMMC [3, 4]. Nowadays, the development of AMMC is based on the wide range of options in the requirement and choice of materials for numerous applications by materials designer to meet working standards in tandem with prevailing technological [5]. The current technological requirements, such as energy-efficient materials, low weight ratio, high strength, and low-cost effectiveness, command that the researchers hunt for new materials. The constraint in designing good AMMC depends upon the fabrication route to meet the recent engineering demands. The AMMC are conventional cast materials in the previous decade, but casting-oriented defects limit its performance and usage [6]. The recent development squeeze casting has high credentials in casting AMMC with the avoidance of process-orientated defects such as shrinkage, porosity, enhanced mechanical property, process capability, and benefit being reviewed in this article.

## 2 Squeeze Casting

In 1800, squeeze casting originated, but it was successfully patterned in 1994 after various challenges. In the current decade, squeeze casting shows the better performance of AMMC when compared with stir casting in liquid metallurgical operation [7]. The process involves stir effects in liquid metals stages with reinforcement and applied pressure during solidification in die as single-stage processes known as squeeze casting which is represented in Fig. 1 [8]. The liquid forging of molten metals during solidification avoids free solidification behaviour, which happens in



**Fig. 1** Graphical representation of squeeze casting process

normal die casting process led to AMMC's avoidance of conventional casting defects [9].

The construction feature of squeeze casting has been equipped with modern features such as an electronic control unit maintaining process parameter level and can be automated in later stages depending on the application requirement [10]. The key parts of squeeze casting are a hydraulic pressure unit with a plunger, electric furnaces, liquid metals flow path with heater, die preheater, and movements of the plunger in both longitudinal and horizontal direction. The success of squeeze casting depends upon the optimum setting of process capability such as hydraulic pressure applied during solidification, duration of applied pressure during solidification known as dwell time, melts' temperature, and die during the casting process [11]. The functional benefits of applied pressure interact with melted metal, enabling quick heat dissipation in the die surface and yielding porous free cast components with imminent mechanical properties [12]. The squeeze casting ensures the premium quality of cast products, and higher heat removal rates during solidification lead to the very close interface of liquid metals and die surfaces, which are not found in any other casting process.

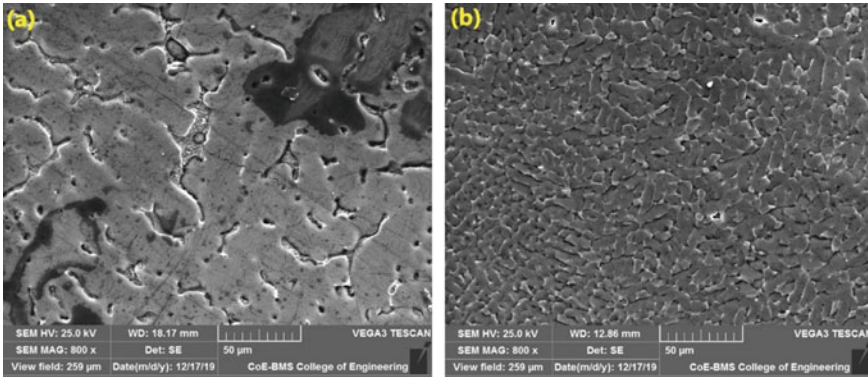
Another vital feature of squeeze casting in the near net shape of casted components is applied pressure during solidification, which avoids the extensive machining process for casted components, usually in the conventional casting process. The near net shape of component is related to the yield of internal soundness, no shrinkage, dimensional stability, and highest grade of surface finish [13]. Squeeze casting also suits the fabrication of wrought alloys [14], which gains the economic importance of recycled AMMC; almost some quality is ensured [15].

## 2.1 Cast Microstructure

The applied pressure during solidification leads to the formation of refined grain in AMMC since applied pressure hinders the rapid grain growth and results in an increase in dislocation density and refinement of grains. The stir action before the pouring molten metals into expected results in the homogenous distribution of Al grains and reinforcement enables us to achieve excellent cast microstructure. The combined effects result in avoidance of porosity and shrinkage defects with the improved mechanical property [9, 16].

The solid solvability of the second phase reinforced particles high compared to the conventional casting process also allows various reinforcement to meet engineering applications' requirements [17]. Many researchers have reported high-dense rare oxides [18, 19] and ceramic powder [20, 21] in AMMC to develop a new aluminium alloy series.

The AA2219 as casted SEM micrograph represented in Fig. 2a reveals the coarse grain, which is the characteristic feature of free solidification of AMMC with porosity. Meanwhile, the squeeze cast of AA2219-2wt% CeO<sub>2</sub> represented in Fig. 2b reveals



**Fig. 2** SEM micrograph of AMMC **a** As cast AMMC (AA2219) **b** Squeeze cast AMMC (AA2219 + 2 wt% CeO<sub>2</sub>) [18]

the fine grain due to the grain refinement action mainly due to applied squeeze pressure during solidification. The squeeze casting enables the solubility of high-dense cerium oxide rare earth oxide in AMMC and benefited by the stir of reinforcement resulting in homogenous cast microstructure [18].

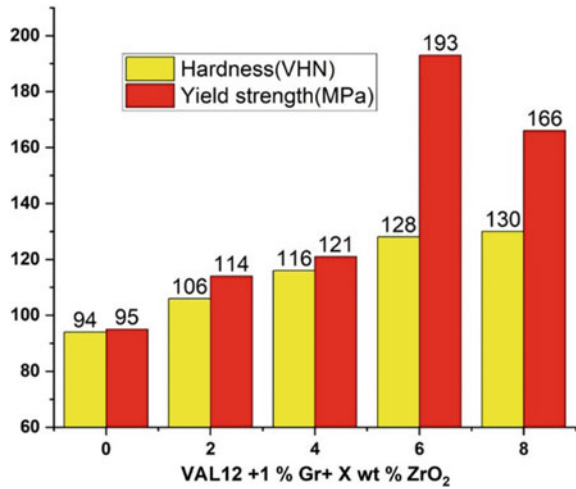
## 2.2 Mechanical Property

Several scientific reports claim the improvement of mechanical property of AMMC such as hardness, tensile strength, and yield strength with improved density. The grain refinement action due to applied pressure during solidification which ensures rapid cooling rate [22] and reinforcement is high compared to the conventional casting process. According to Hall–Petch relation, the reduction of grain size strength, the hardness, and yield values of AMMC state that a decrease of grain size improves the yield strength [17]. The addition of ZrO<sub>2</sub> to VAL Al matrix improves the mechanical property fabricated by squeeze casting process represented in Fig. 3 [23].

## 2.3 Tribological Behaviour

The enhanced mechanical property leads to wear resistance of the AMMC during the interaction between surfaces and second phase reinforcement particles that have a pronounced effect on the tribological behaviour of AMMC, mainly due to the process capability of squeeze casting [24], as explained above. Many researchers have reported the improved wear behaviour of AMMC in different loads, sliding distance, and different weight percentages of the second phase particles [19, 25]

**Fig. 3** Improvement of mechanical property of AMMC by squeeze casting process [23]



### 2.4 Optimum Process Control

All the benefits and process-orientated advantages can be enjoyed if the process parameter is kept in optimum range-based design of component and AMMC [26, 27]. Since the increase of higher squeeze pressure produce, cracked component and accumulation effects can also take place. The high melt and die preheating temperature can cause an increase in grain size. Even the lower range of applied pressure produces less forging effects, leading to defect components and lower temperature range, which ends up improper solidification of molten AMMC [28]. The dwell time and stir time also place a critical role in deciding the property of AMMC. Many researchers reported that the optimization of process variable key obtained the salient feature of squeeze casting [29].

The squeeze casting application in AMMC is automotive wheels, pistons, disc brakes, and several structural components [30]. The several benefits of squeeze casting have tremendous improved AMMC performances as reported by the researcher, but tailor-made squeeze casting processes need to improve for commercial usage. The intricate die design and application of applied pressure during solidification will be constrained for R&D engineers before squeezing commercial practices.

### 3 Conclusion

The review articles mainly focused on squeeze casting merits and developments obtained by AMMC in terms of mechanical property, excellent cast microstructure obtained along with excellent dimensional stability, and avoidance of conventional

defects. This article will be an eye-opener for more application of squeeze casting in commercial and research aspect.

## References

1. Olusegun A, Makun HA, Ogara IM, Edema M, Idahor KO, Oluwabamiwo BF, Eshiett ME (2012) We are IntechOpen , the world ' s leading publisher of Open Access books Built by scientists , for scientists TOP 1 %. Intech 2012, i, 38. <https://doi.org/10.1016/j.colsurfa.2011.12.014>.
2. Hirsch J (2014) Recent development in aluminium for automotive applications. *Trans Nonferrous Met Soc China, English Ed.* 24:1995–2002. [https://doi.org/10.1016/S1003-6326\(14\)63305-7](https://doi.org/10.1016/S1003-6326(14)63305-7)
3. Bodunrin MO, Alaneme KK, Chown LH (2015) Aluminium matrix hybrid composites: a review of reinforcement philosophies. *Mechanical, Corrosion and Tribological Characteristics J Mater Res Technol* 4(434):445. <https://doi.org/10.1016/j.jmrt.2015.05.003>
4. Das DK, Mishra PC, Singh S, Thakur RK (2014) Properties of ceramic-reinforced aluminium matrix composites—a review. *Int J Mech Mater Eng* 9. <https://doi.org/10.1186/s40712-014-0012-9>
5. Surappa MK (2003) Aluminium matrix composites: Challenges and opportunities. *Sadhana - Acad. Proc. Eng. Sci.* 28:319–334. <https://doi.org/10.1007/BF02717141>
6. Fiorese E, Bonollo F, Timelli G, Arnberg L, Gariboldi E (2015) New Classification of Defects and Imperfections for Aluminum Alloy Castings *Int J Met* 9(55):66. <https://doi.org/10.1007/BF03355602>
7. Yue TM, Chadwick GA (1996) Squeeze casting of light alloys and their composites. *J. Mater. Process. Technol.* 58:302–307. [https://doi.org/10.1016/0924-0136\(95\)02148-5](https://doi.org/10.1016/0924-0136(95)02148-5)
8. Ghomashchi MR, Vikhrov A (2000) Squeeze casting: An overview. *J Mater Process. Technol.* 101:1–9. [https://doi.org/10.1016/S0924-0136\(99\)00291-5](https://doi.org/10.1016/S0924-0136(99)00291-5)
9. Gangopadhyay S (2014) Optimisation of casting parameters of squeeze cast LM-24 Al-Si Alloy. *Int J Eng Res Technol* 3:916–921
10. Senthil P, Amirthagadeswaran KS (2012) Experimental study and squeeze casting process optimization for high quality AC2A aluminium alloy castings. *Arab. J. Sci. Eng.* 39:2215–2225. <https://doi.org/10.1007/s13369-013-0752-5>
11. Yue TM (1997) Squeeze casting of high-strength aluminium wrought alloy AA7010. *J Mater Process Technol* 66:179–185. [https://doi.org/10.1016/S0924-0136\(96\)02516-2](https://doi.org/10.1016/S0924-0136(96)02516-2)
12. Chandra VS, Blessto B, Divya S, Dhanasekaran S, Ravi M, Sivaprasad K (2020) Microstructural, Mechanical and Tribological Behavior of Gravity- and Squeeze-Cast Novel Al–Si–Cu–Mg–Fe Alloy. *Trans Indian Inst Met.* <https://doi.org/10.1007/s12666-020-01923-x>
13. Vijayaram TR, Sulaiman S, Hamouda AMS, Ahmad MHM (2006) Fabrication of fiber reinforced metal matrix composites by squeeze casting technology. *J. Mater. Process. Technol.* 178:34–38. <https://doi.org/10.1016/j.jmatprotec.2005.09.026>
14. Souissi N, Souissi S, Niniven C, Amar M, Bradai C, Elhalouani F (2014) Optimization of Squeeze Casting Parameters for 2017 A Wrought Al Alloy Using Taguchi Method. *Metals (Basel)*. 4:141–154. <https://doi.org/10.3390/met4020141>
15. Soundararajan R, Ramesh A, Sivasankaran S, Sathishkumar A (2015) Modeling and analysis of mechanical properties of Aluminium Alloy (A413) processed through squeeze casting route using artificial neural network model and statistical technique. *Adv Mater Sci Eng.* <https://doi.org/10.1155/2015/714762>
16. Wu Y, Du W, Zhang Y, Zuo T, Sadeghian Z, Lotfi B, Enayati MH, Beiss P, Soundararajan R, Ramesh A et al (2017) Effects of squeeze casting parameters on density, macrostructure and hardness of LM13 alloy. *Mater Sci Eng A* 4:135–140. <https://doi.org/10.1016/j.msea.2006.04.099>



17. Maeng DY, Lee JH, Won CW, Cho SS, Chun BS (2000) The effects of processing parameters on the microstructure and mechanical properties of modified B390 alloy in direct squeeze casting. *J Mater Process Technol* 105:196–203. [https://doi.org/10.1016/S0924-0136\(00\)00527-6](https://doi.org/10.1016/S0924-0136(00)00527-6)
18. Karthik A (2020) The Investigation of Microstructure and Mechanical Property of Incorporation of Cerium Oxide to AA2219 Through Liquid Forging Technique. *J Inst Eng Ser D*. <https://doi.org/10.1007/s40033-020-00212-7>
19. Srinivasan SA, Babu SPK, Thirumaran B, Vallimanan A (2020) Wear Behavioral and Mechanical Studies on Liquid Forged VAL12 Alloy Strengthened by Lanthanum Oxide Dispersoids. *J Inst Eng Ser D*. <https://doi.org/10.1007/s40033-020-00224-3>
20. Karthik A, Karunanithi R, Srinivasan SA, Prashanth M (2019) Microstructure and mechanical properties of AA 2219-TiB<sub>2</sub> composites by squeeze casting technique. *Mater Today Proc*. <https://doi.org/10.1016/j.matpr.2019.10.143>
21. Ipekoglu M, Nekouyan A, Albayrak O, Altintas S (2017) Mechanical characterization of B4C reinforced aluminum matrix composites produced by squeeze casting. *J. Mater. Res.* 32:599–605. <https://doi.org/10.1557/jmr.2016.495>
22. Boschetto A, Costanza G, Quadrini F, Tata ME (2007) Cooling rate inference in aluminum alloy squeeze casting. *Mater. Lett.* 61:2969–2972. <https://doi.org/10.1016/j.matlet.2006.10.048>
23. Srinivasan SA, Kumaresh Babu SP, Gaurav V (2019) Elucidation on the microstructural and mechanical properties of tailored val12 hybrid composites with zro2 dispersoids fabricated by squeeze casting technique. *Mater Sci Forum* 2019, 969 MSF, pp 813–818. <https://doi.org/10.4028/www.scientific.net/MSF.969.813>
24. Patel GC, Shettigar M, Parappagoudar AK (2018) A systematic approach to model and optimize wear behaviour of castings produced by squeeze casting process. *J Manuf Process* 32:199–212. <https://doi.org/10.1016/j.jmapro.2018.02.004>
25. Senthil P, Amirthagadeswaran KS (2013) Enhancing wear resistance of squeeze cast AC2A aluminium alloy. *Int. J. Eng. Trans. A Basics* 26:365–374. <https://doi.org/10.5829/idosi.ije.2013.26.04a.05>
26. Ravikumar AR, Amirthagadeswaran KS, Senthil P (2014) Parametric optimization of squeeze cast AC2A-Ni Coated SiC p composite using taguchi technique. *Adv Mater Sci Eng*. <https://doi.org/10.1155/2014/160519>
27. Zyska A, Konopka Z, Lstrok Agiewka M, Nadolski M (2013) Optimization of squeeze parameters and modification of AlSi7Mg Alloy. *Arch Foundry Eng* 13:113–116. <https://doi.org/10.2478/afe-2013-0048>
28. Moorthy G, Rajeswari B (2018) Optimization of squeeze casting process parameters of Aluminium LM25 8:571–580
29. Patel GC, Parappagoudar M (2015) K.P. modelling in squeeze casting process-present state and future perspectives. *Adv Automob Eng* 04. <https://doi.org/10.4172/2167-7670.1000111>
30. Prasad SV, Asthana R (2004) Aluminum metal-matrix composites for automotive applications: Tribological considerations. *Tribol Lett* 17:445–453. <https://doi.org/10.1023/B:TRIL.0000044492.91991.f3>

# Analysis of Internal Hydrodynamic Behavior of Pressure Swirl Atomizer for Liquid Rocket Engines



Kabaleeswaran Manikandan, Boyapati Krishna Vamsi, Pola Anusha, and Chaturya Reddy

**Abstract** The combustion performance and instability behavior of liquid rocket engines are inaudibly related to the effective performance of an injector, thus understanding its internal and external flow characteristics are decisive to enhance its efficiency. The single element pressure swirl injector model is fabricated through a transparent acrylic for enhanced visualization in the internal segment of an injector. The cold flow method is performed for a fixed duration of sixteen seconds to reveal the nature of the formation of an air-core and spray during a transient as well as steady-state operation of an injector. The injector performance parameters like discharge coefficient, injection velocity, volume flow rate, and differential pressures are observed and tabulated for the fluid injection pressure range of 0.5 to 3 bar. In the same manner, air-core and spray formations are also recorded for the entire test duration. Results of image processing show that the complete formation of air-core possesses three phases of transformation. In the first phase, the tornado-like structure is formed, in the second phase it transformed into a twisted water sheet-like shape, and finally in the third phase air-core settles down with the nearly constant cylindrical shape of minimal disturbances around its perimeter. Once the air-core reaches the end of the third stage, spray formation also reaches its nearly steady-state cone angle.

**Keywords** Pressure swirl injector · Unsteady state · Cold flow · Air-core · Spray pattern

## 1 Introduction

The simplex (or pressure swirl) atomizers are used in diverse engineering applications like spray drying, cooling, painting, chemical, sprinklers intended for agricultural, aircraft engines, engines of automobiles, and also as an atomizer of liquid rocket engine industry. Though it is used for different applications, both aviation and rocket industries are adopted simplex atomizers for its engines due to its natural

---

K. Manikandan (✉) · B. Krishna Vamsi · P. Anusha · C. Reddy  
SASTRA Deemed to be University, Thanjavur, Tamil Nadu 613401, India  
e-mail: [manikandan@mech.sastra.edu](mailto:manikandan@mech.sastra.edu)

simplicity, trustworthy combustion instability, and elevated atomization performance [1–6]. The internal and external flow characteristics of injectors are closely related to the combustion efficiency of liquid rockets. Hydrodynamic characteristics like the nature of air-core formation, liquid film thickness, and spray pattern are needed to be analyzed to optimize the injector efficiency. In a swirl injector, working fluid is injected into the swirl chamber through the tangential inlets to induce the centrifugal force. The induced centrifugal forces in the swirl chamber facilitate the swirling film to attach with the chamber wall, thus allowing the creation of the gap for the formation of hollow air-core in the central region of an injector. The centrifugal force forces the thin film of a hollow-cone liquid sheet to exit from the injector orifice, unsteady propagation from the air-core reaches out the thin film to disintegrate into ligaments, and subsequently into very fine droplets. These fine droplets can advance the evaporation as well as the mixing rate in the liquid rocket engines [7]. However, the performance of an injector is decided by the nature of the formation of the air-core and its stability, film thickness, and spray patterns also need to be explored to enhance the injector efficiency. Among the above distinctiveness, the steadiness of the air-core (i.e., invariant contour and height) plays a vital role in the performance behavior of the swirl atomizer. Apart from the stable air-core, the nature of the cone angle also plays a vital role in the performance behavior of simplex injectors [8, 9]. The air-core formation in a swirl injector is an extremely speedy process, which happens for adequately elevated inlet velocity fluid (i.e., elevated differential pressure as a driving force) [10]. Numerous research papers on swirl atomizer describe the performance behavior of air-core and spray pattern through experimental as well as theoretical methods have been published [11, 13]. Datta et al. [12] have measured the geometrical features of air-core in a 2D axis-symmetric conical swirl spray nozzle exit using the least resistance theory. Chinn et al., have done the experimental work on the liquid air-core interaction in the simplex injector for different tangential inlet and injection pressure (i.e., high inlet velocity). Results show that localized regions of air-core might expand and contract for the regular time interval also discontinuity in the liquid film thickness is liable for the disintegration of liquid sheet, which initiates the process called atomization [15]. Mahottamananda et al. [16, 17] studied the effect of number of inlet tangential ports and their angle on spray characteristics of plug type swirl injector. So, nearly all works of literature are broadly focusing on the steady-state air-core formations and their behavior. Hence, investigating the way of the configuration of an air-core during transient state also must be focused to advance the performance behavior of the swirl injector. In this current work, the experimental method of cold flow analysis is adopted for the investigation of air-core behavior from transient to steady-state conditions for the different fluid injection pressure, also the formation of the spray pattern is analyzed at steady-state conditions simplex injector.

## 2 Experimental Setup and Research Methodology

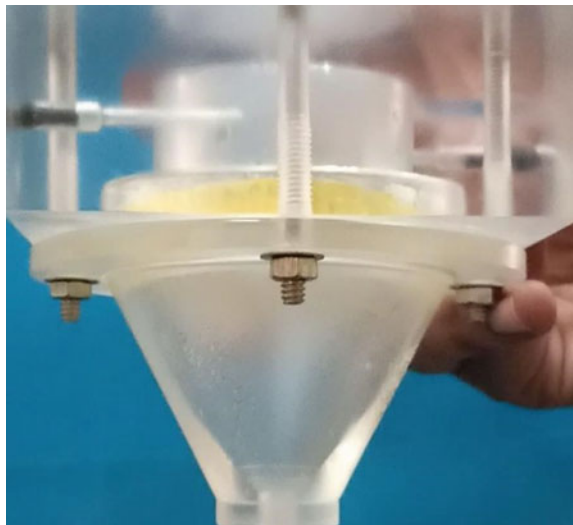
A complete setup for swirl atomizer to conduct cold flow analysis includes the subsystems like an air compressor, pressure regulator, water storage tank, flow meter, Y-junction value, swirl atomizer, collecting tank, and Nikon DSLR D5100 camera. The atomizer consists of two tangential orifices of 2.5 mm diameter with  $90^\circ$  to the injection plane, a swirl chamber of diameter 50 mm, the convergent nozzle of length 60 mm, and an exit orifice of diameter 5 mm. The fabricated swirl atomizer is shown in Fig. 1. This swirl injector is manufactured using acrylic material to enable transparency for visualizing the internal hydrodynamic behavior of a working fluid.

The flow meter is incorporated with the experimental setup to measure the volume flow rate of working fluid with a frequency of 2 Hz (i.e., Hertz (Hz) unit of frequency). The flow sensor YF-S201 is connected with the Arduino UNO board as interference between the flow meter and computer. The flow meter connection with Arduino is shown in Fig. 2.

The flow sensor YF-S201 works based on the Hall effect principle. The pictorial representation of the working principle behind the flow meter is described in Fig. 3. The three wires of water flow sensor are act as interface between microcontroller and Arduino board. It requires only + 5 V Vcc ( Vcc—Voltage at common collector) and provides pulse yield, and the sensor should be properly connected with the experimental setup of a water pipeline.

The outlet of the reservoir tank is connected to the flow sensor followed by the Arduino-a microcontroller and then connected into the computer for recording the output values for the entire duration of 16 s. However, mass flow rate is obtained based on the conservation of mass principle. The relationship between mass flow and volumetric flow is given in the Eq. (1) as below:

**Fig. 1** Acrylic made swirl atomizer



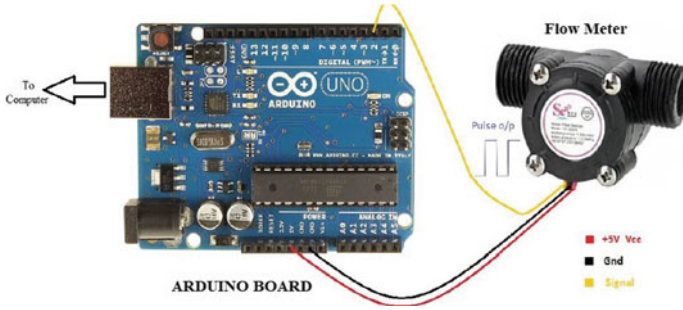


Fig. 2 Flow meter connection with Arduino

$$\text{Mass flow rate of working fluid} = \text{density of fluid} \times \text{volume flow rate} \quad (1)$$

Flow properties like discharge coefficient, injection velocity, differential pressure and spray cone angle are measured for each running duration of 16 s. The spray cone angle is measured as the angle formed between two tangential lines drawn along the surface of the liquid sheet from the nozzle exit which can be seen from Fig. 8, and the cone angle is influenced by the interior geometry and size of the nozzle and also by aerodynamic impact (i.e., rate of entrainment) [15]. The former three values are measured using empirical relations, and later two values are obtained using image processing techniques. Corresponding empirical relations are given below. The discharge coefficient equation  $C_d$  can be calculated from the below Lefebvre equation [14]. From Eq. 3, the differential pressure ( $\Delta P_L$ ) can be obtained, where,  $D_s$  = swirl chamber diameter,  $A_p$  = inlet port area,  $D_o$  = discharge diameter of the nozzle,  $C_d$  = coefficient of discharge,  $\dot{m}_L$  = liquid mass flow rate,  $A_o$  = exit area of nozzle orifice, and  $\rho_L$  = liquid density.

$$C_d = \left( 0.35 \left( \left( \frac{D_s}{D_o} \right)^{0.5} \right) \left( \frac{A_p}{D_s D_o} \right)^{0.25} \right) \quad (2)$$

$$C_d = \frac{\dot{m}_L}{(A_o \sqrt{2 \rho_L \Delta P_L})} \quad (3)$$

### 3 Result and Discussion

The cold flow technique (i.e., water as a working fluid) is adopted for exploring the formation of air-core during the transient phase as well as steady state; for all different injection pressure the test run is conducted for the fixed duration of 16 s to ensure the sufficient time accessible for the internal as well as external flow pattern of the swirl injector to reach steady-state condition. Through the cold flow analysis,

fluid volume flow rate, injection velocity, differential pressure, and spray cone angles are measured and plotted to explore the characteristics of swirl injector from transient state to steady-state condition. Internal flow behavior for the corresponding duration is recorded as a video using the Nikon DSLR D5100 camera to evaluate the sequential behavior of air-core formation. Similarly, the flow meter readings are recorded and tabulated for the subsequent run duration. The cold flow analysis on the simplex injector is carried out for the following different fluid injection pressure 0.5 bar, 1.0 bar, 1.5 bar, 2.0 bar, 2.5 bar, and 3.0 bar. From Fig. 4a, it can be seen that the water is rushing into the swirl chamber with spiral formation because of the tangential mode of entry, where the working fluid gets the induced tangential component of velocity as mentioned by Chang et al. [11].

Likewise, a strong helical wave-like formation can be observed. Similarly twisted liquid sheet of DNA like structure formation can be observed from Fig. 4d. After the fourth second, the twisted helical nature is diminishing into a nearly constant circular cross section of cylindrical air-core showing a helical shape of minimal twists and a few minor turbulence, which can be seen from Fig. 4f.

From Figs. 5 and 6 for all injection pressures, impulsive opening of the valve causes the volume flow and injection velocity to reach peak (i.e., higher initial driving impulse differential pressure) value and then settles down to constant values after the transient phase of an injector coming to an end. However, from Figs. 5 and 6, it can be observed that after the sixth second, fluid volume flow rate, as well as injection velocity, reaches the constant value (i.e., steady state). Hence, the transient phase exists only for six seconds which is almost independent of the fluid injection pressures that also can be observed from both the graphs. Also, at the end of the transient phase only spray cone angle reaches the nearly constant value. Spray cone angles are also varying for the increase in the volume flow rate of fluid (i.e., increase in fluid injection pressure). From Fig. 5, it can be observed that initial peak values of volume flow rate for the injection pressures of 0.5 bar, 1 bar, 1.5 bar, 2 bar, 2.5 bar, and 3 bar are 176 L/h, 208 L/h, 240 L/h, 288 L/h, 320 L/h, and 356 L/h, respectively. Likewise, the steady-state values for the values of volume flow rate for the injection

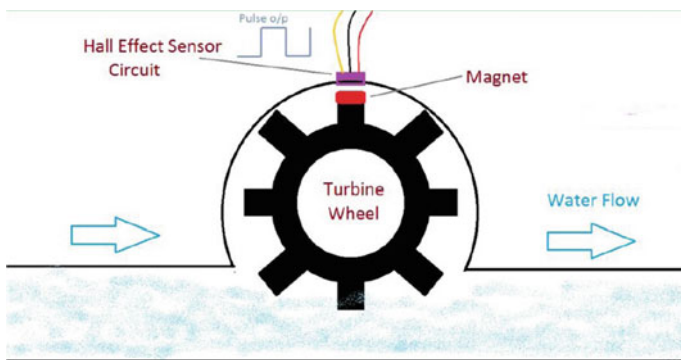
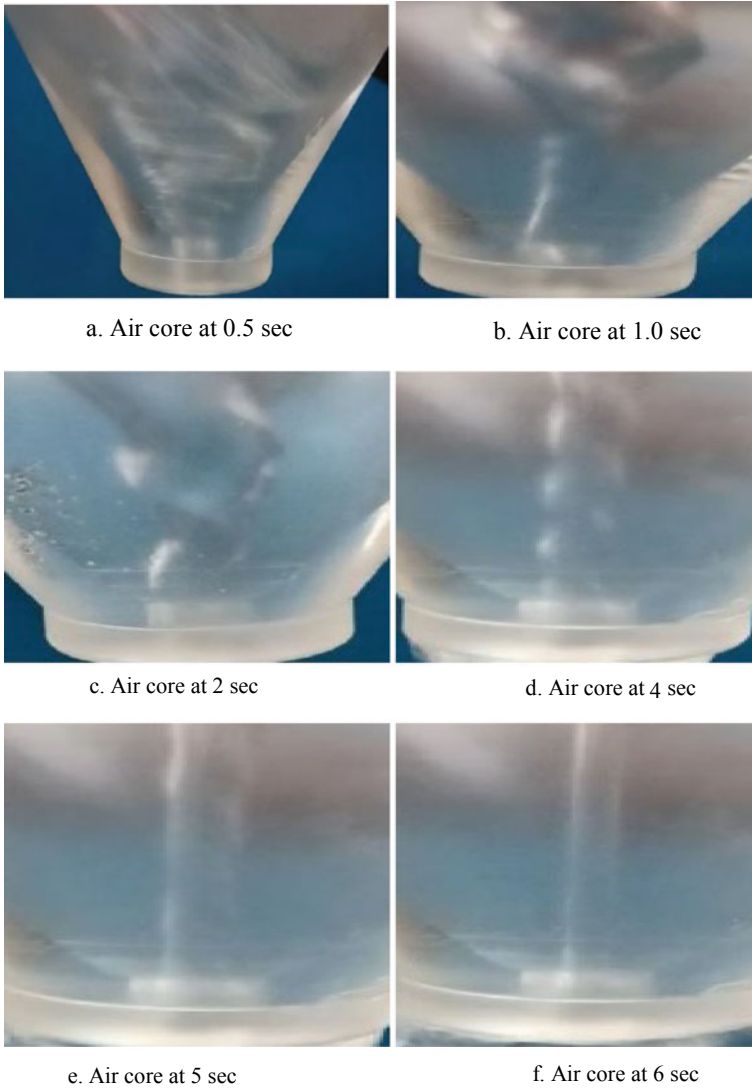


Fig. 3 Flow meter working principle



**Fig. 4** Air-core formation for the extent of the transient as well as steady state

pressures of 0.5 bar, 1 bar, 1.5 bar, 2 bar, 2.5 bar, and 3 bar are 120 L/h, 144 L/h, 168 L/h, 192 L/h, 216 L/h, and 232 L/h, respectively. Injection velocity behavior over the test duration can be visualized from Fig. 6, which is also exhibiting the same trend as Fig. 5, for both transient and steady-state conditions. Fluctuation in injection velocity values is noticed until six seconds, which is again confirming the predicted transient duration from Fig. 5, from sixth second to till the end measured values settle down with a constant value. It can be observed that initial peak values of injection velocity

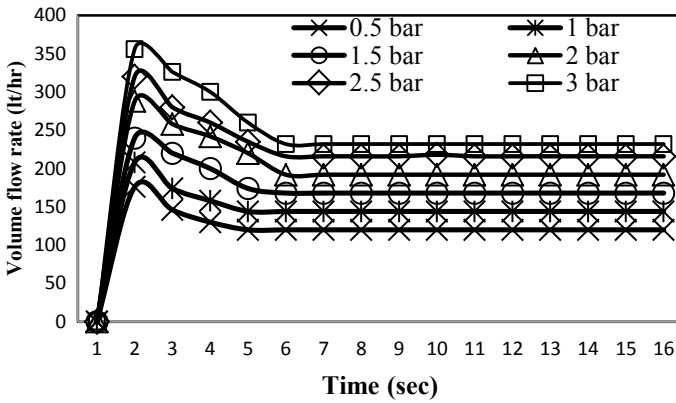


Fig. 5 Volume flow rate versus cold flow test duration

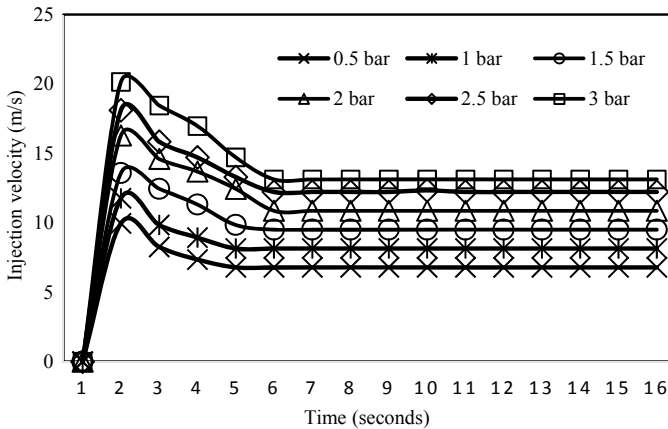
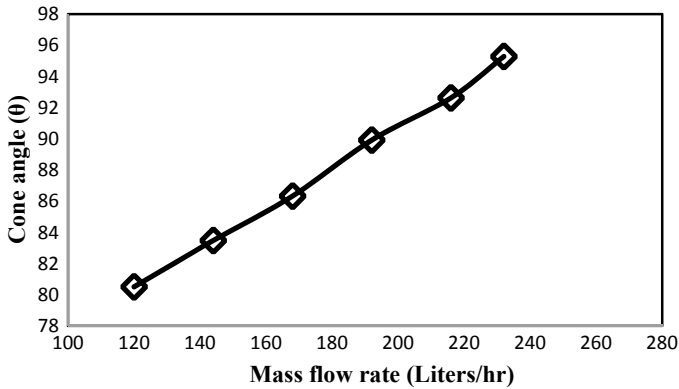


Fig. 6 Fluid injection velocity versus cold flow test duration

for the injection pressures of 0.5 bar, 1 bar, 1.5 bar, 2 bar, 2.5 bar, and 3 bar are 10 m/s, 11 m/s, 13 m/s, 16 m/s, 18 m/s, and 20 m/s, respectively. Likewise, the steady-state values for the values of volume flow rate for the injection pressures of 0.5 bar, 1 bar, 1.5 bar, 2 bar, 2.5 bar, and 3 bar are 6.5 m/s, 8 m/s, 9.5 m/s, 11 m/s, 12 m/s, and 13.5 m/s, respectively.

Measured spray cone angles corresponding to fluid mass flow rate are shown in Fig. 7, and the cone angle increases almost in a linear manner for the increase of volume flow rate of the fluid. The observed cone angle reaches 80° for the minimum volume flow rate of 120 L/h (i.e., injection pressure of 0.5 bar), likewise for the maximum volume flow rate of 232 L/h reaches more than 90°. For all different fluid injection pressure spray cone angle from the injector, exit begins to establish spray pattern nearly at the end of the transient phase only (i.e., Phase I). After the injector





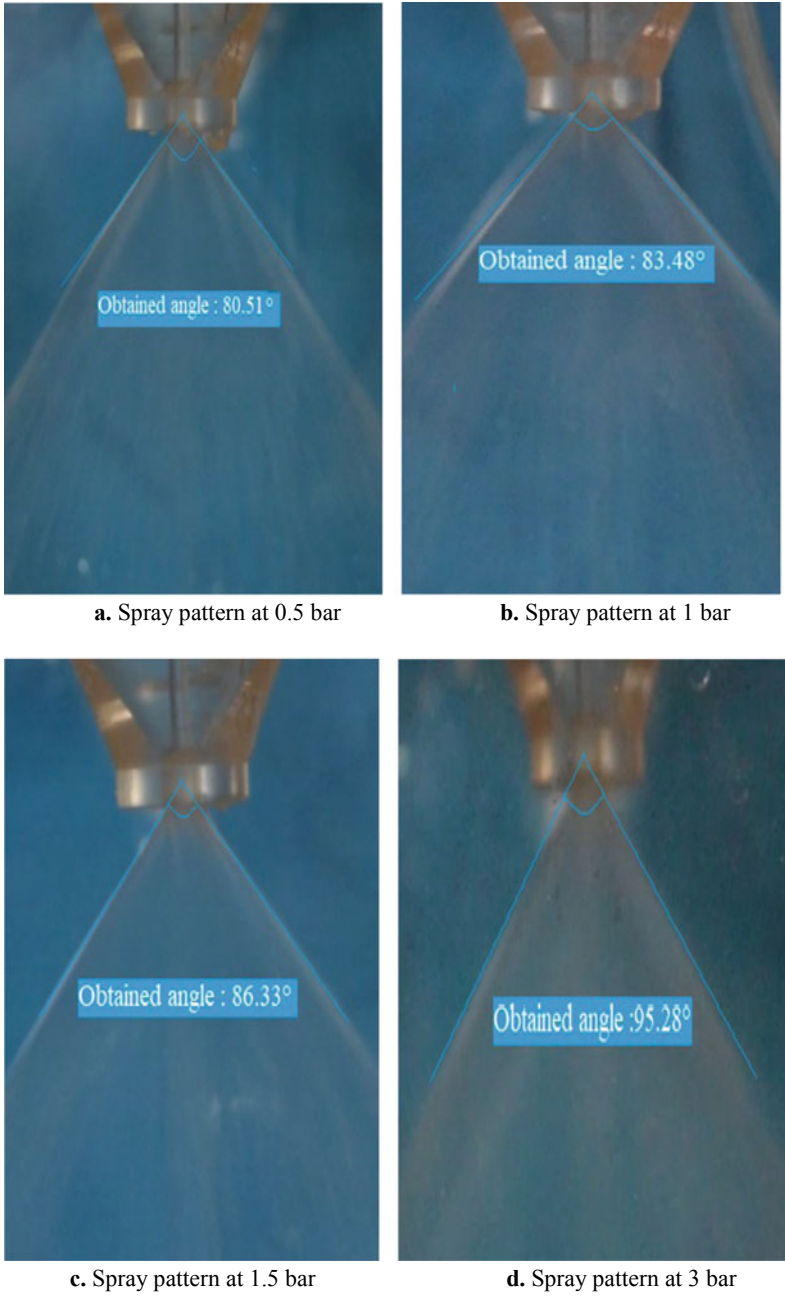
**Fig. 7** Cone angle versus fluid mass flow rate

reaches the constant volume flow rate, the spray cone angle also virtually shown reaches steady value for the remaining test duration. Fully developed spray pattern images are given in the following Fig. 8a–d for the corresponding volume flow rate of 120 L/h, 144 L/h, 168 L/h, and 232 L/h, respectively. Measured spray cone angles at steady state (i.e., after six seconds) are given in Fig. 8–d for the injection pressures of 0.5 bar, 1.0 bar, 1.5 bar, and 3.0 bar, respectively.

Overall it can be observed that transient and steady-state phases can be distinguished into three major regimes in the air-core formation: the first regime where no air-core is established due to very small centrifugal force (i.e., significant fluctuation in spray pattern); second the transitional phase (i.e., formation of unstable air-core); finally, the tired phase shows the formation of constant geometry air-core because of sufficient and less fluctuating centrifugal force inside the swirl chamber of an injector (i.e., constant area and length). The same developmental trend of air-core formation is reported by Lee et al. [15].

## 4 Conclusion

The internal and external flow behavior of the pressure swirl injector is analyzed using cold flow simulation method for sixteen seconds. The primary focus is to analyze unsteady and steady-state formations of an air-core inside the swirl chamber for the fixed run time of the cold flow test. The values of tabulation show that the volume flow rate varies between 120 Liters per hour and around 232 Liters per hour for the injection pressures of 0.5 bar and 3 bar, respectively. Likewise, the injection velocity also varies between 6 m/s to nearly 13 m/s for the injection pressures of 0.5 bar and 3 bar, respectively. Also, the spray cone angle varies between  $80.51^\circ$  and  $95.28^\circ$  for the corresponding injection pressures of 0.5 bar and 3 bar, which is also showing linear increment for the increase of fluid mass flow rate. The unsteady duration of



**Fig. 8** Spray pattern cone angle at different fluid injection pressures

an injector is almost independent of the fluid injection pressures. Image processing result is showing that the development of air-core consists of three main phases also nearly a stable spray pattern arrives at the orifice exit after the air-core reaches its third phase.

## References

1. Huntington DH (2004) The Influence of the spray drying process on product properties. *Dry Technol* 22: 1261–1287
2. Li BQ, Cader T, Schwarzkopf J, Okamoto K, Ramaprian B (2006) Spray angle effect during spray cooling of microelectronics: experimental measurements and comparison with inverse calculations. *Appl Therm Eng* 26(2006):1788–1795
3. Nasr GG, Sharief RA, Yule AJ (2006) High pressure spray cooling of a moving surface. *J Heat Transfer* 128(2006):752–760
4. Zhao F, Lai MC, Harrington DL (1999) The automotive spark ignited direct injection gasoline engines. *Prog Energy Combust Sci* 25:437–562
5. Singh A, Mehregany M, Phillips SM, Harvey RJ, Benjamin M (1998) Micromachined silicon fuel atomizers for gas turbine engines. *Atomization Sprays* 8:405–418
6. Lefebvre A (2000) Fifty years of gas turbine fuel injection. *Atomization Sprays* 10:251–276
7. Rizk NK, Lefebvre AH (1985) Internal flow characteristics of simplex swirl atomizers. *American Institute of Aeronautics and Astronautics* vol 1, no 3
8. Rayleigh WS (1892) On the instability of cylindrical fluid surfaces. *Philos Mag* 34:207
9. Ponstein J (1959) Instability of rotating cylindrical jets. *Appl Sci Res* 8:425–456
10. Dash SK, Halder MR, Peric M, Som SK (2001) Formation of air core in nozzles with tangential entry. *ASME. J Fluids Eng* 123(4): 829–835
11. Chang KC, Wnag MR, Wu WJ, Hong CH (1993) Experimental and theoretical study on hollow cone spray. *J Propulsion Power* 9(1):28–34
12. Datta A, Som SK (2000) Numerical predictions of air core diameter, co-efficient of discharge and spray cone angle in a swirl spray nozzle. *Int J Heat Fluid Flow* 21:412–419
13. Som SK, Mukherjee SG (1980) Theoretical and experimental investigations on the formation of air core in a swirl atomizing nozzle. *Appl Sci Res* 36:173–176
14. Lacava PT, Bastos-Netto D, Pimentar AP (2004) Design procedure and experimental evaluation of pressure-swirl atomizers. In: 24th international congress of the aeronautical sciences. 29-August-3-September-2004-Yokohama-Japan
15. Lee EJ, Oh SY, Kim HY, James SC, Yoon SS (2010) Measuring air-core characteristics of a pressure-swirl atomizer via a transparent acrylic nozzle at various Reynolds numbers. *Experimental Thermal, and Fluid Science*. 34:1475–1483
16. Jayapal SNM, Rafnaz M, Kadiresh PN (2018) Spray characteristics of plug type swirl injector. In: *Advances in Science and Engineering Technology International Conferences (ASET)*, Abu Dhabi, IEEE Explore, pp 1–6
17. Mahottamananda SN, Dilli Babu DN, Kadiresh PN (2021) Effect of number of inlet tangential ports and their angle on spray characteristics of plug type swirl injector. In: *Innovative Design, Analysis and Development Practices in Aerospace and Automotive Engineering. Lecture Notes in Mechanical Engineering*. Springer, Singapore

# Preparation of Low-Cost Oil Resistance Rubber Formulation for an Industrial Oil Seals from Leather Waste



N. Srirangarajalu, R. Dhanasekar, and S. Ponsubbiah

**Abstract** Oil seals are used to arrest the leakage of the fluid of the system during mechanical operation. Oil seals are widely used in automobile and aircraft, industrial machines, medical devices and farm equipment. The role of polymers and its ingredients play vital role in the development of excellent oil resistance properties in oil seals. In this research, the effort is made to use the waste generated by leather industry as a low-cost reinforcing short fibre in rubber formulations to make oil seal. Excellent oil resistance performance can be achieved through effective blending of elastomers and fillers with suitable cure systems and modifying the level of other compounding ingredients such as zinc oxide, stearic acid, coumarone indane resin and paraffin wax. Cost reduction is achieved through increasing filler loading and also with incorporation of the fibrous nature of chrome shavings obtained from leather processing industries. Compound formulations are prepared on the basis of critical studies which include employing various cure system, increasing zinc oxide content, stearic acid content, blending of rubbers and fillers. Based on these technical approaches served, formulations are developed. Out of these formulations, NBR 60 Phr/SBR 40 Phr with leather chrome shavings up to 30 Phr rubber formulation compound exhibit excellent oil resistance performance at lower cost.

**Keywords** l seals · Leather waste · Zinc oxide · Stearic acid and rubber

## 1 Introduction

Felipe Nunes Linhares et al. [1] analysed the effect of different sulphur-based crosslink networks on the nitrile rubber resistance to biodiesel. They used different

---

N. Srirangarajalu (✉)  
Madras Institute of Technology, Chennai, Tamil Nadu, India  
e-mail: [nsrirangarajalu@mitindia.edu](mailto:nsrirangarajalu@mitindia.edu)

R. Dhanasekar  
Institute of Chemical Technology, Chennai, Tamil Nadu, India

S. Ponsubbiah  
Institute of Leather Technology, Chennai, Tamil Nadu, India

types of cure system with different types of accelerators and concluded that the choice of accelerator played an important role on the resistance of rubber to the biodiesel and the crosslinking density was not a key factor with respect the resistance. Ponsubbiah and Sanjeev Gupta [2] investigated on preparation of low-cost shoe soling material from leather waste and they concluded that solid waste generated by leather industry could be reused in low-cost shoe soling materials for footwear applications. Rajasekar et al. [3] analyses nano-composites based on NBR with nano-clay in ENR compatibilizer by solution mixing technique to study about the change in morphological properties, mechanical properties, swelling resistance and cure properties are increased by reinforcing effect.

The predominant property of rubber is the elastic behaviour after deformation in compression or tension. In addition to this, rubbers are characterized by toughness under static and dynamic stresses, abrasion resistance, impermeability to air, water, resistance to swelling in solvents and chemicals. Also, rubbers are capable of adhering to textile, fibre and to metals.

Oil resistance is the phenomenon of rubber products and ability to resist swelling in dynamic oil environmental service condition. If suitable measures are not taken to account for increasing oil resistance, service life of the product will come down. Leather processing involves discharge of enormous quantities of solid wastes. Land-filling is an easy option for the disposal of solid wastes like chrome shavings and trimmings, but it is subjected to stringent environmental regulations because of the presence of chromium in these materials. An efficient way of utilization of these fibrous waste materials may be to combine them in NBR/SBR blends to make composite materials. Such applications based on the fibrous nature of the chrome shavings and trimmings would circumvent the environmental problem as well as evolve value-added products based on these waste materials.

In this study, a compound formulation with increasing oil resistance performance at lower cost, which could be employed for manufacturing oil seals with the incorporation of leather chrome waste in NBR/SBR blends was made. The blend was prepared by soften compounding in two roll mill mixing, in order to obtain uniform dispersion and distribution of the leather chrome waste in NBR/SBR blends with sulphur with delayed action accelerators as a curing system which meets efficient or semi-efficient cure medium. The changes obtained in the curing characteristics, mechanical properties, swelling and compression set have been analysed.

## 2 Materials

The following materials were used for the preparation of compound formulation with increasing oil resistance performance at lower cost material from leather waste (chrome shaving) (Table 1).

Chrome shavings are derived when the wet blue leathers are subjected in shaving operation in order to reduce thickness desirable thickness chrome shavings are tiny, thin and fibre protein material. This is harmful waste category and across the country

**Table 1** Name and role of the material

S. no	Name of the material	Role of the material
1	Nitrile rubber	Base polymer
2	Styrene-butadiene rubber 1702	Base polymer
3	Zinc oxide	Activator
4	Stearic acid	Activator
5	Red oxide/leather chrome shaving	Reinforcing filler
6	Coumarone indane resin	Tackifier
7	Diocetyl phthalate	Plasticizer
8	Silica	Filler
9	Whiting TiO <sub>2</sub>	Filler
10	High abrasion furnace carbon black N330	Reinforcing filler
11	General purpose furnace	Reinforcing filler
12	Fast extrusion furnace	Reinforcing filler
13	Trimethyldihydro quinolone (TDQ)	Antioxidant
14	4020 Dimethyl Butyl, PheylParaphenylenediamide	Anti-ozonant
15	Sulphur	Curative
16	Cyclohexyl benzothiazole sulphonamide (CBS)	Delayed primary accelerator
17	Tetramethylenethiurim disulphide (TMTD)	Secondary accelerator

about 35% of the total tannery wastes are generated during leather processing as trimmings and chrome shavings. Every year about 20,000 tons of chrome shavings are generated in India. Chrome shavings alone constitute to an extent of 10% of the total weight of raw hides/skins.

### 3 Design of Control Compounds

After going through various literatures, which provided information on the effect of various compounding ingredients on oil resistance, the following inference was drawn. The increase in oil resistance can be achieved by any one of methods of compounding or a combination of them.

- i. Employing cure semi-efficient system
- ii. Increasing the ZnO content
- iii. Increasing stearic acid content
- iv. Going for blend of basic rubbers and reinforcing fillers.

Based on the above inference, a critical study of the available choices and their suitability for the service condition is made prior to actual compounding. Selection of ingredients for compounds is arrived through systematic technical approach based on the research papers related to the enhancement of oil resistance of NBR rubber.

**Table 2** Compounds formulations

S. no	Ingredients name	Parts per hundred parts of rubber					
		F1	F2	F3	F4	F5	F6
1	Nitrile rubber	40	60	80	100	25	60
2	Styrene-butadiene rubber 1702	60	40	20	–	75	40
3	Zinc oxide	<b>4</b>	<b>5</b>	<b>6</b>	<b>7</b>	<b>3</b>	<b>5</b>
4	Stearic acid	<b>2.1</b>	<b>2.15</b>	<b>2.18</b>	<b>2.2</b>	<b>2.0</b>	<b>2.15</b>
5	Leather chrome shaving	–	–	–	–	15	30
6	Coumarone indane resin	<b>6.2</b>	<b>6.0</b>	<b>5.8</b>	<b>5.5</b>	<b>6.5</b>	<b>6.0</b>
7	Diocetyl phthalate	6	7	8	10	5	7
8	Silica	20	20	15	15	25	20
9	Whiting TiO <sup>2</sup>					45	
10	High abrasion furnace carbon black N330			10	10		
11	General purpose furnace	10	10				10
12	Fast extrusion furnace	45	40	45	45		40
13	Wood rosin	4	5	2	1	3	5
14	Paraffin wax	<b>0.4</b>	<b>0.6</b>	<b>0.8</b>	<b>1</b>	<b>0.2</b>	<b>0.6</b>
15	Trimethyl dihydroquinolone (TDQ)	1.5	1.5	1.5	1	1.5	1.5
16	4020 Dimethyl Butyl, PheylParaphenylenediamide	0.4	0.6	0.8	1	0.2	0.6
17	Sulphur	1.75	2	1.5	2.2	3.5	2
18	Cyclohexyl benzothiazole sulphonamide (CBS)	0.35	0.75	0.95	1.0	0.2	0.75
19	Tetramethylenethiurim disulphide (TMTD)	1.4	1.25	1.20	1.2	1.5	1.25

They could result in excellent oil resistance, low compression set and high hardness. Six different formulations (F1 to F6) were prepared as per Table 2 given.

## 4 Preparation and Curing

The homogeneous rubber mixes were prepared by using a two-roll mill. The following parameters were considered at the time of compounding process. (1) Temperature of the rolls is 303–312 K. (2) Roll speed is 16 rpm. (3) Pressure is 160 kg/cm<sup>2</sup>. The standard tensile slab is prepared by curing the stocks at 150 degree

centigrade for 10 min in the laboratory upstroke press, which is hydraulically operated and at a pressure of 125 kgf /cm<sup>2</sup>. Breathing is to be done to exclude any entrapped air, which otherwise may lead to blister formation.

## **5 Characterization**

### **5.1 Rheology**

The rheometer helps the compounder to choose the right material and its appropriate dose to meet the end requirement of the product. The rheometer exhibits the curing characteristics of the rubber compound and also monitors the processing characteristics as well as the physical properties of the material. The “cure curve” obtained with a rheometer is a fingerprint of the compound’s vulcanization and processing character. For characterization of compounds, the following tests were conducted. They are tensile strength, modulus at 300% elongation, at break, hardness, specific gravity and ash content percentage of swelling, abrasion strength, compression set and heat ageing.

### **5.2 Scanning Electron Microscopy**

The SEM micrographs (500X) of the fractured surfaces of the tensile tested specimens were taken using S150 stereo scan model. In order to provide visual data, to support the physico-mechanical behaviour of the polymeric compositions tensile fractured surfaces of the specimens were subjected to SEM micrograph study.

## **6 Results and Discussion**

### **6.1 Rheological Characteristics**

The curing characteristics are tested (Table 3).

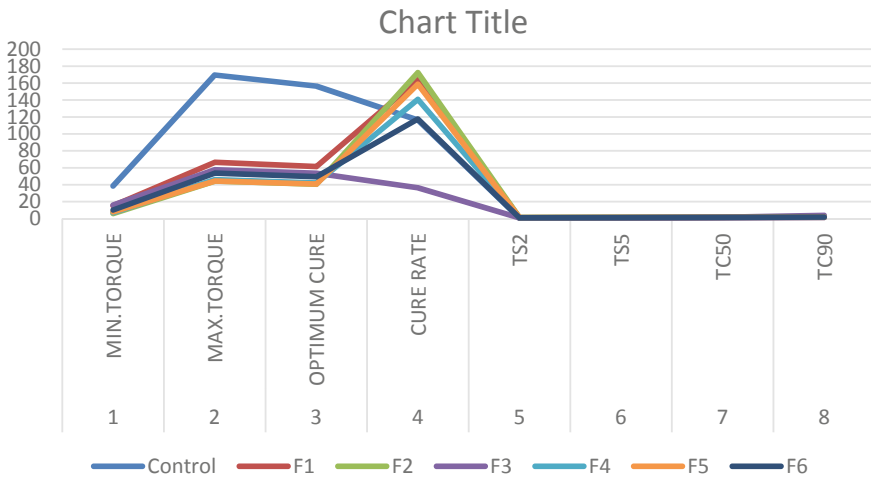
### **6.2 Micrographs**

See Fig. 1.



**Table 3** Cure properties of formulations

S. no	Parameters	F1	F2	F3	F4	F5	F6
1	Min. torque	15.2	6.1	16.0	7.2	8.1	10.2
2	Max. torque	66.5	44.3	57.7	45.9	44.4	53.6
3	Optimum cure	61.4	40.5	53.5	42	40.8	49.3
4	Cure rate	163.9	172.4	36.4	140.8	158.7	117.6
5	TS2	0.8	1.29	0.92	1.27	1.22	0.94
6	TS5	0.96	1.49	1.11	1.46	1.42	1.11
7	TC50	1.18	1.67	1.63	1.65	1.64	1.33
8	TC90	1.41	1.87	3.67	1.98	1.85	1.79



**Fig. 1** Curing characterization of different trials

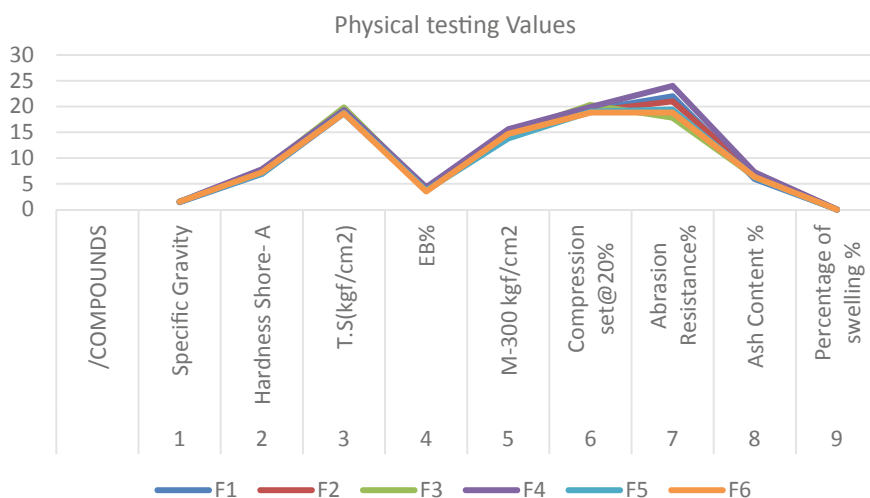
### 6.3 Physical Testing Values of Different Formulations

Tensile strength, modulus at 300% elongation, elongation at break, hardness, specific gravity, ash content, percentage of swelling, abrasion strength, compression set and heat ageing tests were conducted in our laboratory. The obtained values are tabulated for comparison in Table 4 (Fig. 2).

To achieve the excellent oil resistance, a control compound was (based on previous research as per the literature survey) developed followed with compounded, mixed, cured and tested. Based on the properties of reference control compound (Trail-4), seven numbers of required design compounds were developed, compounded, mixed, cured and tested. Table 4 shows that properties of design compounds for various tests performed for both performance and quality check. Oil resistance property is achieved through the technical approach which includes increasing content of zinc

**Table 4** Properties of oil seal design compounds

S. no	Properties/compounds	F1	F2	F3	F4	F5	F6
1	Specific gravity (gm/cm <sup>3</sup> )	1.388	1.490	1.492	1.510	1.520	1.518
2	Hardness shore-A	69	72	75	78	70	72
3	Tensile strength (kgf/cm <sup>2</sup> )	18.7	18.9	19.8	19.3	18.8	18.7
4	%Elongation	385	410	390	430	370	350
5	Elastic modulus 300 kgf/cm <sup>2</sup>	14.9	15.3	14.8	15.6	13.8	14.7
6	Compression set @20%	19.3	19.1	20.3	19.9	19.0	18.8
7	Abrasion resistance%	22.0	21.0	17.8	24.0	19.4	18.8
8	Ash content %	5.9	7.1	6.4	7.2	6.2	6.3
9	Percentage of swelling %	0.000	0.000	0.000	0.000	0.0000	0.000

**Fig. 2** Physical characterization of different trials

oxide from 4 to 7 Phr, increasing content of stearic acid content from 2 to 2.2 Phr, increasing content of dioctyl phthalate content from 5 to 10 Phr, increasing content of paraffin wax content from 0.2 to 1.0 Phr, decreasing content of CI resin from 6.5 to 5.5 Phr, decreasing content of SBR content from 50 to 20 Phr, blending of elastomers NBR and SBR, blending of fillers and by varying cure systems. Tensile strength increases progressively with increasing content of zinc oxide level from 4 to 7 Phr, stearic acid content from 2 to 2.2 Phr, dioctyl phthalate content from 5 to 10 Phr and paraffin wax content from 0.2 to 1.0 Phr. These observations are recognized due to increasing crosslink density of the polymeric chain of rubbers. Modulus at 300% increases progressively with increasing content of zinc oxide level from 4 to 7 Phr, stearic acid content from 2 to 2.2 Phr, dioctylphthalate content from 5 to 10 Phr and paraffin wax content from 0.2 to 1.0 Phr. These observations are recognized only

due to increasing crosslink density of the polymeric chain of rubbers. Elongation at break referring to Table 4 for design compounds 8 to 14, the elongation at break decreases with increasing content of zinc oxide level from 4 to 7 Phr, stearic acid content from 2 to 2.2 Phr, dioctyl phthalate content from 5 to 10 Phr and paraffin wax content from 0.2 to 1.0 Phr due to crosslink density and reduction in molecular chain mobility. Likewise increasing properties of oil resistance, swelling resistance, ash content, abrasion resistance, hardness and specific gravity were depended on the cure systems (efficient and semi-efficient) and blended fillers and rubbers with even though comparable values. Also, these approaches prove the decreasing properties of compression set and elongation at break in analogous manner. The cost of the designed superior oil resistance rubber compound further can be reduced by addition of leather chrome shaving (leather industry waste) up to 30 Phr as a powdered fibrous form, which are acted as reinforcing fillers, with increasing excellent oil resistance performance for medium duty oil seal commercial production. This statement was proved by test results of formulation-6.

## 7 Scanning Electron Microscopy

The SEM images of the sample are shown in Fig. 3, while individual SEM image of sample FS1, FS2 and FS3 shows individual fibres of chrome shavings without much aggregation. The SEM image of sample FS5 and FS6 shows the aggregation of fibre due to blending of NBR/SBR blend Phr of chrome shavings. The SEM image reveals that in all three samples chrome shavings are intermingled with polymers and also can see that in all the three samples chrome shavings are closely knitted.

## 8 Conclusion

The following conclusions were drawn are as follows.

Design and development of superior oil resistance performance rubber compound formulation at lower cost have been performed for industrial oil seal by varying the cure system, increasing level of ingredients loading and blending of rubber and blending of fillers, finally incorporation of leather chrome waste. From characterization of compounds under quality check, performance check and mechanical properties testing, it has been found that improvement in all properties except compression set property due to reinforcement effect and fine dispersion ingredients. From rheograph of compounds, it has been found that improvement the cure characteristics like increase in maximum torque, fast scorch time and effective cure time due to higher reinforcement of leather chrome shaving materials. Based on the results, compound formulations number-3 is to be used for general duty purpose applications, which were satisfied the most important service condition like superior oil resistance at lower cost and conforms to the specifications. Based on the results, compound

formulations formulation-6 could be used for medium duty purpose applications, which were satisfied the most important service condition like superior oil resistance at lower cost and conforms to the specifications. Based on the results, compound formulations formulation-4 is to be used for heavy duty purpose, which was satisfied the most important service condition like superior oil resistance at lower cost and conforms to the specifications.

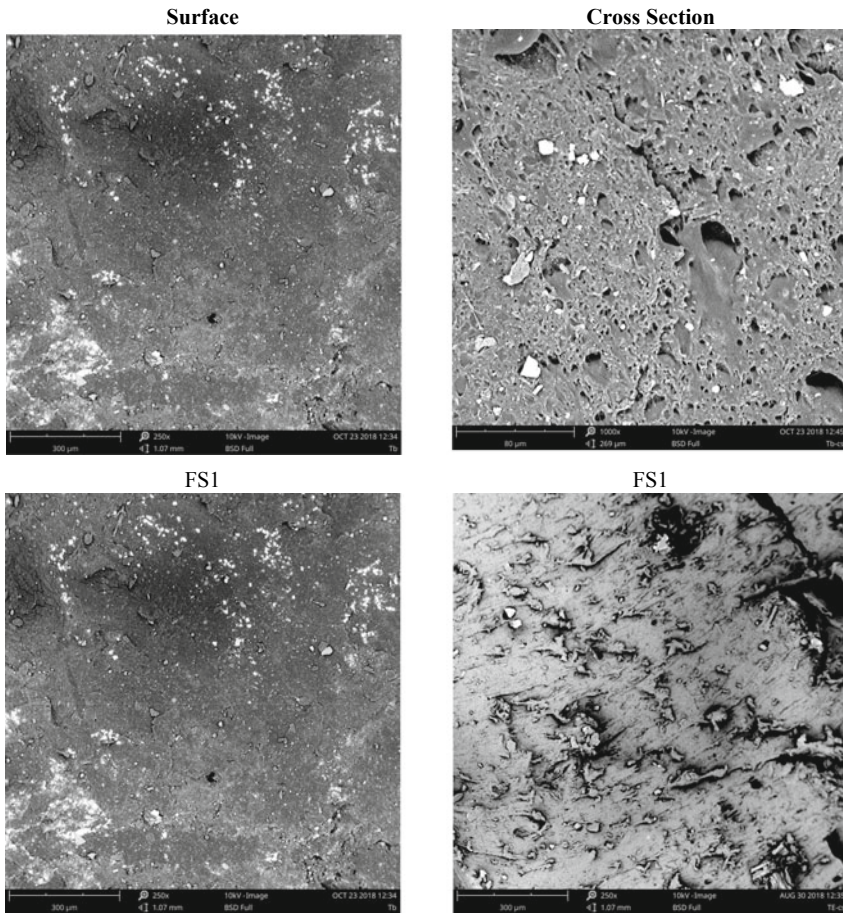


Fig. 3 SEM image of formulation-1 to formulation-6

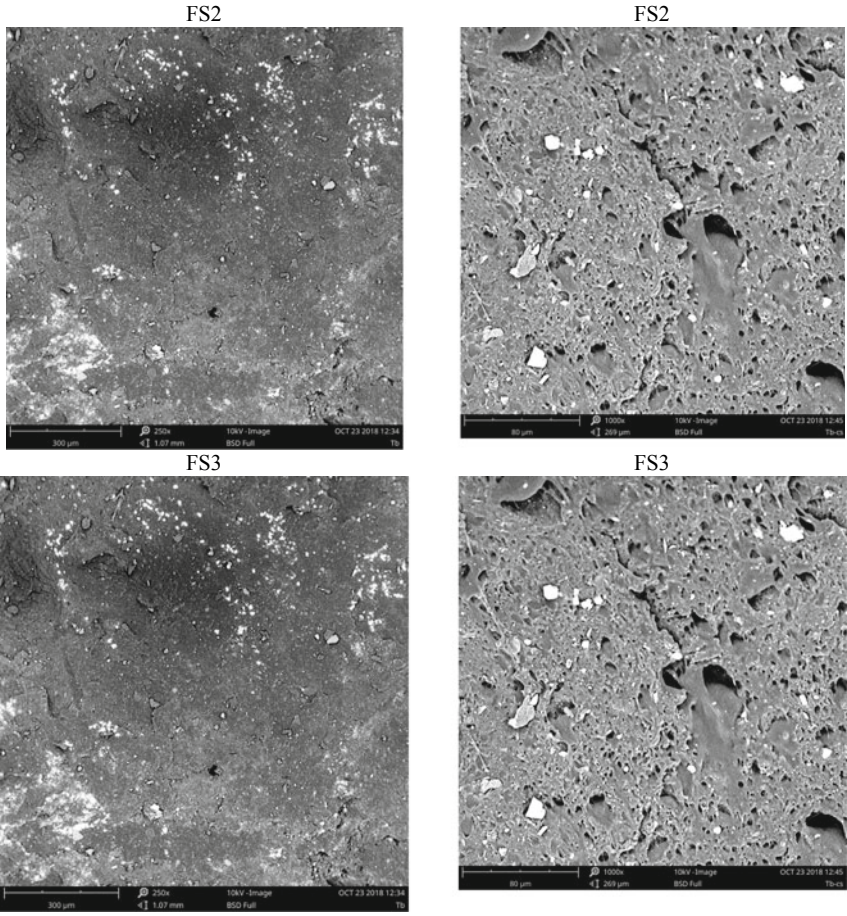


Fig. 3 (continued)



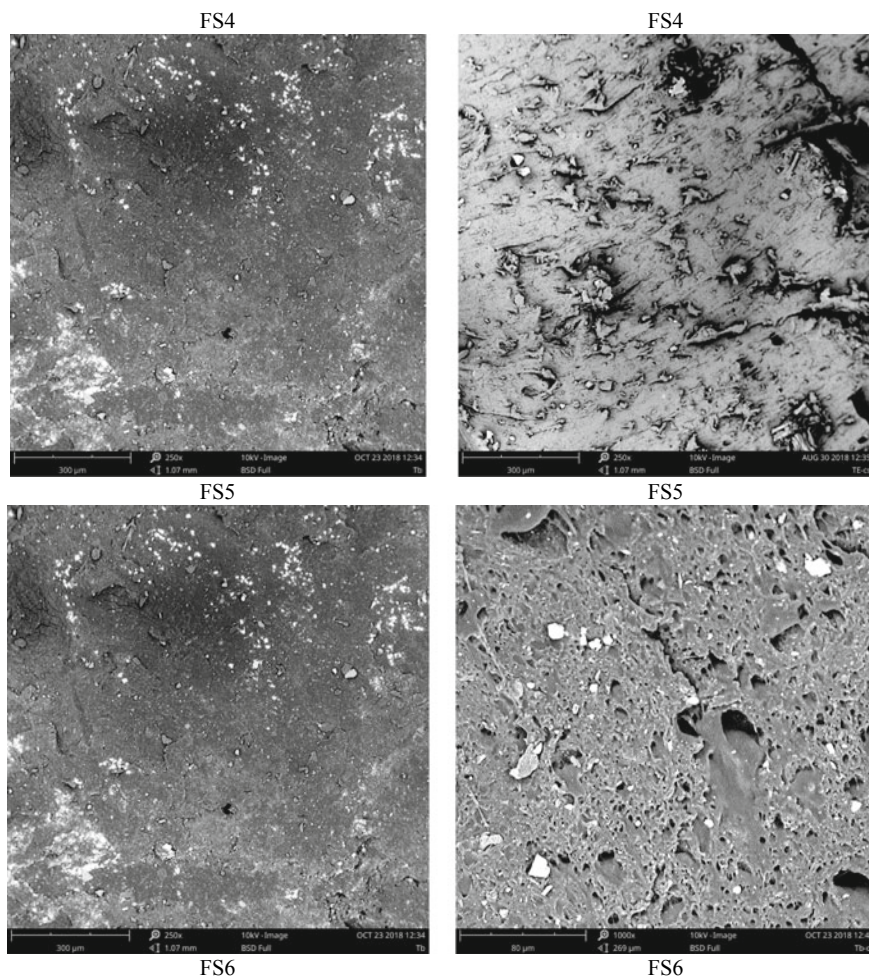


Fig. 3 (continued)

## References

1. Linhares FN, Kesch M, Neibergall U (2017) Effect of different Sulphur based crosslink networks on the Nitrile Rubber resistance to biodiesel. *Fuel* 191:130–139
2. Ponsubbiah S, Gupta S (2019) Preparation of low cost shoe soling material from leather waste. *Int J Res Advent Technol* 7(3), E-ISSN:2321–9637
3. Rajasekar R, Pal K, Heinrich G (2009) Development of NBR-Nano clay composites with ENR as compatibilizer. *Material Design* 30:3839–3845

# Effect of Two-Step Sintering Cycle by Chen and Wang (TSS-CW) on Aluminium (Al) Metal Matrix Reinforced with Niobium Carbide (NbC)



R. Raj Mohan, R. Venkatraman, S. Raghuraman, P. Sunil Kumar, and S. Yokesh Kumar

**Abstract** The aluminium metal matrix composites are significant material for the application of automobile mechanical transmission element like gears due to their excellent physical and mechanical properties. Generally, the addition of carbide reinforcements like silicon carbide (SiC) and tungsten carbide (WC) in pure aluminium (Al) metal matrix improves the hardness. Till now, research work related to pure Al and niobium carbide (NbC) combination for the improvement in mechanical properties has not been addressed widely. The hard-ceramic material like NbC reinforced with Al finds a replacement owing to its high strength and enhanced mechanical properties. In this study, NbC is reinforced with Al metal matrix with different proportions followed by mixing, compaction and subsequent two-step sintering method by Chen and Wang (TSS-CW) to obtain Al-NbC composites. This two-step sintering method was employed, and specimens were fabricated with varying percentage of NbC of 1, 5 and 10% to find out the effect of NbC in aluminium on micro-hardness and density. The micro-hardness test was performed after the sintering process shows that NbC increased the hardness of the specimen by increasing its percentage, whereas the density of the two-step sintered specimen varies concerning the addition of the reinforced element in the metal matrix.

**Keywords** Metal matrix composites (MMC) · Two-step sintering method by Chen and Wang (TSS-CW) · Aluminium · Niobium carbide · Micro-hardness · Density

## 1 Introduction

Powder metallurgy is an art and science technique for the processing of a mixture of metal alloys and ceramic powders by mixing/mixing powders, compaction and sintering of compacted powders, to obtain a specimen with the desired properties [1]. Powder metallurgy technique was established for the manufacture of metal powders into precision engineering components with properties equal to those produced by

---

R. Raj Mohan (✉) · R. Venkatraman · S. Raghuraman · P. Sunil Kumar · S. Yokesh Kumar  
School of Mechanical Engineering, SASTRA Deemed to be University, Thanjavur, India  
e-mail: [rajmohan@mech.sastra.edu](mailto:rajmohan@mech.sastra.edu)



forging [2]. Powder metallurgy industry involved in the production of a wide range of ferrous and non-ferrous materials, including composites, during the Second World War [3]. Powder metallurgy offers the advantage of obtaining a composite material with a high reinforcement content and therefore with high hardness, as well as the possibility of changing the composition according to the requirements [4]. Powder metallurgy techniques are desirable for the construction of metal matrix composites, achieving a homogeneous distribution of the reinforcement in the metal matrix [5]. Aluminium metal matrix composites (Al-MMC) are playing a vital role in enhancing the properties of different automotive and aircraft components [6]. The aluminium and its alloys are essential materials for the transportation industry as they contribute to the development of lightweight structures. The dispersion of hard-ceramic particles in the Al soft matrix can lead to a substantial reinforcement effect, resulting in composite materials exhibiting interesting mechanical properties and inspiring their technological use in sectors such as automotive and aerospace industries. About the two-step sintering method developed by Chen and Wang (TSS-CW) or reverse two-step sintering process, the first stage ( $T_1$ ) and the second stage ( $T_2$ ) temperature reduction, given the longer holding time in  $T_2$ , allow smaller grain sizes to be obtained at the same relative density compared to conventional sintering. The decrease in grain size for the same densification allows materials with improved properties to be achieved, particularly in terms of mechanical properties. The two-step sintering (TSS) indirectly enhances these properties. The TSS method is an efficient microstructure control method compared to expensive methods such as spark plasma sintering (SPS) [7]. The development of Al-MMC, Al is reinforced with oxides such as  $ZrO_2$ , carbides such as TiC, WC, NbC, (W, TiC) and boron carbide, and  $MgB_2$  has improved the mechanical properties, in particular, the resistance to fracture, hardness and wear. It is thermo-mechanically compatible with  $Al_2O_3$  and NbC. Recent works published in the literature have shown the feasibility of using of NbC as an inhibitor of grain growth in WC-Co hard metals, and as a hardening reinforcing agent in  $ZrO_2$ . It indicates that the use of niobium carbide as a possible source for strengthening it requires further study. Due to its combination of excellent chemical, thermal and electrical properties, niobium carbide (NbC) studies are also scientifically and technically impressive. The Al-NbC combination in powder metallurgy technique has not yet been investigated in the manufacture of products using two-step sintering processes to achieve the high hardness and proper densification. The objective is to compare the micro-hardness of samples provided by TSS-CW with a different percentage of NbC reinforced in aluminium and to study the effect of varying percentages of NbC in the density of aluminium.

## 2 Methodology

### 2.1 Material Selection

Pure aluminium and niobium carbide were chosen as the candidate materials for the manufacture of aluminium-based metal matrix composite (Al-MMC). The product specification of pure aluminium powder, Purity: 99.9%; Density: 2.7 g/cc; Melting Point: 660 °C; Boiling Point: 2470 °C; Average Particle Size (APS): <80 μm and for NbC powder, Purity: 99.9%; Density: 7.82 g/cc; Melting Point: 3490 °C; Boiling Point: 4300 °C; APS: <30 μm.

### 2.2 Material Processing

In high-energy planetary ball milling (HEPBM), the powders (Al and NbC) were mixed, and ball milling parameters are shown in Table 1. The powder was tested for its particle size after high-energy planetary ball milling (Table 2).

The sintering process is then performed on the Al-MMC followed by compaction under the optimum pressure of 280 MPa. The compaction pressure of the powder was at the correct level to reach a density of around 85–90% of the theoretical density, which is the optimum level. Explicitly concerning the two-step sintering developed by Chen and Wang (TSS-CW), the temperature reduction of the first step ( $T_1$ ) and the second step ( $T_2$ ), despite the longer holding time in  $T_2$ , make it possible to obtain smaller grain sizes for the same relative density compared to

**Table 1** HEPBM parameters

Parameters	
Time	5 h
Material of balls	Zirconium
Diameter of balls	8–10 mm
Weight-to-ball ratio	1:1
Speed	200 rpm
Process control agent	Methanol of 1% weight of Al-NbC powder

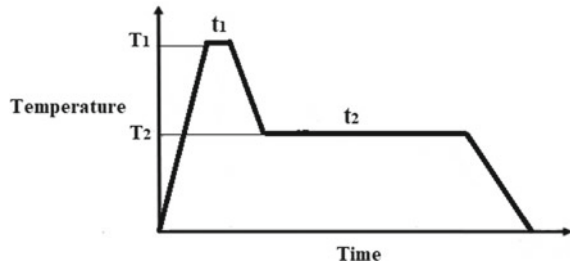
**Table 2** Average particle size (APS)

Material	APS (in nm)
Pure aluminium	955.5
Al-1% NbC	674.7
5% NbC	713.2
10% NbC	722.5

conventional sintering. The Chen and Wang two-step sintering cycle (TSS-CW) is shown in Fig. 1. The sintering conditions that allow densification to occur while at the same time stimulating the growth of grain are suitable for microstructural refining. The distinction between densification and grain growth allows the development of highly dense and nano-metric grains.

As a result, the two-step sintering cycle proposed by Chen and Wang is followed to control grain growth and increase density. Two-step sintering has been performed in the Muffle furnace (Fig. 2), and the input parameters for two-step sintering are shown in Table 3. Figure 3 shows the sintered specimens at different weight percentage of NbC.

**Fig. 1** Two-step sintering process by Chen and Wang



**Fig. 2** Muffle furnace

**Table 3** Parameters of two-step sintering

Temperature (°C)	Holding time (in minutes)
$T_0$ to $T_1$ —0 to 580 °C	Raised by 10 °C/min till it reached $T_1$ temperature
$T_1$ —580 °C	3 min
$T_2$ —462 °C	300 minutes at $T_2$ and then furnace cooled



Fig. 3 Sintered specimens

### 3 Results and Discussion

#### 3.1 Density Calculation

After the two-step sintering process, the specimen is taken from the muffle furnace, and density has been calculated. The actual density of all sintered specimens with varying percentage of NbC was calculated using Archimedes’ principle. The theoretical density calculation method uses the mixture rule (Eq. 1). The theoretical density of an Al-NbC is the maximum density that can be achieved without any voids in a hypothetical state. The actual density was calculated using an electronic balance (Make: SHIMADZU with least count 0.001 mg)

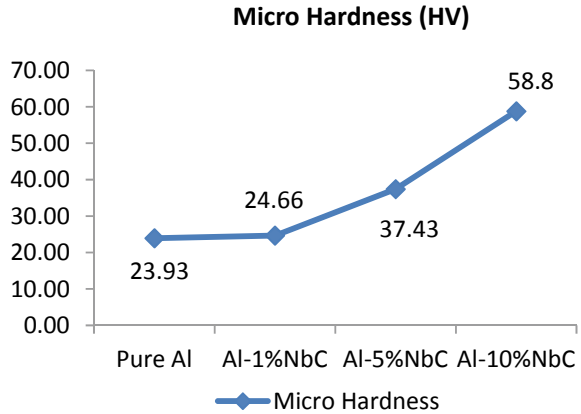
$$\text{Theoretical Density of the Specimen, } \rho_{th} = \frac{100}{\frac{\% \text{ Wt of Al}}{\rho_{Al}} + \frac{\% \text{ Wt of NbC}}{\rho_{NbC}}} \quad (1)$$

From Table 4, the Al-MMC density is initially decreased up to 5% of NbC, and again it increases slightly at 10% of NbC. Generally, the longer holding time ‘ $t_2$ ’ at a sintering temperature of 462 °C affects densification of pure metals such as aluminium. Nevertheless, in the case of the addition of transition metal carbide such as NbC to aluminium, the percentage of density obtained is decreased due to the effect of the reverse two-step sintering process. In reverse two-step sintering process, grain

Table 4 Density of the specimen after TSS-CW

Percentage of NbC (% wt.)	Al density g/cc	NbC density g/cc	Theoretical density g/cc	Actual density g/cc	Percentage of density achieved
0	2.7	7.82	2.7	2.610	96.77
1	2.7	7.82	2.7170	2.440	90.00
5	2.7	7.82	2.7913	2.440	87.40
10	2.7	7.82	2.8891	2.553	88.40

**Fig. 4** Micro-hardness of the sintered specimen



growth was restricted to a higher sintering temperature of 580 °C with a minimum dwell time ' $t_1$ ' of 3 min. Thus, the proper distribution of NbC in the aluminium matrix is not supposed to reduce the pores in the matrix. Besides, the percentage of density reached after the introduction of NbC is less than 90% relative to pure aluminium.

### 3.2 Micro-hardness of the Sintered Specimen

The average value of the micro-hardness was determined using a micro Vickers hardness testing machine (Make: SHIMADZU). A diamond indenter with a square pyramid base has been used and load applied on the sample was 5 kN with the dwell period of 10 s. From Fig. 4, the micro-hardness of aluminium metal matrix composite is increased by adding niobium carbide to aluminium. Up to 5% of NbC, the micro-hardness value increases gradually due to its proper distribution in the matrix, followed by a rapid rise in the micro-hardness value to 10% of NbC, which contributes to the rupture of the specimen.

## 4 Conclusion

From the observations,

- There is a change in Al-MMC density and micro-hardness with an increase in NbC weight percentage.
- TSS-CW affects the densification of the sintered specimen while increasing the weight percentage of NbC.

- The addition of NbC has more influence on the micro-hardness of the Al-MMC, but the percentage of density achieved is less than 90%.
- Highest micro-hardness value was achieved at 10% NbC reinforcement, but it leads to the rupture of the specimen.
- Finally, to increase the densification as well as to control the attainment of higher micro-hardness, further subsequent treatment is required.

## References

1. Abirami, Thirupathi K, Raghuraman S (2017) Investigations on the influence of mechanical behaviour of copper aluminium nickel powder compacts processed through powder metallurgy. In: Lecture notes of mechanical engineering (F9), pp 281–292
2. Pickens JR (1981) Aluminium powder metallurgy technology for high-strength applications. *J Mater Sci* 16(6):1437–1457
3. Froes FH, Eylon D, Suryanarayana C (1990) Thermo chemical processing of titanium alloys. *JOM* 42:26–29
4. Ruiz-Navas EM, Garcia R, Gordo E, Velasco, FJ (2003) Development and characterisation of high-speed steel matrix composites gradient materials. *J Mater Process Technol* 143–144(1):769–775
5. Travessa DN, Silva, MJ, Cardoso KR (2017) Niobium carbide-reinforced al matrix composites produced by high-energy ball milling. *Metall Mater Trans B Process Metall Mater Process Sci* 48(3):1754–1762
6. Chidvilas M, Raj Mohan R, Raghuraman S (2019) Machinability study on Al-SiC metal matrix composite (MMC) using electrical discharge machining (EDM). *Int J Recent Technol Eng* 8(1):41–50
7. Loh NJ, Simao L, Faller CA, De Noni A, Montedo ORK (2016) A review of two-step sintering for ceramics. *Ceram Int* 42(11):12556–12572

# Drilling Performances of Kenaf Fibre/Steel Mesh Reinforced Hybrid Epoxy Composites



K. Jamesha Ibrahim, M. Thirumurugan, P. D. Jeyakumar,  
A. Arockia Julias, and S. Mohamed Fahad

**Abstract** Drilling is one of the important machining operations in polymer matrix composites, which is used to join the polymer composites temporarily. The fiber reinforced polymer composites are widely used in automobile and aerospace fields in which the polymer composites are to be joined with similar or dissimilar materials. The present work focuses on the effects drilling parameters (speed and drill diameter) on kenaf fiber/steel wire mesh hybrid epoxy composites. To obtain the better mechanical properties, the hybrid composites are designed in such way that two layers of kenaf fiber and one layer of steel wire mesh reinforced in epoxy resin matrix. Delaminations, fiber pullout, and cracks are observed in microscopic examinations. Two different parameters of drilling speed and drill diameters are varied to cognizance the mechanism of delamination. The acceptable quality level of drilled holes was measured using toolmakers microscope through by calculating the circularity of drilled holes.

## 1 Introduction

Composite materials are the preferred materials for automobile, marine, and aeronautical applications because of their tailor-made properties and lower manufacturing cost. Even though the polymer composites are used in many engineering applications, fibers are reinforced with polymers to obtain better physical and mechanical properties. Fiber reinforced polymer (FRP) composites are provided the high-specific strength and specific stiffness compared to other composite materials [1–4]. The reinforced materials should have good mechanical properties and lightweight [3–9]. Newer composite materials are developed with the wide range of reinforcing materials with different polymer matrix based on the specific requirements of industries. Kenaf fiber is the biodegradable and recyclable material which contains 65%

---

K. Jamesha Ibrahim (✉) · M. Thirumurugan · P. D. Jeyakumar · A. Arockia Julias ·  
S. Mohamed Fahad

Department of Mechanical Engineering, B.S. Abdur Rahman Crescent Institute of Science and  
Technology, Chennai 600048, India

e-mail: [jameshaibrahim@crescent.education](mailto:jameshaibrahim@crescent.education)

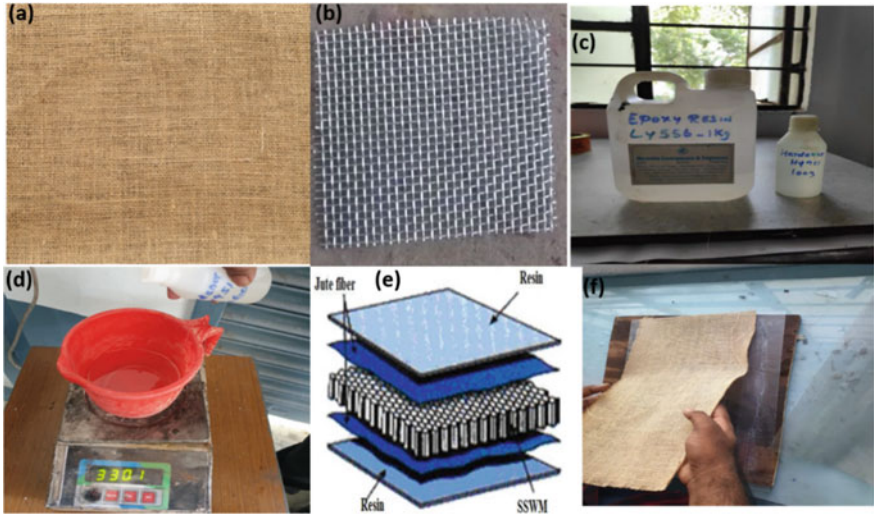
of cellulose and 16% lignin. Kenaf fiber possesses good mechanical properties and offers a great serviceability. Steel wire mesh has good corrosion resistance which widely used in many industries. A wire mesh contains uniformly spaced and crossed wires in regular patterns to form a screen. Based on the applications, the wire mesh patterns may be in the shape of regular square, circular, or any other polygonal shape. Hybrid composites are the one developed to meet the needs of industries with better strength–weight ratio [10, 11]. Machining is considered as one of the important processes for the composites to prepare the parts according to suits the customer needs. Among the machining processes, drilling operation is very much important to fabricate/join the components. In hybrid or laminate polymer composites, delamination is one of the predominant phenomena which are very much useful to understand the failure modes of composites. The heterogeneous structure with multi-phase materials in hybrid composites severely leads to inter-ply failure during drilling operation which may further lead into rejection of the parts or may lead into poor joints [12, 13]. Brinksmeier et al. [14] performed the orbital and conventional drilling process on three different aluminum/CFRP/titanium materials and measured the surface quality of drilled holes. The orbital drilling gives the quality surfaces with less cracks and fiber damages compared to the conventional drilling process. Arul et al. [15] related the cutting parameters with acoustic emission parameters and used the acoustic emission technique to improve the surface quality of drilled holes. Abhishek et al. [16] optimized the drilling parameters using Taguchi technique and minimized the subsurface defects for CFRP composites. Eneyew and Ramulu [17] analyzed the surface quality of drilled holes by varying the cutting direction and fiber orientation on CFRP composites. In this work, two layers kenaf fiber and one layer of steel wire mesh are used as reinforcements with epoxy resin as matrix to fabricate hybrid composites. The main objective of this paper is to study the delamination behavior for the different speeds and drill diameters in hybrid epoxy composites.

## 2 Experimental Procedure

### Preparations of composite:

The woven kenaf fiber and 304 steel wire mesh ( $\Phi$ 500 mm wire) were used as a reinforcement. LY 556 epoxy resin and HY 956 hardener were used as a matrix for the composite preparation. The LY 556 and HY 956 were mixed in the ratio of 10:1. The composite preparation was carried out in the mold with the size of 400 \* 400 \* 8 mm. To avoid sticking of resin in the mold, a release agent was applied on its surfaces. The sequential order of woven kenaf fiber/stainless steel mesh/woven kenaf fiber was stacked and the resin applied by maintaining the fiber/matrix ratio as 40:60. The fiber/mesh orientations were maintained as 0°, and the composites were prepared by hand lay-up technique. Utmost care was given not to form air pockets during the preparation of composites. The images of composite preparation are shown in Fig. 1.





**Fig. 1** a Woven kenaf fiber, b steel wire mesh, c LY 556 epoxy resin, d weight measurements, e stacking order, f hybrid composite preparation

The composites are cured for 24 h at room temperature by applying the compressive load 200 kg through hydraulic press. The entire thickness of the sample was maintained at 3 mm to avoid deviations. The hydraulic press and the prepared hybrid composites are shown in Fig. 2.

The prepared sample was cut with the dimensions of 20 \* 20 \* 3 mm for the drilling operations through waterjet machine. The following parameters were used for water jet cutting: Abrasive flow rate—400 g/min, transverse speed—650 mm/min, standoff

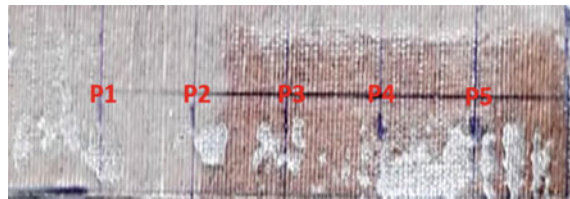


**Fig. 2** a Hydraulic press, b prepared composite



**Fig. 3** a Waterjet machine, b cut sample of hybrid polymer composite

**Fig. 4** Positions (P1, P2, P3, P4, P5) marked for drilling process



distance—2 mm, water pressure—3500 bar, nozzle diameter—1.1 mm, and abrasive used—GMA GARNET 80 MESH. The waterjet machine and the cut sample are shown in Fig. 3.

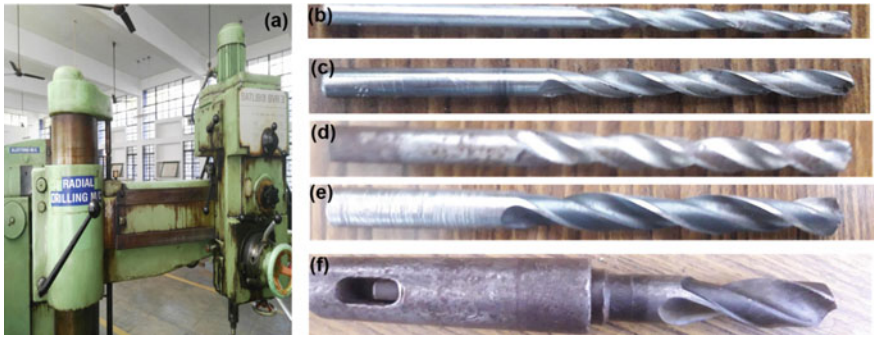
On the cut samples, the drilling positions were marked with markers to perform the drilling operation for the different diameters and drill speeds (Fig. 4). Equally spaced five drilling positions were marked, and similar five samples were kept ready for the drilling process.

#### **Drilling of composites:**

Drilling of composites was done by the radial drilling machine (shown in Fig. 5) using the high-speed steel (HSS) tool.

Drilling tool was attached on the radial arm and can be accustomed and fixed to any chosen point. The prepared hybrid composites were kept on the work-hold area of the radial drilling machine and fixed firmly by using the clamps and drilling was performed. Different speeds were kept based on the gear set available with the drilling machine. The different diameters of the drill tools were used as per Table 1.

A universal toolmaker microscope was used for checking the quality of the drilled holes. The toolmaker microscope positioning mechanism works similar like screw gauge with the least count of  $0.05 \mu\text{m}$  to position the drilled holes under the microscope. Toolmakers microscope have sample holder which has three axis movements. The sample holder was made of glass plate in which the drilled hybrid composites

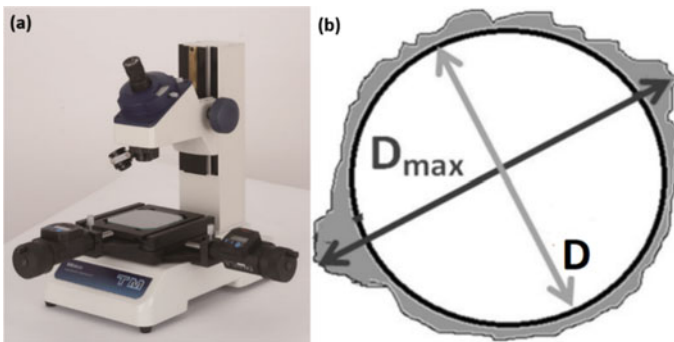


**Fig. 5** a Radial drilling machine; drill tool dimensions, b  $\phi$  2 mm, c  $\phi$  4 mm, d  $\phi$  6 mm, e  $\phi$  10 mm, f  $\phi$  16 mm

**Table 1** Drilling parameters used in polymer composites

Sl. No.	Drilling tool diameter ( $\phi$ , mm)	Speed (rpm) ( $S$ )	Feed (mm/min) ( $F$ )
1	2	280 ( $S_1$ )	50
2	4	450 ( $S_2$ )	
3	6	710 ( $S_3$ )	
4	10	1120 ( $S_4$ )	
5	16	2800 ( $S_5$ )	

were placed for the measurements. Two movements of sample holder in  $X$ - and  $Y$ -directions, whereas the rotation of the table considered as third movement. A 30X magnification is used in experiment for measuring the diameter of drilled holes. The toolmaker microscope is shown in Fig. 6. Delamination in hybrid composites is shown in Fig. 4. The delamination factor ( $F_d$ ) is calculated from the following



**Fig. 6** a Toolmakers microscope, b measurement of maximum diameter

equation  $F_d = D_{\max}/D$ , where  $D_{\max}$  is the maximum diameter of drilled holes and  $D$  is diameter of the drill.

### 3 Results and Discussion

From Fig. 7, it is clearly understand that different drilling speeds result in different surface quality of holes which are obtained.

Delamination is the important factor in fiber reinforced polymer composites. The present work of hybrid composites contains the kenaf fiber and steel wire mesh. Both kenaf fiber and steel wire mesh are different materials which results in homogeneity in the composite structure and results in the delamination occurs which is clearly visible from microscopic images (Fig. 8). From the delamination results, the mode of failure can be easily predictable. Delamination causes the separation of adjacent layers by weakening the interface layers present in the composites. The small diameter of drilled holes ( $\Phi 2$  and  $\Phi 4$  mm) has shown more damages than the bigger diameter of drilled holes irrespective of speeds.

More than ten readings of deviation values are measured from the toolmaker microscope. Initially, the center positions of holes are fixed by matching the cross wires given in microscope by adjusting the thimble. Now, the center positions are marked as (0, 0) in  $x$ - and  $y$ -directions by moving the thimble the deviation values are



**Fig. 7** Macroscopic images of drilled holes in hybrid polymer composite for different diameter of drill tool. **a** 2 mm, **b** 4 mm, **c** 6 mm, **d** 10 mm, **e** 16 mm



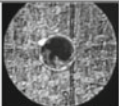
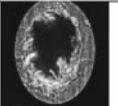
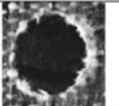

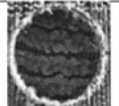
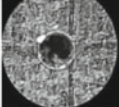
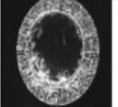
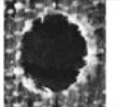
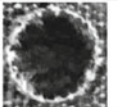

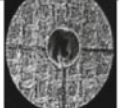
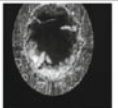
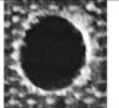
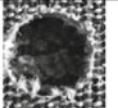

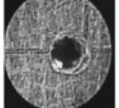
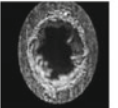
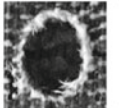
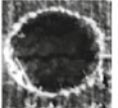

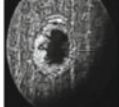
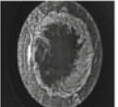
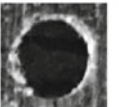
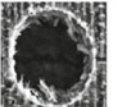
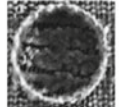
Sl. No.	Speed (rpm)	Drilled hole diameter (mm)				
		2	4	6	10	16
1	280					
2	450					
3	710					
4	1120					
5	2800					

Fig. 8 Microscopic images of different diameters of drilled holes for different speeds

measured and thereby the  $D_{max}$  values are calculated. The  $X$ -axis and  $Y$ -axis deviation values are given in Fig. 9. For the smaller diameters, the deviation values are greatly differing with respect to  $X$ - and  $Y$ -axes. But in bigger diameters, the deviation values are minimal difference with respect to the two different axes.

Delamination can affect the compression strength of composite laminate, and it may leads to failure during loading. The brittle nature of epoxy resin (matrix) results low fracture toughness which also leads to the failure of composites. The delamination factor was calculated for the average  $D_{max}$  for the different diameter of holes and the graph is plotted in Fig. 10.

High delamination factor values are observed for 2 mm diameter holes for different speeds. The non-uniform pressure distribution may occur in drilling operation when small diameter of drill is performed. The resistance given by the steel wire mesh (particularly in smaller diameters) creates the non-uniform pressure distribution. A common value of delamination factor is observed in bigger diameter holes for different speeds.

#### 4 Conclusion

The hybrid composites was fabricated using kenaf fiber and steel wire mesh as reinforcement with epoxy resin as matrix by hand lay-up technique. The hybrid

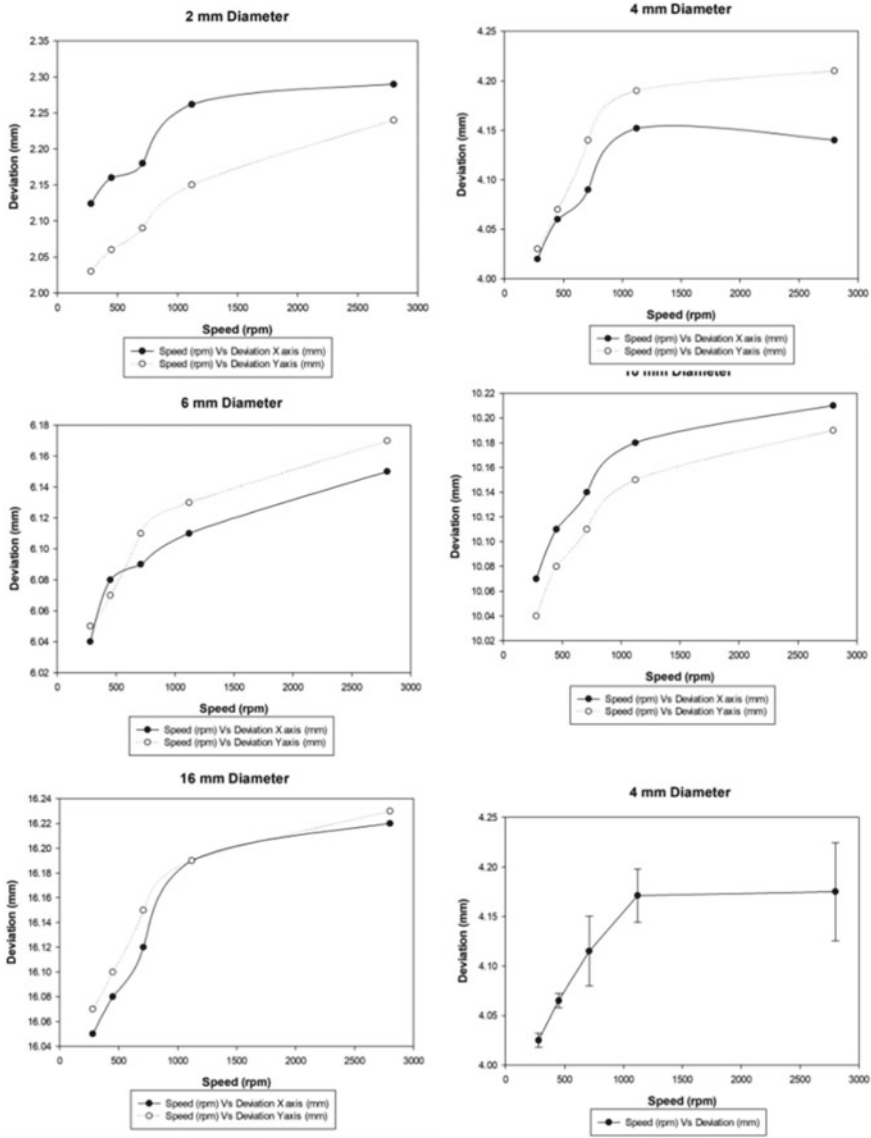


Fig. 9 Deviation values versus rpm for different diameters of drilled holes

composites were cut by using waterjet machine, and the drilling operations was performed on the cut samples. Using five different speeds by keeping the feed rate as constant holes were created by using five different diameters of drill tools. The microscopic examination was carried to understand the delamination behavior which resulted a non-uniform delamination (ovality) occurs in smaller hole diameters and the uniform delamination occurred for bigger hole diameters. For the hole diameter of

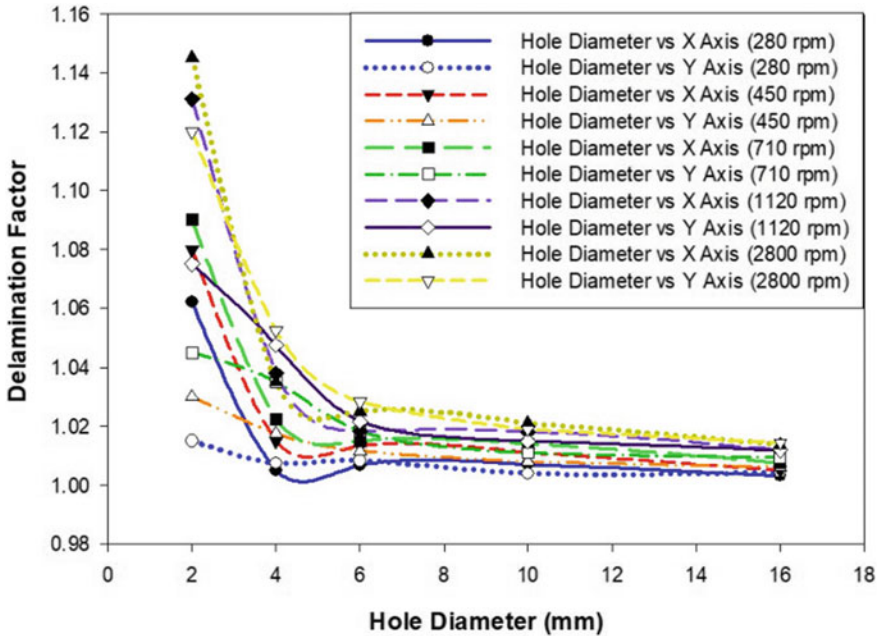


Fig. 10 Delamination factor versus hole diameter

2 mm showed 14% higher delamination factor for speeds from 280 to 2800 rpm. The steel wire mesh reinforcement created the non-uniform pressure when small diameter holes were drilled in hybrid composites. Very closer values of delamination factor were observed for bigger diameter of holes for all drill speeds.

### References

1. Astrom BT (2002) Manufacturing of polymer composites. Nelson Thrones, UK
2. Davim JP, Pedro R (2003) Drilling of carbon fiber reinforced plastics manufactured by autoclave experimental and statistical study. *Mater Design* 24:315–324
3. Omar F, Andrzej KB, Hans-Peter F, Mohini S (2012) Biocomposites reinforced with natural fibers. *Prog Polym Sci* 37(11):1552–1596
4. Sheikh-Ahmad J (2009) Machining of polymer composites. Springer, New York
5. Liu DF, Tang YJ, Cong WL (2012) A review of mechanical drilling for composite laminates. *Compos Struct* 94:1265–1279
6. Zhang X, Wang P, Haosiang Neo H, Lim G, Malcolm AA, Yang E-H et al (2016) Design of glass fiber reinforced plastics modified with CNT and pre-stretching fabric for potential sports instruments. *Mater Des* 92:621–631
7. Rajamurugan TV, Shanmugam K, Palanikumar K (2013) Analysis of delamination in drilling glass fiber reinforced polyester composites. *Mater Des* 45:80–87
8. Bonnet C, Poulachon G, Rech J, Girard Y, Coastes JP (2015) CFRP drilling: fundamental study of local feed force and consequences on hole exit damage. *Int J Mach Tools Manuf* 94:57–64

9. Samuel Raj D, Karunamoorthy L (2016) Study of the effect of toolwear on hole quality in drilling CFRP to select a suitable drill for multi-criteria hole quality. *Mater Manuf Process* 31:587–592
10. Khalina A, Jalaluddin H, Yeong HA (2010) Properties of kenaf (*Hibiscus Cannabinus* L.) Bast fibre reinforced unsaturated polyester composite. In: *Research in natural fibre reinforced polymer composites*, pp 233–246
11. Salleh Z, Berhan MN, Hyei KM, Isaac DH (2012) Cold-pressed kenaf and fiberglass hybrid composites laminates: effect of fibre type. *World Academy of Science Engineering and Technology*, pp 1509–1513
12. Sheikh-Ahmad JY (2009) *Machining of polymer composites*. The Petroleum Institute, Department of Mechanical Engineering, United Arab Emirates, ISBN 978-0-38735539-9. Ed. Springer Science, Abu Dhabi
13. Mohan NS, Kulkarni SM, Ramachandra A (2007) Delamination analysis in drilling of glass fibre reinforced plastic (GFRP) composite materials. *J Mater Process Technol* 186:265–271
14. Brinksmeier E, Fangmann S, Rentsch R (2011) Drilling of composites and resulting surface integrity. *Manuf Technol* 60:57–60
15. Arul S, Vijayaraghavan L, Malhotra SK (2007) Online monitoring of acoustic emission for quality control in drilling of polymeric composites. *J Mater Process Technol* 185:184–190
16. Abhishek K, Datta S, Mahapatra SS (2014) Optimization of thrust, torque, entry, and exit delamination factor during drilling of CFRP composites. *Int J Adv Manuf Technol*
17. Eneyew ED, Ramulu M (2014) Experimental study of surface quality and damage when drilling unidirectional CFRP composites. *J Mater Res Technol* 3:354–362
18. Starost K, Njuguna J (2014) A review on the effect of mechanical drilling on polymer nanocomposites. In: *IOP conference series: material science and engineering*, p 64



# Hardness–Elastic Modulus Relationship for Nitrile Rubber and Nitrile Rubber–Polyvinyl Chloride Blends



D. Murali Manohar, Bikash C. Chakraborty, and S. Shamshath Begum

**Abstract** Nitrile rubber (NBR) and nitrile rubber–polyvinyl chloride (NBR–PVC50/50) (NVC55) blends are vulcanized by sulphur curing system using high abrasion furnace carbon black (CB–HAF) and graphite (GT) as reinforcements in the present investigation. The mechanical properties of the compositions are evaluated. The relationship of durometer hardness with Young’s modulus ( $E$ ) is determined and compared with theoretical models of the literature. It is observed that the relationship is not in good agreement with any literature model for full range of hardness from 49 to 88 Shore ‘A’ ( $S_A$ ). While some models are more applicable to low hardness range, some others are better applicable to higher range. However,  $\log$  (modulus) is found to be varying linearly with Shore ‘A’ hardness. The compressive modulus ( $E_C$ ) of the compositions is calculated using the theoretical relationship with hardness from the literature. The ratio of calculated compressive modulus to measure Young’s modulus for NBR and NVC55 compositions is evaluated as a function of hardness and compared with the available literature data. The ratio for NBR compositions is almost identical for two models, while for NVC55 compositions, one model results in constant ratio irrespective of hardness, and the other predicts a widely varying ratio depending on hardness.

**Keywords** NBR · NBR/PVC · Carbon black · Graphite · Hardness · Modulus

## 1 Introduction

Nitrile rubber and its blend with PVC are versatile elastomeric materials and are widely used in vibration damping applications because of their high damping capability [1–9]. One of the criteria of shock and vibration (S&V) mounts for machinery is

---

D. Murali Manohar (✉) · S. Shamshath Begum  
Department of Polymer Engineering, B.S. Abdur Rahman Crescent Institute of Science and Technology, Chennai, India  
e-mail: [murali@crscent.education](mailto:murali@crscent.education)

B. C. Chakraborty  
Polymer Nanotechnology Centre, B.S. Abdur Rahman Crescent Institute of Science and Technology, Chennai, India

© The Author(s), under exclusive license to Springer Nature Singapore Pte Ltd. 2021  
L. Ganippa et al. (eds.), *Advances in Design and Thermal Systems*, Lecture Notes in Mechanical Engineering, [https://doi.org/10.1007/978-981-33-6428-8\\_24](https://doi.org/10.1007/978-981-33-6428-8_24)

301

natural frequency which depends on compressive modulus of the elastomer. However, nonlinearity in elastic properties is exhibited by these elastomers even at very low stress and strain levels. In addition, the relaxation is also quite dominant, for most applicable temperatures. These factors may result in errors in the determination of modulus in tensile or compression experiment. A very simple method of estimation of elastic modulus of an elastomer is hardness by indentation. Measuring hardness is very simple and is precisely described in American Society for Testing and Materials (ASTM) standards and in some literatures [10–13].

It has been established that the hardness, expressed in durometer or International hardness Rubber Degree (IHRD) can be correlated to Young's modulus by theoretical and empirical equations [14–19]. There are also reports of experimental verification and applicability of these standard equations [20–23]. The derived relation of Young's modulus and Shore 'A' durometer is given by Gent [14] in Eq. (1).

$$E(\text{kg/cm}^2) = \frac{56 + 7.66S_A}{2.67r(254 - 2.54S_A)} \quad (1)$$

where  $E$  is Young's modulus,  $S_A$  is the Shore 'A' hardness and  $r$  is the radius of the round tip of the indenter. Gent [14] considered the indenter tip as a cylinder of round tip having a radius of 0.0515 mm for Shore 'A'. Therefore, the final equation can be written as:

$$E(\text{MPa}) = \frac{5.4936 + 0.747852S_A}{34.92627 - 0.349263S_A} \quad (2)$$

where  $E$  is expressed in  $\text{N/mm}^2$  or MPa. The above relationship was found to be in good agreement with the theoretical relationship of Young's modulus and British Standard (BS) and IRHD from 40° A onwards. For large indentation, i.e. in case of soft rubbers, some variations were observed. However, the theory on linear elasticity was considered in the derivation.

Qi et al. [15] used nonlinear finite element method (FEM) simulation of hardness tests that were used to correlate Shore 'A' and 'D' hardness and stress–strain behaviour of elastomers. The soft rubbers were characterized by higher relaxation and nonlinearity which results in more deviation if linear elastic theory was used. The authors also observed the following relationship of hardness and Young's modulus:

$$\begin{aligned} \log_{10} E &= 0.0235S_A - 0.6403 \\ S_A &= \text{Shore } A \quad 20 < S_A < 80 \\ \text{Shore } D + 50 & \quad 80A < S_A < 85D \end{aligned} \quad (3)$$

However, the nonlinear FEM analysis gives higher values of elastic modulus compared to those obtained by Gent [14]. The authors used two formulations of poly (butadiene) (BR) and one polyurethane (PUR) elastomer varying in elastic modulus to validate the prediction. They also considered stress relaxation of elastomers used

for experimental validation of the prediction. The predicted values by these authors are more or less similar to those predicted by Gent [14].

Equation (2) does not satisfy the relationship below a Shore ‘A’ hardness 40, and Eq. (3) is valid for a range of Shore ‘A’ 20 to Shore ‘D’ 85. Whereas in British Standard 903 (BS 903), the following expression is valid for Shore ‘A’ range from 0 to 100, correspondingly elastic modulus of any value [17].

$$S_A = 100\text{erf}\left(3.186 \times 10^{-4} E^{\frac{1}{2}}\right) \quad (4)$$

where erf stands for the error function.

Briscoe and Sebastian [16] gave following equations to establish relation between indenting force, indentation, durometer hardness and Young’s modulus of rubber:

$$F = 0.55 + 0.075S_A$$

$$F = \frac{2E^*}{\tan \theta} \left\{ ha \tan \theta - \frac{a^2}{2} \left[ \frac{\pi}{2} - \arcsin\left(\frac{b}{a}\right) \right] + \frac{b}{2} \sqrt{a^2 - b^2} \right\} \quad (5)$$

$$E^* = \frac{E}{1 - \nu^2}$$

Cao et al. [24] used FEM to develop an expression relating the load and indentation for any arbitrary ratio of the radius of the indenter to the thickness of the rubber. Huang and Lu [25] studied poly (methyl methacrylate) (PMMA) and poly (vinyl acetate) (PVAc) having widely varying relaxation time for prediction of bulk and shear relaxation function (modulus), using nanoindentation method.

The hardness measurement is by compressive indentation force, and the theory of compression in rubber is quite complex. The main problems are (1) incompressibility or limited compressibility in bulk, hence uncertainty in assuming a reasonable Poisson’s ratio, (2) mode conversion (to shear deformation) in transverse direction during compression and (3) dependence of modulus on shape factor. Various aspects of compression of rubber blocks were studied by researchers with respect to strain, shape, aspect ratio, thickness, etc. [26–29]. Compressive modulus ( $E_C$ ) is predicted through a relationship with Durometer hardness by Horton et al. [30], Rocard [31], Iken [32], Kunz and Studer [33] and with Young’s modulus by Gent and Lindley [26]. Commonly used expression of  $E_C$  is given by Gent and Lindley [26] as:

$$E_C = E(1 + 2kS^2) \quad (6)$$

where  $S$  is the shape factor and  $k$  is a constant, termed as ‘material modifying factor’, determined by experiment. Yeoh et al. [27] have studied thin strips, cylindrical discs and rectangular blocks for prediction of compression force considering bulk compressibility of rubbers. They have given a similar expression as Eq. (6) for compression force for a cylindrical button considering plain compression force and shear force needed to restore the surface points on the bonded surfaces.

However, the analysis and experimental result shown by the authors indicate no significant deviation of the value of compression force for shape factor ( $S$ ) up to 4.0, compared to Gent and Lindley [26] and Yeoh et al. [27]

The earliest equation of  $E_C$  and hardness is given in Eq. (7) [30–32].

$$E_C = \frac{H^{1.9}}{972.02} \left[ \frac{1 + k_1 S^2}{1 + k_2 S^2} + 2S^2 \right] \text{ MPa} \quad (7)$$

where  $H$  is the hardness in Shore ‘A’ and  $S$  is the shape factor. Typically, for low shape factor,  $k_1 = 4.8$  and  $k_2 = 4$ . The rubber is assumed to be incompressible in bulk and the shape factor is as small as about 0.55. Typically, a circular disc-shaped rubber button of diameter 30 mm and height 12 mm shall have shape factor of 0.625, which is quite small.

Kunz and Studer [33] studied the hardness–elastic modulus in compression for commonly available rubbers of varying hardness from Shore ‘A’ 30 to 95 and suggested a simple expression for this relationship as in Eq. (8).

$$E_C = \left[ \frac{1 - \nu^2}{2RC_3} \right] \frac{C_1 + C_2 S_A}{100 - S_A} \text{ N/m}^2 \quad (8)$$

where  $C_1 = 0.549 \text{ N}$ ,  $C_2 = 0.07516 \text{ N}$  and  $C_3 = 0.025 \text{ mm}$ , while  $\nu$  is Poisson’s ratio and  $R$  is the radius of the indenter and  $N$  stands for Newton. The agreement with the experimental result was good for harder rubber ( $S = 85 \text{ Shore ‘A’}$ ) and does not agree for rubbers of medium and low hardness ( $S_A = 30\text{--}50 \text{ Shore ‘A’}$ ). The assumption of incompressibility by taking  $\nu = 0.5$  may result in some errors in prediction of compressive modulus from hardness data.

In the present study, a series of NBR and NVC55 blend vulcanizates reinforced with CB-HAF and GT was used to investigate the relation among Young’s modulus, compressive modulus and Shore ‘A’ hardness according to the relevant equations with experimental data.

## 2 Experimental

### *Nomenclature:*

NBR	Nitrile Rubber
PVC	Polyvinyl chloride
NVC55	Nitrile–Polyvinyl chloride blend of ratio 50/50 by weight
CB-HAF	Carbon black—High Abrasion Furnace
GT	Graphite filler
NBR-xxH	xx parts CB-HAF in 100 part NBR. Similarly, NVC55-xxH
NBR-xx GT	xx parts GT in 100 part NBR. Similarly, NVC55-xx GT
ASTM	American Society for Testing and Materials

## 2.1 Materials and Methods

Raw NBR having 33% acrylonitrile content was obtained from Kumho Petrochemical, Korea. NVC55 (w/w), unvulcanized, having acrylonitrile content of 33% in NBR was obtained from Aarchem Corporation, Chennai, India. Commercial grades of sulphur as curative, accelerator tetramethylthiuram disulphide (TMTD), processing aids stearic acid and zinc oxide were used. CB-HAF N326 of average agglomerate size of 2–5  $\mu\text{m}$  was obtained from Birla Carbon India Pvt. Ltd., Chennai, India. GT of average particle size 250  $\mu\text{m}$  was obtained from Loba Chemie, Chennai, India. All items were used as received, except zinc oxide which was dried in a vacuum oven at 70  $^{\circ}\text{C}$  for 24 h before use. The recipe of all compositions with NBR and NVC55 blends is listed in Table 1.

The rubbers were compounded as per standard procedure, and the curing process was studied by a moving die rheometer (Ektron, Taiwan) to find out  $T_{90}$  at 150  $^{\circ}\text{C}$  for each composition. The  $T_{90}$  was about 6.52 min to 9.20 min. Vulcanized sheets of size 150 mm  $\times$  150 mm and 2 mm thickness and circular discs of 30 mm diameter and 12 mm height were fabricated in a hot platen hydraulic press at 150  $^{\circ}\text{C}$  and under 14 MPa pressure for 15 min followed by post-cure at 70  $^{\circ}\text{C}$  for 8 h. All specimens were conditioned in a room maintained at  $23 \pm 1$   $^{\circ}\text{C}$  and  $\leq 45\%$  relative humidity

**Table 1** Recipe of all compositions with NBR and NVC55 blends

Composition	Rubber (by wt.)	CB-HAF phr	Graphite (GT) phr	Volume fraction of filler
NBR-00	100	0	0	0
NBR-10H	100	10	0	0.047
NBR-20H	100	20	0	0.090
NBR-30H	100	30	0	0.13
NBR-45H	100	45	0	0.18
NBR-10GT	100	0	10	0.042
NBR-20GT	100	0	20	0.081
NBR-30GT	100	0	30	0.116
NBR-45GT	100	0	45	0.165
NVC55-00	100	0	0	0
NVC55-10H	100	10	0	0.05
NVC55-20H	100	20	0	0.10
NVC55-30H	100	30	0	0.14
NVC55-45H	100	45	0	0.20
NVC55-10GT	100	0	10	0.047
NVC55-20GT	100	0	20	0.09
NVC55-30GT	100	0	30	0.13
NVC55-45GT	100	0	45	0.182

for 24 h before undertaking any test. The tensile test was done according to ASTM D412 Type-C using a dumbbell-shaped rubber specimen in a Dak system Inc., India, (Model No. UTB9251). The cross-head speed was 50 mm/min. Durometer hardness test was done according to ASTM D 2240-86 [10] using circular discs of 30 mm diameter and 12 mm thickness using BSE SHR-A Shore 'A' Hardness Tester.

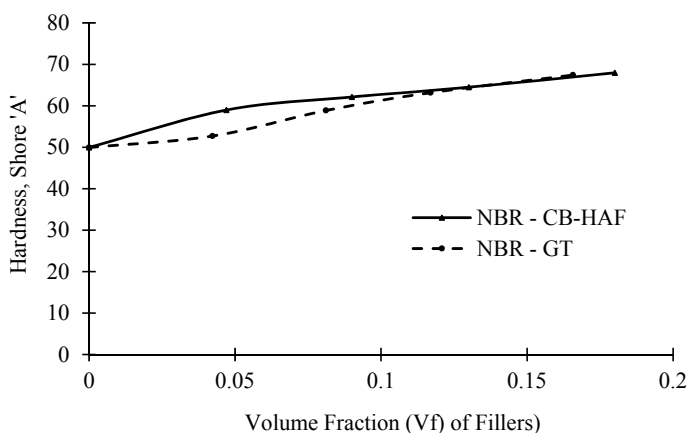
### 3 Results and Discussion

#### Compositions

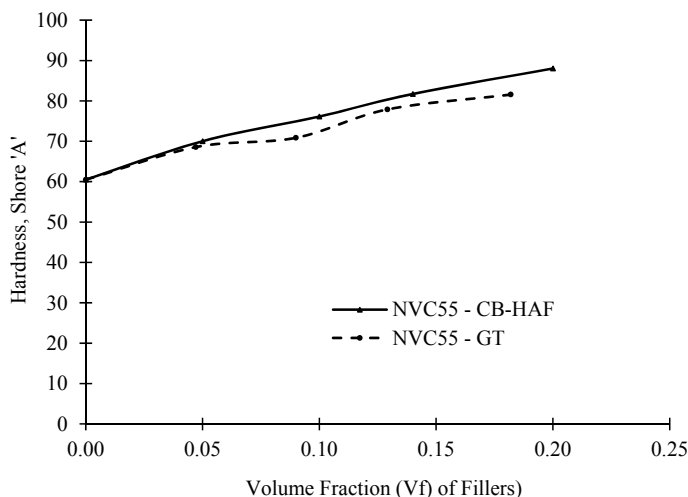
Table 1 shows the compositions of all formulation as expressed parts per hundred parts of rubber (phr) with respect to reinforcing filler content. The curing systems and processing aids were kept identical for all compositions. The  $T_{90}$  of each formulation is also included. The CB-HAF content was restricted to 45 phr since, beyond this limit, it was not possible to obtain homogeneity, particularly in NVC55 blend with graphite filler. The volume fraction of reinforcing fillers was calculated by taking the literature value of densities and measuring the volume and mass of the fabricated buttons.

#### Durometer Hardness

The hardness of all above elastomeric compositions was measured in Shore 'A' scale, and the maximum hardness was found to be 88 for NVC55 + 45 CB-HAF and minimum was 49 for NBR vulcanizate without any reinforcement. Figures 1 and 2 represent hardness data for NBR and NVC55 reinforced with CB-HAF and GT. Initially, the increase in hardness with CB-HAF volume fraction is more, but with more CB-HAF, the increase is not so high as expected. The increase in hardness with GT volume fraction is somewhat less than that with CB-HAF, indicating higher



**Fig. 1** Durometer hardness of NBR vulcanizates reinforced with HAF black and graphite



**Fig. 2** Durometer hardness of NVC55 blend vulcanizates reinforced with HAF black and graphite

reinforcing effect by CB-HAF. However, at a volume fraction beyond 0.12, both CB-HAF and GT loaded NBR had similar hardness values. For NVC55 blends, the reinforcing effect of GT was found to be less at higher loading. The reinforcing by carbon black is due to very large surface area per unit mass and presence of very minute polar organic groups which facilitates adhesion with the rubber. Therefore, graphite, which is purer form of carbon with practically no organic groups, has less reinforcement efficiency.

#### *Young's modulus and Hardness*

Young's modulus was determined by the stress–strain ratio at 1% elongation in tensile experiment. At such low strain, the stress–strain relationship is linear for all compositions with <10% variation in modulus in the strain range from 0.9 to 1.5%. Figure 3 shows few data on dependence of modulus on strain for some compositions. It shows that the Modulus at 1% is well within linear viscoelastic range. Young's modulus for NBR and NVC55 compositions versus filler volume fraction is shown in Fig. 4. The values are similar to those reported in the literature [34–37]. For NVC55 blend compositions, the reinforcing effect of CB-HAF is more compared to GT, while for NBR, the difference is marginal. This could be due to low modulus and high free volume of NBR elastomer compared to its blend with PVC which is an engineering plastic. The dependence of Young's modulus on filler volume fraction is not linear, and the rate of increase in modulus is more at higher loading. This is attributed to more agglomerate–rubber interface as volume occupied by filler particle increases and also, increased aspect ratio compared to spherical individual particles as also reported by Guth [38].

Dependence of Young's modulus on durometer hardness in Shore 'A' scale is given in Fig. 5 for NBR and Fig. 6 for NVC55 blend vulcanizates with CB-HAF

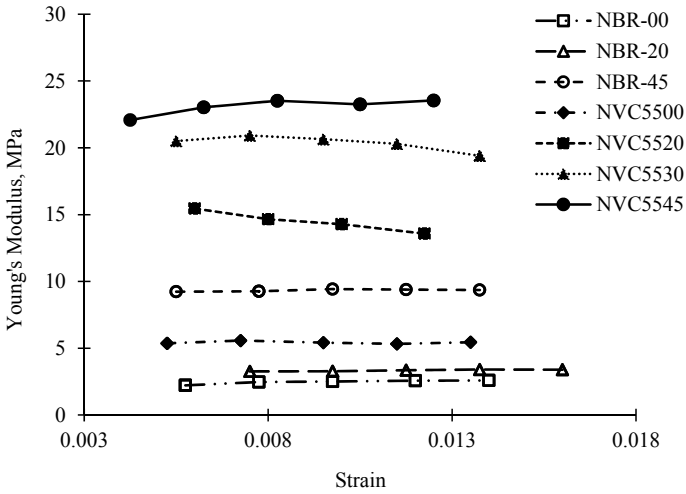


Fig. 3 Dependence of Young’s modulus on the strain

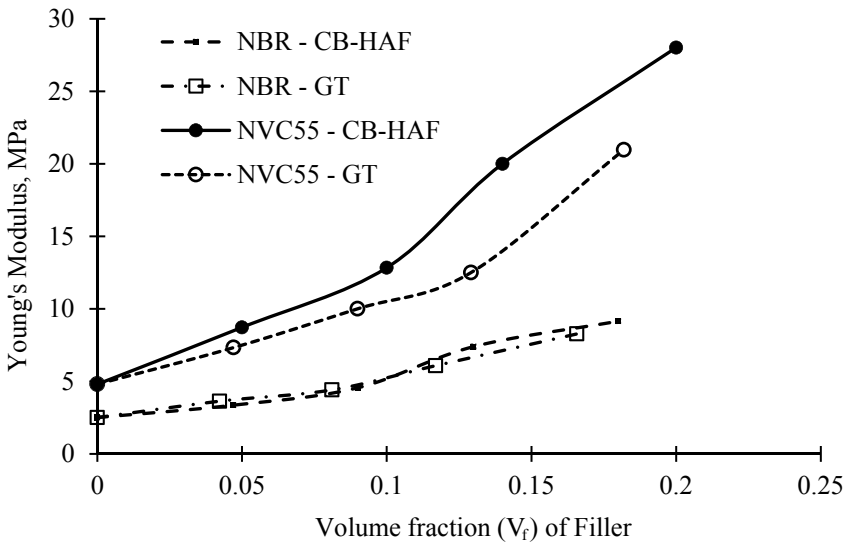
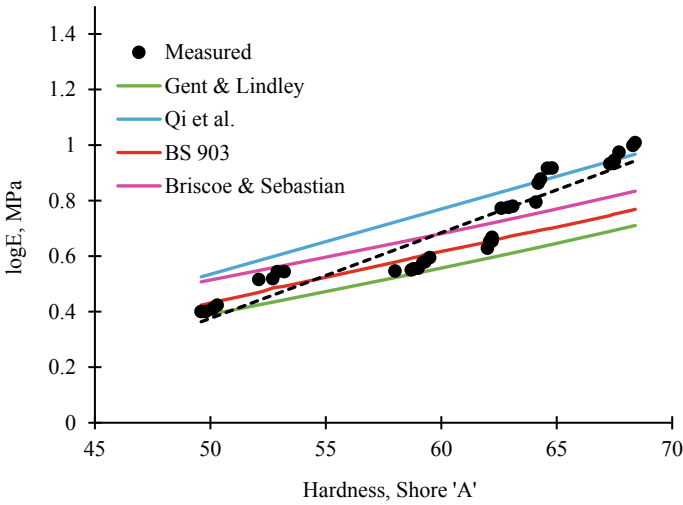


Fig. 4 Young’s modulus (at 1% strain) for NBR and NVC55 vulcanizates filled with HAF black and graphite: variation with filler volume fraction

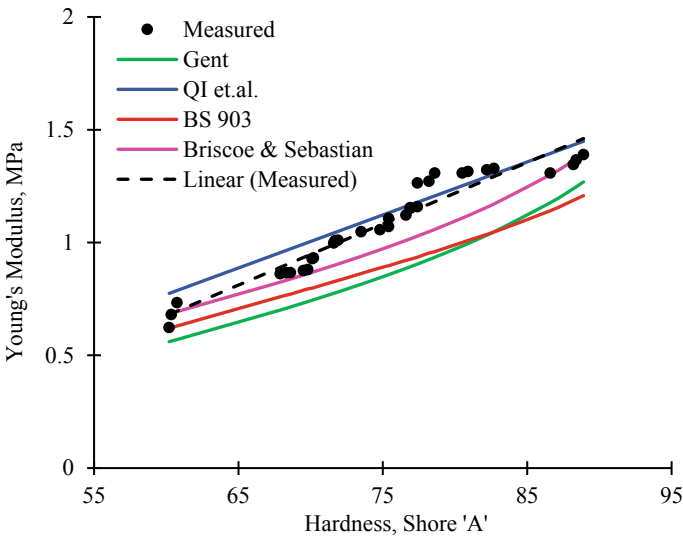
and GT. The experimental hardness data were used in Eqs. (2)–(4) to examine the agreement of the experimental values of Young’s modulus with literature predictions [14–16] for all compositions at 1% elongation.

It is seen from Fig. 5 that none of the theoretical or empirical equations are fully applicable to the entire hardness range. The experimental data at lower hardness





**Fig. 5** Relationship of hardness and Young’s modulus of NBR compositions



**Fig. 6** Relationship of hardness and Young’s modulus of NBR-PVC compositions

are closer to the prediction by BS 903 [17] and Gent [14] predicted lower Young’s modulus.

The data are fairly matched better with the theory by Briscoe and Sebastian [16] calculated by Eq. (5), compared to all others. Qi et al. [15] predict a higher value of modulus in general, but the better agreement is observed at hardness values beyond 62 Shore ‘A’. The experimental data can be fitted better to the following empirical

expression similar to that by Qi et al. [15] as shown by a dotted line in Fig. 5:

$$\log(E) = 0.0308S_A - 1.1653 \quad (9)$$

Comparing the above expression with Eq. (3), it was seen that at lower values of hardness, Eq. (9) predicts the lower value of Young's modulus, but with increased hardness, the two expressions would predict identical modulus values.

The better fit with Eq. (3) confirms that the NBR elastomeric compositions are nonlinear and show greater relaxation characteristics in mechanical deformations. However, harder compositions gave a better fit with Eq. (3). However, the values of Young's modulus determined for NBR-based composition are well in the band of the theoretical equations derived by the four methods shown in Fig. 5, which means that the measured values are somewhat very close to predictions by reported theories.

Similarly, referring to Fig. 6 for NVC55 blend vulcanizates, it was seen that the experimental data are in much better agreement with the prediction by Qi et al. [15] followed by Briscoe and Sebastian [16]. Here, the best fit for the experimental data almost coincides with Eq. (3). Since NVC55 blends have moderate relaxation, the data are more in agreement with Eq. (3). The best correlation similar to Eq. (3) is shown as a dotted line in Fig. 6 and is given by:

$$\log(E) = 0.272S_A - 0.9521 \quad (10)$$

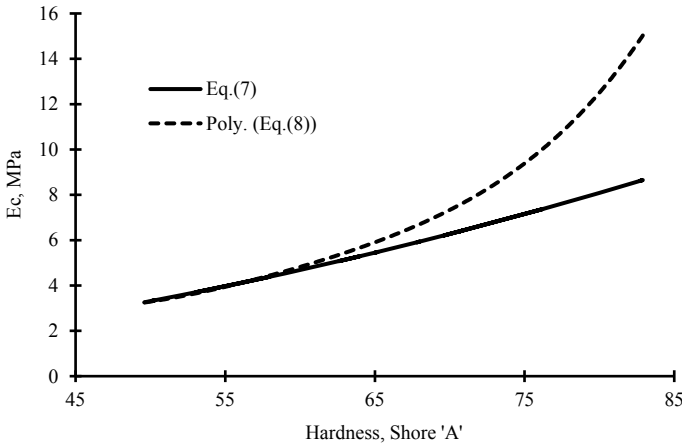
The expression by BS 903 is a relation of IRH and Young's modulus. The IRH is related to Shore 'A' scale as:

$$\text{IRH} = S_A + 4 \quad (11)$$

as suggested by Briscoe and Sebastian [16]. Accordingly, the Shore 'A' values were converted into IRH value and Young's modulus was calculated using Eq. (5).

The fact is that Young's modulus of NVC55 blend compositions are not in full agreement with predictions by the theories in respect of the relationship with measured hardness data. It must be noted that the theories give approximate estimation of Young's modulus in a close range, which is very relevant when selection of an elastomer is desired from a large number of compositions.

The reason for deviation, to even minimal extent, from predictive equations is that the rubber elasticity is heavily dependent on stress relaxation, and at ambient conditions, the effect is significant. This is readily explained by numerical example in the literature [39]. Secondly, all derivations do not include the transverse deformation and the energy spent due to that which results in reduction in hardness measured by indentation. The transverse deformation in rubber in tensile measurement is less since the aspect ratio is much lower (0.6 for hardness measurement sample and 0.2 for tensile sample).



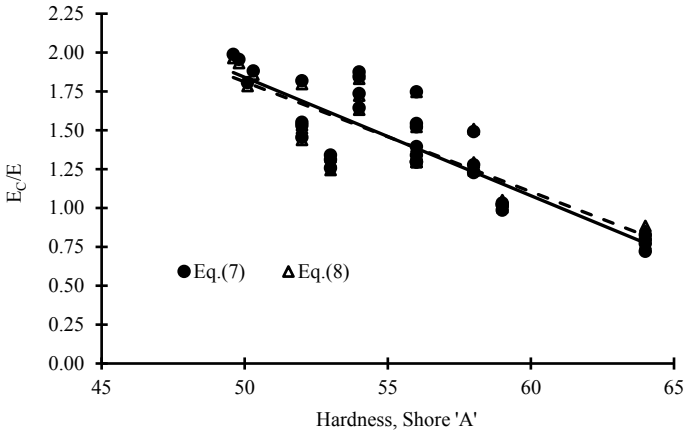
**Fig. 7** Calculated compressive modulus as a function of hardness

*Compressive modulus and hardness*

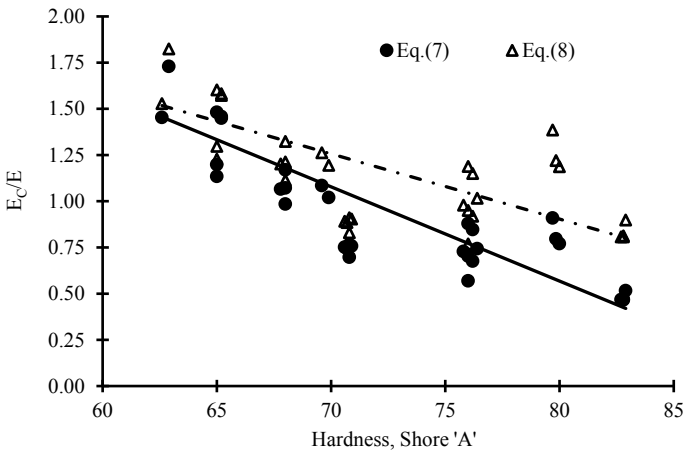
Experimentally measured hardness was used to calculate the compressive modulus using the expressions given in Eqs. (7) and (8). Figure 7 shows the calculated compressive modulus as a function of hardness (Shore ‘A’). The modulus values by these two equations differ in case of hardness beyond 65 as shown in Fig. 7. The drastic increase in modulus for Eq. (8) beyond 65 hardness is due to the consideration of the radius of the flat tip of the Shore ‘A’ indenter (0.395 mm).

The comparison of compressive modulus thus calculated as in Fig. 7 with measured Young’s modulus as a ratio ( $E_C/E$ ) is shown for NBR vulcanizates as Fig. 8 and for NVC55 blend vulcanizates as Fig. 9. The data on the ratio ( $E_C/E$ ) for both Eqs. (7) and (8) were almost identical for NBR compositions since their hardness values are within 70 Shore ‘A’.

Ideally, the tensile and compression modes should give same Young’s modulus value at a very linear elastic range, say 1% deformation. The difference comes due to loss of force by transverse deformation and also at high compression, progressive packing of rubber molecules along with fillers. However, the ratio varies nominally at about 20% with variation in hardness and the average ratio can be taken as 1.08. For NVC55 compositions, having higher hardness values, the ratio is almost uniformly 0.82 on an average when Eq. (8) is considered. The ratio is quite varying at about 70% with variation in hardness when Eq. (7) is used. The ratio for NBR compositions (moderate hardness) and harder NVC55 compositions is of a similar trend as those obtained for natural rubber (NR) ( $S_A \sim 50$  Shore ‘A’) at about 1.4 and polyurethane rubber (PUR) ( $S_A \sim 85$  Shore ‘A’) about 1.0 [11]. It is to be noted that the ratio tends to be lower when the hardness is high. Taking the average value of the ratio ( $E_C/E$ ), the average material modifying factor ( $k$ ) according to Eq. (6), for NBR vulcanizates was found to be 0.11 and of NVC55 compositions, the value was  $-0.23$ , for the shape factor ( $S$ ) as 0.625 which is for the ASTM sample disc for compression experiment.



**Fig. 8** Ratio of calculated compressive modulus and measured Young’s modulus of NBR vulcanizates



**Fig. 9** Ratio of calculated compressive modulus and measured Young’s modulus of NVC55 vulcanizates

Compressive modulus ( $E_C$ ) depends on the shape factor ( $S$ ). In the present study,  $S$  was 0.625. If an elastomeric item has a quite different  $S$  than the laboratory test sample, corrected expressions can be used as discussed in the literature, particularly by Horton et al. [31] and Aiken et al. [32]. In designing machinery mount,  $S$  of a full-size shock mount can be kept almost similar to ASTM circular disc sample even with different sizes and shapes. For example, an elastomeric shock mount of 100 mm  $\times$  130 mm cross section and 50 mm thickness will have a shape factor of 0.565 as against 0.625 for an ASTM sample.

The shape factor sharply increases with a decrease in thickness. Hence, thin sheets will behave differently in compression than thick blocks. This aspect is very important in designing thin sheet damping coating deployed under a heavy structure. It is expected that for a thin damping sheet (1–5 mm thickness) of moderate hardness,  $E_c$  could be much higher than that of the laboratory sample as per ASTM. Therefore, the corrected compressive modulus can be predicted through the studies on interrelationships of hardness, Young's modulus and shape factor.

## 4 Conclusions

NBR and NVC55 blend vulcanizates reinforced with CB-HAF and GT were evaluated for hardness and Young's modulus. The effect of reinforcement was observed to be more for CB-HAF compared to GT. The increase in hardness was more with filler volume fraction up to 0.12 compared to further increase in filler concentration. A linear relation of  $\log(E)$  and shore hardness was found to be the most appropriate one. The coefficients of such expressions being purely empirical. The mathematical models available in the literature were compared with experimental data. In general, no good agreement was found for the full range of hardness studied. However, some reasonable match was found with the model by Qi et al. [15] followed by Briscoe and Sebastian [16].  $E_c$  was calculated using available equations relating to hardness expressions by Rocard [31] and Kunz and Studer [33]. There is considerable higher value of calculated  $E_c$  by Kunz and Studer [33] compared to that predicted by Racord [31]. The ratio of the calculated compressive modulus to measured Young's modulus was seen to vary with hardness. However, the ratio calculated using the model of Kunz and Studer [33] was more or less independent of hardness for NVC55 compositions while for NBR compositions, both expressions were similar and the ratio was found to be varying only by 20% in the full range of hardness from 49 to 68. The average material modifying factor,  $k$ , was found to be 0.11 for NBR vulcanizates and  $-0.23$  for NVC55 vulcanizates.

**Acknowledgements** The authors acknowledge Mr. S J Ali Asgar and Mr. D Prasanna of Polyhose India Pvt. Ltd, Chennai, for their technical support in this investigation. The assistance rendered by Mr. Gopi Ravichandran and Mr. Azeez Taher of B.S. Abdur Rahman Crescent Institute of Science and Technology is also acknowledged.

## References

1. Niwa T, Shimizu Y (1993) US Patent 5213879
2. Chen ACF, Williams HL (1976) J Appl Polym Sci 20(12):3403–3423
3. Mahmoud WE, El-Eraki MHI, El-Lawindy AMY, Hassan HH (2006) J Phys D Appl Phys 39(11):2427–2432
4. Yano K, Saito H, Niwa T (1999) US Patent 5939179

5. Mahmoud WE, Mansour SA, Hafez M, Salam MA (2007) *Polym Degrad Stab* 92:2011–2015
6. Mizumachi H (1970) *J Adhesion* 2(4):292–298
7. Mathew A, Chakraborty BC, Deb PC (1994) *J Appl Polym Sci* 53:1107–1114
8. Shi XY, Weina B, Shugao Z (2011) *J Appl Polym Sci* 120, 1121–1125
9. Xiang P, Zhao X-Y, Xiao D-L, Lu Y-L, Zhang L-Q (2008) *J Appl Polym Sci* 109:106–114
10. ASTM Designation D2240-03
11. ASTM Designation D1415-88 (Reapproved 2004)
12. Sneddon IN (1965) *Int J Engg Sci* 3:47–57
13. Chang WV, Sun SC (1991) *Rubber Chem Technol* 64:202–210
14. Gent AN (1958) *Trans Inst Rub Ind* 34:46–57
15. Qi HJ, Joyce K, Boyce MC (2002) *Rubber Chem Technol* 76:419–435
16. Briscoe BJ, Sebastian SK (1993) *Rubber. Chem Technol* 66:827–836
17. BS 903 Methods of testing vulcanised rubber Part 19 (1950) and Part A7 (1957)
18. Iranthi MM, Parker S, Patel MP, Braden M (2009) *Dent Mater* 25:956–959
19. Mandal UK, Aggarwal S (2011) *Polym Testing* 20:305–311
20. Fediuc DO, Budescu M, Fediuc V, Venghiac V-M (2013) *Bul Inst Polit Iași t, LIX (LXIII), f. 2, 157–165*
21. Larson K (2017) Home page. <https://www.researchgate.net/publication/336239577>
22. Ucar H, Basdogan I (2018) *J Low Freq Noise V A* 37(3):509–518
23. Sherif HA, Almufadi FA (2019) *J Eng Mater-T ASME* 141:1–8
24. Cao Y, Ma D, Raabe D (2009) *Acta Biomaterialia* 5:240–248
25. Huang G, Lu H (2007) *Experimental mechanics*, pp 4787–4798
26. Gent AN, Lindley PB (1959) *Proc Instn Mech Engrs* 173(3):111–122
27. Yeoh OH, Pinter GA, Banks HT (2002) *Rubber Chem Technol* 75:549–561
28. Gent AN (1994) *Rubber Chem. Technol.* 67:549–558
29. Anderson ML, Mott PH, Roland CM (2004) *Rubber Chem Technol* 77:293–302
30. Horton JM, Tupholme GE, Gover MJC (2002) *J Appl Mech* 69(6):836–843
31. Rocard YJ (1937) *Phys Radium* 8(5):197–203
32. Aiken ID, Kelly JM, Tajirian FF (1989) Report to the Rockwell International Corporation: Report No. UCB/EERC-89/13, Earthquake Engineering Research Center, College of Engineering, University of California at Berkeley
33. Kunz J, Studer M (2006) *Kunststoffe international* (6/2006)
34. Vinayasree S, Soloman MA, Vijutha S, Mohanan P, Kurian P, Anantharaman MR (2013) *Compos Sci Technol* 82:69–75
35. Al-Maamori MH, Al-Zubaidi AAA, Subeh AA (2015) *Acad Res Int* 6(2):28–37
36. Hafezi M, Khorasani SN, Ziaei F (2006) *J Appl Polym Sci* 102:5358–5362
37. Omran AM, Youssef AM, Ahmed MM, Abdel-Bary EM, Hellipolis C (2009) *Elastomere Und Kunststoffe*, presented in IRC 2009, Nuremberg
38. Guth E (1945) *J Appl Phys* 16:20–25
39. Chakraborty BC, Ratna D (2020) *Polymers for vibration damping application* (Chap. 3). Elsevier Publications, pp 136–138

# Parametric and Nonparametric Modeling of Magnetorheological (MR) Damper



A. J. D. Nanthakumar, J. Jancirani, Aditya Mishra, and Parth Patel

**Abstract** Semi-active suspension provides better handling characteristics and passenger comfort characteristics than passive suspension as well at a lower cost than the active suspension. The implementation of a control system is essential for the incorporation of the magnetorheological (MR) damper in the suspension setup and to achieve this implementation, the working characteristics of the MR damper need to be analysed. In this direction, an MR damper was designed, fabricated, and experimentally tested. The force–displacement and force–velocity characteristics were obtained. Rheological models were formulated based on the characteristics of the MR damper. Two types of rheological models have been formulated—parametric type model and nonparametric model. Bingham model was utilized as a base for formulating the parametric type model, and a polynomial expression was utilized for formulating the nonparametric model. The model coefficients were evaluated. The proposed models can be utilized to develop control algorithms to be implemented in semi-active suspension systems.

**Keywords** Semi-active suspension · Magnetorheological damper · Parametric model · Nonparametric model

## 1 Introduction

The vehicle handling performance and ride comfort performance of vehicles are influenced by the suspension system. The weight of the vehicle is supported by the suspension system which also aids in providing relative motion between the road surface and the chassis structure. A typical suspension system is composed of components like suspension arms, tires, springs, and dampers. Theoretically, the control of

---

A. J. D. Nanthakumar (✉) · A. Mishra · P. Patel  
Department of Automobile Engineering, SRM Institute of Science and Technology,  
Kattankulathur 603 203, India  
e-mail: [ajd.nanthakumar@gmail.com](mailto:ajd.nanthakumar@gmail.com)

J. Jancirani  
Department of Production Technology, Anna University, MIT Campus, Chennai 600 044, India

suspension system can be implemented by varying any one of the suspension system components. But in practice, the cause and effect of controllability is easily achievable by controlling the damper or the shock absorber. The possibility of control of damping characteristics of the suspension system can be utilized as a controlling tool to influence the output of a suspension system. Engineers have attempted many methods and techniques to control the damping characteristics.

### ***1.1 Types of Suspension Systems***

The control of suspension system is a fundamental problem of vibration dynamics and control. In a similar sense, the suspension system can be classified as passive suspension system, semi-active suspension system, and fully active suspension system.

In a passive suspension system, the damping force characteristics cannot be changed dynamically. In practical cases, the road conditions impose rapidly changing force inputs and the passive suspension system cannot provide an optimum response and is a compromise for all the road conditions. The same suspension and damping characteristics are applied for all the road surface conditions. The active suspension system on the other hand utilizes an actuator to generate the necessary counterforces to balance the road disturbances. Active suspension system though an ideal case for suspension setup has drawbacks which render them impractical. The cost of active suspension is prohibitively high. Moreover, the space requirements and implementation of active system components are so complex that fitment in utility vehicles is almost impossible. The energy requirements of the active suspension systems too make them impractical for commercial applications.

The aforesaid disadvantages present in passive, and active suspension systems are overcome by semi-active suspension systems. The semi-active suspension system can be implemented with minor modifications made in the passive suspension system. Even though the theoretical performance of semi-active suspension system is lower than that of fully active suspension system, it is well within the acceptable levels for the cost involved. The energy requirements also have been very low when compared with fully active suspension systems. Hence, semi-active suspension systems have gained wide spread acceptance by the researchers as well as the vehicle manufacturers. Extensive research activities have been carried over in the semi-active suspension domain. When a current flows in the electromagnetic coil, it leads to the formation of magnetic field and the viscosity of the magnetorheological fluid changes based on the strength of the magnetic field.



## 1.2 Magnetorheological Damper

Many techniques are available to implement semi-active technology for a suspension system including variable orifice damper, magnetorheological damper, etc. Magnetorheological damper has been preferred by many researchers and has found in a variety of applications due to their relatively simpler construction, immediate response to the control signal, and necessity for lower power levels. Magnetorheological fluid is used as the working fluid whose viscosity can be changed across a magnetic field. This results in a corresponding change in the damping force capacity of the magnetorheological damper, thereby influencing the damper output characteristics.

It is to be noted that electrorheological fluids were initially preferred for similar applications as there had been many issues with Magnetorheological fluids such as settling issues and uneven dispersion. Due to the advancements in material science and engineering, these issues have been solved of late and magnetorheological fluids have been the preferred choice of researchers thereafter.

## 2 Literature Survey

Nanthakumar et al. [1] presented the design and analysis of magnetorheological damper. The procedure for the determination of the design parameters for a magnetorheological damper was illustrated. Ashaq et al. [2] designed and fabricated a magnetorheological damper. The fabricated damper was experimentally tested using a damper test rig. The damper output plots for force–velocity were discussed. Revabhai [3] presented the design and construction of a magnetorheological damper. The constructed damper was tested in a damping force testing machine, and its force–velocity characteristics were studied. Song [4] presented the algorithm and strategies for vibration control for various applications using magnetorheological damper. A numerical analysis was also performed. Sahin et al. [5] evaluated the various parametric models utilized for modeling magnetorheological dampers. It was concluded that simpler models were able to predict the magnetorheological damper performance better than complex models in many of the practical situations. Boada et al. [6] proposed a nonparametric model for the magnetorheological damper based on neural networks concept and conducted experimental tests to compare the accuracy of the model. Eshkabilov [7] reviewed the models that depicted the hysteretic behavior of magnetorheological dampers through MATLAB simulation. The models were then implemented in a quarter car model.

Hong et al. [8] presented a dimensional analysis model for the mixed mode operation of the magnetorheological damper. The model was then validated using experimental data. The flow mode damper and mixed mode dampers were compared. Sapinski et al. [9] analyzed a linear magnetorheological damper using various parametric models. Soltane et al. [10] proposed the regularized form of Bingham model

to represent magnetorheological dampers. The operating parameters of the Bingham model were found out so that the model represents closely the experimental data. Then the model was applied for the free vibration case and forced vibration conditions for cable vibrations. Khan et al. [11] explained the various models of operation of a magnetorheological damper and its applications. Bingham model and Herschel Bulkley model were utilized for creating the necessary parametric model to represent magnetorheological dampers. Nugroho et al. [12] utilized adaptive neuro-fuzzy inference system (ANFIS) and developed a control system to control the vibrations in a quarter car model. The damping force was calculated using the fuzzy hybrid sky hook–ground hook controller. Krauze et al. [13] analyzed the damping of vibrations arising out of varying road profile surface. The semi-active suspension was considered for a quarter car model. The front portion of the suspension system was controlled using sky hook control algorithm and the rear portion using FxLMS algorithm.

Many researchers have applied various algorithms and techniques for modeling a magnetorheological damper. Some of the researchers deployed simpler models that aided in easier computations but lacked in accuracy and some of the researchers deployed complex and accurate models that possessed the disadvantage of computational complexity and control system implementation. This research paper considers this as the research gap and identifies a relatively simple as well as computationally efficient model for representing magnetorheological dampers.

### 3 Design

The previous research work of the authors [1] explained in detail about the constructional details of the geometry of the magnetorheological dampers. The geometrical parameters like radius of the piston, flow length were considered, and their effect on the base damping force capacity of the dampers has been analyzed. The parameters for ON state condition and OFF state condition were analyzed. ON state represents the magnetorheological damper operation during flow of current and OFF state represents the damper operation under no current conditions. The base damping capacity of the damper is dependent on the OFF state parameters, and the damping capacity under the flow of current is decided by the ON state parameters. The parameters found out in the previous research work [1] of authors have been extended in this research work. The list of ON state geometrical parameters with their lower bound values and upper bound values is given in Table 1. The list of OFF state geometrical parameters is given in Table 2.

**Table 1** ON state geometrical parameters

ON state geometrical parameters	Lower bound value (mm)	Upper bound value (mm)
Distance between piston rod and coil	3	7
Pole length	5	15
Magnetorheological fluid flow gap	0.5	1.5
Outer pole thickness	4	8

**Table 2** OFF state geometrical parameters

OFF state geometrical parameters	Value (mm)
Piston radius	20
Flow length	20

## 4 Fabrication

The design data obtained from the afore-mentioned design steps were used to fabricate a physical prototype model of a magnetorheological damper. The damper is of double tube construction type so that the fluid compensation is accommodated in the damper design itself. The outer tube and the inner tube of the fabricated damper were made of CEW1 material possessing higher magnetic permeability. The piston rod was fabricated of stainless steel material to possess low permeability values. The coil was wound for 300 turns with SWG 35 copper wire. The fabricated magnetorheological damper was tested in a damper testing machine.

## 5 Rheological Modeling

The rheological models for the behavior of the magnetorheological fluid inside the damper were formulated. Two approaches were followed to create the rheological models. A parametric model based on the Bingham constitutive equation was attempted, and a nonparametric model based on a third order polynomial expression was also attempted. The data obtained from damper testing machine consisted of load and displacement values taken at 0.0001 s time interval. The fabricated magnetorheological damper was tested at five velocity values of 0.25, 0.50, 0.75, 1.00, and 1.25 m/s. The corresponding frequency values for the velocities for the testing machine were found to be 2.65, 5.31, 7.96, 10.61, and 13.26 Hz. The magnetorheological damper coil was supplied zero current (no current flow), 0.50 A of current and 1.00 A of current. The velocity information of the damper testing was arrived from the displacement data. The force–displacement curves and the force–velocity curves were plotted from the experimental data.

### 5.1 Bingham Model

The damping force generated by the magnetorheological damper with reference to the time ( $t$ ) is given in Eq. 1.

$$F_d = C_d V + F_y \text{sgn}(V) + F_0 \tag{1}$$

where  $V$  denotes the velocity of the damper piston,  $C_d$  denoted the damping coefficient,  $F_y$  represents the frictional force generated due to yield stress in the magnetorheological fluid,  $F_0$  represents the force offset value due to the presence of the accumulator. As per Bingham models constitutive equation, the viscoplastic flow of the magnetorheological fluid starts only when the damping force ( $F_d$ ) exceeds the frictional force due to yield stress ( $F_y$ ). The damping coefficient ( $C_d$ ) can be taken from the slope of the force–velocity curve. The expression stated in Eq. 2 has been fitted on the experimental data which represents the parameters that are to be estimated.

$$\text{Parameters} = [C_d, V, F_y, F_0] \tag{2}$$

#### Estimation of parameters:

The parameters of the Bingham model were estimated using the least squares method. After estimating the parameters, the expression given by the Bingham equation was fitted to the experimental data. The parameters of the Bingham equation were determined for each of the frequencies and current values and have been provided in Table 3. The confidence level of the least squares fit was found to be 95%, and the  $R^2$  fit was also found to be good.

**Table 3** Bingham model parameters

$V$ (m/s)	$C_d$			$F_0$			$F_y$		
	0.0 A	0.5 A	1.0 A	0.0 A	0.5 A	1.0 A	0.0 A	0.5 A	1.0 A
0.25	311	323.9	479.5	-48.26	-47.01	-47.35	18.64	13.74	18.45
0.50	407	400.9	517.2	-61.39	-59.35	-64.48	-2.02	2.71	1.10
0.75	198.5	496.1	541.3	-66.98	-70.07	-73.13	4.98	1.90	6.40
1.00	536.4	553.4	608.4	-78.77	-92.53	-10.44	29.46	27.34	3.11
1.25	532.6	530.6	567	-101.56	-113.7	-124.7	69.57	73.44	78.09

## 5.2 Polynomial Model

The polynomial model is a type of nonparametric model. The parameters that are to be determined for the polynomial model are the coefficients of the polynomial expression considered. The complexity of the polynomial models is generally lower than the parametric models. This results in the reduction of complexity of the control system that is to be deployed for the magnetorheological damper control. The degree of the polynomial to be utilized depends on the nature of the experimental data. It was chosen such that the amount of data lost is kept at a minimal level. It was decided to consider a polynomial of order 3 so that the experimental data was well considered, and the accuracy was maintained as well as the complexity was also at a considerable level for control system design. The third degree polynomial for the damping force ( $F_d$ ) is given in Eq. 3.

$$F_d = AV^3 + BV^2 + CV + D \quad (3)$$

where  $V$  denotes the velocity of the magnetorheological damper piston and  $A, B, C, D$  are the coefficients of the cubic polynomial relating the damper force with velocity. The experimental data for the damper testing was fitted to the above equation with the coefficients given in Eq. 4.

$$\text{Parameters} = [A, B, C, D] \quad (4)$$

### Estimation of coefficients:

The values of the coefficients of the polynomial model were estimated using the least squares method. The coefficients of the polynomial equation were determined for each of the frequencies and current values and have been provided in Table 4. The confidence level of the least squares fit was found to be 95%, and the  $R^2$  fit was also found to be good. The residual plot for the least squares fit was also obtained.

Figures 1, 2, and 3 depict the force–velocity curve and the Bingham curve fit for the respective current values of 0, 0.5 and 1.0 A. Figures 4, 5, and 6 depict the force–velocity curve and the cubic curve fit for the respective current values of 0, 0.5, and 1.0 A.

## 6 Results and Discussion

The rheological models for the fabricated magnetorheological damper have been formulated. The parameters of the Bingham model for different testing frequencies and coil currents have been presented in Table 3. The coefficients of the polynomial model for different testing frequencies and coil currents have been presented in Table 4.

**Table 4** Polynomial model coefficients

V (m/s)	A				B				C				D			
	0.0 A	0.5 A	1.0 A	1.0 A	0.0 A	0.5 A	1.0 A	1.0 A	0.0 A	0.5 A	1.0 A	1.0 A	0.0 A	0.5 A	1.0 A	1.0 A
0.25	-1683	-1566	-2311	-108.3	-18.79	-90.94	-108.3	-108.3	557.8	541.6	792.3	792.3	-45.5	-43.68	-42.6	-42.6
0.50	-110.9	-202.3	-328.4	-88.03	-75.3	-103.2	-88.03	-88.03	438.5	470.8	612.2	612.2	-51.6	-46.06	-56.5	-56.5
0.75	-91.52	-86.32	-95.65	-99.9	-86.2	-68.89	-99.9	-99.9	555.5	546.6	603	603	-43.5	-51.57	-45.0	-45.0
1.00	-219.2	553.4	-201.3	-46.24	-10.9	-92.53	-46.24	-46.24	757.6	27.34	798.8	798.8	-87.9	-	-91.7	-91.7
1.25	-183.8	530.6	-204	-40.92	-26.05	-113.7	-40.92	-40.92	806.4	-	867.9	867.9	-95	-	-99.1	-99.1

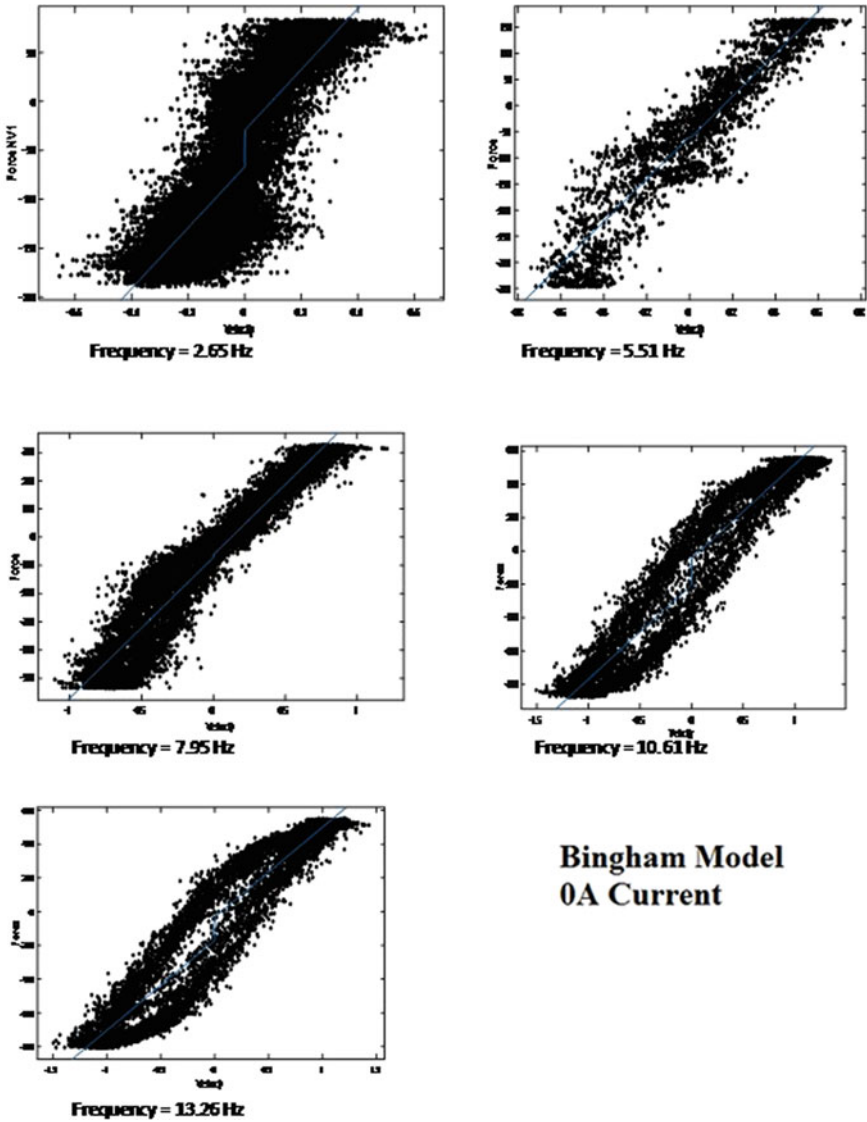


Fig. 1 Bingham model for 0 A current

### Scope for research work

The rheological models with their coefficients formulated in the presented research work could be utilized for designing a control system for the semi-active suspension system employing a magnetorheological damper. The control system design when compared with Bouc–Wen model is relatively simple and robust.

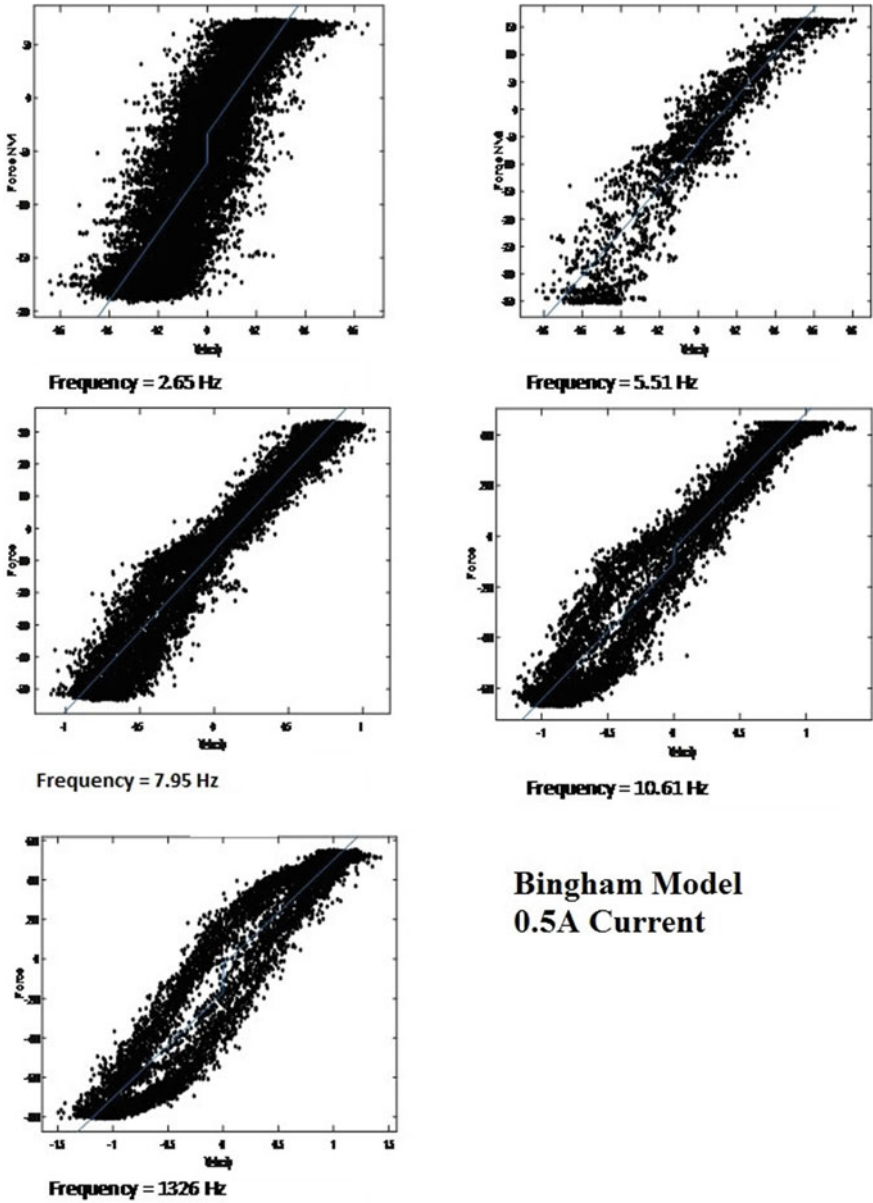


Fig. 2 Bingham model for 0.5 A current



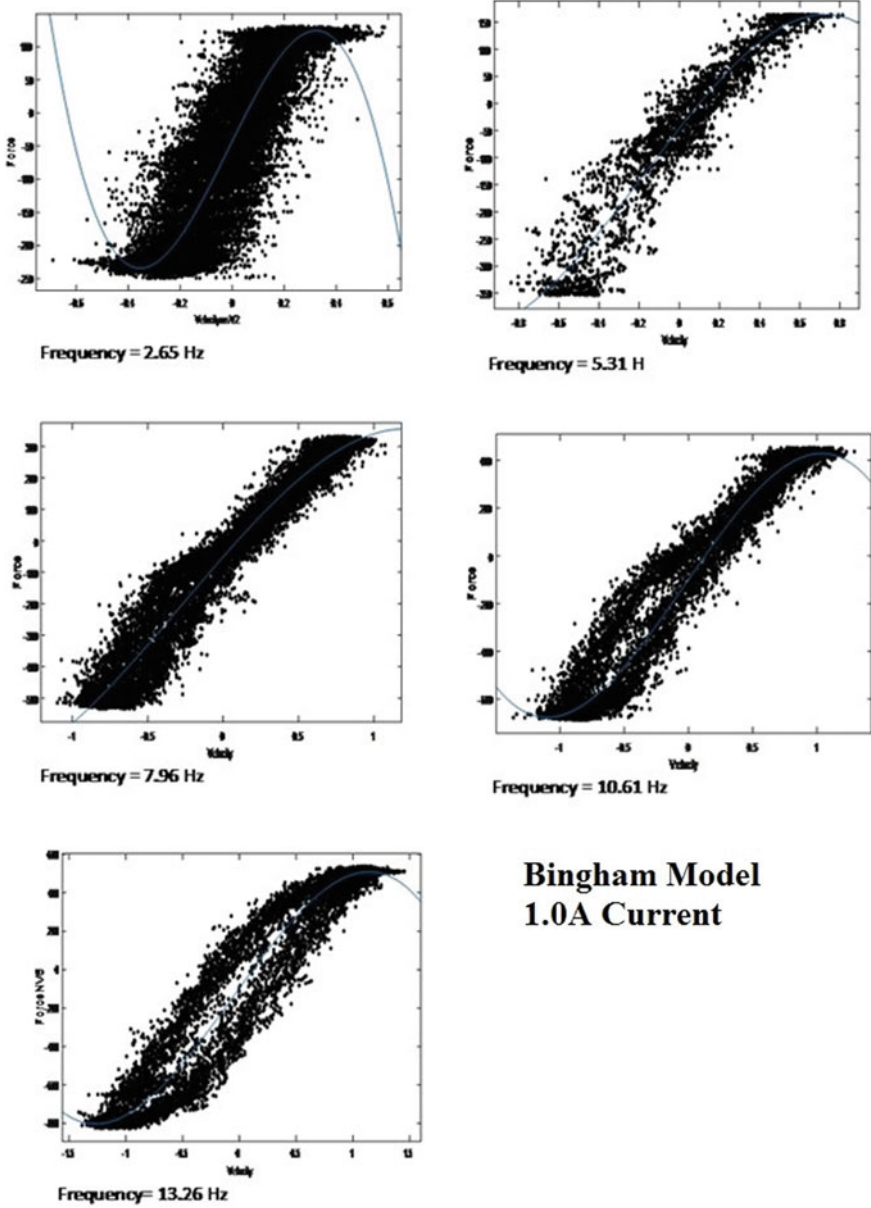


Fig. 3 Bingham model for 1.0 A current

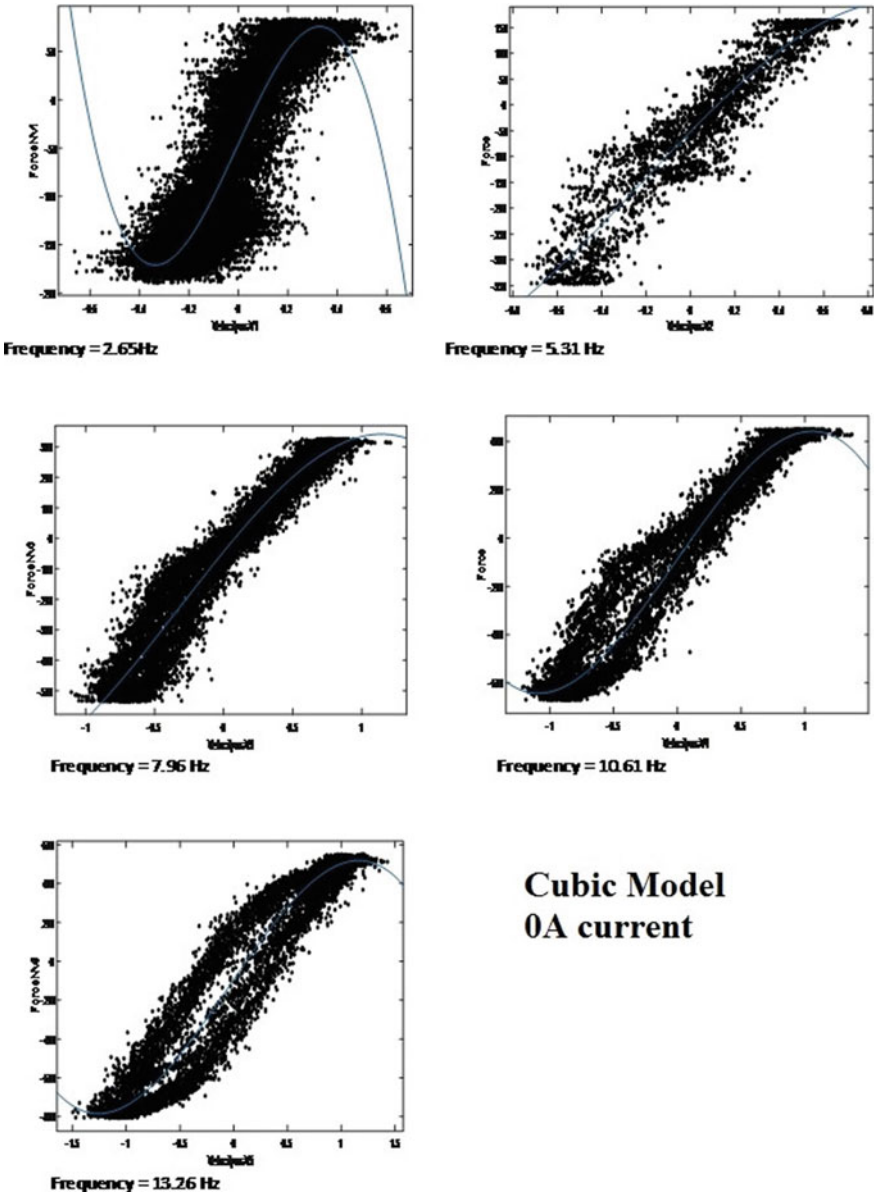


Fig. 4 Cubic model for 0 A current

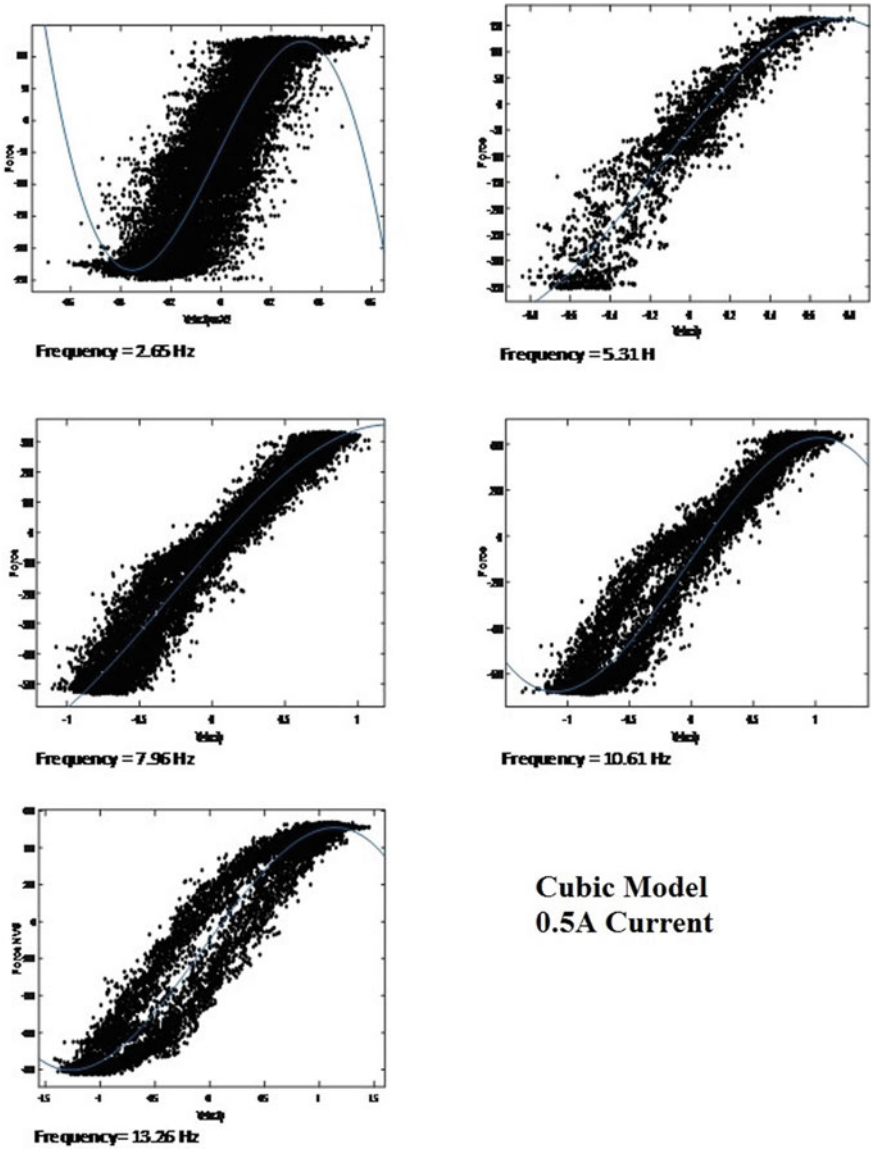


Fig. 5 Cubic model for 0.5 A current

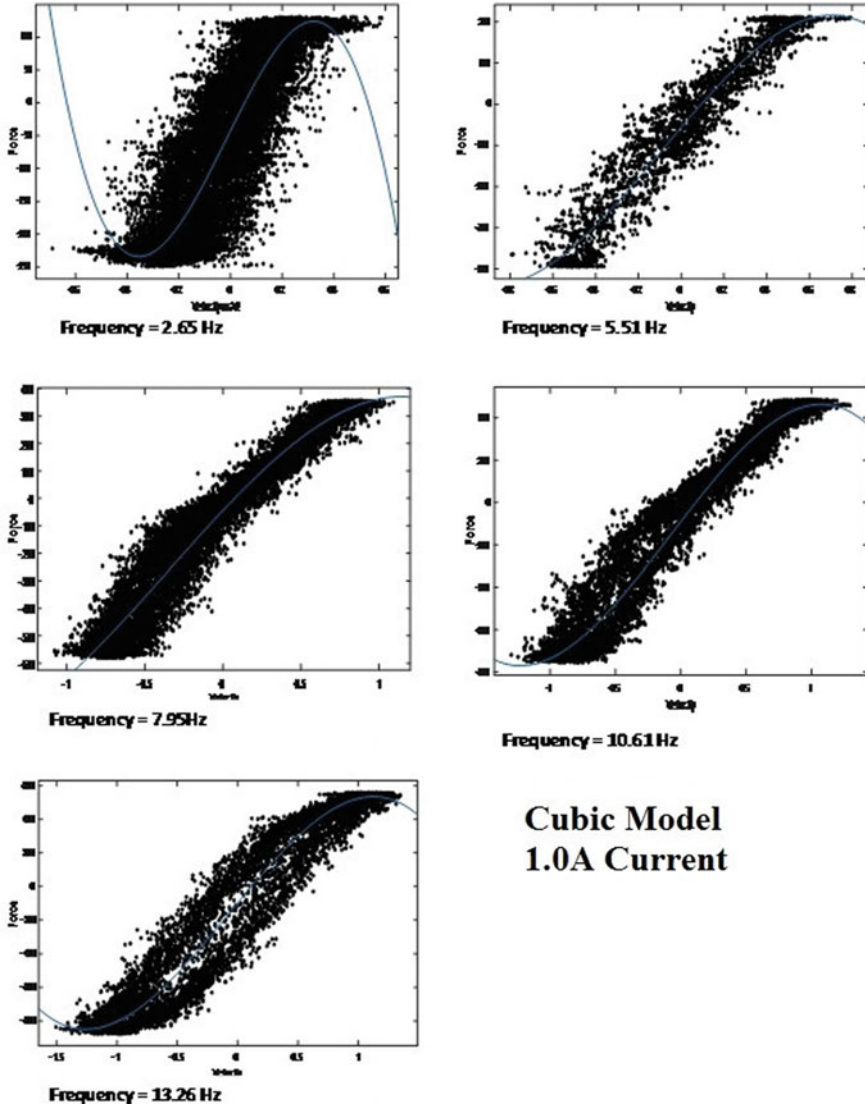


Fig. 6 Cubic model for 1.0 A current

### References

1. Nanthakumar AJD, Jancirani J (2019) Design optimization of magnetorheological damper geometry using response surface method for achieving maximum yield stress. *J Mech Sci Technol* 33(9):4319–4329
2. Ashfak A, Saheed A, Rasheed KA, Jaleel JA (2011) Design, fabrication and evaluation of MR damper. *Int J Aerosp Mech Eng* 1:27–33

3. Rewabhai SH (2017) Design and development of magneto rheological fluid base damper. Doctoral dissertation, Gujarat Technical University
4. Song X (1999) Design of adaptive vibration control systems with application to magnetorheological dampers. J Doctoral dissertation, Virginia Tech
5. Sahin I, Engin T, Cesmeci S (2010) Comparison of some existing parametric models for magnetorheological fluid dampers. *Smart Mater Struct* 19(3):035012
6. Boada M, Calvo J, Boada BL (2009) A new non-parametric model based on neural network for a MR damper. In: ASME 2008 9th biennial conference on engineering systems design and analysis, pp 297–602
7. Eshkabilov S (2016) Modeling and simulation of non-linear and hysteresis behavior of magnetorheological dampers in the example of quarter-car model. *Commun Control Sci Eng* 4:12–29
8. Hong SR, Wereley NM, Choi YT, Choi SB (2008) Analytical and experimental validation of a nondimensional Bingham model for mixed-mode magnetorheological dampers. *J Sound Vib* 312(3):399–417
9. Sapinski B, Filus J (2003) Analysis of parametric models of MR linear damper. *J Theoret Appl Mech* 41(2):215–240
10. Soltane S, Montassar S, Ben O, El Fatmi R (2015) A hysteretic Bingham model for MR dampers to control cable vibrations. *J Mech Mater Struct* 10(2):195–206
11. Khan SA, Suresh A, Seetharamaiah N (2014) Principles, characteristics and applications of magneto rheological fluid damper in flow and shear mode. *Procedia Mater Sci* 6:1547–1556
12. Nugroho PW, Li W, Du H, Alici G, Yang J (2014) An adaptive neuro fuzzy hybrid control strategy for a semiactive suspension with magnetorheological damper. *Adv Mech Eng* (6):487312
13. Krauze P, Kasprzyk J (2016) Mixed skyhook and FxLMS control of a half- car model with magnetorheological dampers. *Adv Acoustic Vibr* 2016:01–13

# Product Development Process Concept—Industrial Perspective



Chitta Ranjan Tripathy and Arvind Katyayn

**Abstract** Product development is a continuous process of evaluating the product and implementing the new solution. This process is based on the nature of competitiveness, marketing and strategies. The product development process also includes a new product introduction based on the requirement of the market and consumers. This process has to pass through various stages of research and development which depends on the type of product to be launched. Therefore, this paper focuses on the various product development concepts. The objective is to explore various processing stages of product development processes incorporated by the companies to increase their profitability. Through the discussion of the various concepts, it is found that the product is developed in physical form by implementing the theoretical knowledge, which is insufficient for selecting the final developed model. To get an aesthetically good and ergonomically better product, one needs to incorporate engineering analysis as well as using CAD/CAM tools and rapid prototyping (RPT) technology. In addition to that, market research needs to be done to increase the certainty of new products introduced in the market and increasing the ROI (return on investment). It helps the industry peoples to predict the life of the product.

**Keywords** CAD/CAM · RPT · Productivity · Product development

## 1 Introduction

The requirement of creating customer-relevant business processes is not a continuous theme in marketing—especially those dealing with the nature of competitiveness, marketing and strategies. Today’s scenario is to consider the dynamics of competitors, consumers and technologies for the firm to be successful, which requires reviewing and reconstituting the product and services offered to the market by the companies [1]. Therefore, the continuous development of an existing product is required along with the new product introduction. The process of product development process

---

C. R. Tripathy (✉) · A. Katyayn  
GNA University, Phagwara 144401, India  
e-mail: [crtripathy@gnauniversity.edu.in](mailto:crtripathy@gnauniversity.edu.in)

undergoes through various steps usually known as product life cycles such as research and development, pre-operations, fully operations, maturity, decline and termination. The various stages of development depend on the type of product to be developed, i.e., existing product or new product. In both cases, the approach of developing a product is different. The developed product should satisfy the need of the market to attract the customers instantly and should be easily differentiable from competitors. We cannot ignore the product's impact on safety and the environment. The business plan should be organized to provide suitable areas for the development of products and also facilitate the development process to compare it with different opportunities. The risk can be minimized by considering the constraints found during product development time. The methods to identify those constraints are to re-check market requirements, criteria for the product, low development and operation cost, project management which is implemented to deliver the product upon its expected criteria and all of these via a programme management system.

In the present work, the product development process is analysed for the existing product as well as a new product. The focus has been made to explore the importance of the various steps involved in the new product development process.

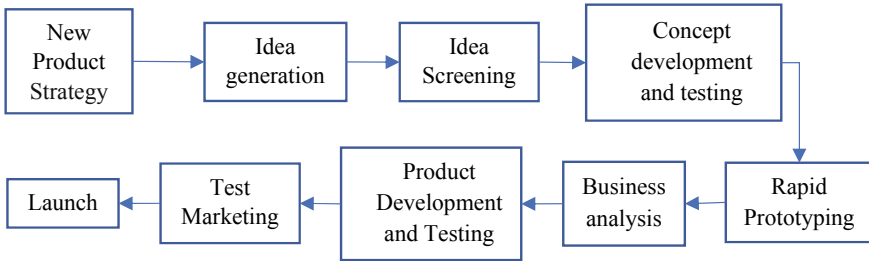
## **2 The Process of Developing an Existing Product**

The development of existing product depends on the feedback from consumers based on its aesthetic, mechanical and chemical properties. The feedback obtained is analysed. and the problem statement is defined for further modification. The problem statement is in the form of key points indicating the flaw in the product, based on these key points some changes in the product are suggested by experts present in the industry. The modified product is then developed using rapid prototyping for its re-evaluation (test). On successful testing of the product, its production and re-launch are carried out. For some cases of product development processes, reverse engineering method is used, which allows reproducing the surface model of the product by 3D-scanning technique, and subsequently manufacturing the components, and sometimes tools also can be manufactured in a short development time [2, 3]. In addition to that, the demand and market scenario on productivity is also analysed to increase the company profit margin.

## **3 New Product Development Process**

Developing a new product for the market including from idea to launch is a challenging job for any industry as it is required to give a physical shape to an idea which describes the function related to the idea.

This idea defines the need of the customer, and they are ready to pay the price to fulfil their needs. Therefore, the product development process has to be managed



**Fig. 1** Sequence of new product development [4]

very carefully. For managing the product development process, one needs to work on a set of activities which ensure that the product is according to the customers need and are manufacturable, affordable, reliable and attractive to customers. The sequence of the new product development process is shown in Fig. 1, and a brief description of the various tasks necessary to carry out at different stages to complete the development and launch of a new product is discussed further (Fig. 2).

The product development process includes brainstorming with artists, painter and multimedia designers for the development of a new concept. It also requires taking feedback of existing product in the similar segment from the market based on its material, aesthetic, colour, mechanism and consumer demand. The manufacturing and production process required for product development are also needed to be reviewed before finalizing the product.

### 3.1 *New Product Strategy*

The purpose of a new product strategy is to:

- Market survey for identifying the various opportunities and threats.
- Analysing the strengths and weaknesses of the competitor’s company.
- Acts like valuable input to later stages.

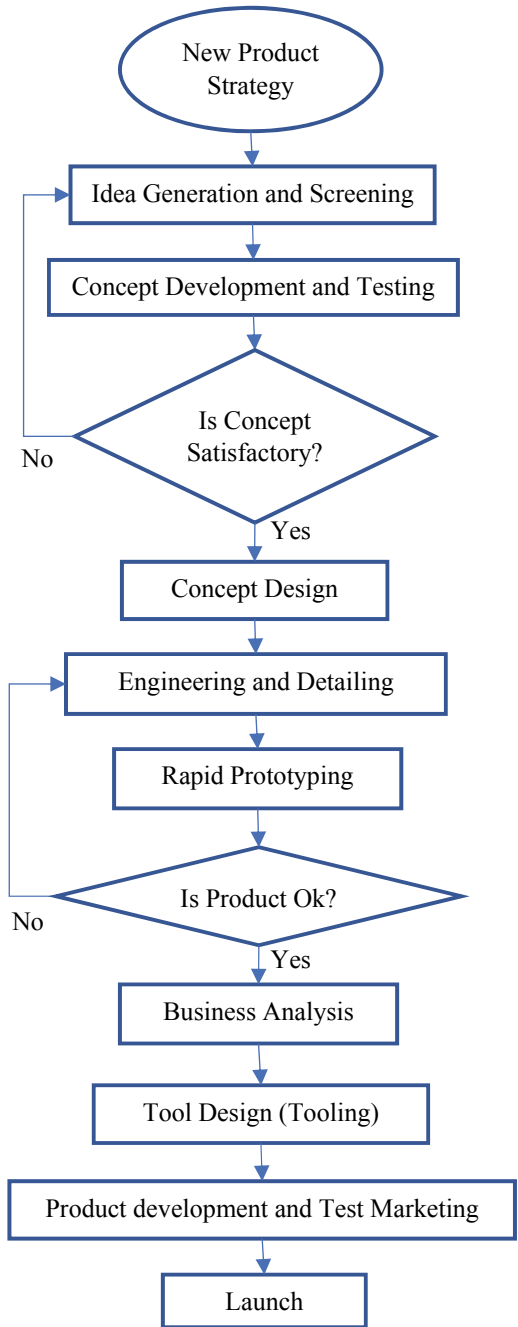
### 3.2 *Idea Generation*

The purpose of idea generation is to come up with multiple concepts in terms of product ideas. Sources of the concept generation are:

1. Customers
2. Company research and development
3. Sales representatives or employees
4. Suppliers
5. Competitors



**Fig. 2** Flow diagram of new product development [5]



### 3.3 *Idea Screening*

It is the process of selecting appropriate ideas out of all generated ideas and dropping the ideas which are not well suited according to the product requirement based on the following criteria [6]:

- Market size as per demand.
- Product price as per consumer.
- Development time and budget.
- Manufacturing and production costs.
- Rate of return and profit.

### 3.4 *Concept Development and Testing*

The concept of a new product is developed from nature, images and hidden ideas. Before generating the concept, viability and feasibility of the concept are ensured by the designer through a market survey. The stages of concept generation and testing are as follows.

- Product concept—this elaborates the idea in detail and usually defined in terms that a customer or client can easily understand and the product image is the way in which the client perceives the product.
- Concept testing—the product concepts are tested with groups of target consumers and retailers.
- At last, the best concept is chosen as per the above test.

### 3.5 *Business Analysis*

**Marketing strategy development:** Everything cannot be done by an organization accurately. It must only focus on only one or two predefined objectives and be competent in other areas [7]. The objectives of various strategies are listed below.

**Overall strategies are:**

- Targeted market
- Planned positioning of the product
- Goals related to sales and profit in the market
- Market share related to the product

**Short-term strategies are:**

- A planned price of the product
- Product distribution in the market
- Overall budget related to marketing

**Long-term strategies are:**

- Product life
- Long-term goals on sales and profit
- Mix strategies on Marketing

**3.6 Product Development**

A prototype is made out of the selected concept by using RPT materials, and the developed prototype should be attractive in appearance, easy to produce and affordable. After the prototype is developed, it will go to laboratory and field testing [8]. To evaluate the overall strategies, the following criteria are considered to develop the product on a positive note:

- Review of the overall sell of the products
- Product cost should be affordable
- Profits projections

If the above criteria are achieved according to the company objectives, then the decision will be taken to move ahead, otherwise, if it does not satisfy, then we need to regenerate the product concept again, and evaluation is again carried out for new selected concepts.

**3.7 Test Marketing**

The purpose of test marketing is to look at the targeted consumers, how they are responding to the developed product, and other marketing mix elements are also analysed.

1. Standard test market:
  - The full marketing campaign is to be made in a small number of targeted consumer cities.
2. Controlled test market:
  - The controlled test market indicates that few stores have agreed to sell the new products for a fee.
3. Simulated test market:
  - This test is to carry out in a simulated shopping environment with a few sets of consumers.

### **3.8 *Launch/Commercialization***

This stage involves

- Placing the product in the market.

It also involves the following:

- To set up manufacturing facilities
- Distribution channel needs to be finalized
- Product's promotion needs to be carried out
- Will often use a regional rollout.

## **4 Importance of Product Development for a Real-Life Situation**

Products come into existence from a set of ideas or concepts which normally generated from nature, images and hidden ideas, on that moment one considers the application of the product for which it will be used and the environment under which it is used. However, there is a large gap between imagination and reality, and therefore, to overcome this gap and to ensure optimum ease of consumer during product's real-time application, a test for checking the performance of the newly developed product should be carried out under the conditions in which it will be used. It is actually done to get valuable feedback on the product, and for doing this, one needs to include targeted customers, partners or anyone who is not familiar with the producing company [7] as a participant. At this point of time, the product should satisfy its planned launch model in all aspects; therefore, more frequent interaction with the participants should be made to increase the resemblance of the new product with its planned model. The participants know all the features and benefits of the product, which can be utilized to increase the quality of the product as per expectation. One needs to achieve three primary objectives during this stage. The first objective is to identify the interest of the customer towards the product. It is also valuable to identify the attributes in which consumers are more attracted. Next objective is to figure out how the newly developed product is used by the customer and how durable that product is, while used by the customer [9]. Apart from these, it also explores the information related to the environment in which that product is being used by the customers. The final step of field testing is to record and analyse the feedback from the valuable costumers. The evaluated feedback can be further used as a tool to improve the design of the product to fully satisfy the customers. The Sales and Marketing team will also get benefited from the feedback. They can use the feedback information to help with their sales presentation and make it easier when they are trying to market the product.

## 5 Focus on Consumer Insight

The entire product development process is consumer-based and related to how consumers think, feel and act while using the product. Consumer insight also indicates how consumers approach towards the products. To get actual market scenario, organizations have to conduct interviews and also visit households, fairs, exhibition or some other places on a large scale. Consumers talk about their own experiences and needs, and then, they are observed as they use the products in their everyday life. The answers and observations are analysed, and the results are then used as a master key in the development of new products or re-launch of existing ones, as well as in marketing activities and campaigns.

## 6 Conclusion

The present work is focused to analyse the key steps of the product development process and their importance in industrial perspective is also presented. Through the study, it is found that the product is developed in physical form by implementing the theoretical knowledge, which is insufficient for selecting the final developed model. In order to get an aesthetically good and ergonomically better product, one needs to incorporate engineering analysis as well as using CAD/CAM tools and rapid prototyping (RPT) technology. CAD/CAM technology helps to analyse the product feasibility in terms of cost, design and manufacturing. In addition to that, market research needs to be done for increasing the certainty of new products introduced in the market and increasing the ROI (return on investment). It helps the marketing and product manager to predict the life of the product and also helps to identify the attractiveness of the product. However, RPT technology can make the market analysis much efficient by creating the physical model. All the staff involved in the process of development should be awarded an incentive in the form of encouragement and reward for their innovative ideas.

## References

1. Marianna K (2017) New product development process—an example of the industrial sector. *Manag Syst Prod Eng* 25(4):246–250
2. Sokovic M, Kopac J (2006) RE (Reverse Engineering) as necessary phase by rapid product development. *J Mater Process Technol* 398–403
3. Zhang Y (2003) Research into the engineering application of reverse engineering technology. *J Mater Process Technol* 139(1–3) SPEC, pp 472–475. [https://doi.org/10.1016/S0924-0136\(03\)00513-2](https://doi.org/10.1016/S0924-0136(03)00513-2)
4. Consumer Insight. Retrieved 21 Feb 2010. <https://newsroom.electrolux.com/files/2009/07/fact-sheet-consumer-insight-final.pdf>

5. Sallati C, Bertazzi JdeA, Schutzer K (2019) Professional skills in the product development process: the contribution of learning environments to professional skills in the industry 4.0 scenario. In: *Procedia CIRP*, pp 203–208.
6. <https://www.patagonia.com>
7. Soldatos J, Hardy J (2007) The new product development process in Australian grocery organisations. *VADYBA Manag* 14(1):61–67
8. Tavell P (2010) Professional mountain biker and product developer at Craft sportswear. Borås, Sweden
9. Santos K, Loures E, Piechnicki F, Canciglieri O (2017) Opportunities assessment of product development process in Industry 4.0. *Procedia Manuf* 11:1358–1365

# Classification of Road Profile Using Golden Car Parameters for Quarter Car Model



A. J. D. Nanthakumar, Karan Jariwala, Kumawat Harshit, S. Yokeshwaran, and S. Madhankumar

**Abstract** The primordial objectives of an automotive suspension system are the ride comfort and stability. To achieve these objectives, the control system utilized for the semi-active suspension should be capable of understanding the road profile and issue subsequent control signals. Hence, a thorough understanding of the road profile is essential. In this direction, this research paper analyzes the road profile and proposes a classification method. A quarter car model is simulated with the golden car parameters as reference values. The classification is based on the sprung mass displacement and sprung mass acceleration values. The proposed classification method can be utilized as a base for control logic formation of a semi-active suspension control system. The proposed classification algorithm can be fed to the controller for taking appropriate control actions to achieve better ride comfort and stability.

**Keywords** Road profile · Road classification · Golden car parameters · Ride comfort

## 1 Introduction

The analysis of the dynamic behavior of vehicles is quintessential in improving the ride comfort and the stability of a vehicle. A number of factors play an important role in influencing the ride comfort and stability of a vehicle. The most fundamental parameter is the nature of the road profile. Road profile can be considered as the input to the dynamic vehicle system. Usually, road profile is represented as roughness parameter. Though road deviations occur in both longitudinal as well as lateral directions, the initial study about the effect of road roughness starts from considering the vertical deviations of the road profile along the longitudinal direction. The roughness scale plays a vital role in determining the ride comfort and stability. There are various factors that are responsible for this. One of the major factors is the road profile. The road profile is very irregular and contains various deviations. This is

---

A. J. D. Nanthakumar (✉) · K. Jariwala · K. Harshit · S. Yokeshwaran · S. Madhankumar  
Department of Automobile Engineering, SRM Institute of Science and Technology,  
Kattankulathur 603 203, India  
e-mail: [ajd.nanthakumar@gmail.com](mailto:ajd.nanthakumar@gmail.com)

referred to as road roughness. There have been many methods to determine and interpret the road roughness for improved ride quality. This road profile is then taken as an input for the suspension system, quarter car model in this case. To generalize this further, the parameters for the golden car are taken. This helps in forming a system that is acceptable all around the world. The quarter car model is designed using MATLAB/SIMULINK and then simulated. The quarter car model was analyzed for ride comfort with sprung mass acceleration parameter for the various road profile functions. Based on this, the classification of various road types is done.

## 2 Literature Survey

Tyan et al. [1] explains how the sinusoidal approximations can be used in deriving a random road profile. This road profile can further be used in the quarter car or half car models. Tudon-Martinez et al. [2] explain the effect of road profile on the comfort and ride quality of a passenger because there is a direct relation between the road profile and the vehicle stability and control. Wambold et al. [3] explained how road roughness is the deviation of road surface from a perfectly smooth surface with minimal characteristic variables that affect the ride quality, comfort, and stability. Also various methods for the measurement of various types of roads are explained.

Buchanan et al. [4] explained the various ways of measuring the road roughness. They found ways to plot the road profile by understanding and measuring the vertical vibrations or oscillations of the wheel. Sayers et al. [5] tell about the growing trend in measuring the road profiles and their measurement methods. Due to this, various countries have come up with different indices. These indices are explained and provided for reference. Ben Bruscella et al. [6] focus on the vertical vibrations as they are after all a function of the road roughness for the plotting of the road profile. They use the International Roughness Index (IRI) for reference; however, this only provided a simple road profile and not the exact one. So they came up with a new road profile analysis methodologies. Rouillard et al. [7] introduce various classifications of road profiles based on the data available universally with special attention to their non-Gaussian and non-stationary properties. Peter AndreAn [8] explains the importance of Power Spectral Density (PSD) and also how it helps in the plotting of the road profile. He also explains how.

PSD can be taken as an input for the vehicle dynamics. Qin et al. [9] propose a new method for measuring the road profile which acts as an input for the semi-active suspension system that is being widely used in the production vehicles. Peter Mucka [10] uses the ISO 8606 road classification as a comparison parameter for determining the accuracy of the road classification. He compares ISO 8608 with the real roads and finds its accuracy. He found significant differences among the road profiles which were used for the simulation from the real-time profiles. Louhghalam et al. [11] states the major factor and parameters responsible for the energy dissipation in a vehicle dynamic system. To further prove this, he uses a system containing the golden car parameter which is taken as the base on which all the properties are dependent. Sayers



[12] explains how the International Roughness Index (IRI) is widely used, but there are no short reference data available. He then tries to create this data that is required for plotting a road profile.

### 3 Road Roughness

Road roughness is defined as the variations and the irregularities that are experienced on the road while traveling. This is one of the major factors that taken into consideration for the analysis of the road profile. The road roughness consists of a number of different wavelengths and elevation data. This data has been collected by a number of engineers and consolidated in the International Roughness Index (IRI). Road roughness can be seen throughout the surface. A road profile having more roughness means that its quality is less. The data that is available to engineers is vast and discontinuous, so this cannot be used for the analysis. So, the alternate method uses the Power Spectral Density (PSD) concept which can be used for dynamic analysis as well as its design.

Power spectral density can be explained as the summation of various data in the form of sinusoidal waves of any random road profile with variations in its wavelength and amplitudes. More the number of sinusoidal waves integrated, better will be its accuracy. As a result of increasing the number of sinusoidal functions, their respective amplitudes decrease as the quality of the road decreases. The PSD value also increases as the wave number increases. The reason for this is that lower wave numbers result in a higher wave length which in turn results in a larger amplitude. This can be seen in almost all types of roads. As per ISO 8608 regulations, there are two methods of representing the road profile data in the form of PSD:

1. Displacement PSD
2. Acceleration PSD

The general form of PSD is given by:

$$G_d(n) = \pi_d(n_0)(n/n_0)^{-w}$$

$$G_d(\omega) = \pi_d(\omega_0)(\omega/\omega_0)^{-w}$$

where  $G_d$  is displacement PSD,  $n$  is spatial frequency, and  $\omega$  is angular spatial frequency.

Buchanan was one of the first people to devise an equipment to measure road roughness. He founded the horizontal pendulum. This was operable for hundreds of miles without failure. Later with the introduction of the CHLOE profilometer, the accuracy was increased. The CHLOE profilometer had disadvantages like design complexity, costlier installation and very slow operation. To overcome these problems, Mays road meter was introduced. Though it did not have as high precision as

the CHLOE profilometer, it had its own advantages like its simple operation, low maintenance, low initial cost, and faster operation. The roughness data obtained from profilometric equipment's after rigorous analysis and the roughness data obtained from response type equipment's showed excellent correlations under acceptable variations. A single index termed as the International Roughness Index (IRI) was proposed that is measurable and compatible with all the roughness measuring equipment's deployed worldwide. Brickman et al. discussed about the features and characteristics of amplitude analysis and frequency analysis of road roughness data and concluded that frequency analysis of road roughness data yielded useful results.

Based on the data gathered by earlier research work, it can be stated that various road profiles can be plotted using that data. Taking the ISO standard as the basis for this research paper, the road is classified into five different types based on their roughness. They are namely road type A, road type B, road type C, road type D, and road type E, with road type A being the best road type and road type E being the worst. For the plotting of these road profiles, a basic SIMULINK model was designed and studied.

## 4 Quarter Car Model

Vehicle simulation can be done using a number of models, whereas for dynamic simulations, the major models are the full car model, half car model, and the quarter car model. The full car model represents all the four wheels and suspension systems of a four wheeler. A half car model represents only half the vehicles wheels and suspension systems, i.e., two wheels and suspension systems. For this generally, one front wheel and one rear wheel is considered. The last one being the quarter car model consists of only one wheel and suspension system taken into consideration. The quarter car model being very fundamental is generally used for the basic vehicle simulations.

The quarter car model has two major masses: Sprung mass and the unsprung mass. The sprung mass refers to all the masses present above the suspension system. This includes the whole body mass. Unsprung mass refers to all the masses present below the suspension system. This includes the wheels and the suspension system itself.  $M_s$  refers to the sprung mass, and  $M_u$  refers to the unsprung mass.  $K_s$  is the stiffness constant for the sprung mass, and  $K_u$  is the stiffness constant for the unsprung mass.  $C_s$  is the damping constant for the sprung mass.  $X_s$ ,  $X_u$ , and  $Y$  are the displacements of the sprung mass, unsprung mass, and the road surface, respectively.

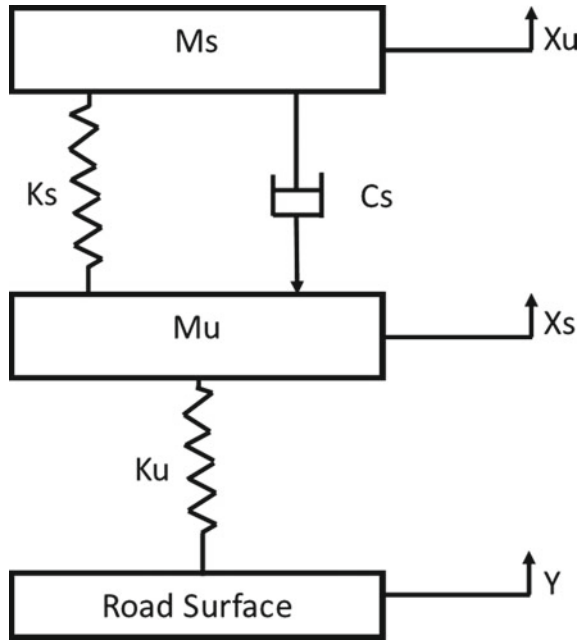
## 5 Golden Car Parameters

To standardize the values of the quarter car model, the golden car parameters were introduced. These values are the basic values taken as an average of the vehicle

**Table 1** Golden car parameters values

Parameter	Value	Unit
$k_t/m_s$	653	$s^2$
$k_s/m_s$	63.3	$s^2$
$c_s/m_s$	6.0	$s^{-1}$
$m_u/m_s$	0.15	1

**Fig. 1** Quarter car model



parameters to make universally accepted values. As stated by Louhghalam [11], these values are taken as ratios. The values are provided in Table 1.

Sayers [12] had iterated the quarter car model using a number of different values for each of the parameters. He came to the conclusion that the golden car parameter values gave the best correlation between the actual values and the simulated values (Fig. 1).

## 6 Simulink Model

See Fig. 2.

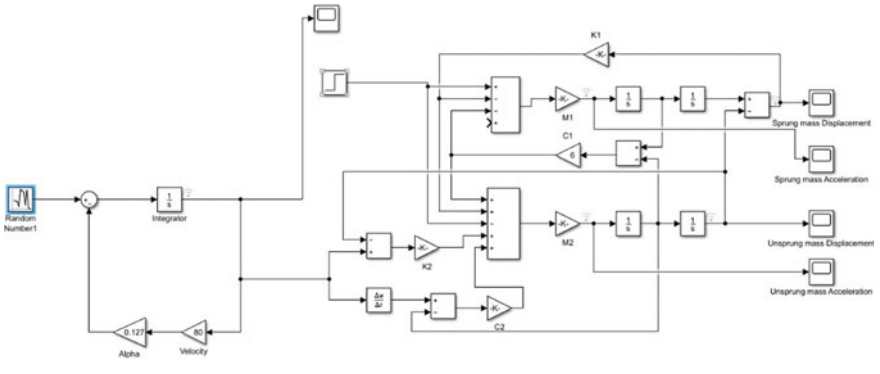


Fig. 2 Quarter car model in SIMULINK

### 7 Results and Discussion

The road profile out was taken using the SIMULINK model. The output graphs show the significance difference between the road profiles (Figs. 3 and 4).

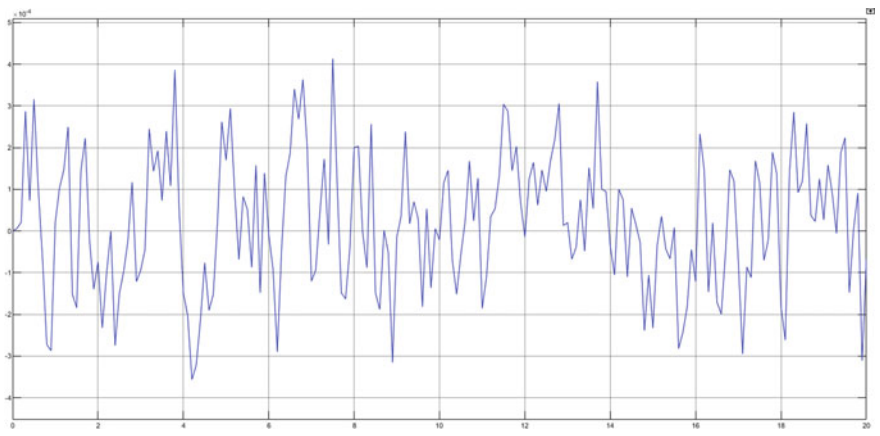
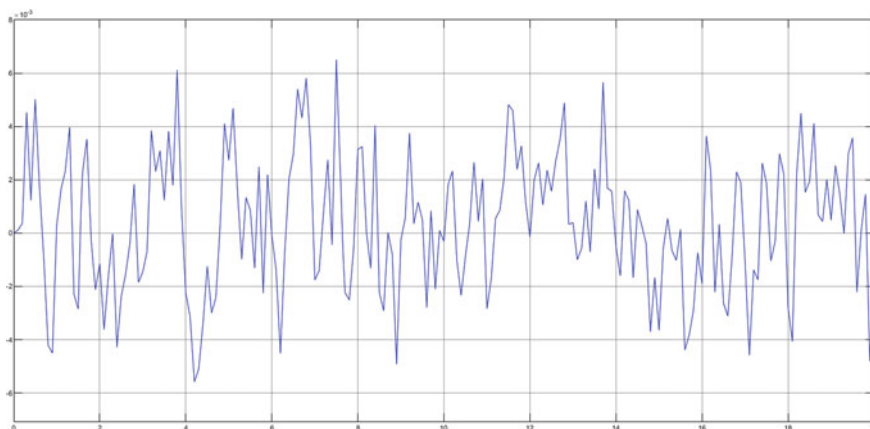


Fig. 3 Road profile A



**Fig. 4** Road profile E

## References

1. Tyan F, Hong Y-F (1999) Generation of random road profiles. *J Adv Eng (B04)*
2. Rewabhai SH (2017) Design and development of magnetorheological fluid base damper. Doctoral dissertation, Gujarat Technical University
3. Wambold JC, Deffrain LE, Hegmon RR, Mecghee J, Reicher J, Spangler EB (1986) State of the art of measurement and analysis of road roughness. *Transportation Research Record*
4. Buchanan JA, Catudal AL, Greenshields BD, Moyer RA (1941) Proceedings of the twentieth annual meeting of the highway research board. In: *Standardisable equipment for evaluating road surface roughness*, vol 20, pp 621–638
5. Sayers MW, Gillespie TD, Queiroz CAV (1986) The international road roughness experiment establishing correlation and a calibration standard for measurements
6. Bruscella B, Rouillard V, Sek M (1999) Analysis of road surface profiles. *J Transp Eng* 125(1)
7. Rouillard V, Bruscella B, Sek M (2000) Classification of road surface profiles. *J Transp Eng* 126(1):41–45
8. Andrian P (2005) Power spectral density approximations of longitudinal road profiles. *Int J Veh Des* 40(1):02–14
9. Qin Y, Xiang C, Wang Z, Dong M (2017) Road excitation classification for semi-active suspension system based on system response. *J Vibr Control* 24(13):2732–2748
10. Mucka P (2016) Simulated road profiles according to ISO 8608 in vibration analysis. *J Test Eval* 46(1):405–418
11. Louhghalam A, Tootkaboni M, Ulm F-J (2015) Roughness-induced vehicle energy dissipation: statistical analysis and scaling. *J Eng Mech* 141(11)
12. Sayers MW (2005) On the calculation of international roughness index from longitudinal road profile. In: *Monograph: pavement-vehicle interaction and traffic monitoring*, vol 1501, pp 01–12

# Development of Onboard Engine Management System—Prediction of Oil Degradation



K. Prabu, P. D. Jeyakumar, C. Dineshkumar, B. Vasanthan,  
A. Arockia Julius, and M. Thirumurugan

**Abstract** The purpose of engine oil lubrication is to reduce the wear and tear of the engine parts due to friction, corrosion, and to dissipate some amount of heat from the engine. The engine oil quality directly influences the service life and performance of the engine. The part manufacturers specify and list down the oil replacement period depending on the capacity of the engine at the standard test conditions. Conveniently, it is very difficult to determine the condition of the engine lubricating oil in normal operating condition. In this work, a coaxial capacitance sensor is developed to monitor the quality of the engine-lubricating oil. The quality of the oil is monitored by the sensor which will provide suitable capacitance value for the different oil conditions. The obtained capacitance values are monitored with the help of the LCR meter. The capacitance and the dielectric constant increase when the quality of the oil decreases. The different oil samples are tested to predict the parameters such as capacitance and dielectric constant. Finally, the obtained values are compared with the fresh oil to estimate the quality of the oil.

**Keywords** Lubrication oil · Sensor · Engine oil degradation · Capacitance sensor · Automobile · Dielectric constant

## 1 Introduction

The service life of the vehicle is mainly governed by the smooth operation of the engine. The engine operation depends on the condition of the lubrication oil and filter used in the engine. Also, this process assists in removing the dirt particles and sludge in the lubricating oil. The Society of Automotive Engineers (SAE) developed

---

K. Prabu  
VIT, Vellore, India

P. D. Jeyakumar (✉) · C. Dineshkumar · A. A. Julius · M. Thirumurugan  
B S Abdur Rahman Crescent Institute of Science and Technology, Chennai, India  
e-mail: [pdjeyakumar@gmail.com](mailto:pdjeyakumar@gmail.com)

B. Vasanthan  
Anna University, MIT Campus, Chennai, India

a grade for the engine oil based on the resistance to thinning at a high temperature, called viscosity. The proper lubrication oil change removes the heat developed due to friction from all the moving parts of the engine. The removal of wear particles and the sludge optimizes the time of oil change and helps improve the fuel efficiency of the vehicle. This process enhances the life of the engine components. All engine manufacturers recommend the engine oil change period for the efficient operation of the engine. But practically due to the different operating conditions, the condition prediction of the engine lubricating oil aging is challenging process. The engine oil degradation occurs due to fuel, high operative temperature, water, engine coolant (ethylene glycol), metal chips which are the important factors.

Presently, the engine lubricating oil condition is found by the physical and chemical properties like total base number, viscosity, total acid number, and dielectric constants. Among these, the viscosity measurement is one of the approaches to monitor the engine oil condition. The sensors capable of measuring the acoustic, electrical, or chemical properties are available [1–3]. The selection of these sensors is very limited owing to the price and complication [4]. The operating condition is not limited, and also the oil degradation depends on the condition of operation and the driving style [5]. Since the nineteenth century, the car manufacturers have been using the onboard diagnostics tools to provide real-time details from the sensors, like crank speed, coolant temperature, ride height, fuel quality, and trouble codes [6, 7]. The metal particles, water contamination, soot particle, permittivity, antifreeze, and oxidation are the indicators of the condition of lubricating oil [8]. There are a few authors who have preferred capacitive technique to study the condition of lubricating oil and the level of lubricating oil. A micro-electro-mechanical system based capacitive sensor is fabricated, and the radio-frequency identification system is used to capture the signal from the sensor. The captured data are processed, and they display the lubrication oil degradation [9].

All these parameters are not required for measuring the quality of the oil and life prediction of the lubricating oil. From the previous studies, the authors have identified that it is problematic to estimate the condition of the lubricating oil. Nonetheless, by considering the essential requirement of the current study, the cylindrical capacitance sensor for estimating the oil condition at different time intervals has been developed. The condition of the oil is monitored by suitable capacitance with the help of an LCR meter. The different oil samples are tested on the automotive single cylinder diesel (APE) engine to predict the parameters such as capacitance and dielectric constant. The actual capacitance and dielectric constant values are compared with the new fresh oil to predict the quality of the oil.

## 2 Material and Methods

The oil monitoring system has done a great job in evaluating the lubricating oil condition in different environments. Most of the monitoring systems are used to estimate the degradation of the engine lubricating oil.

### 2.1 Co-axial Capacitance Sensor

Different methods such as acoustic, electrical conductivity, mathematical, temperature, and viscosity, are used for monitoring the conditions of the oil. Among these techniques, the coaxial capacitance sensor is one of the notable systems preferred for this application. The physical and the electrical properties of the cylindrical capacitance sensor are deliberated by dielectric constant and capacitance. The cylindrical capacitance sensor consists of positive and negative conductive electrodes separated by an insulator (mica, ceramic, or any non-conductive material), and it is developed by using the principle of the capacitor. The insulator is dielectric medium. The measured energy is accumulated by the stored in conductive electrodes when the switch is closed (Fig. 1).

The charging time of the capacitor is estimated by constant(s), where 'R' is the resistance value of the resistor associated with the capacitor and 'C' denotes the capacitance value. The time charging constant(s) is assessed by the mathematical relation

$$s = \frac{1}{4} RC \tag{1}$$

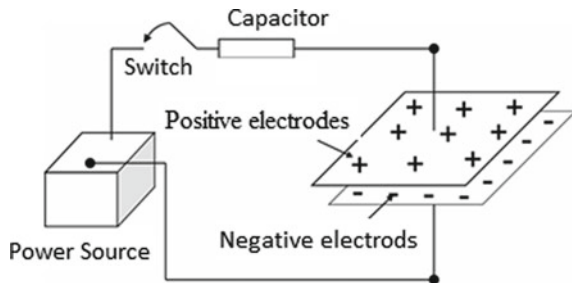
The capacitance is an important property in the prediction of lube oil. The capacitance is mathematically defined by

$$C = \frac{Q}{V} \tag{2}$$

where 'C' is the capacitance in Farad (F), 'Q' is magnitude of charge, and the applied voltage is denoted by 'V'. The typical magnitude of the capacitance is from 1 pF to about 1000 pF range. The resulting electric field is due to the difference between the electric charges stored on the surface of each plate.

The dielectric constant is another parameter considered to estimate the condition of the oil. The capacitance will vary based on the dielectric material. It is increased by increasing the permittivity which allows storing the electric field.

**Fig. 1** Capacitor used in a circuit to store electrical charge





$$C = kC_0 \quad (3)$$

where ' $C_0$ ' is the capacitance with no dielectric between the plates, ' $C$ ' is the capacitance, and ' $k$ ' is the dielectric constant of the material. The dielectric constant has different magnitudes for dissimilar materials. The cylindrical capacitive sensor transforms dielectric constant into an electric signal. If there is a variation in capacitance, area, dielectric constant, and distance, the sensor sends some electric signals.

## 2.2 Development of Cylindrical Capacitance Sensor

Figures 2 and 3 describe the details of the cylindrical capacitive sensor which is developed for measuring the quality of the engine oil. The capacitance for the cylindrical geometry is denoted as capacitance per unit length.

The expression for calculating the capacitance is expressed as

$$\frac{C}{L} = \frac{2\pi k\epsilon_0}{\ln\left[\frac{b}{a}\right]} \quad (4)$$

The cylindrical coaxial sensor's inner diameter ( $a$ ), outer diameter ( $b$ ), dielectric constant ( $k$ ), and capacitance per unit length (and  $C/L$ ) are essential parameters to determine the oil capacitance. Cylindrical tube capacitor has a simple design, and it is easy to manufacture. It consists of two concentric cylindrical tubes. The positive terminal is attached to the inner cylinder cell, and the external part of the cylinder is

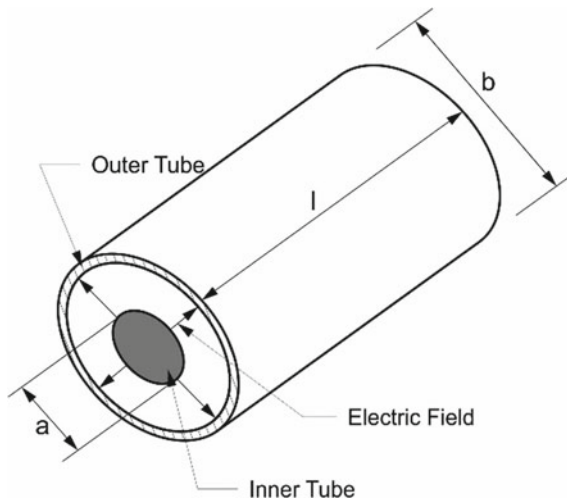


Fig. 2 Schematic view of the cylindrical capacitance sensor

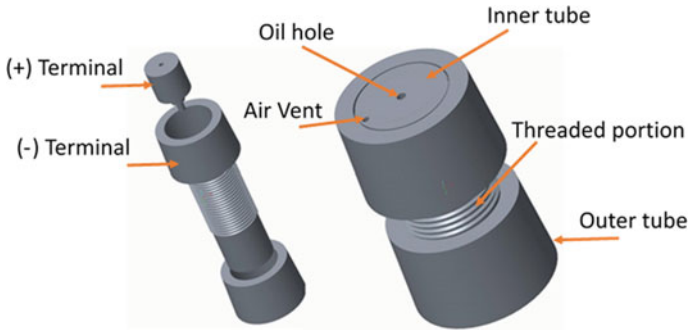


Fig. 3 CATIA model of the cylindrical capacitance sensor

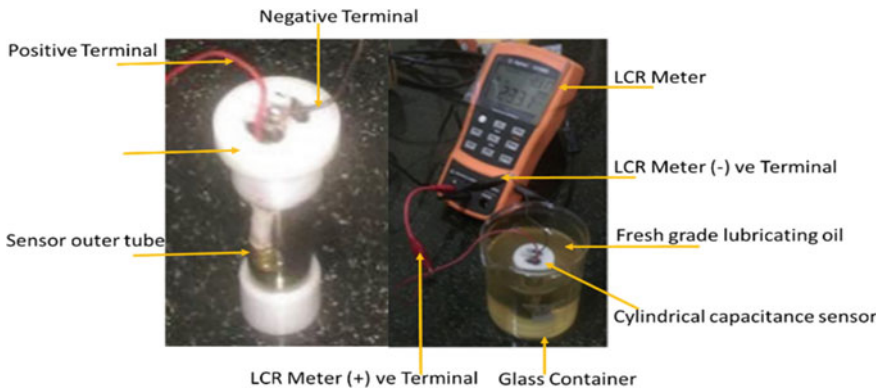


Fig. 4 Schematic view of the cylindrical capacitance sensor

connected the negative terminal. When the voltage is applied between the inner and external cells, an electric field is developed between the cells (Fig. 4).

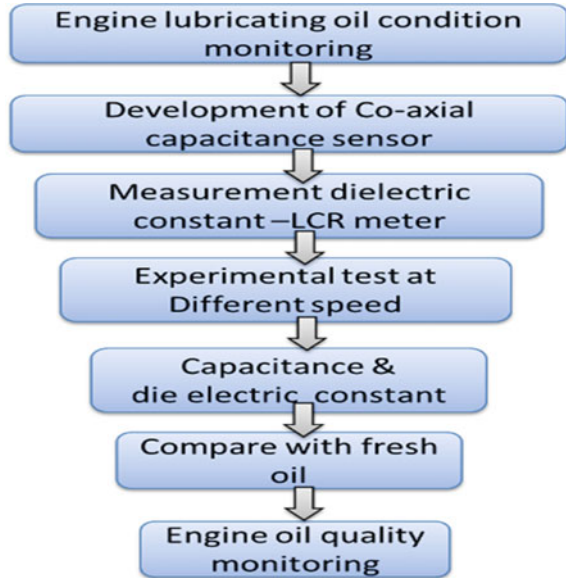
### 2.3 LCR Meter

Electronic LCR meter [6, 8] is preferred to measure the inductance, capacitance, and resistance. This instrument is capable of measuring the impedance and transformed magnitude of capacitance or inductance value.

#### a. Methodology

The engine oil condition monitoring is performed by a capacitive-type coaxial sensor that is proposed to be developed. In the previous study, a capillary tube viscometer was used for measuring the viscosity of the oil [9, 10]. This study attempts to measure the quality of the oil by the cylindrical capacitance sensor which works based on the

**Fig. 5** Methodology for monitoring oil condition



principle of capacitance. The sensor measures the dielectric constant according to the condition of the lubricating oil. The dielectric constant depends upon the dipole moment of the oil. When the oil gets degraded, the dipole moment increases and the capacitance also increases. By using the LCR meter, the value of the dielectric constant is monitored. Figure 5 explains the methodology to be adopted for monitoring the engine lubricating oil.

## 2.4 Engine Test Rig Setup

The experimental test rig includes a four-stroke single-cylinder variable-speed direct-injection automotive engine (PIAGGIO APE) coupled with water cooler dynamometer. The control panel consists of a speed regulator, engine on/off control, and an overload indicator. The burette is used to estimate the fuel consumption for the unit time and the test bench is shown in Fig. 6. Table 1 shows the details of the specifications of the engine setup used for testing.

## 3 Results and Discussions

The quality of the oil was graded by measuring the viscosity and the electrical conductivity of the degraded oil and fresh oil. A single-cylinder (PIAGGIO APE) engine

**Fig. 6** Variable speed test rig with eddy current dynamometer



**Table 1** Specifications of the test engine

Engine	4S single-cylinder variable-speed, water cooled, DI (PIAGGIO APE)
Emission norms	BS-IV
Displacement (CC)	395
Max power	8.04 bhp@3400 rpm
Max torque	22.2 Nm@200 rpm
Transmission	manual
Clutch and gearbox	Multi-disk wet type, 4 speed
Fuel tank capacity (l)	18.13
Gradability (%)	18
Mileage (kmpl)	36

was considered for the experimental analysis. The degraded engine oil’s viscosity and the temperature were measured at different operating speeds (1500, 2000, and 2500 rpm) of the engine. Three different oil samples were collected from the experiment. The viscosity, dielectric constant, and capacitance values were observed for the different tests using a cylindrical coaxial sensor and LCR meter. The viscosity was observed to be around 4.917 mm<sup>2</sup>/s in the experimental test-1 conducted at 1500 rpm which is shown in Fig. 7. The increase in temperature (50–90 °C) resulted in a diminishing trend in viscosity by 1.824 mm<sup>2</sup> at an operating temperature of 90 °C. The obtained results proved that with the increase in temperature, the viscosity reduced

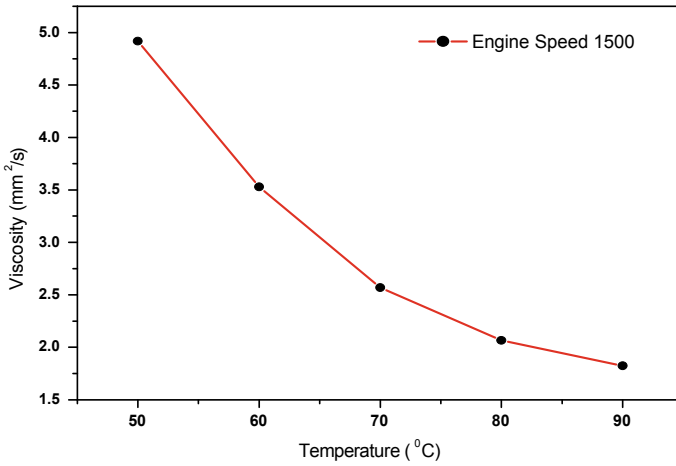


Fig. 7 Test-1 experiments at 1500 rpm engine speed

at all observed temperatures. A 48.1% reduction in viscosity was observed by the rise in temperature from 50 to 90 °C at a speed of 1500 rpm.

The experimental test-2 was conducted at an engine speed of 2000 rpm and temperature range of (50–90 °C) which is shown in Fig. 8. The obtained result revealed that the viscosity of the oil decreased from 4.375 to 1.816 mm<sup>2</sup>/s with the oil temperature going up from 50 to 90 °C. A 58% reduction in viscosity was observed due to the rise in temperature from 50 to 90 °C at a speed of 2000 rpm.

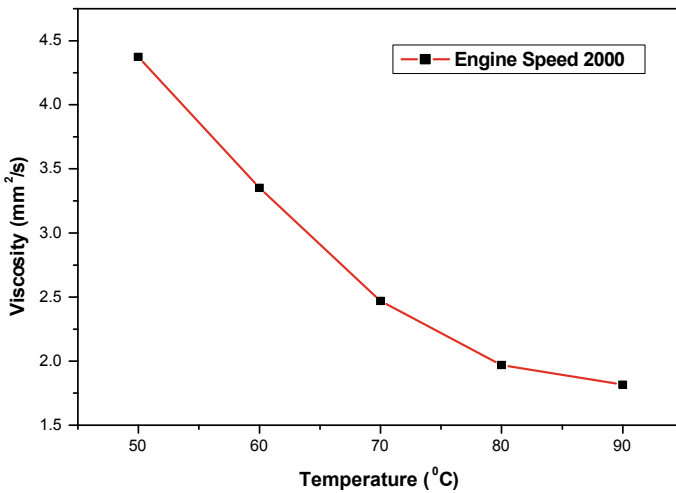
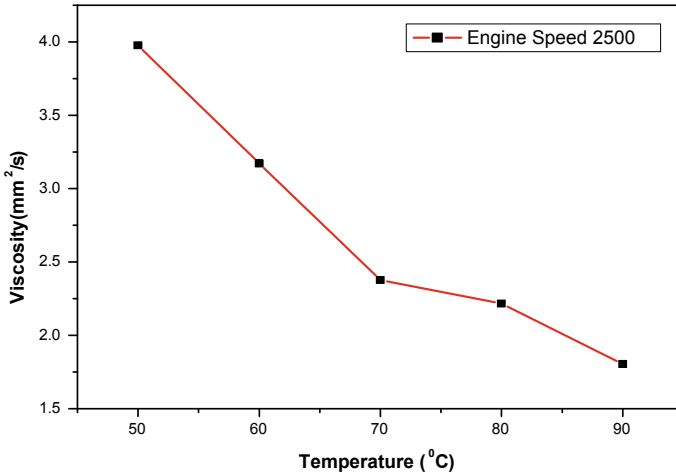


Fig. 8 Test-2 experiments at 2000 rpm engine speed



**Fig. 9** Test-3 experiments at 2500 rpm engine speed

Test-3 was conducted at an engine speed of 2500 rpm. The viscosity values ranged between 3.977 and 1.804 mm<sup>2</sup>/s as shown in Fig. 9. The reduction in viscosity was observed as 54% for the rise in temperature up to 90 °C at an engine speed 2500 rpm.

The five different fresh grades of lubricating oils were procured from the commercial market. The dielectric constant and the viscosity of fresh grade oil were measured by using a cylindrical coaxial sensor and LCR meter. From the fresh graded oils test, it was observed that if the viscosity of the fresh oil increased, simultaneously the dielectric constant also increased (Table 2) when compared with degraded oils obtained from test-1, 2, and 3. From the different fresh and degraded oil tests, the accuracy of the cylindrical coaxial capacitance sensor was validated.

The different degraded oil samples were collected after 100 h test and evaluated by a cylindrical coaxial capacitance sensor with LCR meter. When the oil was degraded, the dipole moment decreased and the capacitance increased as shown in Fig. 10. When the operating temperature was increased from 50 to 90 °C, the viscosity and the dielectric constant reduced from the higher value to lower value, whereas the temperature raised the capacitance value linearly from 39 to 42.51 pF.

**Table 2** Different graded fresh oil sample test

S. No.	Viscosity (mm <sup>2</sup> /s)	Dielectric constant (pF)
1	13.2	2.14
2	13.96	2.17
3	14.15	2.21
4	14.28	2.25
5	14.32	2.30

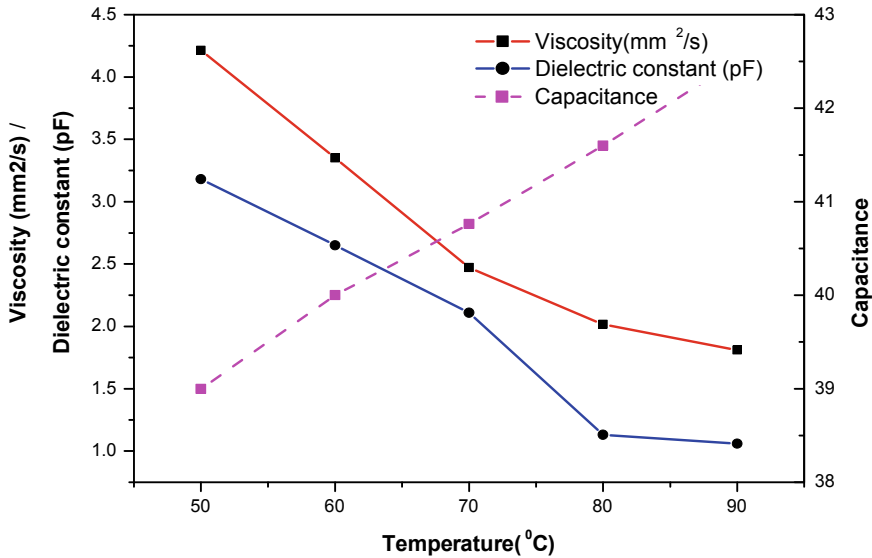


Fig. 10 Relation of viscosity, dielectric constant, and capacitance

## 4 Conclusions

The viscosity and the dielectric constant were measured for fresh graded and degraded oils from different tests.

- In degraded oil, the dielectric constant was 25% higher than that of the fresh grade oil. From this study, it was found that the viscosity of the fresh grade oil was directly proportional to the dielectric constant.
- From the analysis of the degraded oil, it was concluded that the reduction in oil viscosity caused a decrease in the dipole moment and an increase in the capacitance.
- The fresh oil had the capacitance in the range of 36–39 pF. Nevertheless, the degraded oil's capacitance was estimated using a cylindrical coaxial capacitance sensor, and the capacitance was estimated to be in the range of 45–47 pF.
- The future scope of this work is to develop a driver information system to indicate the condition and the level of the lubricating oil which can be obtained from a look-up table consisting of dielectric and capacitance readings.

## References





1. Jakoby B, Scherer M, Buskies M, Eisenschmid H (2003) An automotive engine oil viscosity sensor. *IEEE Sens J* 3(3):562–568

2. Zhu J, Yoon JM, He D, Que Y (2013) Lubrication oil condition monitoring a remaining useful life prediction with particle filtering. *J Chem Sci Tech* 20:1–15
3. Mujahid A, Dickert F (2012) Monitoring automotive oil degradation: analytical tools and on-board sensing technologies. *Anal Bioanal Chem* 40(4):1197–1209
4. Kumar S, Mukherjee PS, Mishra NM (2005) Online condition monitoring of engine oil. *Ind Lub Trib* 57(6):260–267
5. Mujahid AA, Dickert FL (2012) Monitoring automotive oil degradation, analytical tools and onboard sensing technologies. *Anal Bioanal Chem* 404(4):1197–1209. <https://doi.org/10.1007/s00216-012-6186-1>
6. Zhu J, He D, Bechhoefer E (2013) Survey of lubrication oil condition monitoring, diagnostics, prognostics techniques and systems. *J Chem Sci Tech* 2(3):100–115
7. Prabu K, Jancirani J, Jeevamalar J (2012) Development of an actively controlled vehicle suspension for passenger vehicles. In: Internal conference on advance engineering. IEEE Digital Library, pp 206–210
8. Kraljr J, Konecny B, Kral J, Madac K, Fedorko G, Molnar V (2014) Degradation and chemical change of long life oils following intensive use in automobile engines. *Int J Measur* 50:34–42
9. Dineshkumar C, Subramian M, Deepan V, Muthaya J (2019) Health monitoring system for automobile vehicles to enhance safety. *Int J Veh Struct Syst* 10(6):395–398
10. Dineshkumar C, Subramian M (2018) Experimental investigation of onboard driver condition monitoring system for passenger vehicles. *Int J Mech Eng Technol* 9(6):01–09



# Synthesis and Characterization of Water in Diesel Emulsions



Anumula Shiva Kumar , Mallampati Krishna Deepika ,  
Chippa Sri Haasa , P. S. Raghavan, and Purushothaman Nandagopalan 

**Abstract** Air pollution from the combustion of diesel has demonstrated significant interest in synthesizing a non-polluting diesel fuel for an enhanced and clean environment. One such example is the emulsion fuel; water in diesel (WinD). In the present work, the goal is to synthesize an alternative fuel system consisting of (WinD) emulsions focusing on the reduced exhaust emissions, high mileage, and increased efficiency of engines. The effect of surfactant concentration on the emulsion stability plays a vital role and it is studied through the formulation of the emulsions with different fuel blend proportions. The dispersion of the surfactant resulted in a clear emulsion with a high transparency level is considered as a stable emulsion. Here, the SPAN 80(S) and Brij 30(B) are used as the surfactants, and the stabilized emulsions are obtained using high energy homogenizer; with the various proportions. Furthermore, the fuel characteristics such as viscosity, density, flash and fire point, the heat of combustion, and stability of the emulsions were compared with standard values of diesel. The physical stability under the ambient conditions was noticed to be stable for 40 days. The more stable proportion to be synthesized were WinD 24, WinD 27, WinD 30, WinD 36, WinD 37.

**Keywords** Pollution · Water in diesel emulsion · Surfactant · Stability · Viscosity

---

Anumula Shiva Kumar, Mallampati Krishna Deepika, Chippa Sri Haasa and P. S. Raghavan are equal contribution.

---

A. S. Kumar · M. K. Deepika · C. S. Haasa · P. S. Raghavan · P. Nandagopalan (✉)  
Hindustan Institute of Technology and Science, Padur, Chennai 603103, India  
e-mail: [npurush@hindustanuniv.ac.in](mailto:npurush@hindustanuniv.ac.in)

A. S. Kumar  
e-mail: [askumal79@gmail.com](mailto:askumal79@gmail.com)

M. K. Deepika  
e-mail: [krishna.deepika.m@gmail.com](mailto:krishna.deepika.m@gmail.com)

C. S. Haasa  
e-mail: [srihaasa1999@gmail.com](mailto:srihaasa1999@gmail.com)

P. S. Raghavan  
e-mail: [raghavan@hindustanuniv.ac.in](mailto:raghavan@hindustanuniv.ac.in)

# 1 Introduction

## 1.1 Diesel

Diesel-powered engines are significant in energy production by combustion. However, pollutant emissions, particularly, particulate matter, CO, and NO<sub>x</sub> emissions, are the main problem with diesel during its combustion. Other existing issues like fossil fuel depletion, ever-changing fuel prices, and high demands for transportation inwardly affect the role of diesel fuel in the future energy production. Thus, there exists a requirement for introducing a solution to counteract this predicament. Emulsifying the diesel by water has been implemented as one of the key modifications to fuel. A diesel engine runs with a surplus of air that creates nitrogen oxide build up. Water's latent heat of vaporization and high thermal capacity reduces the overall temperature of the combustion chamber, which retards NO<sub>x</sub> formation [1]. Zones with an over-rich mixture give rise to incomplete combustion and unburned HC emissions. The direct vaporization of water improves fuel distribution by increasing the concentration of OH oxidation species, thereby limiting particulate emissions. These emulsions also have better lubricity and thermal efficiency. The thermal efficiency of a unit using emulsified fuel increases (expansion of gases) or decreases (heat transfer) compared to the unit using non-emulsified diesel, depending on the combustor type or characteristic of fuel [2]. Secondary atomization and micro-explosions are also observed in the combustion of emulsified fuels during combustion.

The objective of this study is to obtain stable water in diesel emulsions (WinD), which are stabilized with emulsifying agents, cutting down additional handling and equipment, thereby reducing costs, emissions, and fuel consumption. Before using (WinD) as a fuel, the crucial step is to define their properties as it will affect those engine operating parameters such as design calculations, injection timing, and mixing mechanism. In the works of Abdul Karim et al., density and viscosity were found to be higher for all WinD samples as compared to diesel at all measured temperatures, whereas the carbon contents for WinD with 10 and 20% water were low [3]. However, in our works, the density of unstable emulsions was high and some of the emulsions showed similar densities due to surfactant Brij 30 usage. Emulsions with high viscosities are found to be stable and a stable emulsions droplet size is very minute so that Brownian motion is produced by thermal collision forces of continuous phase molecules [4]. The Brij 30 surfactant used in our emulsions showed stable emulsions with low viscosities and fine droplets with small sizes. It depicted that a fine emulsion with adequate amounts of oil and different emulsifiers can produce stable and tight emulsions.

## 1.2 Materials and Methodology

Emulsified fuel was synthesized using Indian oil diesel, distilled water, Sigma-Aldrich's Brij 30, and Fisher Scientific's Span 80. The properties of the materials used are given in Tables 1, 2 and 3.

The primary role of surfactant is to lower the interfacial tension with the adsorption of more surfactant at the interface, and consequently droplet coalescence is delayed.

## 2 Experimental Procedure

An emulsion is a dispersion of liquid in a liquid system. The two liquids in the system are immiscible. Synthesis of an emulsion is done by either comminution or condensation. Comminution is a process where mechanical energy or pressure is

**Table 1** Properties of diesel

Properties	Values
Chemical formula	C <sub>12</sub> H <sub>24</sub>
Ash, by mass, max	0.01%
Carbon residue, by mass, max	0.30%
Cetane number, min	51
Cetane index, min	46
Pour point, max: a. Winter b. Summer	a. 3° C b. 15° C
Distillation, 95% v/v, recovery, °C, max	360
Flashpoint, Abel, min	35 °C
Kinematic viscosity at 40 °C	$(2.0-4.5) \times 10^{-6} \frac{\text{m}^2}{\text{s}}$
Density at 15 °C	(0.815–0.845) Kg/l
Total sulfur, mg/kg	50
Water content, mg/kg, max	200

Source Indian Oil Corporation

**Table 2** Properties of Span80 (Polysorbate 80)

Properties	Values
Chemical formula	C <sub>64</sub> H <sub>124</sub> O <sub>26</sub>
Viscosity (25 °C)	340–450 (cS)
Specific gravity (25 °C)	1.026–1.09
Sulphated ash	0.20%

Source Fisher Scientific: Lab Equipment and Lab Supplies

**Table 3** Properties of Brij 30 (polyethylene glycol dodecyl ether)

Properties	Values
Chemical formula	$(C_{20}H_{24}O_5)_n$
Physical state	Semi-solid melting to a liquid
Color	White
Density (25 °C)	0.95 kg/l
Flash point (closed cup)	113 °C
Water (kF)	1%
Freezing point	(39–43) °C
Boiling point	100 °C at 1.013 hPa

Source Sigma-Aldrich

applied to the mixture to form an emulsion. Emulsifiers are used for promoting the formation of an emulsion, making it easier to prepare, producing finer droplet size, aiding stability to the dispersed state. The following procedures are implemented to prepare an emulsified fuel.

### ***2.1 Emulsification: Ultrasonicator Bath***

The beaker (100 ml) is filled with diesel and water, and surfactant was injected in assigned proportions. It was enclosed with aluminum foil to cease evaporation of emulsion as to not alter the emulsified fuel proportions. The ultrasonicator bath was filled with water to the specified level on the machine and is switched on. The beaker was positioned on the tray accordingly; thus, agitation of a heterogeneous mixture is initiated. After the completion of homogenization, the emulsion is obtained (transparent) (Fig. 1).

### ***2.2 Emulsification: Magnetic Stirrer***

The beaker (100 ml) is filled with diesel and water; surfactants were injected in assigned proportions. The beaker was enclosed with aluminum foil to cease evaporation of emulsion as to not alter the emulsified fuel proportions. It was positioned at the center of the magnetic stirrer. The stir bar is immersed in the beaker. The magnetic stirrer is turned on and mechanical mixing is initiated. The mechanical mixing was observed for an hour continuously. The emulsion obtained (milky white) is stored for further tests (mainly stability) (Fig. 2).

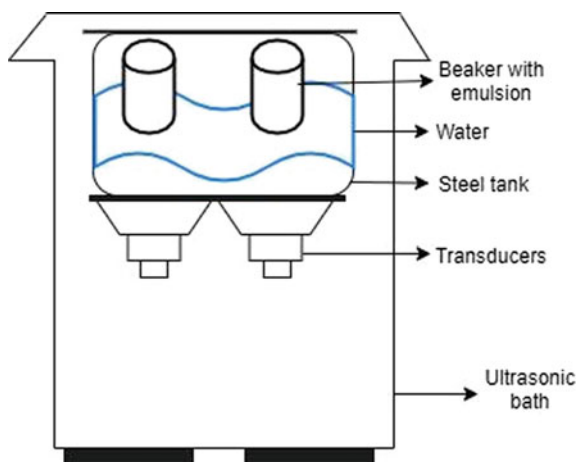


Fig. 1 Ultrasonic bath (schematic)

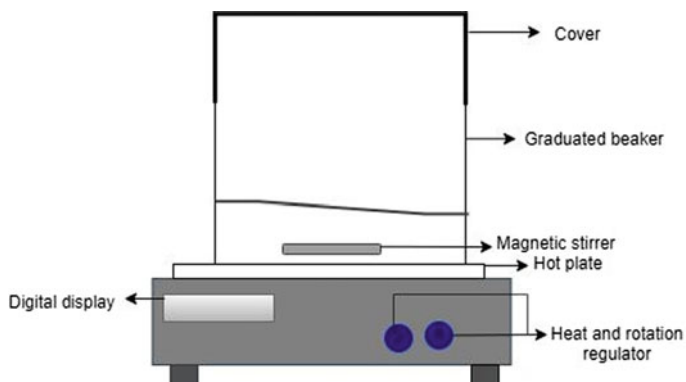


Fig. 2 Magnetic stirrer (schematic)

### 2.3 Emulsification: Mechanical Shaking

The test tube (10 ml) is filled with diesel and water; surfactants were injected in assigned proportions. The test tube was enclosed with hand and shaken continuously and vigorously for 30 min. The emulsion obtained (milky white) is stored for further tests (main stability).

**Table 4** Characterization of WinD emulsions

Characteristics	Method or equipment
Density	Water displacement method
Flash and fire point	Open-cup test
Viscosity	Redwood viscometer
Heat of combustion	API specific gravity method

## 2.4 Experimental Tests Conducted

Viscosity is determined by a redwood viscometer and the result is expressed as the number of redwood seconds required for the flow. The following formula is used to calculate viscosity from redwood seconds (Table 4).

$$V = \left( ct - \frac{B}{t} \right) \times 10^{-6} \frac{\text{m}^2}{\text{s}} \quad (1)$$

The open-cup test was used to estimate the flash and fire point (5% error). The gross heat of combustion of diesel is calculated using an indirect method.

$$Q = 12,400 - 2100d^2 \quad (2)$$

where  $d$  is the specific gravity ( $\frac{15.5}{15.5} \text{ } ^\circ\text{C}$ ).

## 3 Results and Discussion

### 3.1 Stability

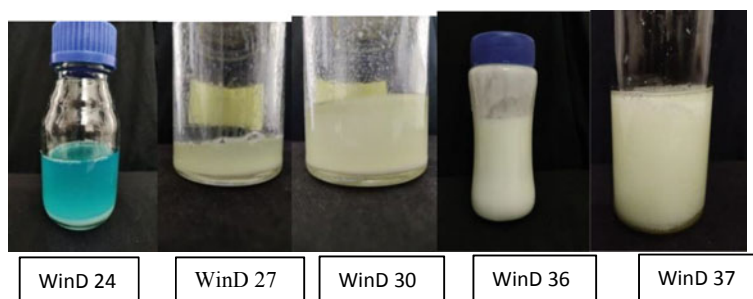
Stability and type of emulsion are dependants on the type of emulsifier and its amount in the emulsions. Types of homogenization which can emulsify the fuels perfectly are also an important factor. The homogenizer power, ambient temperature, and time taken for synthesis play a vital role in the type of emulsion obtained. Hydrophile-lipophile balance characterizes an emulsion. The following are the emulsions synthesized (Table 5).

The synthesized WinD emulsions were stored and examined for 40 days. Few were noticed to sediment due to coalescence leading to an unstable emulsion. But most of them depicted no changes and are stable (Figs. 3 and 4).

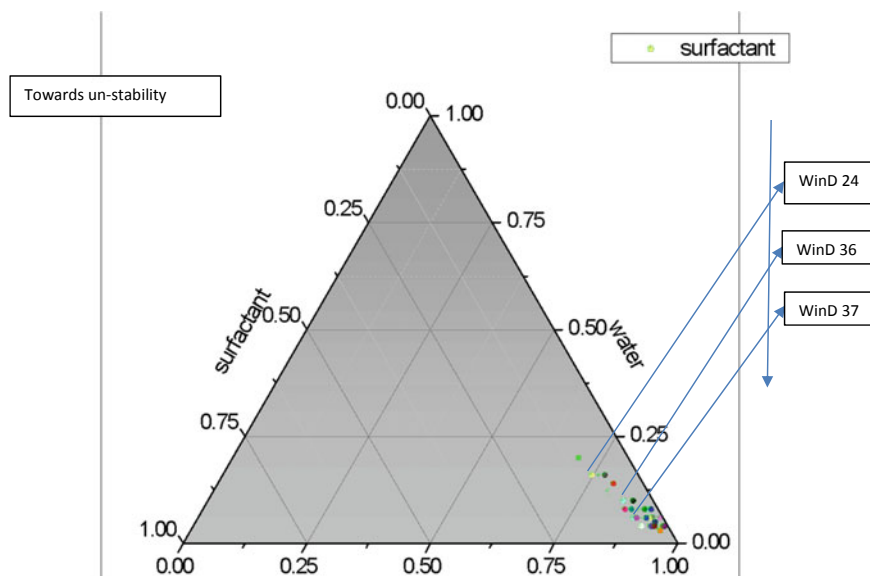
The WinD emulsions were synthesized by mechanical shaking, magnetic stirrer, ultrasonicator. After shaking stirring (900 rpm) and sonication (55 Hz) continuously, the WinD obtained were observed to resemble milky white, translucent, and transparent appearances (Fig. 5).

**Table 5** WinD emulsions synthesized

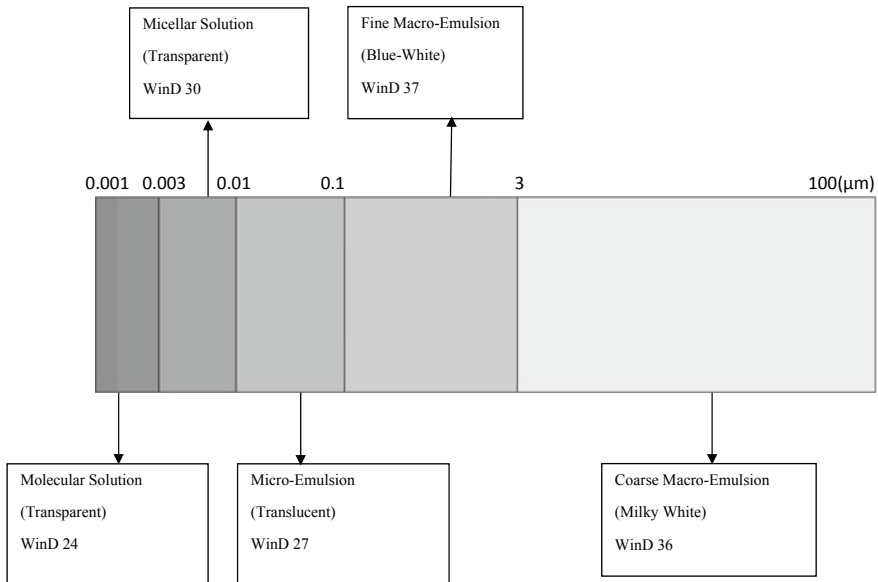
Diesel	Water	Span 80	Brij 30	Code	Method
0.88	0.08	0.04	0	WinD 24	Ultrasonicator
0.92	0.04	0.04	0	WinD 25	Mechanical shaking
0.88	0.08	0.04	0	WinD 26	Magnetic stirrer
0.94	0.04	0.01	0.01	WinD 28	Magnetic stirrer
0.88	0.08	0.02	0.02	WinD 29	Magnetic stirrer
0.76	0.16	0.04	0.04	WinD 36	Magnetic stirrer
0.88	0.06	0.03	0.03	WinD 37	Magnetic stirrer



**Fig. 3** WinD Emulsion



**Fig. 4** Ternary plot of WinD emulsions



**Fig. 5** Scaling of stable emulsion

### 3.2 Density

In the present study, density is observed to increase with water content in comparison with the original fuel. It is due to higher densities of water and surfactants which are added to the diesel of lower density. However, few proportions (WinD 24, WinD 27) have a density similar to the diesel used. This phenomenon is due to the finer homogenization of the emulsions. The decrease in density is due to the destabilization of emulsions (WinD 30, WinD 37) (Fig. 6).

### 3.3 Viscosity

The viscosity of fuels is commonly used in design calculations like an injector, combustion chamber, etc. Viscosity also plays an essential part in an emulsion's stability so that coalescence and de-emulsification do not occur [5–7]. (Fig. 7).

The decrease in kinematic viscosity of the emulsion with water and surfactant content (difference in viscosities) may be due to fine homogenization of emulsion leading to a reduction in viscosity. Further dispersion of molecules uniformly results in the overall effect of improving the rheological behavior of blends. The viscosity of WinD emulsions decreases with an increase in temperature.



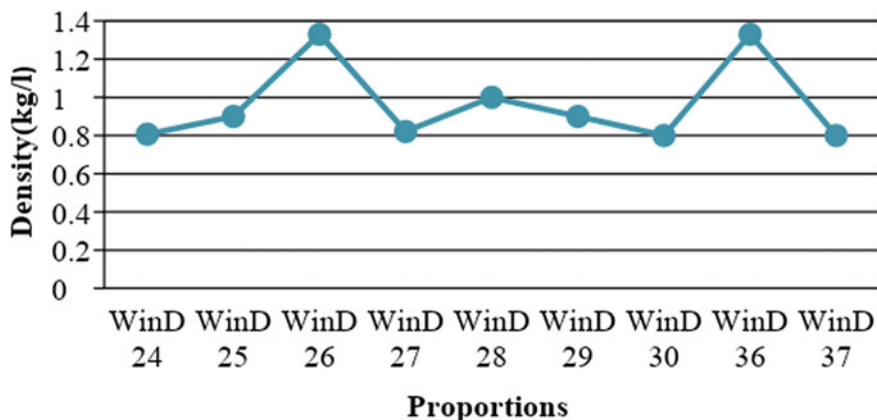


Fig. 6 Variation of density with respect to various proportions

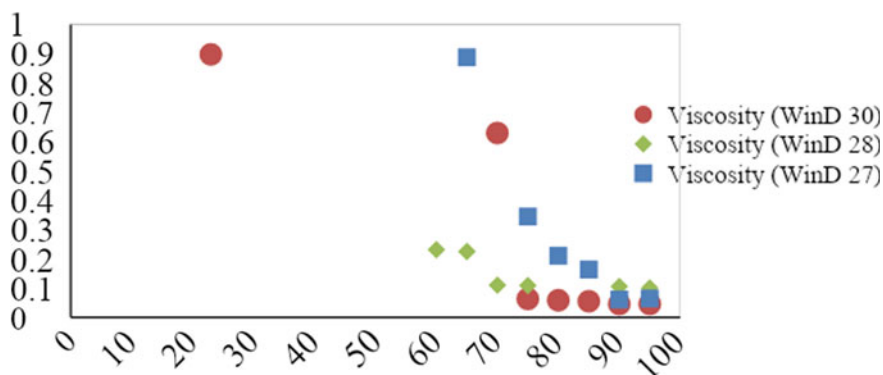


Fig. 7 Variation of the viscosity of WinD emulsions with respect to temperature

### 3.4 Flash and Fire Point

Flash and fire points are estimated to assess the safety hazards of fuel concerning its flammability. The lower the points, the potential for hazards are high (Fig. 8).

The flash and fire point increased when compared to the diesel increases due to the water content. No stabilization additives for flash and fire points are required to add for emulsion. The emulsified fuel has a flash point greater than 60 °C which falls out of hazard combustible fuels. Safety from the flammability of fuel will be achieved by increasing water content, however, high water content reduces heating value.

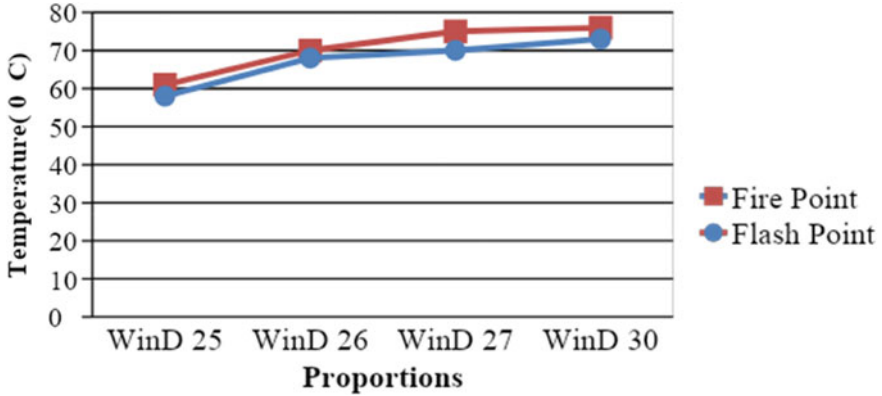


Fig. 8 Variation of flash and fire point with respect to various proportions

### 3.5 Heat of Combustion

Figure 9 depicts the heat of combustion variation with water content. There is a large decrease in heating value in WinD 36 and WinD 26 due to higher water content. The difference in heating value with water content illustrates the influence of this constituent on heat transfer, ignition delay, and better expansion of gases.

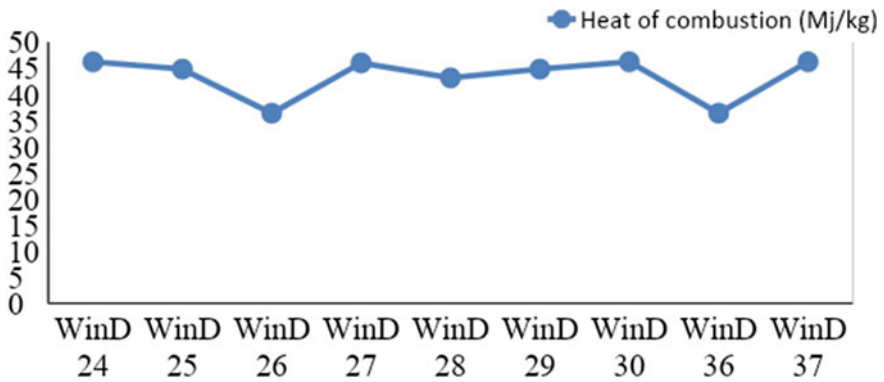


Fig. 9 Variation of the heat of combustion with respect to various proportions

## 4 Conclusion

WinD emulsions of various proportions were synthesized satisfactorily with the use of different homogenizers and are observed to be stable. The physiochemical properties of emulsions were investigated and discussed. The following conclusions were made from the emulsion investigation:

- Density was observed to increase with an increase in water content when compared to the diesel.
- Viscosity decreased due to the difference in viscosities among diesel, water, and surfactants.
- Flash and fire point increased as water is inflammable.
- The heat of combustion decreased slightly due to heat being required for water evaporation and a slight decrease in combustion temperatures.

Further investigations are required for assessing the complete combustion characteristics of WinD emulsions. The WinD emulsions are required to be tested in the engine for spray characteristics emission formations and combustion behavior.

**Acknowledgements** The authors are thankful to Dr. K. Nanda Kumar, Director Research, Hindustan Institute of Technology and Science, and Mr. Thankadurai, Fuel and Lubricants laboratory in charge for their support.

## References

1. Won J et al (2019) The viscosity and combustion characteristics of single-droplet water-diesel emulsion. *Energies* 12(10):1963. <https://doi.org/10.3390/en12101>
2. Sarkar S (1988) *Fuels and combustion*, 2nd edn, Orient Longman, Hyderabad, India
3. Abdul Karim ZA, Yahaya Khan M, Aziz AAR, Tan I (2014) Characterization of water in diesel emulsion. In: MATEC web of conferences, p 13. <https://doi.org/10.1051/mateconf/20141302006>
4. Goodarzi F, Zendejboudi S (2018) A comprehensive review on emulsions and emulsion stability in chemical and energy industries. *Can J Chem Eng* 97(1):281–309. <https://doi.org/10.1002/cjce.23336>
5. Turysbay M, Toncu D (2017) Physico-chemical analysis of alcohol-kerosene blend for alternative jet fuels. *Int J Eng Sci Res Technol* 6(4):464. <https://doi.org/10.5281/zenodo.556365>
6. Gasic S, Jovanovic B, Jovanovic S (2002) The stability of emulsions in the presence of additives. *J Serb Chem Soc* 67. <https://doi.org/10.2298/JSC0201031G>
7. Perdih TS et al (2019) Revision of the mechanisms behind oil-water (O/W) emulsion preparation by ultrasound and cavitation. *Ultrason Sonochem* 51:298–304. <https://doi.org/10.1016/j.ultrasonch.2018.10.003>

# Design of Home Study Furniture for Students of 14–18 Years



Gurmeet Singh and T. Manu

**Abstract** This study was conducted for students of 14–18 years of age and their existing home study furniture to evaluate the ergonomic and usability aspects. Home study furniture has a major impact on students' academic performance and their learning behaviour. The target users were selected from three districts of Kerala—Kollam, Trivandrum and Ernakulum—to study their pain points, concerns and ethnography of their study settings. A huge ergonomic mismatch was found and correlated with the users' attitude towards studies. Further, key insights were drawn to design an ergonomic, highly suitable and effective furniture for the target group in context with their pain points and various academic needs. The final solution of the home study furniture was selected after the concept evaluation matrix and strengths, weaknesses, opportunities and threats (SWOT) analysis of the concepts generated during the ideation phase. Afterwards, the CAD model and prototype of the final solution were made, tested with the prospective users, and their feedback was incorporated into the final product.

**Keywords** Student furniture · Study furniture usability · Desk ergonomics · Kerala anthropometric dimensions · User testing

## 1 Introduction

Proper seating is an important element to ensure a student's relative well-being and efficiency as a learner. There are evidences that improper seating may result in wrong skeletal growth in 11–16 years old children [1, 2]. The right design of study furniture can be crucial to the academics of students, keeping them away from the musculoskeletal and other physiological disorders [3]. Students may be tired from the ergonomic mismatch of school furniture as most of the schools use 'one size fits all' furniture and neither the school authorities nor the parents think on this aspect of students' daily life routine [4, 5]. An average student spends almost 36 h sitting at

---

G. Singh (✉) · T. Manu  
Kerala State Institute of Design (KSID), Kollam, Kerala, India  
e-mail: [gurmeet4design@gmail.com](mailto:gurmeet4design@gmail.com)

school and more than 14 h sitting at home in a week. This is a considerable amount of time and decides the physical and mental wellness of the student [1, 3].

In accordance with the importance of seating, the posture theory has been developed by Max Banfield [6]. Poor posture places the head and shoulders forward of the spine and puts a strain on the spinal joints and muscles, and in the long term causes neck and back pain, arthritis and injuries to the spine. The wrong posture creates pressure on the chest causing problems between the ribs on the lower left and right side [3, 7]. Furthermore, as all pupils have a different character, routines and lifestyle, the home study furniture required need to be adaptable to meet different types of requirements. As the theory of interaction states, individuals select and create their social surroundings, including the physical setting, which is appropriate to their personality, moods and favourite artefacts. People portray their living and working space by decorating it with their preferable elements of favourite colours, patterns, etc. Parents and the pupils take the secondary classes (class 9th onwards) very seriously and assume that those are the years for the right career foundation. Hence, the studies for those years are crucial to having more impact on a student's academic and personal life [8, 9].

By system, most schools and classroom desks make students sit stagnantly. And with time, desks become a second home for students [10, 11]. In 1881, the Sidney School Furniture Company started making the popular "Fashion" school desk. The desk had a patent T-head removing the need for screws and bolts. In 1920, the wooden "Welsh School Desk" was built featuring a double partition top on an iron base. French architect and a prominent furniture designer Jean Prouvé created a tandem school desk in 1946. In 1950, Arne Jacobsen created 'Munkegård' school desk having a hook for school bags [12]. Global furniture maker Steelcase Inc. introduced its 'Node' chair in 2010. This chair had a swivel seat with a large work surface and a base to hold students' things. Arthur Brutter and Ido Bruno made an earthquake-proof desk in 2012 as their final project at the 'Bezalel Academy of Arts and Design' [12]. Some Indian study desks critical to mention are the colonial study desk used by the moneylenders and account keepers, the cardboard desk developed by 'Aarambh' as an aid to assist school students with a bag and the furniture both, a study chair having the note pad attachment and basic storage facility and the officer's table having an inclined small tabletop for writing and reading purposes.

Researches have confirmed that a huge number of learners are using chairs that are either too high or too low for their body dimensions. This makes their feet hanging in the air and escalates back pressure leading to a crunching of the knee area, which imposes bad posture with a compressing of the leg muscles. By retaining classroom work at the appropriate position, more of the page stays in focus at one time and reduces the strain on the eyes [13]. Alongside, while using a sloped work surface, pupils reduce the exhaustion felt during the writing and gain control over the task. A bad sitting can develop many health issues such as aching knees and tightness in the back and shoulders [14]. The education setting comprises of all those physical-sensory components such as lights, colour, sound, space and furniture that portray the place where a pupil is anticipated to study. This setting should be planned to make the learning happen with the least stress and the most effectiveness [11].

The United Nations International Children’s Education Fund (UNICEF) worked on school furniture to pinpoint issues and scopes for design and development of school furniture specifications in 2013. UNICEF hired a design studio for the development of different innovative, ergonomically fit, inexpensive, long-lasting and workable prototypes of classroom furniture. Five categories: size, type, design, technical specifications and materials were considered to identify the needs and scope of design as given in Table 1 [15].

During 2013–2014, the prototypes, as shown in Fig. 1, and guidelines designed under this project were tested for authentication in Malawi (East Africa) by the UNICEF. These products were made using plywood, tubular steel and nut-bolts.

Furniture must reflect the change from teacher-centric to student-centric education and should be versatile enough to meet the changing educational requirements. Students spend nearly 15,000 h deskbound in their school time. Roughly, 13% of teenagers aged 10–16 years have a substantial incidence of repeated back pain. This rises to severe intensities by the age of 16 years and can be accredited to numerous aspects, including bad seats that do not match the children’s anthropometry, and tables having wrong dimensions [16].

**Table 1** Factors considered by the UNICEF to design school furniture

Concerns	Features
Size	Furniture categorization as per the height and age range <ul style="list-style-type: none"> <li>• Small-6–9 year olds</li> <li>• Medium-10–12 year olds</li> <li>• Large-13–17 year olds</li> </ul>
Type	Furniture is fit for various setups—classroom, lecture, exam, individual and group-work <ul style="list-style-type: none"> <li>• Most suitable (single desk and chair)</li> <li>• Most space-efficient in overcrowded contexts (double desks/bench)</li> <li>• Severe overcrowding (triple desks/bench)</li> </ul>
Design	Design considerations should incorporate <ul style="list-style-type: none"> <li>• Structural stability and strength</li> <li>• Adjustability and child-friendliness</li> <li>• Quality, manufacturing simplicity and durability for five years</li> <li>• Weather resistance against extreme temperature, humidity and corrosion</li> <li>• Storage/packing, aesthetics, transport/assembly and cost</li> </ul>
Technical specifications	Furniture should adopt <ul style="list-style-type: none"> <li>• Applicable regional, national and international standards</li> <li>• Warranty and quality assurance</li> <li>• Training, finishing and packaging (should be flat packed)</li> </ul>
Material	Materials should be <ul style="list-style-type: none"> <li>• Locally available and sustainable</li> <li>• Environment friendly</li> <li>• Certified for origin</li> <li>• Cost-effective, durable and recyclable</li> </ul>



Fig. 1 UNICEF’s study furniture prototypes tested in Malawi

## 2 Market Analysis

The competition study and analysis were done to understand the trends in the current market with a focus on the price, form, colour and functionality of the furniture as summarized in Table 2.

After this, the existing good products (selected based on the customer reviews on e-commerce websites) were also studied in particular as summarized in Table 3.

Table 2 Competition analysis of various brands selling study furniture

Aspects	Godrej Interio	Nilkamal	Featherlite	IKEA	Urban Ladder
Price range (INR)	6000–18,000	3000–12,000	6000–16,000	4000–22,000	6000–22,000
Style	Minimal	Minimal	Minimal	Pleasing	Functional
Form	Elegant	Classical	Geometric	Decorative	Elegant
Colour Theme	Cool	Vibrant	Greys	Cool	Cool
USP	Reliable	Lightweight	Looks	Reliable and ease to buy and install	Variety and online buying
Function (primary and secondary)	Sitting-writing and storing	Sitting and writing	Sitting and writing	Sitting-writing and storing	Sitting-writing and storing
Main Material	MDF	Plastics	Particle board	MDF and metals	MDF
Strengths	Brand value	Brand value	Style	Brand value	E-commerce
Weaknesses	No variety and suitable features	No variety and suitable features	No variety and suitable features	Store locations and outreach	Trust issue among new buyers

**Table 3** Different aspects of the analysis of existing study furniture products

Aspects	Fiesta study unit (Godrej)	Perfo study chair (Featherlite)	Arkelstorp desk (IKEA)	Study desk (Nilkamal)	Study desk ( <a href="https://www.amazon.com">amazon.com</a> )
Price (INR)	8000	3000	12,000	9000	12,000
Style	Classic and suede finish	Minimal	Elegant	Multipurpose	Contemporary
Form	Rigid Geometric	Flexible	Pleasing	Rigid geometric	Geometric and flexible
Colour	Jakarta teak	Black	Natural wood	Brown	Stained wood
USP	Lightweight and easy to maintain	Lightweight and easy to maintain	Spacious	Lightweight	Lightweight and dynamic
Function (primary and secondary)	Study and store	Seat and study	Study and store	Study, computer and storage	Study and store
Main material	MDF	Metal	Solid pinewood	MDF	Hardwood
Strengths	Knockdown	Indoor-outdoor use	Knockdown	Compact	With chair
Weaknesses	Straight and rigid	No storage	Price	Short lifecycle	Limited usability

### 3 Research Hypothesis

Based on the literature review and the market study in the previous sections, it was concluded that the ergonomic mismatch is the biggest problem in students' study furniture. Further, the usability, proper features and cost were other issues contributing to this problem. It was found that the students of class 9th–12th need to study more, sitting for hours, as those are the foundation years for their career and life. Based on these findings, it was hypothesized that students of class 9th–12th need ergonomically well-designed study furniture with the price range of rupees 8000–12,000.

## 4 Research Design

### 4.1 Research Methodology

The study was done with a mixed methodology approach. A questionnaire and semi-structured interview were designed based on the literature review and the concluded hypothesis. Respondents were selected conveniently based on the criterion that they



or their children-students use the home study furniture. The field studies were carried out with convenient and judgmental sampling techniques.

### 4.2 Sample Plan for the Study

Students of 14–18 years, who use the home study furniture in any manner, in Trivandrum, Kollam, and Ernakulum districts of Kerala; both boys and girls composed the sample size of this project.

### 4.3 Respondents’ Sample Composition and Size

The following method was considered to calculate the right sample size with a statistical approach:

- Standard deviation (Variability of population characteristics)-*s*
- *Z* value (Level of confidence desired)-taken as 1.64 for 90% confidence level desired
- Degree of precision desired to predict population characteristics-*D*

Following is the equation used to calculate the right sample size (*n*):

$$n = s^2 * Z^2 / D^2 \tag{1}$$

To get a representative and accurate sample size, the results of sample sizes from two settings were compared and the average of both as the final sample size was considered:

- **Setting 1:** A low standard deviation (*s* = 1/2) and a high degree of precision (margin of error, *D*—9%).
- **Setting 2:** A high standard deviation (*s* = 1) and a low degree of precision (margin of error, *D*—16%).

This is summarized in Table 4.

Sample size (average of setting 1 and 2 values) =  $n = n1 + n2/2 = 94$  (rounded off).

**Table 4** Sample size calculation taking different values of *s* and *D* in two settings

Parameters	Setting 1	Setting 2
<i>s</i>	0.5	1
<i>Z</i>	1.64	1.64
<i>D</i>	0.09	0.16
<i>n</i>	83	105

The composition of this sample size was as follows: Students—60, Parents—24, Furniture Sellers—10.

#### ***4.4 Instruments of Data Collection***

The instruments used to collect the data were: Survey questionnaires, semi-structured personal interviews, ethnographic observations and secondary data research. Judgmental and convenience sampling techniques were employed for the study.

### **5 Data Collection and Analysis**

After the collection of the data, the information was analysed to identify themes, problems and triggers related to the scope of the project. Primarily, the analysis was categorized in five groups—activities, environments, interactions, objects and the users. When combined, these five groups form the system which was the prime focus of this study. The analysis was further enhanced with the addition of two more refined groups—pleasure points and the pain points. To complement the analysis holistically, the influencing factors such as the cost, features, materials and trends from the market study were also considered. During the field research, body measurements of the target group students were taken and analysed as presented in Table 8.

The ergonomics, cost and lack of dedicated features were the main issues that emerged in the field study as shown in Fig. 2. The ethnographic observations showed the usability and task management difficulties for the users.

**Design Scopes:** Technology-enabled design, ergonomic design, knockdown design and modular design were considered as the major design directions.

**Problem Statement:** Students have musculoskeletal disorders and are not comfortable, physically and mentally, with the furniture they use for home studies. They needed an ergonomically well-designed and visually appealing set of furniture for their effective home study hours.

**Design Brief:** Design an ergonomic home study furniture for students of 14–18 years, which is flexible to meet their daily academic needs efficiently.

**Constraints:** The target group was from upper- and middle-class Indian families of urban and semi-urban settings. The ideal cost range was rupees 8000–12,000. The furniture could not be bulky and heavy. The ideal life span of the product was 5–6 years without any major maintenance and repair.

**Parameters of Success:** Students should feel comfortable and efficient while using the furniture. The solution should be intuitive and inviting for the student. Durability, mobility and affordability should not be overlooked.

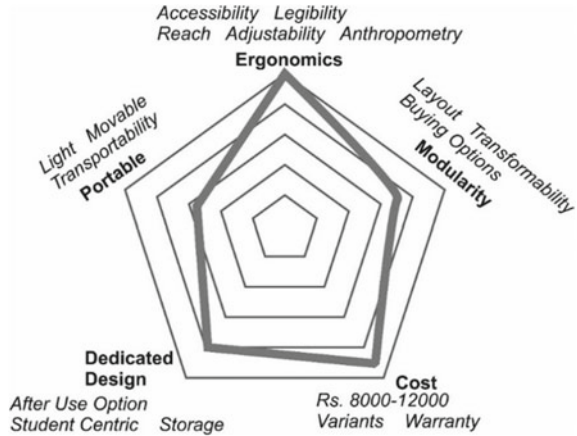
**Table 5** Definitions of various anthropometric dimensions measured during the field study

S. No.	Code	Anthropometric dimensions (mm, kg)	Description
1	TH	Total height	Vertical distance from the crown of the head to the floor
2	ShB	Shoulder breadth	Extreme straight breadth across the shoulders
3	HB	Hip breadth	Extreme horizontal distance across the hips while sitting
4	SiH	Sitting height	Vertical distance from the vertex to the sitting surface
5	EH	Sitting eye height	Vertical distance from the eye level to the sitting surface
6	ShH	Height of shoulder	Vertical distance from the top of the shoulder to the seat
7	EIH	Sitting elbow height	Vertical distance from the underside of the elbow to the seat surface
8	BK	Buttock to front of knee length (sitting)	Horizontal distance from the front of the kneecap to the back of the uncompressed buttock
9	BP	Buttock to popliteal length (sitting)	Horizontal distance at the back of the knee, from the popliteal angle to the back of the uncompressed buttocks
10	KH	Knee height	Vertical distance from the upper surface of the knee to the floor
11	PH	Sitting popliteal height	Vertical distance at the underside of the knee from the popliteal angle to the floor
12	TT	Sitting thigh thickness	The vertical distance from the utmost uncompressed point of thigh to the seat
13	AL	Horizontal reach	Distance from the acromion to the fingertip keeping the elbow and wrist straight
14	BW	Body weight (kg)	Body weight

## 6 Ideation and the Final Concept

A total of 38 concepts were generated as possible solutions for the design brief. Those concepts were discussed with the peers and the faculty. The best three concepts were taken forward for further detailing and development. Then, those concepts were analysed with the concept evaluation matrix (CEM) as given in Table 6 [17] and SWOT analysis as given in Table 7.

**Fig. 2** Scale of thematic issues emerged in the data analysis (centre being zero and the outermost vertices being five)



**Table 6** Concept evaluation matrix showing the concept no. 2 as the most suitable concept

Shortlisted concept no.	Cost	Feasibility	Durability	Effectiveness	Usability	Safety	Maintenance	Total score
1	7	8	8	7	8	9	8	55
2	7	8	8	9	9	8	8	58
3	7	8	8	9	8	8	8	56

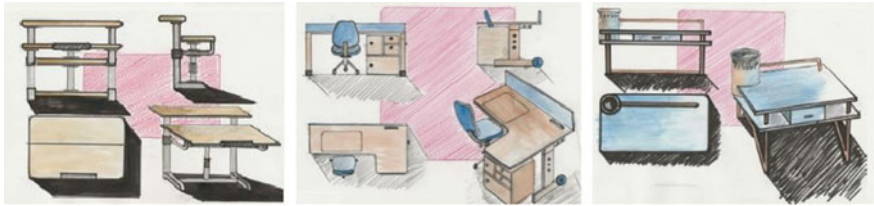
**Table 7** SWOT analysis of the final concept

Aspect	Description
Strengths	Better usability Modern look Aligns with the design brief
Weaknesses	May turn up heavy No footrest
Opportunities	Maybe a good workstation May be customized in variants
Threats	Economic trends may lead to a price hike Improved competitive products or the emergence of new competitors

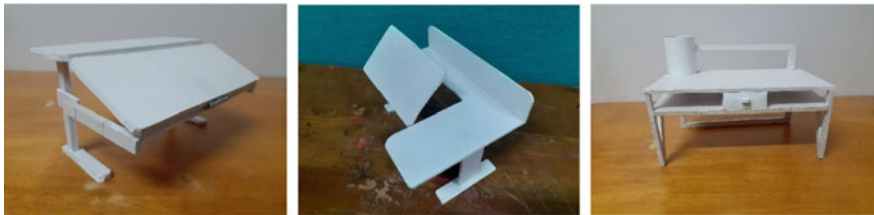
Figures 3 and 4 show the shortlisted concepts and their mock-up models, respectively. Concept number 2 was chosen as the final concept with the CEM and SWOT analysis.

**Table 8** Users' anthropometric dimensions collected and analysed during the study

S. No.	Code	Female anthropometric dimensions (mm, kg)						Male anthropometric dimensions (mm, kg)					
		Max.	Min.	Mean	SD	5th p.	95th p.	Max.	Min.	Mean	SD	5th p.	95th p.
1	TH	1682	1503	1563	1.61	1512	1643	1763	1613	1626	1.14	1632	1741
2	ShB	413	346	392	2.36	356	406	444	363	408	1.88	374	419
3	HB	398	345	368	2.10	357	381	374	323	352	3.79	331	361
4	SiH	468	398	436	1.35	409	452	495	385	462	1.12	389	481
5	EH	701	511	531	2.13	523	687	732	621	548	1.97	631	712
6	ShH	641	503	523	2.10	524	629	646	504	542	2.61	517	625
7	EIH	268	171	193	1.15	189	249	303	193	229	1.09	209	286
8	BK	549	477	501	3.21	493	524	561	491	524	2.32	501	543
9	BP	428	374	401	1.16	382	416	443	392	424	1.17	408	439
10	KH	513	459	483	2.19	461	502	574	514	546	3.43	523	564
11	PH	436	382	416	1.53	395	421	485	422	444	2.16	436	461
12	TT	176	141	147	1.47	152	162	161	121	136	3.21	129	153
13	AL	691	624	657	1.31	631	668	783	692	738	3.56	706	767
14	BW	58	46	52	2.15	48	55	80	49	63	4.17	51	77



**Fig. 3** Shortlisted concepts 1, 2 and 3 taken for further exploration



**Fig. 4** Mock-up models of the shortlisted concepts 1, 2 and 3

## 7 Usability of the Final Product

This final concept is highly fit to the design brief as per the CEM and SWOT analysis as it is ergonomically adjustable and could cover the 90% (5th–95th percentile) population. It is having a dedicated and easily accessible storage, customizable notes and reminders panel, sloped and flat working surface options and easily moving feature with two wheels. The weakness of not having a footrest was removed by iterating the design to add the footrest. The chair was chosen to be without any armrests for free movements and intentional affordance to sit straight and attentive while studying in companion with the table. This solution suits to various writing, reading, drawing and storage needs of the users.

## 8 Ergonomics of the Final Product

Furniture that is intended for use by adults should be designed for approximately 90% of the adult population, i.e., between the 5th (female) and 95th (male) percentile of the population’s physical characteristics [5, 10, 18] (Table 8).

The following aspects were taken into consideration for anthropometric measurements of the users during the field study and the final design of the home study furniture: Standing, sitting, reaching, moving, adjustability, accessibility, arrangement and legibility. The following values were considered for the ergonomic design of this study furniture: the 5th and 95th percentile values for the female and male sitting popliteal height, respectively, 50th percentile value for male shoulder width, 50th percentile value for female shoulder height, the 95th percentile value for the female hip-width and thigh thickness, the 5th percentile value for the female buttock-knee length and horizontal reach. As per the anthropometric data analysis for the 90% (5th–95th percentile) population, the dimensions presented in Tables 9 and 10 were

**Table 9** Study table–chair dimensions

Table		Chair	
Dimensions	Measure (mm)	Dimensions	Measure (mm)
Tabletop height (adjustable)	620–760	Seat height (adjustable)	420–500 (20 mm shoe allowance)
Tabletop length	1100	Seat width	400
Slope surface length	740	Seat depth	410
Slope surface width	400	Backrest height	400
Notes panel width	1100	Backrest width	380
Notes panel height	200	Backrest angle (adjustable)	95–113
Tabletop and notes panel thickness	15		

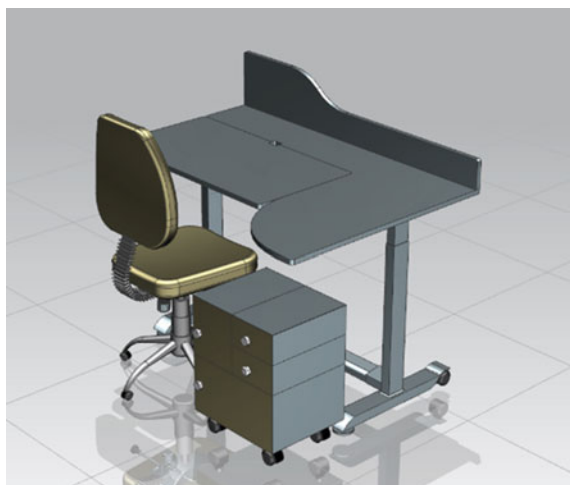
**Table 10** Storage cabinet dimensions

Storage cabinet			
Dimensions	Measure (mm)	Dimensions	Measure (mm)
Ground height	400	Bottom compartment width	356
Width	360	Bottom compartment height	197
Depth	300	Top left compartment width	177
Wheel clearance	80	Top left compartment height	197
Sheet metal thickness	2	All drawer widths	173
All compartment depths	296	All drawer heights	96

chosen for the final product. In the final product dimensions, a 20 mm shoe allowance was also considered.

The selected concept was explored for a better form and appealing aesthetics. The notes and reminders panel and the legs were redrawn and improved. Before starting the final product prototype, a CAD model was made using the Siemens NX CAD modeling software as presented in Fig. 5. Then, the prototype, shown in Fig. 6, was

**Fig. 5** CAD model of the final concept



**Fig. 6** Final concept prototype



fabricated using stainless steel and medium density fibreboard (MDF) as the main materials for the table and stainless steel, iron, foam and rexine for the chair. An 80 N Hettich pneumatic piston was used in the table for the slope surface part.

## 9 User Testing

The prototyped product was tested with 22 users which were respondents of the field study also (Fig. 7).

The users found the product quite comfortable and efficient for their daily academic needs. Initially, 14 users showed their concern about no armrests of the chair, but they found it good as they were using the chair with the table. The storage unit top was suggested to be usable and modified accordingly. The table was tested for reading, writing and drawing activities. The tilt angle of the sloping surface was modified to  $0^{\circ}$ – $45^{\circ}$  with three steps of  $15^{\circ}$  each. A stopper mechanism was also suggested to be attached to the tabletop to prevent the books from falling when in tilted position. Users felt comfortable and worked efficiently while using the furniture. Durability and mobility were tested by sitting, moving and repositioning of the furniture. The total prototyping cost was less than 6000 rupees including the cost of the labour, materials and finishes.





Fig. 7 Final products' ergonomic and usability testing with the users

## 10 Limitations

The anthropometric dimensions used for this design of home study furniture were derived from a small sample size of 60 students from three districts of Kerala. Hence, the design may need ergonomic iterations if employed to other populations in India or abroad and even in other parts of Kerala. For the anthropometric measurements, more accurate and sophisticated instruments may be used for future projects. The stopper mechanism is also needed to be designed and incorporated as identified during the user testing phases. The prototype of the proposed solution is needed to be tested with more users for better optimization.

## 11 Conclusion

The ergonomic mismatch is the biggest problem with existing home study furniture which may lead to negative experiences and attitudes of the learners towards studies [1–3, 7, 14, 16]. Thus, the right ergonomic furniture is highly needed for


such students [19]. The present solution fits the target group's needs and aspirations on both usability and functionality while being highly ergonomic with height adjustability features to support their crucial career deciding period [8, 9]. This solution meets the cost, usability, comfortability and durability aspects as per the design brief. The user testing also confirmed these aspects of the final product.

## References

1. Castellucci HI, Arezes PM, Viviani CA (2010) Mismatch between classroom furniture and anthropometric measures in Chilean schools. *Appl Ergon* 41(4):563–568
2. Sarı Mİ, Şahin İ (2020) Ergonomic analysis based on digital human modelling: adjustable school furniture design for secondary school students. *Politeknik Dergisi* (2020)
3. Obinna FP, Sunday AA, Babatunde O (2020) Ergonomic assessment and health implications of classroom furniture designs in secondary schools: a case study. *Theoret Issues Ergon Sci* 1–15
4. Ergonomic research findings and design guidelines for the learning environment. In: *The handbook of research for educational communications and technology*. <https://members.aect.org/edtech/ed1/36/36-03.html>. Last accessed 10 Aug 2020
5. Gouvali MK, Boudolos K (2006) Match between school furniture dimensions and children's anthropometry. *Appl Ergon* 37(6):765–773
6. The posture theory. <https://www.theposturetheory.com/wp-content/uploads/2013/05/PostureTheoryDiagramGrey-e1367991544540.png>. Last accessed 15 Aug 2020
7. Parcels C, Stommel M, Hubbard RP (1999) Mismatch of classroom furniture and student body dimensions: empirical findings and health implications. *J Adolesc Health* 24(4):265–273
8. Fouad NA, Kim SY, Ghosh A, Chang WH, Figueiredo C (2016) Family influence on career decision making: validation in India and the United States. *J Career Assess* 24(1):197–212
9. Sharma P, Ahuja A (2017) A study on career maturity of Indian adolescents with respect to their educational settings. *Int J Home Sci* 3(1):242–245
10. Parvez MS, Parvin F, Shahriar MM, Kibria G (2018) Design of ergonomically fit classroom furniture for primary schools of Bangladesh. *J Eng* 2018 (Jan)
11. Tunay M, Melemez K (2008) An analysis of biomechanical and anthropometric parameters on classroom furniture design. *Afr J Biotechnol* 7(8)
12. Akanegbu A (2020) A visual history of school desks. <https://edtechmagazine.com/k12/article/2012/10/visual-history-school-desks>. Last accessed 08 Aug 2020
13. Castellucci HI, Arezes PM, Molenbroek JFM, De Bruin R, Viviani C (2017) The influence of school furniture on students' performance and physical responses: results of a systematic review. *Ergonomics* 60(1):93–110
14. Wingrat JK, Exner CE (2005) The impact of school furniture on fourth grade children's on-task and sitting behavior in the classroom: a pilot study. *Work* 25(3):263–272
15. UNICEF: School furniture innovation project: field trial results, pp 3–5. [https://www.unicef.org/supply/files/School\\_Furniture\\_Innovation\\_Project.pdf](https://www.unicef.org/supply/files/School_Furniture_Innovation_Project.pdf). Last accessed 11 Aug 2020
16. Furniture Industry Research Association (FIRA) International: safe seats of learning. <https://www.fira.co.uk/images/safe-seats-of-learning.pdf>. Last accessed 11 Aug 2020
17. Saldana C, Design evaluation methods. Georgia Tech, pp 17–19. [https://2110.me.gatech.edu/sites/default/files/documents/Lecture\\_Slides/me2110\\_spring\\_2019\\_lecture\\_06\\_evaluation.pdf](https://2110.me.gatech.edu/sites/default/files/documents/Lecture_Slides/me2110_spring_2019_lecture_06_evaluation.pdf). Last accessed 11 Aug 2020
18. Lawson S (ed) (2013) *Furniture design: an introduction to development, materials and manufacturing*. Laurence King Publishing, London
19. Colim A, Carneiro P, Costa N, Arezes PM, Sousa N (2019) Ergonomic assessment and workstation design in a furniture manufacturing industry—a case study. In: *Occupational and environmental safety and health*. Springer, pp 409–417

# Mechanical Characteristics of Ethylene Vinyl Acetate Mixed Beeswax Fuel for Hybrid Rockets



Jayapal Sri Nithya Mahottamananda , Dubey Vanchhit Kumar, Abdul Khaleel Afreen, S. Dinesh, Wahab Ashiq, P. N. Kadiresh, and M. Thirumurugan

**Abstract** The hybrid rocket has several advantages than solid and liquid rockets which uses two different states of matter that includes solid fuel burned with gas or liquid oxidizer. Beeswax is bio-derived, eco-friendly hydrocarbon fuel which has similar properties of paraffin wax like higher fuel regression rate (3–4 times) used in hybrid rocket applications. However, beeswax has poor mechanical properties. To increase the mechanical characteristics, ethylene vinyl acetate (EVA) and charcoal are mixed with the beeswax fuel. Five different compositions of beeswax with EVA and charcoal are prepared, and their mechanical properties are evaluated. The measured porosity range of 0.42–0.84% confirms the good quality of prepared fuel sample. The FTIR spectrum confirms the homogeneity of beeswax mixed with EVA and charcoal fuel without any chemical reaction. The ultimate tensile strength rises up to about 8.1% and the elongation increases to 42% for beeswax fuel mixed with 20% EVA. Further, the tensile strength rises to 8.8% and the elongation increases to 13.4% for beeswax-EVA compositions mixed with 2% activated charcoal.

**Keywords** Mechanical properties · Blended beeswax-EVA fuel · EVA and charcoal fuel · FTIR spectrum · Hybrid rocket fuel

## 1 Introduction

The rocket propulsion system researches have concentrated on secure propulsion system which seeks higher reliability, better efficiency, and focusing toward eco-friendly future. Both the solid and liquid rocket propellants are applied in propulsion, each one having its own advantages and limitations [1, 2]. Solid rocket propulsion

---

J. Sri Nithya Mahottamananda (✉) · D. Vanchhit Kumar · A. K. Afreen · S. Dinesh · W. Ashiq · P. N. Kadiresh  
Department of Aerospace Engineering, B.S. Abdur Rahman Crescent Institute of Science and Technology, Chennai 600048, India  
e-mail: [mahottamananda@gmail.com](mailto:mahottamananda@gmail.com)

M. Thirumurugan  
Department of Mechanical Engineering, B.S. Abdur Rahman Crescent Institute of Science and Technology, Chennai 600048, India

system has certain limitations like low specific impulse and zero throttling; also the solid propellant combustion has much more sensitive than other combustion process because the minor cracks/voids present in solid propellant grain may damage the rocket motors. The liquid rocket propulsion systems are more complex than solid propulsion system, and also it is very much difficult to include the solid additives in propellants. To resolve this, hybrid rocket propulsion system has emerged with throttling option, restart capability, easy inclusion of solid additives, and higher specific impulse [3–7]. But hybrid rocket system also suffers with few shortcomings like low regression rate, low combustion efficiency, and low volumetric loading efficiency. Nowadays, the paraffin wax and beeswax are used as a fuel in hybrid rockets. Paraffin wax is derived from petroleum, and the beeswax is naturally obtained from beehive. During burning, paraffin wax produces lot of soot and forms sticky smoke on the walls of burning cylinders. But beeswax produces a less soot and ensures clean burning [8]. As an alternate to paraffin wax, the naturally obtained beeswax is used in our research work. The beeswax is selected because of its matching regression rate value to paraffin wax, natural availability, non-toxic, inexpensive, and easy moldability into fuel grains. So when beeswax is used as a solid fuel in hybrid rockets, it could lower the operating cost and vary stringent safety precautions compared to other rocket propulsion systems. Beeswax has good regression rates of 2–3 times higher than HTPB. Even though the paraffin wax and beeswax have shown higher regression rate, but both suffer with poor mechanical properties and melt flow effects. Because, melt flow effects can reduce the combustion efficiency [9–11]. To increase the mechanical properties, researchers mixed the wax with different materials. DeSain et al. [12] added the low-density polyethylene (LDPE) with paraffin wax to improve its mechanical properties. The elongation increased to 50% and tensile strength increased to 100% after the addition of 4% LDPE with paraffin wax. Maruyama et al. [13] studied blended paraffin wax with EVA (ethylene vinyl acetate) fuel. With paraffin wax, 20% EVA was added [13] and found that the tensile stress and percentage of strain increased to 60% and 100%, respectively. From the results, it is found that even with enhancement in tensile strength and percentage of elongation, the absolute values were below the desired range of values. To improve the mechanical properties of paraffin wax, HTPB was blended [14]. The solid fuel has required mechanical properties that need to be explored. Beeswax and EVA are promising candidate to satisfy the mission requirements.

Present work, an attempt is made to enhance the mechanical properties of beeswax by blending EVA and charcoal. EVA is a co-polymer extensively used with wax to modify the wax crystals [15]. The addition of EVA changes the wax crystal size, viscosity, and pour point depression [16–18]. The charcoal is a black carbon which is lighter in weight compared to other elements in hybrid rocket fuel and enhances the mechanical properties and burning efficiency. In this study, five different compositions of beeswax mixed with EVA and charcoal are prepared, and their mechanical properties are evaluated.

**Table 1** Five different compositions of beeswax solid fuels

S. No.	Sample name	Beeswax (wt%)	EVA (wt%)	Activated charcoal (wt%)
1	Sample 1 (BW)	100	0	0
2	Sample 2 (BW10EVA)	90	10	0
3	Sample 3 (BW20EVA)	80	20	0
4	Sample 4 (BW10EVA1C)	90	10	1
5	Sample 5 (BW20EVA2C)	80	20	2

## 2 Materials and Methodology

### 2.1 Solid Fuel Sample Preparation

Five different fuel compositions of beeswax mixed EVA and charcoal were prepared. Pure beeswax was taken as a baseline (100% beeswax), and the beeswax was mixed with EVA and activated charcoal in different weight ratios. The detailed compositions of solid fuel are given in Table 1. Beeswax was hammered into small chunks and heated in the bowl to the melting temperature of 64 °C. The EVA and charcoal were added into the molten beeswax as per the proportions and the temperature was raised to 100 °C, further the mixture was stirred for 30 min to obtain uniform mixture of beeswax, EVA, and charcoal. Then, the molten uniform mixture was poured into dog bone shape aluminum die and kept in the vertical position for 4 h in open air to get it solidified. After solidification, the beeswax sample was carefully removed out from the die. The macrostructure of prepared fuel samples is shown in Fig. 1.

### 2.2 Quality and Microscopic Analysis of Prepared Fuel Sample

The porosity of prepared fuel samples were calculated by density measurement. Using Archimedes principle and a gravimetric method, the prepared solid fuel sample density was measured. Solid fuel sample density was estimated theoretically by additive rule of mixture. The difference between measured and theoretical density gives the porosity of prepared fuel sample. To study the surface morphology of fuel samples, scanning electron microscopic analysis was conducted using JEOL Model JSM-6390LV. Surface morphology was investigated under a 5 kV beam, to understand the mixing of beeswax and EVA.

**Fig. 1** Dog bone shape solid fuel samples (BW10EVA)



### ***2.3 Chemical Composition of Prepared Fuel Sample***

To find out the chemical composition of prepared solid fuel samples, Fourier transform infrared spectroscopy (FTIR) studies were conducted using FTIR-JASCO 6390. From the FTIR results, chemical reactions during the mixing and curing process can be found.

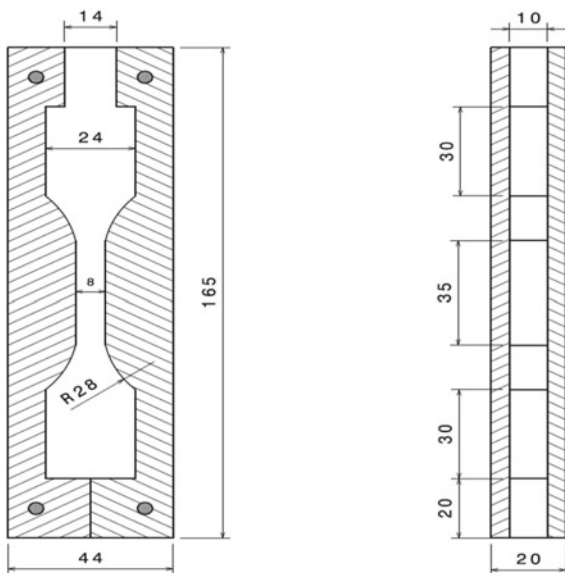
### ***2.4 Prepared Fuel Sample Mechanical Properties***

To find out mechanical properties of prepared fuel samples, the tensile test was done using the Instron UTM machine of 9000 series as shown in Fig. 2. The mechanical properties were such as tensile strength, maximum stress, strain, and Young's modulus. Each fuel composition three specimen were prepared and tested the mechanical properties. The size and shape of the fuel specimen was prepared as per ASTM standard D412. Figure 3 shows the die prepared as per the ASTM standard D412. The solid fuel test specimen was fixed in the specimen holder. The specimen holder has wedge grips to hold the specimen tightly. The specimen holder's one side was attached with a screw and an electric motor. This facility enables to move up and down and used to select the speed required by user. The other side of the specimen holder was fixed permanently.

**Fig. 2** Universal testing machine—9000 series



**Fig. 3** Dog gone shape die—ASTM standard D412





**Table 2** Density variations of beeswax-EVA based solid fuel compositions

Sample name	Experimental density (kg/m <sup>3</sup> )	Theoretical density (kg/m <sup>3</sup> )	Porosity (%)
Sample 1 (BW)	955	960	0.52
Sample 2 (BW10EVA)	950	958	0.84
Sample 3 (BW20EVA)	949	956	0.73
Sample 4 (BW10EVA1C)	948	953	0.52
Sample 5 (BW20EVA2C)	944	948	0.42

### 3 Results and Discussion

#### 3.1 Density of Prepared Fuel Sample

The density measurements were made for blended beeswax-EVA-charcoal-based solid fuel. All five compositions density was calculated, and results were summarized in Table 2. The experimental density was measured using buoyancy techniques of Archimedes' principle. There is not much difference in density values between the experimental and theoretical. The differences in values refer the porosity of the prepared samples. The porosity value decides the quality of prepared sample. Lower porosity range of 0.42–0.84% is observed for all five different compositions of fuel samples. The lower porosity values depict the good quality blending of beeswax, EVA, and charcoal. Porosity present in the fuel samples may not influence the regression rate, but lower porosity leads to low volumetric loading of fuel in hybrid rocket motor.

#### 3.2 Surface Morphology of Blended Beeswax-EVA Solid Fuel Compositions

Figure 4 shows the SEM images of different beeswax/EVA/charcoal compositions. To understand the mixing behavior of different beeswax/EVA/charcoal compositions, SEM images are analyzed. Figure 4 illustrates the most important features revealed by microscopic analysis. BW sample details that the edges are homogeneous and appear with micro voids in random places. BW10EVA sample shows relatively uniform composition and a homogeneous mixture throughout the sample. The formation of flake-like structure seen in this composition confirms the presence of EVA. Compositions with the addition of charcoal refine the grain structures and appear as small particles in the samples of BW10EVA1C and BW20EVA2C.



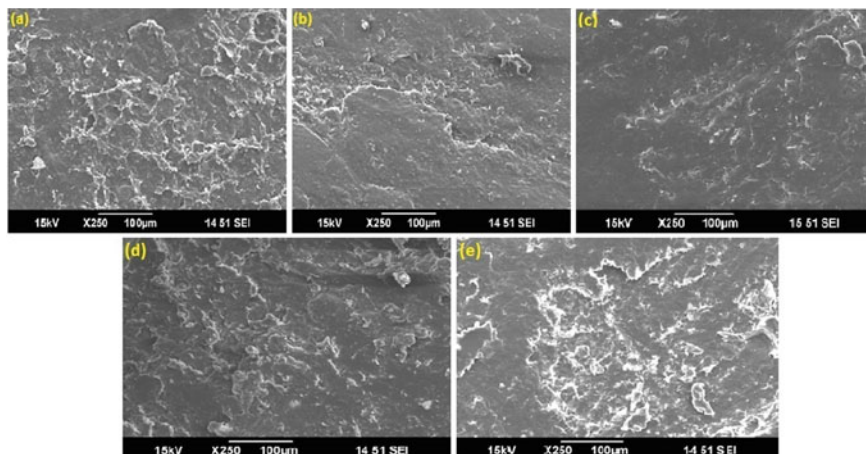


Fig. 4 SEM images of different solid fuel compositions a BW b BW10EVA c BW20EVA d BW10EVA1C e BW20EVA2C

### 3.3 Chemical Composition of Blended Beeswax-EVA Solid Fuel Compositions

The FTIR spectra of all samples are presented in Fig. 5. The absorption wave numbers  $2914.88\text{ cm}^{-1}$  and  $2848.35\text{ cm}^{-1}$  correspond to  $-\text{CH}_3$  and  $-\text{CH}_2$  groups [19]. The wave numbers  $1464.67\text{ cm}^{-1}$  and  $1375\text{ cm}^{-1}$  correspond to the methylene and methyl

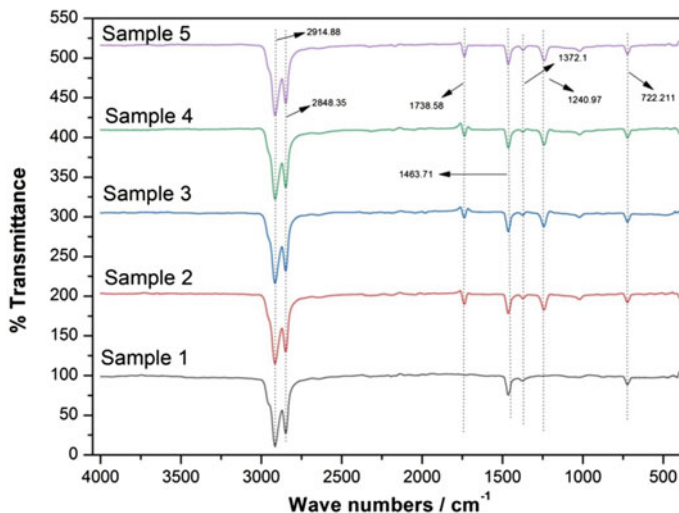


Fig. 5 FTIR spectra of blended beeswax-EVA solid fuel compositions

C–H asymmetrical/symmetrical bend, respectively [20]. The wave number  $722\text{ cm}^{-1}$  corresponds to the methylene  $\text{-(CH}_2\text{)}_n\text{-}$ ; where  $n \geq 3$ ) aliphatic chain rocking. The wave numbers 2914.88, 2848.35, 1463.67, and  $722.211\text{ cm}^{-1}$  are collectively confirm the presence of beeswax [21, 22].

In all samples, the absorption wave number  $1737.55\text{ cm}^{-1}$  corresponds to the ester of cerotic acid, which is a major component of beeswax and thus confirms the presence of beeswax. The wave numbers 1242.9 and  $1022.09\text{ cm}^{-1}$  correspond to the unit absorbance of the vinyl acetate and thus confirming the presence of EVA. These results are collectively confirming the presence of beeswax and EVA physically without any chemical reaction. In the samples BW20EVA and BW18EVA2C, the wave numbers 3656.37 and  $3617.8\text{ cm}^{-1}$  correspond to the presence of non-hydrogen bonded alcohol (OH group) or free OH group either on the surface, or embedded within a crystal lattice and free from interactions with other ions or groups. This is observed only in the samples with 20% EVA. The OH group presence is also indicative of the triacontanol which is a constituent of the beeswax. Similar type of study was done for blended HTPB-paraffin based fuel [23].

### 3.4 Mechanical Properties of Blended Beeswax and EVA Solid Fuels

As per the ASTM standards, five different beeswax compositions were prepared and conducted experiments using UTM machine of 9000 series. From experimental results, the tensile strength and percentage of elongation are measured. To get accuracy of measured mechanical properties, three fuel samples were prepared and tested for each fuel composition, and the stress versus strain values is recorded. The strain rate applied on the fuel specimen is 5 mm/min. Figure 6 represents the tensile behavior of 100% pure beeswax at room temperature. It is observed that stress increases linearly with strain up to maximum stress due to elastic modulus, and then, elongation due to plastic deformation finally reaches to failure. The values maximum stress, strain, and Young's modulus of beeswax samples are given in Table 3. It is observed from beeswax sample that the maximum stress of the samples was  $100 \pm 5\%$  ( $\text{N/m}^2$ ), and the maximum strain was  $0.0231 \pm 5\%$ . The average Young's modulus for pure beeswax was  $42.81 \pm 5\%$ .

Beeswax has poor mechanical properties, and to improve its properties, the additives are added to beeswax. EVA and activated charcoal are selected as additives. EVA is added to beeswax to improve the mechanical properties, whereas activated charcoal is added to beeswax to improve its mechanical and thermal properties. More amount of activated charcoal addition to the beeswax increases the brittleness of material. Figure 7 shows the stress–strain of five different beeswax compositions with addition of EVA and activated charcoal. The BW sample was having tensile strength of  $93.960 \times 10^4\text{ N/m}^2$ , whereas the BW20EVA sample had higher tensile strength of  $101.563 \times 10^4\text{ N/m}^2$ . It is confirmed that when the EVA added to the

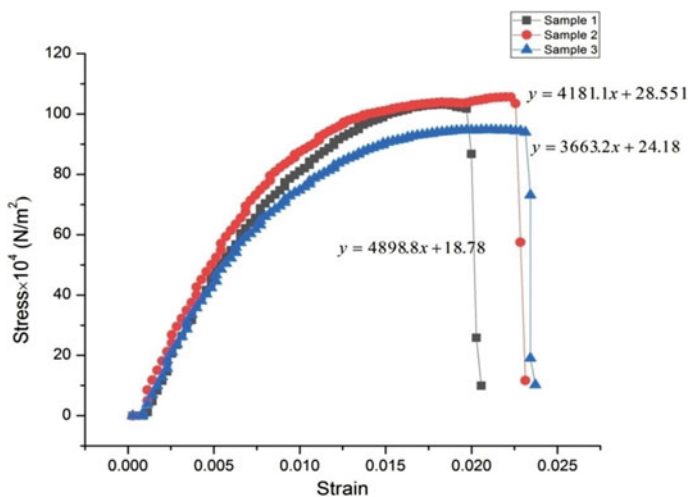


Fig. 6 Stress versus strain curve for pure beeswax sample

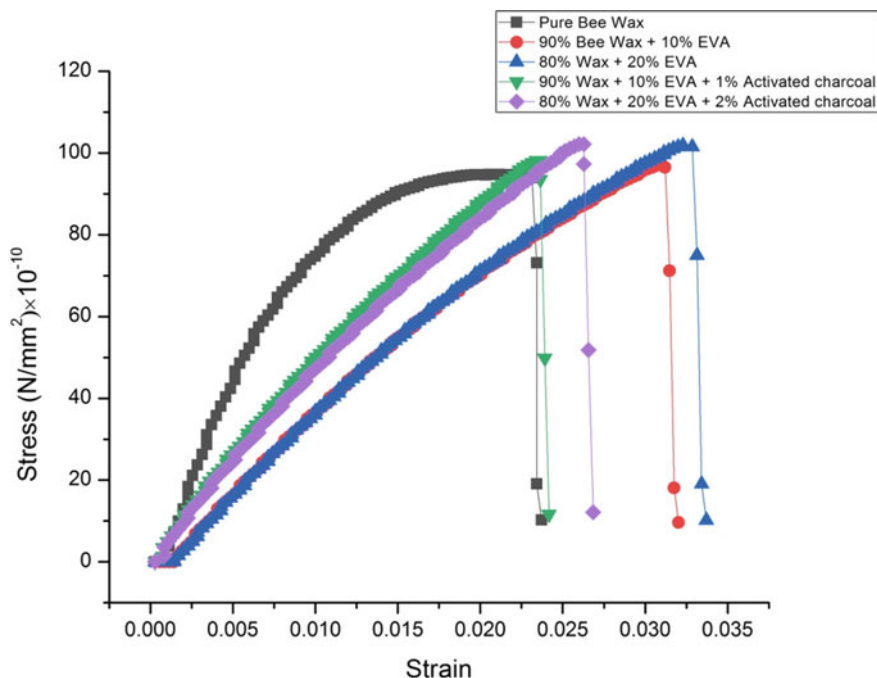
Table 3 Max stress, maximum strain, and Young’s modulus for pure beeswax

Pure beeswax specimen	Max. stress × 10 <sup>4</sup> N/m <sup>2</sup>	Maximum strain	Young’s modulus (MPa)
1	101.784	0.0197	48.98
2	103.525	0.0225	41.81
3	93.960	0.0231	36.63

beeswax, tensile strength is increased to maximum of 8.1%. Strain of beeswax is 0.0231 and BW20EVA sample having increased strain of 0.03285. It is observed that when the EVA was added, the percentage of elongation had increased in the range of 35–42%. It is observed when the EVA was added, Young’s modulus had decreased in the range of 15.21–15.23%.

### 3.5 Effect of Addition of Activated Charcoal with Blended Beeswax-EVA

Table 4 shows the effect of addition of activated charcoal with blended beeswax/EVA/charcoal on mechanical properties. For BW10EVA1C sample, tensile strength is increased 1.8%, percentage of elongation is decreased by 24.4%, and Young’s modulus is increased by 28.1% compared to BW10EVA results. It is also observed that tensile strength of BW20EVA2C sample is increased by 0.62%,



**Fig. 7** Stress versus strain curve for five different solid fuel compositions

**Table 4** Ultimate stress, maximum strain (percentage elongation), and Young's modulus for different fuel compositions

Sample	Max. stress $\times 10^4$ N/m <sup>2</sup>	Maximum strain	Young's modulus (MPa)
BW	93.960	0.0231	36.6 $\pm$ 5%
BW10EVA	96.485	0.0312	31.06 $\pm$ 5%
BW20EVA	101.563	0.03285	31.05 $\pm$ 5%
BW9EVA1C	98.203	0.0236	39.78 $\pm$ 5%
BW18EVA2C	102.188	0.0262	37.25 $\pm$ 5%

percentage of elongation is decreased to 20.2%, and Young's modulus is increased to 20% compared to BW20EVA composition.

## 4 Conclusion

In this study, beeswax-mixed EVA and charcoal solid fuel density, porosity level, chemical composition, surface morphology, percentage of elongation, tensile strength, and Young's modulus were evaluated experimentally.

- From the FTIR results, it is found that no chemical reaction occurred during mixing and curing process. SEM analysis also proved that the beeswax and EVA are mixed homogeneously, and the level of porosity obtained confirmed the good quality of prepared solid fuel samples.
- 80% beeswax+ 20% EVA fuel sample shown increased tensile strength, percentage of elongation and decreased Young's modulus than 100% pure beeswax and 90% beeswax+ 10% EVA fuel samples.
- 90% beeswax+ 10% EVA with 1% activated charcoal sample shown increased tensile strength and Young's modulus and decreased percentage of elongation than 90% beeswax+ 10% EVA sample.
- 80% beeswax+ 20% EVA with 2% activated charcoal sample shown increased tensile strength and Young's modulus and decreased percentage of elongation than 80% beeswax+ 20% EVA sample.
- 80% beeswax+ 20% EVA with 2% activated charcoal sample is best suited based on their good mechanical properties. So it could be a potent candidate for the future hybrid rocket application.

## References

1. Sutton GP, Biblarz O (2016) Rocket propulsion elements. Wiley
2. Altman D, Hybrid rocket development history. In: 27th joint propulsion conference. American Institute of Aeronautics and Astronautics
3. Mahottamananda SN, Joshi PC (2016) Combustion study of HTPB–sugar hybrid fuel with gaseous oxygen. *J Therm Anal Calorim* 123:1927–1934. <https://doi.org/10.1007/s10973-015-4608-y>
4. George P, Krishnan S, Varkey PM, Ravindran M, Ramachandran L (2001) Fuel regression rate in hydroxyl-terminated-polybutadiene/gaseous-oxygen hybrid rocket motors. *J Propul Power* 17:35–42
5. Chiaverini MJ, Serin N, Johnson DK, Lu Y-C, Kuo KK, Risha GA (2000) Regression rate behavior of hybrid rocket solid fuels. *J Propul Power* 16:125–132
6. Mahottamananda SN, Kadiresh NP, Pal Y, Regression rate characterization of HTPB-paraffin based solid fuels for hybrid rocket. *Propellants Explos Pyrotech*. <https://doi.org/10.1002/prop.202000051>
7. Mahottamananda SN, Rafnaz M, Kadiresh PN, Spray characteristics of plug type swirl injector. In: 2018 advances in science and engineering technology international conferences (ASET). IEEE, pp 1–6
8. Tarmizi Ahmad M, Abidin R, Taha AL, Anudip, Amzaryi (1930) Feasibility study of palm-based fuels for hybrid rocket motor applications. In: AIP conference proceedings, vol 1, 2 Feb 2018, p 020010
9. Karabeyoglu A, Ziliac G, Cantwell BJ, DeZilwa S, Castellucci P (2004) Scale-up tests of high regression rate paraffin-based hybrid rocket fuels. *J Propul Power* 20:1037–1045
10. Ziliac G, Karabeyoglu M, Hybrid rocket fuel regression rate data and modeling. In: 42nd AIAA/ASME/SAE/ASEE joint propulsion conference and exhibit. American Institute of Aeronautics and Astronautics
11. Lee T-S, Tsai H-L (2008) Combustion characteristics of a paraffin-based fuel hybrid rocket. In: 9th Asia-Pacific international symposium on combustion and energy utilization, pp 2–6

12. DeSain J, Brady B, Metzler K, Curtiss T, Albright T (2019) Tensile tests of paraffin wax for hybrid rocket fuel grains. In: 45th AIAA/ASME/SAE/ASEE joint propulsion conference and exhibit. American Institute of Aeronautics and Astronautics. Accessed 4 Sept 2019
13. Maruyama S, Ishiguro T, Shinohara K, Nakagawa I, Study on mechanical characteristics of paraffin-based fuel. In: 47th AIAA/ASME/SAE/ASEE joint propulsion conference and exhibit. American Institute of Aeronautics and Astronautics
14. Mahottamananda SN, Kadiresh PN (2020) Mechanical characteristics of paraffin wax-HTPB based hybrid rocket fuel lecture notes in mechanical engineering. Springer, Singapore. [https://doi.org/10.1007/978-981-15-4756-0\\_9](https://doi.org/10.1007/978-981-15-4756-0_9)
15. Kumar R, Ramakrishna PA (2016) Studies on EVA-based wax fuel for launch vehicle applications. *Propellants Explos Pyrotech* 41:295–303
16. Ashbaugh HS, Guo X, Schwahn D, Prud'homme RK, Richter D, Fetters LJ (2005) Interaction of paraffin wax gels with ethylene/vinyl acetate co-polymers. *Energy Fuels* 19, 138–144
17. Farazmand S, Ehsani MR, Shadman MM, Ahmadi S, Veisi S, Abdi E (2016) The effects of additives on the reduction of the pour point of diesel fuel and fuel oil. *Pet Sci Technol* 34:1542–1549
18. Wei B (2015) Recent advances on mitigating wax problem using polymeric wax crystal modifier. *J Petrol Explor Prod Technol* 5:391–401
19. Sari A, Alkan C, Bilgin C (2014) Micro/nano encapsulation of some paraffin eutectic mixtures with poly(methyl methacrylate) shell: preparation, characterization and latent heat thermal energy storage properties. *Appl Energy* 136:217–227
20. You M, Wang X, Zhang X, Zhang L, Wang J (2011) Microencapsulated n-Octa decane with styrene-divinyl benzene co-polymer shells. *J Polym Res* 18:49–58
21. Lv X, Zha M, Ma Z, Zhao F, Xu S, Xu H (2017) Fabrication, characterization, and combustion performance of Al/HTPB composite particles. *Combust Sci Technol* 189:312–321
22. Varol M, Atımtay AT, Bay B, Olgun H (2010) Investigation of co-combustion characteristics of low quality lignite coals and biomass with thermo gravimetric analysis. *Thermochim Acta* 510:195–201
23. Mahottamananda SN, Kadiresh PN, Pal Y (2020) A study on thermal stability and combustion performance of hydroxyl-terminated polybutadiene-paraffin blended fuel. *Energy Sources, Part A: Recovery, Utilization, and Environ Effect*. <https://doi.org/10.1080/15567036.2020.1815902>

# Safety-Enhanced Driver Condition Monitoring System for Preventing Road Accidents in Automobile



C. Dineshkumar, P. D. Jeyakumar, B. Mohamed Asarudeen,  
G. Mohamed Uvaize, and A. K. Ahamed Kabeer

**Abstract** In present day, most of the automobile manufacturers depend on active safety systems to prevent collisions because collisions and accidents increase day by day in automobiles. Research statistics reported that 20% of collision occurs due to driver's fault in the event of driving. It also points out that the causes of fatality rate in vehicles are not only due to fault of the vehicles. The causes of accidents are mainly due to drivers faults in automobile such as health-related issues which are the foremost reason for the accidents. In this study, the proposed system is used to analyze the condition of the driver in the event of health issues while driving tends to warn the driver. The sensor is mounted in the steering wheel for sensing the pulse of the driver during driving. The driver positioning of hands or palm in steering wheel is sensed by the pulse sensor fitted on steering wheel and at the time of abnormality in driver's pulse rate. The sensor alerts the driver and co-passenger by displaying warning signal in dashboard. The research is carried out especially for the taxi drivers prolong time and for the low-cost vehicles to prevent the fatality rate, injury and damage to the vehicle.

**Keywords** Steering wheel · Pulse sensor · Positioning of hands · Collision

## 1 Introduction

The National Highway Traffic Safety Administration estimates that approximately 100,000 crashes occur every year due to physical illness. The main reason for crashes in highway roads is mostly due to the drowsiness of the drivers during driving. Drivers are continuously driving without enough sleep which leads to stress while traveling. So this not only affects the drivers but also the environment [1]. It is dangerous to both

---

C. Dineshkumar (✉) · B. Mohamed Asarudeen · G. Mohamed Uvaize · A. K. Ahamed Kabeer  
Department of Automobile Engineering, B.S. Abdur Rahman Crescent Institute of Science and  
Technology, Chennai, Tamil Nadu, India  
e-mail: [contactdinesh90@gmail.com](mailto:contactdinesh90@gmail.com)

P. D. Jeyakumar  
Department of Mechanical Engineering, B.S. Abdur Rahman Crescent Institute of Science and  
Technology, Chennai, Tamil Nadu, India

© The Author(s), under exclusive license to Springer Nature Singapore Pte Ltd. 2021  
L. Ganippa et al. (eds.), *Advances in Design and Thermal Systems*, Lecture Notes  
in Mechanical Engineering, [https://doi.org/10.1007/978-981-33-6428-8\\_32](https://doi.org/10.1007/978-981-33-6428-8_32)

401

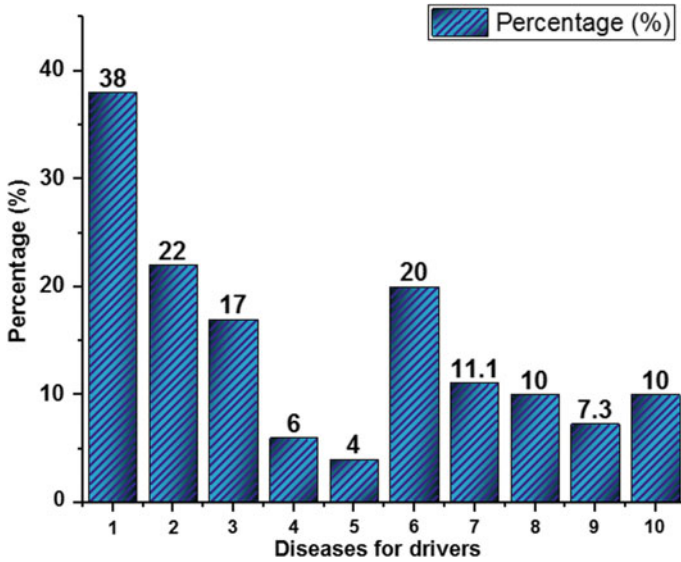
**Table 1** Factors responsible for road accidents (4)

S. No.	Diseases for drivers	Percentage (%)
1	Hypertension	38
2	Hyperlipidemia	22
3	Diabetes	17
4	Heart disease	6
5	Gastrointestinal ulcer	4
6	Fatigue	20
7	Respiratory issues	11.1
8	Anxiety	10
9	Headaches	7.3
10	Others	10

drivers and passengers. Accidents due to drowsiness or physical illness of drivers are very high in past decade. An efficient safety measures is required to mitigate the impact of accidents. Implementation of heart-rate sensor on the steering wheel for detecting the pulse rate of driver alerts the rescue team about the driver's drowsiness. According to World Health Organization (WHO) report, 35+ age is the starting age of heart diseases and attacks. Unfortunately, in India, half of the vehicle drivers are above 35 years. Therefore, design of health emergency system for drivers, by fitting the heart-rate sensor, helps in monitoring the driver pulse which is useful for finding the condition of driver in any abnormal situation. The health emergency system takes over the control of vehicle control and stops the vehicle on road side and also contacts the nearby hospital with the help of GPS [2]. Drowsiness, consuming alcohol during driving and physical illness lead to accidents. Driver's drowsiness contributes to 20% of the accidents. Advanced technology offers some hope in avoiding these up to some extent. This study involves measuring and controlling of the eye blink using IR sensor [3].

Table 1 and Fig. 1 show the diagnosed diseases for the drivers. Major causes of prevalent health conditions among the drivers are listed: fatigue or tiredness, respiratory illness and psychological factors such as anxiety and headaches or panic, heart attack, hypertension, hyperlipidemia and heart disease. The causes of health issues and list of factors that lead to collision are listed in Table 2 given by the Department of Legal Medicine, Japan. The hypertension plays major role of 38% of health issues in drivers and 22% of hyperlipidemia; second major role of 22% is the health -related motor vehicle collisions. Seventeen percentage of diabetes drivers are diagnosed. The heart-related diseases play a dominate role which depends on health condition, and some of the country heart diseases plays a vital role by increasing the percentage of fatality in the case of heart-related diseases. Sudden cardiac death while driving is often seen in the motor vehicle crashes. Working stress is also a serious health problem in taxi drivers as well 10% of due to fatigue or tiredness, 7.3% of drivers are diagnosed by headaches, 11.1% are due to respiratory issues which are significantly caused by prolong driving; 11% of diseases in drivers are





**Fig. 1** Diagnosed diseases for the drivers

**Table 2** Effect of measured heart rate on accurate heart rate

Age group	Actual rate ECG (BPM)	Measured rate (calculated) (BPM)	Error rate
35	76	77	0.013
36	75	77	0.026
37	75	74	0.013
38	82	83	0.012
39	83	84	0.012
40	86	87	0.011

diagnosed. The unknown cases are 10% which is equal to the anxiety as well 4% of ulcer is diagnosed. Therefore, the above issues play a major role in health-related issues [4].

The process covers list of factors that influence the driver’s performance, experience or skill, ability of driving, stress or mental disorder, psychological factors, heart disease. The automatic messaging during heart attack is passed to nearby hospitals, and monitoring system is used even though the collisions occur due to uncontrolled of vehicle. Heart beat detector is a device to detect the pulse of the driver to monitor the beats fluctuation and the information easily displayed or tracked the health condition.

## 2 Methodology

The intelligent system is used not only to reduce driver injury but it also saves the life of the drivers from demise while driving. The existing systems have many sub-systems to reduce the speed of vehicle but not enough to prevent injury during health issues in normal Indian vehicles. The proposed research is made up of pulse monitoring that senses the heartbeat of the driver. The proposed system is tested and analyzed by the age group in static and trail method. One of the main physiological signs of drowsiness is a lowered pulse heart rate. A heart-rate sensor is implemented in the steering wheel of passenger vehicle; it will constantly monitor the drivers pulse as long as his hand is on the steering wheel. This will help the driver to be aware of any problem arising while driving. The heart-rate sensor is implemented in multiple parts of the steering wheel; the use of this is to read the pulse of the driver. The sensor is connected to the car’s system via programming; once a problem is detected, it alerts the driver. Using functions in the programming, the system identifies the driver’s pulse rate via the driver’s finger placed on the steering wheel. Once the engine is ON, the sensor gets ON and starts monitoring the driver pulse and save that data to cloud. If there is any abnormal pulse rate monitored by the sensor, first the system will confirm the abnormal situation by giving some task to the driver to test the consciousness of the driver for 5 s by asking the driver to press some random button from the system. If the driver does not respond to the comments properly, then the system of emergency alert, i.e., emergency alarm stat.

The steering wheel is considered as wall clock. The “4 and 8” and “3 and 9” positions of hand on steering wheel are the two major used positions. The survey had been taken for analyzing the position for the age group and shown in Fig. 2 for present-day comfort to the drivers. The result shows that the survey abides with the NHTSA for the proposed system. These different hand positions refer to visualizing the steering wheel as the clock face and positioning the left hand at 9 or 8 and the right hand at the 3 or 4 o’clock position. Today, the National Highway Traffic Safety Administration recommends drivers to place their hands at the 3 and 9 o’clock positions [5, 6].

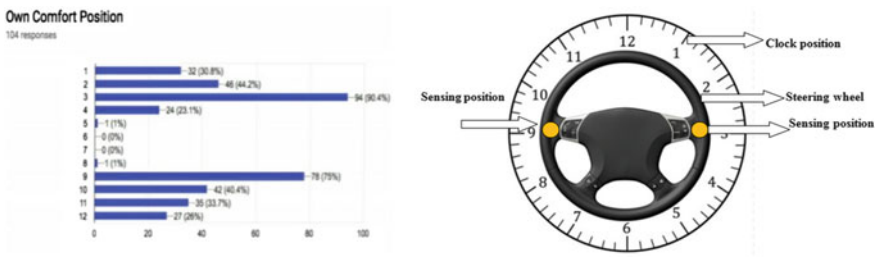


Fig. 2 Comfort position and sensor position in steering wheel

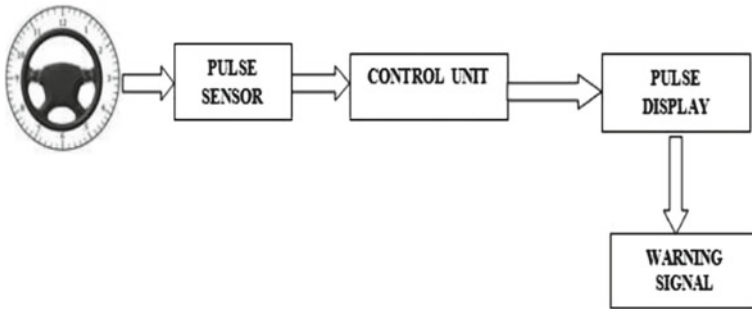


Fig. 3 Block diagram of proposed system

### 2.1 Control System

The layout of proposed system is shown in Fig. 3. The sensor is placed in the steering of a car. The sensor has two sides; one end of the sensor is connected to the steering wheel, and the other end is connected to the circuit of controller. The LED is placed on the steering wheel to sense the driver’s pulse rate. The LED light passes to the fingers of the vein of the driver. The receiver receives the light which is done by the reflector to determine the heart rate. The pulse sensor pin configuration is connected to the ground of the system.

The  $V_{cc}$  pin is connected to the +5–3.3 V supply voltage. The signal pin is connected to the pulsating output signal. The pulse causes the variation in the blood flow, and the detector output is in the form of electrical signal which is proportional to the heart rate.

Based on the range of heart beat for various drivers or people between age group of 40. The IR light-emitting diode transmits the light into the finger arteries, an element of that is mirrored back from the blood within the finger arteries. The photodiode detects the portion of the light that is mirrored back to micro-controller utilized for proposed project and automatic voltage regulator (AVR) family is preferred. At mega 328P CMOS 8-bit AVR micro-controller with 32 KB bytes of in-system programmable ISP flash memory, 2 KB bytes of RAM, 32 I/O lines. A liquid crystal display is used to display the heart beat which is beats per minute (bpm). When the driver falls asleep or another health-related issues the pulse of the driver’s body significantly required to perform less physical and mental tasks. LM 324 chip used in the controller is shown in Fig. 4, and the pulse display is used to display the actual heart rate of the driver. The control unit is programmed the range of the pulse beat and the normal pulse range is 60–100 beats for the adults, and it is measured continuously. Whenever the pulse range is less than 60 bpm or higher than the 100 bpm, the signal is given to the control unit to warn the driver by alarm. If the driver is not responding, a signal is given to the hydraulic actuator to activate the brake. The prototype model of sensing system is shown in Fig. 5 which is coupled with the Arduino. The sensing of driver pulse is tested and calculated by changing the mode from less than 60 to

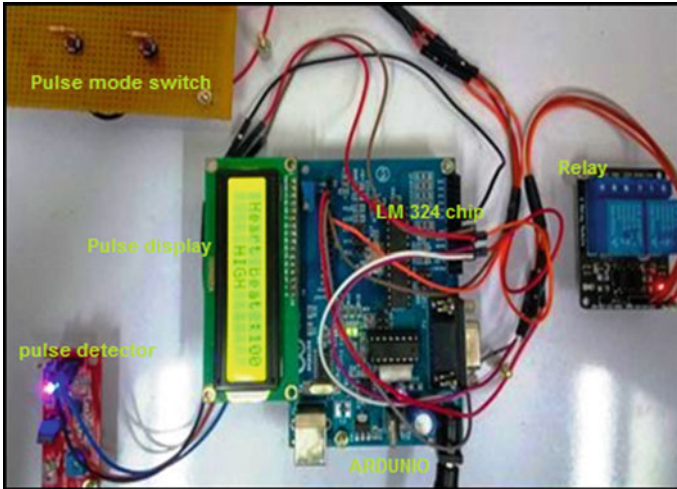


Fig. 4 Controller unit

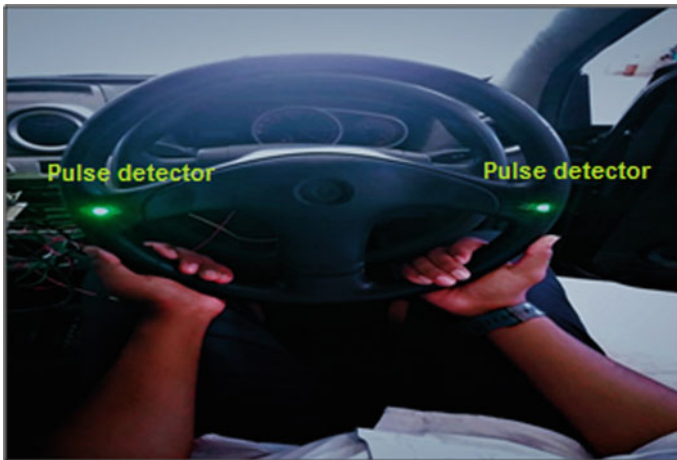


Fig. 5 Steering wheel sensing area

less than 80 bpm. The normal pulse range for the human in adult is 60–100 bpm. For testing, the system is programmed to 80 bpm manually. Whenever the pulse range is less than 80 bpm, the system gets triggered and gives signal to the alarm [7–9].

### 3 Results and Discussions

The proposed system sensing output is compared with the efficiency of the conventional system. The proposed system is tested in prototype and also in real-time model of the vehicle. The pulse sensor output is tested and validated with the conventional electrocardiogram. The proposed system is tested with maximum trials with individual people of different age groups, and the average pulse rate is taken for the study, and it is shown in Table 2. The results and discussion points out the output of the monitoring or sensing efficiency of the driver during driving when demand. The electrocardiogram output is tested for the age groups in hospital and supported by doctor (cardiologist). The output data from ECG is taken by trail methods as well analyzed with efficient sensing methods. The proposed system pulse sensor placed in steering wheel for testing in static and idling conditions. The testing is carried out with the age group for different trails for accuracy with repeatability. The testing is done by 12 people at the age group of under 40 for strive and for accuracy. The sensor is analyzed for repeatability using trail people. The sensor is placed in steering wheel and measured the pulse rate in the real time model. Table 2 shows the measured rate for the adult age groups. The measured pulse rate for the 35 age adult is 77 beats per minute which has 0.013 error rate compared with the conventional ECG pulse rate. The measured pulse rate for the 36 age adult is 77 beats per minute which has 0.026 error rate compared with the conventional ECG pulse rate. The measured pulse rate for the 37 age adult is 74 beats per minute which has 0.013 error rate compared with the conventional ECG pulse rate. The measured pulse rate for the 38 age adult is 83 beats per minute which has 0.012 error rate compared with the conventional ECG pulse rate. The measured pulse rate for the 39 age adult is 84 beats per minute which has 0.012 error rate compared with the conventional ECG pulse rate. The measured pulse rate for the 40 age adult is 87 beats per minute which has 0.011 error rate compared with the conventional ECG pulse rate. The maximum error is 0.026 for the actual ECG pulse rate which is 75 beats per minute, and for the proposed pulse sensor, it gives 77 beats per minute. The maximum acceptable margin error universally is 4–8%.

The error rate is calculated

$$[E] = [A - C] \times [100]/A \quad (1)$$

- A Actual heart rate
- C Calculated heart rate
- E Error rate.

The pulse range is monitored with the help of the sensor in steering wheel. For the error analysis, the sensor is compared with the electrocardiogram and results are carried out from the proposed system. The test is conducted with the help of trail method with individual person for 10 times. The calculated values are tested again and again for accuracy. The maximum error rate for the proposed system is 0.026,

and the minimum error rate for the proposed system is 0.012 (Fig. 6). The effect of adult age on pulse rate and tested readings is shown in Fig. 7.

Figure 7 shows the margin error of the pulse sensor and electrocardiogram; by using this graph, maximum percentage for the margin error rate is 2% for the static condition. The maximum peak of the curve at 0.026 for the adult age of 36. The remaining age group people are less than 0.013 errors and by percent are 1.3% of typical error rate. The 37 age adult had the error of 0.013 which is the second

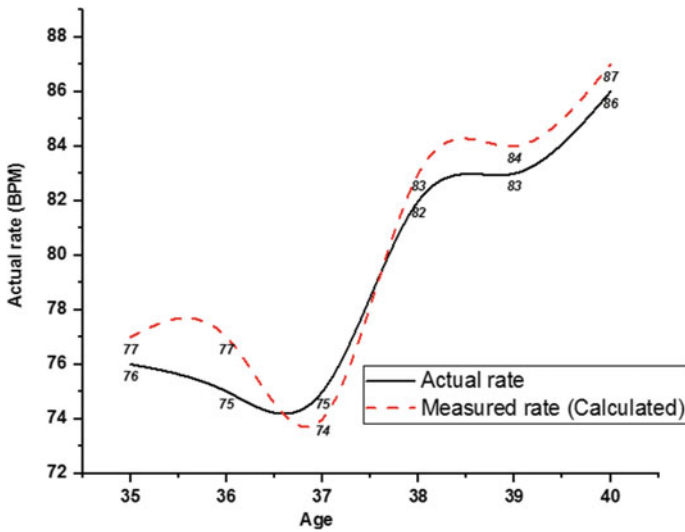
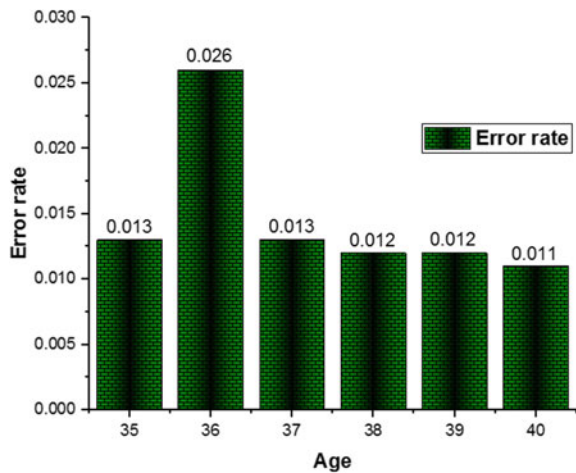


Fig. 6 Effect of adult age group on pulse rate

Fig. 7 Effect of adult age group on error rate



maximum error. The 40 age adult had the error of 0.011 which is minimum error for the pulse sensor while comparing with the electrocardiogram of the pulse monitor.

## 4 Conclusion

The proposed system monitors the driver condition during driving using sensors continuously for the safety. The system can also be used in low-cost vehicles and a supporting system for the drivers. The driver's health condition status is monitored and displayed in onboard. At the time of fluctuation of pulse, the signal from control unit gives warning or alarm signal to the driver. The proposed system reduces the fatality and makes the driver to slow down the vehicle during emergency. The driver condition monitoring system analyzed the condition of driver or driver fault during driving the vehicle. The proposed system reduces not only the damage to the vehicle but it also safeguards the driver from the collision.

## 5 Future Work

The designed system is used to sense the condition of driver and warns the driver only; probably the system will be tested in dynamic condition in different speeds for accuracy and also implemented further more by adding the GPS system with cloud access for connecting to the nearby clinics and hospitals for emergency if the driver's health is in serious condition. The GPS tracking system is already available, and the proposed system explores with the system to enhance the active safety desperately.

## References

1. Praveen Kumar B, Mahendran K (2014) Prevention of accident due to drowsy by using eye blink. *Int J Innov Res Sci Eng Technol* 3(5)
2. Dineshkumar C, Subramanian M (2017) automotive braking system for passenger vehicle to enhance safety. *Int J Pure Appl Math* 117(20):1011–1020
3. Punitha R, Suchithra G, Sujitha A (2015) Automatic car control during heart attack with an emergency messaging and comprehensive health monitoring system. *Int J Sci Eng Res* 6(1)
4. Road Accidents in India (2016) Government of India ministry of road transport & highways transport research. Wing, New Delhi
5. Highlights of 2009 motor vehicle crashes, Traffic safety facts, research notes, NHTSA (National Highway traffic Safety Administration) [Online]. Accessed on 16 Oct 2018
6. Dineshkumar C (2020) Security and privacy preserving for patient's E-health care applications. *Test Eng Manag* 82:1781–1786
7. Dineshkumar C (2019) On board driver monitoring system with safety enhanced brake system. *Int J Eng Adv Technol (IJEAT)* 8(6S3). ISSN: 2249-8958
8. Dineshkumar C, Subramanian M, Muthaya J, Deepan V (2019) Health monitoring system for automobile vehicles to enhance safety. *Int J Veh Struct Syst* 10(6). ISSN 09753040

9. Dineshkumar C, Subramanian M (2018) Experimental investigation of onboard driver condition monitoring system for passenger vehicles. *Int J Mech Eng Technol (IJMET)* 9(6):01–09. Article ID: IJMET\_06\_07\_001
10. Sales K, Jose X, Mary A, Mathew N (2013) ARM-7 based accident alert and vehicle tracking system. *Int J Innov Technol Explor Eng (IJITEE)* 2(4)
11. Veena SL, Subhashini R (2014) Driver alertness based on eye blinking and bio-signals. *Int J Adv Res* 2(3):666–670
12. Meiera A, Gontera M, Kruse R (2014) Precrash classification of car accidents for improved occupant safety systems
13. Hamersma HA, Schalk Els P (2014) Improving the braking performance of a vehicle with ABS and a semi-active suspension system on a rough road, 28 Sept 2014
14. Deepan V, Subramanian M, Dineshkumar C (2018) Motorcycle rider fatigue analyze: results of an online survey. *Int J Mech Product Eng Res Dev (IJMPERD)* 8. ISSN (P): 2249-6890; ISSN (E): 2249-8001
15. Alonso F, Esteban C, Sanmartin J, Useche SA (2017) Reported prevalence of health conditions that affected drivers. *Publ Health Res*. Article First Published: 09 Mar 2017
16. Hitosugi M, Hasegawa M, Yamauchi S, Morita S, Furukawa S (2015) Main factors causing health-related vehicle collisions and incidents in taxi drivers. *Romanian Society of Legal Medicine*
17. Hashem MMA, Shams R, Kader MA, Sayed MA (2014) Design and development of a heart beat measuring device using fingertip. *Int J Comput Sci Eng (KUET)*. Khulna, Bangladesh
18. Bhumkhar SP, Deotare VV, Babar RV (2012) Intelligent car system for accident prevention using ARM-7. *Int J Emerg Technol Adv Eng* 2(4)
19. Lőrincz AE, Ristoiu MN, Ionica A, Leba M (2017) Driver monitoring system for automotive safety. In: *IOP conference on series: materials science and engineering*
20. Ananth C, Shalaysha SS, Vaishnavi M, Sabena JSR (2014) Real-time monitoring of cardiac patients at distance using tarang communication. *SSRN Electron J* 9(3):15–20
21. Gulhane M, Mohod PS (2014) Intelligent fatigue detection and automatic vehicle control system. *Int J Comput Inform Technol* 6(3)
22. Gopalakrishnan S (2012) A public health perspective of road traffic accidents. *J Fam Med Primary Care Fam Med Prim Care* 1(2):144–150. <https://doi.org/10.4103/2249-4863.104987>



# Fabrication and Evaluation of Optimized Parametric Condition During EDM Machining of Al-CSA Composite Using Taguchi Orthogonal Array



C. J. Rao, R. Siva Sankara Raju, D. Sreeramulu, and Y. Sagar

**Abstract** In the modern decades, machining of components plays a vital role in manufacturing sector, hence with limited resources need to produce best results. This work has been details on fabrication of Al-coconut shell ash (CSA) composites produced via stir casting. The Al-CSA composites have prepared with varying 5 wt% of CSA fabricated upto 20% and identified mechanical and physical properties of composites. A detailed electric discharge machining (EDM), study on Al-15%CSA composite and identified optimal condition. The experiments are designed using Taguchi Orthogonal Array. The machining parameters such as current ( $I$ ), time of pulsing ( $T$ ), voltage ( $V$ ), pressure of dielectric fluid ( $P$ ) are affecting responses, i.e., metal removal rate (MRR), tool wear rate (TWR), and surface roughness (SR). The experiments are designed based on Taguchi OA (L27). Macroscopic examination was done on machining surface at various conditions. ANOVA revealed that current ( $I$ ), voltage ( $V$ ), and pressure ( $P$ ) is most influence on MRR, TWR, and SR, respectively. A regression model was developed and results were corroborates with existing once.

**Keywords** Amcs · Coconut shell ash · EDM · Taguchi OA · MRR · TWR and SR

## 1 Introduction

EDM can be a non-old form of machining that uses thermo-electric energy to extract material. The removal of material occurs through the erosive action of partly separate high-frequency electrical discharges (sparks) with high power density between two electrodes, one being the instrument and the alternative being the work piece itself with a material fluid inside the distance between them. The substance fluid appliance helps scoured particles to flush away from the gap and funky it. EDM provides a cost-efficient and effective method for the processing into specialized shapes of high strength, heat-resistant materials. EDM has well tried to be successful in the

---

C. J. Rao · R. Siva Sankara Raju (✉) · D. Sreeramulu · Y. Sagar

Department of Mechanical Engineering, Aditya Institute of Technology and Management, Tekkali 532201, India

e-mail: [sivaraju80@gmail.com](mailto:sivaraju80@gmail.com)

manufacture of composite materials amongst the non-standard machining techniques [1, 2].

On account of the incredible bodily and mechanical properties of aluminium metal matrix composites (AMCs), are extensively used in plane technology, digital engineering and automobiles too. Major served sector via automobile include bolstered pistons for diesel engines, cylinder bores, exhaust valves, and brake components. The needs on matrices face up to temperature versions, be conductors or resistors of energy and own moisture sensitivity. The matrix can also offer weight benefits, ease of managing, and other deserves which may additionally turn out to be relevant relying. Materials should accommodate stresses because of incorporation of different parts and also offer a sturdy bond for the reinforcing phase form capacity matrix substances. Reinforcement for the composites may be fibers, particles or whiskers. Fibers are basically characterized via very lengthy axis with other two axes either often round or close to round. Particles don't have any favored orientation and so does their shape. Whiskers have a preferential shape but small both in diameter and length as compared to fiber [3–5].

Ramesh et al. [6] studied on Al6061-SiC-B4C composites using EDM and identified optimal condition based on fuzzy-based model. They revealed that SiC is a influencing parameter on MRR and SR. MRR decreased with increase in SiC and B4C, whereas SR shows inverse character to reinforcement. Kerf width increased with pulse on time and decreased with addition of SiC and B4C.

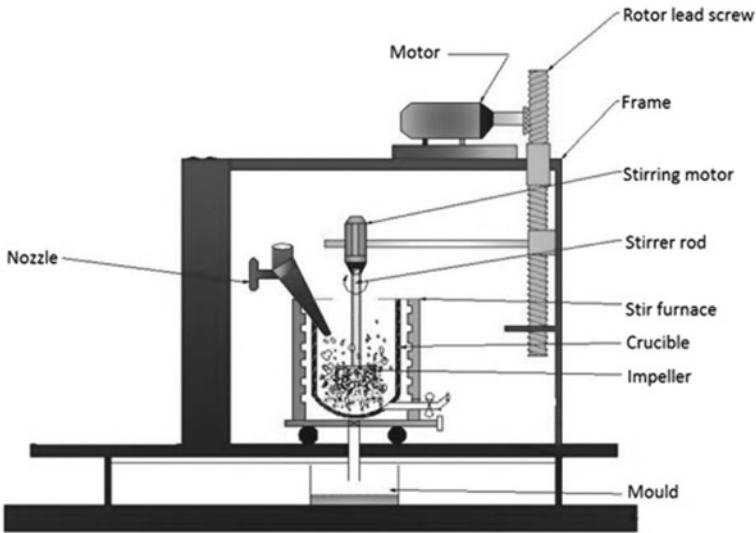
Kumar et al. [7] studied on Al-SiC composites based on RSM and revealed surface roughness decreased due to composite defects like porosity. Higher MRR achieved with escalating current. Liu et al. performed machining on Al-10%Al<sub>2</sub>O<sub>3</sub> and Al-20% Al<sub>2</sub>O<sub>3</sub> composites, comparing performance in neutral and emulsified oil. SR decreased with addition of oil.

The use of non-conventional machining techniques for shaping AMCs has generated large interest inside the production of complex contours which include dies. EDM is one of the promising methods for machining composites. Investigation on the influence of EDM procedure parameters on machining performance criteria of Al-CSA composite debris were accomplished through the development of mathematical correlations.

This work emphasize on machining of Al-CSA composite using Taguchi OA (L27). The input parameters such as current ( $I$ ), time of pulsing ( $T$ ), voltage ( $V$ ), pressure of dielectric fluid ( $P$ ), whereas affecting responses are metal removal rate (MRR), tool wear rate (TWR), and surface roughness (SR).

## 2 Investigation Scheme and Experimental Design

Fabrication of CSA composites were done by stir casting and setup was illustrated in Fig. 1. Al-Si-Mg alloy is held inside the electric induction furnace in graphite crucible. The alloy was pre-heated at 579 °C. After successful degassing, pre-heated reinforcement particles with a CSA quantity of size 50–65 μm was poured into



**Fig. 1** A detailed setup of stir casting

the whirlpool of melt. A graphite stirrer was used to achieve exciting the melt over a period of 9 min. The stirrer speed had been held at 590 rpm. The melt poured in a mould and cooled at normalizing temperature and then collected [8–10]. On the FANUC ROBOCUT machine was performed a series of EDM. Metal matrix composite of 15 vol per cent CSA reinforced alloy Al–Si–Mg was the work—piece material. Al-CSA composites’ tensile properties are measured at a velocity of  $1 \text{ mm s}^{-1}$  with Hounsfield tensometer (model: ETM-ER3/772/12). The Brinell hardness test was carried out using 5 mm steel ball indenter under a load of 250 kg. The experiments are designed using Taguchi OA (L27) with thrice in replicates of each experiment. The selected input parameters were four along three levels, illustrate in Table 1. The work piece is 200 mm long and has a diameter of 50 mm. The EDM experimental interface appears in Fig. 2. The finishing interfaces value ( $R_a$ ) was measured using SURTRONIC 25. The direction in which roughness is measured being perpendicular to the cutting axis. To minimize the responses, a randomized experimental test was performed. Variance analysis (ANOVA) was used to analyze

**Table 1** Constraint and their levels

Factor	Unit	Symbol	Level		
			1	2	3
Current	Amp	$I$	3	9	15
Pulse on time	$\mu\text{s}$	$T$	200	400	600
Servo voltage	V	$V$	30	50	70
Flush pressure	psi	$P$	1	3	5

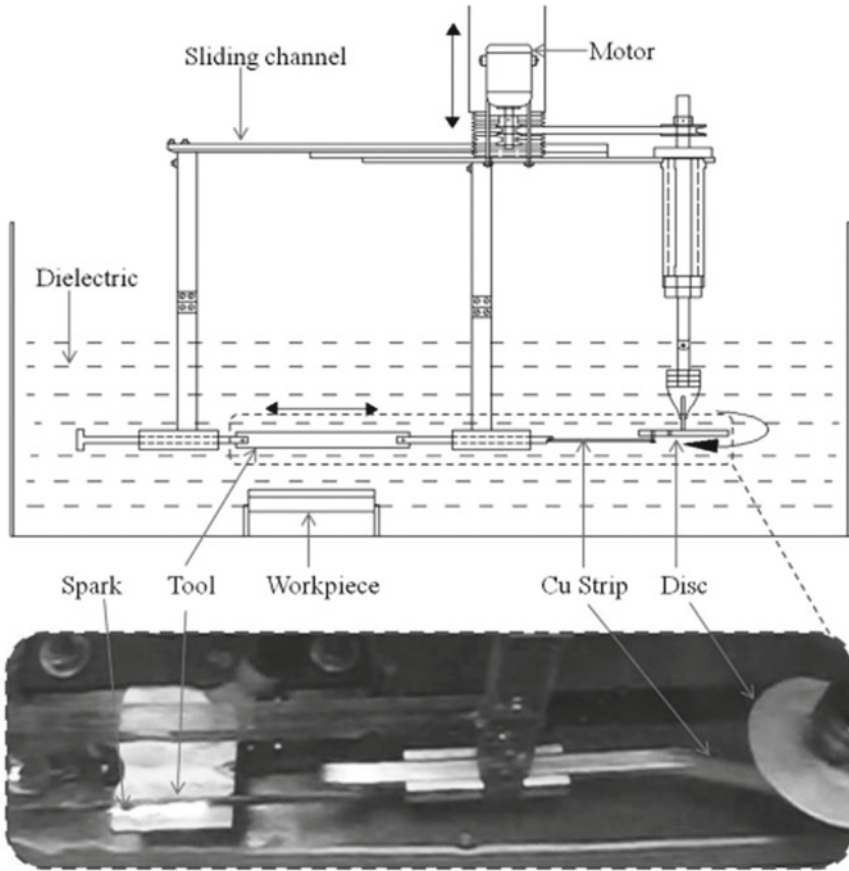


Fig. 2 EDM schematic setup used for machining

the entity, association, and square effects of control parameters on the outcome. ANOVA was run using the program MINITAB 16.

### 3 End Result and Debate

#### 3.1 Mechanical Properties

Figure 3a shows the tensile stress comparison plot with the strain for different CSA-AMCs. It is obvious that tensile strength is rising with an increasing percentage CSA. The yield strengths for pure Al, 5, 10, 15, and 20% of CSA MMCs are found to be 90, 101, 127, 142, and 148 N/mm<sup>2</sup>. Increases in hardness and decreases in percentage

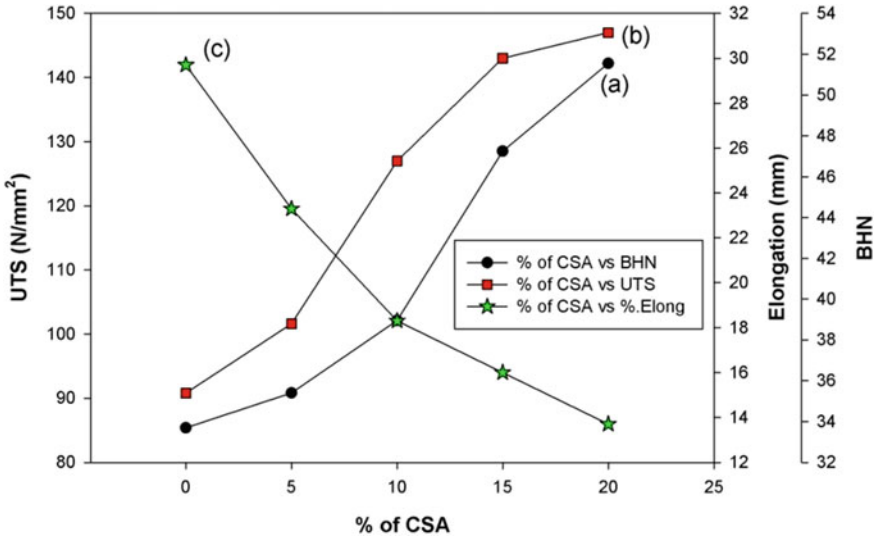


Fig. 3 Effect of CSA composites on a Tensile strength b Hardness c Elongation

of elongation with an increase in CSA are seen in Fig. 3b, c, which is attributed to composite strain hardening. CSA particles are strong, which increases the flexibility of load bearing, and limits matrix dislocation movement.

### 3.2 Regression Analysis

Table 2 shows the layout of experiments on Al-15%CSA composite response. The effects of variable parameters ( i.e.,  $I$ ,  $T$ ,  $V$  and  $P$ ) with relationships on surface roughness (SR) of the material removal rate (MRR), tool wear rate (TWR) have been developed using ANOVA and regression models as shown in Eqs. (1), (2) and (3). The value of  $R^2$  is 0.986 specifies that 98.6% of the variation in the MRR has explained by the model. Similarly,  $R^2$  value of TWR and SR are 0.996. From regression, revealed MRR decreased with increased voltage. Similarly, TWR has positive impact on pulse on time and flushing pressure. Also, SR increased with increasing all factors.

$$MRR = 0.392 + 0.0332 I + 0.00750 T - 0.0131 V + 0.0133 P \quad (1)$$

$$TWR = 0.0299 + 0.00150 I - 0.00311 T + 0.00511 V - 0.00200 P \quad (2)$$

$$SR = 0.644 + 0.308 I + 0.492 T + 1.02 V + 1.79 P \quad (3)$$

**Table 2** Experimental design with outcomes of Al-15%CSA composite

Run	<i>I</i>	<i>T</i>	<i>V</i>	<i>P</i>	MRR	TWR	SR
1	-1	-1	-1	-1	0.434	0.032	4.175
2	-1	-1	-1	-1	0.434	0.032	4.175
3	-1	-1	-1	-1	0.434	0.032	4.175
4	-1	0	0	0	0.453	0.032	7.706
5	-1	0	0	0	0.453	0.032	7.706
6	-1	0	0	0	0.453	0.032	7.706
7	-1	1	1	1	0.456	0.033	10.775
8	-1	1	1	1	0.456	0.033	10.775
9	-1	1	1	1	0.456	0.033	10.775
10	0	-1	0	1	0.492	0.034	9.314
11	0	-1	0	1	0.492	0.034	9.314
12	0	-1	0	1	0.492	0.034	9.314
13	0	0	1	-1	0.455	0.041	7.009
14	0	0	1	-1	0.455	0.041	7.009
15	0	0	1	-1	0.455	0.041	7.009
16	0	1	-1	0	0.495	0.026	7.259
17	0	1	-1	0	0.495	0.026	7.259
18	0	1	-1	0	0.495	0.026	7.259
19	1	-1	1	0	0.494	0.043	8.617
20	1	-1	1	0	0.494	0.043	8.617
21	1	-1	1	0	0.494	0.043	8.617
22	1	0	-1	1	0.534	0.029	8.867
23	1	0	-1	1	0.534	0.029	8.867
24	1	0	-1	1	0.534	0.029	8.867
25	1	1	0	-1	0.513	0.034	7.023
26	1	1	0	-1	0.513	0.034	7.023
27	1	1	0	-1	0.513	0.034	7.023

A level mean is the average value of response at specific level. The machining parameters (i.e., *I*, *T*, *V* and *P*) on EDM responses (i.e., MRR, TWR and SR) are observed, shown in Fig. 2. The optimal conditions for MRR, TWR, and SR are I3T3V1P3, I1T3V1P3, and I1T1V1P1, respectively. The plot of signal noise ratio of mean effectives for MRR, TWR, and SR are shown in Fig. 4.

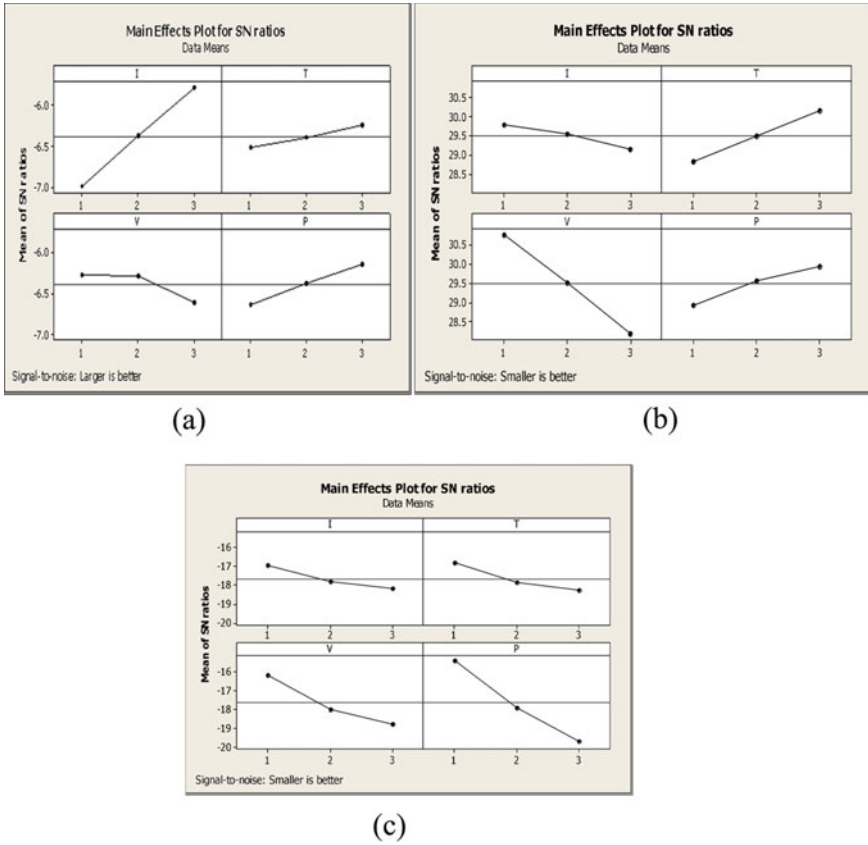


Fig. 4 Mean effective plots for a MRR b TWR c SR

### 3.3 Analysis of the Process Parameters and Interactions

The experiments seek to obtain correlation between process variables and output in machining. Factorial style, level mean are calculated and shown in Table 4. From the ANOVA of MRR (Vide in Table 3), current (76%) is most effecting parameter followed by flushing pressure (13%).

ANOVA Table 4 revealed voltage is most control parameter on TWR of Al-CSA composites with 68% of contribution. Pulse on time (*T*) is the second influencing factor. The overall contribution is 99.6% on TWR of Al-CSA composites.

Similarly, ANOVA (Table 5) revealed, flushing pressure (63%) is mainly control parameter followed voltage (24%) on surface roughness (SR). The contributions of overall factors are performed 99.6% of the total variance in SR.

**Table 3** ANOVA of MRR

Source	DF	SS	A-SS	AD MS	<i>P</i>	% Cont (%)
<i>I</i>	2	2.15366	2.15366	1.07683	1.53E−20	76
<i>T</i>	2	0.11449	0.11449	0.057245	1.08E−07	4
<i>V</i>	2	0.21121	0.21121	0.105605	9.91E−10	7
<i>P</i>	2	0.35426	0.35426	0.17713	2.97E−12	13
Total	8	2.83363				

$S = 0.00413$   $R\text{-Sq} = 98.6\%$   $R\text{-Sq}(\text{adj}) = 98.3\%$

**Table 4** ANOVA of TWR

Source	DF	SS	A-SS	AD MS	<i>P</i>	% Cont (%)
<i>I</i>	2	0.631	0.631	0.3155	2.37E−14	4
<i>T</i>	2	2.5597	2.5597	1.27985	2.53E−19	17
<i>V</i>	2	9.9475	9.9475	4.97375	1.03E−25	68
<i>P</i>	2	1.5401	1.5401	0.77005	5.8E−17	10
Total	8	14.6783				

$S = 0.000365563$   $R\text{-Sq} = 99.6\%$   $R\text{-Sq}(\text{adj}) = 99.5\%$

**Table 5** ANOVA of SR

Source	DF	SS	A-SS	AD MS	<i>P</i>	% Cont (%)
<i>I</i>	2	2.547	2.547	1.2735	2.37E−14	6
<i>T</i>	2	3.2726	3.2726	1.6363	2.53E−19	8
<i>V</i>	2	10.4203	10.4203	5.21015	1.03E−25	24
<i>P</i>	2	27.2516	27.2516	13.6258	5.8E−17	63
Total	8	43.4916				

$S = 0.120453$   $R\text{-Sq} = 99.6\%$   $R\text{-Sq}(\text{adj}) = 99.5\%$

### 3.4 Confirmation Test and Corroboration of SEM Results

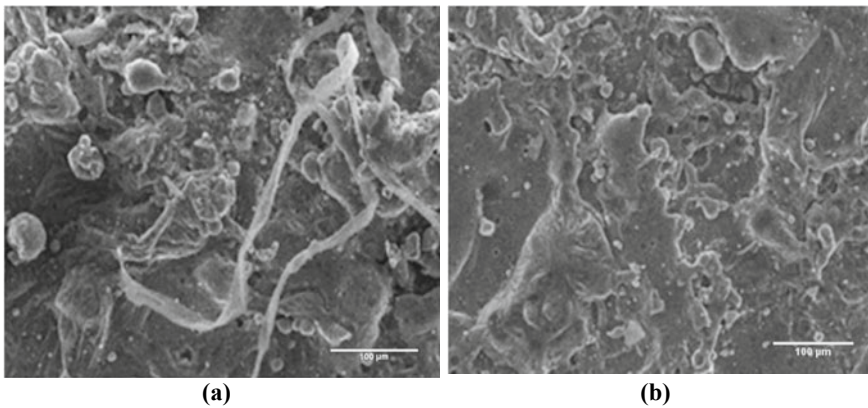
From the confirmation test (Table 6), it is clear that the regression model equation are satisfied and error within the limits.

When current increasing, electric spark strike the surface of specimen intensely. Owing to this attribute, the diameter and void intensity increases and causes to increase of surface roughness. The reinforcement particles have padding nature with extraordinary arcing, and random spark discharges arise in which micron sized reinforcements are visible. The machined surface at the condition of current (15 A), pulse on time of 400 μs, as shown in Fig. 5a, Bands and craters establish on machined surfaces of composites as shown in and Fig. 5b. In preferred, at low discharge craters are seen to be shallow with less indiscretion in surface. At high discharge, craters



**Table 6** Confirmation test results

<i>I</i>		<i>T</i>		<i>V</i>		<i>P</i>		
6		300		40		2		
12		500		60		4		
9		400		30		1		
MRR Exp	MRR Cal	Error	TWR Exp	TWR Cal	Error	SR Exp	SR Cal	Error
0.459	0.461	0.345	0.0327	0.0319	-2.514	7.065	6.962	-1.482
0.507	0.491	-3.279	0.0297	0.0292	-1.674	8.48	8.945	5.199
0.48	0.502	4.467	0.0335	0.0319	-5.043	6.837	6.523	-4.82



**Fig.5** EDM surfaces of Al-15% CSA composite at **a** I:15A,T:400 μs **b** I:9A,T:600 μs

are deeper and more abnormality in surfaces. While the flushing stress turned into extended, solidification of particles scattered over the surface by way of molten fabric droplets between electrode and work piece also increased, which cause of decreasing surface roughness.

### 4 Conclusions

In this work, Al-CSA composites are prepared with varying % of CSA indigenously in laboratory scales. The following points are highlighted in present study.

- Al-CSA composites increase the mechanical properties up to 15% then decreased due to porosity, hence Al-15%CSA composite considered in further case study, i.e., EDM.
- MRR is decreased and surface roughness decreased with increasing wt% of CSA.

- The optimal conditions for MRR, TWR, and SR are I3T3V1P3, I1T3V1P3, and I1T1V1P1, respectively.
- The optimal value of MRR, TWR, and SR is 0.664, 0.0229, and 4.175, respectively.
- ANOVA revealed that current, pulse on time ( $T$ ), flushing pressure is most effecting parameter on MRR, TWR, and SR, respectively.
- The experiments results are correlates with SEM findings.

## References

1. Kachhup S, Singh A, Kumar S (2019) Performance evaluation of different electrode geometries in electric discharge drilling of MMCs. *Int J Mech Eng Robot Res* 8:531–535. <https://doi.org/10.18178/ijmerr.8.4.531-535>
2. Liu JW, Xiao YJ, Guo ZN, Wang SJ, Yue TM, Tang ZW (2016) Electrical discharge machining of metal matrix composites with a high speed non-round electrode. *Adv Compos Lett* 25:137–142. <https://doi.org/10.1177/096369351602500603>
3. Siva Sankara Raju R, Panigrahi MK, Ganguly RI, Srinivasa Rao G (2017) Investigation of tribological behavior of a novel hybrid composite prepared with al-coconut shell ash mixed with graphite. *Metall Mater Trans A* 48:3892–3903. <https://doi.org/10.1007/s11661-017-4139-1>
4. Siva Sankara Raju R, Srinivasa Rao G, Samantra C (2019) Wear behavioral assessment of Al-CSAp-MMCs using grey-fuzzy approach. *Measurement* 140:254–268. <https://doi.org/10.1016/j.measurement.2019.04.004>
5. Raju SS, Murali GB, Patnaik PK (2020) Ranking of Al-CSA composite by MCDM approach using AHP–TOPSIS and MOORA methods. *J Reinf Plast Compos* 39:721–732. <https://doi.org/10.1177/0731684420924833>
6. Ramesh S, Natarajan N, Krishnaraj V (2014) Experimental investigation of Al6061/SiCp/B4Cp hybrid MMCs in wire electrical discharge machine. *Indian J Eng Mater Sci* 21:409–417
7. Kumar R, Singh I (2017) Electric discharge sawing of hybrid metal matrix composites. *Proc Inst Mech Eng Part B J Eng Manuf* 231:1775–1782. <https://doi.org/10.1177/0954405415611360>
8. Vikash Kumar K, Siva Sankara Raju R (2020) Statistical modeling and optimization of Al-MMCs reinforced with coconut shell ash particulates. In: Deepak B, DRK P, Jena PC (eds) *Innovative product design and intelligent manufacturing systems. Lecture notes in mechanical engineering*. Springer Nature Singapore Pte Ltd., Rourkela, India, pp 703–712. [https://doi.org/10.1007/978-981-15-2696-1\\_67](https://doi.org/10.1007/978-981-15-2696-1_67)
9. Sankara Raju RS, Panigrahi MK, Ganguly RI, Srinivasa Rao G (2019) Tribological behaviour of Al-1100-coconut shell ash (CSA) composite at elevated temperature. *Tribol Int* 129:55–66. <https://doi.org/10.1016/j.triboint.2018.08.011>
10. Siva Sankara Raju R, Rao GS (2017) Assessment of tribological performance of coconut shell ash particle reinforced Al–Si–Fe composites using grey-fuzzy approach. *Tribol Ind* 39:364–377. <https://doi.org/10.24874/ti.2017.39.03.12>

# Prediction and Modeling of Tool Wear with Cutting Force and Fine Gaussian Support Vector Machine in Drilling



G. Mahendran, M. A. Sai Balaji, J. Susai Mary, and D. Dinakaran

**Abstract** The tool wear is a vital problem in machining which affects the accuracy, geometry of the workpiece and also productivity. This paper presents a cutting-force-based monitoring method with a Gaussian Support Vector Machine for tool wear prediction in a drilling process. The experimental results show that the tool wear has a significant effect on the cutting forces. Statistical features in time and frequency domains are extracted from the measured force signals and are used as inputs to the Support Vector Machine (SVM). The machining parameters speed and feed are also taken as inputs for tool wear prediction as they greatly influence the cutting force. The fine Gaussian SVM algorithm is able to model the tool wear with a prediction accuracy of 88% and can be used for online diagnosis of tool wear. The results of the Gaussian SVM algorithm are compared with standard algorithms like ANN to prove its efficiency.

**Keywords** Condition monitoring · Fine Gaussian SVM drilling · Force · Tool wear

## 1 Introduction

Drilling is a very essential operation which includes 40% of the machining operations and finds its applications in many manufacturing industries [1]. The monitoring and classification of tool wear in drilling are needed to provide timely and precise

---

G. Mahendran · M. A. Sai Balaji  
Department of Mechanical Engineering, B S Abdur Rahman Crescent Institute of Science and Technology, Chennai, India  
e-mail: [saibalaji@crecident.education](mailto:saibalaji@crecident.education)

J. Susai Mary (✉)  
Department of Electronics and Instrumentation Engineering, B S Abdur Rahman Crescent Institute of Science and Technology, Chennai, India  
e-mail: [susaimaryj@gmail.com](mailto:susaimaryj@gmail.com)

D. Dinakaran  
Center for Automation and Robotics, Hindustan Institute of Technology and Science, Chennai, India  
e-mail: [drddinakaran@gmail.com](mailto:drddinakaran@gmail.com)

estimation of the tool state. The progression of tool wear from sharp to worn state is a dynamic process and will possibly lead to the breakage of tool [2]. It is difficult to predict the tool wear in real time due to the influence of various parameters and tool performance variations [3]. As a result, many indirect methods of tool wear prediction using vibration, force, acoustic emission, ultrasound, etc., have been proposed by many researchers.

Wear classification in end milling based on force and current signals in linear axis has been presented. The mean, median and standard deviation were taken as inputs for wear classification [4]. In drilling EN24, the RMS of vibration signal was used for tool wear and surface roughness prediction. Desirability optimization was presented to find the optimal machining conditions [5]. A multisensory approach for prediction of tool wear has gained popularity in recent years. Susai Mary et al. have presented a method for surface roughness modeling using vibration and force sensors with a cubic SVM model with an accuracy of 94% [6]. The statistical features and wavelet packet decomposition of sound and vibration signals were used for wear detection during drilling in [7]. The features extracted from the measured secondary signals are used as input to train various modeling techniques to predict the tool wear state in real time.

Many machine learning algorithms have attracted attention in recent years such as Artificial Neural Networks (ANNs), Support Vector Machines (SVMs) and decision tree algorithms have been used by many researchers in condition monitoring of tools, surface roughness, runout, etc. ANN has been widely used in condition monitoring because of its ability to model nonlinear systems. A neural-network-based modeling of tool wear and metal removal rate has been presented and proven to predict the parameters with a regression of 0.97 and 0.98 [8]. Thangarasu et al. have presented a tool wear prediction method in turning EN8 steel with cutting force measurements. They have compared various NN modeling methods and have stated that BFGS quasi-Newton back propagation algorithm gives the best result [9].

SVMs are machine learning algorithms capable of modeling and classifying nonlinear data by mapping their inputs in infinite dimensional space with the help of kernel functions. Sun et al. have presented a SVM approach with one versus one method to classify the tool wear states with acoustic emission signals to reduce the manufacturing losses [2]. Jaydeep Karandikar has used SVM and logistic approach for tool life prediction and has proved that the machine learning algorithms provide better results in shop floor [3]. A comparison study was done on SVM and random forest (RF) models to classify the wear states in end-milling and was found that the SVM outperformed the RF with an accuracy of 99.8 and 98% on the test and validation data [4]. A LS-SVM model for runout monitoring during drilling with the frequency domain features of force and vibration was presented, and the model was proved efficient in predicting the runout states with 80% accuracy [10]. A review on the application of SVM for modeling machining operations was carried out and verified that SVMs are powerful tools for classification, estimation and regression. It is also concluded that Radial Basis Function (RBF) Kernels are mostly used in the SVM [11]. The feature selection (force at 100 Hz) and the use of SVM for modeling

and prediction of tool wear are the novel contribution of this work. The results showed that the model is simple and effective.

## 2 Experimental Setup and Measurements

A three-axis CNC vertical milling machine LV-45 (LMW) was used to conduct the drilling experiments, shown in Fig. 1. A high-speed steel twist drill of 6 mm diameter with a straight cylindrical shank was used for drilling through holes in an EN24 workpiece with a diameter and thickness of 120 and 10 mm. Drill bits with various states of wear from 0.1 to 0.4 mm were selected randomly, and the wear was measured using vision measurement. Experiments were conducted at various speeds of 800, 950, 1100, 1300 and 1450 rpm and feed rates of 90, 100, 120 and 140 mm/min. The speed and feed levels were selected based on a L20 orthogonal array. No coolant was used during the experiments.

During drilling, a milling tool dynamometer (RATNA, RDMT-303) capable of measuring force up to 9000 N with an accuracy of  $\pm 0.1\%$  was used to measure the axial cutting force in Z-direction. A NI9233 data acquisition card interfaced with LabVIEW was used for acquiring the force signals at a rate of 5K samples/second. After every drilling, the drill flank wear was measured with a vision system (SIPCON, SVI-CH). A total of 30 drilling experiments were conducted in the recommended cutting range out of which 20 are used for training and 10 data are used for validation. The drill wear was measured at four different places on the flank surface, and the maximum value was taken as the value of tool wear. A total of 12 drill bits were

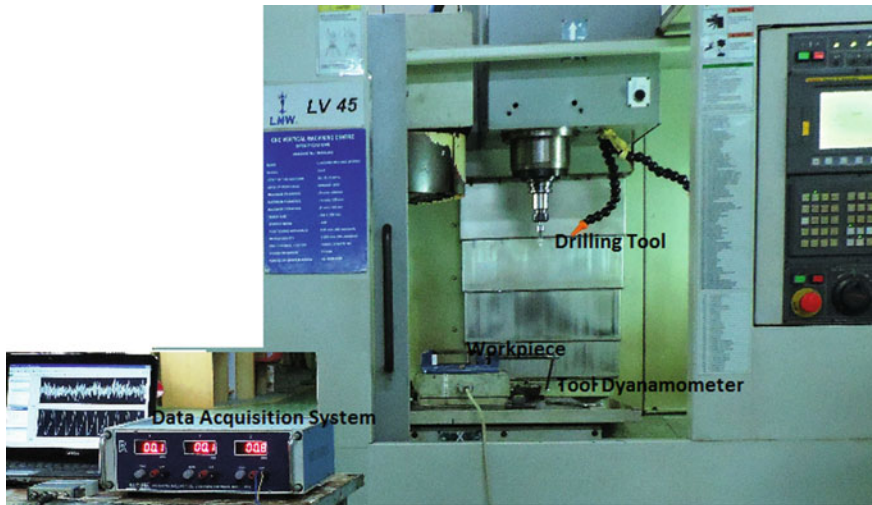


Fig. 1 Experimental setup with data acquisition

used and changed randomly. The measured tool wear values for 20 experimental conditions which are used for training are represented graphically in Fig. 2.

The cutting force signals recorded during drilling were further processed for feature extraction. To eliminate the discontinuities and spectral leakage in the signals, a Hanning window is used [12]. In time domain, the RMS of the force signal associates well with tool wear and changes in machining conditions [13]. Thus, the RMS is taken as a measure of tool wear, and the variations of RMS of force signal with tool wear are given in Fig. 3.

From Fig. 3, it is found that the RMS of force varies proportional to tool wear and is also influenced by the speed and feed of machining. From the frequency analysis of the recorded force signals, it is observed that the axial force magnitude at 100 Hz

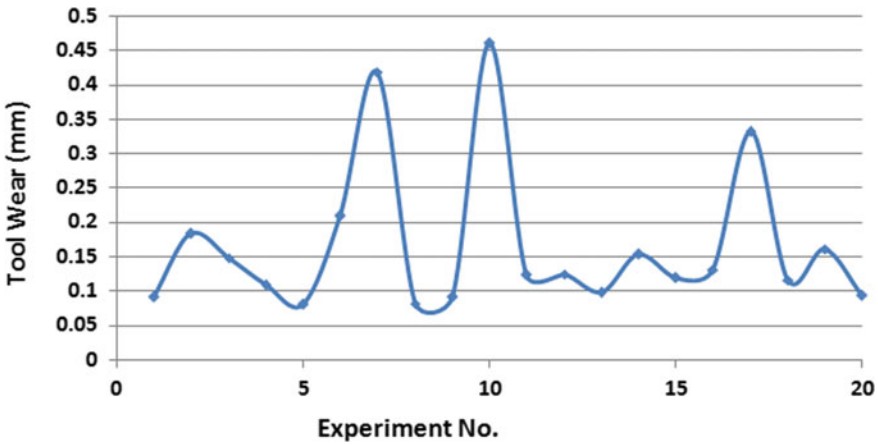


Fig. 2 Tool wear values measured at different cutting conditions

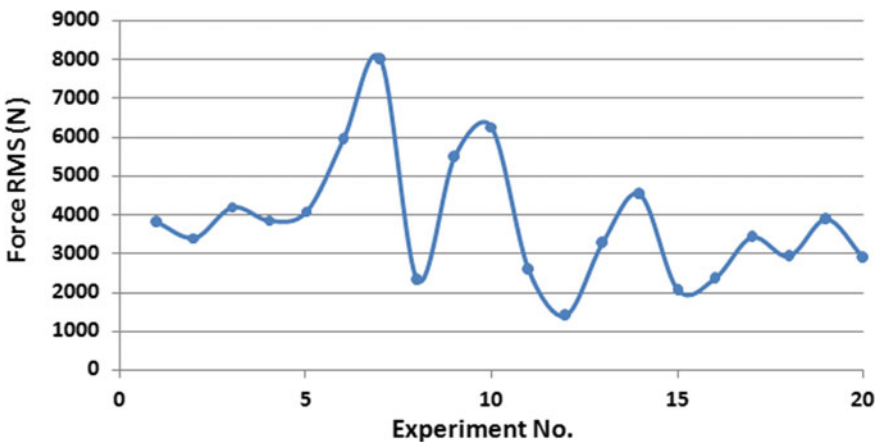


Fig. 3 Force RMS for different experimental conditions

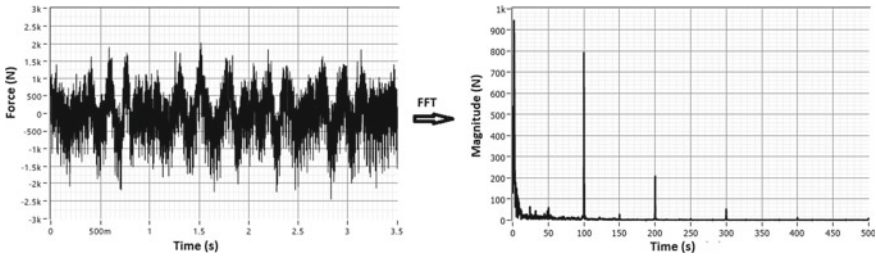


Fig. 4 Frequency spectrum for a sample force signal (Experiment No. 17)

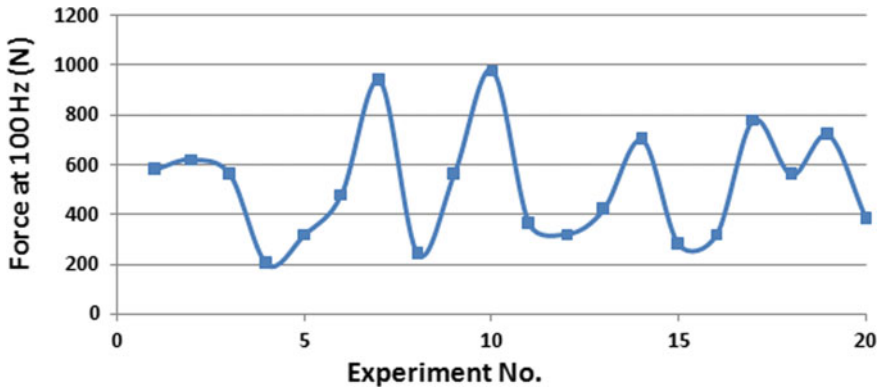


Fig. 5 Force amplitude at 100 Hz

depicts clearly the relation between tool wear, speed and feed of machining [14]. A sample of the recorded force signal with its frequency components is shown in Fig. 4. The amplitude of force signals at 100 Hz for the all experimental conditions is given in Fig. 5. The force amplitude increases as the tool wear increases, and at certain places the amplitudes vary randomly due to the influence of machining conditions.

### 3 Modeling of Tool Wear Using Fine Gaussian SVM

Tool wear monitoring and prediction is very essential in tool condition monitoring. There is a need to monitor and predict the tool wear progression considering the effects of machining conditions in real time. Support Vector Machine (SVM) is a supervised machine learning model used for classification and regression analysis. An advantage of SVM is that the solutions are global and unique, whereas in ANNs the solutions can get stuck in multiple local minima. Moreover, SVMs have a sound theory, simple geometrical interpretations and are less prone to overfitting of data. SVM classifier helps to minimize the structural risk instead of the empirical risk

[15]. A fine gaussian SVM is proposed for modeling the tool wear. The RMS of force signal, amplitude at 100 Hz, the spindle speed and feed are taken as inputs for tool wear modeling. The block diagram for fine gaussian SVM modeling of tool wear is given in Fig. 6.

The fine gaussian SVM was modeled with 20 experimental data, and the model was capable of predicting the tool wear with a root mean square error (RMSE) of 0.0375 and a regression ( $R^2$ ) of 0.88. The measured and predicted values of tool wear for the training dataset are shown in Fig. 7. Later, the model was tested with a different dataset of 6 values and found that the model was able to predict the tool wear with an accuracy of 93% as shown in Fig. 8.

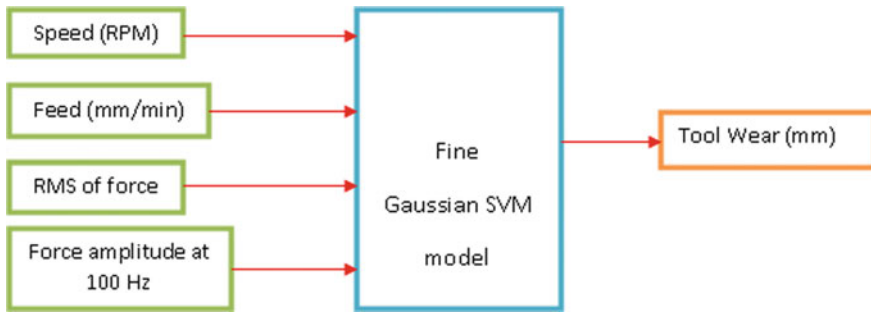


Fig. 6 Block diagram for tool wear modeling using SVM

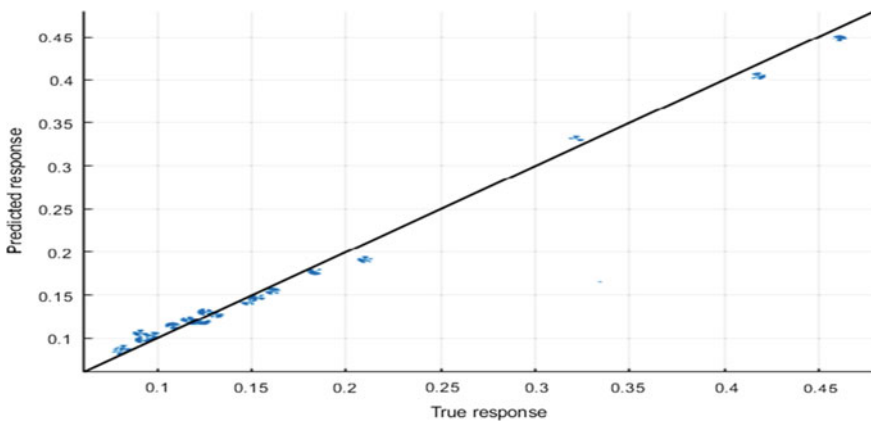


Fig. 7 Actual versus predicted values of tool wear for training data



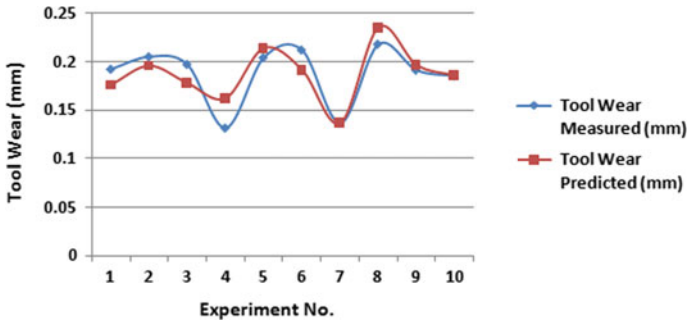
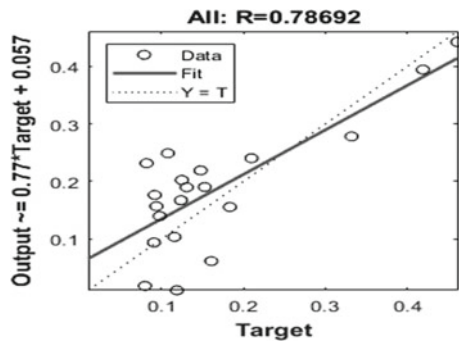


Fig. 8 Validation output of fine Gaussian SVM model

Fig. 9 Regression plot for the neural network model



### 3.1 Comparison of SVM with Neural Networks

Many researchers have proved that the SVM models give the best and maximum accuracy compared to ANN, Hidden Markov Model (HMM) and Random Forest (RF) models [12, 15–17]. To prove the efficiency of the fine Gaussian SVM model, the results are compared with artificial neural networks (ANNs). In this work, the same dataset which was used to model the SVM was used to model the ANN. A Levenberg–Marquardt algorithm was used to train the network. The experimental data was classified as training (75%), testing (15%) and validation (15%). The overall regression obtained by the neural network was 0.78 which is less compared to the fine Gaussian SVM model as given in Fig. 9.

## 4 Conclusion

The paper presented gives a new idea for prediction of tool wear with fine Gaussian SVM model. It includes features of force signal in time and frequency along with varying machining conditions for better accuracy. It is found that the force RMS

and amplitude in frequency domain increase with increase in tool wear and are also influenced by the speed and feed of machining. However, the experiments are carried out at different machining conditions and with tools of varying tool wear, this model can be used to predict wear states from 0.1 to 0.45 mm at recommended speed and feed. To prove the efficiency of SVM models for tool wear prediction, it is compared with ANN model. Results prove that the SVM model is able to model the tool wear with 88% accuracy than ANN model with 78%.

## References

1. HMT (1980) Production technology. Tata McGraw-Hill Publishing Co. Ltd.
2. Sun J, Rahman M, Wong YS, Hong GS (2004) Multi-classification of tool wear with support vector machine by manufacturing loss consideration. *Int J Mach Tools Manuf* 44:1179–1187
3. Karandikar J (2019) Machine learning classification for tool life modeling using production shop floor tool wear data. *Procedia Manuf* 34:446–454
4. Schwenzer M, Miura K, Bergs T (2019) Machine learning for tool wear classification in milling based on force and current sensors. In: *IOP conference series: materials science and engineering*, vol 520, 012009
5. Susai Mary J, Sabura Banu U, Dinakaran D, Nakandhrakumar RS (2017) Adaptive control by multi-objective optimisation for drilling process with fuzzy inference system and neural predictive controller. *Insight Non-Destruct Testing Condition Monit J Br Ins Non-Destruct Testing* 59(1):38–44
6. Susai Mary J, Sai Balaji MA, Dinakaran D (2019) Prediction and Geometric Adaptive Control of surface roughness in drilling process. *FME Trans* 47(3):424–429
7. Rafezi H, Akbari J, Behzad M (2012) Tool condition monitoring based on sound and vibration analysis and wavelet packet decomposition. In: *2012 8th International symposium on mechatronics and its applications*, pp 1–4
8. Susai Mary J, Sabura Banu U, Dinakaran D (2015) Adaptive optimization using Grey relational analysis and PID control of CNC drilling process. In: *2015 International conference on robotics, automation, control and embedded systems (RACE)*, Chennai, pp 1–5
9. Thangarasu SK, Shankar S, Mohanra T, Devendran K (2019) Tool wear prediction in hard turning of EN8 steel using cutting force and surface roughness with artificial neural network. *Proc Inst Mech Eng Part C: J Mech En Sci* 234(1):329–342
10. Susai Mary J, Sai Balaji MA, Krishnakumari A, Nakandhrakumar RS, Dinakaran D (2019) Real time monitoring of drill runout using Least square support vector machine classifier. *Measure J Int Measure Confederation Elsevier* 146:24–34
11. Deris AM, Zain AM, Sallehuddin R (2011) Overview of support vector machine in modeling machining performances. In: *2011 International conference on advances in engineering, procedia engineering*, vol 24, pp 308–312
12. Alexandre FA, Lopes WN, Ferreira FI, Dotto FBL, de Aguiar PR Bianchi EC (2018) Chatter vibration monitoring in the surface grinding process through digital signal processing of acceleration signal. *Proceedings MDPI* 2:1–5
13. Jantunen E (2002) A summary of methods applied to tool condition monitoring in drilling. *Int J Mach Tools Manuf* 42:997–1010
14. Alessandra, Centobelli P, Nele L, Teti R (2017) Multiple sensor monitoring in drilling of CFRP/CFRP stacks for cognitive tool wear prediction and product quality assessment. *Procedia CIRP* 62:3–8
15. Binsaeid S, Asfour S, Cho S, Onar A (2009) Machine ensemble approach for simultaneous detection of transient and gradual abnormalities in end milling using multisensor fusion. *J Mater Process Technol* 209:4728–4738

16. Wang G, Yang Y, Li Z (2014) Force sensor based tool condition monitoring using a heterogeneous ensemble learning model. *Sensors* 14:21588–21602
17. Wu D, Jennings C, Terpenney J, Gao RX, Soundar Kumara (2017) Comparative study on machine learning algorithms for smart manufacturing: tool wear prediction using random forests. *J Manuf Sci Eng*, 139(7):1–9

# Toughness Property Evaluation of Additive Welded Low Carbon Steel Weldments



Mohd Durvesh Mohiuddin and S. Rasool Mohideen

**Abstract** This paper investigates the impact toughness of low carbon steel weldments produced by the WAAM technique along with the microstructure analysis and hardness survey. The properties are compared with the properties of AISI 1018 steel which is the conventionally rolled steel plate with matching chemical composition. Additive welded specimens were made by GMAW additive welding technique using ER70S-6 electrode (Copper-coated MS wire). The conventional Charpy impact test was performed on the specimens extracted from the additively manufactured bar as per ASTM E23-18 and the microstructure analysis was carried with optical microscopy. Microstructure and chemical composition of both the additive welded and as received specimens indicate relatively homogeneous material properties. An interestingly predominant variation in toughness and hardness was observed between the specimens, though a significant variation in the microstructure is not observed. In general, the results indicate that the additive welding process is capable of producing components with good toughness property when compared to the conventional steel counterpart.

**Keywords** Additive welding · Toughness · Microstructure · Mechanical properties · Low carbon steel

## 1 Introduction

American Society for Testing and Materials (ASTM) refers additive manufacturing (AM) as a material joining process to make objects from 3D model data, building layer upon layer, which is opposite to subtractive manufacturing [1, 2]. Additive layer manufacturing involves the deposition of metal using powder or wire feed through protected atmosphere. This technique focuses on zero wastage to manufacture near net shape objects with min. finishing operation and without need for complex tooling, moulds, and dies.

---

M. D. Mohiuddin (✉) · S. R. Mohideen  
Department of Mechanical Engineering, B.S. Abdur Rahman Crescent Institute of Science & Technology, Vandalur, Chennai 600048, India  
e-mail: [durvesh88@gmail.com](mailto:durvesh88@gmail.com)

Additive layer manufacturing method uses electron beam melting (EBM) [3–5], laser beam deposition (LBM) [6–8], plasma additive manufacturing (PAM) [9], gas tungsten arc welding (GTAW) [10], and gas metal arc welding (GMAW) [11]. Among these, manufacturing industry is getting attracted with arc-based additive manufacturing technique due to its potential to manufacture large metal component in short production lead time with low cost. Interestingly, for additive manufacturing large components, arc welding has been widely used over the past three decades due to its unlimited build envelope with higher deposition rates and lower capital investment [12]. A significant amount of work has been done to produce parts by additive welding using layer-by-layer weld deposition technique. Until now, this technology is not fully automated. Moreover components produce by WAAM technique requires metal removal, and it can be as little as 1 mm in order to obtain surface finish [13]. There is no specific commercial arc-based additive manufacturing system available in market which can produce parts by wire arc additive manufacturing from CAD model [14].

In the field of various industrial fabrications, an arc heat source is used as it has advantages features, such as low cost and increase productivity. Deposition of metal in additive manufacturing technique can be achieved with various arc welding processes (GMAW, GTAW & PAW). EBM, SLM, laser cladding, powder sintering, among are other techniques [15]. The criteria for adopting additive manufacturing process are determined by geometry of the component. Small components having complex geometry require low deposition rates, thus electron beam or laser process is more desirable whereas many require processes with higher deposition rates, such as arc welding [16]. Recent studies revealed that compared to conventional methods of machining from forged and cast materials, additive manufacturing is more economical and eco-friendly [17, 18]. To study the material characterization of additive welded components, full density weldment of the selected material has been successfully produced using gas metal arc welding (GMAW).

The wire arc additive manufacture (WAAM) process melts the electrode wire onto a base plate or previously deposited layers at a controlled wire feed rate using electric arc or plasma arc. The major advantage of arc-based additive manufacture produces large and near-net shaped components with a high deposition rate, at an acceptable cost within a reasonable time, as compared to powder-based additive manufacturing. But, optimized molten material transfer mode can be achieved by recent developments that have synchronized both wire-feeder and power source. This process is known as “mechanically assisted droplet deposition”, which is applied in controlled short-circuit by retracting the wire from the short-circuiting [19, 20]. However, parts produced by wire arc additive manufacturing require less surface machining, because of lower-dimensional accuracy and surface roughness [21].

Practically, WAAM technique can produce components of variable dimensions by changing different welding process parameters, such as voltage (V), current (A), wire-feed (WF), and speed of torch (TS). Although there is an upper limit for bead thickness, for a thickness larger than one bead, it can be achieved by laying beads parallel to each other, which totals the sum of all beads minus the overlap. As an

alternate, another technique to achieve larger thickness is the use of oscillation of welding torch.

Several studies have been performed on the fabrication of different materials such as Ti-6Al-4V using the WAAM technique but not on steels even though it is the most commonly used material in various industrial sectors [22, 23]. Therefore, the aim of this study is to fabricate low carbon low alloy steel using (ER 70S-6) electrode by WAAM technique and to evaluate the impact toughness and microstructure of weldment produce by WAAM.

## 2 Experimental Procedure

### 2.1 Gas Metal Arc Welding (GMAW)

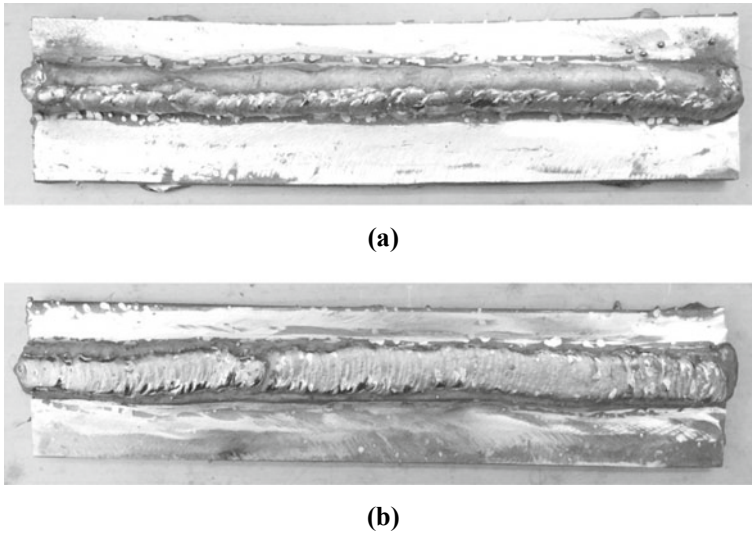
Gas metal arc welding can be used to weld a wide range of metal such as steel, aluminium and to weld unalloyed, low-alloyed, and high-alloyed materials at any position. Weld quality achieved by gas metal arc welding depends on voltage (V), current (A), wire-feed speed (Wf), and torch speed (Ts). Hence, control over these process parameters is required to produce a good quality weld.

Gas metal arc welding process was employed to prepare the additive weldments with a build-up length of 200 mm, width 12 mm, and height 12 mm. The process parameters adapted in the weldment preparation are given in Table 1.

Gas metal arc welding is done using ER70S-6 electrodes for metal deposition. Layer by layer deposition of metal requires careful consideration, the slight movement of the operator's hand and the corresponding changes in arc length are unavoidable in GMAW. This can lead to a change in the electrode melting rate and hence may affect the consistency of the weld. To prevent any such fluctuation in the melting rate, the welding power source best suited for the purpose is of the constant current type. To produce a sound weld with maximum penetration, flat welding is done to produce weldments. Figure 1a shows the weldment produced using a parallel bead deposition strategy and Fig. 1b shows the weldment produced using oscillation bead deposition strategy.

**Table 1** Welding process parameters

Voltage	26–28 V
Current	130–150 A
Wire-feed speed	2.5 m/min
Torch speed	0.25–0.30 m/min
Shielding gas	CO <sub>2</sub>
Electrode	ER70S-6
Electrode wire diameter	1.2 mm
Post-weld heat treatment if any	Atmospheric air cooling



**Fig. 1** **a** Weldment produced using parallel bead deposition strategy. **b** Weldment produced using oscillation bead deposition strategy

**Table 2** Chemical composition mild steel specimen and welded specimen

Element→ Specimen↓	C%	Mn%	Si%	S%	P%	Cr%	Ni%	Mo%	Cu%	V%
Mild steel specimen	0.154	0.904	0.455	0.013	0.022	0.015	0.017	0.003	0.078	0.001
Welded specimen	0.138	0.868	0.496	0.15	0.019	0.018	0.011	0.002	0.090	0.001

## 2.2 Chemical Composition

Table 2 shows the chemical composition of the mild steel specimen and additive welded specimen.

## 2.3 Charpy Impact Test

The impact toughness properties of weldments were evaluated using the Charpy impact test. The impact toughness is a measure of energy absorbed during fracture. It is measured using the notched bar impact specimen  $55 \times 10 \times 10$  mm. The specimen is prepared as per ASTM E23-18 and specimen geometry is given Fig. 2.

The specimens in required numbers were extracted from additive weld build-up plates which were produced using both parallel bead deposition strategy and oscillation bead deposition strategy, and mild steel plate for comparative study.

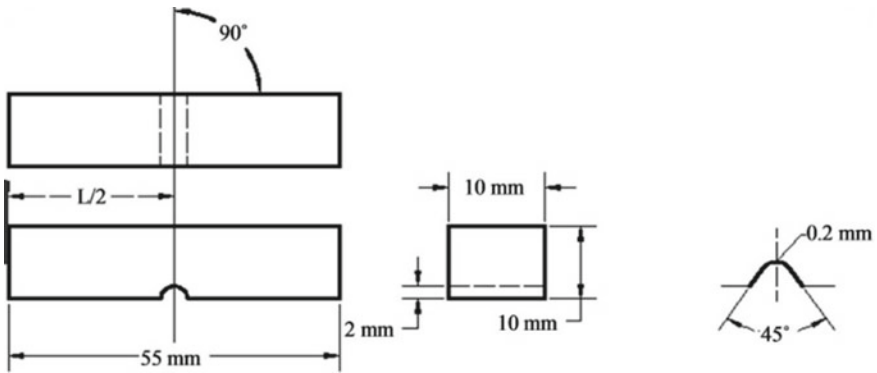


Fig. 2 Geometry of Charpy test specimen as per ASTM E23-18

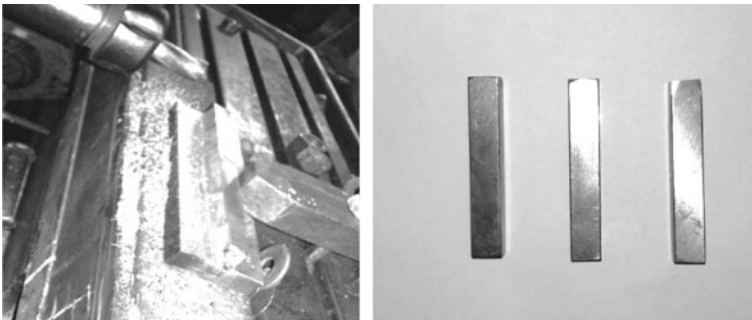


Fig. 3 Specimen preparation from wire arc additive manufacture plate

### 2.4 Hardness Test

Hardness measurements were taken using static indentation procedure with ball indenter 2.5 mm mounted on Brinell hardness testing machine. To measure the hardness of the test specimens, the Brinell hardness test is carried out by applying 187.5 Kg load with ball indenter 2.5 mm on surface of the specimen using IS 1500:2005 test procedures.

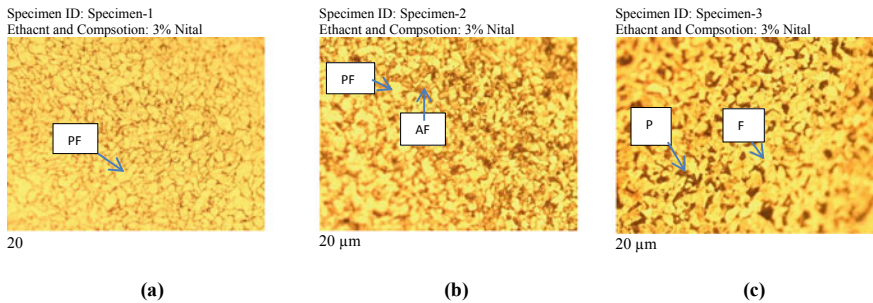
## 3 Results and Discussion

### 3.1 Microstructure

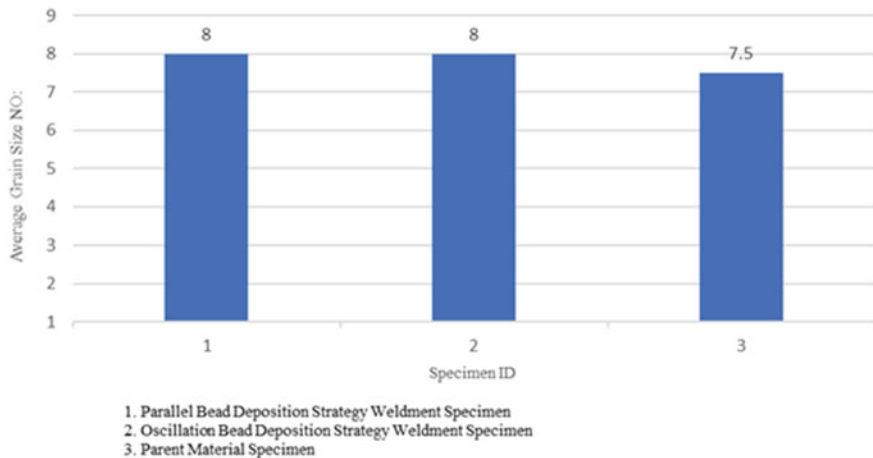
The microstructural examination was carried out at 200X magnification using an optical microscope equipped with a digital camera that was used to study the



microstructure. ASTM E112 standards are used for analysis. The etchant used is 3%Nital. Figure 4a shows the microstructure of weldments produced by parallel bead deposition strategy which consists of lesser pearlite and more ferrite regions when compared to parent metal; Fig. 4b shows the microstructure of weldments produced by oscillation bead deposition strategy which consists of some amount of acicular ferrite along polygonal ferrite and pearlite structures. The average ASTM grain size number 8 for both parallel bead deposition strategy and oscillation bead deposition strategy, Fig. 4c shows the microstructure of parent metal which consists of Ferrite, Pearlite uniformly distributed with average ASTM grain size number 7.5. A similar microstructure appeared in past studies done for WAAM fabricated ER 70S-6 additive welded wall [22]. Also, Fig. 5 shows the average grain size for various specimens.



**Fig. 4** a Microstructure of weldment produced by parallel bead deposition strategy. b Microstructure of weldment produced by oscillation bead deposition strategy. c Microstructure of parent metal



**Fig. 5** Bar chart showing average grain size of various specimens

**Table 3** Hardness values of weldment specimen and parent material specimen

S. No.	Specimen	Observed values (BHN)			
		Impression 1	Impression 2	Impression 3	Average
1	Parallel bead deposited weldment	131	129	131	130.33
2	Oscillation bead deposited weldment	138	135	135	136
3	Parent material specimen	229	224	224	225.67

### 3.2 Hardness Measurement

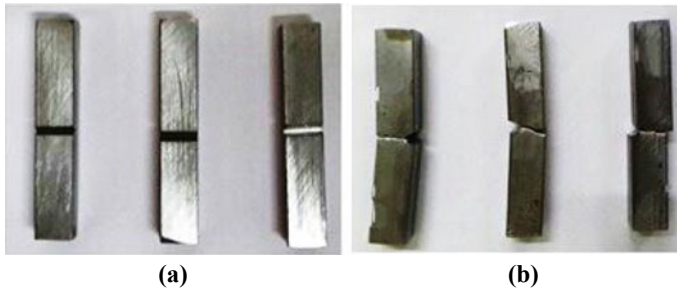
The observed hardness values of both the weldment specimens produced by parallel bead deposition strategy and oscillation strategy are given in Table 3. The average hardness of the weldment specimen produced by the parallel bead deposition strategy is around 130 BHN; the weldment specimen produced by the oscillation bead deposition strategy is around 136 BHN and for the parent material is around 225.67 BHN.

### 3.3 Toughness Measurement

The impact toughness of both the weldment specimens produced by parallel bead deposition strategy and oscillation strategy has been higher compared to those of parent material specimens. In the case of parallel bead deposition strategy, presence of more ferrite may be the reason for higher toughness value whereas in case of oscillation bead deposition strategy, acicular ferrite regions would have caused increase in toughness than the parent metal. The impact toughness values are presented in Table 4. The average impact toughness of 152, 120, and 8.67 J has been respectively produced by parallel bead deposition strategy, oscillation bead deposition strategy, and parent metal. Figure 6a shows the extracted specimens from weldment before

**Table 4** Impact values of weldment specimen and parent material specimen

S. No.	Specimen	Observed values (J)			
		Impact 1	Impact 2	Impact 3	Average
1	Parallel bead deposited weldment	144	152	160	152
2	Oscillation bead deposited weldment	70	150	140	120
3	Parent material specimen	10	8	8	8.67



**Fig. 6** **a** Extracted specimens from weldments before impact test. **b** Broken specimens after impact test

performing the impact test, and Fig. 6b shows the broken specimens after performing the Impact test.

## 4 Conclusion

This paper has highlighted the wire arc additive manufacturing of low carbon low alloy steel additive welded walls using ER 70S-6 electrode for parallel bead deposition strategy and oscillation bead deposition strategy. The following conclusion can be drawn:

1. Charpy impact toughness of both the weldment specimens produced by parallel bead deposition strategy and oscillation bead deposition strategy has relatively higher toughness and lower hardness compared to the parent material. This is because of grain refinement in wire arc additive manufacturing due to multiple thermal treatments in additive welding. Therefore, it can be concluded that additive welded components have higher toughness compared to its parent material.
2. During additive welding, contribution of cooling intervals between the consecutive layers is to form similar microstructure in different layers of additive welded wall which contributes to the consistency of mechanical properties.
3. There is a grain refinement in both the weldment which has led to increase in toughness with a decrease in hardness.

**Acknowledgements** We gratefully acknowledge B.S. Abdur Rahman Crescent Institute of Science & Technology for supporting the presented investigations.

## References

1. ASTM-International (2012) ASTM Standard F2792-12a: standard terminology for additive manufacturing technologies
2. Ivanova O, Williams C, Campbell T (2013) J Additive manufacturing and nanotechnology: promises and challenges. Rapid Prototype 353–364
3. Wang P, Tan X, Nai MLS, Shu BT, Wei J (2016) Spatial and geometrical-based characterization of microstructure and Microhardness for an electron beam melted Ti-6Al-4V component. Mater Des 95:287–295. <https://doi.org/10.1016/j.matdes.2016.01.093>
4. Hinojos A, Mireles J, Reichardt A, Frigola P, Hosemann P, Murr LE, Wicker RB (2016) Joining of Inconel 718 and 316 stainless steel using electron beam melting additive manufacturing technology. Mater Des 94:17–27. <https://doi.org/10.1016/j.matdes.2016.01.041>
5. Wanjara P, Brochu M, Jahazi M (2007) Electron beam freeforming of stainless steel using solid wire feed. Mater Des 28:2278–2286. <https://doi.org/10.1016/j.matdes.2006.08.008>
6. Farshidianfar MH, Khajepour A, Gerlich AP (2016) Effect of real time cooling rate on microstructure in laser additive manufacturing. J Mater Process Technol 231:468–478. <https://doi.org/10.1016/j.jmatprotec.2016.01.017>
7. Wang F (2012) Mechanical property study on rapid additive layer manufacture Hastelloy X alloy by selective laser melting technology. Int J Adv Manuf Technol 58:545–551. <https://doi.org/10.1007/s00170-011-3423-2>
8. Zhang YN, Cao X, Wanjara P, Medraj M (2014) Tensile properties of laser additive manufacture Inconel 718 using filler wire. J Mater Res 29:2006–2020. <https://doi.org/10.1557/jmr.2014.199>
9. Lin JJ, Liu YX, Xu BS, Sun Z, Li ZG, Wu YX (2016) Microstructural evolution and mechanical properties of Ti-6Al-4V wall deposited by pulsed plasma arc additive manufacturing. Mater Des 102:30–40. <https://doi.org/10.1016/j.matdes.2016.04.018>
10. Baufeld B, Biest OVD, Gault R (2010) Additive manufacturing of Ti-6Al-4V components by shaped metal deposition: microstructure and mechanical properties. Mater Des 31:S106–S111. <https://doi.org/10.1016/j.matdes.2009.11.032>
11. Zhao H, Zhang G, Yin Z, Wu L (2011) A 3D Dynamic analysis of thermal behaviour during single-pass multi-layer weld-based rapid prototyping. J Mater Process Technol 211:488–495. <https://doi.org/10.1016/j.jmatprotec.2010.11.002>
12. Ding D, Pan Z, Cuiuri D et al (2015) Wire-feed additive manufacturing of metal components: technologies, developments and future interests. Int J Adv Manuf Technol 81:465–481
13. Kapustha N, Harris ID (2014) Exploring Arc welding for additive manufacturing of titanium parts. Weld J 93:32–35
14. twi-global (2018) Arc-based additive manufacturing. Accessed on <https://www.twi-global.com/technical-knowledge/job-knowledge/arc-based-additive-manufacturing-137/>
15. Frazier EW (2014) Metal additive manufacturing: a review. J Mater Eng Perform 23:1917–1928
16. Silva RJ, Barbosa GF, Carvalho J (2015) IFAC-PapersOnLine 48–3(2015):2318–2322
17. Williams SW, Martina F (2015) Wire+arc additive manufacture. Mater Sci Technol IoM. <https://doi.org/10.1179/1743284715Y.0000000073>
18. Frazier WE (2012) Metal additive manufacturing: a review. F Mater Eng Perform 23:1917–1928
19. Huisman G (1999) Introduction of new MIG process—Advantages and possibility. In: Proceeding of conference, IIW 1999 Doc. 212
20. Wu Y, Kovcevic R (2002) Mechinal assisted dropted transfer process in gas metal arc welding. Proceeding of the Institution of Mechanical Engineering. J Eng Manuf 216(B):555–564
21. Brandl E, Baufelt B, Leyens C (2010) Additive manufactured Ti-6Al-4V using welding wire: comparison of laser and arc beam deposition and evaluation with respect aerospace material specifications. Phys Procedia 5:595–606
22. Haden CV, Zeng G, Carter FM et al (2017) Wire and arc additive manufactured steel: tensile and wear properties. Additive Manuf 16:115–123
23. Hu R, Chen X, Yang G et al (2018) Metal transfer in wire feeding based electron beam 3D printing: modes, dynamics, and transition criterion. Int J Heat Mass Transfer 126:877–887

# Performance Enhancement of Solar Water Heater Incorporated with Latent Heat Storage Material



M. Ajees Aboobucker, N. Muthu Saravanan, R. Mayilraj Sathish, S. Aakhash, and M. Gunasekaran

**Abstract** The present work has been undertaken to study the effect of latent heat storage materials in solar water heater with flat plate collector, and the numerical results observed from the open-air measurements were analyzed. Two configurations have been explored for solar water heater namely without PCM and with PCM. The preferred energy storage material was sodium thiosulfate pentahydrate as a PCM and tested under various operating conditions. The water heater was evaluated for the different quantity of materials and the energy competence, and the length of time the solar water heater that can supply hot water has been compared before and after using of PCM in the tank. Also, it is scrutinized that the heater with PCM can offer hot water with precise heat at longer time. Overall efficiency of solar water heater increases 34.5% with use of phase change material.

**Keywords** Water heater · Renewable energy · Latent heat storage · Solar collector

## Nomenclature

### Symbols

HTF Heat Transfer Fluid  
SWH Solar Water Heater  
TES Thermal Energy Storage  
PCM Phase Change Material

---

M. Ajees Aboobucker (✉) · N. Muthu Saravanan · R. Mayilraj Sathish · S. Aakhash  
National Engineering College, K.R. Nagar, Kovilpatti, Tamilnadu 628503, India  
e-mail: [Ajees619@gmail.com](mailto:Ajees619@gmail.com)

N. Muthu Saravanan  
e-mail: [saravananmech@nec.edu.in](mailto:saravananmech@nec.edu.in)

M. Gunasekaran  
Anna University Regional Campus, Tirunelveli, Tamilnadu 627007, India

## 1 Introduction

Water is an essential component for all living things. For healthy purposes, the raw water must be heated to remove the unwanted impurities. By heating the water, the sediments were settled down, and the water becomes pure and fit for human health. Generally, the water is heated by burning the wood or fossil fuels. It is not economical and not user-friendly. A solar water heater is a device which utilizes the solar energy to heat the water and supplies the hot water without affecting the atmosphere. A renewable source of energy is the most promising one to overcome the limitations and be an eco-friendly one. In the current work, a newly modified solar water heater was designed and fabricated. Its performance was investigated under the normal operating conditions in the open atmosphere. The main drawback of solar-assisted application was the energy demand in the period of afternoon. In order to enhance the efficiency of solar water heater, thermal energy storage material was inbuilt within the system. In this way, latent heat storage material was selected to increase the temperature of water during the sun offset time. Touaba et al. [1] used a novel solar water heater. A flat plate collector was attached as an additional unit to increase the performance of water heater. The waste engine oil was preferred as a thermal energy storage medium in their work. It acts as an energy absorber and heat transfer fluid in the system. They investigated that the result was good as 65% of heating efficiency was attained when the flat plate collector is with solar water heater and waste engine oil as a heat transfer medium. Mahfuz [2] et al. carried out an experimental work to investigate the effect of thermal energy storage system with PCM in a shell and tube solar water heating applications. They used paraffin wax as a latent heat storage material in the heater. With different flow rates of heat transfer fluid, the solar water heater efficiency were analyzed and compared. Finally, the overall life cycle cost was compared with flow rates and concluded that the life cost and exergy efficiency were reduced with increasing the flow rates. Xue [3] performed an experimental work in domestic solar water heater to increase the efficiency of water heater which is integrated with a solar collector and is coupled with phase change materials. For the same collector area, they compared the output of heater coupled with solar collector and PCM to that of the water heater with evacuated tube collector. The demonstration results were compared for the energy efficiency variation with the tank volume and collector area ratio. Fazilati and Alemrajabi [4] uses a jacketed shell type heat exchanger as a water-heating system. They studied the effect of the intensity of solar radiation likely weak, medium, and strong characteristics. The energy density was increased up to 39% by using a PCM in the tank. The exergy efficiency was increased to 16%. Also the length of time by which the temperature of water could be maintained was observed as 25% higher than conventional solar water heater. Bouadila et al. [5] experimentally carried out a work with latent heat storage in the flat plate collector with solar water heater. The simple modification was that the two rectangular cavities were made behind the flat plate collector's absorbers plate surface. The two rectangular-shaped cavities were filled by the commonly used latent heat storage materials such as phase change materials. The performance

of flat plate collector incorporated with cavities and PCM was analyzed, and its efficiency was improved. The thermal stratification inside the PCM filled cavity was studied. They concluded that the outlet temperature was not affected, and the heater provides the uniform heat of water for five hours after the sunset. Abdelsalam [6] developed and validated a numerical model to analyze the effect of sensible heat storage materials and hybrid energy storage with phase change materials coupled with domestic water heating applications. By using the immersed heat exchanger with the water heater, the mechanism of direct heat exchange and the indirect heat exchange were compared. They experimentally prove that the efficiency of water heater was enhanced by the direct heat exchange mechanism only. Li and Zhai [7] designed a storage system for mid-temperature application using 97% of erythritol and 3 wt% of expanded graphite as a composite phase change material (PCM) filled in aluminum pipes. The experimental and numerical analysis concluded that the addition of external graphite increases thermal conductivity by 241.41% than pure erythritol, and composited PCM exhibits higher storage efficiency. Xiao et al. [8] selected sodium acetate trihydrate (SAT) as a phase change material by analyzing its parameter using transient system simulation software (TRNSYS). They carried out the process with different systems like series, parallel, and single tank system. On comparing the efficiency, he concluded by saying that the series system with solar fraction of 5–12% higher than the parallel system and 30% higher than the single tank system. Mehta et al. [9] selected stearic acid as a phase change material for horizontal shell and tube-type latent heat storage unit (LHSU). Due to natural convection, the upper half melts faster than the lower half. Deliberately, the rate of melting of the lower half can be increased by installing heat transfer fluid (HTF) or multi-tube configuration. When the HTF temperature is increased to 85 °C, the storage of energy takes place at a faster rate, and melting time is reduced significantly. Pourakabar and Darzi [10] carried out a numerical study where the PCM is melted fewer than nine different cases with different shapes of shells and arrangements. By changing the number of arrangements the rate of melting and solidification has increased. But he noticed some significant effect in melting and solidification process, so he inserted copper foam inside the PCM. As a result, the melting and solidification rate has increased to 92% and 94%, respectively. Gao et al. [11] investigated the efficiency of the PCM in centralized hot water systems. The Paraffin wax with expanded graphite is taken under consideration as a PCM to test the properties of heat storage, thermal insulation, and heat releasing rate with materials having melting point of 55 and 60 °C. After analyzing the heat transfer rate and rate of heat storage, the 60 °C PCM is more efficient than 55 °C PCM in centralized hot water system.

The objective of the present work is to investigate the possibility of enhancing the performance of a solar water heater by using TES. The operational modes are without PCM and with pure PCM. Lot of research works have been done by introducing the TES coupled with solar concentrating collectors. It needed to change the entire collector setup. In addition, paraffin wax was widely used as a latent heat storage material. To the best of the author's knowledge, no study was carried out by using sodium thiosulfate pentahydrate as energy storage material for solar water heating

system. Comprehensive investigation and laborious works are still needed to clarify the feasibility of using PCM in domestic solar water heaters.

## 2 Methodology

The experimental setup is open-loop conventional passive solar energy system with natural circulation, which is generally used to provide domestic hot water requirements in buildings. It consists of solar collectors, hot water storage tank, and measurement systems, and photograph of the experimental setup is shown in Fig. 1. The flat plate solar collector with fixed plate of  $1.425 \text{ m} \times 0.925 \text{ m} \times 0.11 \text{ m}$  have single cover glass and black-painted absorber plate.

Solar collectors faced to the south also have the net absorption area of  $1.32 \text{ m}^2$  and the tilt angle of  $9.5^\circ$  with horizontal plane. Insulated hot water storage tank has the maximum volume of 50 l. The system has a capacity of 45 l and water level in the storage tank 0.7 m above from collector inlet. All of the pipes and fittings used in the experimental system were also insulated. The storage tank contains six cylindrical copper tube having a length of 0.45 m, inner diameter of 0.015 m, and 0.6 mm thickness. Each container have a PCM mass of 83 g and totally 500 gm. PCM filled in the container lower than total volume of container to minimize various problems detected during the melting and solidification of PCM. The measurement system includes a total of six digital thermometer: One at the absorber plate and one top of the glass cover, three distributed at the upper, middle, and lower sections of the storage tank, one thermometer inserted in a PCM container of the tank, and one to measure the ambient air temperature (Fig. 2).

During charging process, solar collector continuously absorbs solar radiation to heat water in the collector pipe. According to thermosiphon effect, hot water in the collector move upward to top of the storage tank, cold water in the storage tank



**Fig. 1** Experimental setup of solar water heater





**Fig. 2** Photographic view of the water container

move to bottom of collector, and this process continued. Hot water in the storage tank exchange heat to the PCM container. Therefore, PCM can store the heat energy until charging period. During the discharging period, temperature of the hot water decreases below melting point of the PCM, due to heat transfer from PCM to storage water. During this period, experiment is to measure varying temperature and solar intensity data for every ½ hours' time period and without consumption of water. This same experiment is conducted to take more than three trials for each case of with and without condition and comparing result of with and without condition based on approximately similar intensity data (Tables 1, 2 and 3).

**Table 1** Properties of sodium thiosulfate pentahydrate

Melting temperature, $T_m$	48.5 °C
Heat of fusion, $H$	210 kJ/kg
Thermal conductivity, $k$	0.57 W/m K
Density, $\rho$	1667 kg/m <sup>3</sup>
At solid	1.46 kJ/kg K
At liquid	2.38 kJ/kg K

**Table 2** Specification of solar collector

Flat plate solar collector		
Collector	Dimension	Material
Runner tube	9.5 mm inner dia $\times$ 1110 mm length—10 tubes	Copper
Riser tube	28 mm inner dia $\times$ 1180 mm length—2 tubes	Copper
Absorber plate	1400 mm $\times$ 910 mm $\times$ 0.4 mm	Aluminum
Collector box	1425 mm $\times$ 925 mm $\times$ 110 mm	Wood
Insulation	3/4 in. thickness	Thermocol
Transparent cover	5 mm thickness	Glass
Aperture area	1.32 m <sup>2</sup>	—

**Table 3** Specification of solar water heater

S. No.	Parameters	Values
1	Collector area, $A_c$	1.425 $\times$ 0.925 m <sup>2</sup>
2	Thickness of collector, $l_3$	0.11 m
3	Center-to-center tube spacing, $W$	0.06 m
5	Outside diameter of the tube, $D$	9.5 mm
6	Thermal conductivity of tube, $K_t$	386 W/m K
7	Tube thickness, $m_t$	0.6 mm
8	Plate thickness, $m_p$	0.404 mm
9	Thermal conductivity of plate, $K_p$	204 W/m K
10	Space between the absorber plate and glass, $L$	6 mm
11	Bottom insulation thickness, $l_i$	1.9 cm
12	Thermal conductivity of bottom insulation, $K_i$	0.035 W/m K
13	Side insulation thickness, $l_i$	1.25 cm
14	Thermal conductivity of side insulation, $K_i$	0.115 W/m K
15	Emissivity of glazing, $\epsilon_g$	0.88
16	Emissivity of absorber plate, $\epsilon_p$	0.95
17	Absorptance of the absorber plate, $\alpha$	0.96
18	Transmittance of the cover plates, $\tau$	0.95

### 3 Results and Discussion

#### 3.1 Hourly Variation of Various Temperature in SWH Without PCM

Figure 3 shows the relation between time and temperature of storage water, ambient, absorber plate, and glass cover in solar water heater working without PCM condition.

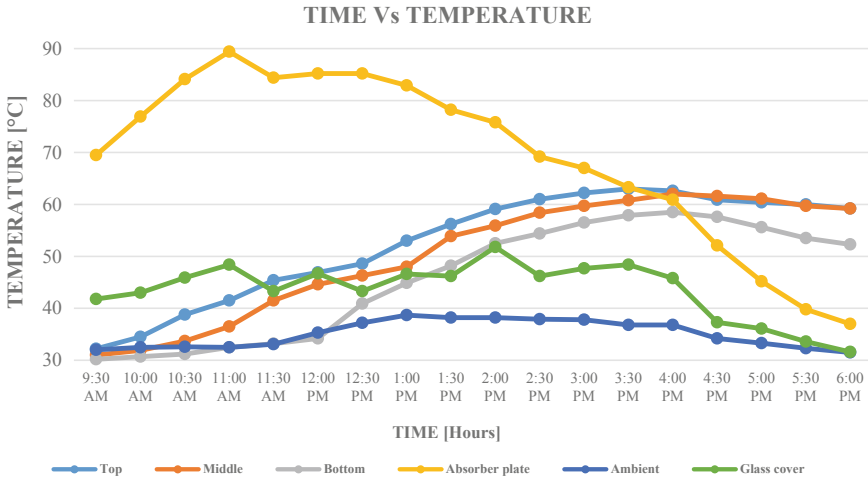


Fig. 3 Temperature variation of water heater without PCM

During the period of time temperature of water, ambient and glass cover gradually increased than decreased according to the solar intensity. But absorber plate temperature curve has sudden rise and drop due to the cloud appearance. Maximum water and ambient temperature is 63 °C and 38.7 °C attained at time of 3:30 pm and 1:00 pm, respectively.

### 3.2 Hourly Variation of Various Temperatures in SWH with PCM

Figure 4 shows that the relation between time and temperature of storage water, ambient, absorber plate, and glass cover in solar water heater working with PCM condition. During the period of time temperature of water, ambient and glass cover gradually increased than decreased according to the solar intensity. But water temperature increases gradually up to melting point (48.8 °C) of PCM and after that increases slowly because of phase change that occurs in the PCM. Maximum water, PCM, and ambient temperature is 59.2, 52.9 °C, and 38.5 °C attained at 3:30 pm, 3:00 pm, and 12:00 pm, respectively.

### 3.3 Charging Process

Figure 5 shows the temperature distribution of water during the charging period. Temperature water increased approximately linear in without PCM condition. But

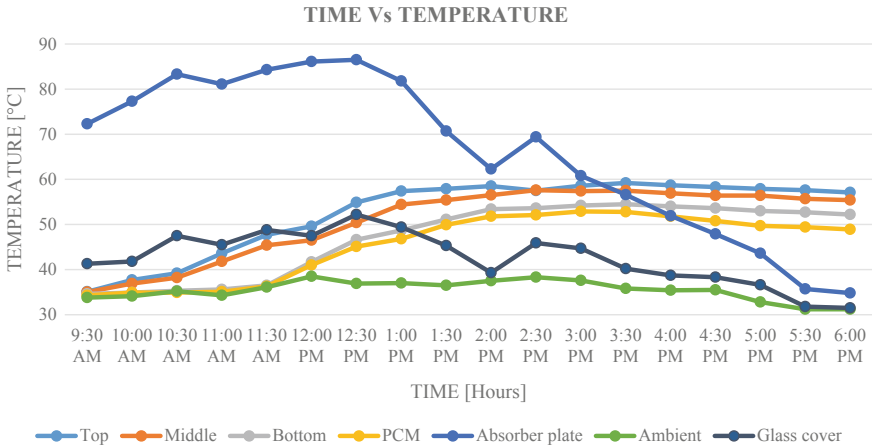


Fig. 4 Variation of temperatures in water heater with PCM

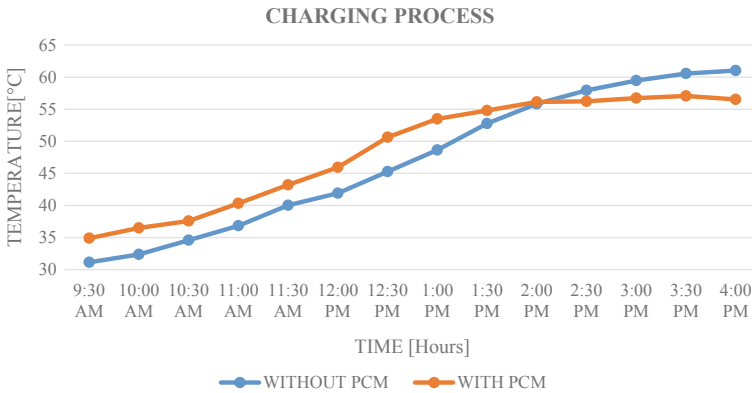


Fig. 5 Charging characteristics

with PCM condition temperature increased linear up to melting point of PCM than increase slowly. Average temperature water increased from 31.13 to 61.03 °C in 6 h at without PCM condition. For with PCM condition, average temperature water increased from 34.9 to 57.06 °C in 6 h.

### 3.4 Discharging Process

From the graphical result, it was showed that the temperature distribution of water during the discharging period. Average temperature of water decreased from 60

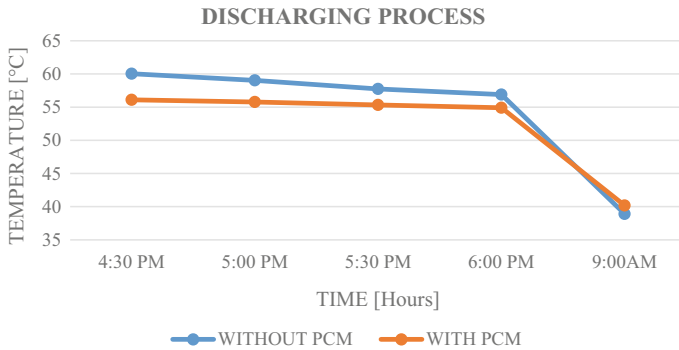


Fig. 6 Discharging characteristics

to 38.9 °C in 16.5 h at without PCM condition. For with PCM condition, average temperature of water decreased by 56.1–40.17 °C in Fig. 6

### 3.5 Useful Heat Gain During Charging Process

Figure 7 show the variation of useful heat gain during period of charging. Maximum useful heat gain attains in charging process for without and with condition is 778.78 and 885.55 kJ at the time of 1:30 PM and 12:30 PM (Tables 4, 5 and 6).

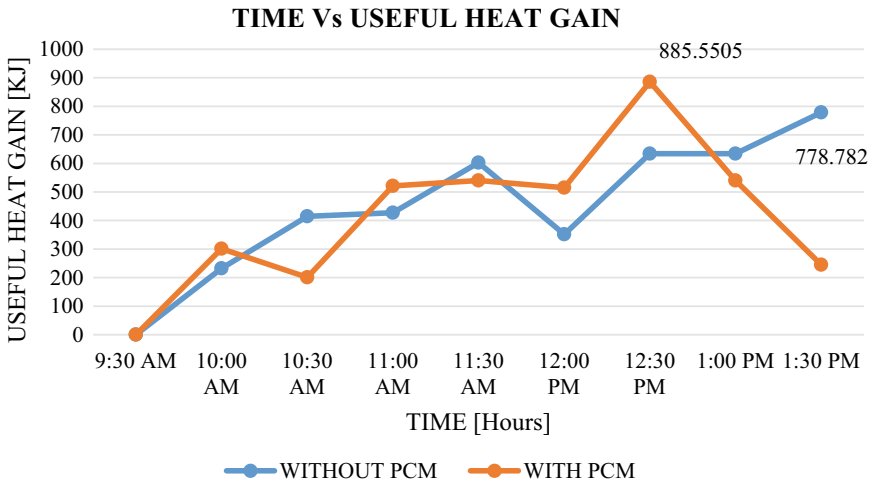


Fig. 7 Heat gain in water heater

**Table 4** Temperature variations without PCM

Time (h)	Solar intensity ( $W/m^2$ )	Temp. of water in the tank			Temp. of absorber plate ( $^{\circ}C$ )	Ambient temp. ( $^{\circ}C$ )	Temp. of glass cover top ( $^{\circ}C$ )
		$T_{top}$ ( $^{\circ}C$ )	$T_{mid}$ ( $^{\circ}C$ )	$T_{bottom}$ ( $^{\circ}C$ )			
9:30 AM	503	32.2	31	30.2	69.5	32	41.8
10:00 AM	593	34.5	31.9	30.7	76.9	32.5	43
10:30 AM	646	38.8	33.7	31.2	84.1	32.6	45.9
11:00 AM	686	41.5	36.5	32.5	89.4	32.5	48.4
11:30 AM	759	45.4	41.5	33.2	84.4	33.1	43.3
12:00 PM	770	46.9	44.6	34.2	85.2	35.3	46.7
12:30 PM	780	48.6	46.3	40.9	85.2	37.2	43.3
1:00 PM	775	53	48	44.9	82.9	38.7	46.6
1:30 PM	749	56.2	53.9	48.2	78.2	38.2	46.2
2:00 PM	695	59.1	55.9	52.5	75.8	38.2	51.8
2:30 PM	659	61	58.4	54.4	69.2	37.9	46.2
3:00 PM	550	62.2	59.7	56.5	67	37.8	47.7
3:30 PM	483	63	60.8	57.9	63.3	36.8	48.4
4:00 PM	375	62.6	62	58.5	60.9	36.8	45.8
4:30 PM	268	60.9	61.6	57.6	52.1	34.2	37.3
5:00 PM	175	60.4	61.1	55.6	45.2	33.3	36.1
5:30 PM	83	60	59.7	53.5	39.8	32.3	33.6
6:00 PM	41	59.2	59.2	52.3	37	31.5	31.6

**Table 5** Temperature variations when PCM is inbuilt

Time (h)	Solar intensity (W/m <sup>2</sup> )	Temp. of water in the tank			Temp. of PCM (°C)	Temp. of absorber plate (°C)	Ambient temp. (°C)	Temp. of glass cover top (°C)
		$T_{top}$ (°C)	$T_{mid}$ (°C)	$T_{bottom}$ (°C)				
9:30 AM	512	35.1	35	34.6	34.3	72.3	33.8	41.3
10:00 AM	613	37.7	36.9	34.9	34.9	77.3	34.1	41.8
10:30 AM	696	39.2	38.2	35.3	34.9	83.3	35.2	47.5
11:00 AM	750	43.6	41.8	35.6	35.1	81.1	34.3	45.5
11:30 AM	779	47.7	45.4	36.5	36.3	84.3	36.1	48.8
12:00 PM	823	49.6	46.5	41.7	41	86.1	38.5	47.5
12:30 PM	833	54.9	50.4	46.6	45.1	86.5	36.9	52.2
1:00 PM	825	57.4	54.4	48.7	46.8	81.8	37	49.4
1:30 PM	824	57.9	55.4	51.1	49.9	70.7	36.5	45.3
2:00 PM	638	58.5	56.5	53.4	51.8	62.3	37.5	39.3
2:30 PM	613	57.5	57.6	53.6	52.1	69.4	38.3	45.9
3:00 PM	506	58.6	57.4	54.2	52.9	60.8	37.6	44.7
3:30 PM	375	59.2	57.5	54.5	52.8	56.6	35.8	40.2
4:00 PM	305	58.7	56.9	54	51.8	51.9	35.4	38.7
4:30 PM	272	58.3	56.4	53.6	50.8	47.9	35.5	38.3
5:00 PM	86	57.9	56.4	53	49.7	43.6	32.8	36.6
5:30 PM	35	57.6	55.7	52.7	49.4	35.7	31.2	31.8
6:00 PM	30	57.1	55.4	52.2	48.9	34.8	31.2	31.5

**Table 6** Comparison of present study with previous published work

Ref. no	PCM used	% Increment	Title of the work
1	Waste engine oil and heat transfer fluid	Temp.—50 °C (<3 h) Mean eff.—65% Max eff. —80%	Experimental investigation of solar water heater equipped with a solar collector using waste oil as absorber and working fluid
2	Paraffin wax	Efficiency increases from 63.88 to 77.41%	Performance investigation of thermal energy storage system with phase change material (PCM) for solar water heating application
3	BaCO <sub>3</sub>	Energy efficiency increases to 52%	Experimental investigation of domestic solar water heater with solar collector coupled phase-change energy storage
4	Paraffin wax in a cylindrical capsule	Energy storage eff. increases to 39%	Phase change material for enhancing solar water heater, an experimental approach
5	Integrated paraffin wax in a rectangular cavities	Energy eff. varied between 25 to 35%	Enhancement of latent storage material in a rectangular cavity: Solar water heater case study
6	Paraffin and fatty acids	Solar fraction 18–23% > indirect system	Hybrid thermal energy storage with phase change materials for solar domestic water applications: Direct versus indirect heat exchange systems
7	Erithritol	Energy storage eff. increases to 40.17%	Experimental investigation and theoretical analysis on a mid-temperature solar collector/storage system with composite PCM
8	Disodium hydrogen phosphate dodecahydrate	Solar fraction increased by 30%	Improvement of the efficiency of solar thermal energy storage systems by cascading a PCM unit with a water tank

(continued)



**Table 6** (continued)

Ref. no	PCM used	% Increment	Title of the work
10	N-eicosane	Melting and solidification rate improved by 70 and 44%	Enhancement of phase change rate of PCM in cylindrical thermal energy storage
11	Paraffin wax in a stainless steel ball	Solar fraction increases to 75%(55 °C) 80%(60 °C)	Research on the application of phase-change heat storage in centralized solar hot water system
Present work	Sodium thiosulfate pentahydrate	34.5%	

## 4 Conclusion

From the experimental analysis, it is concluded that the use of PCM in solar water heater helps to reduce cooling rate of water; thus, it enhances the maximum utilization of solar energy and hence improves its efficiency. The following points are noteworthy:

- Selection of suitable phase change material for solar water heater is done. It has melting point of 48.5 °C and has higher latent heat fusion which is 210 kJ/kg.
- Maximum water temperature attained in solar water heater without and with PCM condition is 63 °C and 59.2 °C, respectively.
- Maximum charging and discharging temperature for solar water heater without phase change material is 29.9 °C and 21.13 °C, respectively.
- Maximum charging and discharging temperature for solar water heater with phase change material is 21.63 °C and 15.93 °C, respectively, and in water temperature 5–6 °C advantage.
- Overall efficiency of solar water heater increases 34.5% with use of phase change material.
- Percentage of energy stored in sensible and latent heat form in PCM is 12.9% and 87.06%, respectively.
- Difference between theoretical and actual efficiency is 31.58%.

**Acknowledgements** It is acknowledged that M. Gunasekaran was involved in fabrication work. M. Ajees Aboobucker and N. Muthu Saravanan wrote the manuscript. R. Mayilraj@Sathish and S. Aakhash done the correction/grammatical error.

## References

1. Touabaab O, Prof. Cheikh MSA, El-Amine Slimani M Ph.D., Bouraiou A Ph.D., Ziane A Ph.D., Necaibia A, Ph.D., Harmim A (2020) Experimental investigation of solar water heater equipped with a solar collector using waste oil as absorber and working fluid. *Sol Energy* **199**:630–644
2. Mahfuz MH, Anisur MR, Kibria MA, Saidur R, Metselaar IHSC (2014) Performance investigation of thermal energy storage system with Phase Change Material (PCM) for solar water heating application. *Int Commun Heat Mass Transfer* **57**:132–139
3. Sheng Xue H (2016) Experimental investigation of a domestic solar water heater with solar collector coupled phase-change energy storage. *Renew Energy* **86**:257–261
4. Fazilati MA, Alemrajabi AA (2013) Phase change material for enhancing solar water heater, an experimental approach. *Energy Convers Manage* **71**:138–145
5. Bouadila S, Fteïti M, Oueslati MM, Guizani A, Farhata A (2013) Enhancement of latent heat storage in a rectangular cavity: Solar water heater case study
6. Abdelsalam MY, Teamah HM, Lightstone MF, Cotton JS (2020) Hybrid thermal energy storage with phase change materials for solar domestic hot water applications: Direct versus indirect heat exchange systems. *Renew Energy* **147**:77–88
7. Li B, Zhai X (2017) Experimental investigation and theoretical analysis on a mid-temperature solar collector/storage system with composite PCM. *Appl Thermal Eng* **124**:34–43
8. Huang H, Xiao Y, Lin J, Zhou T, Liu Y, Zhao Q (2019) Improvement of the efficiency of solar thermal energy storage systems by cascading a PCM unit with a water tank. *J Clean Prod*
9. Mehta DS, Solanki K, Rathod MK, Banerjee J (2019) Thermal performance of shell and tube latent heat storage unit: Comparative assessment of horizontal and vertical orientation. *J Energy Storage* **23**:344–362
10. Pourakabar A, Ali Rabienataj Darzi A (2019) Enhancement of phase change rate of PCM in cylindrical thermal energy storage. *Appl Therm Eng* **150**:132–142
11. Zhou Z, Liu J, Wang C, Huang X, Gao F, Zhang S, Yu B (2018) Research on the application of phase-change heat storage in centralised solar hot water system. *J Clean Prod*

# Performance Analysis of Oil Expelling Using Vaagai Wood Crusher



S. Stephen Bernard, M. Bakkiyaraj, Md. Javeed Ahmed, M. V. Niranjana, R. Nirmal, and K. Hemanand

**Abstract** This research work focus on the performance of vaagai wood in oil expelling wood crusher. It is based on crushing the seeds by the wood crusher. The requirements of wood are not to absorb oil during seed crushing and there should not be any physical and chemical reactions between the wood and the seed. This oil expeller is made by using available material in local. The experiments are conducted with three different crushers (Stainless steel, redwood and vaagai wood). The results show that temperature of extracted oil is low for vaagai wood crusher. This crusher also extracts high viscosity 31, 26, and 37% compared to steel crusher for peanut, sesame, and soybean oil, respectively. Finally, the quantity of oil extracted is nearly equal to stainless steel crusher. These machines are very compact and can be used for domestic purpose.

**Keywords** Vagai wood · Oil expeller · Crusher · Viscosity · Friction

## 1 Introduction

Edible oil is used for cooking purpose; they are important in the nutrition, by ensuring their purity. Price plays a major role in purity. It effects the health due to the impurity or change in the viscosity which causes liver problems, heart disorder, etc. [1]. Oil extraction technology is used in India for a long time. Among many method, cold press for oil extraction is better than other due to its low cost, good quality oil with high nutrition, easy to handle, low manpower, environmentally friendly, and presence of organic solvents [2, 3]

Economic requirement, cost plays a major role in the manufacturing of machine. So the material selected should be low in cost and easily available in local. The wood

---

S. S. Bernard (✉) · M. Bakkiyaraj · M. V. Niranjana · R. Nirmal · K. Hemanand  
Department of Mechanical Engineering, Rajalakshmi Institute of Technology, Kuthambakkam,  
Chennai, India  
e-mail: [Stephenbernard.s@ritchennai.edu.in](mailto:Stephenbernard.s@ritchennai.edu.in)

Md. J. Ahmed  
BS Abdur Rahman Crescent Institute of Science and Technoogy, Vandalur, Chennai, India

is cheaper than metal which it is organic and does not alter the property of the oil [4]. Life cycle is important in the machine; life cycle of the product says the standard of the product.

The material chosen for the crusher is vaagai wood. These woods do not absorb oil and do not react with oil or cannot alter the oil properties. In ancient, woods are used for the oil extraction process which gives a major advantage in health [5, 6]. Nowadays, metal crusher is used where the property of the oils is altered.

Vaagai wood is rich in medical properties and it is called as marachekku. In metal crusher, the heat is produced during the process of crushing the seeds. This heat destroys the nutrients of the oil where it leads to the many health disorders [7]. In vaagai wood, it absorbs the heat and maintains the atmospheric temperature. These processes are called cold oil press. These woods are rich in antioxidants which increases the immunity. In addition to these, vaagai plays a major role in healing the wounds [8]. These woods are used in ancient times. Vaagai consists of pack of nutrients in it. After the advancement of technology, the woods usage in oil extraction is reduced. The reason for using wood crusher instead of metal crusher because, the metal crusher produces more heat during the crushing of seeds, where it changes the purity of oil and changes the standard value of viscosity [9]. The requirements of woods for the crushing are it should not absorb oil. And there should be no reaction between the wood and the seed.

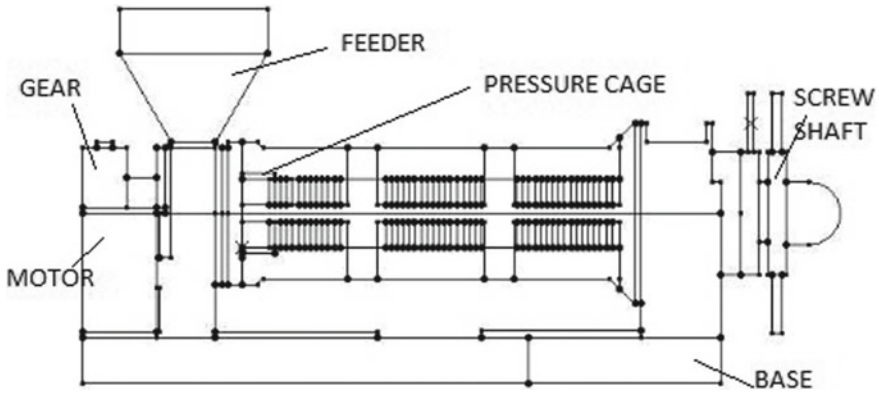
It is the mechanical method for oil extraction, where the raw material is squeezed under high pressure in between the crusher and the surface of the hollow cylinder. In this case, when the raw material pressed, friction is generated and produces heat [10, 11]. The crusher used in these machines is screw types, where it has thread-like structure on it. It is similar to the lead screw. When raw materials are crushed due to the helix thread pushes the raw material forward along the surface of the hollow cylinder [12].

In this research, in order to reduce the health issues, a compact oil extraction using wood crusher is developed and different oil (peanut, sesame, and soybean oil) is tested with metal crusher.

## 2 Experimental Setup

For a good efficiency and for good results, selection of method, design, materials is very important. The selection is based on the requirements, properties of the product. The factor influencing for the selection of material is strength, weight, appearance, manufacturing method, and the cost.

The vaagai wood oil expeller is shown in Fig. 1. The components of the machine are motors, motor shaft, flat belt, pulley, roller bearing, wood crusher, wood hollow cylinder, and machine stand. Motor specifications are the 24 V DC motor, where the flat belt is used for the power transmission. Bearing is used at the end of the crusher, and it transmits the rotary motion from motor to the wood crusher.

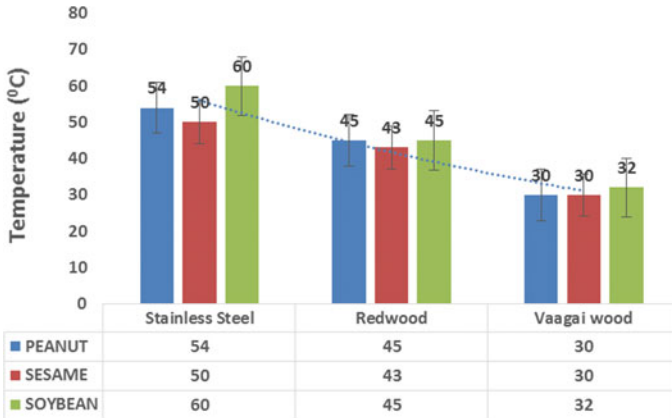


**Fig. 1** Vaagai wood crusher oil expeller

Wood crusher, it is the main core of the research. The material chosen for the crusher is vaagai wood. The diameter of the crush at the end is 20 mm and the diameter at the middle portion of the thread is 38 mm. Hollow cylinder, it is casing for the wood crusher and it contains tiny holes at the bottom where oil comes from it. The length of the cylinder is similar to the crusher. The diameter is 40 mm [13]. The crusher and hollow cylinder are placed horizontally. It is supported by stand vertical to the wood plank. Two stand for the hollow and two for the bearing. The crusher is kept inside the hollow cylinder and at the end of the crusher bearing is inserted and the bearing supported by the stand. Bearing and motor are connected with the help of pulley and flat belt. And the seeds are introduced on the top of the hollow cylinder in the hopper which situated on the top of the cylinder.

### 3 Result and Discussion

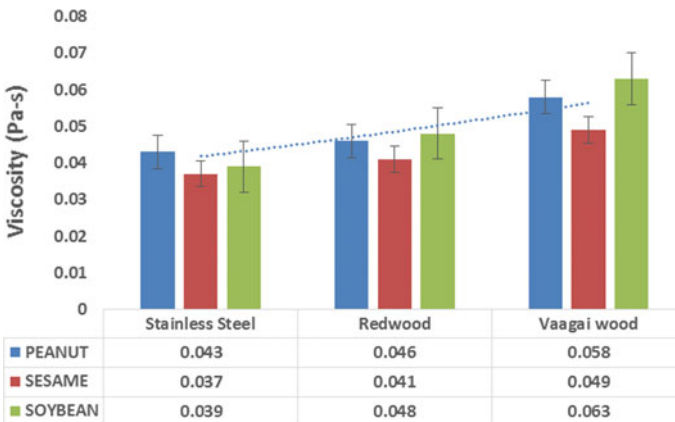
Figure 2 shows the temperature of various extracted oil for various materials (stainless steel, redwood, and vaagai wood). The figure clearly indicates that temperature of extracted oil using vaagai wood is near to atmospheric temperature. This is due to vaagai wood able to absorb heat created during crushing and maintain the atmospheric temperature [14]. In stainless steel crusher, temperature increased was 94, 82, and 104% for peanut, sesame, and soybean, respectively. This heat generated during the crushing in the metal crusher destroys the oil nutrition and taste. When compared to stainless steel crusher, the redwood crusher generates low temperature. This clearly indicates that metal crusher rises the temperature of oil due to pressure and friction between crusher and seed. The wood is organic and no reaction will occur between the crusher and the seeds [15]. Temperature plays major role in the quality of the oil, where the heat destroys the nutrition of the oil.



**Fig. 2** Temperature of various extracted oil for stainless steel, redwood, and vaagai wood

From the figure, it is evident that sesame oil generates a low temperature compared to peanut and soybean oil. In stainless steel, it generates 16.6% low temperature compared to soybean and 7% compared to peanut oil. Similarly, 4% low temperature generates in redwood for soybean. In vaagai wood, all these oil generates low temperature and it does not affect the nutrition energy in oil.

Viscosity of various extracted oil for stainless steel, redwood, and vaagai wood was clearly shown in Fig. 3. Generally, viscosity says nutrition of the oil and also it alters the nutrition of the oil. Viscosity of oil from stainless steel crusher is low due to high temperature generated during oil production [16]. It seems high for vaagai wood compared to redwood. This is due to low absorbing property of vaagai and its porosity structure is negligible [17]. For all type of crusher, sesame oil viscosity is low compared to peanut and soybean oil. High viscosity is found in soybean oil for



**Fig. 3** Viscosity of various extracted oil for stainless steel, redwood, and vaagai wood

both the wood crusher but it seems low in steel crusher compared to peanut oil. Vaagai wood crusher extracts high viscosity 31, 26, and 37% compared to steel crusher for peanut, sesame, and soybean oil, respectively. Redwood crusher also produces a good viscosity of oil compared to stainless steel.

Vaagai wood extracts 0.058 Pa s viscosity for soybean oil but it is lower for other two oil. 18 and 21% produce a higher viscosity for soybean oil compared to peanut and sesame oil. These trend follows in redwood crusher also. So this viscosity variation depends on the oil properties not due to crusher. But the trend is different in stainless steel crusher, i.e., peanut oil produces a high viscosity oil compared to other two oil.

Oil quantity of various extracted oil for stainless steel, redwood, and vaagai wood were clearly shown in Fig. 4. Stainless steel crusher extracts more than 50% of oil from their seeds. Vaagai wood crusher extracts high quantity oil 6, 4 and 2% compared to redwood crusher for peanut, sesame, and soybean oil, respectively, but it extracts low quantity compared to stainless steel crusher. This is due to addition of high density additives with seeds during extraction process [18, 19]. These additives require high pressure during crushing which reduces the extraction of oil in wood crusher compared to steel crusher.

In all the crusher, peanut oil produces a high quantity of oil compared to other two oils. In stainless steel, peanut oil produces 520 ml which is 9.9 and 3.6% high compared to sesame and soybean oil. Similar trend is followed in vaagai wood but in redwood, soybean oil produces 490 ml whereas peanut and sesame oil produce 470 ml.

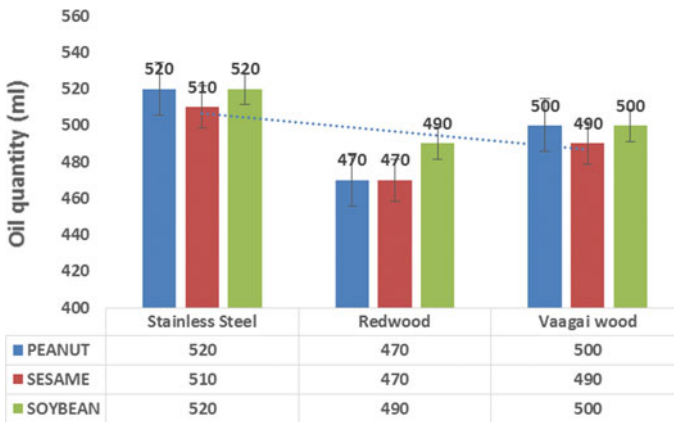


Fig. 4 Oil quantity of various extracted oil for stainless steel, redwood, and vaagai wood

## 4 Conclusion

The following conclusions were drawn after the fabricated and constructed compact oil extraction machine using wood crusher.

It is observed that the temperature of extracted oil is less for vaagai wood crusher when compared to steel crusher. Viscosity of oil is also high for vaagai wood and also the nutrition and the taste of the oil are not altered. Though quantity of oil extracted more in stainless steel crusher, the vaagai wood also extracts near to it. Vaagai wood crusher extracts high quantity oil 6, 4, and 2% compared to redwood crusher for peanut, sesame, and soybean oil, respectively.

It is found that vaagai wood crusher is superior to the redwood and stainless steel crusher, because quantity of oil production is higher and the oil extraction time is shorter and oil has good quality. The machine is also cheap, compact, portable, and easy to operate.

## References

1. Savoire R, Lanoisellé JL, Vorobiev E (2013) Mechanical continuous oil expression from oilseeds: a review. *Food Bioprocess Technol* 6(1):1–16. <https://doi.org/10.1007/s11947-012-0947-x>
2. Chemat F, Strube J (2015) *Green extraction of natural products: theory and practice*. Wiley, pp 108–113. <https://doi.org/10.1002/9783527676828>
3. Uitterhaegen E, Evon P (2017) Twin-cold extrusion technology for vegetable oil extraction: a review. *J Food Eng* 212:190–200 (2017). <https://doi.org/10.1016/j.jfoodeng.2017.06.006>
4. Matthaus B, Brühl L (2003) Quality of cold-pressed edible rapeseed oil in Germany. *Food* 47(6):413–419. <https://doi.org/10.1002/food.200390092>
5. Rabadán A, Pardo JE, Gómez R, Álvarez-Ortí M (2018) Influence of temperature in the extraction of nut oils by means of cold pressing. *LWT* 93:354–361. <https://doi.org/10.1016/j.lwt.2018.03.061>
6. Suresh G, Stephen Bernard S, Vivek S, Sai Krishnan G, Ashwin Kishore V, Ivon Paul A, Mohideen Fowzan K (2020) Study of mechanical performance of E-Glass fiber reinforced (IPN) interpenetrating polymer networks. *Mater Today: Proc.* <https://doi.org/10.1016/j.matpr.2020.02.332>
7. Rombaut N, Savoire R, Thomasset B, Castello J, Van Hecke E, Lanoisellé JL (2015) Optimization of oil yield and oil total phenolic content during grape seed cold cold pressing. *Ind Crops Prod* 63:26–33. <https://doi.org/10.1016/j.indcrop.2014.10.001>
8. Stephen Bernard S, Jayakumari LS (2018) Pressure and Temperature Sensitivity Analysis of Palm fiber as a biobased reinforcement material in brake pad. *J Braz Soc Mech Sci Eng* 40:152. <https://doi.org/10.1007/s40430-018-1081-0>
9. Burg P, Mašán V, Rutkowski K (2017) Evaluation of the pressing process during oil extraction from grape seeds. *Potravinárstv* 11:1. <https://doi.org/10.5219/690>
10. Al Juhaimi F, Özcan MM, Ghafoor K, Babiker EE, Hussain S (2018) Comparison of cold-pressing and soxhlet extraction systems for bioactive compounds, antioxidant properties, polyphenols, fatty acids and tocopherols in eight nut oils. *J Food Sci Technol* 55(8):3163–3173
11. Frančáková H, Ivanišová E, Dráb Š, Krajčovič T, Tokár M, Mareček J, Musilová J (2015) Composition of fatty acids in selected vegetable oils. *Potravinárstvo* 9(1):538–542. <https://doi.org/10.5219/556>



12. Hardie WJ, O'Brien TP, Jaudzems VG (1996) Morphology, anatomy and development of the pericarp after anthesis in grape. *Vitis vinifera* L. Aust J Grape Wine Res 2(2):97–142 (1996). <https://doi.org/10.1111/j.1755-0238.1996.tb00101.x>
13. Stephen Bernard S, Srinivasan T, Suresh G, Ivon Paul A, Mohideen Fowzan K, Ashwin Kishore V (2020) Production of biogas from anaerobic digestion of vegetable waste and cow dung. Mater Today Proc. <https://doi.org/10.1016/j.matpr.2020.07.129>
14. Gros C, Lanoisellé JL, Vorobiev E (2003) Towards an alternative extraction process for linseed oil. Chem Eng Res Des 81(9):1059–1065. <https://doi.org/10.1205/026387603770866182>
15. Pradhan RC, Meda V, Rout PK, Naik S, Dalai AK (2010) Supercritical CO<sub>2</sub> extraction of fatty oil from flaxseed and comparison with screw press expression and solvent extraction processes. J Food Eng 98(4):393–397. <https://doi.org/10.1016/j.jfoodeng.2009.11.021>
16. Stephen Bernard S, Jayakumari LS (2014) Effect of the properties of natural resin binder in a high friction composite material. Polimeros- Ciencia Tecnologia 24(2):149–152 (2014). <https://doi.org/10.4322/polimeros.2014.038>
17. Yılmaz C, Gökmen V (2013) Compositional characteristics of sour cherry kernel and its oil as influenced by different extraction and roasting conditions. Ind Crops Prod 49:130–135. <https://doi.org/10.1016/j.indcrop.2013.04.048>
18. Moura JM, Campbell K, Mahfuz A, Jung S, Glatz CE (2008) Enzyme-assisted aqueous extraction of oil and protein from soybeans and cream de-emulsification. J Am Oil Chem Soc 85:985–995. <https://doi.org/10.1007/s11746-008-1282-2>
19. Do LD, Sabatini DA (2010) Aqueous extended-surfactant based method for vegetable oil extraction: proof of concept. J Am Oil Chem Soc 8710:1211–1220. <https://doi.org/10.1007/s11746-010-1603-0>

# The Effect of Quenching Mediums on Heat Treatment Properties of Multi-pass Welding of 0.3% C-Cr Mo V Steel



K. Radhakrishnan and V. Muralidharan

**Abstract** This paper brings out the correlation between microstructure and mechanical properties of 0.3% C-CrMoV steel, welded with manual gas tungsten arc welding (GTAW) process with a combinations of weld parameters as per the principle of Taguchi's design of experiments (DOE). After welding the test plates, test specimens were cut from it, hardened and tempered, quenched in forced air, water, and oil. Test samples were drawn from these combinations and microstructure evaluation was studied. Mechanical properties like hardness, tensile strength, yield strength, %elongation, % reduction in area, and impact strength were evaluated. The fracture morphology features of failed impact specimens were observed using scanning electron microscope. The mechanical properties of the weldment were compared and it was observed that, the test specimens quenched in oil give maximum UTS 1430 MPa, water quenching gives 1395 MPa, and forced air cooling gives 1260 MPa. Maximum weld strength obtained with the combinations of root gap of 1 mm, number of passes two or three and oil as quenching medium. All the tensile test specimens are broken outside the weldment during tensile testing. The maximum impact properties were obtained from the test plates welded in annealed condition with multi-pass welding, which was 52 J. When forced air was used as a quenching medium, with multi-pass welding, it gives lower tensile strength and higher percentage elongation and impact strength. This study was an attempt to optimize the weld parameters, heat treatment methods, quench mediums, and correlate mechanical properties with microstructure.

**Keywords** 0.3%C-CrMoV steel · GTAW · UTS · Hardening · Tempering · Quenching mediums

---

K. Radhakrishnan (✉)  
Vikram Sarabhai Space Centre, Trivandrum 695022, India  
e-mail: [radhakrishnan3263@gmail.com](mailto:radhakrishnan3263@gmail.com)

K. Radhakrishnan · V. Muralidharan  
B.S. Abdur Rahman Crescent Institute of Science &Technology, Chennai 600048, India  
e-mail: [v.muralidharan2@gmail.com](mailto:v.muralidharan2@gmail.com)

## 1 Introduction

Structural steel with minimum yield strength of 1400 MPa is referred as ultra high-strength steel. These steels are used in critical applications like rocket motor casings, aero space components, aircraft components, pressure vessels, aero space structures, etc. Some of these steels, like maraging steels, are highly alloyed and are very expensive. Therefore, search for less expensive steels with improved properties is taking place continuously. These steels must have good weldability, hardenability, formability with good ductility and toughness. Few examples of such steels are medium carbon low alloy steel, medium alloy air hardening steel, and high alloy hardenable steel.

15CDV6 [1] steel is high-strength low-alloy steel used in the fabrication of booster motor casings and pressure vessels. For larger space boosters and pressure vessels, new ultra high-strength materials with higher specific strength are explored. For these applications, material like maraging steel is used. Due to its higher cost, a new alloy known as 0.3%C-CrMoV [1, 2] steel was developed which is considered to be a cost-effective alternative to maraging steel.

In this study, weld parameters are selected using the principle of Taguchi's design of experiment (DOE) with three levels and four variables. Totally, nine experiments with different combinations of weld parameters were conducted on the test plates (TP) of size 8 mm × 200 mm × 150 mm. The chemical composition of parent metal and welding filler rod [3] is same. For three levels of current, voltage, variables, like root gap, number of passes, welding speed, and types of quenching media were employed. The amount of shielding, purging gas used and quantity of its flow are noted. Hardness, ultimate tensile strength (UTS), 0.2% proof strength, % elongation, % reduction in area, impact strength are chosen as responses. After welding, all the nine test plates were subjected to visual, dimensional [4], liquid penetrant test (LPT) [5], X-ray radiography inspections.

## 2 Experimental Work

Manual GTAW was carried on the test plates by maintaining weld geometry with 60° V-groove and root face of 1 mm. Nine test plates were welded using the principle of Taguchi's design of experiments. DOE is a systematic approach employed in the investigation of a process. As per Taguchi's orthogonal array selection table, L9 orthogonal array was selected.

Using the above methodology, nine test plates were welded by varying the root gap, number of passes, etc. The size of the plates was 8 mm × 200 mm × 150 mm and length of welding is 200 mm for each test plate. Totally, nine test plates were welded. After welding, these test plates were inspected by measuring [4] bead width ( $B$ ), reinforcement height ( $H$ ), penetration width ( $b$ ), and penetration height ( $h$ ). The weld penetration in all the plates was flush grounded and the weld was subjected to

**Table 1** Chemical composition (% in weight)—0.3%C-CrMoV steel [1, 2]

C	Mn	Si	Mo	V	Cr	Nb	S	P	Fe	O <sub>2</sub>	H <sub>2</sub>	N <sub>2</sub>
0.29	0.93	0.16	0.87	0.26	1.38	0.1	0.003	0.005	Bal	50 ppm	2 ppm	125 ppm

liquid penetrant test (LPT) [5], X-ray radiography and found defect free (Tables 1, 2, 3, 4 and 5).

Heat treatment was carried in a laboratory scale furnace as per the heat treatment cycle (Table 6) by electric heating and rate of heating of 100 °C/hour was maintained. The test specimens cut from the test plates TP-1, 5, 9, the quenching media was forced air, for TP-2, 6, 7, the quenching media was water, for TP-3, 4, 8, the quenching media was oil. Tensile [6]/Impact test [7] specimens were cut by water jet machining process and dimensions were maintained as per ASTM-A 370, ASTM E23 standard. By this method, the specimens are not subjected to any heating process. These test specimens are cleaned by wire brushing to remove the scaling, corrected to maintain the dimensions [8] by fitting process. Hardness [9] survey carried on PM, HAZ, WM and found between 40/48 HRC (Fig. 1) (Table 7).

**Table 2** Proposed welding parameters as per DOE

Experiment	Current (A)	Voltage (V)	Number of passes	Root gap in mm (mm)	Heat treatment quenching medium
TP1	160	18	2	1	Air
TP2	206	20	3	1.5	Water
TP3	200	20	4	2	Oil
TP4	200	20	2	1.5	Oil
TP5	206	19	3	2	Air
TP6	160	16	4	1	Water
TP7	200	20	2	2	Water
TP8	160	16	3	1	Oil
TP9	205	19	4	1.5	Air

**Table 3** Welding parameters for two pass welding

Experiment	Current in amps	Voltage in volts	Number of pass	Root gap in mm	Length of filler wire consumed for 200 mm length	Weight of filler wire deposited per 100 mm gms	Welding speed (mm/min)
TP1	160/160	19/18	2	1	350/420	13/16	99/46
TP4	202/160	20/19	2	1.5	680/930	26/36	65/47
TP7	200/165	20/18	2	2	970/1040	37/40	64/37

**Table 4** Welding parameters for three pass welding

Experiment	Current in amps	Voltage in volts	Number of pass	Root gap in mm	Length of filler wire consumed for 200 mm weld length	Weight of filler wire deposited per 100 mm (in gms)	Welding speed in mm/min
TP2	206/180	20/18	3	1.5	450/650	17/25	87/71
TP5	206/180	19/18	3	2	550/600	21/23	75/64
TP8	160/158	16/18	3	1	340/550	13/21	71/62

**Table 5** Welding parameters for four pass welding

Experiment	Current in volts	Voltage in amps	Number of pass	Root gap in mm)	Length of filler wire consumed for 200 mm length	Weight of filler wire deposited per 100 mm in gms	Welding speed in mm/min
TP3	203/181	20/18	4	2	600/425	23/20	98/75
TP6	160/160	16/18	4	1	350/450	13/17	56/52
TP9	204/180	19/18	4	1.5	400/600	15/23	75/105

**Table 6** Heat treatment cycle

Process	Temperature at loading (°C)	Temperature at soaking (°C)	Soaking time	Quenching medium <sup>a</sup>
Hardening	≤600 °C	920	1 h	Air/Water/Oil
Quench delay	≤45 s			
Stress relieving	≤200 °C	300	1 h	Air
Tempering	≤300 °C	505	2 h	Air/Water/Oil
Quench delay	≤45 s			

<sup>a</sup>For TP-1,5,9-quench medium was air, For TP-2,6,7-quench medium was water, For TP-3,4,8-quench medium was oil



**Fig. 1** Tensile test specimens

**Table 7** Tensile test [6] values—As welded condition

Specimens	T-1	T-2	T-3	T-4	T-5	T-6	T-7	T-8	T-9
UTS:MPa	690	651	657	706	648	695	663	679	688
0.2% PS: MPa	558	479	484	509	459	479	446	521	439
% Elongation (G.L = 50 mm)	16.2	16.3	16.1	18	16.3	18	18.2	17.8	17.7
% Reduction in area	39.1	34	31.8	32.3	45	39	41.4	31.4	42.5

Location of fracture: outside the gauge length

Tensile Test values—Heat treated—Parent metal.

### 3 Microstructure of 0.3% C-CrMoV Steel

1. Microstructure in annealed condition shows ferrite and pearlite.
2. Welded-Heat treated, air cooled.

Microstructure shows fine-tempered martensite in base metal, combined microstructure of bainite, martensite in heat affected zone and in fusion zone.

3. Welded-heat treated, water quenched

Microstructure shows fine-tempered martensite in base metal, combined microstructure of bainite, martensite in heat affected zone and in fusion zone.

4. Welded-heat treated, oil quenched

Microstructure shows fine-tempered martensite in base metal, combined microstructure of bainite, martensite in heat-affected zone and in fusion zone.

## 4 Fractography

The fractured surface of the impact test specimens quenched in various conditions were studied using scanning electron microscopy (SEM) (Fig. 6).

## 5 Fractography Study

From the SEM image, it is observed that the fracture [10] is highly ductile mode showing uniformly distributed fine dimples [10, 11] as shown.

## 6 Observations and Conclusions

1. From this study, it was observed that maximum weld strength was obtained with a combinations of 1 mm root gap, two/three weld passes and oil as quenching medium. The microstructure observed was fine-tempered martensite.
2. All the tensile test specimens failed outside the weld show weld efficiency was more than 90%. In annealed condition welding, the weld attains the maximum hardness, even though the parent metal region shows less. This is because the molten weld pool reaches to austenising temperature followed by air cooling.
3. From the impact test results, it is observed, maximum impact strengths obtained from the plates welded in annealed condition with multi-pass welding. This may be due to multiple thermal cycles the weld is subjected during multi-pass welding.
4. It was observed, with multi-pass welding and oil as quenching medium, gives higher UTS, impact strength, and % elongation (Table 10). This infers ductility is more in multi-pass welding.
5. Optical microstructure of this material in annealed condition reveals ferrite with carbides (Fig. 2). The microstructures in hardened and tempered condition followed by rapid air cooling reveals bainitic structure [3, 12] along with martensite, ferrite, and carbides.
6. nRamkumar et al., reported similar microstructures by using Plasma arc welding process. Similarly, other authors also reported the same microstructures using different fusion welding process [13] (Fig. 3).
7. Micro structure of air quenched specimens shows upper bainite coupled with lath martensite and small fraction of ferrite. Saravanan et al., reported similar microstructures in the heat treatment studies [10, 11] done on parent metals (Fig. 3).
8. The optical microstructure of the specimens hardened, tempered, and quenched in oil shows fine-tempered martensite in base metal, combined microstructure of bainite and martensite in heat affected zone and in fusion zone (Fig. 5).

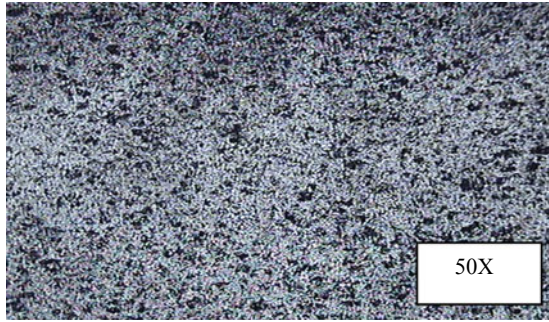


Fig. 2 Optical microstructure of weld-welded in annealed condition

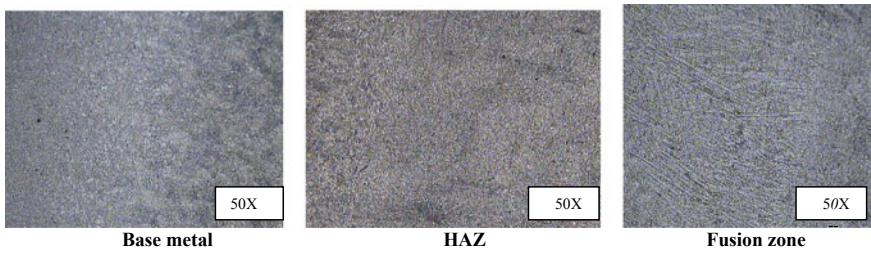


Fig. 3 Optical microstructure of weld-Heat treated, air cooled

- 9. The microstructure of the specimens heat treated and quenched in water shows fine-tempered martensite in base metal [10, 11], combined microstructure of bainite and martensite in heat affected zone and in fusion zone [3, 12] (Figs. 4 and 6).
- 10. The broken impact specimens show shear fracture and the sheared surfaces exhibit dimples (Figs. 7, 8, 9 and 10). Similar features reported in the fractography [10] studies done by Sravanan et al. on heat-treated parent metal.
- 11. The fracture [10] is highly ductile mode showing uniformly distributed fine dimples [10, 11].

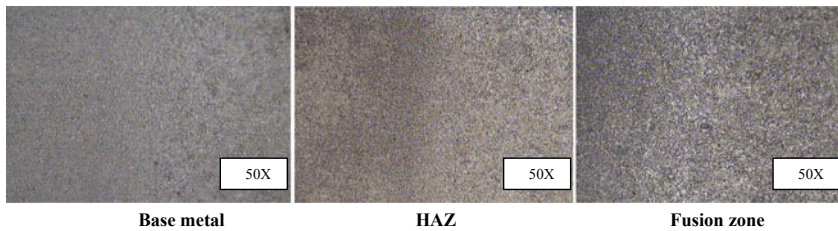
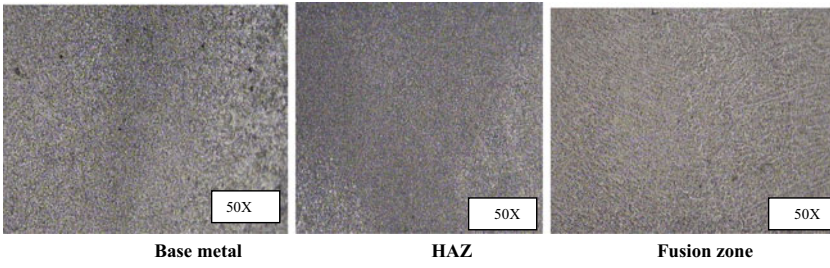
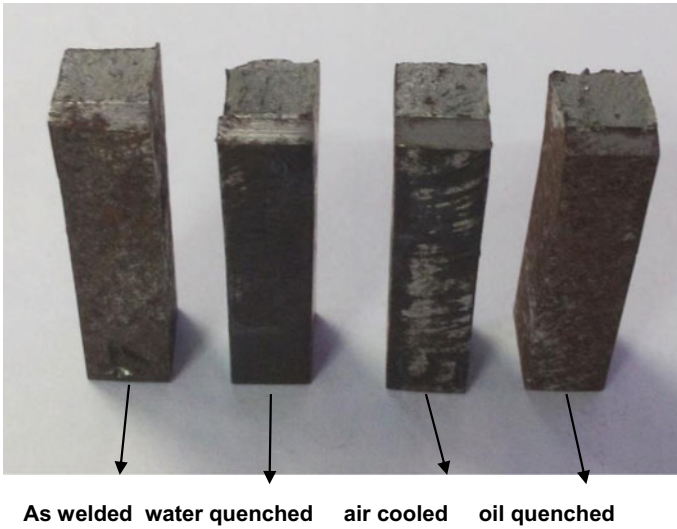


Fig. 4 Optical micro structure of weld-heat treated and cooled in water

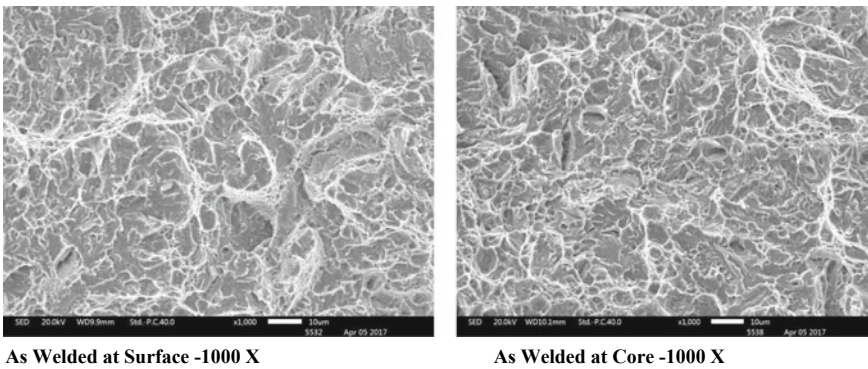




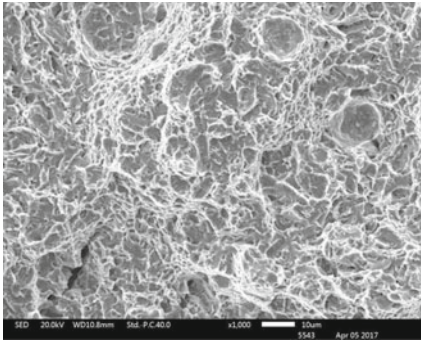
**Fig. 5** Optical microstructure of weld-Heat treated, oil cooled



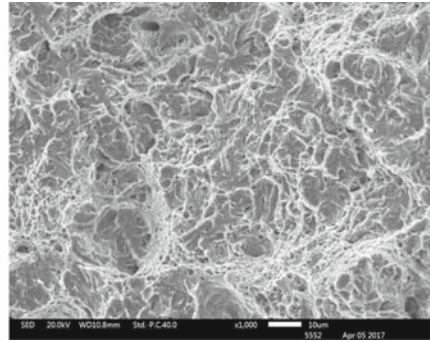
**Fig. 6** Impact test samples, after breaking



**Fig. 7** Fracto graphic image of weld-welded in annealed condition

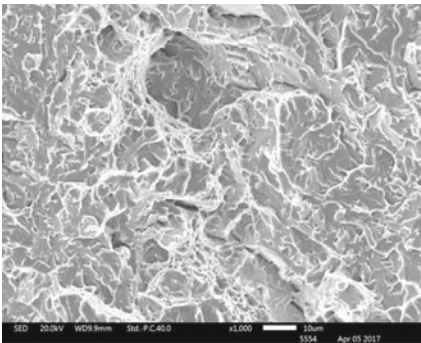


**Water Quenched ,at Surface -1000 X**

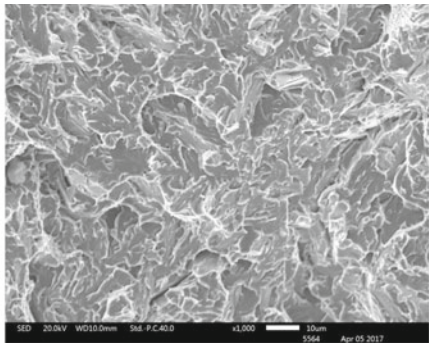


**Water Quenched ,at Core -1000 X**

**Fig. 8** Fracto graphic image of weld-heat treated, cooled in air

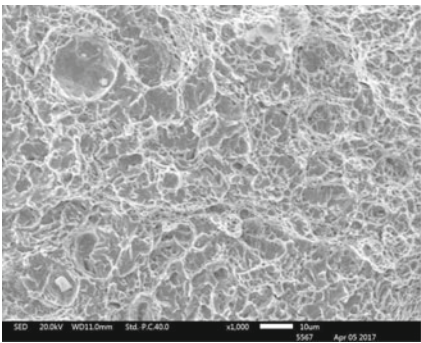


**Air Quenched, at Surface - 1000 X**

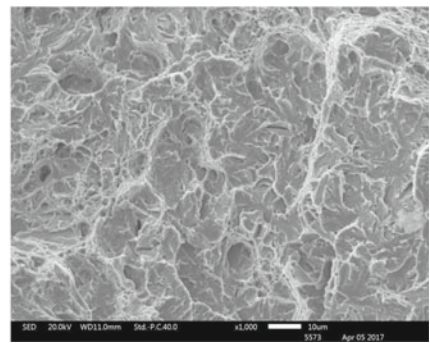


**Air Quenched, at Core -1000 X**

**Fig. 9** Fracto graphic image of weld-heat treated, cooled in water



**Oil Quenched, at Surface -1000 X**



**Oil Quenched ,at Core -1000 X**

**Fig. 10** Fracto graphic image of weld-heat treatrd, cooled in oid

**Table 8** Average tensile test [6] values—Heat treated, Quenching medium: Air

Specimens	TP-1	TP-5	TP-9
UTS:MPa	1200	1254	1225
0.2%PS: MPa	1074	1183	1110
% Elongation (G.L = 50 mm)	14	12	13
% Reduction in area	32	25	25

Location of fracture: outside the gauge length

**Table 9** Tensile test [6] values—Heat treated, quenching medium: Water

Specimens	TP-2 TP-2/2	TP-6	TP-7
UTS:MPa	1329	1371	1325
0.2%PS: MPa	1278	1323	1287
% Elongation (G.L = 50 mm)	11.0	12.0	12.0
% Reduction in area	26.0	24.0	30.0

Location of fracture: outside the gauge length

12. It was observed from this study that oil quenching gives maximum strength (Table 10) followed by water quenching (Table 9). When forced air is used as quenching medium, the values of UTS (Table 8) come down because the rate of cooling is less compared to oil and water. Average difference of around 100 MPa of UTS and 50 MPa of 0.2%PS was observed between oil, water, and air (Tables 11, 12, 13 and 14).

**Table 10** Tensile test [6] values—Heat treated, quenching medium: Oil

Specimens	TP-3	TP-4	TP-8
UTS: MPa	1301	1404	1417
0.2%PS: MPa	1192	1374	1380
% Elongation (G.L = 50 mm)	11.0	12.0	10.0
% Reduction in area	28	23.0	17

Location of fracture: outside the gauge length

**Table 11** Impact test [7] values—As welded condition

Specimens	TP-1	TP-2	TP-3	TP-4	TP-5	TP-6	TP-7	TP-8	TP-9
Impact strength (J)	27	44	52	25	24	52	28	34	30

**Table 12** Impact test [7] values—Heat treated, quenching medium: Air

Specimens	TP-1	TP-5	TP-9
Impact strength (J)	16	17	25

**Table 13** Impact test [7] values—Heat treated, Quenching medium: Water

Specimens	TP-2	TP-6	TP-7
Impact strength (J)	18	19	19

**Table 14** Impact test [7] values—Heat treated, quenching medium: Oil

Specimens	TP-3 TP-3/2	TP-4 TP-4/2	TP-8 TP-8/2
Impact strength (J)	20	16	17

## References

1. Bandyopadhyay et al T. Improvement in Mechanical Properties of standard 15CDV6 steel by increasing Carbon and Chromium content and inoculation with titanium by ESR. IIT, Mumbai
2. Maity SK et al (2009) Development of ultrahigh strength low alloy Steel through electro slag refining process. ISIJ Int 49(6):902–910
3. Suresh MR et al Study of welding characteristics of 0.3%C-CrMoV (ESR) ultra high strength steel. J Mater Sci 42(14)
4. AIR 9112/A condition for checking and receiving steel parts and assemblies made by welding
5. ASTM E 165 test method for liquid penetrant examination
6. ASTM E 8 test method for tension testing of metallic materials
7. ASTM E 23 test method for notched bar impact testing of metallic materials
8. ASTM: A 370-10 Standard test methods and definition for mechanical testing of steel products
9. ASTM E 18 Test method for rockwell hardness of metallic materials
10. Saravanan K, Kumar S et al (2012) Effect of tempering temperature on strength and fracture toughness of 0.3%C-CrMoV(ESR) steel. Mater Sci Forum 710(2012):433–438

11. Magudam C et al (2017) Heat treatment of 0.3%C-CrMov (ESR) segment-NAMS-2017
12. Ramkumar P et al (2017) Plasma arc welding of high strength 0.3%C-CrMoV (ESR) steel. Trans Ind Inst Metals
13. Chandra Sekar M et al (2014) Welding development in ESR modified 15CDV6 material. Int J Mech Eng Rob Res 3(3). ISSN 2278-0149
14. Karthikeyan MK et al (2017) Effect of Quench Media on mechanical properties of 3%C-Cr-Mo-V steel NAMS

# A Study on the Welding and Heat Treatment of 0.3% C-Cr-MoV Steel



K. Radhakrishnan and V. Muralidharan

**Abstract** 15CDV6 steel is a high-strength low-alloy steel widely used in aerospace applications to make pressure vessels, components, and structures. This steel has good fabricability and attains strength by simple heat treatment process of hardening and tempering. The unique property of this steel is, it can be welded in annealed and hardened and tempered conditions. This material has a ultimate tensile strength of minimum 980 MPa. The 0.3% C-CrMoV steel is modified version of 15CDV6 steel and is considered as a substitute for ultra high-strength material like maraging steel. This paper deals with study of weld bead dimensions, optimising weld parameters, and heat treatment process to get the maximum strength. In this work, the welding parameters, its response on the variables, and influence on weld properties are studied. The test plates after welding were subjected to liquid penetrant test (LPT), X-ray radiograph. Dimensional measurements were carried on weld beads. Tensile and impact test specimens were cut from these test plates, heat treated, and quenched in different cooling mediums. These test specimens were subjected to hardness, tensile, and impact testing. The test results were compared to find out the combinations of weld parameters which gives the maximum properties.

**Keywords** 15CDV6 steel · 0.3% C-CrMoV steel · GTAW · Radiography · LPT · Weld bead dimensions

## 1 Introduction

15CDV6 [1] (Table 1) steel is high-strength low -alloy steel used in the fabrication of booster motor casings and pressure vessels in aero space applications. For larger

---

K. Radhakrishnan (✉)  
Vikram Sarabhai Space Centre, Trivandrum 695022, India  
e-mail: [radhakrishnan3263@gmail.com](mailto:radhakrishnan3263@gmail.com)

K. Radhakrishnan · V. Muralidharan  
B.S. Abdur Rahman Crescent Institute of Science & Technology, Chennai 600048, India  
e-mail: [v.muralidharan2@gmail.com](mailto:v.muralidharan2@gmail.com)

**Table 1** Chemical composition (% in weight)—15CDV6 [1] steel

C	Mn	Si	Mo	V	Cr	S	P	Fe	O <sub>2</sub>	H <sub>2</sub>	N <sub>2</sub>
0.12–0.16	0.81–1.0	0.20	0.80–0.90	0.20–0.30	1.25–1.50	0.015 max	0.02 max	Bal	70 ppm max	3 ppm max	150 ppm max



space boosters and pressure vessels, new ultra high-strength materials with higher specific strength are explored. So a new alloy known as.

0.3%C-CrMoV [2] steel (Table 2) is developed which is considered to be a cost-effective alternative to maraging steel. In this study, combinations of weld parameters were selected using the principle of Taguchi's design of experiment (DOE) with three levels and four variables. Nine experiments with different combination of weld parameters were carried on the test plates of size 8 mm × 200 mm × 150 mm. As per Taguchi's orthogonal array selection table, L9 orthogonal array was selected. For three levels of current, voltage, variables like root gap, number of passes, welding speed, and types of quenching media were employed. Hardness, ultimate tensile strength, 0.2% proof strength, %elongation, %reduction in area, impact strength were responses. Using the above methodology, nine test plates were welded by varying the current, voltage, root gap, number of weld passes, etc. (Tables 4, 5 and 6). These test plates were inspected by measuring [3] bead width, reinforcement height, depth of penetration (Tables 7, 8 and 9). All the nine test plates were subjected to visual, dimensional, liquid penetrant test (LPT), and X-ray radiography inspections (Table 3).

## 2 Experimental Methods

Manual GTAW [4] was done on the test plates (Fig. 1) by maintaining weld geometry of V-groove with included angle of 60° and a root face of 1 mm. Nine test plates were welded using the principle of Taguchi's design of experiments. These test plates were inspected by measuring bead width ( $B$ ), reinforcement height ( $R$ ), depth of penetration ( $r$ ), and width ( $b$ ) After visual check, liquid penetrant testing (LPT) and X-ray radiography were taken. The X-ray films were processed, interpreted, and found defect free. Tensile and impact test specimens (Fig. 2a, b, c) were cut by water jet machining and dimensions were maintained as per ASTM-A 370 [5], ASTM E 23 [6] standards.

## 3 Experimental Procedure

One specimen from each plate was tested to represent the weld property in as welded condition (Idn. T1–T9). Heat treatment was carried out for other specimens in an electrically heated laboratory scale furnace as per the heat treatment cycle shown (Table 10) and the rate of heating 100 °C/hour was maintained during heating. For the test specimens cut from test plates TP-1, 5, 9, the cooling media was forced air, for test plates TP-2, 6, 7, the quenching media was water, for test plates TP-3, 4, 8, the quenching media was oil. Similar simulations of heat treatment process were reported by others [3, 7–11] also. These test specimens after heat treatment were



**Table 2** Chemical composition (% in weight)—0.3%C-CrMoV steel (ESR MOD.15CDV6) [1, 2]

C	Mn	Si	Mo	V	Cr	S	P	Nb	Fe	O <sub>2</sub>	H <sub>2</sub>	N <sub>2</sub>
0.27-0.31	0.81-1.0	0.20 max	0.80-0.90	0.20-0.30	1.25-1.50	0.015 max	0.02 max	0.1	Bal	50 ppm max	2 ppm max	125 ppm max

**Table 3** Process details for multi-pass welding

Material	0.3%C-Cr MoV steel
Test plate size	8 × 200 × 150 mm
Filler metal [3]	Size $\phi$ 2.5 mm × 700 L, chemical composition same as parent metal
Welding method	Manual GTAW
Welding machine	Lincon pulse TIG
Maximum current	350 A

**Table 4** Two-pass welding parameters

Experiment	Current (A)	Voltage (V)	No. of pass	Root gap (mm)	Length of filler wire consumed for 200 mm weld length (mm)	Weight of filler metal deposited (per 100 mm in gms)	Weld speed (mm/min)
TP1	160	19	1st	1	350	13	99
	160	18	2nd	–	420	16	46
TP4	202	20	1st	1.5	680	26	65
	160	19	2nd	–	930	36	47
TP7	200	20	1st	2	970	37	64
	165	18	2nd	-	1040	40	37

**Table 5** Three-pass welding parameters

Experiment	Current (A)	Voltage (V)	No. of pass	Root gap (mm)	Length of filler wire consumed for 200 mm weld length (mm)	Weight of filler metal deposited (per 100 mm in gms)	Weld speed (mm/min)
TP2	206	20	1st	1.5	450	17	87
	206	19	2nd	–	550	21	78
	180	18	3rd	–	650	25	71
TP5	206	19	1st	2	550	21	75
	206	19	2nd	–	560	21	63
	180	18	3rd	–	600	23	64
TP8	160	16	1st	1	340	13	71
	160	16	2nd	–	360	14	62
	158	18	3rd	–	550	21	62

**Table 6** Four-pass welding parameters

Experiment	Current (A)	Voltage (V)	No. of pass	Root gap (mm)	Length of filler wire consumed for 200 mm weld length (mm)	Weight of filler metal deposited (per 100 mm in gms)	Weld speed (mm/min)
TP3	203	20	1st	2	600	23	98
	203	20	2nd	–	350	13	103
	203	18	3rd	–	525	20	75
	181	18	4th	–	425	16	67
TP6	160	16	1st	1	350	13	56
	159	17	2nd	–	250	10	57
	160	18	3rd	–	350	13	66
	160	18	4th	–	450	17	52
TP9	204	19	1st	1.5	400	15	75
	203	19	2nd	–	350	13	97
	205	19	3rd	–	300	11	105
	180	18	4th	–	600	23	74

**Table 7** Weld bead dimensions (in mm) of two-pass welding

Test plates TP 1, TP 4, TP 7	Width— <i>B</i>	15/12	14.1/12.1	13.8/11.4
	Height— <i>H</i>	2/0.9	1.6/0.9	1.9/0.7
	Penetration width— <i>b</i>	9/6.9	7.9/6.9	10.1/6.9
	Penetration height— <i>h</i>	1.9/0.8	3.7/2.3	2.8/0.8

**Table 8** Weld bead dimensions (in mm) of three-pass welding

Test plates TP 2, TP 5, TP 8	Width— <i>B</i>	11/10	11.8/10.1	10.7/10
	Height— <i>H</i>	2.0/0.9	2.2/1.0	2.0/1.4
	Penetration width— <i>b</i>	7.6/5.0	8.2/5.3	6.5/5.1
	penetration height— <i>h</i>	0.8/0.5	1.0/0.6	1.1/0.5

**Table 9** Weld bead dimensions (in mm) of four-pass welding

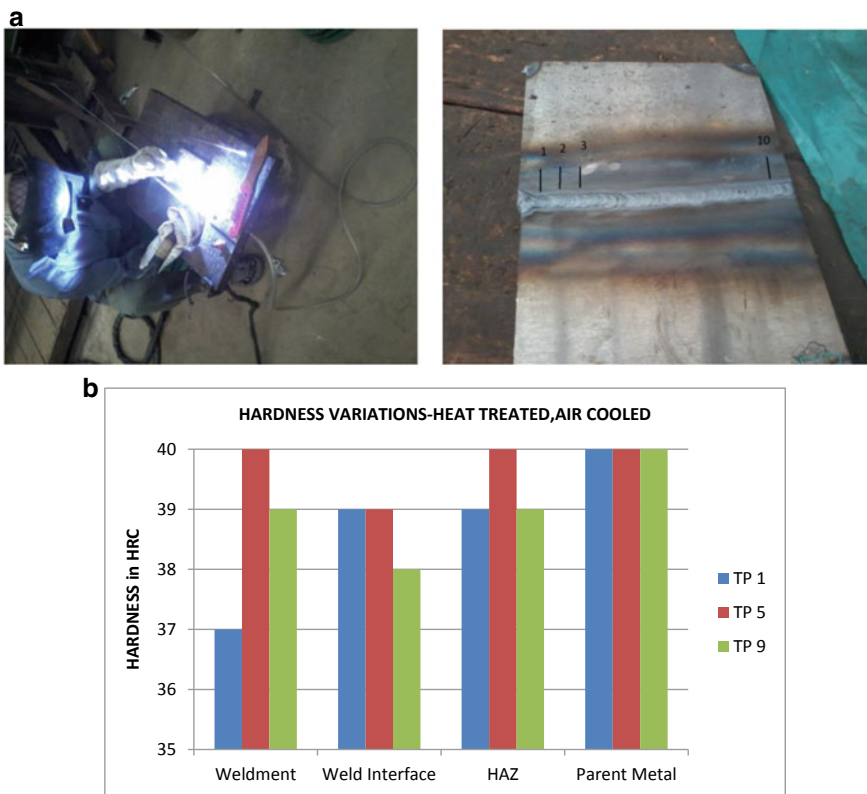
Test plates TP 3, TP 6, TP 9	Width— <i>B</i>	11.9/10.7	10.9/9.9	12.3/10
	Height— <i>H</i>	1.0/0.4	1.8/0.8	2.5/0.7
	Penetration width— <i>b</i>	10.5/5.0	7.0/4.0	6.5/5.1
	Penetration height— <i>h</i>	2.6/0.5	2.4/0.4	1.5/0.3

cleaned by wire brushing to remove the heat treatment scaling, corrected to maintain the dimensions by fitting process using hand files.

### 4 Results and Discussions

Hardness survey [12] carried in all the welded test specimens at the portions of fusion zone (FZ), weld interface (WI) between fusion zone and heat affected zone, heat affected zone (HAZ), on the parent metal, and the values are tabulated below. Table 11 for annealed condition and Tables 12, 13 and 14 and Fig. 1b–d for respective heat treated and quenched conditions (Tables 15, 16, 17, 18, 19, 20, 21 and 22).

Tensile tests [13] were conducted on the specimens (Fig. 2a, b) using 20T capacity computerised UTM machine and 0.2% proof stress was measured using electronic



**Fig. 1** a Weld set up and test plate after welding, b Hardness variations in (HRC)-Heat treated, air cooled, c Hardness variations in (HRC)-Heat treated, water cooled, d Hardnes variations in (HRC)-Heat treated, oil cooled

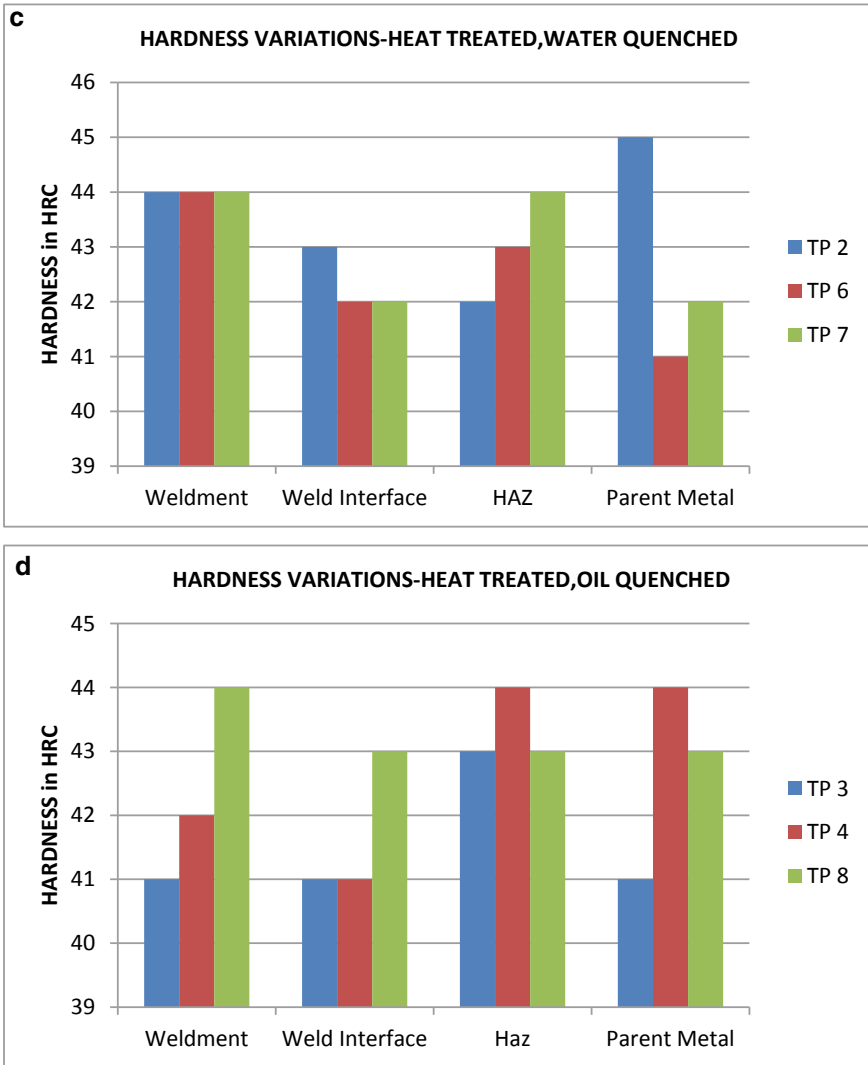
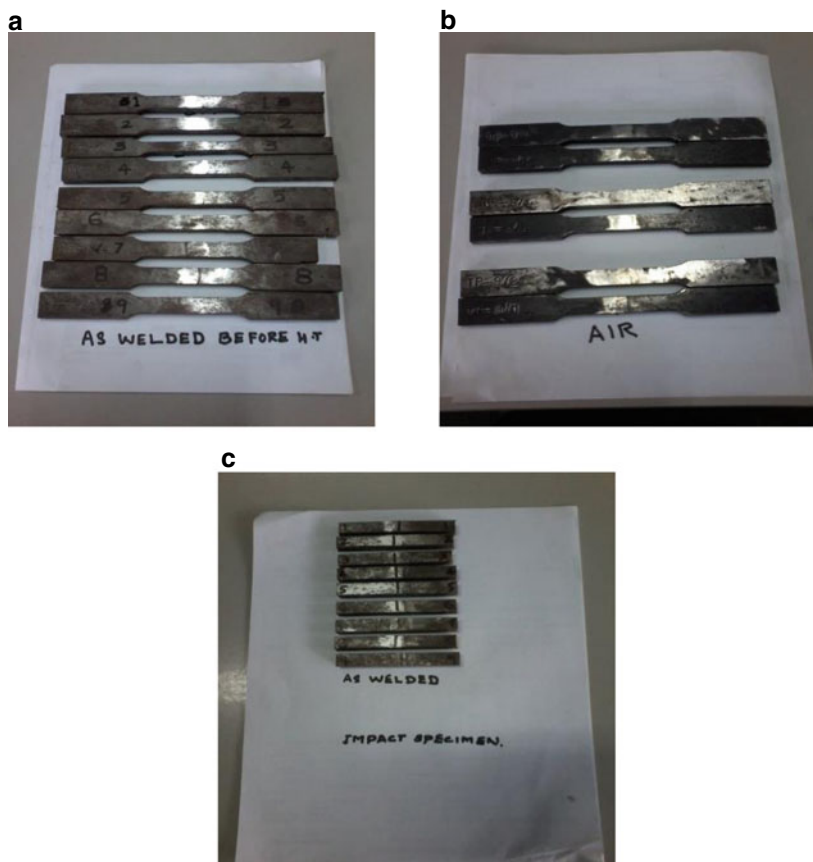


Fig. 1 (continued)

extensometer with autographic recording facility. The tensile test values obtained with different quenching media were tabulated.

The variations of UTS with respect to number of weld passes and root gap at different quench conditions are shown in Fig. 3a, b

Sub-size charpy V-notch [6] impact test specimens (size 55 mm × 10 mm × 7.5 mm, with a notch depth of 2° × 45°, Fig. 2c) were machined and the V-notches were cut using broaching notch cutter machine. Impact testings were carried out at room temperature and the values are given in Figs. 4, 5 and 6.



**Fig. 2** a–c Tensile and impact test specimens

**Table 10** Heat treatment cycle

Process	Temperature at loading	Temperature at soaking	Soaking time	Quenching/cooling medium
Hardening	<600 °C	920 °C	1 h	Air for TP-1, 5, 9 Water for TP-2, 6, 7 Oil for TP-3, 4, 8
Quench delay	<45 s			
Stress relieving	<200 °C	300 °C	1 h	Air
Tempering	<300 °C	505 °C	2 h	Air for TP-1, 5, 9 Water for TP-2, 6, 7 Oil for TP-3, 4, 8
Quench delay	<45 s			

**Table 11** Hardness (in HRC)—As welded condition

Idn No.	Weldment	Weld interface	HAZ	Parent metal (annealed) in BHN (HRC)
T-1	36	38	40	200 (20)
T-2	38	36	40	195 (20)
T-3	37	36	39	205 (21)
T-4	36	37	38	200 (20)
T-5	35	36	38	200 (20)
T-6	36	37	39	195 (20)
T-7	36	37	39	200 (20)
T-8	35	36	38	205 (20)
T-9	36	37	40	200 (20)

**Table 12** Hardness (in HRC)—Heat treated, air cooled

Idn No.	Weldment	Weld interface	HAZ	Parent metal portion
TP-1	37	39	39	40
TP-5	40	39	40	40
TP-9	39	38	39	40

**Table 13** Hardness (in HRC)—Heat treated, water quenched

Idn No	Weldment	Weld interface	HAZ	Parent metal portion
TP-2	44	43	42	45
TP-6	44	42	43	41
TP-7	44	42	44	42

**Table 14** Hardness (in HRC)—Heat treated, oil quenched

Idn No.	Weldment	Weld interface	HAZ	Parent metal portion
TP-3	41	41	43	41
TP-4	42	41	44	44
TP-8	44	43	43	43

**Table 15** Mechanical test [13] values—As welded condition (without heat treatment)

	T-1	T-2	T-3	T-4	T-5	T-6	T-7	T-8	T-9
Root gap	1	1.5	2	1.5	2	1	2	1	1.5
Number of passes	2	3	4	2	3	4	2	3	4
UTS: MPa	690	651	657	706	648	695	663	679	688
0.2% PS Mpa	558	479	484	509	459	479	446	521	439
% Elongation	16.2	16.3	16.1	18	16.3	18	18.2	17.8	17.7

**Table 16** Mechanical test [13] values—Heat treated, cooling medium—Air

	TP-1/1	TP-1/2	TP-5/1	TP-5/2	TP-9/1	TP-9/2
Root gap	1	1	2	2	1.5	1.5
Number of passes	2	2	3	3	4	4
UTS:MPa	1209	1191	1272	1216	1190	1260
0.2%PS: MPa	1075	1073	1217	1148	1088	1132
% Elongation	12.6	14.4	11.8	12	12.9	12.8
% Reduction in area	30.4	32.7	22.3	28.3	29.1	21

**Table 17** Mechanical test [13] values—Heat treated, quenching medium—Water

	TP-2/1	TP-2/2	TP-6/1	TP-6/2	TP-7/1	TP-7/2
Root gap	1.5	1.5	1	1	2	2
Number of passes	3	3	4	4	2	2
UTS: Mpa	1324	1334	1395	1346	1308	1341
0.2%PS Mpa	1268	1287	1323	1323	1267	1306
% Elongation	11.8	10.9	11.9	12	11.8	12
% Reduction in area	23.4	29.4	23.1	24.9	30.9	28.6

**Table 18** Mechanical test [13] values—Heat treated, quenching medium—Oil

	TP-3/1	TP-3/2	TP-4/1	TP-4/2	TP-8/1	TP-8/2
Root gap	2	2	1.5	1.5	1	1
Number of passes	4	4	2	2	3	3
UTS: MPa	1295	1307	1404	1403	1430	1404
0.2%PS MPa	1142	1241	1372	1375	1383	1377
% Elongation	11.7	10.5	10.8	12.5	8.5	10.1
% Reduction in area	28	27	23.8	21.4	18.4	16.1

<sup>a</sup>In all the specimens, the location of failure was outside the weldment

**Table 19** Impact test [6] values—As welded condition

Impact energy	T-1	T-2	T-3	T-4	T-5	T-6	T-7	T-8	T-9
Joules	27	44	52	25	24	52	28	34	30

**Table 20** Impact test [6] values-Heat treated, cooling medium—Air

Impact energy	TP-1/1	TP-1/2	TP-5/1	TP-5/2	TP-9/1	TP-9/2
Joules	16	16	16	18	26	24

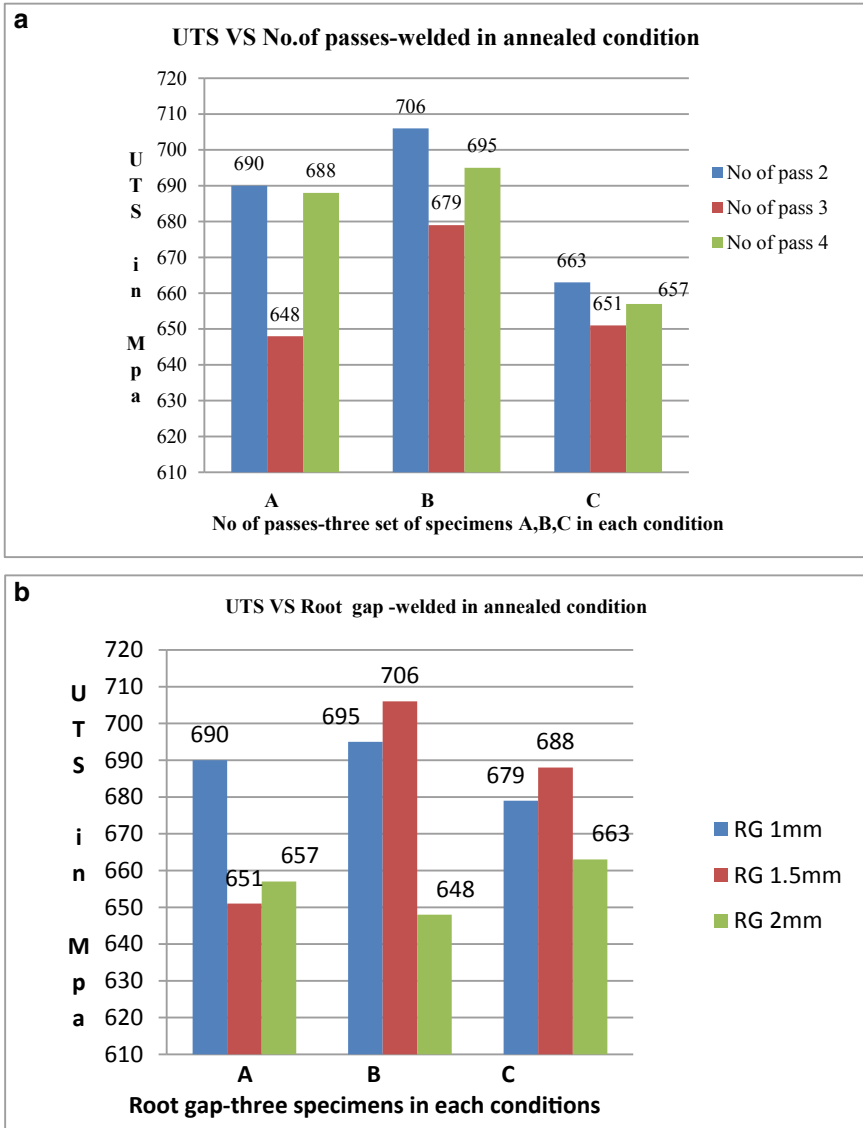
**Table 21** Impact test [6] values—Heat treated,quenching medium—Water

Impact energy	TP-2/1	TP-2/2	TP-6/1	TP-6/2	TP-7/1	TP-7/2
Joules	16	20	20	18	20	18



**Table 22** Impact test [6] values—Heat treated, quenching medium—Oil

Impact energy	TP-3/1	TP-3/2	TP-4/1	TP-4/2	TP-8/1	TP-8/2
Joules	22	18	18	14	16	18



**Fig. 3** UTS Vs no. of weld pass in annealed conditions

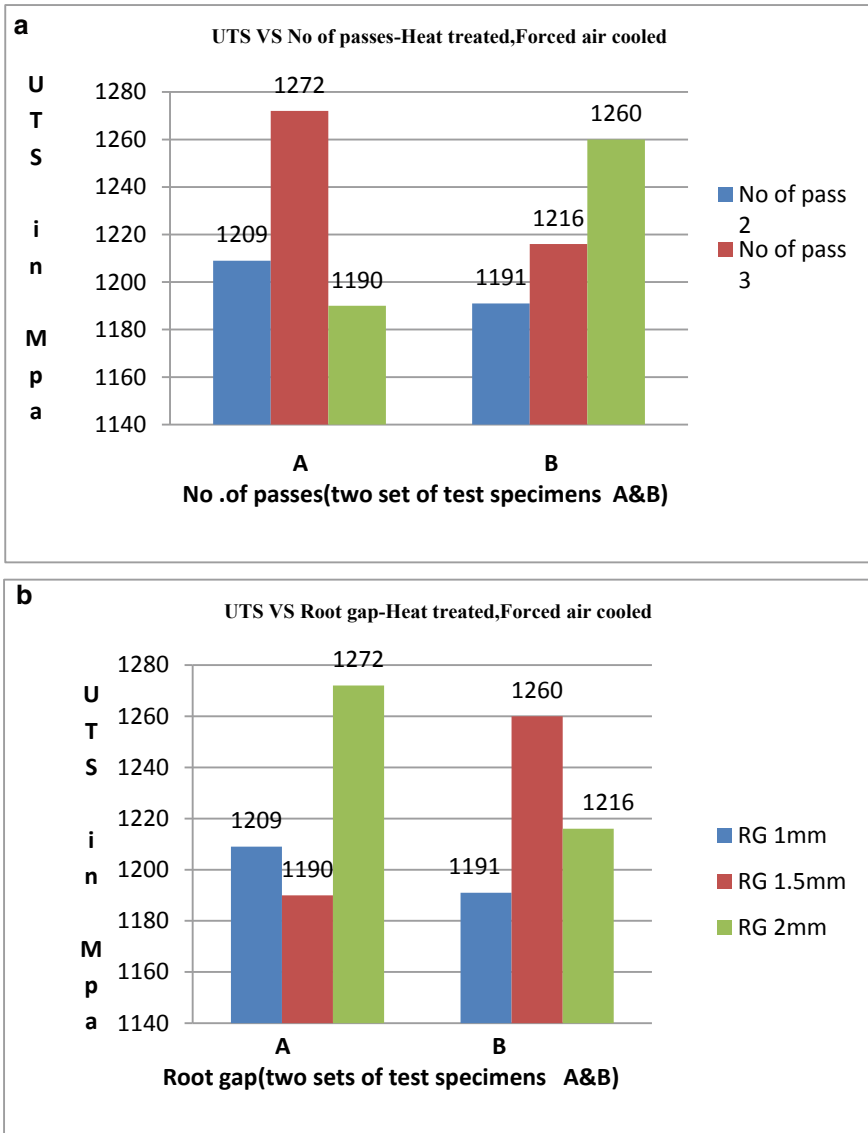


Fig. 4 UTS Vs no. of weld pass, heat treated, air cooled

### 5 Weld Microstructure in Annealed Condition

Optical microstructure of this material, in the as welded condition, reveals ferrite with carbides (Fig. 7a).

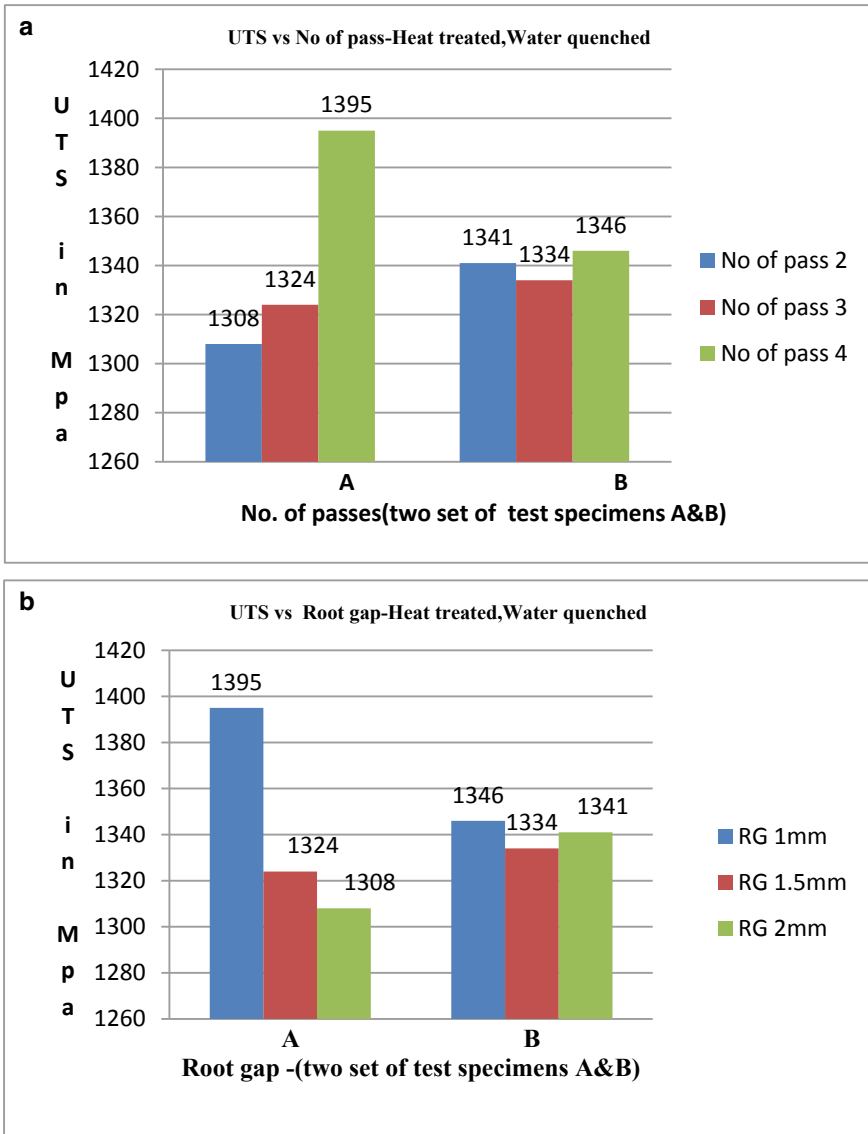


Fig. 5 UTS Vs no. of weld pass, heat treated, water cooled

The optical microstructure of the weldment, heat treated, and quenched in oil and water shows combined microstructure of bainite, martensite in fusion zone (Fig. 7c, d).

The optical microstructure weldment hardened and tempered followed by rapid air cooling shows bainitic structure along with martensite, ferrite, and carbides (Fig. 7b).

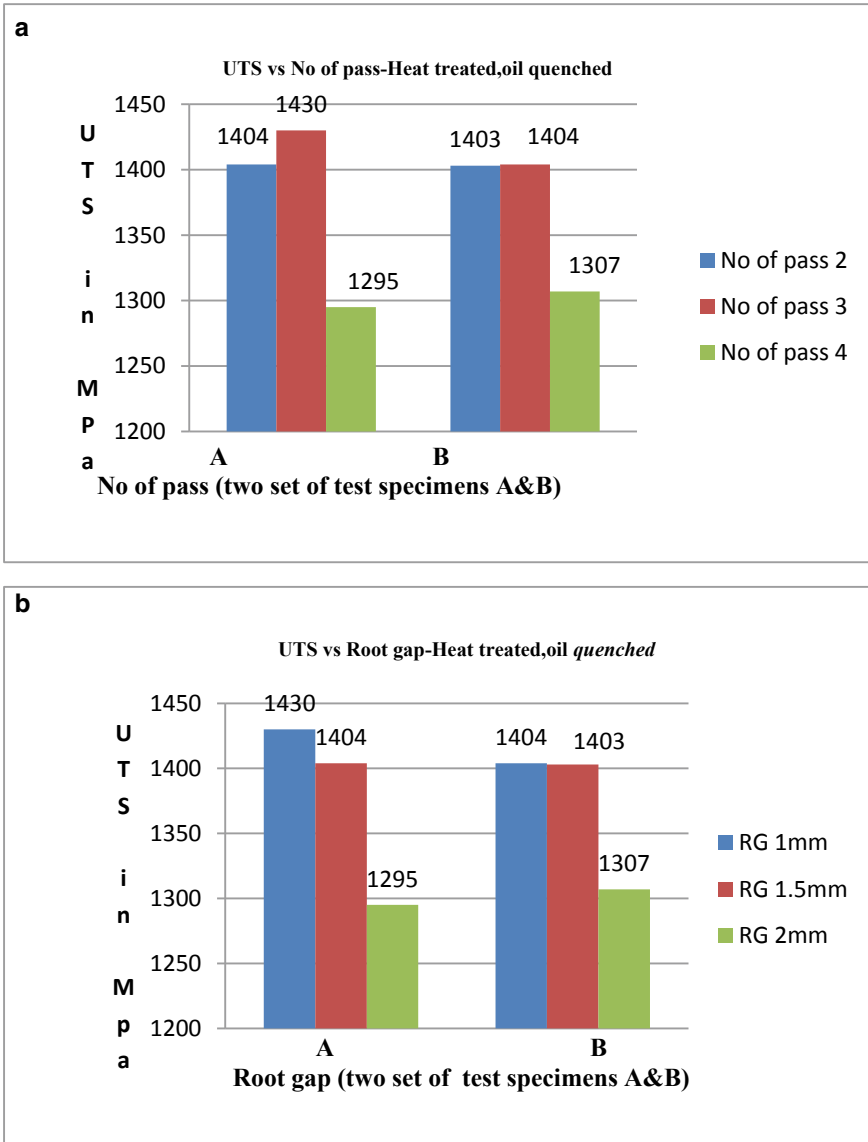
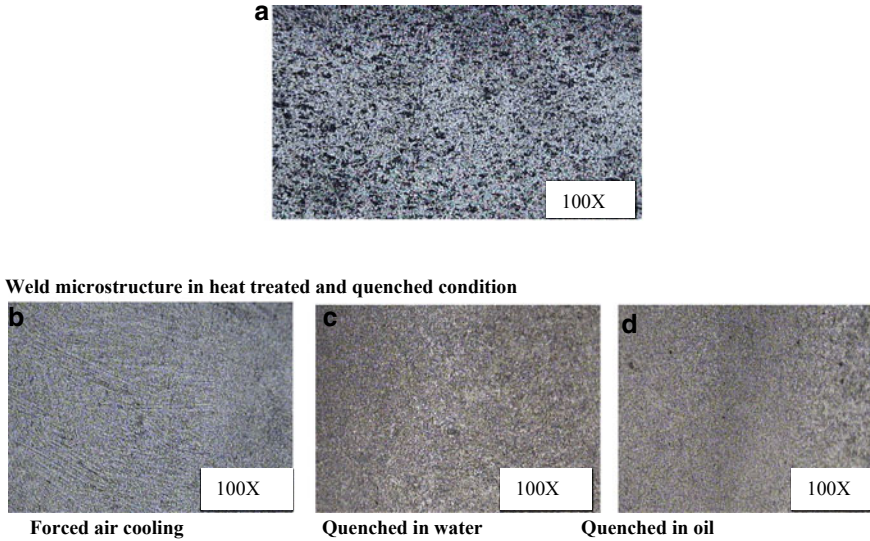


Fig. 6 UTS Vs no. of weld pass, heat treated, oil cooled

Similar microstructure was reported in parent metal weld studies in both annealed and hardened conditions [3, 7–9]



**Fig. 7** **a** weld micro structure, welded in annealed condition, **b** weld micro structure, heat treated, air cooled, **c** weld micro structure, heat treated, water cooled, **d** weld micro structure, heat treated, oil cooled

## 6 Observations

1. The 0.3%C-Cr-Mo-V steel is welded with manual GTA welding in annealed condition gives good bead forming, reinforcement, and penetration.
2. The test plates were welded with different combination of welding parameters, which gave defect free weldment.
3. In multi-pass welding, the weld parameter variations were same irrespective of number of passes.
4. The welding current and voltage required were less when the root gap maintained is 1 mm irrespective of the number of passes.
5. When the root gap is between 1.5 and 2 mm, the current required for the root pass welding and the subsequent passes was more. The closing pass needed lesser current.
6. The rate of filler wire consumption and the welding speed was less when the root gap is less and vice versa.
7. The rate of filler metal deposition was more, when root gap increases, irrespective of number of passes.
8. The dimensional variations of weld bead remain almost same in all the combinations.

## 7 Conclusions

1. In this work, the 0.3%C-Cr-Mo-V steel of 8 mm thickness is used. These plates were welded by using manual GTA welding by employing the weld parameters as per DOE principle. The welded test plates were subjected to NDT methods, then hardened and tempered and quenched using forced air, water, and oil as quenching mediums.
2. The significant outcome of these work is, in all the cases, the tensile tests specimen rupture occurred at the parent material. This shows the strength of both HAZ and the weldment is not lower than that of parent material. Similar trends of tensile properties were reported by Ramkumar [3] in using PAW process.
3. The weldment attains the hardness (Table 11) when welded in annealed condition even though the parent metal region shows less. This is because of hardening effect of the weldment in multi-pass welding.
4. It is found that oil quenching gives maximum strength. Water-quenched specimens give slightly lower properties. Similar trends in the mechanical properties were reported by P.Ramkumar and others [3, 8, 11]
5. When forced air is used as quenching medium, the values of UTS come down since the rate of cooling is less compared to oil and water. Karthikeyan [7] and others reported the same in Parent metal heat treatment studies.
6. Maximum weld strength was obtained in the combinations of 1 mm root gap with number of passes two to three and oil as quenching medium, (Table 10; Fig. 6a, b)
7. The higher strength of weldment was the result of faster cooling which leads to the formation of higher amount of martensite [8].
8. The maximum impact properties were obtained from the plates welded in annealed condition with multi-pass welding.

## References

1. Bandyopadhyay T et al. Improvement in mechanical properties of standard 15CDV6 steel by increasing Carbon and Chromium content and inoculation with titanium by ESR. IIT, Mumbai
2. Maity SK et al (2009) Development of ultrahigh strength low alloy steel through electro slag refining process. ISIJ Int 49(6):902–910
3. Ramkumar P et al (2017) Plasma arc welding of high strength 0.3%C-CrMoV (ESR) steel. Trans Ind Inst Metals
4. Suresh MR et al. Study of welding characteristics of 0.3%C-CrMoV (ESR) ultra high strength steel. J Mater Sci 42(14)
5. ASTM: A 370-10 Standard test methods and definition for mechanical testing of steel products
6. ASTM E 23 Test method for notched bar impact testing of metallic materials
7. Karthikeyan MK et al (2017) Effect of quench media on mechanical properties of 3%C-Cr-Mo-V steel NAMS-2017
8. Saravanan K, Kumar S et al (2012) Effect of tempering temperature on strength and fracture toughness of 0.3%C-CrMoV(ESR) steel. Mater Sci Forum 710: 433–438

9. Magudam C et al (2017) Heat treatment of 0.3%C-CrMov (ESR) segment NAMS-2017
10. Chandra Sekar M et al (2014) Welding development in ESR modified 15CDV6 material. *Int J Mech Eng Rob Res* 3(3). ISSN 2278-0149
11. Sapthagiri et al (2015) Comparison of mechanical properties on 15CDV6 steel plates by TIG welding with or without copper coated filler wires. *Int J Adv Res Found* 2(5)
12. ASTM E 18 Test method for rockwell hardness of metallic materials
13. ASTM E 8 Test method for tension testing of metallic materials
14. Rajkumar V et al. Study of welding maraging steels. In: ICMAT symposia proceedings
15. Yayla P (2007) Effect of Welding processes on the mechanical properties of HY 80 steel materials. *Mater. Des* 28
16. Ramesh MVL et al. Structure-properties evaluation in laser beam welds of high strength low alloy steels. In: 4th International conference on material processing and characterization
17. Naveen Kumar P et al (2014) Study on Dissimilar welding of 15CDV6 and SAE4130 steel by inter pulse GTA welding. In: International conference on advances in manufacturing and materials engineering, AMME 2014. *Procedia Material Science*, vol 5
18. ASTM E 165 Test method for liquid penetrant examination
19. AIR 9112/A Condition for checking and receiving steel parts and assemblies made by melting welding

# Investigation on Tribological Properties of Chromium-Filled Particle Damper During Hard Boring Process



G. Lawrance, P. Sam Paul, R. Gokul, M. Subhash, M. Ezhil, and J. Ebi Ashish

**Abstract** In boring process, surface roughness and tool wear are considered as important parameters which affect the quality of the product due to the overhanging length of tool holder. An appropriate method has to be implemented to reduce tool wear and surface roughness which enhances the productivity in manufacturing industries. In the present study, an effort was made to decrease the tool wear and surface roughness during boring using chromium particle damper. From the result, it was observed that the use of chromium spheres enhances rigidity of the tool and tribological properties.

**Keywords** Particle damper · Chromium sphere · Tribological properties

## 1 Introduction

In modern metal cutting and manufacturing, industrialists are more concern in achieving the product with reduced ecological effect. Also with the good standard end of the product. The product should also possess the dimension accuracy, good surface quality, and increased production rate. The increase in surface roughness results in surface imperfection in the workpiece with variable chip thickness and reduced tool life [1]. Production industries are expecting improved quality, increase in productivity, decrease in production cost, and enhanced practice to reduce surface roughness and tool wear. To increase tool life and surface finish, impact damper is a cost-efficient technique. Friend and Kinra [2] proposed particle damping method which is 50% enhancement in a cantilever beam. Devaraj et al. [3] used impact damper technique on boring process to enhance surface quality of workpiece. Experimental results show that use of different masses of silicon, zinc, aluminum, and copper particles on impact damper reduce the surface roughness of the boring work piece. Alexander et al. [4] used global optimization combined with Pareto optimization technique on chromium nitride system and found that thermodynamically stable

---

G. Lawrance (✉) · P. Sam Paul · R. Gokul · M. Subhash · M. Ezhil · J. Ebi Ashish  
Karunya Institute of Technology and Sciences, Coimbatore, India  
e-mail: [lawrancedevaraj@gmail.com](mailto:lawrancedevaraj@gmail.com)



chromium nitride phases display high hardness up to 30GPa using Vickers hardness calculated by Chen's model. Hones et al. [5] conclude that dichromium nitride coating shows 2950 HV as maximum hardness while crystallized chromium nitride coating displays hardness below dichromium nitride.

In this study, boring tool is partially filled with chromium spheres whose diameter is smaller than the boring tool cavity. The chromium sphere present in the boring bar aids to escalate the stability of the tool holder which inturn increases the tool life and surface finish. During machining process, vibration is reduced due to the energy dissipation from one sphere to another sphere and inturn enhances the tool life and surface finish. Experimental analysis was performed to investigate the effect of chromium particle damper on tribological properties during boring process.

## 2 Experimental Analysis

### 2.1 Chromium Sphere Particle Damper

In this study, widax tool is used with a specification of S25T PCLNR 12 F3 which consist of sim, insert, and tool shank with a dimension of 300 mm length and 25 mm diameter [6]. The cavity of the boring tool consists of 200 mm length and 10 mm diameter which is drilled by spark machining [7]. The chromium sphere of 8 mm diameter is partially filled in a boring tool and sealed by means of adaptable screw [8]. Figure 1. shows the boring tool filled with chromium sphere as particle damper. The workpiece used in this study is AISI 4340 steel and it consists of 100 mm length, 80 mm and 40 mm as outer and inner diameter, respectively [9].

The cutting experiments were performed using Kirloskar turn master-35 lathe. Surface roughness is measured by means of Mitutoyo SJ-210 and tool wear is measured by means of tool maker's microscope. The experimental study was carried out at two repetitions with 60 s each at dry condition.

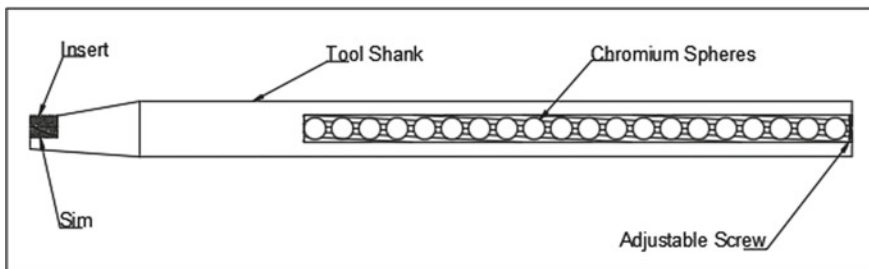


Fig. 1 Boring tool cavity is filled with chromium sphere

## 2.2 Design of Experiments

Taguchi technique is used to optimize the cutting parameters which consist of tolerance design, system design, and parameter design. In this study, parameter design is used with the stages as (i) quality characteristics is to be identified and design parameters should be selected and evaluated; (ii) design parameters levels should be determined; (iii) a suitable orthogonal array should be selected and assigned; (iv) based on the orthogonal array arrangement, experiments should be conducted; (v) S/N analyses used to analysis the experimental results; (vi) optimal levels of design parameters are to be selected; and (vii) optimal design parameters should be verified through the confirmation experiment. In this present study, an orthogonal array ( $L_9$ ) consist of nine rows and three columns. The design parameter can handle three level of eight degree of freedom. Each column consist of cutting parameter with nine cutting combinations. So entire parameter space consists of nine experiment with orthogonal array of  $L_9$ . So, in this study,  $L_9$  orthogonal array is selected based on Taguchi technique with variables as feed rate, cutting speed, and the depth of cut and shown in Table 1 [9]. Table 2 shows orthogonal array of  $L_9$  with three cutting parameters as experimental layout [10].

**Table 1** Levels of input parameters

S. no	Variable	Level 1	Level 2	Level 3
1	Cutting speed (m/min)	60 ( $S_1$ )	80 ( $S_2$ )	100 ( $S_3$ )
2	Feed (mm/rev)	0.06 ( $P_1$ )	0.08 ( $P_2$ )	0.1 ( $P_3$ )
3	Depth of cut (mm)	0.5 ( $W_1$ )	0.6 ( $W_2$ )	0.7 ( $W_3$ )

**Table.2** Response values and S:N ratios

Runs	Factors			Responses		Signal-to-noise ratio	
	Cutting speed	Feed rate	Depth of cut	Surface roughness ( $\mu\text{m}$ )	Tool wear (mm)	Surface roughness (dB)	Tool wear (dB)
1	$S_1$	$P_1$	$W_3$	3.16	2.62	-10.00	-8.36
2	$S_1$	$P_2$	$W_1$	2.25	2.57	-7.04	-8.19
3	$S_1$	$P_3$	$W_2$	3.26	3.28	-10.27	-10.31
4	$S_2$	$P_1$	$W_2$	1.80	2.31	-5.12	-7.29
5	$S_2$	$P_2$	$W_3$	2.10	2.90	-8.31	-9.24
6	$S_2$	$P_3$	$W_1$	2.80	1.78	-8.95	-5.00
7	$S_3$	$P_1$	$W_1$	0.67	0.71	3.46	2.97
8	$S_3$	$P_2$	$W_2$	2.17	1.65	-6.74	-4.34
9	$S_3$	$P_3$	$W_3$	2.17	3.21	-8.53	-10.13

### 2.3 S:N Ratio Characteristics

It is the mean to the standard deviation and measure the quality characteristic deviating from the desired value. The S:N ratio ( $\eta$ ) is calculated by the following equation

$$\eta = -10 \log(\text{M.S.D.}) \quad (1)$$

To obtain optimal cutting performance for tool wear and surface roughness for the mean square deviation.

$$\text{M.S.D} = \frac{1}{M} \sum_{i=1}^m S_i^2 \quad (2)$$

where  $m$  is the number of tests and cutting parameters value,  $S_i$  for surface roughness and tool wear in the  $i$ th test [10].

## 3 Results and Discussion

### 3.1 S:N Ratio

Table 2 shows the experimental values of surface roughness and tool wear and the response parameters which are converted into S:N ratio using the Taguchi method are also presented. The ‘smaller the better’ quality characteristics were used in signal-to-noise ratio to calculate surface roughness and tool wear [11]. From Figs. 2 and 3, optimal machining parameters for reduced surface roughness and tool wear were determined. Table 3 specifies signal-to-noise ratios for surface roughness value, cutting speed as Level 3, feed rate as Level 1 and depth of cut as Level 1. Similarly, signal-to-noise ratios for tool wear were identified as cutting speed as Level 3, feed rate as Level 1 and depth of cut as Level 1. Figures 2 and 3 identify optimum cutting parameters as 100 m/min ( $S_3$ ) as cutting speed, 0.06 mm/rev ( $P_1$ ) as feed rate and 0.5 mm ( $W_1$ ) as depth of cut. The tribological properties were studied and signal-to-noise ratio was analyzed by means of MINITAB16 software [12].

The confirmatory test was conducted for chromium particle damper with boring bar and an ordinary boring bar through which parameters were obtained. From Table 4 clearly shows that chromium sphere-filled particle damper increases the surface finish by 77.5% and tool life by 78.8%.

The impact from the tool is transferred to the spheres using a linear momentum. The damping force is caused by means of linear momentum of the spheres and it is influenced by material and mass of the sphere [13]. So the large amount of damping

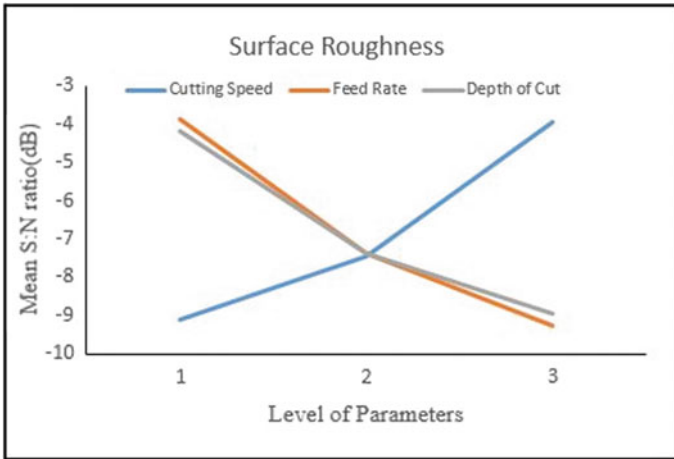


Fig. 2 Signal-to-noise ratio plot for surface roughness

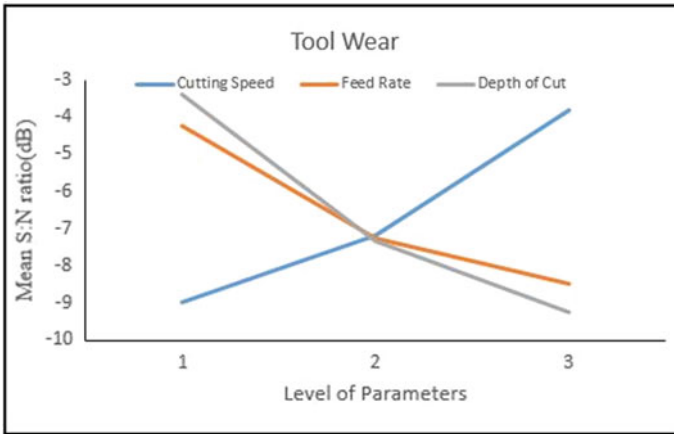


Fig. 3 Signal-to-noise ratio plot for tool wear

Table 3 Signal-to-noise ratio table

S. no	Cutting parameter	S:N ratio (dB)					
		Surface roughness			Tool wear		
		L 1	L 2	L 3	L 1	L 2	L 3
1	Cutting speed	-9.10	-7.46	-3.93	-8.96	-7.18	-3.83
2	Feed rate	-3.88	-7.36	-9.25	-4.22	-7.26	-8.48
3	Depth of cut	-4.17	-7.38	-8.95	-3.41	-7.31	-9.24

**Table 4** Comparison test with and without chromium-filled particle damper

S. no	Cutting parameters	With impact damper	Without impact damper	% Reduction
1	Surface roughness ( $\mu\text{m}$ )	0.72	3.2	77.5
2	Tool wear (mm)	0.70	3.3	78.8

effect is provided by chromium sphere particle damper. It is found that chromium sphere particle damper provides larger damping by means of confirmatory test.

## 4 Conclusions

In this study, chromium sphere particle damper was developed and to study its influence on surface roughness and tool wear during boring of hardened AISI 4340 steel. Cutting experiments were conducted, signal-to-noise ratio analysis was done, and finally, the performance of chromium sphere particle damper with conventional boring tool was compared. From this study, the following observations were made:

1. The chromium spheres were partially filled to achieve decrease in surface roughness and tool wear.
2. The chromium spheres particle damper is less expensive and simple in design which can function in any environments.

## References

1. Sam Paul P, Varadarajan AS, Ajay Vasanth X, Lawrance G (2014) Effect of magnetic field on damping ability of magneto rheological damper during hard turning. *Archives of Civil and Mechanical Engineering* 14:433–443 (2014)
2. Friend RD, Kinra VK (2000) Particle impact damper. *J Sound Vib* 233(1):93–118
3. Shivalingappa DS, Channankaiah D, Jangaler RS (2014) Surface quality enrichment using fine particle impact damper in boring operations. *Int J Res Eng Technol* 3(2):531–535
4. Kvashnin AG, Oganov AR, Samtsevich AI, Allahyari Z (2017) Computational search for novel hard chromium-based materials. *J Phys Chem Lett* 8(4):755–764
5. Hones P, Sanjines R, Levy F (1997) Characterization of sputter-deposited chromium nitride thin films for hard coatings. *Surface Coatings Technol* 94–95:398–402
6. Lawrance G, Sam Paul P, Varadarajan AS, Paul Praveen A, Ajay Vasanth X (2017) Attenuation of vibration in boring tool using spring controlled impact damper. *Int Journal on Int Des Manuf* 11:903–915
7. Lawrance G, Sam Paul P, Ezhil M, Ebi Ashish J, Gokul R, Subhash M Influence of stainless steel impact damper on tribological properties during boring process. *Mater Today: Proceedings*. <https://doi.org/10.1016/j.matpr.2020.06.260>
8. Diniz AE, Alves da Silva WT, Suyama DI, Pederiva R, Albuquerque MV (2019) Evaluating the use of a new type of impact damper for internal turning tool bar in deep holes. *Int J Adv Manuf Technol* 101:1375–1390

9. Lawrance G, Sam Paul P, Ajay Vasanth X, Varadarajan AS, Daniel E (2019) Influence of magnetorheological elastomer on tool vibration and cutting performance during boring of hardened AISI4340 steel. *J Mech Sci Technol* 33: 1555–1561(2019)
10. Yang WH, Tarn YS (1998) Design optimization of cutting parameters for turning operations based on the Taguchi method 84(1–3):122–129
11. Lawrance G, Daniel E, Sam Paul P, Shaji J, Thankachan T (2020) Study on the influence of multi-layered nano metal oxide coating on cutting performance during boring of hardened steel. *Materials Today: Proceedings* 22:1731–1736
12. Thankachan T, Soorya Prakash K, Loganathan M (2018) WEDM process parameter optimization of FSPed copper-BN composites, *Mater Manuf Proces* 33:350–358
13. Kanase Sandip S, Jaydeep SP, Sainand MJ (2013) Improvement of Ra value of boring operation using passive damper. *Int J Eng Sci* 2(7):103–108

# Frictional Performance on Various Speed and Pressure for Cardanol as a Binder in High Friction Composite Material Using Pin on Disc



G. K. Kannan, S. Stephen Bernard, Md. Javeed Ahmed, A. Ivon Paul, and G. Suresh

**Abstract** The main objective of this research work is to develop an environmentally friendly brake pad with the incorporation of bio based binder, filler, reinforcement and friction modifiers. This study suggests that maintaining the high friction stability at high speed and load for a brake pad material can be sustained by cardanol resin, a natural resin binder. The tribo test procedure of JASO 406C was performed on two different cardanol (15CF and 20 CF) compositions by maintaining the two test parameters such as pressure sensitivity (effectiveness test). Result shows that 3–(8,11,14-Pentadecatrienyl) phenol Cardanol in phenolic resin is found to be more superior and most suitable binder resin combination, for the given ingredients compared to using only a cardanol resin as a binder in brake pad. Furthermore, the morphology of wear debris, contact plateaus and transient patches are analysed by scanning electron microscope.

**Keywords** Cardanol · Brake pad · Pressure sensitivity · Temperature sensitivity · Friction

## 1 Introduction

Friction materials requires a combination of friction controlling additives, fiber, fire resistant ingredients, and binder. Out of these ingredients, binder plays the major role of binding all the ingredients as a single composite and these exhibits exemplary friction quality during contact of two surface [1]. This materials also require wear

---

G. K. Kannan

Department of Mechanical Engineering, Chennai Institute of Technology, Chennai, India

S. Stephen Bernard (✉) · A. Ivon Paul · G. Suresh

Department of Mechanical Engineering, Rajalakshmi Institute of Technology, Kuthambakkam, Chennai, India

e-mail: [Stephenbernard.s@ritchennai.edu.in](mailto:Stephenbernard.s@ritchennai.edu.in)

Md. J. Ahmed

Department of Mechanical Engineering, BS Abdur Rahman Crescent Institute of Science and Technology, Vandalur, Chennai, India

resistance and high friction stability. More than 10 ingredients used for the production of composite which are abundantly available and significantly economical in manufacturing sector [2, 3].

Phenolics resins are generally used as a binder materials for the production of high friction composites. Phenolic resin enhance the inhaling disease to the manufacturer due to their harmful particle passes through the respiratory system [4]. It also has poor shelf life, shrinkage and voids. The phenolic resin enhance the friction and squealing noise during contact between two surface [5]. Succeed in dealing with these complication, phenolic resin can be an alternate with a tribo-evaluated thermosetting phenolics. The production of new thermosetting resin must be low cost with high mechanical strength compared to phenolics. Thermosetting are highly cross linked polymer material which was cured using pressure and heat.

Many researcher works on developing the applications of renewable thermosetting materials for the production of high friction materials. It may help industry to produce with high strength and thermal stress resistance with the inclusion of renewable energy. This leads to the reduction of inhaling disease to the operator who's directly involve in the production of high friction materials [6]. Using of renewable material in thermosetting polymer such as epoxy, phenolics and polyester.

Research on novolac-type resins synthesized based on cardanol which was derived from cashew nut shell liquid. Production of cardanol resin at distinctive experimental conditions to synthesize a better output with diverse extent of conversion. cardanol-based novolac-type phenolic resins increased the strength and stability of the friction composite to large extent [7]. Cashew nut have the renewable binder materials such as cardanol, cardols, anacardic acids and cashew nut shell liquid. Cashew apple are mostly used in poultry feed, paint and varnish. Cashew seed shell have the high content of binding quality and a more cost effective ingredients. It is also determined that the wear resistances, chemical bonding, and the life span of the composite is high.

The analysis on wear, friction and lubrication during a material contact gives a importance due to their function of force on a mating surface. During contact of two different material, low strength material will experience a material loss from a contact surface and resistance to motion [8]. Pin on disc experiments are used to measure the coefficient of friction and wear of the composites during their initial development because it is too costly to analyze the composites for particular application testing kit. Using Pin on disc, tribology and wear readings nearly same compare to inertia dynamometer test but the measurement of various environment condition is not possible.

In this paper frictional performance and friction stability of cardanol resin in high friction composite material is analysed using pin on disc tribometer. Also wear for all the specimen analysed.



## 2 Materials and Methodology

All ingredients used in the production of high friction materials are purchased. Five specimens are prepared and friction test were conducted. Cardanol and phenolic resin are varied and the remaining ingredients kept constant as shown in the Table 1.

Friction performance and stability was measured using DUCOM wear and friction monitor. C.I is used as a counter material and tested specimen is shown in the Fig. 1. The readings are automatically entered by a data acquisition system. Testing procedure followed is ASTM G-99. Motor runs under stationary load conditions and velocity remains constant during a measurement. The reading parameter from a test kit are specific wear rate, friction force and coefficient of friction.

Length and diameter of the composite specimen are 32 and 8 mm. Cast Iron disc was fixed on a table with eight screw and renewed after each reading. Specimen tightened on a top screw and placed on a cast iron disc. The tests were carried out at various load for different time and speed. In this experiment, load 20, 30 and 40 N are maintained at a velocity of 2–4 m/s for distance of 6.3 km. At beginning the speed is maintained at 300 rpm for 700 s and gradually augment to 500 rpm for 700 s and then the speed is augmented to 700 rpm for another 700 s. Specimen and disc were removed from the table after taking reading then it is cleaned by using acetone. Then the specimen is weighed in an electronic machine with a precision of 0.1 mg.

Average COF ( $\mu$ ) of specimen was measured using the below equation

**Table 1** Formulation of friction material by varying cardanol content

Ingredients (Wt %)	PR	5% CF	10% CF	15% CF	20% CF
CF Resin	<b>0</b>	<b>5</b>	<b>10</b>	<b>15</b>	<b>20</b>
PR Resin	<b>20</b>	<b>15</b>	<b>10</b>	<b>5</b>	<b>0</b>
Reinforcement	40	40	40	40	40
Friction and lubricant additive	40	40	40	40	40

Bold indicates the determining factors of the entire research work



**Fig. 1** Ducom wear and friction tester with data acquisition and specimen tested

$$\mu = \frac{F_f}{F_n} \quad (1)$$

where,  $F_f$  is the average friction force, and  $F_n$  is the applied load.

Friction Stability (F.S) is calculated using the below Equation

$$F.S = \frac{\mu_{avg}}{\mu_{max}} \times 100 \quad (2)$$

where,  $\mu_{avg}$  is the average COF and  $\mu_{max}$  is the maximum COF.

### 3 Results and Discussions

#### 3.1 Friction Performance

Coefficient of friction of cardanol formaldehyde resin is shown in Fig. 2. It is evident that 5, 10 and 15% forms a same trend. Phenol formaldehyde resin and 20% cardanol resin forms a very distinct than other specimen. Phenolic resin manifest clearly the unstable coefficient of friction during starting and then the friction stability is maintained. Friction instability is normal and usually fade away after a contact between the specimen and cast iron [8].

It is found that friction values are high during siding on cast iron. It depends on binder strength and lubricant properties of all chemicals. Highest Coefficient of friction value is 0.57 for phenolic resin. This is because the resin changes its physical characteristics when it reaches the glass transition temperature and form as a char [9]. 10% cardanol formaldehyde resin found friction stability from the beginning to the end of sliding. It may be presence of low hardness properties of cardanol which

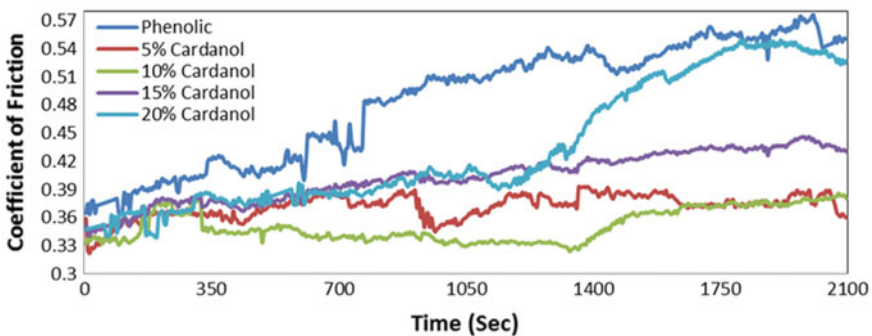


Fig. 2 Coefficient of friction on various speed and time for the load of 2 MPa

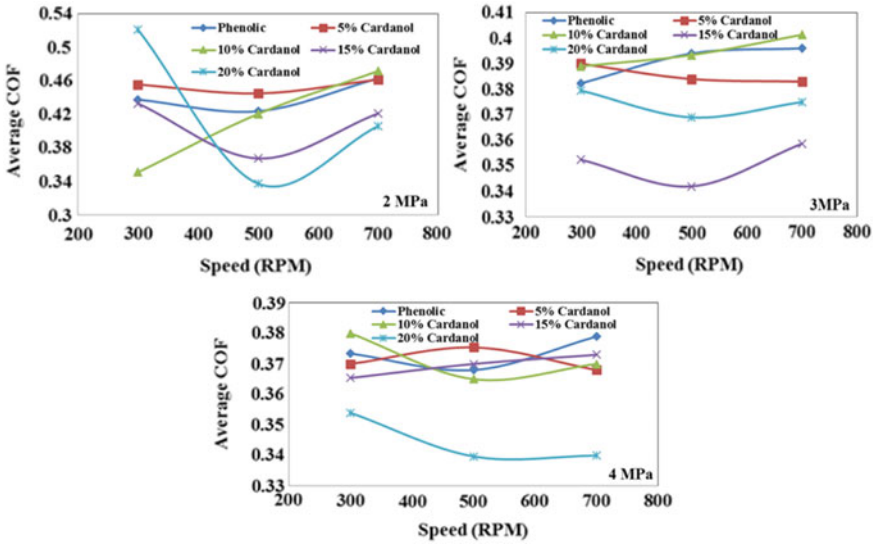


Fig. 3 Average COF under various pressure and speed

smoothen the contact between specimen and cast iron [10]. COF for 5 and 10% is less than 0.39, which is an acceptable range for friction values.

Average COF value for the load of 2, 3 and 4 MPa is shown in Fig. 3. It is found that average friction value range is between 0.34 and 0.52 for all the specimen. In all load at 300 rpm average friction value of phenolic resin is high compared to all cardanol resin. But the trend is changed for the speed of 500 and 700 rpm. In general temperature is directly related to pressure at constant volume, this leads the cardanol to hold other resin very poor because it is a polymeric materials [11].

From the figure it is clear that average COF decreases when the pressure is increased for all the specimen. The reason behind this characteristics are the real contact surface is increased at high pressure to a large extent seeing that cardanol are viscoelastic in nature [12]. Reduction of friction value is due to degradation of cardanol at the asperity contact surface leads to form a carbon dioxide [13].

### 3.2 Friction Stability

Friction stability of phenolic and cardanol resin is represented in Fig. 4. Friction stability is good for the specimen ranges from 85 to 100. In phenolic resin, the friction stability is high at 300 rpm and it is continuously reduced for 500 and 700 rpm. The reason behind this the hardness of the phenolic resin [14]. Among all the specimen, 15 and 20% cardanol resin have high friction stability. This may be

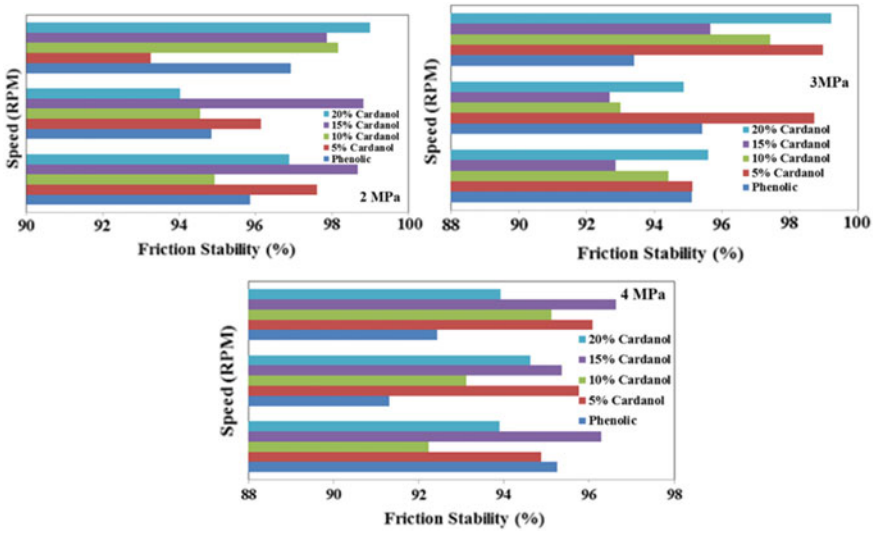


Fig. 4 Friction stability under various pressure and speed

due to low content of cardanol presence in specimen which ascribe steric hindrance and lessen the interaction of intermolecules in C15 side chain [15].

Friction stability for 15 and 20% cardanol remains constant for all pressure which gives an ideal nature of the specimen. But at the mean time the frictional behavior is totally varied at 300 rpm for all load. The reason behind this the fact that at lower rpm, initially entire contact between the specimen and cast iron is not formed which gives unsteady behavior of friction values which is been described in the Fig. 5.

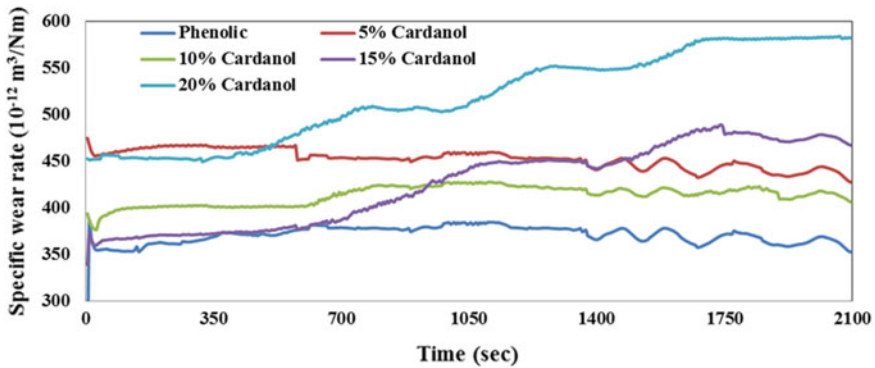


Fig. 5 Specific wear rate of cardanol resin for various sliding speed

### 3.3 Wear

For all the five specimen the testing method are similar and hence the extra care has been taken to analyze the wear amount for each speed and pressure. It is found that phenolic resin specimen have low wear rate compared to cardanol resin specimen. This may be due to internal strength of binder over the other ingredients [16]. It is also noted that at higher rpm wear is gradually increased due to temperature of the specimen increase. For 20% cardanol specimen the specific wear rate is rapidly increased to  $583 \times 10^{-12} \text{ m}^3/\text{Nm}$ . This is an unexpected result because the friction stability is high at 700 rpm. Lubricating property for cardanol resin is reduced by adding a large quantity instead of phenolic resin. Selecting a cardanol range plays a role of wear and lubrication in friction.

## 4 Conclusion

From the experiment it was evident that the friction stability is high at high pressure and speed for all the specimen. Similarly, it shows the poor stability at low pressure and speed. Phenolic resin have the higher friction value which creates a wear in the specimen or cast iron disc. 5 and 10% cardanol resin have lower friction value which reduce a contact surface.

15 and 20% cardanol resin have friction value from 0.35 to 0.45, which is an acceptable range. Also it shows high friction stability at all the pressure and speed. So applying 15 or 20% of cardanol as a binder materials gives the high strength, low wear rate and good friction stability for all the conditions. Specific wear rate is high for higher rpm for all the composites. Phenolic resin have lower wear rate at all speed. 10% cardanol resin shows  $400 \times 10^{-12} \text{ m}^3/\text{Nm}$  for all the speed, which is the minimum wear for high friction material since friction is also considered.

## References

1. Devi A, Srivastava D (2007) Studies on the blends of cardanol-based epoxidized navolac resin and CTPB. *Eur Polymer J* 43:2422–2432. <https://doi.org/10.1016/j.eurpolymj.2007.03.006>
2. Stephen Bernard S, Javeed Ahmed M, Dasaprakash J, Saroj Nitin MR, Vivek S, Kannan GK (2019) Friction and Wear Properties of Bio-Based Abrasive in a High-Friction Composite Material. *Advances in Manufacturing Technology. Lecture Notes in Mechanical Engineering*. 577–585. [https://doi.org/10.1007/978-981-13-6374-0\\_63](https://doi.org/10.1007/978-981-13-6374-0_63)
3. Le Hwong N, HuuNieu N, Tan TTM, Ullrich J, Griesser, (1996) Cardanol-phenol-formaldehyde resin Thermal analysis and characterization. *Die Angewandte Makromolekulare Chemie*. 243:77–85. <https://doi.org/10.1002/apmc.1996.052430107>
4. Yadav R, Srivastava D (2009) Studies on the process variable Condensation reaction of cardanol and formaldehyde by response surface methodology. *Eur Polymer J* 45:946–952. <https://doi.org/10.1016/j.eurpolymj.2008.11.019>

5. Stephen Bernard S, Jayakumari LS (2014) Effect of the Properties of Natural Resin Binder in a High Friction Composite Material. *Polimeros- Ciencia Tecnologia*. 24; 2: 149–152. <https://doi.org/10.4322/polimeros.2014.038>
6. Sai Krishnan G, Jayakumari LS (2019) Investigation on the physical, mechanical and tribological properties of areca sheath fibers for brake pad applications. *Mater Res Express* 6:085–109. <https://doi.org/10.1088/2053-1591/ab2615>
7. Mwaikambo LY, Ansell MP (2003) Hemp fibre reinforced cashew nut shell liquid composites. *Compos Sci Technol* 63:1297–1305. [https://doi.org/10.1016/S0266-3538\(03\)00101-5](https://doi.org/10.1016/S0266-3538(03)00101-5)
8. Stephen Bernard S, Jayakumari LS (2018) Pressure and Temperature Sensitivity Analysis of Palm fiber as a biobased reinforcement material in brake pad. *J Brazilian Soc Mechanical Sci Eng* 40:152. <https://doi.org/10.1007/s40430-018-1081-0>
9. Sultania M, Rai JSP, Deepaksrivastava, (2011) Process modeling, optimization and analysis of esterification reaction of cashew nut shell liquid (cnsl)-derived epoxy resin using response surface methodology. *J Hazard Mater* 185:1198–1204. <https://doi.org/10.1016/j.jhazmat.2010.10.031>
10. Oztrk B, Ozturk S (2011) Effect of resin type and fiber length on the mechanical and tribological properties of brake friction materials. *Tribol Lett* 42:339–350. <https://doi.org/10.1007/s11249-011-9779-5>
11. Stephen Bernard S, Jayakumari LS (2016) Effect of rockwool and steel fiber on the friction performance of brake lining materials. *Materia- rio de janeiro*. 21: 656-665. <https://doi.org/10.1590/S1517-707620160003.0063>
12. Sharifah H, Aziz Martin P, Ansell (2004) The effect of alkalization and fibre alignment on the mechanical and thermal properties of kenaf and hemp bast fibre composites: part 2—cashew nut shell liquid matrix. *Composites Sci Technol* 64:1231–1238. <https://doi.org/10.1016/j.compscitech.2003.10.002>
13. Ikeda R, Tanaka H, Uyama H, Kobayashi S (2002) Synthesis and curing behaviors of a crosslinkable polymer from cashew nut shell liquid. *Polymer* 43:3475–3481. [https://doi.org/10.1016/S0032-3861\(02\)00062-9](https://doi.org/10.1016/S0032-3861(02)00062-9)
14. Yun R, Filip P, Lu Y (2010) Performance and evaluation of eco-friendly brake friction materials. *Tribol Int* 43: 2010–2019. <https://doi.org/10.1016/j.triboint.2010.05.001>
15. Bijwe J, Kumar M (2007) Optimization of steel wool contents in non-asbestos organic (NAO) friction composites for best combination of thermal conductivity and tribo-performance. *Wear* 263:1243–1248. <https://doi.org/10.1016/j.wear.2007.01.125>
16. Malhotra VM, Valimbe PS, Wright MA (2002) Effects of fly ash and bottom ash on the frictional behaviour of composites. *Fuel* 81:235–244. [https://doi.org/10.1016/S0016-2361\(01\)00126-0](https://doi.org/10.1016/S0016-2361(01)00126-0)

# Studies on Mechanical and Physical Characteristics of Cardanol in a High-Friction Composite Material



S. Stephen Bernard, G. Suresh, G. K. Kannan, S. R. Lohesh Srinath, M. Vishweshwaran, and Md. Javeed Ahmed

**Abstract** This work presents the influence of cardanol in a high-friction material as a binder resin. Cardanol is a natural derived resin which has a phenolic structure bonding which holds all the ingredients during mechanical stress. Five specimens were prepared (phenolic resin and 5, 10, 15, 20% cardanol resin) by varying cardanol resin. Fourier transform infrared spectroscopy analysis of phenolic and cardanol resins was done. Thermogravimetric analysis, physical and mechanical testing were done for all the samples. Result shows that 20% cardanol shows a better result for specific gravity, heat swell and loss of ignition. It also shows a low weight gain in water, salt water and lubricating oil. SEM analysis shows small broken metallic materials and be lost from the contact zone immediately after being broken from the composite surface.

**Keywords** Cardanol · TGA · FT-IR · Friction · SEM

## 1 Introduction

Binder plays a major role in a high-friction composite material, which maintains a structural integrity at high pressure and thermal stresses. More than 10 ingredients are used to manufacture a high-friction composite material. All these ingredients are held together and prevent from crumbling apart from the composites [1]. At all operating and environmental condition, the binder effectively controls the deterioration of the

---

S. Stephen Bernard (✉) · G. Suresh · S. R. Lohesh Srinath · M. Vishweshwaran  
Department of Mechanical Engineering, Rajalakshmi Institute of Technology, Kuthambakkam,  
Chennai, India  
e-mail: [Stephenbernard.s@ritchennai.edu.in](mailto:Stephenbernard.s@ritchennai.edu.in)

G. K. Kannan  
Department of Mechanical Engineering, Chennai Institute of Technology, Kundrathur, Chennai,  
India

Md. Javeed Ahmed  
Department of Mechanical Engineering, BS Abdur Rahman Crescent Institute of Science and  
Technoogy, Vandalur, Chennai, India

ingredients. Choosing the type and quantity of binder added in a composite is by trial and error method [2, 3].

Generally, phenolic resins are used as a binder material which is a synthetic resin. It creates harm to the respiratory system. More volume of phenolics added in composite leads to friction drop at elevated temperature and also affects cross-linking [4, 5].

Instead of using phenolic resin, researchers are doing studies on renewable material. Many researches deal on the ingredients of reinforcement and friction modifier in composite such as banana peel, hemp and jute [6]. Cardanol is one of the best alternatives for synthetic phenolic resin. Cardanol is extracted from cashew nut shell liquid. It is a byproduct of cashew seed. Among all countries, India is the major exporter of cashew (around 55%). So, the abundantly available cardanol can be used as a binder in friction material [7, 8].

CNSL is considered as the phenol derivative which was mainly composed of four meta-alkyl phenols differing by the unsaturation degree of aliphatic chain—monoolefinic (MO) 48.5%, diolefinic (DO) 16.8%, triolefinic (TO) 29.3% and saturated chains (SC) 8.4% chains—and acts as an outstanding monomer for thermosetting polymers [9].

Nguyen Le hwong explained cardanol synthesized from CNSL. The result gives hope to the researcher that the addition of 15% cardanol in a phenolic resin enhances the mechanical strength and tribological properties. It also stated that the phenolic resin has higher thermal stability compared to cardanol resin [10]. On the other side, Mikael Ericson states that organic binder has low bulk strength and inhomogenous mixing over the other ingredients [11].

Mwaikambo found that using a cardanol with alkali-treated hemp fibre reduces the noise level during contact. It also increases the compressive strength, hardness and specific gravity of the composite [12].

Cardol, anacardic acid, cardano and CNSL are synthesized from cashew seed. Cardanol is used in paint and varnish industry to hold the paint in the wall. So, applying the cardanol as a binder in friction material gives a good result as like phenolic resin. Cardanol can react with formaldehyde by condensation polymerization to produce cardanol–formaldehyde (CF) resins.

Friction coefficient of CF resin has very less sensitivity to temperature changes, than phenolic binder. Normally, the CF resins possess distinct properties such as modulus retention at elevated temperatures, high-temperature resistance, resistance against chemicals as well as against detergents, high surface hardness and low cost. Pin on disc is the best method to analyse the friction and wear characteristics of the high-friction composite material.

In this paper, role of cardanol resin in high-friction composite material is analysed by studying the physical and mechanical properties. Also, FT-IR and TGA results were plotted. SEM image after hardness test is also analysed.



**Table 1** Formulation of friction material by varying cardanol content

Ingredients (Wt %)	PR	5% CF	10% CF	15% CF	20% CF
CF resin	<b>0</b>	<b>5</b>	<b>10</b>	<b>15</b>	<b>20</b>
PR resin	<b>20</b>	<b>15</b>	<b>10</b>	<b>5</b>	<b>0</b>
Reinforcement	40	40	40	40	40
Friction and lubricant additive	40	40	40	40	40

## 2 Materials and Methodology

The materials which are used in this course of study are cardanol and cashew dust purchased from Satya Cashew chemicals Pvt. Ltd., Chennai. All ingredients used in the production of high-friction materials are purchased. Five specimens are prepared, and the weight % is shown in Table 1.

To examine the curing behaviour of phenolic and cardanol formaldehyde resin, the Perkin-Elmer spectrum device was used. The pellets were used to examine the solid sample of potassium bromide. All the sample spectra were recorded at the level of  $1\text{ cm}^{-1}$  with a scan range of  $450\text{--}4000\text{ cm}^{-1}$ . The background spectrum of each sample was initiated and kept in run mode. The polystyrene film was used in the instrument in order to study the spectral calculation at regular interval of time.

The thermal stability of cured phenolic, cardanol formaldehyde resin and a blend of cardanol and phenolic resin at different compositions were studied by thermogravimetric analysis using TA-SDT Q600 at a heating rate of  $10\text{ }^{\circ}\text{C}/\text{min}$  in nitrogen atmosphere from ambient temperature to  $700\text{ }^{\circ}\text{C}$ . Throughout the process, the nitrogen flow rate was maintained at  $60\text{ mL}/\text{min}$ .

## 3 Result and Discussions

### 3.1 Spectroscopic Characterization Using FT-IR

From Fig. 1, it evidences that the OH group associated with the phenyl ring was seen at  $3431\text{ cm}^{-1}$  for successive cardanol and phenol systems of resin. The peak which was found at  $1206$  and  $1224\text{ cm}^{-1}$  was the evidence or presence of linkage of ether. Furthermore, the methylene groups were found at  $2852\text{ cm}^{-1}$ ,  $2879\text{ cm}^{-1}$  and  $2919\text{ cm}^{-1}$ , as well phenolic resin was found at  $2919\text{ cm}^{-1}$ . The methyl group peak was found at  $2852\text{ cm}^{-1}$  and  $2920\text{ cm}^{-1}$  in the neat cardanol resin system. The value which is found at the (monosubstitution) peak of  $753\text{ cm}^{-1}$  and  $780\text{ cm}^{-1}$  are considered as the phenyl ring, actually the values shown the intensity in decreasing mode which confirms the ortho or para positions [13].

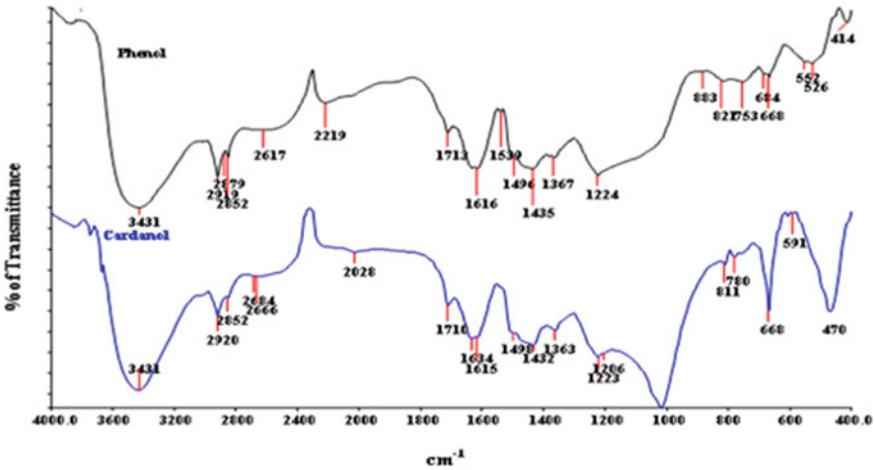


Fig. 1 Fourier transform infrared spectroscopy analysis of cardanol and phenolic resin

### 3.2 Thermal Characterization Using TGA

See Fig. 2.

The thermogravimetric analysis (TGA) was used to assess the thermal stability. The consequent temperature of a 10% weight loss is a crude index of thermal stability, and  $T_{max}$  represents the temperature at which maximum degradation takes place. The TGA thermogram for the two compositions is shown in Fig. 3. The data related to thermal stability and maximum degradation temperature are char residue which are presented in Table 2.

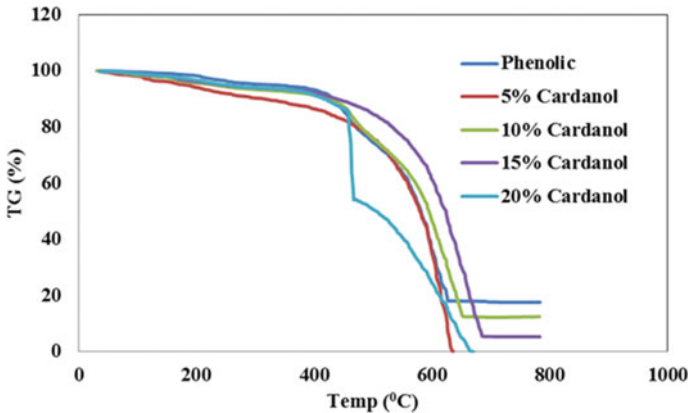
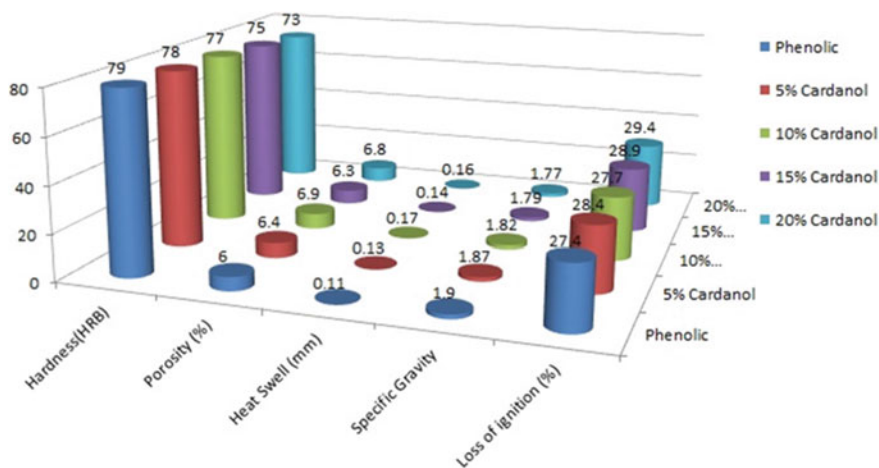


Fig. 2 Thermogravimetric analysis of the cured resin system



**Fig. 3** Physical and mechanical properties of cardanol and phenolic resins in a high-friction composite material

**Table 2** Thermogravimetric analysis data of cured resin

Material	Thermogravimetric analysis		
	T <sub>10</sub> °C	T <sub>max</sub> °C	Obtained char yield %
Phenolic	462	589	18
5% cardanol	319	609	–
10% cardanol	459	611	19
15% cardanol	491	629	8
20% cardanol	419	509	–

From Table 2, it is observed that the phenolic resin exhibited an onset of degradation at 485°C with a higher char residue of 19%. When the cardanol is mixed as an alternate for phenolic resin for 10 and 15%, the degradation is established to move towards right. For 5% CF resin, the degradation moves on left of phenolic resin at 22 wt %. Pure cardanol resin (20% CF) has a lower thermal resistance of 425 °C. This may be due to breaking of intermolecular interaction of C15 alkyl chain present in pure cardanol resin [14].

### 3.3 Physical and Mechanical Properties of Cardanol-Based Resin Composites

The physical and mechanical properties of cardanol and phenolic resin are shown in Fig. 3. Specific gravity of 20% cardanol resin is 1.77 which is found to be low

compared to other four specimens. The reason for this low value for high content of cardanol in a specimen is during a cure; close packing of molecules is prevented by alkyl group [15]. The above reason is also the cause of loss of ignition increase in cardanol nearly 8.3%. Loss of ignition is found 29.4 in cardanol resin, whereas phenolic resin has the value of 27.4. By increasing the cardanol content in the composite increases the heat swell. This may be due to the internal plasticizing effect of alkyl group present in cardanol moiety [16].

The porosity value for phenolic resin is 6%, and by adding a cardanol in a composite, the porosity value is gradually increased to 6.9% up to 10% and then decreased to 6.3 at 15% cardanol. This effect is happened in the composite due to the low bonding molecule structure. Cardanol resin composite has lower hardness compared to phenolic resin because polymeric materials in cardanol do not transmit high cross-link density to all the ingredient present in the specimen [17]. But phenolic resin transmits high cross-link density to all the ingredients.

Weight gain of cardanol resin on water, SAE20w-40 lubricating oil and salt water is shown in Fig. 4. It is evident from the figure that the addition of cardanol in high-friction composite reduces the absorption of water, SAE20w-40 lubricating oil and salt water. 15% and 20% cardanol resin composite is not shown much difference during the test. Phenolic resin shows 0.21% of weight gain, whereas 0.15% of weight gain is absorbed for 15% cardanol resin composite. This weight reduction is due to the long alkyl group present in cardanol molecular structure which is hydrophobic in nature [18]. This leads to repulsion between non-polar substance and water. Similar trend is followed in lubricating oil and salt water as 0.165% and 0.21% for phenolic resin and for 15% cardanol resin as 0.12% and 0.16%.

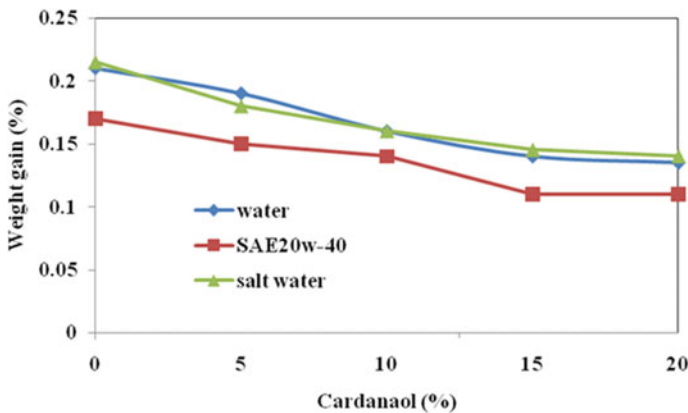


Fig. 4 Absorption of cardanol resin on water, salt water and lubricating oil

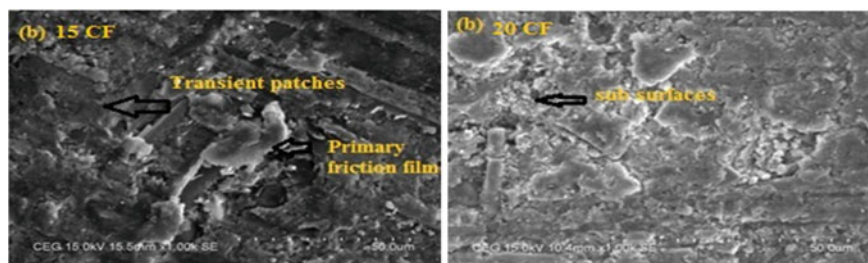


Fig. 5 SEM image of 15 and 20% cardanol resin composite after hardness test

### 3.4 Scanning Electron Microscope of Cardanol Resin Friction Material

Figure 5 shows the SEM image after hardness test specimen. In 15% cardanol resin composite, some of the common formation of plateaus which depends on pressure and their associate contact temperature is formed. Contact plateaus are formed due to the presence of lower removal rate of the mechanically stable and thermal-resistant ingredients of the cardanol in phenolic resin, and also, it may be due to protruding hard phases which form nucleation sites for the growth of secondary plateaus [19]. These secondary plateaus normally require stable conditions and a normal force to exist. As in all other sliding contact situations, the area of real contact transfers the friction forces. The size and composition of the plateaus thus have a crucial influence on the friction behaviour of the pad.

20% cardanol resin composite shows the shear-deformed polymer matrix, which consists of the small broken metallic materials. These particles can either be lost from the contact zone (interface) immediately after being broken from the composite surface or remain there for a while as transferred and back-transferred layers.

## 4 Conclusion

The following conclusions were made by the experimental reading of high-friction composite material.

Methyl and ether group present in cardanol and phenolic resin were found using FT-IR. The peak which was found at  $1206$  and  $1224\text{ cm}^{-1}$  was the evidence or presence of linkage of ether. The methyl group peak was found at  $2852\text{ cm}^{-1}$  and  $2920\text{ cm}^{-1}$  in the neat cardanol resin system.

20% cardanol shows a better result for specific gravity, heat swell and loss of ignition as 8, 19 and 7% compared to phenolic resin. Hardness and porosity have a better result for phenolic resin.

20% cardanol shows a low weight gain in water, salt water and lubricating oil as 0.15, 0.13 and 0.16% compared to phenolic resin. SEM analysis shows a small broken metallic materials and be lost from the contact zone immediately after being broken from the composite surface.

## References

- Ikeda R, Tanaka H, Uyama H, Kobayashi S (2002) Synthesis and curing behaviors of a crosslinkable polymer from cashew nut shell liquid. *Polymer* 43:3475–3481. [https://doi.org/10.1016/S0032-3861\(02\)00062-9](https://doi.org/10.1016/S0032-3861(02)00062-9)
- Yun R, Filip P, Lu Y (2010) Performance and evaluation of eco-friendly brake friction materials. *Tribology Int* 43: 2010–2019. doi.org/<https://doi.org/10.1016/j.triboint.2010.05.001>
- Bijwe J, Kumar M (2007) Optimization of steel wool contents in non-asbestos organic (NAO) friction composites for best combination of thermal conductivity and tribo-performance. *Wear* 263:1243–1248. <https://doi.org/10.1016/j.wear.2007.01.125>
- Bulent O, Sultan O (2011) Effect of resin type and fiber length on the mechanical and tribological properties of brake friction materials. *Tribol Lett* 42:339–350. <https://doi.org/10.1007/s11249-011-9779-5>
- Stephen Bernard S, Jayakumari LS (2018) Pressure and Temperature Sensitivity Analysis of Palm fiber as a biobased reinforcement material in brake pad. *Journal of the Brazilian Society of Mechanical Science and Engineering*. 40:152. <https://doi.org/10.1007/s40430-018-1081-0>
- Malhotra VM, Valimbe PS, Wright MA (2002) Effects of fly ash and bottom ash on the frictional behaviour of composites. *Fuel* 81:235–244. [https://doi.org/doi.org/10.1016/S0016-2361\(01\)00126-0](https://doi.org/doi.org/10.1016/S0016-2361(01)00126-0)
- Devi A, Srivastava D (2007) Studies on the blends of cardanol-based epoxidized navolac resin and CTPB. *Eur Polymer J* 43:2422–2432. <https://doi.org/10.1016/j.eurpolymj.2007.03.006>
- Sharifah H, Aziz Martin P, Ansell (2004) The effect of alkalization and fibre alignment on the mechanical and thermal properties of kenaf and hemp bast fibre composites: part 2—cashew nut shell liquid matrix. *Composites Sci Technol* 64:1231–1238. <https://doi.org/https://doi.org/10.1016/j.compscitech.2003.10.002>
- Patnaik A, Kumar M, Bhabani K, Satapathy Bharat S, Tomar (2010) Performance sensitivity of hybrid phenolic composites in friction braking: Effect of ceramic and aramid fibre combination. *Wear*. 269: 891–899. <https://doi.org/10.1016/j.wear.2010.08.023>
- Le Hwong N, HuuNieu N, Tan TTM, Ullrich J, Griesser (1996) Cardanol-phenol-formaldehyde resin Thermal analysis and characterization. *Die Angewandte Makromolekulare Chemie*. 243:77–85. <https://doi.org/10.1002/apmc.1996.052430107>
- Eriksson M, Jacobson S (2000) Tribological surfaces of organic brake pads. *Tribol Int* 33:817–827. [https://doi.org/10.1016/S0301-679X\(00\)00127-4](https://doi.org/10.1016/S0301-679X(00)00127-4)
- Mwaikambo LY, Ansell MP (2003) Hemp fibre reinforced cashew nut shell liquid composites. *Compos Sci Technol* 63:1297–1305. [https://doi.org/10.1016/S0266-3538\(03\)00101-5](https://doi.org/10.1016/S0266-3538(03)00101-5)
- Stephen Bernard S, Javeed Ahmed M, Dasaprakash J, Saroj Nitin MR, Vivek S, Kannan GK (2019) Friction and Wear Properties of Bio-Based Abrasive in a High-Friction Composite Material. *Advances in Manufacturing Technology. Lecture Notes in Mechanical Engineering*. 577–585. [https://doi.org/https://doi.org/10.1007/978-981-13-6374-0\\_63](https://doi.org/https://doi.org/10.1007/978-981-13-6374-0_63)
- Yadav R, Srivastava D (2009) Studies on the process variable Condensation reaction of cardanol and formaldehyde by response surface methodology. *Eur Polymer J* 45:946–952. <https://doi.org/10.1016/j.eurpolymj.2008.11.019>
- Raquez JM, Deléglise M, Lacrampe MF, Krawczak P (2010) Thermosetting (bio) materials derived from renewable resource: A critical review. *Prog Polym Sci* 35:487–509. <https://doi.org/10.1016/j.progpolymsci.2010.01.001>

16. Stephen Bernard S, Jayakumari LS (2014) Effect of the Properties of Natural Resin Binder in a High Friction Composite Material. *Polimeros- Ciencia Tecnologia*. 24; 2: 149–152. dx.doi.org/<https://doi.org/10.4322/polimeros.2014.038>
17. Sai Krishnan G, Jayakumari LS (2019) Investigation on the physical, mechanical and tribological properties of areca sheath fibers for brake pad applications. *Materials Research Express*. 6:085–109. <https://doi.org/10.1088/2053-1591/ab2615>
18. Sultania M, Rai JSP, Deepaksrivastava (2011) Process modeling, optimization and analysis of esterification reaction of cashew nut shell liquid (cnsL)-derived epoxy resin using response surface methodology. *J Hazard Mater* 185:1198–1204. <https://doi.org/10.1016/j.jhazmat.2010.10.031>
19. Stephen Bernard S, jayakumari L.S (2016) Effect of Rockwool and Steel fiber on the Friction performance of brake lining materials. *Materia- rio de janeiro*. 21: 656-665. <https://doi.org/https://doi.org/10.1590/S1517-707620160003.0063>

# Influence of 3-(8,11,14-Pentadecatrienyl) Phenol Cardanol as a Bio-Based Binder in a Brake Pad



S. Stephen Bernard, S. Vivek, G. Suresh, and G. K. Kannan

**Abstract** The main objective of this research work is to develop an environmentally friendly brake pad with the incorporation of bio-based binder, filler, reinforcement and friction modifiers. This study suggests that maintaining the high friction stability at high speed and load for a brake pad material can be sustained by cardanol resin, a natural resin binder. The tribo test procedure of JASO 406C was performed on two different cardanol (15CF and 20 CF) compositions by maintaining the two test parameters such as pressure sensitivity (effectiveness test). The result shows that 3-(8,11,14-Pentadecatrienyl) phenol cardanol in phenolic resin is found to be more superior and most suitable binder resin combination, for the given ingredients compared to using only a cardanol resin as a binder in brake pad. Furthermore, the morphology of wear debris, contact plateaus and transient patches are analyzed by scanning electron microscope.

**Keywords** Cardanol · Brake pad · Pressure sensitivity · Temperature sensitivity · Friction

## 1 Introduction

Nowadays, due to developed economic values in India, the importance of health care is grown rapidly [1]. Brake pads are consumable parts in vehicles that cannot be recycled because they are thermosetting composite and need a special attention due to the release of particulate matter to the environment [2, 3]. 3-(8, 11, 14-Pentadecatrienyl) phenol cardanol is known to be an agricultural resource, which is derived from the cashew nut shell liquid (CNSL), by subjecting the same with help of the thermal

---

S. Stephen Bernard (✉) · S. Vivek · G. Suresh  
Department of Mechanical Engineering, Rajalakshmi Institute of Technology, Kuthambakkam,  
Chennai 600124, India  
e-mail: [Stephenbernard.s@ritchennai.edu.in](mailto:Stephenbernard.s@ritchennai.edu.in)

G. K. Kannan  
Department of Mechanical Engineering, Chennai Institute of Technology, Kundrathur, Chennai,  
India



treatment [4]. This research is a part of an approach for reduction of hazardous components for humans and the environment from high-friction brake pad.

The main aim of this work is to find out the usage of biosourced chemicals and their supporting materials in near future exclusively for brake pad preparation [5, 6]. The 3-(8,11,14-Pentadecatrienyl) phenol cardanol has potential industrial applications in friction lining materials and surface coatings. Production of cardanol–formaldehyde is prepared by the condensation polymerization of cardanol with formaldehyde. Friction coefficient of CF resin has very less sensitivity to temperature changes, than phenolic binder [7, 8].

In this study, 3-(8,11,14-Pentadecatrienyl) phenol cardanol resin was loaded to friction material at different compositions; the best composition was selected with respect to physical, thermal and mechanical properties [9]. The trio-evaluation technique was used to obtain the best composition by actively using the full-scale inertia dynamometer, in order to find out a range of performances of the material [10, 11]. In this course of study, physical, mechanical, thermal and tribological characteristics of the cardanol resin as a phenolic binder in an automotive brake system material are analyzed.

## 2 Materials and Methodology

### 2.1 Preparation of Brake Pad Materials

Brake pad is developed by the standard industrial procedure, which consists of the following sequential steps, first mixing of the frictional materials followed with the production of pre-forms. This procedure ends with the shot blast of braking plate and ends up with the curing the same during the machining. The weight fraction methodology has been used to fabricate all set of the specimens as per the composition given in Table 1.

The digital weighing machine is used to gauge all the gradients up to the deviation level of 0.1 g. Initially, the mixtures are blended using electron EBR instrument for the particular duration of 16 min by maintaining an rpm of 4000. All the processes

**Table 1** Ingredients used for brake pad and its percentage in weight

Ingredients ( % in weight)	15 CF	20 CF
3-(8, 11, 14-Pentadecatrienyl) phenol cardanol–formaldehyde resin	15	20
Phenol formaldehyde resin	5	0
Rockwool fiber, steel fiber, palm fiber	20	20
CaCO <sub>3</sub>	20	20
Calcium silicate, cashew dust, silicon, alumina, vermiculate	32	32
Antimony trisulfide, graphite	8	8

were carried out at room temperature (30 °C approx). During the initial processes, all set of fibers were added into the chamber such as steel, rockwool and palm fiber with the exact volume; the same was subsequently mixed for the period of 10 min. In the same way the filler and friction modifiers are well mixed along with the fiber for the period of 3 mins. At last, binder material, which was considered as the base of all the mixtures, was added for the period of 3 min with the same speed which has been maintained to prepare all set of ingredients [12].

120 tonne of hydraulic press has been used to perform the molding process on the preform. The ingredients to about 500 g were taken into the compaction die initially; following this, the pressure of 160 kg/cm<sup>2</sup> was maintained over the perform throughout the entire process for the period of 6 min. Moreover to complete the fabrication process, the braking plate of rigid steel structure was used in order to make the brake pad; it was quite rigid in structure to absorb the additional amount of force which is been used throughout the pressing processes. The surface of the braking plate was completely roughened to ease the operation of making the brake, as well to increase the more adhesion between them [13, 14]. To facilitate this adhesion process, the proper adhesive has been used over the surface of the braking plate to avail the exact bond between them [15].

After completing this process, the preform was placed on the compaction die of the compression molding machine. Around 180 degree celsius with 160 kg/cm<sup>2</sup> pressure was applied over the preform which was placed on the die for the period of 6 min. Further to avoid the volatiles, five intermittent breathing was allowed during the initiation of the curing process. Afterward, the post-curing operation was done by placing the mold in the preheat furnace for the period of 2 h by maintaining the temperature of 140 °C [16]. In addition to this, the mold components were additionally raised to the temperature of 150 °C for exact 2 h and then followed by 180 °C for exact 2 h. In addition to avoid the reduced thermal expansion as well as to make sure the curing uniformity, reducing the pore space and ensuring the compactness, the gradual increase of temperature was opted throughout this process [17]. Examine the proper mixing of the friction materials, the scanning electron microscope (SEM) EVO MA15 was used to characterize the material.

## 2.2 *Experimental Procedure*

The schematic sketch of the inertia brake dynamometer testing machine is shown in Fig. 1. To study the distinctive performance of various parameters of the brake pads, parameters like fade, recovery behavior and effectiveness studies were examined with help of the full-scale inertia dynamometer.

It consists of the variable speed inertia load prime mover with the load capacity of 175 kW, rpm of 1500 apart from that, it has been provided with external cooling facility, as well the system analyze the COF along with the wear of the specimen. The entire process is completely controlled by the pre-program controller. The thermocouple sensor was used to find a temperature of the specimen. Besides infrared

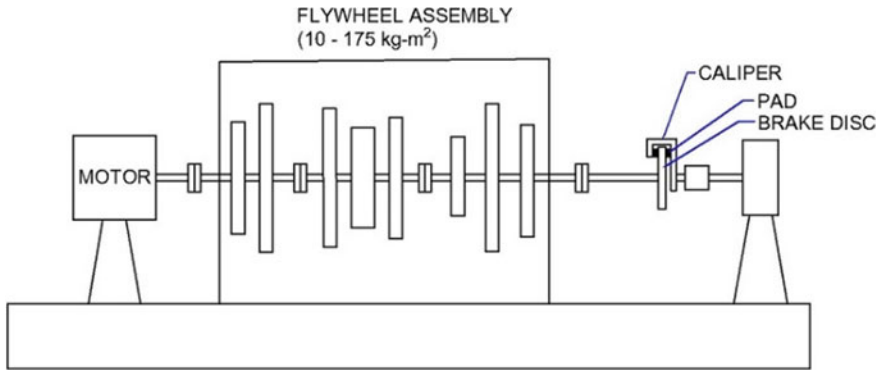


Fig. 1 Inertia brake dynamometer testing machine

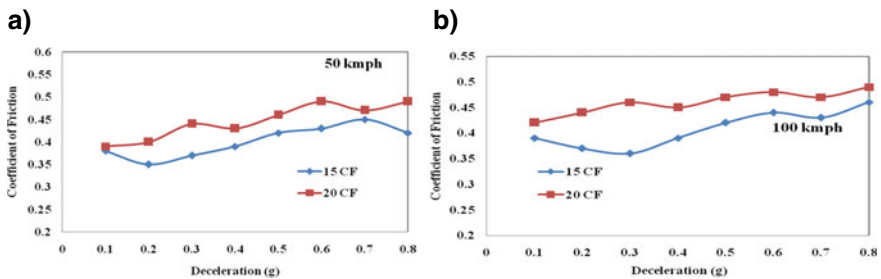


Fig. 2 Performance I effectiveness at a 50 kmph b 100 kmph

sensor, non-contact type was also used to measure the disk temperature. The IR sensor which is been used in this setup successfully sends the analog output to the interface device of the system, and the same has been used to monitor the temperature during testing.

### 2.3 JASO C406 Test Schedule

JASO C 406 testing procedure was followed to test the car pads throughout this study as per Table 2. This method is exclusively for passenger cars, which is widely followed in Japanese automobile giants. The effectiveness measurement was taken place for discrete pressures. During the fade test, 10 brake applications were applied, and similarly, recovery test 20 applications were applied with the inline pressure of 5.86 bar.

To find the friction of the specimen, the speed variation against the deceleration values between 0.1 and 0.8 g was applied. Applying the brake on running condition decelerates the speed. Similarly, eight brakes were applied for each speed. Thus, for

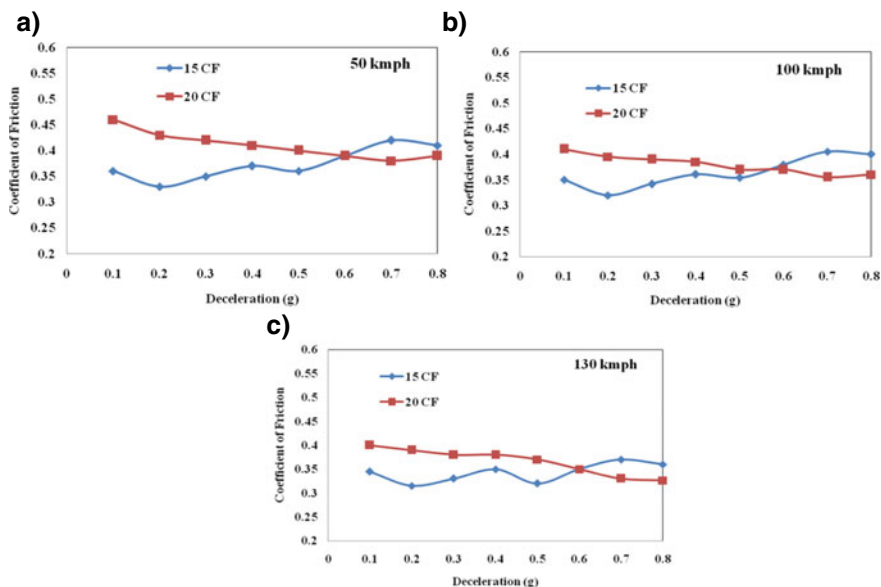


Fig. 3 Performance II effectiveness at a 50 kmph b 100 kmph c 130 kmph

Table 2 Effectiveness schedule followed in JASO C406

	Speed (kmph)	Braking deceleration (g)	Temperature maintained at initial braking (°C)	Number of brakings
Effectiveness I (pressure–speed sensitivity I)	50, 100	0.1–0.8	80	16
Effectiveness II (pressure–speed sensitivity II)	50, 100, 130	0.1–0.8	<80	24

analyzing two composite pads, totally, 16 brake decelerations were applied for every speed. Similarly, the time span was varied for every brakes from braking to halt (zero speed).

### 3 Results and Analysis

#### 3.1 Effectiveness Studies on Cardanol Resin (Pressure-Speed Sensitivity)

Figures 2 and 3 illustrate various speeds against the deceleration (0.1–0.8 g) in order to find out the value of COF, and their corresponding observations were presented.

The customized way of deceleration was kept varied by increasing the pressure; simultaneously the again the pressure was kept varied for the given rate of deceleration which completely depends upon the materials, for every deceleration was brake was applied. Cumulatively, eight brake applications were initiated at each and every speed. In this particular work, to do analysis on the two composite brake pads, totally, 16 brake applications were initiated for every speed [18]. When the deceleration increases, their corresponding severity on braking also tends to increase, as well the stopping distance reduces to a set value [19].

From performance of effectiveness I and effectiveness II results,  $\mu$  (COF) shows the value between 0.315 and 0.49. It clearly shows that the increase in deceleration, increase COF for both the specimen in I effectiveness test but in II effectiveness COF value was decreased and showed an opposite trend for 20 CF.

The acceptable friction coefficient range of standard brake pad composite is 0.35–0.45. The sliding speed and their corresponding applied pressure are the important factors to find out the COF during the braking system, and the COF often shows minimum changes, why because the driver often expects the same level of frictional forces during various conditions of operation [20].

By increasing speed, 15 CF showed less undulations and maximum  $\mu$  showing its least sensitivity for speed. 20 CF showed high slope and moderate undulations, and  $\mu$  value was 0.49 which is far away from the standard values. Hence, the sensitivity toward speed was high for 20 CF. At high rpm, both composites showed the same performance mainly because cardanol is viscoelastic in nature [21]. Finally, this leads to disproportionate minimum pressure reduction in pressure in spite of  $\mu$  fluctuation and makes the same trend for both the composites.

For the supreme value, the corresponding curve inclination and their undulations must be minimum. For a better performance even though the difference in slope is high and  $\mu$  is found to increase, the material has the good sensitivity of braking for continuous load. With an increase in speed, COF of cardanol composite brake pad is decreased. This is due to the fact that with increase in speed, contact surface increases and high heat energy is released at the interface which leads to increased fluctuations [22].

### 3.2 *Speed Spread of Effectiveness II*

The speed variation by each braking (g) shows speed spread for effectiveness II which is shown in Fig. 4. Spread speed is the stability of COF when 50 Kmph changes to 100Kmph and 130Kmph. In this graph, 50 to 100 kmph represents soft condition and 50 to 130 kmph represents rigorous condition.

To obtain the best result, speed spread must be between 90 and 100% and the minimum undulation should be formed. The below-mentioned speed spread data purely depends on the speed fluctuation.

15 CF (96.4%) > 20 CF (89.1%) (50 to 100 kmph).

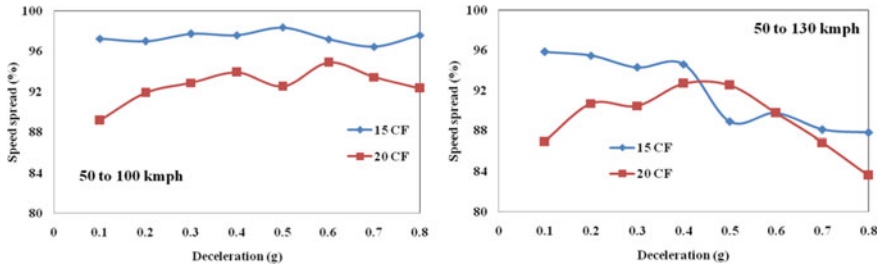


Fig. 4 Speed spread for soft condition (50 kmph to 100 kmph) and rigorous conditions (50 to 130 kmph)

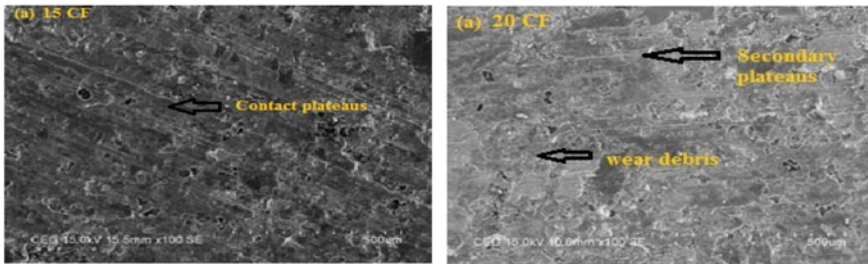


Fig. 5 Friction surface 15 CF and 20 CF brake pad

15 CF (89.7%) > 20 CF (83.5%) (50 to 130 kmph).

The higher percentage always shows better performance, which indicates the least sensitivity toward the speed. In common for the best friction material, SS always should be very close to 100 to the maximum, and their range should be as minute as possible [23]. For both soft and rigorous conditions, 15 CF shows better performance as compared to 20 CF. 20 CF is neat cardanol–formaldehyde resin which undergoes thermal degradation at a faster rate during frictional heat generated at the contact surface between the disk and brake pad [24].

### 3.3 Analysis of Friction Surfaces of Cardanol Brake Pad Using SEM

The friction behavior between pad and disk is closely related to the formation of contact plateaus during braking. Variations in braking are associated with brake pad and disk material; it may also be due to operating condition. In this regard, the worn surfaces after the friction test from 15 and 20 CF were analyzed by scanning electron microscope (SEM).

The SEM images of friction surface of the brake pad are presented in Fig. 5. From the observation, the removal of material can be seen, and this was because of the

mechanical crushing due to the entrapped wear debris. Figure 5a shows a rougher surface exhibiting locally delaminated regions and contact plateaus. It also clearly shows that a shear is developed in a secondary plateaus on peripheral of the surface to the contact side of the brake pad indicating that the high sensitivity of brake pad leads to high wear.

## 4 Conclusion

The following conclusion was obtained by brake pad test for 15 CF and 20 CF cardanol variation and is listed below,

Effectiveness I: 15 CF > 20 CF (during 50 rpm).

: 15 CF  $\approx$  20 CF (during 100 rpm).

Effectiveness II: 15 CF > 20 CF (during 50 rpm).

: 15 CF < 20 CF (during 100 rpm).

: 15 CF > 20 CF (during 130 rpm).

Cardanol percentage beyond 15% imparts poor performance for both effectiveness and fade test. Hence, 15 CF (15% cardanol resin and 5% phenolic resin) is found to be more superior and the most suitable binder resin combination for the given ingredients.

## References

1. Cho MH, Kim SJ, Basch RH, Fash JW, Jang H (2003) Tribological study of gray cast iron with automotive brake linings: The effect of rotor microstructure. *Tribol Int* 36:537–545. [https://doi.org/10.1016/S0301-679X\(02\)00260-8](https://doi.org/10.1016/S0301-679X(02)00260-8)
2. El- NSM, Liew KW (2008) Effect of water spray on friction and wear behaviour of noncommercial and commercial brake pad materials. *Wear* 208:135–144. <https://doi.org/10.1016/j.jmptotec.2007.12.111>
3. Malhotra VM, Valimbe PS, Wright MA (2002) Effects of fly ash and bottom ash on the frictional behaviour of composites. *Fuel* 81:235–244. [https://doi.org/10.1016/S0016-2361\(01\)00126-0](https://doi.org/10.1016/S0016-2361(01)00126-0)
4. Devi A, Srivastava D (2007) Studies on the blends of cardanol-based epoxidized navolac resin and CTPB. *Eur Polymer J* 43:2422–2432. <https://doi.org/10.1016/j.eurpolymj.2007.03.006>
5. Sharifah H, Aziz MP, Ansell (2004) The effect of alkalization and fibre alignment on the mechanical and thermal properties of kenaf and hemp bast fibre composites: part 2—cashew nut shell liquid matrix'. *Compos Sci Technol* 64:1231–1238. <https://doi.org/10.1016/j.compscitech.2003.10.002>
6. Ikeda R, Tanaka H, Uyama H, Kobayashi S (2002) Synthesis and curing behaviors of a crosslinkable polymer from cashew nut shell liquid. *Polymer* 43:3475–3481. [https://doi.org/10.1016/S0032-3861\(02\)00062-9](https://doi.org/10.1016/S0032-3861(02)00062-9)
7. Vivek S, Jayakumari LS, Stephen Bernard S, Suresh G, Javeed Ahmed Md, Arul Murugan S (2020) Tribological and mechanical properties of biobased reinforcement in a friction

- composite material. *Materia- rio de janeiro*. 25: 3 <https://doi.org/10.1590/s1517-70762020003.1085>
8. Rongping Y, Filip Peter Lu, Yafei (2010) Performance and evaluation of eco-friendly brake friction materials. *Tribol Int* 43:2010–2019. <https://doi.org/doi.org/10.1016/j.triboint.2010.05.001>
  9. Bijwe J, Kumar M (2007) Optimization of steel wool contents in non-asbestos organic (NAO) friction composites for best combination of thermal conductivity and tribo-performance. *Wear* 263:1243–1248. <https://doi.org/doi.org/10.1016/j.wear.2007.01.125>
  10. Stephen Bernard S, Javeed Ahmed M, Dasaprakash J, Saroj Nitin MR, Vivek S, Kannan GK (2019) Friction and Wear Properties of Bio-Based Abrasive in a High-Friction Composite Material. *Advances in Manufacturing Technology. Lecture Notes in Mechanical Engineering*. 577–585. [https://doi.org/10.1007/978-981-13-6374-0\\_63](https://doi.org/10.1007/978-981-13-6374-0_63)
  11. Bulent O, Sultan O (2011) Effect of resin type and fiber length on the mechanical and tribological properties of brake friction materials. *Tribol Lett* 42:339–350. <https://doi.org/10.1007/s11249-011-9779-5>
  12. Blau PJ, Meyer III HM (2003) Characteristics of wear particles produced during friction tests of conventional and unconventional disc brake material. *Wear* 255:1261–1269. [https://doi.org/10.1016/S0043-1648\(03\)00111-X](https://doi.org/10.1016/S0043-1648(03)00111-X)
  13. Jang H, Lee JS, Fash JW (2001) Compositional effects of the brake friction material on creep groan phenomena. *Wear* 251:1477–1483. [https://doi.org/10.1016/S0043-1648\(01\)00786-4](https://doi.org/10.1016/S0043-1648(01)00786-4)
  14. Stephen Bernard S, Jayakumari LS (2018) Pressure and Temperature Sensitivity Analysis of Palm fiber as a biobased reinforcement material in brake pad. *J Brazilian Soc Mech Sci Eng* 40:152. <https://doi.org/10.1007/s40430-018-1081-0>
  15. Patnaik A, Kumar M, Satapathy BK, Tomar BS (2010) Performance sensitivity of hybrid phenolic composites in friction braking: effect of ceramic and aramid fibre combination. *Wear*. 269: 891–899. <https://doi.org/10.1016/j.wear.2010.08.023>
  16. Hwong NL, HuuNieu N, Minh Tan TT, Griesser UJ (1996) Cardanol-phenol-formaldehyde resin Thermal analysis and characterization. *Die Angewandte Makromolekulare Chemie*. 243: 77–85. <https://doi.org/10.1002/apmc.1996.052430107>
  17. Eriksson M, Jacobson S (2000) Tribological surfaces of organic brake pads. *Tribol Int* 33:817–827. [https://doi.org/10.1016/S0301-679X\(00\)00127-4](https://doi.org/10.1016/S0301-679X(00)00127-4)
  18. Mwaikambo LY, Ansell MP (2003) Hemp fibre reinforced cashew nut shell liquid composites. *Compos Sci Technol* 63:1297–1305. [https://doi.org/10.1016/S0266-3538\(03\)00101-5](https://doi.org/10.1016/S0266-3538(03)00101-5)
  19. Yadav R, Srivastava D (2009) Studies on the process variable Condensation reaction of cardanol and formaldehyde by response surface methodology. *Eur Polymer J* 45:946–952. <https://doi.org/10.1016/j.eurpolymj.2008.11.019>
  20. Raquez JM, Deléglise M, Lacrampe MF, Krawczak P (2010) Thermosetting (bio) materials derived from renewable resource: a critical review. *Prog Polym Sci* 35:487–509. <https://doi.org/10.1016/j.progpolymsci.2010.01.001>
  21. Stephen Bernard S, Jayakumari LS (2014) Effect of the properties of natural resin binder in a high friction composite material. *Polimeros- Ciencia Tecnologia*. 24; 2: 149–152. <https://doi.org/10.4322/polimeros.2014.038>
  22. Sai Krishnan G, Jayakumari LS (2019) Investigation on the physical, mechanical and tribological properties of areca sheath fibers for brake pad applications. *Mater Res Express* 6:085–109. <https://doi.org/10.1088/2053-1591/ab2615>
  23. Minakshi S, Rai JSP, Deepaksrivastava (2011) Process modeling, optimization and analysis of esterification reaction of cashew nut shell liquid (cnsL)-derived epoxy resin using response surface methodology. *J Hazardous Mater* 185: 1198–1204 <https://doi.org/https://doi.org/10.1016/j.jhazmat.2010.10.031>
  24. Stephen Bernard S, Jayakumari LS (2016) Effect of rockwool and steel fiber on the friction performance of brake lining materials. *Materia- rio de janeiro*. 21: 656–665. <https://doi.org/10.1590/S1517-707620160003.0063>



# Effect of Barium Sulfate on Mechanical, DMA, Wear Analysis of Woven Hybrid with Wire Mesh Composite



M. Arul Murugan and A. S. Selva Kumar

**Abstract** Natural fiber-reinforced polymeric composites interest automotive industries as of their recyclability, cost-effectiveness, lightweight, high strength, rigidity, and eco-friendly production. The natural polymeric fiber-hybrid composite overcomes the difficulty of the mechanical properties of mono-material fiber-reinforced composites. This investigation involves using aloe vera (A), hemp (H), and flax (F) bast fiber in the hybrid natural fiber polymer (HNFPC) composites for different applications. Natural fiber wire mesh laminate (NFWML) plates were fabricated using woven A/H/F along with stainless steel wire mesh (SSWM), aluminum wire mesh (ALWM), and copper wire mesh (CUWM). Totally 15 variants of samples were fabricated using hand layup and compression molding techniques. In the composite materials characterization, the tensile, flexural, impact, and hardness properties were analyzed by mechanical characterization and the viscoelastic properties were estimated by the dynamic mechanical analysis (DMA) and wear analysis. This research work focuses mainly on the effect of barium sulfate ( $\text{BaSO}_4$ ) and wire mesh on the characteristics of hybrid natural fiber-reinforced polymer (HNFPC) composite. The  $\text{BaSO}_4$  was preferred as filler based on the absence of self-motion, high density, and high melting point ( $1580^\circ\text{C}$ ). Finally, the scanning electron microscope images were analyzed to recognize the fractured surface morphology of the prepared composites.

**Keywords** Natural fiber · Wire mesh · DMA · Wear · Mechanical property

## 1 Introduction

Composites are often distinct as constituents of two or more chemically and physically dissimilar parts parted by a definite boundary. The numerous schemes of resources are joined sensibly to obtain a system with added favorable structural or practical properties unattainable by any of the contributing materials. Composites, the marvel materials, are a vital part of today's materials due to benefits like

---

M. Arul Murugan (✉) · A. S. Selva Kumar  
B.S.Abdur Rahman Crescent Institute of Science and Technology, Chennai, India  
e-mail: [Marulm79@gmail.com](mailto:Marulm79@gmail.com)

a reduced amount of weight, corrosion resistance, great fatigue strength, and faster assembly. They are widely used in manufacturing aircraft structures, electronic packaging for medical equipment, and spacecraft to domestic construction [1]. Woven fabric composites, especially, are built by intertwining two fiber tows into one another to make a layer. These layers are formerly impregnated with a resin or matrix material, stacked at the desired orientation, and cured to get a composite laminate [2]. Woven fabrics are good as reinforcements since they supply excellent integrity and conformability. The natural fibers like banana, hemp, flax, ramie, pineapple leaf, and kenaf have the potential to be used as standby for glass or other synthetic, inorganic traditional reinforcement materials in composites [3]. Natural fibers composites exist equally in plants and animals; for instance, bone and wood are composites. Wood contains long cellulose fibers detained collectively by lignin [4]. The cellulose and lignin were collected to make a robust material with weaker substances. For example, a soft and versatile material collagen (which may be a protein) and therefore the hard and brittle material hydroxyapatite (which is especially calcium phosphate) constitute the bone in the physical body [5]. Natural fiber is divided into two classes depending upon whether the fiber is attained from plant source or animal source. These fibers are again segmented into two divisions like natural cellulosic fiber (jute, cotton, sisal, coir, hemp, flax, ramie, abaca, etc.) and protein pedestal fiber like silk [6]. Every part of the natural fiber is designed to get an extensive sort of new product from ropes, textiles, nets, carpets, brushes, mats, and mattresses to paper and panel resources. There is a rising environmental anxiety within the structural, construction, automobile, and packing industries to use natural fibers attained from renewable bases [7]. Bast fibers otherwise called skin fiber are attained from the skin or bastes adjoining the stem of dicotyledonous plants. These fibers retain the conductive cells of the phloem and offer potency to the stem [8]. The natural fiber containing composites are new eco-friendly and are utilized in transport (automobiles, railway coaches, and aerospace), military applications, building and construction industries (ceiling paneling, partition boards), and packaging and consumer products [9].

Two or more differing types of fibers combine together in a common matrix referred to as hybrid composite. Not only fibers, in some cases, fibers with fillers in a common matrix are additionally said to be hybrid composite [10]. The advanced possessions of the composites remained create when wire mesh composites are fabricated. Aloe vera/hemp/SS wire mesh/flax with  $\text{BaSO}_4$  are prepared during this analysis work [11]. Panels for partition and false ceiling, partition boards, and mobile or prefabricated in construction are utilized in times of natural calamities like floods, cyclones, and earthquakes. Automobile parts are dashboard, door panel, head linear, food tray, bottle holder, and seat back [12]. The new material is going to be employed to supply suitable applications. So far, mixture of aloe vera, hemp, and flax with wire mesh has not been studied as an ingredient for the composite materials. There is no literature available on the appliance of AHF as reinforcing material within the epoxy composites [13]. The greater accessibility of natural fibers from renewable springs accelerates the replacement of artificial fibers by natural fibers. New plants and cost-effective, easy extraction procedures should be identified without affecting the nature of the fiber [14]. There are several plant-based natural fibers which possess

high specific mechanical properties. The natural fiber is employed as reinforcement in composites appreciations to the benefits like biodegradability, low weight, and high precise modulus [15]. Since natural fibers are freely available at low price from renewable sources and possess good mechanical properties and low density, make them a beautiful ecological substitute to synthetic fibers like glass, carbon, and other man-made fibers used for the engineering of composites [16]. The alignment and type of composite material improved the binding energy and thus involves in greater strength and modulus of the element formed. Basically, continuous fiber composite produces more strength than the discontinuously aligned matrix material [17]. Kuru villa Joseph et al. (1999) reviewed the sisal fiber reinforced with polymer composite. The author reviewed the different manufacturing methods, processing techniques, and properties of sisal fiber. He also has reviewed its mechanical properties and structure of the sisal fiber. The author finally concluded that the usage of natural fiber will reduce the cost of manufacturing of the composite, [18] the water absorption ability of jute/kenaf/e-glass woven fabric composite. The author carried out the research for understanding the water absorption ability of the woven fabric when hybridized with e-glass [19].

## 2 Experimental Implementation

Aloe vera is a plant that was used for medicinal purpose from the ancient times. They are used for dermatology, skin care and used to produce fibers. Aloe vera comes from the plant family of liliaceous. They were botanically named as *Aloe barbadensis miller*. Hemp is plant that grows extensively in any environment. Hemp plant is from the family of *cannabis sativa* species. They are botanically named as *cannabis*. These plants are used in the past historical decades to produce fiber used for clothing. The plant requires very less water and has no need of pesticides and herbicides. Flax is also a multipurpose plant from the family of *Linum usitatissimum*. Flax is also named as linen. As the name seems familiar, flax fibers are sources of linen clothings. The clothes obtained from flax are very expensive and were used to cover the mummies of the Egyptian tombs in ancient times. Flax seeds are excellent weight reducing agents because of its fiber content which in turn improves the digestive metabolism of a human. Flax plants are 80–120 cm long and have flowers in it.

Manufacturing of composite woven fabric or mats is very much useful. There are two types of directions in weaving a composite warp and weft. According to their weaving patterns, they are classified as follows. Addition on woven mat increases the strength of the composites as well as the reliability of the composite stainless steel wire mesh and as per the requirement, the diameter and area of the mesh are the same as that of aluminum mesh. Figure 3.6 represents the stainless steel wire mesh of wire diameter  $-0.25$  mm and area of  $300 \times 300$  mm. The inorganic compound is obtained from barite which is ore for extracting barium and other barium-based materials. The material is white in color, has no odor, and it is not soluble in aquatic

liquids. The physical appearance of BaSO<sub>4</sub> is like a white powder and looks like bleaching powder.

## ***2.1 Fabrication of Laminate Composites***

### **2.1.1 Chemical Treatment of Fibers**

Chemical treatment of fiber is an important step before utilizing a natural fiber into composite fabrication. The fiber extruder from the plants has some natural wax and celluloid in it, that has to be removed for improving the properties of fiber. After chemical treatment of the fibers, the properties of the fiber are improved in mechanical characters, adhesiveness, structural integrity between the matrix and the fiber as well as flexural properties. There are surfaces of aloe vera, hemp, and flax (AHF) that are treated with alkali, benzoyl peroxide, potassium permanganate, and stearic acid.

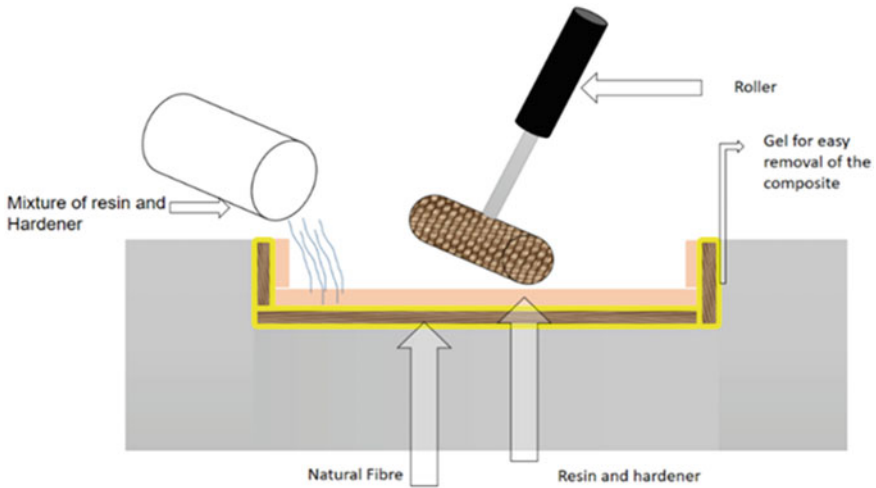
Hand layup method:

Hand layup method is one of the most familiar methods to fabricate many of the industrial component made of composite, as the technique is very simpler, was effective in adhesion, and improves the mechanical ability of the composites. Hand layup method is a molding process that involves placement of fibers by hand and a resin was used to wet the fiber and gives the ability to the composite to bind or adhere together. The process involves mold from smaller to larger molds. A wax is initially applied to the mold to improve the surface finishing of the composite and a spray gun is used for this purpose. The gel is let to dry and the fibers are placed manually in the mold sprayed with gel. The resin for hardening and adhesion may be poured, brushed, or sprayed. Fiber glass rollers (FRP) or pain rollers are used for rolling throughout the wet surface of the laminate to get rid of the air inside the laminates. After that the succeeding layer of the natural fiber is added in the same process. This process involved to produce a layer by layer composite with minimal cost and technic. A good product can be produced with good skilled labor and with reduced rate for the composite (Fig. 1).

### **2.1.2 Compression Molding Technique**

Compression molding is a technique used to manufacture a composite using compressive force. It has two molds; one is the upper half and the other is a lower half. The lower half is preheated and the upper half pushed is toward the lower half placing the fiber between the molds. Basically, a polymer matrix composite is manufactured using this method.

Procedure for fabrication of laminate composite is as follows.



**Fig. 1** Illustration of hand layup process

Initially, mat of aloe vera, hemp, and flax is placed one by one as layers to form the composite. A combination of hardener and resin is prepared and transferred to the custom formatted mat. Wax is smeared above the polyester sheet for easy removal of the mat. A fleece of resin mixture is applied over the mold. A roller is used to level the mold surface. Polyethylene sheet is placed after that and another aluminum sheet is placed over it. A weight is placed over the mold to ensure adhesion. Over a period of 6 h the counter weight is removed and then composite is removed by tapping it out. The procedure is repeated for manufacturing the remaining composite combination.

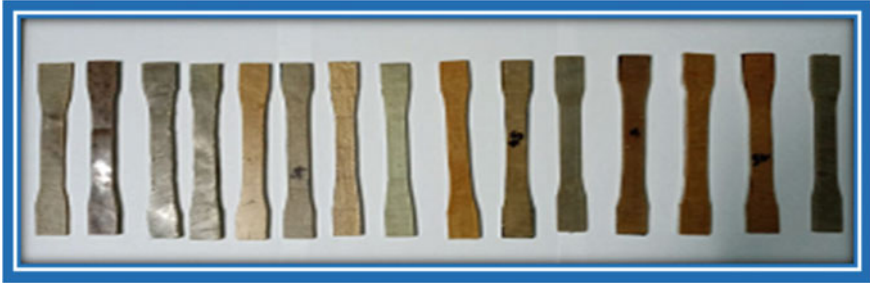
### 3 Characterization of Materials

In this research, there are different ASTM standards depending on the test that have to be carried out throughout the testing process. We shall look after the testing standard that is preceded for our research. We preferred to evaluate our composite using the following test.

Mechanical Characterization:

#### 3.1 Tensile Testing of Composites

Mechanical testing of a material is to study the load withstanding capacity, strength, and elastic property of the composite. In our research, we have done tensile testing,

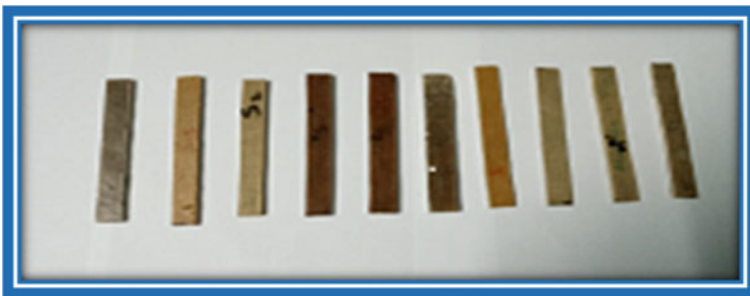


**Fig. 2** Tensile sample of composite

compression testing, flexural testing, impact testing, and hardness for the material. We shall discuss about the mechanical testing of the materials. Tensile testing of material is used to identify the elastic property of the material of the material (Fig. 2).

### ***3.2 Flexural Testing***

Flexural test for a composite is done to understand the materials behavior on bending. The test may be undergone in many ways but in our research the test is carried out in an UTM [17]. The flexural test is otherwise called as three-point bending load, and as the name implies, the test is all about applying three loads at three point as it is in a simply supported beam. The test is followed using samples in ASTM D790 [18] standards. The procedure for conducting the test relies till the breakage of the specimen that is to define that the specimen is subjected to compressive load at the middle and upward acting force or support at both the ends extends the material to be fractured to measure the schematic diagram of the flexural testing setup stress–strain curve of subjected to tensile load and the specimen till it breaks (Fig. 3).



**Fig. 3** Flexural sample of composite

### **3.3 Impact Test**

Impact test for a specimen is conducted for observing the maximum toughness of the material. The specimen required for testing the material is formed as per ASTM D256 standard [15]. The test is conducted to observe the resistance offered by the material against deformation when a sudden impact load is happening in the surface of the specimen.

### **3.4 Hardness Test**

The specimen is tested for hardness in Rockwell hardness machine. The hardness of a material is used to resistive force offered by the material toward indentation and the specimen is prepared as per ASTM D4762 standards. It is measured by depth of indentation of the indent. The depth of cut is reduced mean the material is harder and vice versa. The load applied on the indenter is measured in Rockwell hardness number and the result of these observations is explained in brief in the result and discussion chapter. A steel ball indenter was used for checking the hardness of the composite and was 1/16th diameter ball and the maximum load applied toward the specimen was 60 Kgf the specimen used for hardness testing.

Dynamic mechanical analysis (DMA):

Dynamic mechanical analysis of a material is done to identify the viscoelastic properties of a material in more precise and in dynamic condition; ordinary mechanical testing is done in static condition; by here the same testing is done in computer-controlled dynamic environment. The DMA is analyzed under varying temperature and differentiated sinusoidal forced condition. The equipment used for measurement is DMS6100 SII (Inkar) Nanotechnology Japan. The mechanical properties are tested from 200 °C/minute. The temperature ranges from 250 to 1540 °C. And the loading frequency ranges from 0.2 to 0.5 Hz. The measured quantities are storage modulus, loss modulus, and the damping factor. The properties are observed by varying sinusoidal input force involving the variation of frequencies.

Wear test:

Wear test is carried out for understanding the frictional behavior of the material. The equipment used for the measurement of wear of a material is pin-on-disc apparatus. The apparatus is designed as pin and disc that is say the pin is a probe or the material to be measured for wear and the disc is the frictional surface that is meant to be in contact with the material in dry as well as wet condition. The normal load is varied, a sliding friction is set up between the stylus and the disc. Sensors placed in the probe or the stylus measures the frictional values in proportionate with the load applied, speed, lubrication, or environment. The specimen is designated as per ASTM G99 standards.

### 4 Results and Discussion

The tensile test for a composite material is done to understand the elastic property of the material and to identify the applicability of the material toward industry. The composite manufactured is split into four experimental trials. The values of tensile load of each of the experimental trial are inferred from the results. The best sample in this group is found to be the sample with 5% of the filler BaSO<sub>4</sub> and its tensile stress value is 44.56 N/mm<sup>2</sup>. The S7 sample provided best tensile value because the filler mixed with the resin and the hardener improves the surface integrity of the sample that is to tell that the sample reduces the space between the molecules and atom of the resin and hardener. The tensile strength is enhanced by the addition of BaSO<sub>4</sub> due to the appropriate combination of matrix, interlace of woven fiber, filler addition, and interlocking of the fiber arrangement (Fig. 4).

Flexural testing:

Flexural testing of a composite is done to understand the behavior of the material to withstand load or to deflect. Flexural load may be illustrated as point loads acting in a simple supported beam. The flexural testing of specimens is also carried out in experimental trial or groups ad tested for tensile testing. It shows the experimental trial discrepancies of these composites. The sample S4 is made up of A/H/F all the samples in experimental trial-I. Since three fibers are hand laid, the sample has more flexural strength than the remaining samples that are only made of two fiber (Fig. 5).

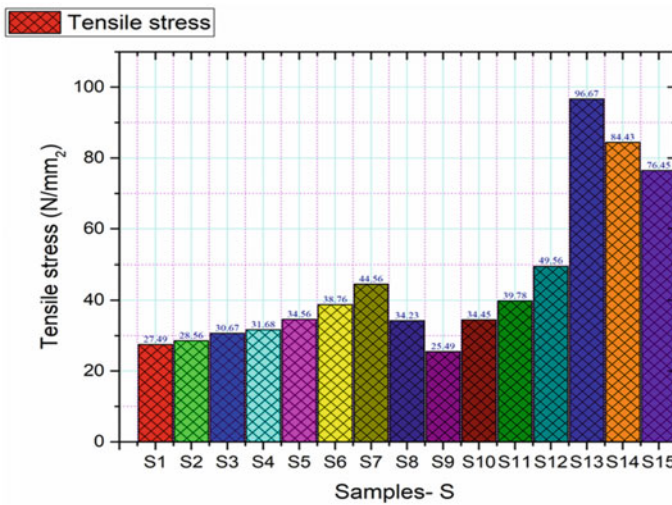


Fig. 4 Tensile stress values of all the samples



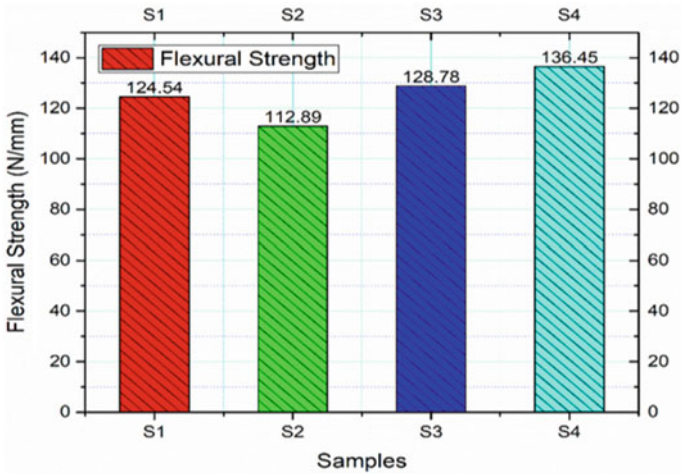


Fig. 5 Flexural value

**Impact Testing**

The impact energy of a material defines the amount of force or energy that the material can withstand during a sudden impact or shock load. As for all the tests, the samples are split into four experimental trials to segment.

The AH composites have more abortion values than most of the other composite’s combination. The toughness values of A/H with filler composite are reduced than flax and hemp composite, this may be owing to the inclusion of filler, and this enhances the toughness values by 32%. Fiber strength, fiber resistivity, and involvement of filler vary the values of wear toughness of the samples in different experimental trials. The woven arrangement of fibers reduces the fiber pull out influence during fracture; this ascendance also involves the weaving distance between the fiber and secondary or tertiary fiber. The involvement of these properties improves the impact toughness.

DMA: DMA for a composite is done for observing the storage modulus (E’), loss modulus (E’'), and damping factor (tan-D) of a composite. The experiment was done by observing the composite in a controlled environment; the apparatus used for this observation involves the supply of heat to observe the change in the values to be measured. Like all the experimentations, the composites are segmented as four experimental trials for easy identification.

**Wear Analysis:**

Wear test for a composite is to understand the frictional stability of the composite; the test is done in a pin-on-disc apparatus. The wear of a material is calculated by the material removal rate. The wear values of the samples are calculated by weight loss rate in volume, more weight removed material.

## 5 Conclusions

These composites were subjected to the characterization of material like mechanical, water absorption, DMA, thermal analysis, wear and AWJM machining. From the obtained results, the following conclusions are made.

- Chemical treatment of fiber improved the tensile property. This treatment eliminates hemicelluloses in fiber, so surface adhesion features of fiber and filler too better quality.
- The BaSO<sub>4</sub> particles enriched the tensile and hardness properties of wire mesh laminate composites and reduced the flexural strength of aloe vera/flax laminate composite. Fillers give more interlocking strength to matrix and fiber.
- The obtained result shows that the mechanical properties of the hybrid composites are mainly influenced by BaSO<sub>4</sub> filler. The effect of filler enhances the tensile strength.
- The physical and woven pattern of the aloe vera, hemp, and flax fiber improved the toughness property. Performance, as those materials only enhances the properties of the materials. Apart from these parameters, flushing pressure of the dielectric fluid plays a role in obtaining the better surface finish.

## References

1. Joseph K, Tolêdo Filho RD, James B, Thomas S, de Carvalho LH (1999) A review on sisal fiber reinforced polymer composites. *Rev Bras Eng Agrícola e Ambient* 3:367–379
2. Venkateshwaran N, ElayaPerumal A, Alavudeen A, Thiruchitrambalam M (2011) Mechanical and water absorption behaviour of banana/sisal reinforced hybrid composites. *Mater Des* 32:4017–4021
3. Balaji A, Karthikeyan B, Swaminathan J, Sundar C (2017) Mechanical behavior of short bagasse fiber reinforced cardanol-formaldehyde composites. *Fiber Polym* 18:1193–1199
4. Almahdi A, Alhwaige A, Ishida H, Qutubuddin S (2020) Chitosan/polybenzoxazine/clay mixed matrix composite aerogels: preparation, physical properties, and water absorbency. *Appl Clay Sci* 184: 105403
5. Alavudeen A, Rajini N, Karthikeyan S, Thiruchitrambalam M, Venkateshwaran N (2015) Mechanical properties of banana/kenaf fiber-reinforced hybrid polyester composites: Effect of woven fabric and random orientation. *Mater Des* 66:246–257
6. Sanjay MR, Yogesha B (2016) Study on water absorption behaviour of jute and kenaf fabric reinforced epoxy composites: hybridization effect of e-glass fabric. *Int J Compos Mater* 6:55–62
7. Navaneethkrishnan G, Karthikeyan T, Selvam V, Saravanan S (2019) Effect of cordia obliqua willd particles on mechanical and fracture toughness of epoxy nanocomposites. *Mater Res Express* 6:115038
8. Sekaran ASJ, Palani Kumar K (2019) Study on drilling of woven sisal and Aloevera natural fiber polymer composite. *Material Today Proc* 16:640–646
9. Charlet K, Jernot JP, Breard J, Gomina M (2010) Scattering of morphological and mechanical properties of flax fibers. *Industrial Crops Product* 32:220–224
10. Sivasaravanan S, Sangeetha M, Prakash S, Dinesh Reddy T, Prabhudev Rahul D (2019) Experimental investigation of composite material laminated with Aloe vera fiber in different composite resin. *Materials Today Proc* 16:832–837

11. Baley C (2002) Analysis of the flax fibers tensile behaviour and analysis of the tensile stiffness increase. *Compos Part A Appl Sci Manuf* 33(7):939–948
12. Sekaran ASJ, Palani Kumar K, Pitchandi K (2015) Evaluation on mechanical properties of woven aloevera and sisal fiber hybrid reinforced epoxy composites. *Bulletin Mater Sci* 38:1183–1193
13. Chaudhary V, Bajpai PK, Maheshwari S (2018) Studies on mechanical and morphological characterization of developed jute/hemp/flax reinforced hybrid composites for structural applications. *J Natural Fiber* 15:80–97
14. Gupta M, Kumar S (2015) Investigation of surface roughness and MRR for turning of UD-GFRP using PCA and Taguchi method. *Eng Sci Technol* 18:70–81
15. Sreenivasan VS, Somasundaram S, Ravindran D, Manikandan V, Narayanasamy R (2011) Microstructural, physico-chemical and mechanical characterisation of *Sansevieria cylindrica* fibers—An exploratory investigation. *Mater Des* 32:453–461
16. Munikenche Gowda T, Naidu ACB, Chhaya R (1999) Some mechanical properties of untreated jute fabric-reinforced polyester composites. *Composite Part A Appl Sci Manuf* 30:277–284
17. Chaitanya S, Singh I (2018) Ecofriendly treatment of aloe vera fiber for PLA based green composites. *Int J Precision Eng Manuf Green Technol* 5:143–150
18. Holbery J, Houston D (2006) Natural-fiber-reinforced polymer composites in automotive applications. *Jom* 58:80–86
19. Palanikumar K, Ramesh M, Hemachandra Reddy K (2016) Experimental investigation on the mechanical properties of green hybrid sisal and glass fiber reinforced polymer composites. *J Nat Fiber* 13:321–331

# Study on the Influence of Auxiliary Mass on Displacement Using Computational Static Analysis



P. Sam Paul, D. S. Shylu, and G. Lawrance

**Abstract** During machining process, tool holder is subjected to vibration, which has considerable influence on productivity and quality of the product. In order to control displacement and provide stability during machining, mass damper was developed in the present investigation. The mass damper used in this paper consists of a specific auxiliary mass attached to the tool shank at a definite location. The size and shape of the auxiliary mass were designed using arithmetic analysis, and the mounting position of the mass on the tool shank was determined using computational analysis. When the auxiliary mass was mounted on the tool holder, the rigidity of the tool holder got enhanced and provides an inherent damping ability to the tool holder for controlling tool vibration. From the computational results, it was observed that the use of auxiliary mass collision on tool holder reduces displacement in cutting tool considerably.

**Keywords** Displacement · Auxiliary mass · Turning tool · Static · Mass damper

## 1 Introduction

In machining process, the existence of vibration in tool holder affects the quality of the product, damages the cutting tool, resulted toward progressive tool wear and irksome noise [1]. Vibration in a cutting tool is a result of interaction between metal cutting process and the dynamics of machine tool which influences the stability of machining system used. This generation of tool displacement can be controlled by enhancing the rigidity of cutting tool which was accomplished by having a damper mechanism. In the past, many researchers attempted the effective implementation of dampers like viscous damper and frictional damper to control vibration in metal

---

P. Sam Paul (✉) · G. Lawrance

Department of Mechanical Engineering, Karunya Institute of Technology and Sciences,  
Coimbatore, India

e-mail: [psam\\_paul@rediffmail.com](mailto:psam_paul@rediffmail.com)

D. S. Shylu

Department of ECE, Karunya Institute of Technology and Sciences, Coimbatore, India

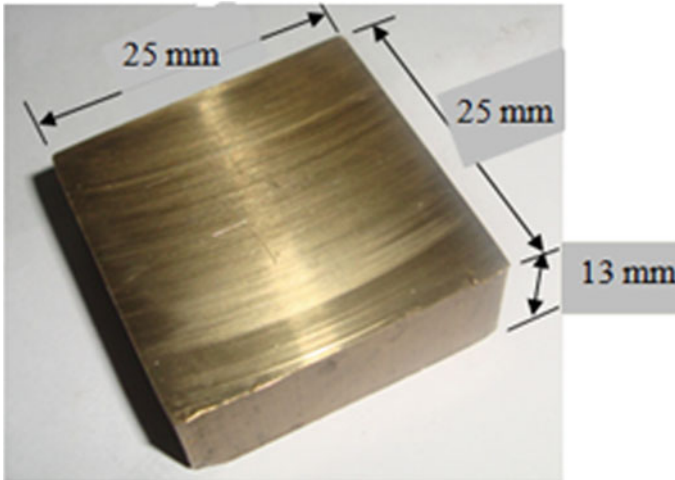
cutting. In machining process, the control of vibration was done effectively through the implementation of viscoelastic dampers [2, 3]. However, it was noticed that the performance of these dampers depends on temperature and it will degrade with wear. In order to overcome this limitation, focus is shifted toward impact dampers, where the working of dampers at high temperature is involved. Also, it is reported that, in metal cutting, tool vibration was controlled effectively by using impact dampers [4]. After much deliberate research, it was concluded that these impact dampers are strong and can operate in situations which are not favourable and suitable for other damping systems [5].

Ema and Maruti [5, 6] developed impact damper which consists of a free mass in the form of a ring and successfully controlled chatter in boring tool. Ramesh and Alwarsamy [7] mentioned that the materials used in impact damper was instrumental in reducing tool vibration and also observed that material with high density controls vibration effectively. Sathish kumar et al. [8] developed particle damper made of copper and lead in powder form and applied the same in boring tool to improve surface finish by 40% and reduced chatter in boring tool. Above-mentioned findings show that the implementation of auxiliary mass collision has proved to be effective for different application. Also, from the literature, it was observed that the concept of auxiliary mass collision damper has not been applied in turning of hardened steel. In the present work, it is planned to develop an auxiliary mass damper and to study the location and effect of auxiliary mass collision on tool vibration in turning tool holder. This work is based on the concept that as the auxiliary mass was attached to the tool holder, there will be mutual collision between them which in turn resulted toward the absorption in the vibrational energy and subsequently decrease in the magnitude of vibration level. The geometric properties of the auxiliary mass were determined using mathematical calculation, and computational static analysis using ANSYS software was performed to arrive at a suitable optimum position for the auxiliary mass on the tool holder so as to attain decrease in tool displacement.

## 2 Design of Auxiliary Mass

An auxiliary mass consists of a concentrated mass of well-defined geometric properties attached to the tool holder and mounted at optimum position. Kun and Vikram through their work suggested that superior damping will be attained provided the mass ratio of the auxiliary mass to the tool shank is 0.1 or greater than 0.1 [10]. The tool holder used here is of 700 g and based on the mass ratio value from literature, the mass of the damper was identified as 70 g. Considering the tool holder size and the complications of mounting the auxiliary mass on the tool holder, the width and the breadth of the auxiliary mass were taken as 25 mm and 25 mm, respectively. As the width of tool holder was found to be 25 mm, any values for the auxiliary mass beyond this will affect the stability of the tool holder.

In this investigation, brass material was used for developing the auxiliary mass and the height of auxiliary mass was estimated as 13 mm which was based on arithmetic



**Fig. 1** Fabricated auxiliary mass

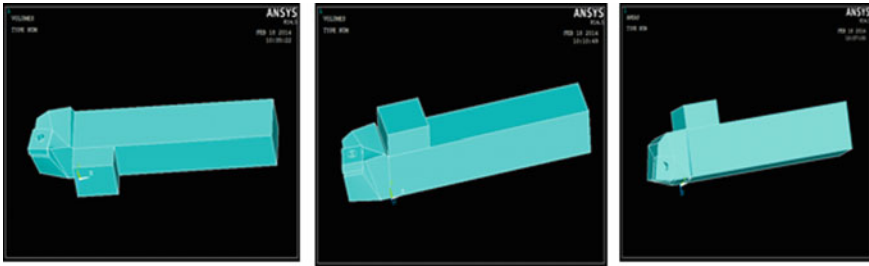
calculation. Even though maximum displacement occurs at the edge of the tool holder, the overhang position for the tool was fixed as 50 mm. This 50 mm was taken by considering the dimension of the work material, contour of the tool holder, geometry constrain of cutting tool, and the ergonomic point of view in handling the tool and work. In order to optimize the optimum position of the auxiliary mass in the tool holder, tool holder assembly along with mass was analyzed using ANSYS software. Figure 1 presents the photograph of the auxiliary mass.

### 2.1 Geometric Model

In this paper, PSBNR 2525 M12 cutting tool and multicoated hard metal inserts having the description of SNMG 120408 MT TT5100, both manufactured by M/s. Taegu Tec was used [9]. Parts connected with this turning tool are tool shank, insert, and shim, and all these parts were modeled in ANSYS software. The material properties detail for tool shank, insert, and shim are stated in Table 1, and the different location of auxiliary mass on tool holder is shown in Fig. 2. Using ANSYS software,

**Table 1** Properties of material for the tool holder and auxiliary mass

Component name	Material	Density (kg/m <sup>3</sup> )	Young's modulus (N/m <sup>2</sup> )	Poisson's ratio
Tool shank and shim	Steel	7850	$2.09 \times 10^{11}$	0.33
Insert	Tungsten carbide	15,800	$5.50 \times 10^{11}$	0.29
Mass	Brass	8450	$0.97 \times 10^{11}$	0.3



**Fig. 2** Geometric model of tool holder with auxiliary mass at different locations

tool holder with auxiliary mass on top, left, and right location was modeled separately. Element used for meshing the geometric model of the tool holder with and without auxiliary mass is 3D Solid 185 element, and this element belongs 8-noded higher-order element family.

## 2.2 Static Analysis

After optimizing the mesh size, the maximum displacement of the tool holder with auxiliary mass placed in three locations of the tool shank, namely on the uppermost position of the tool holder, both the sides of the (left and on the right) tool holder, was determined. Displacement plots obtained using computational analysis were shown in Fig. 3, and the corresponding displacements are shown in Table 2. The maximum displacement obtained for the turning tool with auxiliary mass at different location was compared with turning tool without auxiliary mass. The overhang for the turning tool holder was fixed as 50 mm, and concentrated load of 400 N was applied at the edge of the insert in vertical direction for all the models.

## 3 Results and Discussion

From the computational results shown in Fig. 3 and Table 2, it was found that the tool displacement was reduced, when the auxiliary mass was mounted on the uppermost position of the tool shank. When the tool holder was not supported by auxiliary mass, the maximum deflection was found to be 0.02580 mm whereas the deflection of the tool holder with auxiliary mass mounted on the top of the tool holder was calculated as 0.00733 mm and the auxiliary mass on the right and left was found to be 0.06883 mm and 0.04725 mm, respectively. When the auxiliary mass is attached to the uppermost position of the tool shank, the stability of the tool holder got increased and gathered more strength to withstand higher vertical load. When a vertical load of 400 N was applied at the tool holder edge, tool holder along with auxiliary mass

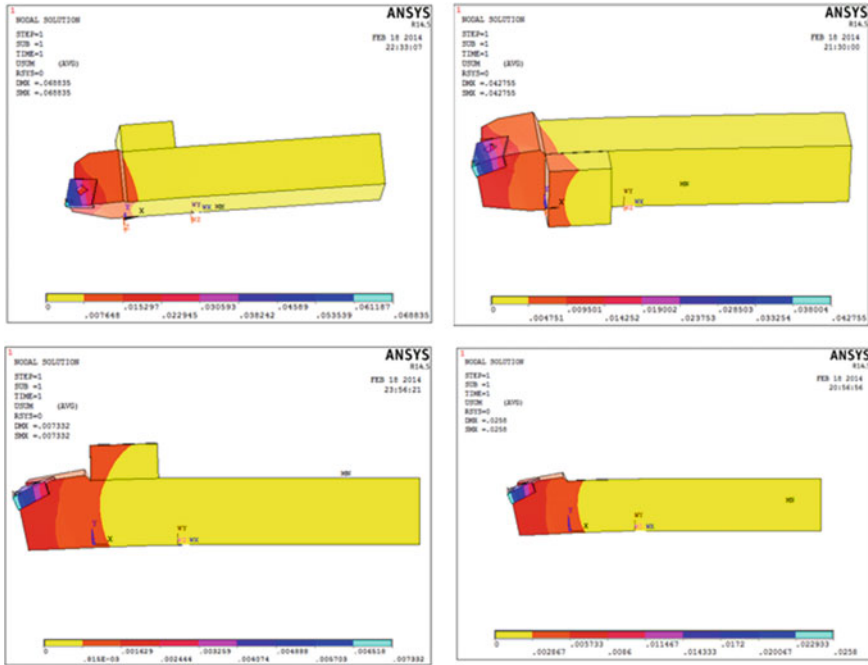


Fig. 3 Displacement plots of tool holder with auxiliary mass at different locations

Table 2 Maximum tool deflection for the auxiliary mass located at different spot

Location of auxiliary mass	Without auxiliary mass	Auxiliary mass on top	Auxiliary mass on right	Auxiliary mass on left
Maximum deflection in the Y-direction (mm)	0.02580	0.00733	0.06883	0.04725

absorbs vibration energy generated by external load thereby subsequently decreasing the vertical deflection. For the auxiliary mass attached to left or right side of the tool holder, it appears that the stability of the tool holder will be altered when a load of 400 N was applied at the edge of the tool shank. This unstable condition will reduce the vibration absorption ability and also reduce the tendency to withstand normal load which leads to marginal rise in deflection. As the deflection increases marginally due to the presence to auxiliary mass at either left or right location of tool holder, auxiliary mass was not located on both sides together. It also appears that when auxiliary mass was mounted at both sides too much load will act at workpiece which will increase the cutting force which will further leads to increase in tool vibration.



## 4 Conclusion

In this paper, auxiliary mass was designed, modeled, and analyzed to study the influence and location of auxiliary mass on the displacement of tool holder. Static analysis was done to identify the optimum location of auxiliary mass on tool shank. Based on the work and the analysis, the following are the inferences:

- (1) Inclusion of auxiliary mass in the turning tool reduces tool vibration effectively.
- (2) For achieving reduction in tool vibration, the auxiliary mass has to be fixed on the uppermost position of the tool shank.
- (3) This auxiliary mass damper is simple to manufacture, tough and can work in situations which are not favorable and suitable for other damping systems.

**Acknowledgements** The authors would like to thank the Department of Mechanical Engineering, Karunya Institute of Technology and Sciences for extending support and help for carrying out this research work.

## References

1. Tobias SA (1965) Machine Tool Vibration. Blackie and sons Ltd., London
2. Sam Paul P, Varadarajan AS (2014) Effect of magnetic field on damping ability of magnetorheological damper during hard turning. *Archives Civil Mech Eng* 14(3):433–443
3. Lawrance G, Sam Paul P, Varadarajan AS, Paul Praveen A, Ajay Vasanth X (2017) Attenuation of vibration in boring tool using spring controlled impact damper. *Int J Interactive Design Manuf* 11:903–915
4. Flint EM (1999) Experimental measurements of particle damping effectiveness under centrifugal loads. In: Proceedings of the fourth national turbine engine high cycle fatigue conference, USAF, Monterey, CA, pp 1–6
5. Ema S, Marui E (1996) Damping Characteristics on an Impact Damper and Its Application. *Int J Mach Tools Manuf* 36(3):293–306
6. Ema S, Marui E (2000) Suppression of chatter vibration of boring tools using impact dampers. *Int J Mach Tools Manuf* 40(8):1141–1156
7. Ramesh and Alwarsamy (2012) Investigation of modal analysis in the stability of boring tool using double impact dampers model development. *European J Sci Res* 80(2):182–190
8. Sathish kumar B, Mohanasundaram KM, Senthil Kumar M (2012) Experimental studies on impact of particle damping on surface roughness of machined components in boring operation. *European J Sci Res* 71(3):327–337
9. Sam Paul P, Varadarajan AS (2012) A multi-sensor fusion model based on an artificial neural network to predict tool wear during hard turning. In: Proceedings of the Institution of Mechanical Engineers, Part B: Journal of Engineering Manufacture, 226(5):853–860
10. Marhadi KS, Kindra VK (2005) Particle impact damping: effect of mass ratio, material and shape. *J Sound Vibration*, 283(1–2):433–448